STRAHL modeling of iron impurity transport with on- and off-axis heating during the first divertor campaign on Wendelstein 7-X

by

Peter Joseph Traverso

A dissertation submitted to the Graduate Faculty of
Auburn University
in partial fulfillment of the
requirements for the Degree of
Doctor of Philosophy

Auburn, Alabama
December 11th, 2021

Keywords: Stellarator, W7-X, Impurity transport, CTH, Plasma

Approved by

David A. Maurer, Chair, Professor of Physics
Sarit Dhar, Andrew T. Hunt Endowed Professor of Physics
Christopher Easley, Professor of Chemistry
Gregory J. Hartwell, Associate Research Professor of Physics
Stuart D. Loch, Professor of Physics
Novimir A. Pablant, Staff Research Physicist at Princeton Plasma Physics Laboratory and
Auburn Affiliate Professor

Abstract

Impurity transport characterization and ultimately impurity control is critical to the future prospects of magnetic confinement fusion energy. In particular for an optimized stellarator like Wendelstein 7-X the characterization of impurity transport is vital for identifying potential advanced scenarios where ideally both screening near the edge and core flushing of impurities can be realized. The experimental characterization of impurity transport in W7-X can be used to validate neoclassical simulations and to compare with turbulent transport predictions. To that end on- to off-axis ECRH scans held at comparable line-integrated densities ($\sim 6 \times 10^{19}\ m^{-2}$) & comparable total input ECRH power were seeded with iron LBO injections in order to investigate the influence of the heating profile on impurity transport. Three total input ECRH power levels (2.8, 3.5, and 4.9 MW), with on- to off-axis variation were measured in the standard magnetic configuration (EJM) in W7-X.

Overall across the entire ECRH on- to off-axis dataset as either more ECRH power is moved off-axis or less total ECRH power is deposited both the $\frac{T_i}{T_e}$ and the τ_I increases. As ECRH was moved off-axis there was an increase in the $\frac{T_i}{T_e}$ ratio for $\rho \leq 0.6$ due to the strong electron temperature variation in the core, $\rho \leq 0.4$, with changes of as much as ~ 1.5 keV. This strong core electron temperature flattening had a marginal effect on the observed iron impurity transport time with τ_I enhanced by at most 27% as core T$_e$ was decreased. On the other hand even though the purely on-axis ECRH power scan from 4.9 to 2.8 MW reduced the core T$_e$ a nearly identical amount as the 4.9 MW on- to off-axis dataset, the resulting global transport time enhancement was substantially larger for the on-axis power scan. The combination of the similar ~ 900 eV drop in core T$_e$ during the 4.9 MW on- to off-axis dataset, the larger enhancement in the global transport time for the on-axis power scan, and the significant variation in the $\frac{T_i}{T_e}$ ratio outside $\rho \geq 0.6$ for the on-axis power scan all indicate that the kinetic profiles' magnitude/shape outside mid-radius has a greater impact on the observed iron impurity transport than core T$_e$ variations.

To better characterize these observational results a least squares minimization was performed to infer the anomalous transport profiles that most accurately produces the measured iron line emission using the transport code STRAHL. These experimentally observed iron spectral signals could only be well-matched when the anomalous diffusion channel was included within the least squares inference with this transport channel clearly dominating all other channels. The fact that an ordinary, charge-independent anomalous diffusion was necessary to match the iron line emission in combination with the dominance of the anomalous diffusive channel strongly suggests that turbulent transport is the main transport mechanism during these W7-X plasma discharges in accordance with gyrokinetic simulations performed by [García-Regaña et al. 1]. Although the inferred anomalous diffusion profiles are still consistent with the concomitant increase of global transport time (τ_I) and the ion-to-electron temperature ratio ($\frac{T_i}{T_e}$), the inferred profiles are only distinguishable in the on-axis ECRH power comparison when the total uncertainties are considered.

Finally to give confidence to the aforementioned inferred anomalous diffusion profiles numerous sensitivity studies were performed on the least squares minimization routine using both synthetic and experimentally derived data. The synthetic sensitivity tests demonstrated that for the inferred anomalous diffusion profile the 1-sigma T_e profile shifts had minimal impact on the inferred accuracy, the LBO injection timing & temporal shape had the largest influences on the profile accuracy, and the STRAHL edge parameterization also induced a large variation. These results from the synthetic sensitivity tests used to determine the accuracy of the least squares fits and to estimate the uncertainty in the anomalous diffusion profile were corroborated by the variational tests performed on experimental data.

Acknowledgments

I am grateful for the guidance and patience provided by my advisor Prof. David Maurer as he helped me navigate through two different thesis projects. His experience and feedback on the many research projects has been invaluable to my development as a scientist. I would also like to extend my deep gratitude to Dr. Novimir Pablant whose support was not only instrumental in making the research collaboration with the W7-X team much easier, but also provided comments and insights that have made the work presented in this thesis much better. I am thankful to Prof. Greg Hartwell for the discussions on diagnostic design and the time spent training me as a CTH operator.

In my long journey of graduate school at Auburn, I am thankful for the support from the physics office staff, the CTH group, and my fellow graduate students. Jennifer Morris, Freddie Killian, Mary Prater, and Glenda Stroud all made the physics department feel like family in addition to making my job much easier. Whether it was class enrollments, package deliveries, equipment orders, or travel reimbursements they made it seamless. I am thankful for the guidance provided by former CTHers Jeffery Herfindal, Mihir Pandya, and Xinxing Ma including the many hours shared in the control room. I am also appreciative of the many fruitful discussions with fellow CThers and officemates Curtis Johnson and Nicholas Allen. Although I have made many friends throughout graduate school, I would like to particularly thank my fellow cohort members for making the process much more enjoyable: Spencer LeBlanc, Chunkun Jiao, Dylan Reedy, Nicole Engleman, Ye li, Cory Nook, Burcu Ozden, and Yongju Zheng.

I am most thankful for my parents Timothy & Marilyn Traverso for their constant love and support throughout my life, encouraging me to always strive for excellence. My parents established an environment where my older siblings and I could be pursue our passions. I am extremely proud and grateful to my siblings Matthew, Carrie, and Andrew for continually setting the bar high and keeping me humble. Finally I would like to my friends Anthony

Yim, Seth Davidovits, Dragos Velicanu, Margaret Wang, Joseph Youssef, and David Xia for willingly being uncomfortable on hiking trips across the world.

Table of Contents

List of Figures

List of Tables

Chapter 1

Introduction

This chapter is structured first to cover the basics of fusion energy going into the challenges and giving context on the difficulty of achieving practical fusion energy on earth. Next a brief overview on magnetic confinement is presented as an introduction to the Wendelstein 7-X (W7-X) experiment where all of the iron impurity transport experiments were performed. After the introduction of W7-X as an optimized stellarator there is a discussion on the basics of particle transport theory. The particle transport discussion is meant to provide an overview of the transport types and relevant regimes pertinent for iron impurity transport in an optimized stellarator like Wendelstein 7-X. The particle transport definitions and their importance to the iron impurity transport studies performed for this thesis will be discussed. Finally the specific iron impurity transport studies with on- to off-axis Electron Cyclotron Resonant Heating (ECRH) scans are presented and given context as to why these studies are relevant in a neoclassically optimized stellarator like W7-X.

1.1 Fusion energy and magnetic confinement

- The difficulties of achieving a sustained fusion reaction can be estimated by the Lawson criterion where a high density (10^{20} m^{-3}), high temperature (10 keV), and long confinement time (1 sec) are necessary. In particular a 10 keV temperature indicates that a reactor relevant device would need good confinement for a one second translating into a distance traveled of $\sim$ 620 miles underscoring the difficulty of fusion-grade plasma confinement.

- A purely toroidal magnetic field will not confine a hot plasma and therefore a magnetic field in the poloidal direction is necessary to give the resultant magnetic field lines helical paths around the torus. This "twistedness" can on average nullify the deleterious effects of the drifts induced from the toroidal magnetic geometry

Creating energy in a safe yet reliable way has been the impetus for developing both fission and fusion reactors since the discovery of the nuclear force in the mid 1930s. The rapid success of the research and development of the fission process is remarkable and unprecedented in modern science. In a little over ten years scientists went from first discovery of the neutron as a subatomic particle to the development of the first fission reactor, the Chicago Pile 1, in 1942 by Enrico Fermi. The reason so much effort was put into the research into nuclear physics was that scientists recognized the amazing energy density stored in nuclear matter. In fact to give some perspective on the enormity of the energy density a quick calculation of how much fuel (in grams) is equivalent to one barrel of oil (42 gallons) can be preformed, where it is important to note that one barrel of oil is equivalent to 6×10^9 Joules. For a typical fusion reaction of deuterium and tritium, as shown in equation (1.1), only 0.018 grams of fuel (^2D and ^3T) is necessary to produce the equivalent energy of a single barrel of oil.

$$^2D + {}^3T \longrightarrow \alpha + n \tag{1.1}$$

For both fission and fusion that's six order of magnitudes less fuel (by mass) to produce the same amount of energy. From these simple calculations, we can start to see that the potential for utilizing the energy stored in an atom is enormous and why scientists would be interested in utilizing a fusion process like the one shown in (1.1) for energy production.

After understanding the huge potential energy density offered by fusion, the question becomes why has a fusion power plant not already been built, especially considering the fast development of fission reactors. To motivate the difficulty of achieving an energy-generating sustainable fusion process, even a quick examination of the necessary parameters for fusion to occur can reveal the depth of the challenge. The first aspect to note is that although there is a huge amount of energy stored in the nucleus, the strong nuclear force holding the nucleus together only generates meaningful amounts of force at extremely short distances. In fact the attractive nuclear force's distance which it can start to overcome the coulomb repulsive force is $\sim 3 \times 10^{-15}$ or roughly 3 femtometers. Meaning for two protons to fuse a simple estimation of the energy necessary to overcome the coulomb repulsive force is shown in the equation (1.2).

$$V_r - V_\infty = \int_\infty^r \frac{Z^2 e^2}{4\pi\epsilon_0 r^2} dr \qquad V_r \approx 7.7 \times 10^{-14} J \quad or \quad 4.8 \times 10^5 eV \tag{1.2}$$

A more intuitive way of understanding this huge amount of energy necessary to achieve fusion between two protons is to convert this into a temperature: $480\, keV$ is equivalent to $5.5 \times 10^9 K$ or ~ 5 billion degrees. Thankfully due to quantum tunneling two ions (e.g. two protons) can fuse at much lower temperatures and in fact most proposed fusion reactor designs have temperatures at $\sim 10\, keV$. However even at this lower temperature, the ions will still need to be heated to ~ 100 million degrees. At these temperatures all particles will be ionized leaving a fluid of electrons and positive ions that generally form the fourth state of matter called a plasma.[a] To achieve these extremely high temperatures requires very high power heating sources and the plasma itself can make this task more complicated due to the potential for fluid velocity differences leading to currents & self-perturbing magnetic fields which can disturb the confinement. Therefore the challenge is not only achieving the high energies needed for fusing two ions together, but also the nontrivial method of sustainably heating those particles up to the necessary temperatures.

Unfortunately the basic challenges of achieving viable fusion do not stop there and to understand another aspect of the challenge the collision between energetic ions should be revisited. An important consideration is the cross section for a nuclear reaction to occur since energetic ions, even if they have the adequate energies for fusion, will never fuse if they don't collide. In our simple model for calculating the necessary temperature to achieve fusion we made the inherent assumption that the ions had the exact velocities to be on a collision course. To examine a more realistic case we must relax this assumption and take into account that there is a finite area (i.e. cross section) for a fusion reaction to occur. In the classical model, where

[a]To be precise, a plasma has to have a critical number density and have collective behavior otherwise it is just an ionized gas.

the ions are modeled as hard spheres, we can actually use the known diameter of an ion to calculate this cross section. Based purely on flux arguments a probability per path length can be derived and leveraged into a basic estimate of the necessary ion density to achieve a realistic fusion power density.[b] Using the specifications for a typical proposed fusion reactor, 2000 MW with a plasma volume of 400 m^3, the necessary fusion power density is roughly $\approx 5 \times 10^6 \frac{W}{m^3}$.

$$Fusion\ \ power\ \ density = E n_i^2 \sigma v \tag{1.3}$$

Then using the energy per ^2D & ^3T fusion event ($E \approx 2 \times 10^{-12} J$), the fusion event cross section ($\sigma \approx 1 \times 10^{-28} m^2$), and the ion velocity at fusion relevant temperatures ($v \approx 1 \times 10^6 \frac{m}{s}$) the resultant ion density required is shown through equation (1.3) to be $n_i \approx 1.5 \times 10^{20}$. Converting this into a pressure roughly results in $P \approx 2.4 \times 10^5 Pa$ where standard air pressure at sea level is $1.01 \times 10^5 Pa$. At face value this magnitude with over double air pressure at sea level doesn't seem extraordinarily large, until the realization that this ion pressure level needs to be maintained at extraordinary particle energies. In fact such a density of high-temperature plasma begins to show why confinement is so important since even small amounts of flux to the reactor walls have the potential to quickly disperse the plasma and even melt the walls. Therefore for any serious sustainable fusion process a high density of particles is necessary to get enough fusion reactions per unit volume and this density needs to be maintained over time for any hope of an operational fusion reactor.

In addition to the already outlined high density and high temperature challenges for a fusion reactor, a third major difficulty arises from the confinement necessary for these highly energetic particles to fuse. A rough estimate for what the confinement time can be estimated by using the probability per path length, the ion's thermal velocity, and the general size of a proposed reactor ($R = 5$ m). The first step is to utilize $Probability\ per\ path\ length = \sigma n_i \approx 1.5 \times 10^{-8} m^{-1}$ to estimate the necessary distance the particle must travel to have any significant probability for a fusion event, where anything $\geq 1\%$ is considered significant.[c] Therefore the

[b] Note that the probability per path length is the inverse of the mean free path, which is defined as the average distance traveled before a collision occurs.

[c] See footnote b.

ions must travel $\sim 10^6$ meters to yield any significant probability of undergoing a fusion event, which for a toroidal reactor with major radius of 5 m corresponds to $\sim$ 32,000 orbits around the torus. With these parameters the time an ion needs to be confined for a $\sim 1.5\%$ probability of a fusion event to occur can be estimated, $time \approx \frac{10^6 m}{10^6 \frac{m}{s}} = 1$ second. From the shear distance that the particle needs to be confined ($\sim$ 620 miles) to have a small (but finite) chance of fusing, the difficulty of confinement is made quite clear. Even in the more feasible toroidal reactor, the hot ions need to make over 30,000 orbits without hitting the wall of the chamber and without its density dropping.

Therefore creating an energy-generating sustainable fusion reactor has a multitude of difficulties to over-come before the fusion reactor can become a reality. More specifically the deuterium tritium fuel must be superheated to achieve the high temperatures and the high densities necessary all the while keeping the formed plasma in a contained equilibrium. Thus the problems of building a fusion reactor stem from three main aspects: temperature, density, and confinement. This is most famously detailed in Lawson's criterion, which is just the product of density (n) and energy confinement (τ_E).[11]

$$Lawson\ \ criterion = n\tau = \frac{12k_bT}{\langle\sigma v\rangle\epsilon_\alpha - 4c_1 Z_{eff}\left(k_bT\right)^{0.5}} \tag{1.4}$$

This equation is important because it is a special form of the ignition condition which tells us the values of density, confinement time, and temperature necessary for a more realistic fusion process to occur. More specifically the ignition condition is really an equation describing the power balance of α particle heating with energy losses stemming from thermal conduction and Bremsstrahlung, the emission of radiation as the particles are accelerated/decelerated during their orbits. In fact these parts can still be seen in the Lawson criterion where $4c_1 Z_{eff}\left(k_bT\right)^{0.5}$ is the term associated with the energy loss of the plasma due to Bremsstrahlung, $\langle\sigma v\rangle\epsilon_\alpha$ is the term associated with the energy from the alpha particles, and $12k_bT$ is the term associated with the internal energy of the plasma that is lost over a confinement time. Therefore the Lawson criterion is an important measuring stick to evaluate the more realistic values of density, confinement time, and temperature to achieve a self-sustaining fusion process (i.e. ignition), which for a ^2D & ^3T fusion process requires a triple product of $(n\tau T) \geq 3.5 \times 10^{21} \frac{s\,keV}{m^3}$. This is very useful for a first order approximation of the conditions necessary to achieve fusion. For example, with T =15 keV and τ = 1 sec a density of n_i = 2.3 $\times 10^{20} m^{-3}$ to achieve fusion. From the Lawson criterion it is evident that the long confinement times necessary for a fusion reactor is most likely the hardest to achieve since doubling the confinement time means our density just decreases by half, but is still in the $\times 10^{20} m^{-3}$ range.[d] This partially explains why properly containing & sustaining fusion reactions in a hot plasma is extremely difficult since it necessitates the simultaneous creation of high temperatures & high densities in a plasma required to keep the hot ions within its bulk for at least one second.

In general there are many different methods and types of devices that have been developed for fusion energy, but historically magnetic confinement fusion has received the majority of development and research causing it to be the leading method for achieving fusion energy. The basic idea of magnetic confinement is to leverage a sufficiently strong magnetic field to control the ionized particle orbits via the lorentz force, $\vec{F} = q\left(E + \vec{v} \times \vec{B}\right)$. This immediately creates an anisotropy for the plasma with directions parallel and perpendicular to the magnetic field experiencing very different particle motion. As will be discussed in section 1.2.1, in a straight field geometry this leads to classical transport due to Coulomb collisions, but in the absence of Coulomb collisions between different plasma species leads to no net particle losses perpendicular to the magnetic field. In a straight magnetic field particles can free-stream parallel to this field meaning they would easily escape any finite plasma.[e] Therefore to prevent these end-losses the magnetic field can be wrapped in on itself to form a torus. As shown in figure 1.1 the toroidal direction (ϕ) corresponds to the long way around the torus, while the poloidal direction (θ) corresponds to the short way around the torus. Although this torodial structure is the most common shape for magnetic confinement devices, a pure toroidal magnetic field does not provide adequate confinement. The reason a purely circular magnetic field has poor confining properties is due to the fact that bending the magnetic field into a finite torus

[d]It is important to remember the nuclear physics requires the temperature to stay at least $\geq$ 10 keV for the ions to have enough energy and slight enough probability of fusing

[e]Remember that at fusion relevant temperatures a cylindrical plasma would need to be $\sim$ 620 miles long to contain a particle for one second.

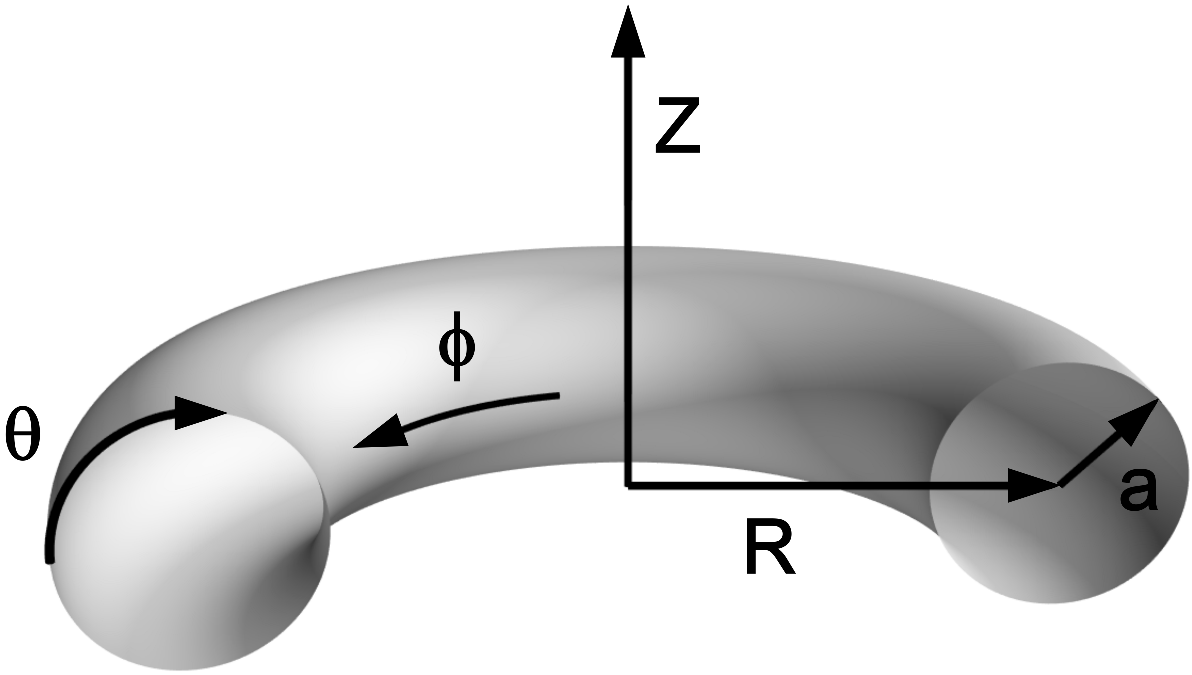

Figure 1.1: An example of the toroidal geometry used for plasma confinement with the key directions and parameters labeled. The major radius (R), minor radius (a), the toroidal direction (ϕ), the poloidal direction (θ), and the vertical direction (Z) are all labeled in the schematic.

introduces forces on the plasma and the electrons & ions in the plasma can respond to these forces in opposite directions. Specifically the bending of a magnetic field into a finite torus causes a gradient in the magnetic field strength due to the field lines being more densely packed on the in-board side of torus. These two forces, i.e. the gradient (∇B) and the curvature (R_C) in the magnetic field, give rise to plasma drifts that are charge-dependent as shown in equation (1.5) with both forces leading to particles drifting in the vertical direction (i.e. $\pm\hat{z}$) as depicted in figure 1.1. The charge-dependence in these drifts mean the ions & electrons drift in opposite directions quickly allowing an electric field to self-generate creating the outward radial flux of the plasma via $\vec{E} \times \vec{B}$ drift.

$$v_{\nabla B} = \frac{mv_\perp^2}{2qB}\frac{\vec{B} \times \nabla B}{B^2} \qquad\qquad v_{R_C} = \frac{mv_\parallel^2}{qB}\frac{\vec{R_C} \times \vec{B}}{R_C^2 B^2} \tag{1.5}$$

In order to restore confinement, a magnetic field in the poloidal direction (see figure 1.1) needs to be added to the existing toroidal field. The resultant field lines trace out helical paths around the torus and critically can on average nullify the deleterious effects from these drifts.

This ”twistedness” of the magnetic field lines is referred to as the rotational transform or to the lowest order approximation the pitch angle of the magnetic field. Formally the rotational transform is defined as $\iota\!\!\!- = \frac{d\psi}{d\phi}$ where ψ is the poloidal magnetic flux and ϕ is the toroidal magnetic flux, but can be expressed in a more intuitive form as simply the number of poloidal transits (n) per the number of toroidal transits (m) as shown in equation (1.6).

$$\iota\!\!\!- = \frac{n}{m} \tag{1.6}$$

These helical field lines fall into three classes of trajectories: rational, erdogic, and stochastic If the ratio of transits can be expressed with integers (i.e. a rational number), then this field line will close on itself after a finite number of toroidal circuits leading to a rational surface. An ergodic trajectory is characterized by a field line making an infinite number of toroidal circuits without closing on itself, but importantly returns arbitrarily close to itself. These ergodic trajectories generate a surface with constant $\iota\!\!\!-$ and give rise to the nested magnetic flux surfaces needed for good confinement. The final class of trajectories are stochastic field lines that do not remain on a surface, but rather fill an entire volume.

1.1.1 Tokamaks and stellarators

- A tokamak utilizes the plasma as a second winding of a transformer to drive a toroidal plasma current in order to create the necessary poloidal field for good confinement, while the stellarator only utilizes external field coils to produce both the toroidal and poloidal fields necessary for good confinement.

- Unlike the axisymmetry of a tokamak that guarantees the existence of flux surfaces necessary for good confinement, the stellarator has to have its magnetic geometry designed carefully to ensure the existence of flux surfaces. Moreover stellarators with an inherently 3D magnetic field can give rise to helically trapped particles that can lead to uncompensated radial outward drifts and rapid loses due to these helically trapped particles being poloidally localized.

- Despite the challenge of designing and building a stellarator given its 3D nature, the inherent steady-state operation using only external field coils and the ability to optimize the field for desired plasma properties make it an intriguing future option for a fusion reactor. In fact the Wendelstein 7-X experiment as a quasi-isodynamically optimized stellarator was built to test and verify the design criterion.

Within toroidal magnetic confining devices there are two main methods to generate the poloidal field necessary for nested flux surfaces and good confinement: a driven toroidal current in the plasma or external field coils. The tokamak follows the first method with a toroidal field generated from equally-spaced planar coils and a poloidal field produced using the plasma as a secondary winding to an inductor and ohmically-driving a toroidal plasma current. This type of device is inherently axisymmetric meaning that the magnetic flux surfaces are identical at every toroidal angle allowing it to have very good confining properties with the first order drifts naturally averaging out. However since a tokamak relies on the plasma response to an induced loop-voltage, the tokamak operation is both intrinsically non-steady state and vulnerable to current-driven instabilities.[f] The stellarator utilizes the second method relying solely on external field coils to produce both poloidal and toroidal fields. Unlike the tokamak, the stellarator is inherently steady-state by eliminating the need to drive an internal plasma current to generate good, nested flux surfaces. In addition to the steady-state operation, the stellarator is less likely to experience major losses of plasma confinement that can occur in tokamaks from instabilities associated with the need to drive current in the plasma. However the current-driven instability avoidance and steady-state characteristics of stellarators come at the cost of a complicated 3D magnetic configuration with both nonplanar coils and non-axisymmetric plasmas. This 3D complexity is compounded by the fact that there is no guarantee for the existence of flux surfaces and even with the presence of nested flux surfaces no guarantee for good confining properties.[2]

[f] There are non-inductive methods to drive the plasma current necessary for plasma confinement in a tokamak (e.g. electron cyclotron current drive)

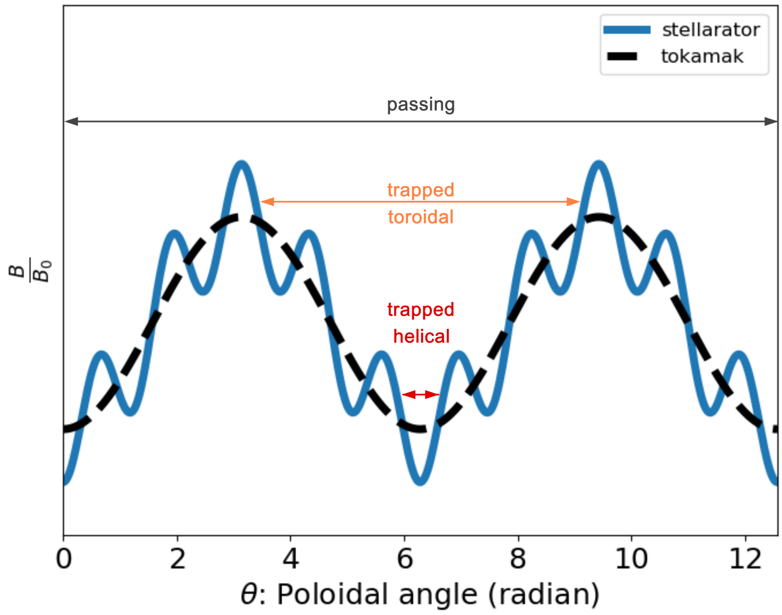

Figure 1.2: A schematic showing the normalized magnetic field strength ($\frac{B}{B_0}$) for a magnetic field line making two poloidal rotations with the common types of particle trajectories labeled.

Understanding why a stellarator's non-axisymmetry doesn't guarantee good confinement properties regardless of magnetic field strength can be explained by examining particle orbits in both these 3D magnetic fields and a tokamak's axisymetric fields.[12,13] In figure 1.2 is a schematic of the normalized magnetic field strength of a single magnetic field line as it makes two poloidal transits (i.e. 4π radians) for both a typical tokamak (dashed black line) and stellarator (solid blue line). Depending on the distribution of the velocity parallel and perpendicular to the magnetic field a particle will fall broadly into two types of particle orbits: passing or trapped. Within the trapped particle trajectories there are two separate subtypes where the particles get mirror-trapped in either a toroidal or helical ripple along a field line as labeled in the figure 1.2. Notice that the representative field line for a tokamak doesn't have the helical magnetic wells that are present in stellarators due to a tokamak's axisymmetry and that the toroidal modulation in field strength is a consequence of the toroidal field being inversely proportional to major radius (i.e. $B \propto \frac{1}{R}$).[g] Therefore a particle trapped in a toroidal ripple will traverse poloidal angles corresponding to positions above and below the magnetic axis

[g]Tokamak's do have small helical-like wells due to the finite number of toroidal field coils introducing a slight modification in the magnetic field strength along a field line.

(see figure 1.1 showing that the outboard mid-plane is the location for $\theta = 0$). Critically this means the toroidal ripple trapped particles experience a constant vertical drift off a flux surface when above the magnetic axis that is offset by the same vertical drift back onto the original flux surface when their orbits are below the magnetic axis. The axisymmetry of a tokamak allows for the exact cancellation of the vertical drift, effectively guaranteeing good confinement properties even for collisionless trajectories. For the non-axisymmetric flux surfaces found in stellarators an additional type of magnetic mirror trapped particle trajectory can occur with the helical modulation in the field strength as shown in figure 1.2. These helically trapped particles lead to an uncompensated radial outward flux due to their orbits being poloidally localized where they will experience a unidirectional vertical drift off their current flux surface. This type of trapped trajectory can lead to rapid losses for stellarators. Moreover these collisionless losses become worse at fusion relevant temperatures, meaning the stellarator has a much harder challenge than tokamak in controlling these neoclassical transport losses.[h]

Nevertheless a stellarator's inherent steady-state operation using only external field coils to generate the confining magnetic surfaces is a distinct advantage over the tokamak design. Furthermore modern engineering capabilities, both in modeling and construction, have enabled the magnetic geometry to be tailored for specific symmetry conditions without compromising on the desired plasma parameters. In fact all modern stellarators are designed to have their magnetic flux surfaces with a symmetry property that the magnetic field at (R, ϕ, Z) and at $(R, -\phi, -Z)$ are equivalent where R is the major radius, ϕ is the toroidal angle and Z is the vertical displacement.[14,15] This so-called "stellarator symmetry" indicates that a poloidal slice of the flux surfaces at ϕ have a vertical mirror symmetry with a corresponding polodial slice of those located at $-\phi$. In addition to this stellarator symmetry property, advanced stellarators are designed with a quasi-symmetry to reduce the large neoclassical transport present at low collisionality (i.e. at high temperatures) stemming from the previously mentioned unfavorable helically trapped particles.[i] A quasi-symmetric design aims to create magnetic surfaces with the magnetic field geometry having the property where there is approximately an ignorable

[h] See section 1.2.1 for a definition and discussion on neoclassical transport

[i] [Helander et al. 16] has a very informative discussion on 3D field confinement and optimization.

coordinate as shown in equation (1.7).[17]

$$\vec{B}\left(\psi,\tilde{\theta},\tilde{\phi}\right) \Longrightarrow \begin{cases} \vec{B}\left(\psi,\tilde{\theta}\right) & \text{quasi-axisymmetry (similar to a tokamak)} \\ \vec{B}\left(\psi,\tilde{\phi}\right) & \text{quasi-poloidal symmetry} \\ \vec{B}\left(\psi,\tilde{\theta}-M\tilde{\phi}\right) & \text{quasihelical symmetry} \end{cases} \tag{1.7}$$

The coordinates in equation (1.7) are in magnetic flux coordinates where ψ is a radial-like coordinate derived from the toroidal flux, while $\tilde{\theta}$ and $\tilde{\phi}$ are generalized angular coordinates representing the poloidal and toroidal directions respectively.[18] There is another type of optimization called quasi-isodynamicity, which isn't symmetric even in magnetic coordinates, that instead makes the second adiabatic invariant along a magnetic field line constant on a magnetic flux surface and makes the constant magnetic field contours close poloidally.[19,20] The quasi-isodynamic optimization is particularly relevant since this is the approach taken by the Wendelstein 7-X experiment on which the impurity transport studies presented in this thesis were performed. In the next two subsections the Compact Toroidal Hybrid and the advanced stellarator Wendelstein 7-X will be introduced.

1.1.2 Wendelstein 7-X (W7-X)

- Wendelstein 7-X is a drift-optimized stellarator built to demonstrate and study a magnetic field optimization approach capable of supporting reactor-relevant plasma parameters.

Wendelstein 7-X is a large, superconducting quasi-isodynamically optimized stellarator built to demonstrate and study a magnetic field optimization capable of supporting reactor-relevant plasma parameters.[21,19,22] In particular the high-level goals of the W7-X experiment are to achieve long discharges with plasmas held at equilibrium, high plasma density & temperatures, density profile control, feasible steady-state divertor performance for both heat-loads & radiated power, and prevention of core impurity accumulation.[23] In order to achieve these high-level priorities, W7-X was designed with modular coils for flexible magnetic configuration control enabling the initial confirmation of the W7-X optimization.[24] The W7-X design with key parameters listed in table 1.1 has a high aspect ratio ($\frac{R}{a} \approx 11$) and a five-field period

Parameter	Dimension
Major radius (R_0)	5.5 m
Average plasma minor radius (a_0)	0.5 m
Toroidally averaged B-field along the magnetic axis (B_0)	2.5 T
Input ECRH heating*	$\leq$ 8.5 MW
Input NBI heating*	$\leq$ 3.5 MW
Central density* (n_e)	$\leq 1.5 \times 10^{20}\,\mathrm{m}^{-3}$
Electron temperature* (T_e)	$\leq$ 10 keV
Ion temperature* (T_i)	$\leq$ 3.5 keV
Discharge length*	$\leq$ 10 s

Table 1.1: W7-X key parameters with * indicating the representative values from the first divertor campaign (OP1.2 a&b) (see [Pedersen et al. 8] & [Klinger et al. 9] for more details)

symmetry with each period composed of ten non-planar and four planar superconducting coils.[j] The five-fold symmetry, similar to the CTH experiment, can be seen in figure 1.3 illustrating the W7-X nested flux surfaces for the standard magnetic configuration with the shaded color corresponding to the magnetic field strength ($|B|$) and the gray lines representing field lines that make up the surfaces.[k]

As briefly mentioned W7-X is a quasi-isodynamically optimized stellarator and to better understand this type of neoclassical optimization an examination of the mirror-trapped particle trajectories along a magnetic field line is useful. In figure 1.4 the CTH and W7-X normalized $|B|$ are plotted for a field line on the flux surface at $\rho = 0.5$ for two complete poloidal transits just like the schematic from figure 1.2. Notice that in the unoptimized CTH case the helical wells are not only much deeper (i.e. $\sim 30\%$ $|B|$ modification), but also they are poloidally localized at $\theta \approx 0, 2\pi$ which correspond to regions of bad-curvature where the $\vec{R_C}$ points in the opposite direction of the pressure gradient making the fluid Rayleigh–Taylor unstable increasing outward transport. On the otherhand the W7-X case shown in figure 1.4b has the exact opposite properties with overall shallower helical wells and with the proportionally deeper wells localized in regions of good-curvature. Understanding the W7-X drift-optimization goes beyond examining the normalized $|B|$ along a field line since a quasi-isodynamic optimization aims to create trapped particle trajectories that form nearly poloidally-closed drift orbits.[19,25]

[j]Each field period was composed of two sets of the five types of non-planar and two types of planar coils.

[k]For more information on the W7-X magnetic configurations and their effects see [Dinklage et al. 24]. All of the experimental data shown in this thesis will be performed in the standard magnetic configuration.

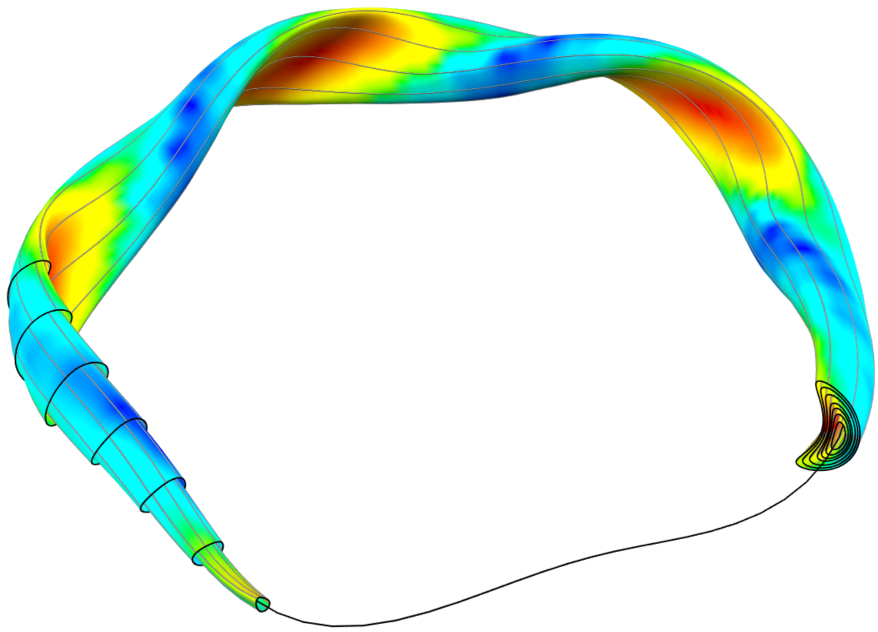

Figure 1.3: The magnetic field lines in gray are displayed on the nested flux surfaces of W7-X in standard magnetic configuration with the color indicating the normalized strength of the magnetic field with red corresponding to higher levels of $\langle |B| \rangle$.

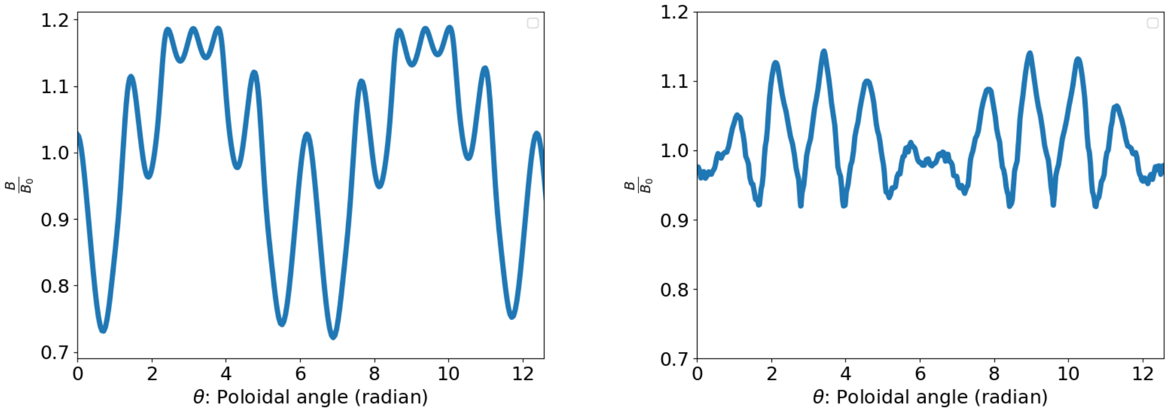

(a) (b)

Figure 1.4: The normalized magnetic field strength ($\frac{B}{B_0}$) is shown for a magnetic field line making two poloidal rotations on the $\rho = 0.5$ surface in CTH during an ohmic discharge (a) and in W7-X for the standard magnetic configuration (b)

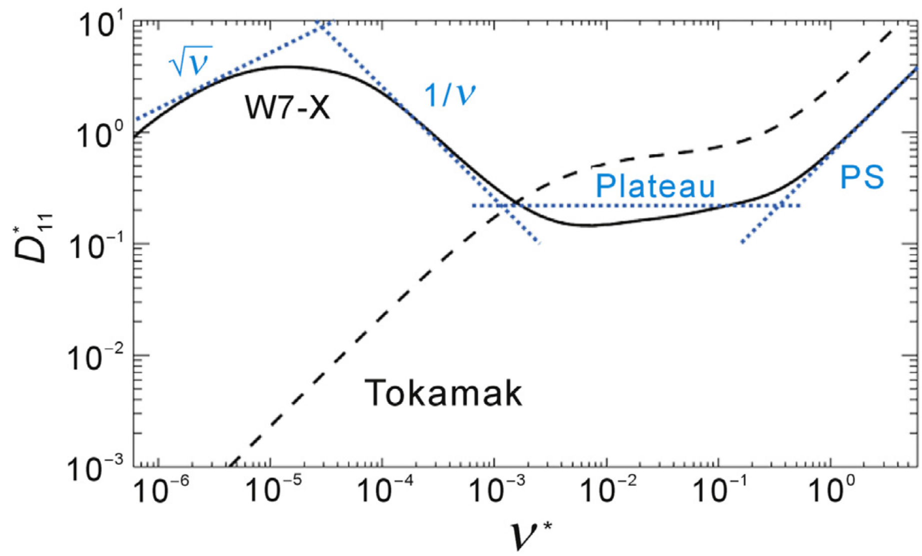

Figure 1.5: Figure taken from [Helander et al. 2] depicting the neoclassical transport coefficient D^*_{11} as a function of normalized collisionality ($\nu^* = \frac{\nu R}{\iota v}$) for W7-X and a tokamak

These nearly poloidally-closed drift orbits mean that trapped particles will precess poloidally during their bounce-orbits with minimal radial excursions off the flux surface due to the small variation poloidally in the minimum-B. This effect is more pronounced at higher plasma pressures and with a magnetic configuration producing a stronger toroidal mirror, the aptly name W7-X high-mirror configuration.[26,27]

As a result of the neoclassical optimization W7-X has favorable transport properties in the high-performance regimes (i.e. the $\sqrt{\nu}$ and $\frac{1}{\nu}$ regimes corresponding to high temperatures & low-collisionalities) as shown in figure 1.5 with the neoclassical diffusion coefficient as a function of normalized collisionality.[2] Therefore it is imperative to characterize the impurity transport properties in an optimized stellarator like W7-X to not only increase the understanding of the cross-field transport physics, but also to make progress toward achieving one of the high-level goals of preventing impurity accumulation in the plasma core.

1.2 Impurity transport basics

1.2.1 Classical & neoclassical transport

- In a toroidal magnetic field geometry the collisional friction forces perpendicular to both the magnetic field and pressure gradients lead to classical transport, while the parallel collisional friction forces lead to neoclassical transport.
- In nonaxisymmetric devices like stellarators particles can be lost on collisionless trajectories meaning these devices are not intrinsically ambipolar, but instead have a radial electric field develop to balance the flux of ions and electrons.
- The ratio of classical to neoclassical particle flux was shown in [Buller et al. 28] to scale as a ratio of $j_\perp$ to $j_\parallel$. With W7-X optimized for minimum $j_\parallel$, the classical transport can be on the same order if not larger than the neoclassical transport.

Fundamentally the distinction between classical and neoclassical transport arises from the magnetic field structure. In a straight homogeneous field only classical transport is present, while a toroidal field structure provides the necessary geometry for both classical and neoclassical transport. As detailed below, coulomb collisions are necessary for the cross-field transport in a straight homogeneous magnetic field, while for a toroidal magnetic field cross-field transport can occur without any collisions. In this way, an experiment with a toroidal magnetic field experiences classical transport stemming from the collisional friction forces perpendicular to the field (and gradients in temperature & density) and neoclassical transport from the parallel friction forces arising as a consequence of the toroidal geometry ([3]).

Even with classical transport in a straight homogeneous field, the Lorentz force causes charged particles to follow helical trajectories that can be decomposed into free-streaming parallel motion and circular motion perpendicular to the magnetic field. A sufficiently strong magnetic field creates this type of anisotropy in the particle motion, naturally allowing the transport characterization to also be separated into parallel and perpendicular directions with respect to the magnetic field. For the classical picture with a straight homogeneous magnetic field, perpendicular particle transport requires collisions. Therefore in this classical picture an iron impurity present in a bulk hydrogen plasma has cross-field transport completely dictated by collisions. Moreover without any gradients in the bulk plasma density, temperature, or electric potential the only net particle transport will occur from collisions between dissimilar particles[l]. Therefore a random walk approach for a pure diffusive transport (e.g. section 1.2 in [29]) can be used to estimate the perpendicular diffusion of the iron impurity from the characteristic step size and the characteristic stepping time as seen in equation[m] (1.8).

$$D_\perp \approx \frac{l^2}{2t} = \frac{\rho_Z^2}{2}\nu_{Zi} \tag{1.8}$$

The characteristic step size and stepping time in this scenario are simply the larmor radius of the iron ions ($\rho_Z = \frac{\sqrt{2m_Z T_Z}}{ZeB}$) and the mean collision time between the iron and hydrogen ions ($\frac{1}{\nu_{Zi}}$). Importantly coulomb collisions conserve momentum meaning that from a fluid perspective the friction forces on each respective species are equal but opposite. The consequence of this momentum conservation is that the charge-weighted perpendicular fluxes are balanced, i.e. $q_Z\left(\Gamma_{Zi}^{\perp}\right) + q_i\left(\Gamma_{iZ}^{\perp}\right) = 0$, which assures the ambipolarity of the total impurity flux $\sum_\alpha q_\alpha \langle \Gamma_\alpha^{\perp} \rangle = 0$ ([R. Dux 3]). This intrinsic ambipolarity is a feature of classical transport and critically indicates that a perpendicular electric field does not contribute to net particle transport in the classical case.[n] Even as gradients in density, temperature, and electric potential are added to the straight homogeneous magnetic field scenario for further complexity, the surprising result is that the heuristic definition of the diffusion coefficient in equation (1.8) turns out to be the exact classical diffusion coefficient under the assumptions that collisions with electrons can be ignored (the electron to impurity ion mass ratio is so small that their contributions to impurity transport is minuscule) and that the impurity ions are present in trace amounts (meaning only collisions with the main ions species are relevant). Therefore writing the classical flux (Γ_Z^C) in this straight homogeneous field scenario yields equation (1.9) where the classical diffusion

[l]Collisions between similar particles will have a symmetric displacement of their gyrocenters meaning the particles will just exchange locations leading to no net transport.

[m]The factor of $\frac{1}{2}$ in equation (1.8) is there to capture the equal probability to make a step parallel or antiparallel to the density gradient.[29]

[n]The $E \times B$ drift is charge independent and will cause the entire plasma to first order drift together.

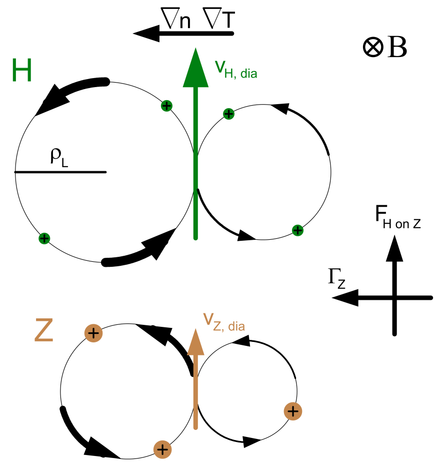

Figure 1.6: Diagram depicting classical transport in presence of density and temperature gradients for the hydrogen main ion. The density and temperature gradients produce diamagnetic flows for both the hydrogen and impurity ions where the left-side orbits have thicker arrows representing increased density and larger larmor radii (ρ_L) representing the increased temperature. There is a collisional friction force on the impurity ions from the hydrogen ions that in the presence of a magnetic field cause the impurity to drift, $v_{drift} = \frac{1}{q}\frac{\vec{F}\times\vec{B}}{B^2}$, contributing to the cross-field transport. Figure adapted from [R. Dux 3]

coefficient (D_Z^C) is given by equation (1.8).

$$\Gamma_Z^C = D_Z^C \left(-\nabla n_Z + Zen_Z \left[\frac{\nabla n_i}{n_i} - \frac{1}{2}\frac{\nabla T_i}{T_i} \right] \right) \tag{1.9}$$

From equation (1.9) the cross-field transport has terms proportional to the impurity density gradient (∇n_Z), the main ion density (∇n_i) gradient, and the temperature gradient (∇T_i), but critically no electric field terms due to the intrinsic ambipolarity. The ion density & temperature gradients perpendicular to the magnetic field will give rise to a diamagnetic velocity as seen in figure 1.6. The difference in the diamagnetic flows between the main and impurity ions will lead to a collisional friction force on the impurity ions parallel to the diamagnetic flow velocity, where generally the lighter main ion species will drag the heavier and slower impurity flows. Therefore from a MHD perspective the impurity fluid will drift perpendicular to both the collisional force and the magnetic field due to this collisional force, i.e. $v_{drift} = \frac{1}{q}\frac{\vec{F}\times\vec{B}}{B^2}$.The simple diagram in figure 1.6 illustrates the previous statement that the collisional forces perpendicular to the magnetic field (and gradients in temperature & density) give rise to classical transport.

Next for toroidal magnetic geometry like W7-X the classical cross-field flux of an iron impurity is not completely described by equation (1.9). The classical impurity flux for this scenario can be expressed as equation (1.10) reproduced from equation (5.7) in [Buller et al. 28], where the radial transport is averaged over a flux surface as indicated by $\langle ... \rangle$ with ψ serving as a flux-surface label.

$$\langle \Gamma_Z \cdot \nabla\psi \rangle^C = -\langle n_{Z0} \rangle \left(\frac{1}{Z} D^C_{N_Z} \frac{d \ln N_Z}{d\psi} + D^C_{n_i} \frac{d \ln n_i}{d\psi} + D^C_{T_i} \frac{d \ln T_i}{d\psi} \right) \tag{1.10}$$

Note that $D^C_{N_Z} = \frac{m_z T_i}{Ze^2} \nu_{Zi} \langle \frac{|\nabla\psi|^2}{B^2} \rangle$, $D^C_{n_i} = -D^C_{N_Z}$, and $D^C_{T_i} = \frac{1}{2} D^C_{N_Z}$ demonstrating that the classical transport in a toroidal geometry is modified by a geometric factor based on the flux surface averaging. This can be simply understood by the fact that the magnetic field is not constant on a flux surface requiring the modification of the straight homogeneous magnetic field's diffusion coefficients.[o]

In contrast to the classical picture, the neoclassical transport is inherent to the toroidal magnetic geometry, where specifically the neoclassical transport is based on the $\vec{E} \times \vec{B}$ and magnetic geometry induced drifts. In this way it is the parallel component of the collisional friction force determining the neoclassical transport due to the curved magnetic geometry coupling the parallel and perpendicular velocities (i.e. the perpendicular fluid flows are not divergence free requiring the parallel fluid velocities to self-assemble ensuring this requirement[p]). However for non-axisymmetric configurations even collisionless particles can lead to radial flux due to the polodially-localalized magnetic wells trapping particles and allowing these particles to drift radially outward (see [31] and [32] for good discussion on helical magnetic wells' contribution to neoclassical transport). In fact the collisionless loss of particles is the reason that stellarators are not intrinsically ambipolar meaning that a radial electric develops to balance the flux of ions and electrons, i.e. the flux of each species is a function of the radial electric field: $\sum\limits_\alpha q_\alpha \langle \Gamma^\perp_\alpha (E_r) \rangle = 0$. In general there is not an analytic solution for the radial electric field and the above-mentioned ambipolarity condition for the particle fluxes can give multiple solutions

[o] For a more general discussion and description of classical transport see [Buller et al. 30], specifically equation (3.9)

[p] To lowest order the density should be constant on a flux surface meaning that the particle fluxes should be divergence free. See [R. Dux 3] for further discussion

for E_r based on magnetic geometry and plasma conditions. Therefore numerical calculations are performed to solve the radial electric field and diffusion coefficients self-consistently with the plasma parameters and magnetic geometry. This means that compared to the classical picture the equation describing the neoclassical impurity flux should look identical except for the inclusion of the radial electric field term and the different values for the transport coefficients that take into account the parallel & perpendicular flow coupling. Thus in the trace limit approximation for a heavy impurity the neoclassical impurity flux is shown in equation (1.11), reproduced from equation (4.5) in [Buller et al. 28].[q]

$$\langle \Gamma_Z \cdot \nabla\psi \rangle^{NC} = -\langle n_{Z0} \rangle \left(\frac{1}{Z} D^{NC}_{N_Z} \frac{d \ln N_Z}{d\psi} + D^{NC}_{n_i} \frac{d \ln n_i}{d\psi} + D^{NC}_{T_i} \frac{d \ln T_i}{d\psi} - \frac{e}{T_i} D^{NC}_{\Phi} \frac{d \ln \langle \Phi \rangle}{d\psi} \right) \tag{1.11}$$

For known plasma parameters the neoclassical transport coefficients, listed in equations (4.10-4.13) in [Buller et al. 28], critically only differ from the classical coefficients by a scaling factor dependent on the magnetic geometry. Typically in axisymmetric devices like a tokamak and especially in non-optimized stellarators the neoclassical transport coefficients are at least an order of magnitude larger than their classical counterparts when these devices are operated in the fusion-relevant temperature regimes.[r] However in the specific case of W7-X, the classical impurity flux can be on the same order if not larger than the neoclassical impurity flux as first reported in [Buller et al. 28] and discussed in [Buller et al. 30]. The reason W7-X's classical transport can be significant when compared to the neoclassical transport is due to W7-X's neoclassical optimization whereby one of the optimization criteria was the minimization of the parallel current, i.e. the bootstrap current.[21] In fact a simple estimate of the relative significance of the classical transport can be estimated by taking the ratio of the classical impurity flux (1.10) to the neoclassical impurity flux (1.11) in the limit that the impurity density is homogeneous ensuring that the ratio is purely dependent on magnetic geometry. This ratio taken from equation (2.1) in [Buller et al. 30] is reproduced in equation (1.12) demonstrating how

[q] The red coloration on the electric field term is added to emphasize the difference with the classical impurity flux equation in (1.10) .

[r] Plasmas unlike gases become less collisional as the temperature increases meaning that trapped particles can complete many bounce orbits before a collision event providing time for radial excursions from these trapped particles.

a minimization of the parallel current, $j_{\|}$, increases the importance of the classical transport channel.

$$\frac{\langle \Gamma_Z \cdot \nabla\psi\rangle^{C}}{\langle \Gamma_Z \cdot \nabla\psi\rangle^{NC}} = \frac{\langle j_{\perp}^2\rangle\langle B^2\rangle}{\langle j_{\|}^2\rangle\langle B^2\rangle - \langle j_{\|}B\rangle^2} \tag{1.12}$$

As reported in [Buller et al. 28] this ratio for the W7-X standard configuration in the mixed-collisionality regime (i.e. collisional trace impurity with low-collisionality main ion) is ~ 3 to 3.5 highlighting possible the importance of including the classical transport channel in modeling the impurity transport experiments.[s] Also equation (1.12) reemphasizes through the $j_{\perp}$ and $j_{\|}$ dependence that it is the collisional friction forces perpendicular to both the magnetic field and the density & temperature gradients that lead to classical transport, while the parallel collisional friction forces lead to neoclassical transport.

1.2.2 Turbulent transport

- In tokamaks and optimized stellarators the observed transport is larger than the neoclassical predictions just discussed. This anomalous transport is attributable to small spatial scale plasma perturbations associated with drift waves stemming from plasma inhomogeneities.

- Although the ion temperature gradient (ITG) and trapped electron mode (TEM) instabilities are expected to contribute the most to impurity transport in W7-X according to [33, 1], the type of instability and the degree to which it contributes to impurity transport needs to be numerically calculated using the specific magnetic geometry and plasma profiles.

In general the measured impurity transport is usually larger than the expected levels calculated from classical and neoclassical transport theory alone. This increased impurity transport has been measured in both tokamaks[34,35,36] and in stellarators[7,37] where this enhancement over collisional transport theory is referred to as anomalous transport. The observed anomalous transport is largely attributable to microinstabilities, small scale plasma fluctuations on length

[s]The W7-X's standard magnetic configuration was used for the on- to off-axis ECRH iron impurity transport dataset presented in this thesis and the one shown in figures 1.4b and 1.3. See footnote k

scales larger than the debye length, associated with drift waves.[38] Drift waves are the cross-field drift motion due to inhomogeneity in the plasma, i.e. density and/or temperature gradients inducing diamagnetic drifts. Specifically these gradients are a source of free energy that can drive these microinstabilities unstable, where a plasma perturbation (i.e. temperature, density, potential) in the presence of a temperature and/or density gradient can cause localized charge separation along the perturbation. The localized charge separation leads to $\vec{E} \times \vec{B}$ fluctuations that either stabilize or destabilize the microinstability depending on the direction of the density/temperature gradient. Even from this basic description of the underlying mechanism for turbulent transport, the clear important factors for determining the stability of these microinstabilities are the magnetic geometry and the plasma kinetic profiles.[t]

In fact these microinstabilities can be classified into different modes depending on the source of free energy, where three main ones are the ion temperature gradient (ITG), the electron temperature gradient (ETG), and the trapped electron mode (TEM). Moreover these modes can be further categorized by their characteristic length scales and frequencies. The ITG and TEM have fluctuations on the order of the ion's larmor radius while the ETG mode has shorter scale length fluctuations on the order of the electron larmor radius. This scale length difference is important since not only has it been shown in [39] that the ETG instability's contribution to turbulent transport should be low for a quasi-isodynamic stellarator like W7-X, but also the fluctuations on the electron larmor radius scale should have minimal impact on impurity transport.[40] Therefore it is expected that ITG and TEM instabilities should contribute the most to turbulent impurity transport in W7-X, although it should be noted that these instabilities listed as independent single modes can mix and be present as hybrid plasma instabilities.[33,1] As such it is important to evaluate the characteristic length scales for the kinetic profiles since they help indicate the regimes where the various instabilities could be driven unstable. Specifically these characteristic length scales are the normalized gradient lengths, i.e. $a/L_T = \frac{a\nabla T}{T}$ and

[t]Remember that the diamagnetic drift from a pressure gradient is the fluid description of the ∇B and curvature drifts in the single particle description. This single particle picture depending on the magnetic geometry reemphasizes how there will be different localized areas more/less prone to the various microinstabilities.

$a/L_n = \frac{a\nabla n}{n}$ where a is the plasma minor radius, which are dimensionless values yielding information on the potential sources that could drive/suppress the various instabilities (see [38] and [41] for more in depth discussion).

Although characteristic length scales and frequencies can help hint at the potential instability causing the increased turbulent transport, the type of instability and the degree to which it contributes to impurity transport needs to be calculated with the specific magnetic geometry and plasma profiles. These predictions can be very computationally expensive due to the nonlinearity and huge scale range necessary to realistically model these microinstabilities even when taking the gyrokinetic approach, i.e. following the gyrocenters of the particles and that equilibrium values are slowly varying compared to the smaller spatial & more rapidly varying turbulent fluctuations.[41] For a good review of turbulent transport in W7-X, the reader is encouraged to review the series of papers [42, 33, 43, 44]. In terms of impurity transport while there has been analytic work on collisional transport effects in W7-X (see [45, 46]), only recently has there been numerical simulations for impurity transport driven by gyrokinetic microturbulence in stellarator geometry for both LHD[47] and W7-X.[1] In particular for W7-X the work done by [García-Regaña et al. 1] demonstrated that for pure ETG driven impurity transport, the radial impurity flux is much smaller than those driven by pure ITG and TEM instabilities. Additionally [García-Regaña et al. 1] demonstrated that whether the turbulence was driven by ITG or TEM instabilities the impurity transport was dominated by ordinary, charge-independent diffusion.

1.3 Impurity transport in an optimized stellarator

Impurity transport characterization and ultimately impurity control is critical to the future prospects of magnetic confinement fusion energy. Similar to tokamaks, impurities present in stellarator plasmas not only cause fuel dilution decreasing the potential fusion power density, but also cause increased radiated power losses cooling the plasma. Such a double negative impact to power balance needs to be mitigated for any implementation of a practical fusion reactor. However the prevention of any impurity contamination in these plasmas might be nearly impossible with sputtering from plasma-wall interactions, usage of certain seed impurities for diagnostic capabilities, and even large impurity injections to cool the edge plasma to further prevent localized heat flux to first wall materials. All of these possibilities underline the importance of impurity transport characterization and begin to indicate why it is a critical topic in stellarator physics.

Across multiple stellarator experiments, it has been observed that impurity confinement times tend to scale with electron density.[37] This is problematic for high performance, high density discharges since an accumulation of impurities can lead to a radiative collapse. In fact theory predicts such scenarios are not just possible, but also probable.[48,49] However there is evidence from LHD's impurity hole to W7-AS's high-density H-mode (HDH) that high energy confinement and avoidance of impurity accumulation are not mutually exclusive.[37] Therefore in high performance steady state operation, both screening near the edge and core flushing of impurities will be important. Before identifying possible advanced scenarios with these characteristics, the impurity transport should be characterized under various conditions. Not only is this useful for understanding impurity transport over parameter space, but also these measurements can be used to validate neoclassical simulations and compare with turbulent transport predictions. Specifically the work in this thesis covers the variation in the ECRH deposition profile which primarily effects the radial electric field and hence the neoclassical transport in W7-X. Therefore comparisons with neoclassical predictions are possible and due to W7-X neoclassical optimization the role of turbulent transport in the different heating scenarios can be evaluated.

1.3.1 Purpose for ECRH deposition position scan during impurity transport experiments

- Performing an on- to off-axis ECRH scan at higher plasma densities can change the radial electric field from an electron-root (positive) to ion-root (negative), which should have a strong impact on the transport properties of a medium Z material like iron.

- A consequence of W7-X's optimization is the reduction of neoclassical transport to low levels making the evaluation into turbulent transport's contribution to the overall impurity transport in a stellarator uniquely possible.

The main objectives of the on- to off-axis ECRH scan were threefold: First, to measure impurity transport effects from the different heating scenarios; Second, to compare the measured impurity transport to neoclassical predictions; Third, to determine the role of turbulent transport in the different heating scenarios.

The methodology of the first objective will be described in detail in chapter 2 with the specific results presented in section 6.1. Critically it is the second objective that will help determine the role the radial electric field plays in impurity transport. From neoclassical considerations, the radial electric field is expected to play an important role in impurity transport. Specifically an ECRH scan from on- to off-axis was performed to investigate a transition from an electron-root confinement regime to an ion-root confinement regime. An electron-root confinement regime is characterized by a peaked electron temperature and a large positive radial electric field in the plasma core transitioning to a negative electric field, ion-root, from approximately mid-radius until the last closed flux surface.[50] Strong central ECRH with a large positive radial electric field in the core has been demonstrated on W7-AS, LHD, TJ-II.[51] Although an electron-root confinement regime has the favorable feature of a strong positive core electric field to prevent/reduce highly charged impurities accumulating, it is not generally foreseen as a model discharge for a future fusion power plant. The simple justification stems from the fact that core electron-root discharges tend to occur at lower plasma densities when the energy equilibration time between the ions and electrons is much longer than their respective confinement times, allowing for ECRH heated plasmas to have a core $T_e > T_i$. On the other hand, high-performance plasma discharges typically exhibits a negative electric field throughout the radial extent of the plasma due to the ion-drift being stronger than the electron-drift. Although this ion-root confinement regime naturally arises at high densities, namely $n_e > 1 \times 10^{20}\ m^{-3}$, this regime can also be accessed whenever $T_e \approx T_i$. Therefore by directing the ECRH further off-axis the central electron temperature can be lowered to where $T_e \approx T_i$ recovering ion-root confinement at lower densities.

To better understand how these regimes can play a significant role in impurity transport it is helpful to examine what would be expected from purely neoclassical transport.The neoclassical particle flux of an impurity Z as detailed in [Maassberg et al. 52] and reproduced in (1.13) is controlled by the kinetic profiles, the gradients of the kinetic profiles, and the magnetic field geometry. The neoclassical flux can be simplified down to a diffusive term, proportional to the impurity density gradient, and a convective term, proportional to the impurity density.

$$\Gamma_Z^{nc} = -n_Z \left\{ D_{11}^Z \left(\frac{\nabla n_Z}{n_Z} - \frac{q_Z E_r}{T_Z} \right) + D_{12}^Z \frac{\nabla T_Z}{T_Z} \right\} = -D_Z \nabla n_Z + n_Z V_Z \tag{1.13}$$

Although the neoclassical coefficients D_{11}^Z and D_{12}^Z depend on the magnetic geometry and the collisionality across the radius of the plasma, only D_{11}^Z is guaranteed to positive.[u]Critically the combination of $D_{11}^Z > 0$ along with a medium Z impurity like iron means that the impurity flux's direction is tied to the sign of the radial electric field. This can be seen in equation (1.14) where the convective velocity is dominated by the radial electric field term leading to convection velocities being negative (positive) for an ion-root (electron-root) regime.

$$V_Z = D_{11}^Z \left(\frac{ZE_r}{T_Z} \right) - D_{12}^Z \left(\frac{\nabla T_Z}{T_Z} \right) \qquad \text{For high Z:} \quad V_Z \approx D_{11}^Z \left(\frac{ZE_r}{T_Z} \right) \tag{1.14}$$

Meaning a heavier impurity in a high performance plasma can lead to an impurity accumulation in the plasma core causing the plasma to radiate and terminate prematurely as already observed in LHD[54] and W7-AS.[37] However recent theoretical work has demonstrated that a temperature screening effect observed in tokamaks can be recovered in stellarators when the plasma is in a mixed-collisionality regime, i.e the impurities are collisional while the main ions are collisionless.[45,46] This neoclassical temperature screening phenomenon can be recovered for high Z impurities if there is a sufficiently steep temperature profile and impurity collisionality for the 2nd term in equation (1.14) to compete with the electric field term. Based on normalized transport coefficients for Fe^{+16} calculated in [Helander et al. 45] there is good reason to believe that the iron impurity transport experiments performed were in the mixed collisionality regime for iron chargestates higher than Fe^{+16} outside the normalized radius of $\rho \approx 0.88$. Therefore these impurity transport experiments were performed during an ECRH deposition scan at medium densities, $\overline{n_e} \approx 6 \times 10^{19}\ m^{-2}$, to tailor the electron temperature profile helping evaluate the

[u]The way that equation (1.13) is written $D_{11}^Z = L_{11}^Z$ and $D_{12}^Z = L_{12}^Z - \frac{3}{2} L_{11}^Z$ from [van Rij et al. 53]

impact of the radial electric field alternating between electron-root to ion-root confinement regimes.

Finally the last objective of the iron impurity transport experiments during an on- to off-axis ECRH scan was to determine the contributions from turbulent transport.Previous impurity transport experiments done on LHD[55] and W7-AS[56] have attributed observed deviations from neoclassical theory to turbulence, but the large uncertainties in the neoclassical modeling made turbulence's role inconclusive. The goal of assessing turbulence's role in impurity transport can be uniquely answered by W7-X due to its optimization of the magnetic field geometry to reduce neoclassical transport to very low levels.[21,22] One significance of turbulence is that it could provide anomalous impurity transport that might help avoid core impurity accumulation that is predicted for the high performance discharges. Moreover turbulence induced anomalous transport is not expected to have a strong mass or charge dependence, potentially flushing all impurities at a similar diffusive rate. Recent work on W7-X[7] and on LHD[57] show strong indications that ion temperature gradient, ITG, caused turbulence can be the dominant transport channel in stellarator plasmas. In fact [Wegner et al. 40] recently demonstrated turbulent dominated transport on W7-X where increases in the ion-to-electron temperature ratio via low power ECRH could suppress the turbulence driven by the ion temperature gradient mode leading to longer iron transport times. Therefore an impurity transport investigation into ECRH deposition position at various power levels on the neoclassically optimized W7-X can help further elucidate the relative importance of turbulent driven anomalous transport.

1.3.2 Iron impurity transport experiments on W7-X

- Previous iron impurity transport experiments on W7-X demonstrated that by placing more ECRH power off-axis the iron transport time increased and that the observed iron impurity transport had anomalous diffusion values two orders of magnitude larger than the calculated neoclassical values.

- Due to the previous iron impurity transport experiments occurring in low density discharges, a robust transition from an electron-root to ion-root confinement regime was not attainable. Therefore both an on-axis ECRH power scan and on- to off-axis ECRH scan were acquired for three heating power levels at constant density of $\overline{n}_e \approx 6 \times 10^{19}$ in the W7-X standard magnetic configuration.

In this subsection recent impurity transport investigations on W7-X will first be summarized before a description of the experiments performed for this thesis work will be discussed. During the first half of the W7-X divertor campaign (OP1.2a), on- and off-axis ECRH iron impurity transport experiments were performed in helium at relatively low densities $\overline{n}_e \approx 1 \times 10^{19}\, m^{-2}$, and at low ECRH input power $P_{total} \approx 1.8$ MW in the standard magnetic configuration (see footnote k for more details on magnetic configuration). Due to external constraints only a limited amount number of experiments were able to be performed, but still a clear dependence in the global impurity transport time was observed as more of the input ECRH power was deposited off-axis. In fact an increase in the iron's global transport time from $\tau_I \approx 80$ ms to $\tau_I \approx 118$ ms was observed for the on- and off-axis cases respectively, all while the global energy confinement time being relatively unaffected.[58]

In addition to the on- and off-axis helium experiments, an iron impurity experiment was performed in a hydrogen electron-root discharge at relatively low density, $\overline{n}_e \approx 2 \times 10^{19}\, m^{-2}$, and high input ECRH, 5 MW, again in the standard magnetic configuration. The anomalous diffusion and convective velocity for the iron impurity was inferred using a similar strategy of a least squares minimization of the various iron chargestate's line emission data. The inferred transport profiles showed anomalous diffusion profile two orders of magnitude larger than the calculated neoclassical one, while the resulting inferred convection velocity profile agreed within the uncertainties of the calculated neoclassical convection profile.[7]

Therefore these two experiments taken together helped motivate a more in depth study of iron impurity transport in high performance hydrogen discharges with various on- and off-axis ECRH levels. These previous experiments were low density discharges due to poor wall conditioning meaning a robust transition from an electron-root to ion-root confinement regime were not attainable in hydrogen.

The iron LBO injection experiments were performed at constant $\overline{n_e} \approx 6 \times 10^{19}\ m^{-2}$ in three primary ECRH powers ($\sim$ 2.8, 3.5, and 4.9 MW) in the W7-X standard magnetic configuration. By keeping the input ECRH power and line-averaged density profiles constant during an iron LBO injection as various gyrotrons were turned off, consistent discharges were attainable. In this way the gyrotron's plasma-facing steering mirrors were not moved during a plasma discharge and provided the most efficient way to scan for ECRH input power and percent of ECRH power deposited off-axis. In conclusion both an on-axis ECRH power scan and on- to off-axis ECRH scan were acquired for the three power levels at constant density in the W7-X standard magnetic configuration.

1.4 Thesis overview

This thesis is organized as follows: Chapter 2 describes the impurity transport diagnostics on W7-X used to measure and derive the iron impurity transport properties during the on- to off-axis ECRH scans. Chapter 3 discusses how the anomalous iron impurity transport coefficients were inferred including the details on the execution of the transport code STRAHL and the structure of the python wrapping code ($lstsq\_STRAHL\_wrap$) specifically written to perform the task. Chapter 4 covers the sensitivity studies for the inferred anomalous transport coefficient profiles using noisy synthetic data generated by the forward modeling of $lstsq\_STRAHL\_wrap$. Chapter 5 then applies the same sensitivity studies from chapter 4 to experimental data in order to reconfirm the total uncertainty stemming from the potential uncertainties and systematics inherent to the STRAHL code and $lstsq\_STRAHL\_wrap$. Finally chapter 6 discussed the observational and inferred results from the on to off-axis ECRH scans performed during the second half of the first divertor campaign on W7-X.

Chapter 2

Impurity transport hardware on W7-X

This chapter describes the critical systems used to perform the iron impurity transport experiments during the on- to off-axis ECRH scan. In total there were five diagnostics and one heating system necessary for the analysis of these impurity iron transport experiments performed during the first divertor campaign on W7-X. Three of the five diagnostics were directly related to the iron measurements used in the impurity transport studies for this thesis work: the Laser Blow-Off (LBO) system, the High Resolution X-ray Imaging Spectrometer (HR-XIS), and the High-Efficiency eXtreme ultraviolet Overview Spectrometer (HEXOS). During the impurity transport experiments the LBO system was used to inject a trace of amount of iron into the plasma and then HR-XIS & HEXOS were used to measure the line-radiation from the various iron chargestates. Meanwhile the thomson scattering diagnostic and the X-ray Imaging Crystal Spectrometer (XICS) provided routine background plasma profiles with the interferometer used to scale the thomson's density profile. Specifically these last three diagnostics enabled the measurement of the electron density & temperature from thomson scattering and the ion temperature & radial electric field from XICS. Finally the Electron Cyclotron Resonance Heating (ECRH) system provided both plasma generation & modification of the electron temperature profile.

The chapter begins by describing the impurity diagnostics used to measure the iron line emissions and inject the iron in trace amounts with details in sections 2.1 & 2.2 and section 2.3 respectively. The following two sections briefly detail the ECRH system and the thomson scattering diagnostic in sections 2.4 and 2.5 respectively.

2.1 X-ray Imaging Crystal Spectroscopy

- The two x-ray imaging spectrometer systems on W7-X provided routine measurements of the ion temperature, radial electric field via poloidal ion flow measurements, the electron temperature, and selected impurity chargestate densities
- The one-dimensional image provided by these systems yield invaluable radial information from the measured helium-like iron spectra, which in the case of characterizing iron impurity transport is critically important.

There are two separate x-ray imaging spectrometer systems installed on W7-X providing complimentary diagnostic capabilities: one system primarily focused on characterizing impurities and the other system focused on providing ion temperatures, electron temperatures, and ion perpendicular flows for radial electric field estimations. Both systems work on the basic concept of Bragg reflection where the incident line emission reflects off of adjacent atomic layers in a crystal and if the path length through the first few atomic layers is an integer multiple of the incoming wavelength then constructive interference occurs.[59] The true advantage for an x-ray imaging spectrometer stems from bending the crystal into a spherical surface that provides simultaneous spatial and wavelength resolution while also increasing the light throughput.[60] An explanation for this advantage can be seen from the geometric properties of a spherical mirror satisfying the Bragg condition shown in figure 2.1 taken from [Ince-Cushman 4]. Specifically the entire curved crystal collects and focuses the light satisfying the Bragg condition to a point on the Rowland circle (the dashed line in figure 2.1) where due to the spherical crystal's astigmatism maps an elongated source at the sagittal focus to a point on the detector. Additionally with the spherical crystal ensuring that a similar elongated source above the meridional plane will focus to a point below the meridional plane at the detector position (shown by the curved red in figure 2.1) effectively giving spatial resolution that is measured vertically along the detector. Therefore in combination with the horizontal wavelength resolution satisfied by light emission with slightly different Bragg conditions, the spherical crystal yields a one-dimensional image of the plasma with spectral information at each spatial point.

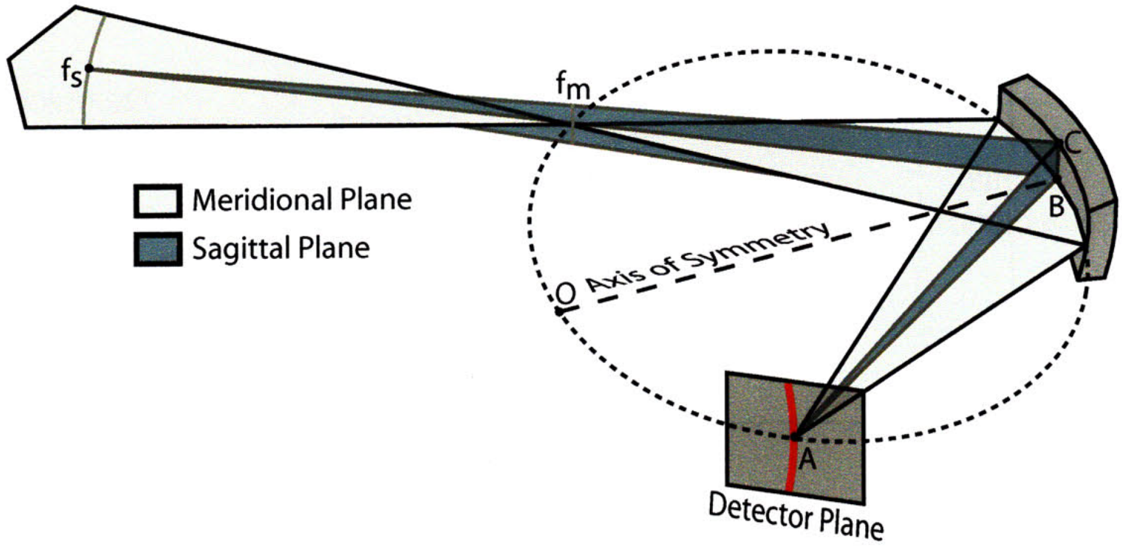

Figure 2.1: Schematic taken from [Ince-Cushman 4] depicting the geometry of a spherically bent crystal and the unique characteristics of an x-ray imaging crystal spectrometer.

The X-ray Imaging Crystal Spectroscopy (XICS) system on W7-X is a great example of this type of diagnostic.[61] As shown in figure 2.2, a time-integrated image of the helium-like argon emission is shown along with the limiting & central sightlines through the central flux surface and the corresponding central sightline's Ar XVII spectra from $\sim$ 3.94 to 4.01 angstroms. This XICS system has a second crystal & detector measuring the hydrogen-like argon spectra and the helium-like iron spectra in second order. Both of the crystals & detectors are fixed in placed and require a small puff of argon gas during the plasma discharge for routine measurements of Ar XVII and Ar XVIII spectra. From Ar XVII's w-line line-broadening the ion temperature profile can be determined with a $\sim$ 2 cm spatial resolution and $\sim$ 2 ms temporal resolution.[62] Additionally the doppler shift of the w-line and its ratio with neighboring dielectronic satellite lines allows the diagnostician to determine the radial electric field and electron temperature respectively.[63] This system was used for the T_i profiles in the STRAHL modeling and the E_r profiles in DKES for comparisons with the neoclassical transport coefficients (see sections 5.2.3 and 5.1.4 respectively for more details).

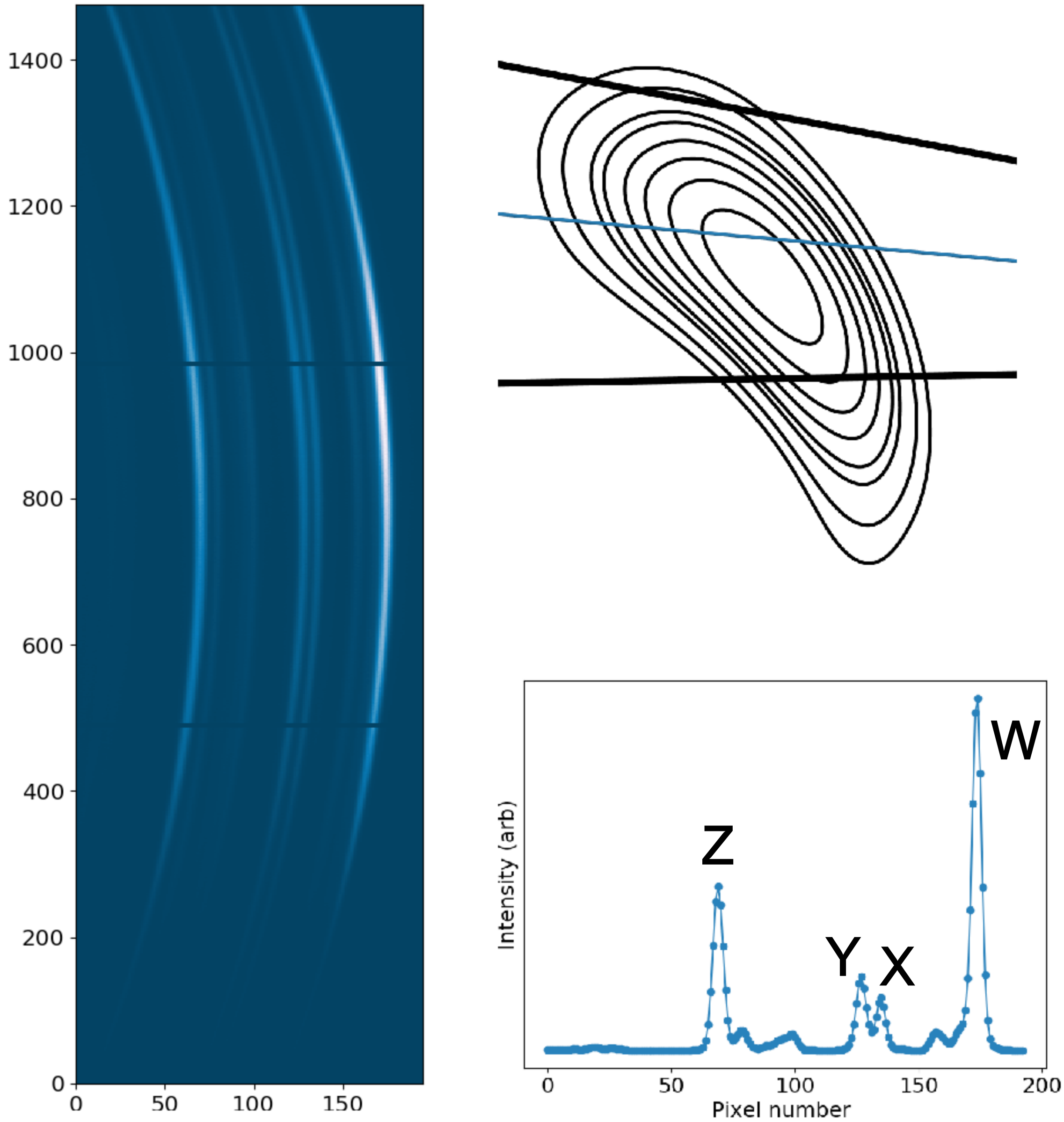

Figure 2.2: On the top right is the central sightline from XICS's He-like Ar detector with the detector's limiting rays colored black over the intersecting flux surfaces. The full XICS image of He-like Ar spectra from discharge 20180919.046 is shown on the left. The blue sightline corresponding to the vertical pixel 749 from the left & the same blue sightline from the top right has its corresponding spectra displayed on the bottom right.

The High Resolution X-ray imaging Spectrometer (HR-XIS) is the second system installed on W7-X with its primary goal to characterize the transport of various impurities in the plasma via helium-like emission spectra measurements.[64,59] This system has eight different crystals installed on a motorized rotation and dual-axis translation stage for remote crystal selection between plasma discharges. This diagnostic flexibility allowed [Langenberg et al. 65] to perform atomic mass & charge scans during the first divertor campaign on W7-X to better characterize impurity transport scalings. With a crystal specifically installed for measuring the helium-like iron spectra in first order, the HR-XIS diagnostic was used to characterize the iron impurity transport in the on- to off-axis ECRH dataset presented in this thesis. Figure 2.3 depicts the time integrated image for the same discharge as shown in figure 2.2 with the eight colored sightlines representing the eight different signals for the $Fe^{+}24$ w-line used within the STRAHL iron transport modeling.[a] The orange sightline's collected emission is seen below the flux surface diagram showing the corresponding iron spectra with key $Fe^{+}24$ spectral lines noted. For the iron transport experiments presented in this thesis the helium-like iron crystal was placed in an incorrect position leading to vignetting (see figure 5.23 for the estimated transmission). The strongest spectral line, i.e. the w-line, was the least effected by the vignetting allowing for eight separate sightlines all with measurable signal levels to be used for the transport analysis.[b] Each sightline was composed of 40 vertically binned pixels & $\sim$ 10 horizontally binned pixels in order to only select the w-line and have an effective spatial resolution of $\sim$ 3.5 cm in the plasma. Also with the center of neighboring sightlines separated by 100 vertical pixels on the detector, there is no overlap of collected emission from the plasma. As discussed in section 4.1.3, having the spatial information from multiple sightlines was absolutely invaluable for inferring a meaningful anomalous transport profile, underlining HR-XIS's importance for characterizing impurity transport. Finally for more details on how each sightline of Fe^{+24} w-line was line-integrated and utilized within the least squares minimization see sections 3.3.3 and 5.2.2.

[a]The Fe XXV w-line corresponds to the atomic transition ${}^1P_1 \longrightarrow {}^1S_0$ leading to 1.85039 $\mathring{A}$

[b]The signal corresponding to the most edge-viewing sightline had the lowest signal levels, but still had a signal-to-noise ratio of at least three.

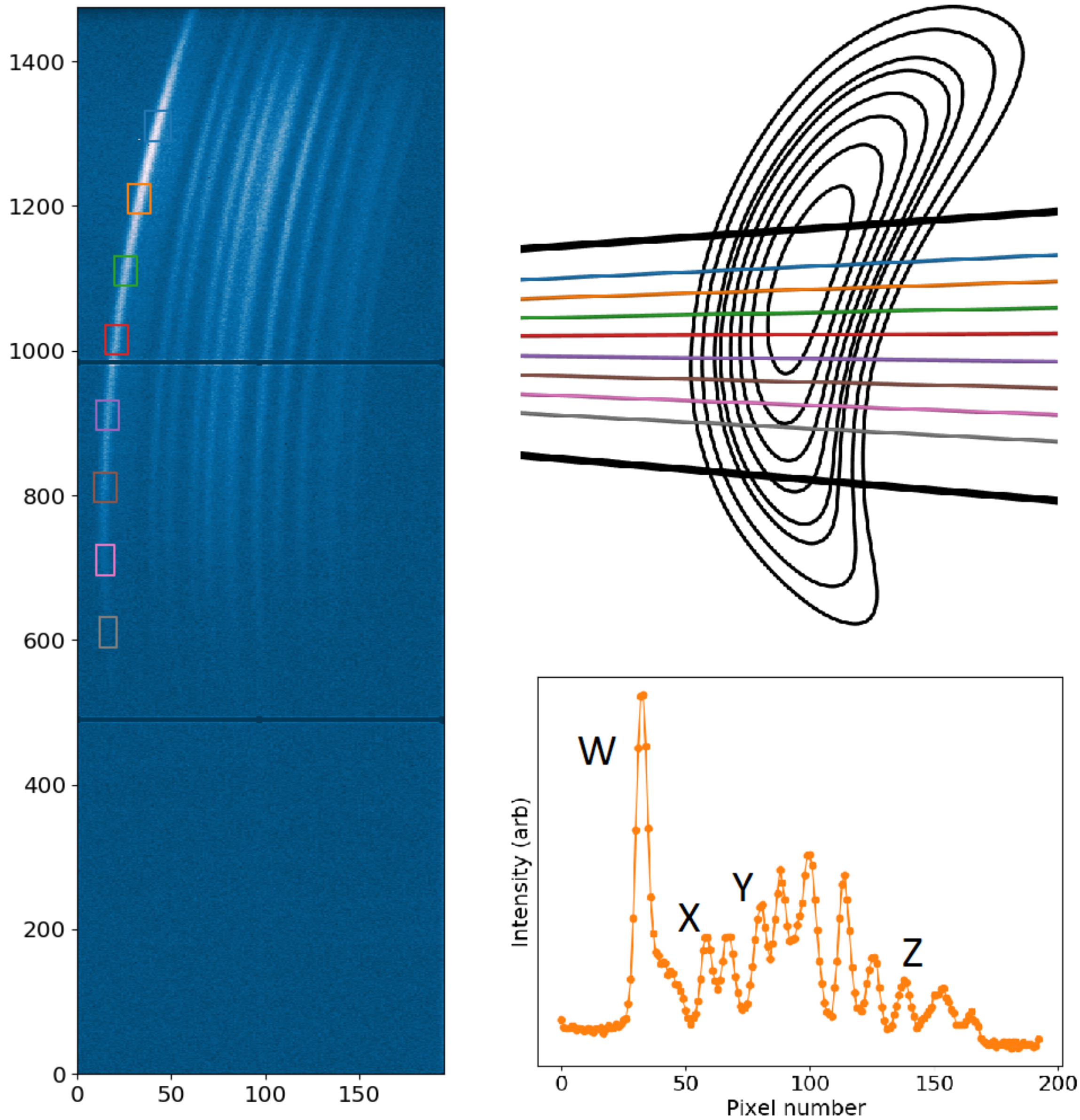

Figure 2.3: On the top right are the eight HR-XIS sightlines for He-like Fe used within the STRAHL modeling with the detector's limiting rays colored black over the intersecting flux surfaces. The full HR-XIS image of the He-like Fe spectra from discharge 20180919.046 is shown on the left. The orange sightline corresponding to the vertical pixel 1210 from the left & the same orange sightline from the top right has its corresponding spectra displayed on the bottom right. Note that there is vignetting on the detector discussed in section 4.1.3 & 4.2

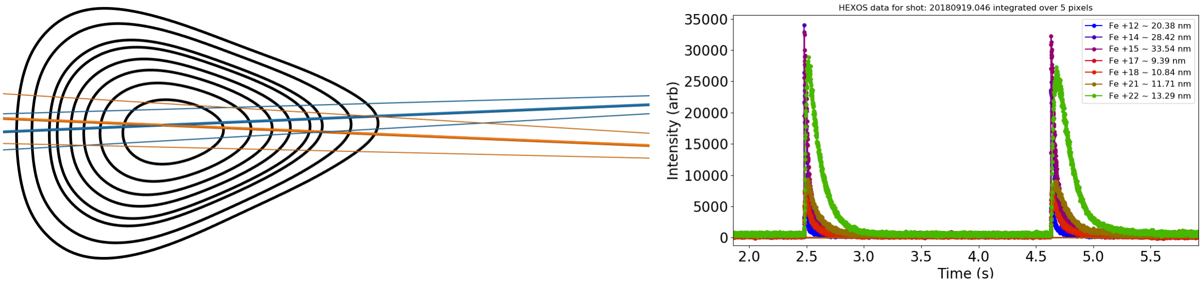

Figure 2.4: HEXOS's single, central sightlines for detector 2 & 3 are shown with limiting rays in the same color (detector 2 in blue and detector 3 in orange) and the intersecting flux surfaces on the left. The corresponding iron signals from discharge 20180919.046 for the first two LBO injections are shown to the right

2.2 High-Efficiency eXtreme ultraviolet Overview Spectrometer (HEXOS)

- HEXOS's wide spectral range and kilohertz time-resolution enabled the simultaneous measurements of iron spectral lines' temporal evolution corresponding to chargestates from Fe^{+6} to Fe^{+23}.

The High-Efficiency eXtreme ultraviolet Overview Spectrometer (HEXOS) consists of four different spectrometers acting as one complete set providing a total spectral range from 2.47 to 161.16 nm.[66,67] The wide spectral coverage allows for the measurement of the most intense Mg-like, Na-like, Be-like and Li-like resonance lines for all elements up to $Z = 42$.[66] In addition to the wide spectral coverage, each spectrometer is equipped with a toroidal holographic diffraction grating & microchannel plate in order to minimize aberration effects and increase signal levels enabling a kilohertz time-resolution.

The combination of these beneficial properties made HEXOS a great diagnostic to capture the impurity iron's spectral lines temporal traces during the transport experiments. Although HEXOS was limited to single, central sightlines for each spectrometer as demonstrated in figure 2.4, the wide spectral coverage in the extreme ultra-violet (EUV) & very ultra-violet (VUV) wavelength ranges enabled the observation of the line emission from the lower iron chargestates. The lack of multiple sightlines providing spatial information on the iron transport was compensated by the wide wavelength range allowing for individual lines from Fe^{+6} to Fe^{+23} to be measured and identified. This characteristic is quite important since the electron temperature profiles generally have steeper edge gradients that can better localize the lower chargestates'

Iron ion	Atomic transition	Wavelength (nm)
Fe XIII	${}^3D_3 \longrightarrow {}^3P_2$	20.38
Fe XV	${}^1P_1 \longrightarrow {}^1S_0$	28.44
Fe XVI	${}^2P_{\frac{3}{2}} \longrightarrow {}^2S_{\frac{1}{2}}$	33.54
Fe XVIII	${}^2S_{\frac{1}{2}} \longrightarrow {}^2P_{\frac{3}{2}}$	9.39
Fe XIX	${}^3P_2 \longrightarrow {}^3P_2$	10.84
Fe XXII	${}^2P_{\frac{1}{2}} \longrightarrow {}^2P_{\frac{1}{2}}$	11.72
Fe XXIII	${}^1P_1 \longrightarrow {}^1S_0$	13.29

Table 2.1: The atomic transitions & corresponding iron chargestates measured on HEXOS and used within STRAHL for the modeling of the impurity iron transport.

abundances which in turn provide better transport characterization from a single line-of-sight measurement like HEXOS (see section 5.2.2 for a more in depth discussion). In the iron impurity transport studies performed for this thesis, the iron lines measured using HEXOS and used within the least squares inference of the anomalous transport coefficients are listed in table 2.1. In figure 2.4 the iron lines detailed in table 2.1 and measured by HEXOS are shown for the first two laser blow-off injections of iron during plasma discharge 20180919.046. These time traces demonstrate the high temporal resolution (1 ms time-resolution), the sensitivity of HEXOS's detectors to a trace injection of iron above the background light levels, and the difference in the observed emission decay times among the iron chargestates. To obtain these signals the NIST defined wavelengths were used to identify and select the spectral lines measured on HEXOS with each spectral signal being the sum of five pixels centered around the NIST defined wavelength. After correcting for a negative offset in the summed signals by using the y-intercept from fitting the last second of data (when no plasma is present), each spectral line's signal uncertainty and plasma background need to be determined within the window used for inferring the iron transport coefficients.

In addition to covering the signal processing in section 5.2.2, a sensitivity study was performed on the impact from the iron line emissions' uncertainty estimations on the inferred anomalous transport coefficients. Moreover the distribution of the iron chargestates associated with the measured spectral lines has an impact on the inference of the anomalous diffusion profile as detailed in section 5.2.2. Critically subsection 5.2.2 describes the importance of the iron chargestates' fractional abundance profiles and its effect on inferring a unique anomalous diffusion profile.

2.3 Laser Blow-Off injection (LBO)

- The LBO system enabled the routine and consistent injection of trace impurity iron for performing the iron impurity transport experiments during the on- to off-axis ECRH scan. However the temporal characterization of the LBO injection had significant uncertainties that did contribute to the inferred uncertainties in the anomalous transport coefficients.

The last critical diagnostic for the iron impurity transport studies is the Laser Blow-Off (LBO) injection system that introduces non-intrinsic impurity particles for a distinct, localized impurity cloud in the plasma edge to characterize the transport in W7-X.[68,40] The LBO system consisted of a Q-switched Nd:YAG laser capable of supplying a 1 Joule pulse within a 6 ns full-width half-max at a 20 Hz repetition-rate, a holder with an ability to hold up to eight glass targets, and a remotely controllable lens and mirror system to scan the laser across a glass target. The glass targets were coated through Physical Vapor Deposition (PVD) ensuring an even coating of the desired impurity. Specifically the iron glass targets had a 5 μm thick iron layer grown on a 100 nm thick titanium layer improving the infrared energy absorption of the target. Therefore the combination of the precise layer thickness, measuring the laser energy, and controlling the spot size ($\sim$ 3.5 mm diameter) on the target meant the amount of iron ablated and entering the plasma was consistent, i.e $\sim 1 \times 10^{17}$ iron atoms. Moreover at the line-integrated densities of $\sim 6 \times 10^{19}\ m^{-2}$ and with a total plasma volume of $\sim 30\ m^3$, the total injected iron atoms of $\sim 10^{17}$ was very much in the trace limit ensuring the background plasma was not perturbed.

Although figure 2.4 demonstrates that multiple iron LBO ablations could reliably be injected during a plasma discharge, the exact timing of the iron cloud entering the plasma edge for accurate STRAHL modeling was not well characterized. The combination of laser jitter and the lack of consistent measurements from the fast spectrometer measuring a neutral iron spectral line allowed for relatively large uncertainties in the LBO injection timing, i.e. ~ 5

ms. This forced the least squares minimization wrapper take the exact LBO injection timing as a fit parameter where sections 4.1.4 & 4.2.2 discuss the LBO injection timing's impacts on the inferred anomalous diffusion profile. In addition to the uncertainty in the LBO injection timing, the aforementioned inconsistent measurements of a Fe I line meant the exact temporal shape of the LBO injection was not well characterized. Without an exact characterization of the temporal shape a standard trapezoidal shape was adopted and the inferred anomalous diffusion profile's sensitivity to the LBO injection's temporal shape was tested with detailed in sections 4.2.7 & 5.1.3.

2.4 Electron Cyclotron Resonance Heating (ECRH)

- A robust procedure for capturing both an ECRH power scan and ECRH deposition position scan was developed. Each gyrotron's antenna was moved between plasma discharges for the desired deposition location and during the plasma discharge the gyrotrons would be selectively turned off.

W7-X's electron cyclotron resonance heating system[69] was instrumental in altering the plasma heating profile and the subsequent electron temperature profiles for the iron impurity transport experiments performed for this thesis. The ECRH system for the first divertor campaign on W7-X included 10 separate gyrotrons operating at a frequency of 140 GHz and having a power rating of 1 MW leading to an average power coupled to the plasma of $\sim$ 0.8 MW (see table 1.1 for W7-X basic parameters during the first divertor campaign). In order to increase the likelihood of successful ECRH power and position scans during the iron impurity transport experiments, the plasma-facing gyrotron antennae[70] were pre-moved to their desired positions and then during the plasma discharge the gyrotrons were selectively turned off as power was stepped down. This plasma discharge plan is demonstrated in figure 2.5, where the total ECRH power is plotted with the individual gyrotron's contributions shown below and with the LBO injections indicated by the measured HEXOS iron spectral lines. All of the iron impurity transport experiments shown in this thesis were performed with ECRH as the only heating source, meaning starting with the highest total ECRH power and stepping down the power by turning

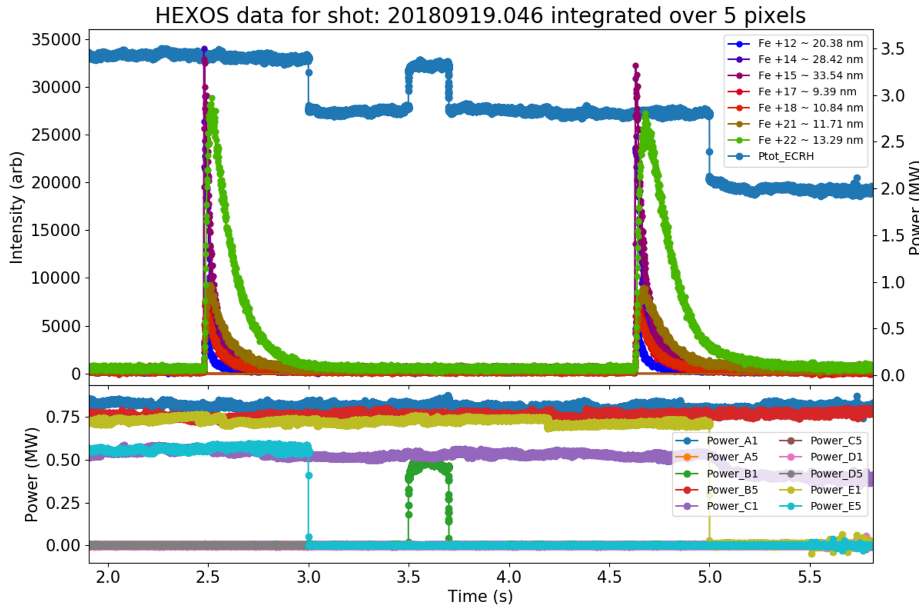

Figure 2.5: The iron spectral lines measured on HEXOS from discharge 20180919.046 are displayed on top of the total ECRH power injected with the individual gyrotrons' powertraces shown below.

off gyrotrons would ensure the plasma discharge would be less prone to a radiative collapse in the beginning. Using this power step-down method and changing the deposition between the discharges provided a robust procedure to obtain the iron impurity transport experiments at the desired heating profile settings.

2.5 Thomson scattering and interferometer

- The thomson scattering measurements were fit using a gaussian process regression technique to determine the electron density and temperature profiles for accurate STRAHL modeling.

The final key diagnostic was the thomson scattering system providing routine electron temperature and density profile measurements.[71] The thomson scattering system consisted of three separate Nd:YAG lasers that shared the same beamline and were phase-shifted from one another turning an individual laser's 10 Hz repetition-rate into a collective measurement rate of 30 Hz. Along the beamline there were 42 optical volumes viewed by the thomson collection optics representing both inboard and outboard measurement locations. Using the three time points centered around an iron LBO injection time the electron temperature and density profiles

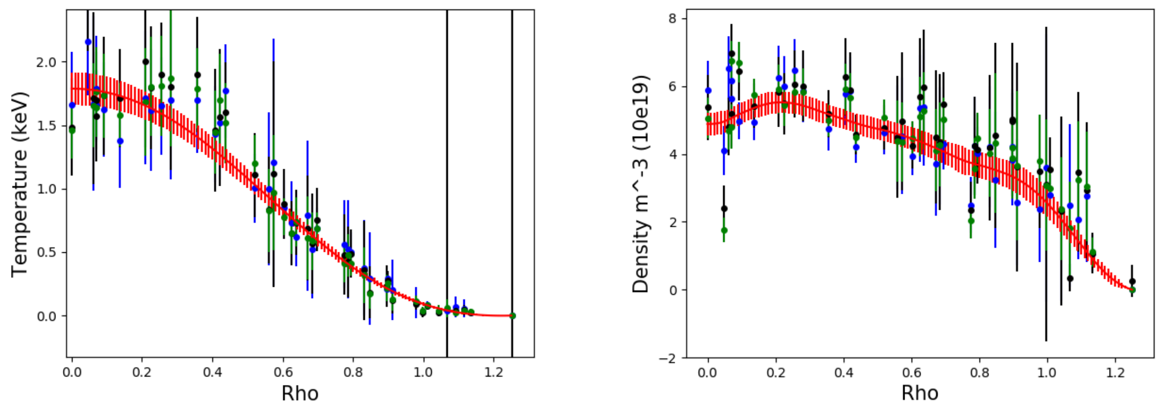

(a)

(b)

Figure 2.6: The thomson scattering electron temperature (a) and density (b) radial measurements for three subsequent times centered around the 1st iron LBO injection from plasma discharge 20180919.046. Shown over the points are the subsequent gaussian process regression fits for the T_e and n_e profiles respectively.

were fit using a gaussian process regression technique.[72] These profile shown in figure 2.6 were used within the STRAHL modeling as time-constant profiles due to the ECRH input power being held constant over the duration of the LBO injection. Also it should be noted that the electron density profile gaussian process regression fit was scaled to the interferometer measurement to ensure that the returned thomson density profile had the same line-integrated density.

The single channel dispersion interferometer provided a central line-integrated electron density measurement for W7-X plasmas.[73] This central line-integrated measurement shared its sightline with the thomson scattering diagnostic's beamline allowing for direct comparisons between the estimated line-integrated density and the radial profiles provided by the thomson system. With time resolutions faster than 1 ms and an accurate estimate for the line-integrated electron density, the thomson's n_e profiles from gaussian process regression fit were scaled to the interferometer's measurement as mentioned.

The iron impurity transport experiments presented in this thesis were performed at approximately the same line-integrated density of $\sim 6 \times 10^{19}\ m^{-2}$ as measured by the interferometer so only the T_e profile varied across the on- to off-axis ECRH dataset. Due to the fact that the ECRH on- to off-axis scans mainly impacted the electron temperature profiles, both synthetic data sensitivity testing (see section 4.2.6) and experimental data sensitivity testing (see section 5.2.3) were performed to estimate the impact of the profile uncertainties on the inferred anomalous diffusion profiles.

Chapter 3

STRAHL modeling and data analysis

The chapter first provides a general overview of the analysis process in evaluating the iron impurity transport experiments. Specifically the overview details the entire process from collecting the experimental data to inferring the anomalous transport parameters from said experimental data. This overview also includes a discussion on the significance of the synthetic data sensitivity studies performed in chapter 4 and the further sensitivity testing performed with experimental data in chapter 5. Following the general overview of the data analysis method, the STRAHL analysis code is presented, highlighting the primary inputs necessary for an iron impurity transport simulation. Finally $lstsq\_STRAHL\_wrap$, the python code written to perform the least squares inference of the anomalous transport parameters, is introduced.

3.1 Overview of the least squares analysis to extract iron transport parameters

3.1.1 General goals of the least squares analysis

The goal of the work performed in this thesis was to determine the radial diffusion and convective velocity profiles of an injected iron impurity in the optimized stellarator Wendelstein 7-X (W7-X) under different plasma heating scenarios. To achieve this goal the general experimental method was to inject a non-perturbative amount of iron at the plasma edge and subsequently measure the iron line emission corresponding to different chargestates. In order to extract transport parameters from the iron impurity diagnostic measurements the one dimensional transport code STRAHL was employed to model both the iron radial transport and the expected iron line radiation. However extracting meaningful radial diffusion and convective velocity profiles from the STRAHL modeling requires that the STRAHL calculated iron line radiation matches the experimentally measured iron line emission. Therefore a python code was written to perform the matching between the experimentally measured signals and the STRAHL modeled signals via a least squares method where the sum of the weighted differences between the experimental and modeled signals are minimized. This python code, named $lstsq\_STRAHL\_wrap$, executes STRAHL within a least squares minimization loop that modifies various input parameters before each STRAHL execution. Critically the updated input parameters describing the radial diffusion and convective velocity profiles can be left as free fit parameters allowing for the minimization to find the most likely iron transport radial profiles given the best match between the measured and modeled signals.[a] In this way an inference of the iron transport profiles can be obtained for each iron impurity injection experiment based on the STRAHL modeled iron line emission that most closely match the experimentally measured signals.

However as a least squares method, the resultant best fit is not guaranteed to be a unique solution meaning that care needs to be taken in both the interpretation of the result and in the consideration of the inference's uncertainties. In order to better understand the sensitivity of various model inputs the $lstsq\_STRAHL\_wrap$ code was written to have the capability to generate noisy synthetic data. As detailed in chapter 4, the noisy synthetic iron line emission, generated using the nominal input values, was then attempted to be matched as if it were experimental data while holding individual input parameters at their low and high estimated values. Therefore given the known inputs that generated the synthetic data, the contribution from each tested model parameter can be evaluated within their estimated variance. This synthetic sensitivity testing gives confidence in the least squares method and understanding about the sensitivity of the inferred transport profiles to key input parameters. Finally in chapter 5 the potential uncertainties inherent to STRAHL and the least squares method were examined. In the discussion of the inherent uncertainties, additional sensitivity studies were performed using real experimental signals providing context for the synthetic sensitivity studies performed in

[a]The anomalous convection velocity profiles were generally not included in the least squares fitting because the synthetic data analysis showed the iron line emission signals were less sensitive to their values (see section 4.2.2) and the experimentally measured signals could be well-matched using only the anomalous diffusion profile (see section 6.1.1)

chapter 4. These additional sensitivity studies performed with experimental signals not only helped reaffirm many of the conclusions from the synthetic studies, but also uncovered aspects of the fitting not previously known.

3.1.2 General procedural method of performing a least squares minimization with $lstsq\_STRAHL\_wrap$

Before the $lstsq\_STRAHL\_wrap$ code can be utilized to perform a least squares minimization between the STRAHL modeled iron line emission and the experimentally measured line emission, the following steps must first be prepared by the user.

1. Generate the STRAHL input files describing background plasma and experimental conditions
   - This includes six separate input files: the magnetic geometry, plasma profiles, the iron atomic data, neutral iron temporal injection, the neoclassical & classical transport coefficients, and the main execution of STRAHL. See section 3.3.1 for more details
   - In order to generate the neoclassical & classical transport coefficients the Neotransp code[74] which takes in plasma profile data as an input needs to be executed first. See section 3.3.1 and 5.1.4 for more details.
2. Generate the $lstsq\_STRAHL\_wrap$'s input file describing the iron emission lines
   - This includes such information as each diagnostic signal's corresponding chargestate, the path to each diagnostic signal's data file & sightline data file, the time window, each diagnostic signal's shot noise, background signal to be added, etc. See section 3.3.2 for more details
   - In order to execute a least squares fit with $lstsq\_STRAHL\_wrap$ each signal's data and time must be stored in .csv files.
3. Specify the initial conditions within $lstsq\_STRAHL\_wrap$ for the first execution of STRAHL within the least squares minimization with the nominal settings detailed below

- Six spline-knots specifying the anomalous diffusion profile with only the four interior knots unique. The nominal initialization is 0.1 $\frac{m^2}{s}$. See section 3.3.1 and 5.2.1 for more details.
- The anomalous convection velocity has the same spline-knots specification, however the nominal scenario fixes their values at 0 $\frac{m}{s}$.
- Each STRAHL-modeled signal has its own free fit scale factor and two fixed parameters specifying any background signal. See section 3.3.3 for more details.
- Although the width of the scrape-off-layer, the distance to the limiter, the connection length to the divertor, the connection length to the limiter, and the Mach number are all specifiable as free fit parameters they are typically held at fixed values. See section 5.1.5 for more details.

Once the above tasks have been performed the $lstsq\_STRAHL\_wrap$ code can be executed. Internally the $lstsq\_STRAHL\_wrap$ code uses the mpfit python module which employs a Levenberg-Marquardt least squares minimization routine to obtain the resultant fit parameters. Once the $lstsq\_STRAHL\_wrap$ code executes it performs the following actions.

1. The experimental signals are read into a python dictionary and then flattened into a one-dimensional array. See section 3.3.2 for more details.

2. A dictionary is formed with the all of the input parameters (including those that are held at fixed values) and their characteristics (e.g. bounded limits, step size, etc). See section 3.3.1 for more details.

3. Through the least squares python module the main STRAHL input file and $lstsq\_STRAHL\_wrap$'s parameter dictionary is passed via command line to execute STRAHL. See section 3.3.1 for more details.

4. Within the STRAHL execution the listed diagnostic iron emission lines in the STRAHL atomic data file are calculated on the native STRAHL spatiotemporal grid.

5. The STRAHL diagnostic iron emission lines on the native STRAHL spatiotemporal grid are then modified according to the $lstsq\_STRAHL\_wrap$'s parameter dictionary with appropriate line-integration, time axis shifts, background signal addition, total signal scaling, and time & space grid interpolations to create the modeled signals that most accurately reflect the experimental signals. See section 3.3.3 for more details.

6. Mpfit, the internal Levenberg-Marquardt least squares minimization module, then calculates the total $\mathcal{X}^2$, the sum of the squares of the weighted residuals between the STRAHL-generated signals and the experimentally provided signals. See section 3.3.1 for more details.

7. Mpfit then adjusts the free parameters within $lstsq\_STRAHL\_wrap$'s parameter dictionary (e.g. diffusion spline-knot values, signal scale factors, etc) to re-run STRAHL for another total $\mathcal{X}^2$ evaluation. See section 3.3.1 for more details.

3.2 Impurity transport modeling using STRAHL

3.2.1 STRAHL modeling basics

- The one dimensional transport code STRAHL was used to model both the iron impurity's radial transport and spectral line emissivity in W7-X.
- To successfully execute STRAHL six separate input files are required: the magnetic geometry, plasma profiles, the iron atomic data, neutral iron temporal injection, the neoclassical & classical transport coefficients, and the main execution of STRAHL

The one-dimensional code STRAHL[75] was employed to model both the iron impurity's radial transport and spectral line emissivity in W7-X. The radial transport equation that STRAHL solves for an impurity I in chargestate Z is reproduced in equation (3.1) from the STRAHL user manual where $n_{I,Z}$, $\Gamma^{\rho}_{I,Z}$, and $Q_{I,Z}$ are the particle density, flux density, and sources/sinks respectively.[76]

$$\frac{\partial n_{I,Z}}{\partial t} = -\left(\frac{\partial V}{\partial \rho}\right)^{-1} \frac{\partial}{\partial \rho}\left(\frac{\partial V}{\partial \rho}\langle \Gamma^{\rho}_{I,Z}\rangle\right) + Q_{I,Z}$$

$$\frac{\partial n_{I,Z}}{\partial t} = -\frac{1}{r}\frac{\partial}{\partial r} r\langle \Gamma^{r}_{I,Z}\rangle + Q_{I,Z} \tag{3.1}$$

Equation (3.1) shows the resultant cylindrically-approximated continuity equation indicated by the transformation of the volume V from the flux surface label ρ into a cylindrical radius r. As shown above and detailed in the STRAHL user manual, [Dux R. 76], the radial continuity equation is solved for each impurity ionization stage allowing for the spatiotemporal evolution of the ionization stages to be modeled for a given diffusive and convective flux. The diffusive and convective flux include options for neoclassical and anomalous channels whereby the sum of the chosen channels is utilized in the numerical solution of the impurity transport. The goal of the STRAHL modeling in this thesis is to infer the most-likely impurity transport coefficients based on the matching between the iron line emission measured by the W7-X spectroscopic diagnostics, detailed in chapter 2, with the STRAHL calculated signals.

With the numerical structure and discussion of input parameterization for STRAHL found in a number of resources, [75, 76, 3], the primary focus of this section is the execution of STRAHL especially in the context of utilizing STRAHL within a least squares minimization routine. In particular STRAHL requires six separate input files for the successful execution, where generally the files describe the magnetic geometry, plasma profiles, the iron atomic data, neutral iron temporal injection, the neoclassical & classical transport coefficients, and the main execution of STRAHL. Examples of each file can be found in appendix C and more details pertaining to the uncertainties introduced from STRAHL on the inferred transport coefficients are discussed in 5.1 For the modeling performed in this thesis, the geometry file (grid_nnnnn.i) only has importance for the specification of the major and minor radii. The plasma profiles input file (pp_nnnnn.i) contains the stationary profiles of electron density & temperature, ion temperature, and neutral hydrogen density profiles. The iron atomic data file (Fe.atomdat) contains all of the switches and pointers for enabling the atomic processes and their respective ADAS[77] files. These supporting atomic data files encompass the ionization (scd00_fe.dat), recombination (acd85_fe.dat), thermal charge exchange (ccd89_fe.dat), and importantly the photon emissivity coefficients for each spectral line (e.g. ben#fe14.dat). It is these diagnostic spectral lines listed in the atomic data file that will have their emission calculated on the inherent STRAHL spatiotemporal grid that will then be used within $lstsq_STRAHL_wrap$ to have their sightlines integrated before comparing to the experimentally measured line emission signals. In order for STRAHL to calculate the diagnostic spectral lines, each iron spectral line needs a corresponding photon emissivity coefficients file detailing the variation with density and temperature. All the supporting atomic data files need to be prepared beforehand through existing temperature and density varying database files from ADAS or calculated using the current ADAS codes.[77] For the modeling presented in this thesis all of the supporting atomic data files were the exact ones used in the previous iron impurity transport work on W7-X performed by [Geiger et al. 7]. Next, the iron flux file (Feflxnnnnn.i) describes the source of neutral iron particles and is important to highlight not only for the critical sensitivity the inferred transport profiles show to the temporal source description[b], but also for its use within the least squares minimization as the file gets automatically rewritten for every STRAHL execution ensuring that the correct LBO injection time parameter is used. The neoclassical & classical transport coefficients file (D_and_v_for_strahl.out_nnnnn.i) contains the radial profiles for the total diffusion and convection velocities for each iron chargestate. As discussed in section 1.2.1, the W7-X optimization leads to the classical transport to be on the same order as the neoclassical transport meaning that it was necessary to calculate and include the classical transport coefficients. To accomplish this the Neotransp code[74] was utilized (see section 5.1.4 for more discussion on the neoclassical & classical transport calculations) to generate the charge-dependent classical transport coefficients and add these values to the DKES[53] generated neoclassical coefficients. Finally the STRAHL main input file contains the calculation details (e.g. specification of temporal & spatial grids, the corresponding step sizes, the pointers to the geometry & plasma profile input files, etc), the impurity type(s) & source description, the plasma boundary characterization, and importantly the anomalous transport channel parameterization. Therefore this main input file is critical to the least squares minimization since the anomalous transport coefficients' radial

[b] See sections 4.2.7 and 5.1.3 for details on how the iron LBO parameterization contributes uncertainty to the inference of the transport profiles

```
                                                Connection lengths [m]      Mach #
cv#     r_bound-r_lcfs (cm)  r_lim-r_lcfs(cm)    to divertor   to limiter     SOL Flow
          10.0                  10.0                250.          1.            0.2
```

Figure 3.1: Example of STRAHL main input file edge parameterization

profiles are the primary parameters that will be inferred and utilized to match the STRAHL-generated iron emission with the experimental signals.

In summary these six input files describing the magnetic geometry, plasma profiles, the iron atomic data, neutral iron temporal injection, the neoclassical & classical transport coefficients, and the main execution of STRAHL need to be prepared before a successful STRAHL execution can be performed (see appendix C for example input files). Many supplementary python codes were written in the course of this thesis project to not only calculate the necessary data (e.g. reading in and generating the plasma profiles using a gaussian process regression, running Neotransp for neoclassical & classical transport coefficients, etc.), but also generate/modify the necessary input files for a successful STRAHL code execution.

3.2.2 STRAHL scrape-off layer parameterization

Due to its importance and impact, an accurate description of the STRAHL parameterization of the scrape-off layer, SOL, is detailed below. The inferred anomalous diffusion can be directly impacted by the SOL parameterization because this region determines the iron impurity fluxes both as a source and sink. Therefore it is critical to correctly establish the edge parameters within STRAHL to ensure accurate anomalous transport inferences. STRAHL separates the SOL into two distinct regions where the first region, closest to the last closed flux surface, connects with the divertor and the second region, furthest from plasma axis, connects to the limiter. As seen in figure C.6 there are two distance parameters $r\_bound - r\_lcfs$ and $r\_lim - r\_lcfs$ which specify the total width of the SOL and the location of the limiter respectively. The values shown in figure 3.1 are the typical values used in this thesis work, where the SOL is 10 cm wide with the limiter placed at outermost edge of the divertor-connected region. In terms of the STRAHL modeling these values translate the limiter-connected region to be the outermost two points of the radial grid, or a $\sim$ 1 cm radial extent. The next two parameters listed are the connection lengths for the divertor and limiter regions of the SOL respectively. These connection lengths are critical in determining the characteristic loss time, $\tau_{\|,edge}$, for each region as seen in equation (3.2).

$$\tau_{\|,edge} = \frac{L_C}{v_{flow}} \qquad\qquad v_{flow} = M\sqrt{\frac{k_b\left(3T_i + T_e\right)}{m}} \tag{3.2}$$

Also equation 3.2 demonstrates the importance of the local flow velocity, which depends on the kinetic profiles, the main ion's mass m, and the mach number M, in determining the characteristic loss time. In fact from a sensitivity perspective on altering the iron loss rate, changing the Mach number (hence flow velocity) is analogous to changing the connection length. Fortunately with a non-recycling impurity like iron, return fluxes from the limiter or divertor do not need to be considered meaning only impurity loss rates are necessary. Equation (3.3) shows it is the ratio of the edge anomalous diffusion and the parallel loss time constant that determines the radial flux loss rate for a chargestate Z.

$$\Gamma_Z = n_{Z,edge}\sqrt{\frac{D_{edge}}{\tau_{\|,edge}}} \tag{3.3}$$

Therefore with the edge anomalous diffusion value coupled into the edge loss rate, establishing an accurate as possible approximation of $\tau_{\|,edge}$ is vital. The Mach number was set to a value of 0.2 based on average Mach probe measurements in similar experiments and modeling for the standard magnetic configuration.[78] In [Sinha et al. 79] the median and mean connection lengths for the typical magnetic configurations used by W7-X are listed. Thus a 250 m divertor connection length was specified since it corresponds to the mean connection length for the W7-X standard magnetic configuration, which was the configuration used for these iron impurity transport experiments. In [Killer et al. 80] the SOL's outermost few centimeters show a dramatic drop in the connection length for all the magnetic configurations from tens of meters to ones of meters. Therefore the connection length for the limiter, concerning the $\sim$ 1 cm outermost radial extent, was estimated to be on the order of the 1 m.[c]

[c] An 1 m limiter connection length was used here also to be consistent with the analysis done in [Geiger et al. 7]

3.2.3 Model assumptions particular to the on- to off-axis dataset analysis

In the process of performing the synthetic data sensitivity studies in chapter 4 and experimental data sensitivity studies in chapter 5, it became obvious that the systematic errors introduced from model inaccuracies had much larger impact on inferring unique and accurate transport profiles than the random errors introduced in the noisy signals. Due to this conclusion, the model used in $lstsq_STRAHL_wrap$ had to be reduced in order to have reasonable comparisons of inferred anomalous diffusion profiles for the on- to off-axis datasets shown in chapter 6. The model assumptions used in the on- to off-axis dataset analysis included:

- Ensuring the SOL parameterization, discussed in section 3.2.2, was fixed across each on- to off-axis dataset since at a constant total ECRH power there should be minimal edge profile variations among an on- to off-axis dataset
  - Holding the anomalous edge diffusion value at a fixed value of D_{edge} = 0.15 $\frac{m^2}{s}$ as described in section 6.1.1
  - Setting all of the T_e SOL profiles in an on- to off-axis dataset equal to the on-axis scenario's T_e profile as discussed in section 6.1.1
  - Setting the T_i profile equal to the T_e profile in the SOL as discussed in section 6.1.1
- Shifting down the anomalously high T_i profiles to more representative levels as described in section 5.2.3
- Restricting the spline-knots to stationary positions to restrict the model from finding non-unique solutions with nonphysical gradients in the inferred anomalous diffusion profiles as discussed in section 5.2.1

3.3 Python least squares wrapper for STRAHL: $lstsq\_STRAHL\_wrap$

In order to accomplish the task of determining the most-likely anomalous transport profiles that are present in the iron impurity transport experiments performed for this thesis work, a python least squares minimization routine, $lstsq\_STRAHL\_wrap$, was written to execute STRAHL and infer these anomalous transport coefficients. The least squares inference routine was designed around the mpfit python module that was originally written for IDL, see [81] for more details. Broadly the python routine is separated into three main portions: the STRAHL execution and minimization of $\mathcal{X}^2$, the handling of experimental signals, and the manipulation of the STRAHL-generated line emission. The structure of the code is very basic with a single class creating a least squares fitting object with the functions and attributes to perform a full least squares minimization between the experimental signals and the STRAHL-generated line emission. Although the least squares minimization python wrapper has a basic structure, it still flexible enough to accommodate the rapid re-execution from resultant least squares fit, the rapid exclusion/inclusion of signals & signal types, and simple control over the parameterization of the radial anomalous transport coefficient profiles. The following subsections will discuss the idosyncrasies of mpfit & how it was utilized to execute STRAHL, the handling of input experimental signals & their associated parameters, and finally the STRAHL generation of the corresponding iron line emission signals.

3.3.1 STRAHL execution & mpfit characterization

- $lstsq\_STRAHL\_wrap$ was written with a single class to perform the least squares minimization using the mpfit module [81]. The STRAHL execution was performed via writing to the command line taking advantage of STRAHL's ability to read input data from the terminal when properly commented within its main input files.

- The mpfit module required the input data to be one-dimensional meaning that signals had to be carefully ordered to ensure the signal appending was performed in the correct order regardless of which signals were chosen.

- The acceptance of keywords as a list within mpfit not only allowed all of the relevant parameters to be explicitly included within a least squares minimization, but also facilitated fast and simple re-executions of $lstsq\_STRAHL\_wrap$ by simply reading in this parameter information list from a previous code execution.

As mentioned above the python wrapper creates a single class that is structured with the necessary attributes and methods to perform a least squares inference of the anomalous transport profiles. One of the integral methods of this class is the function that executes STRAHL. In particular this method interacts with STRAHL through the command line since STRAHL is a compiled Fortran program that is structured to use in a stand-alone manner. STRAHL was designed to facilitate scans that might only vary by a few different parameters and in fact has multiple ways to control these scans.[76] The method chosen was to indicate in the input files which data should be read externally, where technically STRAHL will first look to read the data from a file named ext_parameter.dat but if this file isn't found it will expect the indicated data from the command line.[d] Therefore within the main input file the data blocks corresponding to the neutral iron source, the characteristics of the plasma boundary region, and the anomalous transport coefficient specification were all labeled to be read from the command line, see appendix C for an example main input file. In this way the values listed within these data blocks could all be included as parameters within mpfit, creating a convenient process to modify and pass the values to STRAHL during a least squares minimization.[e]

In addition to executing STRAHL and passing some of the main input file's parameters through STRAHL's command line execution option, $lstsq\_STRAHL\_wrap$'s STRAHL execution method also calculates the anomalous transport coefficients' radial profiles based on the number of spline-knots and their associated values. This is an important aspect of the method because including too many spline-knots will not only lead to overfitting, but also increase the computation time necessary for mpfit to find an adequate solution. $lstsq\_STRAHL\_wrap$'s STRAHL execution method input includes the number of spline-knots and the specific radial positions defining the interior boundary of the core & edge, outside of which the anomalous transport coefficients are forced to be flat. Specifically the radial parameterization is designed such that the most interior and most exterior spline-knots are fixed to their neighboring spline-knot's value, meaning the number of uniquely inferred spline-knots will always be two less

[d] STRAHL uses the free format read function in Fortran77 for reading in the parameters from the input files and uses cv␣ as an indicator to read in the data below the current line. Changing cv␣ to cv# indicates that STRAHL should read the data externally.

[e] In order to initiate the STRAHL execution, the data blocks are converted into strings and issued to the command line via the subprocess python module's check_output() command.

than the total number specified to the STRAHL execution method. Therefore the minimum number of spline-knots for a given anomalous transport coefficient's radial profile is four: two on the absolute boundary of the STRAHL radial profile (e.g. $\rho = 0$ & 1.2) and two defining the inner points of the core & edge region (e.g. $\rho = 0.1$ & 1.1). If more than four spline-knots are specified the remaining interior spline-knots are equally spaced radially inbetween these forced flat regions. Due to concerns of overfitting and coefficient values exceeding realistic limits, the number of spline-knots passed as fit parameters for the analysis in this thesis was six.[f] Finally a monotonic cubic spline is used to interpolate these radial spline-knots onto the STRAHL radial grid ensuring that there are no extrema between the spline-knots and that the anomalous transport profiles are smooth. It is these interpolated anomalous transport profiles that are written to the command line during a STRAHL execution using the subprocess python module.

Moving onto mpfit, the python module used to perform the least squares minimization, the first aspect of mpfit to discuss is the necessary inputs for successful integration within the entire python wrapper. Specifically mpfit's main input requirement is a user-defined function that calculates & returns the total residual according to equation (3.4), where $\mathcal{X}$ is the weighted residual that is calculated using the 1-sigma uncertainties (σ_i), the experimental signals ($\mathrm{Y}_i^{\text{measured}}$), and the modeled signals ($\mathrm{Y}_i^{\text{calculated}}$).

$$\mathcal{X} = \sum_{i=1}^{N} \frac{\mathrm{Y}_i^{\text{measured}} - \mathrm{Y}_i^{\text{calculated}}}{\sigma_i} \tag{3.4}$$

It should be noted that the mpfit module internally uses a Levenberg-Marquardt algorithm to minimize the summed squares of the residuals shown in (3.4) for the given signal data and modeled data.[81] In addition to the user-defined residual function, mpfit's only other required input is an array with the starting values for all the parameters used within the model to calculate the signals for comparison, i.e. $\mathrm{Y}_i^{\text{calculated}}$. Naturally the user-defined residual function also needs these parameter values as an input since it is necessary to update the modeled signals as mpfit varies these fit parameters. Although mpfit only requires these two inputs for successful least

[f]The reader is encouraged to see sections 4.1.2 and 5.2.1 for discussion on anomalous transport coefficient radial parameterization and the associated uncertainties.

squares minimization, mpfit has the ability to accept both keyword data useful for the functions calculating the modeled signal and additional data on parameter fit properties. In fact the ability to pass keyword data to the functions used to execute STRAHL is the first mpfit characteristic that impacted $lstsq\_STRAHL\_wrap$'s design. The ability of mpfit to accept the STRAHL execution method's keywords was invaluable for passing the variables describing the location and the number of spline-knots to this method without the need to create individualized class attributes for each variable. The next two characteristics of mpfit that had the most profound impact on the implementation of the python wrapper were the necessity of the input data to be one-dimensional and the ability to apply sophisticated control on the fit parameters via a list of python dictionaries.

The one-dimensional requirement on the input data meant that signals had to be carefully parsed and coordinated to ensure not only that the appending of each signal was performed in the correct order regardless of which signals were chosen, but also that the corresponding STRAHL modeled signals were accurately selected for the residual calculation. This challenge to allow for user flexibility in selecting the spectral lines to perform the least squares minimization led to an implementation of a json formatted input file that is both easily readable/modifiable by python and by users. An example of the json input file specifying the selected experimental signals and their associated signal parameters can be found in appendix D with a snippet shown in figure 3.2. Although this will be discussed in detail in the following subsection, it is important to note that due to the organization of the nested dictionaries in json format both line-integrated and inverted signals can be passed into STRAHL. In this way the signals can be properly handled and ordered such that any two-dimensional data like inverted data from the HR-XIS diagnostic could be correctly flattened into a one-dimensional array before being appended to the total signal array for least squares minimization.

The next critical characteristic of mpfit is its ability to accept via keyword a list of python dictionaries detailing every parameter's properties. Unlike the one-dimensional constraint, this characteristic not only simplified the process of performing a least squares minimization, but also added practical control over every parameter. Each parameter as an element in the list passed to mpfit contained dictionaries about the parameter's value, its limits, its stepsize, whether it was fixed, its description, etc. (see [81] for more information). In this way all of the relevant parameters can be explicitly included within a least squares minimization using mpfit even if such parameters are usually invariant (e.g. SOL characteristics). This makes cross comparisons between resultant least squares minimizations easier to perform due to the transparency of the included parameters and their properties. Finally this mpfit characteristic facilitates fast and simple re-executions of $lstsq\_STRAHL\_wrap$ by simply reading in this parameter information list from a previous code execution that was written to a json file (more details in the following subsection).

3.3.2 Experimental data handling

- A json formatted file structure was created to organize all of the necessary information associated the input signals to be used within the least squares minimization. The utility of the json structure with its standardized keywords is that a user can easily add/subtract entire signals or their properties providing for rapid modification of a least squares run.

In the previous subsection there were two characteristics of mpfit that defined how the experimental data should be read in and prepared for the least squares minimization. The first was the requirement that the data arrays given to mpfit needed to be one-dimensional. The second was the ability of mpfit to take a singular list of all of the parameters & their fit properties. These two characteristics combined with the desire to have the code be simple yet flexible for adding/removing signals meant that it was best to handle the signals through a single input file. Therefore a json formatted file containing all of the necessary information associated the input signals was created. As shown in figure 3.2 (see appendix D for complete example file) the json formatted file utilized nested python dictionaries where the keys referenced the corresponding iron chargestate, the signal type, and finally the signal number before listing the signal information. The reasoning behind this choice was to provide a template that could accommodate almost every scenario while still being able to have precise control over the signals to be fit. Not only could a single iron chargestate have multiple different spectral lines measured, but also could have multiple signals corresponding to the same spectral line. For example, the x-ray imaging spectrometer systems can provide multiple sightlines through the plasma for the

```
"22": {
    "lineintegrated": {
        "1": {
            "name": "20180919.049_signalFeXXIII_data_from_detect_2_intensity_corrected_over_1000_pixel_width_5",
            "typeofsignal": "lineintegrated",
            "detector": "hexos2",
            "elementsymbol": "Fe",
            "title": "Fe XXIII ~ 13.28 nm",
            "chargestate": 22,
            "backgroundnoisesig": 300,
            "scalingshotnoisesig": 1.24381819,
            "starttime": 6.19,
            "endtime": 6.50,
            "typeofbackground": "linear",
            "slope": 22.59847441,
            "yintercept": 351.73259213,
            "scaleguess": 4.0,
            "rhofilename_lineofsight": "/draco/u/petr/Peter_Python/w7x_20180919.049_HEXOS_sightline_rhopos_fordetector_2.csv"
        }
    }
},
"24": {
    "lineintegrated": {
        "1": {
            "name": "20180919.049_qsx_Wline_horpixel_36to50_vertpixel_1290to1331",
            "typeofsignal": "lineintegrated",
            "detector": "qsx",
            "elementsymbol": "Fe",
            "title": "Fe XXV ~ 1.85 nm (W-line)",
            "chargestate": 24,
            "backgroundnoisesig": 0.0,
            "scalingshotnoisesig": 1.0,
            "starttime": 6.19,
            "endtime": 6.50,
            "typeofbackground": "linear",
            "slope": 1.34461305,
            "yintercept": 0.03704084,
            "scaleguess": 1.6,
            "pixelindex": 1310,
            "rhofilename_lineofsight": "/draco/u/petr/Peter_Python/w7x_20180919.046_HRXIS_sightline_rhopos_forpixel_1310.csv"
        },
```


Figure 3.2: A small portion of the json formatted experimental signal input file used by $lstsq\_STRAHL\_wrap$ is shown with the line emission corresponding to $Fe^{+}22$ and $Fe^{+}24$ displaying the necessary signal information/characteristics for completing a least squares minimization.

same spectral line or these same signals can be used to find an inverted emissivity as a single two-dimensional signal type. Also for future experiments additional diagnostics measuring line emission from the same chargestate could be available (e.g. including the Q-line or the beta line), underscoring the importance of including the signal number as a key in this json format. Under the three signal-identification keys of chargestate, signal type, and signal number are the signal properties necessary to complete a least squares minimization. The power of using the json structure is that a user can easily change these signal properties, can add or remove additional properties, and importantly reference these properties by a standardized label. For example, although figure 3.2 shows the signal properties of spectral lines corresponding to the HEXOS and HR-XIS diagnostic measurements, they have the same keys with the only difference being the HR-XIS diagnostic having an additional property of "pixelindex".

In terms of the experimental data handling the only standardized keys used within the python wrapper to specify/modify the experimental signals are "name", "starttime", "endtime", "backgroundnoisesig", and "scalingshotnoisesig". Specifically these standardized keys were used to define the experimental signals ($\mathrm{Y}_i^{\text{measured}}$) and 1-sigma uncertainties (σ_i) from equation (3.4) by identifying the signal's input file, defining the signal window, and providing data for calculating the uncertainties for every signal type. Note that the experimental input data was saved to a csv file rather than read directly from the W7-X archive in order to perform the least squares fitting on any machine with a linux environment for a STRAHL installation. Therefore just like the STRAHL input files were prepared in advance, each spectral line had its time & emission intensity saved to file and moved to the appropriate folder before a least squares minimization was performed.[g] These time & emission intensity files included an entire plasma discharge, possibly encompassing multiple LBO injections, meaning the "starttime" and "endtime", given in seconds after plasma initialization, were critical in slicing the correct data to be fit. Finally the weights, $\frac{1}{\sigma_i}$, used within the least squares minimization of the residual from equation (3.4) were calculated within $lstsq\_STRAHL\_wrap$ according to equation (5.2)

[g]See section 2.2 for details on how the signal pre-processing was performed.

using the data given by “backgroundnoisesig” ($\sigma_{\text{background}}$), and “scalingshotnoisesig” (α), and the emission intensity.[h]

After understanding how individual signal properties are handled, it is important to return to the discussion of how the entire json formatted input file is parsed into single, one-dimensional arrays for the experimental signals ($\mathrm{Y}_i^{\text{measured}}$) and 1-sigma uncertainties (σ_i). As briefly mentioned before the three signal-identification keys of chargestate, signal type, and signal number were used to categorize and order the signals in a standardized way. The hierarchy followed the nested key structure where the line emission signals were ordered by their corresponding chargestate from high to low then followed by signal type with inverted data placed before line-integrated data and finally by signal number from low to high. Following this ordering all of the individual signals are appended together forming the necessary one-dimensional input data array ($\mathrm{Y}_i^{\text{measured}}$) and uncertainty array (σ_i) for the least squares minimization. Subsequently these arrays are assigned to instance variables (e.g. self.data) of the least squares fitting class within the STRAHL python wrapper so that the class methods (e.g. self.residual) can easily access the data.

The overall process for the experimental data handling starts with the spectrometer data being read from the W7-X database, saved to comma separated value (csv) files after minor pre-processing (see section for more details 2.2), moved to the appropriate directory where the STRAHL execution will occur, loaded into class instance variables via the pre-established json formatted input file, before finally being used within mpfit to minimize the square of the residuals. Therefore the json formatted input file with its standardized keywords is the critical piece that provides the code with the flexibility to change the input data simply and effectively.

3.3.3 STRAHL-generated line emission

- The raw STRAHL generated line emission was matched with the corresponding experimental signals and their associated parameters from the json formatted input file to correctly modify the STRAHL signals. The raw STRAHL signals were line-integrated, had

[h]See section 5.2.2 on the details of how the signal uncertainties were calculated and on how it contributed to the inferred anomalous diffusion’s uncertainties.

background signals added, and finally scaled to match their corresponding experimental signal.

- A class method was written to generate synthetic line emission data by executing STRAHL before adding normally distributed noise to each signal. This method was used extensively for the sensitivity testing performed in chapters 4 & 5

The final major aspect of $lstsq\_STRAHL\_wrap$ to discuss is the code's handling of the STRAHL-generated iron line emission. As previously mentioned in section 3.2, STRAHL calculates all of the spectral lines listed in the atomic data file and saves this spatiotemporal emission within STRAHL's netcdf output file in the order listed. Therefore in the formation of the total model signal array, $\mathrm{Y}_i^{\text{calculated}}$, it was necessary to append the modeled spectral lines in the order corresponding to the total experimental signal, $\mathrm{Y}_i^{\text{measured}}$. To put it simply $lstsq\_STRAHL\_wrap$ takes the synthetic diagnostic output from STRAHL and generates an array in the correct order that can be used to calculate a residual. The ordering within this array is controlled by the json formatted input file. To accomplish this task a function was written to read the atomic data file extracting an ordered dictionary with each chargestate as a key storing the corresponding spectral line's wavelength as a value. This dictionary was then used in conjunction with the json formatted input file containing all of the necessary information associated with the experimental signals to not only ensure the correct STRAHL signals are selected, but also to pass along the correct information to modify these STRAHL modeled signals. In this way the same ordering listed in the previous subsection was used to create the total model signal namely that the individual signals are ordered according to the hierarchy of first chargestate (high to low), then signal type (inverted then line-integrated), and finally signal number (low to high).

Before the total model signal array is formed, the STRAHL line emission data needs to be augmented to more closely reflect the measured signals. Specifically the measured spectral emission corresponds to line-integrated measurements that also have background emission not associated with the iron LBO injection. In order to achieve the most accurate modeling as possible, these aspects need to be taken into account in the modification of the STRAHL-generated line emission. Therefore each spectral line's diagnostic geometry and background signal were determined before any least squares fitting took place. This necessary data was then included in the json formatted input file as shown in figure 3.2 with the keywords: "slope", "yintercept", "scaleguess", "rhofilename_lineofsight". To calculate the appropriate line-of-sight integral and add the background signal to the iron line emission, a non-class function was called within the loop that selected the correct modeled spectral line for a given measured signal. This function is an integral part of $lstsq\_STRAHL\_wrap$ since it was written to handle both inverted and line-integrated signal types in addition to performing all the necessary signal modifications such as line-integration, time axis shifts, background signal addition, total signal scaling, and time & space grid interpolations. Within $lstsq\_STRAHL\_wrap$ this function would be called for every model signal each time mpfit executed the residual method underscoring its importance for generating a closest possible model signal.

Line-integration of model signals

- Each line emission signal was line-integrated using the real detector sightlines and had a distinct scale factor as a free parameter within the least squares routine.

To perform the proper line integral and tie in the spatial information into the $lstsq\_STRAHL\_wrap$, each line-of-sight was parameterized as 1 mm spaced cartesian points that were then converted into a radial coordinate based on normalized polodial flux using the magnetic configuration of the experiment. The STRAHL calculated line emission on the native radial grid[i] is then interpolated onto each line-of-sight's normalized polodial flux radial coordinate. Finally each line-of-sight signal is summed over this radial extent completing the equivalent STRAHL line integral before the last interpolation is performed matching the time array of the measured signal. Each line-of-sight has a free scaling factor which is used within the least squares fitting routine meaning the absolute signal intensities (and by extension the iron impurity density) are not fixed. This fact means that the line integral for a sightline only needs the appropriate relative weighting between points along the line-of-sight. Therefore with the even distribution

[i]Remember that for W7-X that the radial unit derived from flux surface volume is essentially the same as the radial unit based on polodial flux see figure 5.1

of points in real space along a sightline, the only possible introduction of uncertainty in the handling of the sightline integral is field of view effects present in the measured signals.

The process of augmenting the STRAHL-generated line emission starts first with the interpolation of the model emission onto the normalized radius values from the measured spectral emission's sightline.[j] The function was passed the pre-calcualted sightline data file through the keyword "rhofilename_lineofsight" from the json input file. After spatially summing the interpolated emission, this entire signal was scaled by the scaling fit parameter which was initialized from "scaleguess".[k] Next the measured time axis is optionally shifted and the now line-integrated & scaled STRAHL-generated line emission is interpolated onto the measured time axis.[l] Finally the pre-determined linear background is added to this modeled signal using the slope, y-intercept, and the measured time axis all specified through the json formatted input file.

The STRAHL augmenting function had an additional critical usage outside its implementation within the least squares minimization routine. Since this function could generate analogous model signals for both line-integrated and inverted data types, it could be used to generate noisy synthetic data to help evaluate the least squares fitting method. Therefore within the least squares fitting class a method was written to generate synthetic line emission data by executing STRAHL. Within this method normally distributed noise was added at realistic levels for each individual signal after being altered by the above-mentioned STRAHL augmenting function. In this way many of the systematic uncertainties that are difficult to estimate could be examined easily. For example, the STRAHL iron flux file was rewritten every time mpfit called the residual method in order to include an LBO timing offset as a fit parameter in the least squares minimization. Only through attempting to fit noisy synthetic data using a non-generating LBO injection timing could the impact of an incorrect LBO injection time be explicitly estimated for

[j]For inverted emission data the sightline integrals are not performed and a two dimensional interpolation is used to map the STRAHL spatiotemporal grid onto the inverted emission's grid.

[k]Note that every modeled signal had an additional constant scale factor of 10^6 multiplied to it in order raise the modeled signal levels up to the same order of magnitude as the measured signal levels.

[l]The capability to shift the time axis was included to test the sensitivity of the inference to mismatches between diagnostics' timing. See section 4.1.4 for more details.

the inferred anomalous transport profiles. The critical usage of the noisy synthetic data generation for estimating the systematic uncertainties present in the least squares fitting method is covered in detail in chapter 4.

Chapter 4

Synthetic data sensitivity studies

This chapter discusses sensitivity studies using noisy synthetic data generated by the forward modeling STRAHL and $lstsq\_STRAHL\_wrap$, the least squares python wrapper discussed in section 3.3. The synthetic data sensitivity studies' primary goals were to capture inherent model limitations and to improve analysis of real experimental data. Specifically the sensitivity studies' goals can be broken down into four main tasks:

- Determine which model inputs, within their uncertainty levels, limit the recovery of accurate transport profiles
- Understand any potential coupling between model input parameters and, where possible, isolate their effect on the recovery of the accurate transport profiles
- Construct a best-practices procedure for performing the least squares minimization with particular inputs as free fit parameters.
- Establish whether the W7-X impurity transport diagnostic set is well suited to accurately infer the transport profiles.

In order to accomplish these tasks, two main sets of synthetic data were generated mirroring the same real LBO injection experiment on W7-X. The following chapter is separated into a discussion of the first and second synthetic data sets, where the former uses artificially-flat transport profiles while the latter uses experimentally motivated transport profiles.

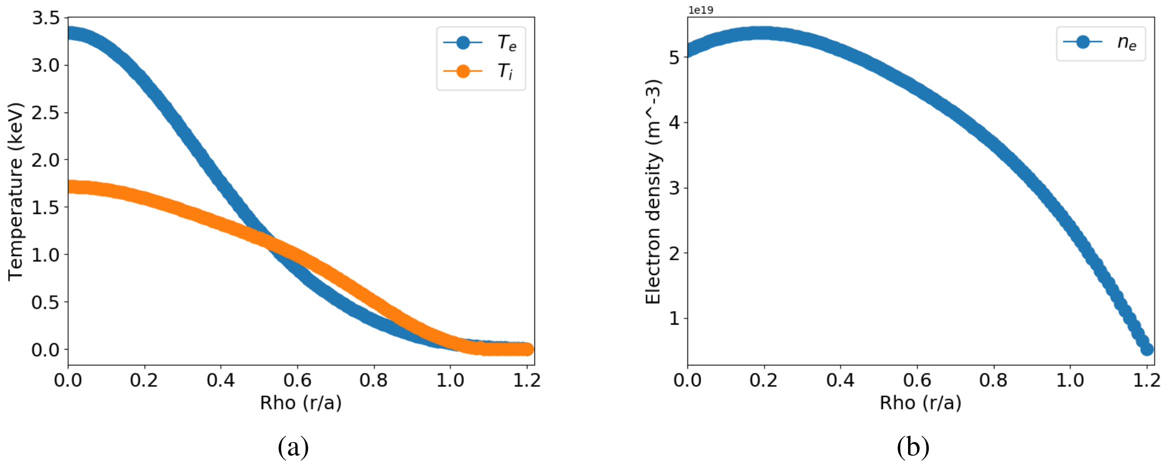

Figure 4.1: Input temperature profiles for the initial synthetic data generation are shown in (a), while the input electron density is shown in (b)

4.1 Synthetic data testing using flat transport profiles

The initial synthetic data study was performed as an intuition building and model testing exercise. Specifically the goal of the initial synthetic data testing was to determine whether the diagnostic measurements on W7-X were well suited to accurately infer the transport profiles. Some of the key questions that needed to be determined were whether the inferred transport profiles are unique, what spline-knot spatial resolution is appropriate, how critical is the spatial and temporal resolution of the input measurements, and which parameters can be freely determined in the fitting procedure.

4.1.1 Model description for synthetic data generation

In order to perform this testing and answer the aforementioned questions, synthetic data was generated using STRAHL and mirroring a real iron LBO injection experiment on W7-X. The synthetic data used input temperature, density, neutral density, and characteristic iron flux modeled after a specific iron LBO injection. Nine different iron spectral lines corresponding to nine distinct chargestates were generated with normally distributed noise and background noise

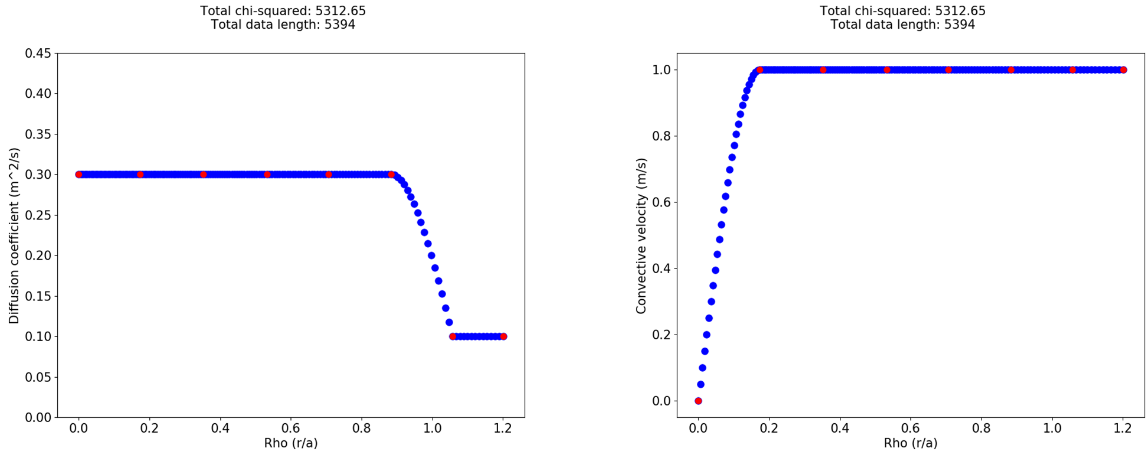

(a) (b)

Figure 4.2: Input anomalous transport profiles for the initial synthetic data generation with the diffusion shown in (a) and convection velocity in (b). The red points represent the spline-knot locations that have a monotonic cubic spline parameterization for the points in-between

added to each signal at levels matched from the chosen discharge.[a] For the helium-like chargestate, a tomographically inverted and central line-of-sight signal representing the w-line were each generated in order to mimic the data obtained from the HR-XIS diagnostic as detailed in section 2.1. Only anomalous transport profiles were used to generate this synthetic data and their profiles were purposefully chosen to be mostly flat at reasonable values, see figure 4.2.

The anomalous diffusion and convection velocity profiles were initialized with eight spline-knots for specifying the radial profile. Analogous to handling of real data, there are three parameters describing each iron spectral line. There are two fixed parameters describing the slope and intercept of linear background noise added in addition to one free magnitude parameter to scale the STRAHL calculated spectral line to the measured signal.[b] In addition to these parameters, a LBO injection timing offset was included within the model as a free fit parameter. As a final check the synthetic data was verified using $lstsq\_STRAHL\_wrap$, the least squares fitting routine, with all of the same generating inputs held at their fixed values and it returned a reduced chi-squared value of $\mathcal{X}_R^2 \sim 1$ with no structure in any of the weighted residuals.

[a]The line emission from FeIX was included within the synthetic data, but has not been utilized in the real data analysis due to the inability to match the signal

[b]It should be noted that for this initial synthetic data the line-of-sight signals did not calculate the proper sightline integral which could effect the spatial information extracted from the iron chargestates. The generation and fitting of the synthetic line-of-sight data were handled in a consistent way.

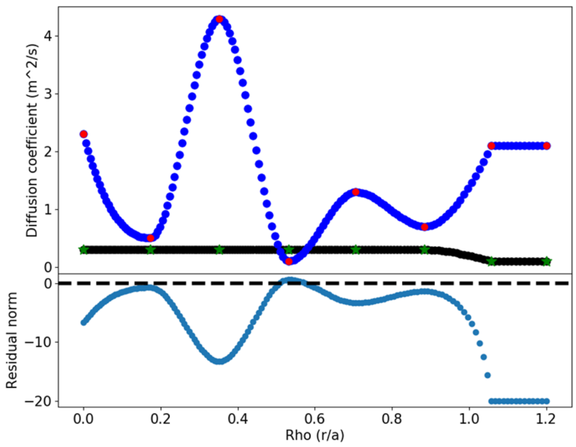

(a)

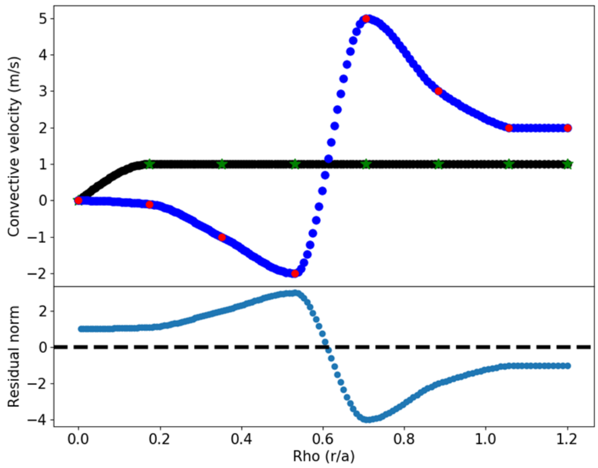

(b)

Figure 4.3: The anomalous transport profiles used to generate the synthetic data are shown in the black with the green star indicating the spline-knot locations. The blue profiles and red spline-knots are the initialization for anomalous diffusion values within the least squares inference.

4.1.2 Radial profile function of anomalous transport

- For the diagnostic coverage and line radiation used, employing eight spatial spline-knots for the anomalous diffusion and convection radial profiles allows for overfitting by the least squares routine

The synthetic data is critical for evaluating the confidence in the radial specifications of the anomalous transport profiles that the least squares fitting routine is attempting to infer. The first illustration of this fact is seen in the number of spline-knots specified as free parameters for the anomalous diffusion and convective velocity profiles. The eight spline-knots for the diffusion and convective velocity were initialized away from the generating values as seen in figure 4.3a and 4.3b, which the least squares routine used as a first estimate to match the signals by varying the knot values and each signal's scaling parameter. As seen in figure 4.4a and 4.4b the blue profiles (with red spline-knot locations) are the resultant inference from the least squares fit. Although these inferred profiles demonstrate the accuracy of the inference due to the close match to the black profiles used to generate the synthetic data, the deviations from core to edge for the diffusion profile and edge to core for the convection profile exhibit an oscillation that is indicative of overfitting. Therefore to understand the variation in uncertainty across the

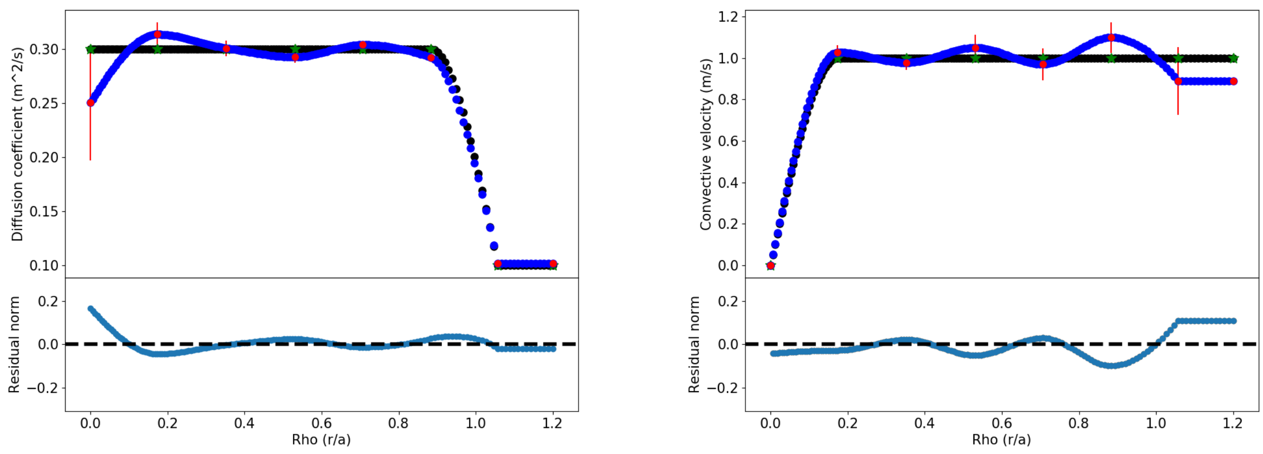

(a) (b)

Figure 4.4: The black profiles are the synthetic data generating transport profiles while the blue are the least squares code's inference. The residuals normalized to the data generating values are plotted below to demonstrate the percent difference from the true transport profiles. The inference had $\mathcal{X}_R^2 \approx 0.99$ with no observable structure in the weighted residuals.

inferred transport profiles, especially in the core region for the diffusion and the edge region for the convective velocity, a closer look will be performed in the next section.

Iron impurity flux analysis

- The anomalous diffusion transport channel is the dominant transport channel during the first $\sim$ 100 ms across the entire radial extent

Examining the total impurity iron flux as seen in equation 4.1 can give some intuition on the impurity density profile evolution after the LBO injection.

$$\Gamma_I = -D_I\left(\nabla n_I\right) + \mathbf{v}_I n_I \tag{4.1}$$

In particular the diffusive flux channel scales with the impurity density gradient while the convective flux scales with the impurity density, meaning that as the iron cloud enters the edge plasma the diffusive flux typically dominates the initial impurity density rise due to the strong impurity density gradient present. This fact can be observed in figure 4.5 with the radial distribution of the iron impurity density evolution in figure 4.5a and the comparison between the

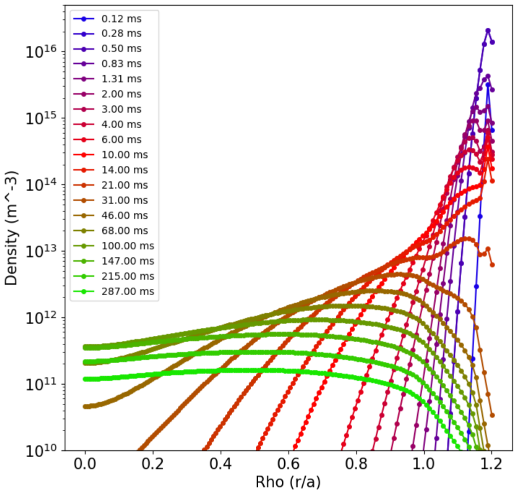

(a)

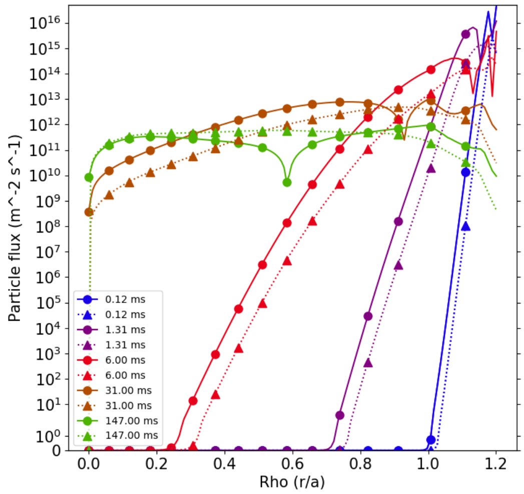

(b)

Figure 4.5: In (a) the radial distribution of the iron impurity density taken at various times after the LBO injection is plotted for the inferred solution in 4.4a and 4.4b. From the same inferred transport profiles the absolute value of the diffusive and convective fluxes are plotted in (b) at the same select times used in (a). The diffusive flux is plotted with circular markers & full lines while the convective flux is plotted with triangles & dashed lines.

absolute value of the diffusive and convective flux channels in figure 4.5b. From figure 4.5b it is clear that the diffusive flux is the dominant transport channel for almost the entire radial extent of the plasma until 147 ms after LBO injection. Each dip observed in the absolute value of the diffusive flux represents the location where the impurity density has peaked and the impurity density gradient is changing sign. As the iron cloud transports inward the spatial distribution of the cloud is extended, decreasing the density gradient and creating regions where the convective flux can become dominant as observed around the dips in the absolute value of the diffusive flux. In this example, it takes $\sim$ 100 ms for the iron impurity density profile to reach an equilibrium shape, after which the convective flux becomes the dominant transport channel in a region stretching from the core to $\rho \sim 0.7$ Consequently the iron line emission from the higher chargestates, Fe^{18+} and up, shows greater efficacy in the inference of the anomalous convective velocity due to their presence in the core and signal length being longer than 100 ms. Therefore the resultant inaccuracy in the core and edge for the anomalous diffusion and convective velocity respectively is completely consistent with which transport channel is dominating both radially and temporally. Even at the relatively low values of anomalous diffusion used in this synthetic data example[c], the anomalous diffusive flux is the primary transport channel for nearly all radial positions and all times before the iron density profile has reach an equilibrium shape. Thus the anomalous diffusive flux should predominantly control the temporal shape of the iron impurity line emission that is used within the least squares minimization to infer the anomalous transport profiles.

Establishing an appropriate number of spline-knots

- The estimated errorbars on the inferred transport profiles calculated from the least squares routine are not guaranteed to encompass the accurate solution even when using the exact noise levels. The systematic errors of using a reduced model or using a model with direct coupling between fit parameters can lead to inaccurate uncertainty estimations.
- Six spline-knots will be used for the anomalous diffusion profile parameterization in the analysis of real experimental data

Armed with an improved understanding of the oscillations in the inferred anomalous transport profiles, reducing the radial resolution of said profiles should minimize any unphysical overfitting. Performing a separate least squares minimization with only five spline-knot locations as seen in figure 4.6a and 4.6b, the fits are equivalently accurate in reproducing the generating transport profiles as the eight spline-knot case with less observed oscillations. Specifically the five spline-knot case's fit quality means that the iron spectral emission could be well matched meaning $\mathcal{X}_R^2 \approx 1$ and no observable structure in the weighted residuals (not shown). Even with the interior moving spline knots case as shown in figure 4.6c and 4.6c, the exact transport profiles show a hint of this oscillation in the regions where the respective transport channels are subordinate (i.e. core for the diffusion and edge for convection). More disturbingly the spline knots' magnitude uncertainties displayed are underestimated even in the case with the extra parameterization of moving interior knots. Naively one would think that the errorbars derived from the least squares fitting routine should encompass the generating transport profiles since the **exact noise levels** in the iron line emission is known and passed into the

[c]see section 4.2 for further discussion

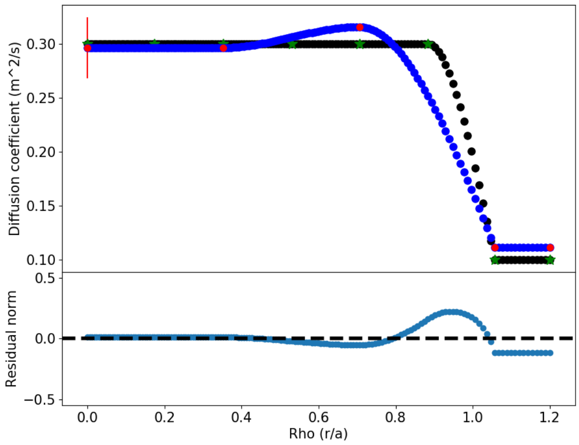

(a)

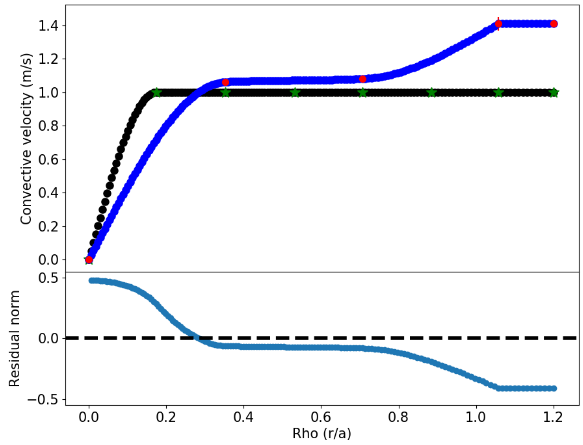

(b)

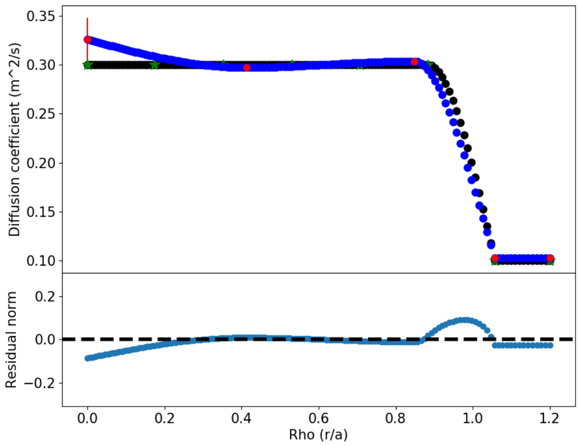

(c)

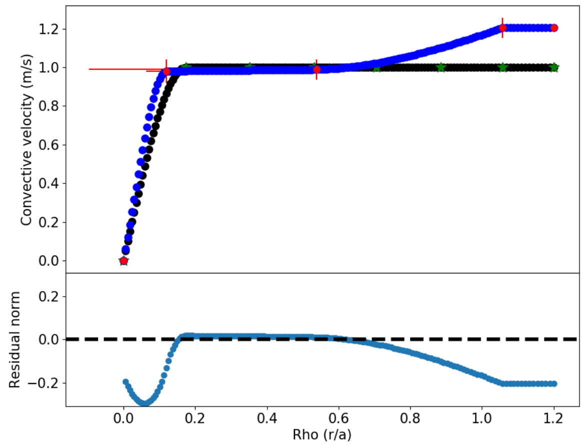

(d)

Figure 4.6: The same synthetic data with the same initialization for the least squares code was used for the fit shown in (a) & (b) and in (c) & (d) with the differences being that (c) & (d) show the 2nd run with radial moving interior knots using the results from (a) & (b) as an initialization. The black profiles are the synthetic data generating transport profiles while the blue are the least squares code's inference. The residuals normalized to the data generating values are plotted below to demonstrate the percent difference from the true transport profiles. The fixed spline knot case shown in (a) & (b) had $\mathcal{X}_R^2 \approx 1.09$ while the moving interior knot case shown in (c) & (d) had $\mathcal{X}_R^2 \approx 0.99$. Neither case had any observable structure in the weighted residuals.

least squares fitting routine as weights. However the reduced model using five spatially-fixed spline-knots cannot reproduce the transport profile shapes characterized by eight spline-knots and used to generate the synthetic data. This systematic uncertainty is impossible to capture by the returned parameter uncertainties through $lstsq\_STRAHL\_wrap$, the least squares fitting routine, as exemplified in figures 4.6a and 4.6b. Moreover when the five spline-knot model has the radial position of the two interior spline-knots as free fit parameters, the correct transport profile shape can be approximated but the direct coupling between these fit parameters (i.e. magnitude and radial position) does not guarantee accurate parameter errors returned from $lstsq\_STRAHL\_wrap$. Therefore it is clear when the number of the spline-knots is reduced from the number used to generate the synthetic data, the uncertainty is not fully captured and is especially significant for the transport channel that is subordinate in that radial region. With this understanding, it is obvious that the number of spline-knots needed to be reduced enough to minimize the overfitting oscillation observed with the the eight spline-knot inference, but still retain the flexibility to match the true solution with the caveat that the transport profiles' uncertainties will not necessarily capture the true solution.

For this initial synthetic data case, the reduction to five spline-knots provided the appropriate balance between minimizing the potential for overfitting, while also providing the radial resolution, when interior moving spline knots are used, to match these flat generating transport profiles. When performing inferences using real experimental data,six spline-knots were used to parameterized the transport profiles where the extra spline knot was used in the core region to force a flat inference exactly like was used in the edge (more details on this topic are discussed in the following section).[d] Therefore a model using a six spline-knot radial parameterization was chosen to minimize the aforementioned overfitting and to accurately infer the transport profiles.

[d]Only four of the six spline-knots are treated as free parameters exactly like the five spline knots used in the inferences shown in figure 4.6

Establishing forced flat anomalous transport in the core and edge regions

- The small radial extent of the core and edge, $\Delta\rho$: 0 to 0.1 and 1.1 to 1.2 respectively, can cause unphysical inference of transport values in these regions especially considering the overfitting observed in section 4.1.2

Continuing the discussion of the radial parameterization of the transport profiles, fixed regions both in the core and edge with flat transport values were established in order to constrain the least squares routine from inferring an unphysical solution. These regions as just mentioned can have large uncertainties and potential inaccuracies in the inferred transport profiles depending on which transport channel is dominant. As a result, regions equivalent to 0.1 $\Delta\rho$, roughly $\sim$ 5 cm radial extent, were chosen for both the core and edge to force radially constant anomalous transport values ensuring these regions are inferred in an average sense. Enforcing a constant inferred anomalous diffusion and convective velocity in the edge region, $\Delta\rho$ from 1.1 to 1.2, is an appropriate parameterization for the work presented here due to the very low iron line emission levels in this region. With low temperatures and sparse abundance of the Fe^{+12} chargestate in this far scrape-off layer region, the line emission for the lowest chargestates used in this work, Fe^{+12}, wouldn't be significant enough to derive radial information there. Moreover in this far scrape-off layer where island structures are present, the parameterization still allows for radial variation across the last closed flux surface which is important for accurately inferring the edge transport parameters. Therefore establishing an edge region with forced flat anomalous transport should limit spurious overfitting and hopefully produce more accurate inferences across the entire profile.

Keeping flat transport values in the central region, $\rho = 0$ to 0.1, is also an appropriate parameterization due to the higher sensitivity of the iron line emission temporal shape to the anomalous diffusion. As already mentioned the core region can be dominated by the convective flux leading to greater uncertainty in the anomalous diffusion in this region, but notably this can take upwards of 100 ms after the LBO injection meaning a larger fraction of the line emission's data points is determined from the diffusive flux. By ensuring the core region has a flat anomalous diffusion profile, the inferred parameter space is constrained from unphysically high anomalous diffusion on axis. The anomalous convective velocity was also enforced to be flat in the core region to parallel the diffusion, inferring this region's average anomalous transport.[e] Overall the requirement on the core and edge anomalous transport to be flat increases the confidence in the accuracy of the inferred transport profiles. The average anomalous diffusive and convective transport are inferred in these regions helping preclude large gradients in the transport parameters in these regions to improve the inference of the main part of the plasma, $\rho = 0.1$ to 1.1

Utilizing moving interior spline-knots

- Allowing the two interior spline-knots' transport value and position to be inferred gives the least squares routine the ability to match a more diverse set of profile shapes. However this does exacerbate the potential inaccuracies of the uncertainties.

Finally the last aspect of the radial parameterization tested within the initial synthetic data was the inclusion of the radial position of the two interior spline-knots as free parameters within the least squares minimization. This is an important consideration because on the one hand without any radially moving spline-knots the true transport profiles (especially locations with large gradients) might not be accurately inferred, but on the other hand an extra free parameter for a spline-knot location couples these spline-knots' magnitude and location fit parameters within the least squares minimization. As mentioned in section 4.1.2 the direct coupling of fit parameters can exacerbate inaccurate uncertainty estimations. More importantly the interdependent spline-knot magnitude and position expands the least squares parameter-space potentially leading to inaccurate inferences due to multiple minima in least squares parameter-space that can reproduce the signals. To minimize the possibility of non-unique solutions, only the two interior spline-knots are permitted to move both in magnitude and position with bounds in place to ensure the two knots do not cross positions. With the flat regions in the core and edge constraining some of parameter space, the two interior moving points strikes the balance between profile inference flexibility and uniqueness. Both the magnitude of the spline-knot

[e] It should be noted that the convective velocity on axis is required for continuity reasons to be zero and hence the flat anomalous convective velocity in the core doesn't include this single point while still extending to $\rho = 0.1$

uncertainties and the uniqueness of the inference can be estimated by the procedure used with the least squares fitting routine. For example, an inference with the two interior spline-knots spatially fixed can be performed first and used as an initialization into a second inference with the interior knots' positions now as free parameters. In addition these sequential inference implementations can be compared to a single inference with all of the parameters free, effectively testing the variance in results. More details on the ordering and procedure used with the least squares fitting routine will be presented in section 4.2. Although the radial shifting of spline-knots can exacerbate the inaccuracy of the anomalous diffusion's uncertainties by coupling the fit position and magnitude together, these potentially incorrect uncertainties are mitigated by the fitter's ability to match more diverse profile shapes. Moreover a best-practices procedure for performing the least squares minimization can be used to establish a strong initialization of the transport profiles close to the accurate solution.

4.1.3 Spatial and temporal resolution of inverted He-like spectral emission

Excluding inverted emissivity leads to non-unique inferences

- Spatially resolved line radiation data is absolutely necessary for ensuring the inferred profiles are unique and accurate.

The most significant conclusion from the initial synthetic data testing is that without the inclusion of spatial information the inferred anomalous transport profiles are not unique and potentially inaccurate. This fact is most clearly observed in figure 4.7 where despite the great matching of the line-of-sight iron line emission, $\mathcal{X}_R^2 \approx 1.0$ with no observable structure in the weighted residuals (not shown), the inferred anomalous diffusion and convective velocity profiles are incorrect. Examining 4.7a closely, the outer four spline-knots are relatively accurate for the diffusion profile, but from $\rho = 0.6$ inwards the diffusion values are unconstrained and the true solution is not captured by the spline-knot uncertainties. This result can be understood by the radial distributions of the various iron chargestates that correspond to the iron line emission signals used within $lstsq\_STRAHL\_wrap$. The higher iron chargestates have a broad radial distributions throughout the plasma core meaning that without the spatial localization provided by the inverted He-like signal the line-integrated measurements do not constrain the diffusion profile within the least squares fit. The lower iron chargestates' radial distributions are more peaked and localized near the plasma edge adding to the lower chargestates line emission's efficacy of accurately inferring the anomalous diffusion in this outer region. This fact helps explain the conclusion found in section 4.1.2 where the diffusive flux is the dominant transport channel in the edge and in the first $\sim$100 ms after the LBO injection. It is also important to note that in 4.7b no part of the profile is accurately inferred. Even with the convective flux being the dominant transport channel in the core for this generated data, the convective velocity profile is totally wrong with incorrect uncertainties. The core inferred diffusion is a factor of $\sim$20 greater than the true generating diffusion values because the inference doesn't have the spatial information to localize the broad Fe^{+24} radial profile. Therefore the least squares fitting routine is attempting to drive the diffusive flux as the dominating transport channel in the core leading to this completely inaccurate convective velocity profile. In conclusion this synthetic data testing demonstrates two important facts: first the anomalous diffusion profile's stronger sensitivity to the iron line emission's temporal shape and second the true necessity to include spatial information in the inference to obtain accurate transport profiles.

Inverted He-like spectral emission spatiotemporal resolution effects

- The temporal and spatial resolution reduction for inverted He-like spectral signal did not impede the accurate inference of the transport profiles.

As seen in the last section the spatial resolution provided by the x-ray diagnostic was absolutely critical for inferring accurate anomalous transport profiles. However to produce accurate inversions for the He-like emissivity a baseline signal-to-noise ratio is necessary.[82] In some cases the nominal 5 ms and 3 cm resolutions used for inverting the data collected by the HR-XIS diagnostic were too high for robust inversions of the w-line from He-like iron. Therefore reducing the spatial/temporal resolution of the experimental data can be performed to increase the singal-to-noise ratio and subsequently make the inversions more robust. The reduction in resolution, especially the spatial resolution, might have strong impacts on the inference of the

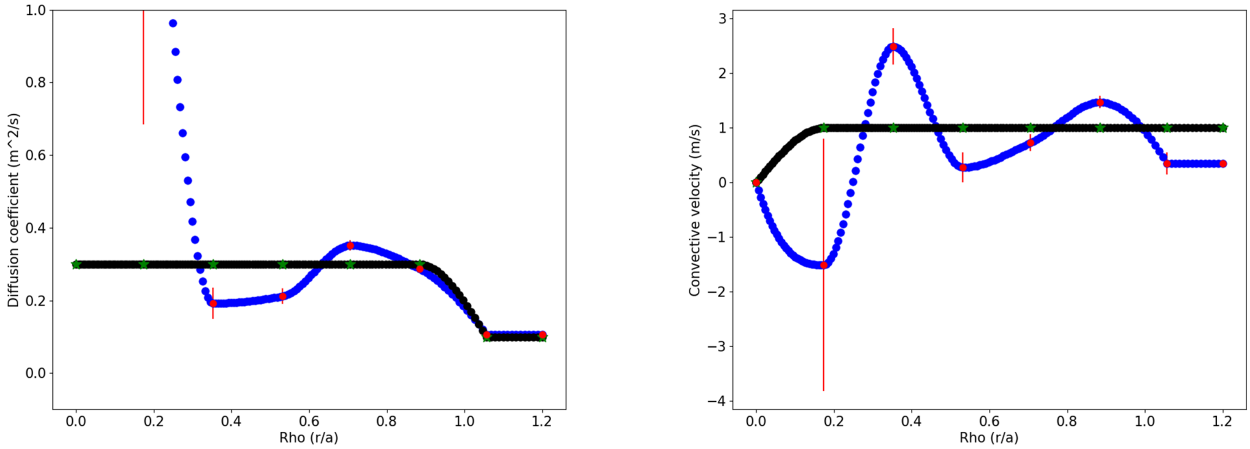

(a) (b)

Figure 4.7: The same synthetic data with the same initialization for the least squares code was used for the fit shown in 4.4a & 4.4b and in a & b with the difference being that the inverted Fe^{+24} emission is not included within the inference here. The black profiles are the synthetic data generating transport profiles while the blue are the least squares code's inference. Also this had $\mathcal{X}_R^2 \approx 1.0$ with no observable structure in the weighted residuals indicating the inference is not unique without including spatial information.

transport profiles. To understand the resolution effects on the inferences prompted this particular synthetic data testing.

In order to test the limitations on the x-ray measurements and their subsequent inversions, synthetic data was generated with different levels of spatial and temporal resolutions. Specifically the reduction in spatial or temporal resolution was modeled as an increase in signal quality due to higher number of counts per spatial/temporal point. This was again performed analogously to how experimentally collected data would be processed whereby the reduction in spatial or temporal resolution increases the signal-to-noise ratio for the downsampled inversions. Therefore two cases were tested, one with a decreased spatial resolution from 3 cm to 12 cm ($\Delta\rho$ =0.025 to 0.1), the other with decreased temporal resolution from 5 ms to 20 ms. As seen in figure 4.8 the reduction in both the temporal resolution and the spatial resolution of the He-like inverted emissivity did not detract from accurately inferring the anomalous transport profiles at all. In particular the reduction from 40 to 10 radial points, corresponding to 3 to 12 cm resolution change, was still perfectly adequate in providing the necessary radial information for accurate inferences. This result coupled with the reduced temporal resolution scenario,

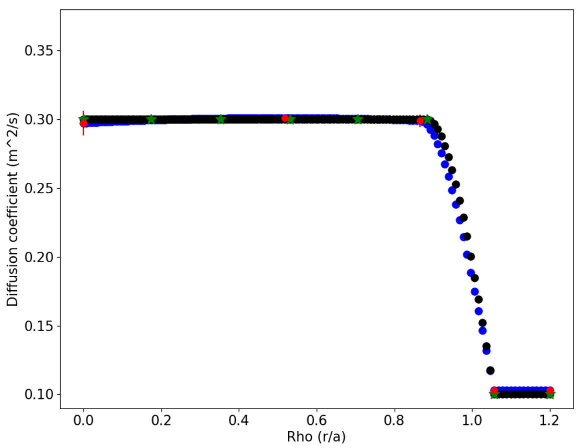

(a)

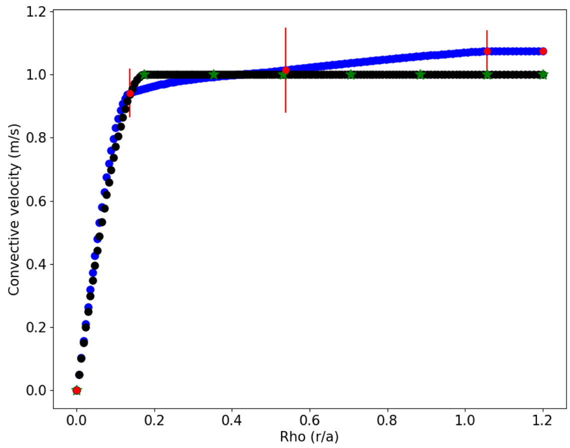

(b)

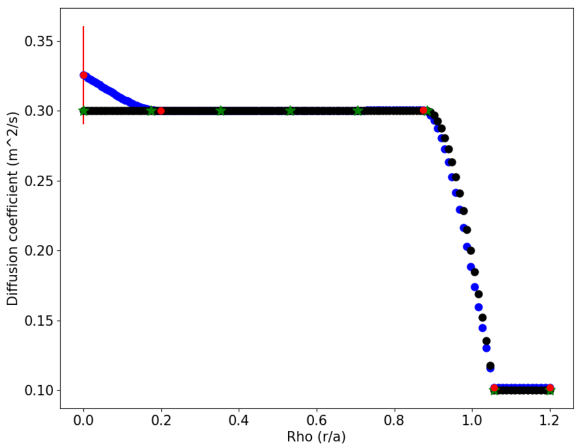

(c)

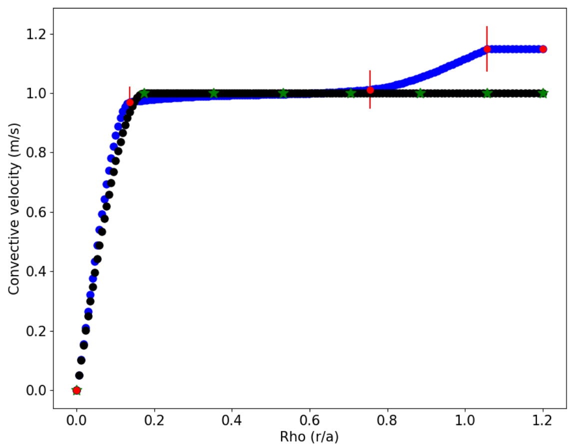

(d)

Figure 4.8: Synthetic data using the same noise levels were used to generate inverted He-like line emission with reduced spatial and temporal resolution in (a) & (b) and in (c) & (d) respectively. In fact (a) & (b) show the effective spatial resolution being reduced from 40 to 10 points (corresponding to a resolution change from 3 cm to 12 cm in the plasma). In (c) & (d) the temporal resolution is decreased from the nominal 5 ms to the 20 ms with the standard 3 cm spatial resolution. The residuals normalized to the data generating values are plotted below to demonstrate the percent difference from the true transport profiles. Both cases shown have $\mathcal{X}_R^2 \approx 1.0$ without any observable structures in the weighted residuals.

5 ms to 20 ms, indicates that individual reduction in experimental resolution to increase the robustness of inversions shouldn't have any impact on anomalous transport inferences.

Regrettably for the work presented in this thesis, the data collected for the x-ray system could not be inverted like the synthetic data presented. There was substantial vignetting on the HR-XIS system, the primary iron impurity x-ray diagnostic, making the inversion process extremely difficult, hence forcing the detector to be broken up into eight evenly spaced, distinct lines-of-sight with eight different scaling parameters rather than a single common factor as shown in figure 2.3 and further discussed in section 5.2.2.[f] Due to the vignetting, all the iron line emission signals used in the real experimental data analysis are line integrated including the spectral lines corresponding to the UV detectors and the aforementioned eight sightlines for the HR-XIS system. Therefore in section 4.2 more synthetic data analysis will be presented utilizing the same eight sightlines to verify the spatial information provided by these individual sightlines were enough to provide accurate transport profile inferences.

4.1.4 Uncertainties from timing offsets between diagnostics

LBO injection timing as a free fit parameter

- The exact LBO injection time has a profound effect on the ability of the least squares routine to match the signals. Fortunately, the signal matching for an incorrect LBO injection time is poor enough that this timing can be included as a free parameter and determined within the least squares routine.

In addition to the synthetic data demonstrating the importance of including spatially unique data in the inference of anomalous transport profiles, the synthetic data clarifies the sensitivity of the inferred transport profiles to timing offsets. During the iron impurity transport experiments, not only was the time base of the fast spectrometer and the LBO laser not the same, but also the laser had jitter in its timing meaning that the exact injection of the neutral iron cloud at the plasma edge could easily be any time within a 5 ms window. With such a large uncertainty

[f]The relative transmission for each pixel has been calculated from the vignetting and in theory the eight different scale factors could be tied together in the inference. However some of the line-of-sights' transmission is extremely low meaning the ratio of scale factors has large uncertainties that would introduce more inaccuracy into the inference of the transport parameters

in the LBO injection time, $lstsq\_STRAHL\_wrap$ was written with the option of leaving the LBO injection time as a free or fixed parameter. As a consistent and measurable initialization, the iron LBO injection time was set to 2.5 ms before the first observed spectral emission which happened to always be the line radiation corresponding to the $Fe^{+14,+15}$ chargestates. Therefore to better understand the ability and sensitivity of the least squares minimization code to determine the exact LBO timing, two different inferences were performed with the LBO injection timing fixed to an incorrect value that was off by $\pm$ 5 ms. The results of those inferences can be observed in figure 4.9 where although the inferred profiles for much of the plasma are unexpectedly accurate, the reduced least squares values of 4.5 and 3.37 for the fixed cases of 5 ms late and 5 ms early respectively indicate quite poor matching of the spectral emission. In addition to the $\mathcal{X}_R^2$ being much larger than unity the inferred edge transport parameters are completely inaccurate. The inaccuracy in the edge transport parameters is consistent with the least squares routine attempting to match the temporal shape of the lower chargestates, $Fe^{+8,12}$ in this example, that are strongly localized near the last closed flux surface due to the strong electron temperature gradient. Taking into account the inaccurate edge transport parameters and the poor matching of the iron spectral emission in the edge, all indicate that the iron LBO injection timing parameter can be included in the model and accurately inferred without any issues. Moreover this demonstrates that uncertainty introduced from any potential LBO injection timing ambiguity can be completely resolved with the inclusion of the LBO injection time as a free parameter within the fit.

Timing offset between VUV and x-ray diagnostics

- The x-ray to UV timebase shift leads to inaccurate inferences of the transport profiles without a large, $> 1\mathcal{X}_R^2$, increase in the signal mismatching. This indicates the UV to x-ray timing offset probably shouldn't be included as a free parameter within the least squares fit.

Although both the HEXOS and HR-XIS spectrometers utilized the hardware trigger signal from the central CoDaC system,[83,84] at least one plasma discharge was observed with a potential timing offset between the two time bases. To understand whether a timing offset was

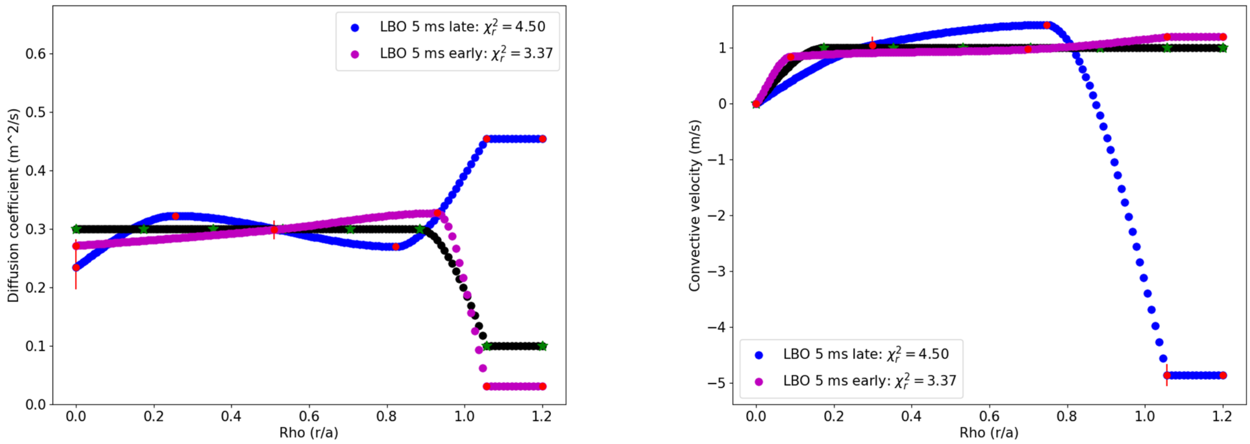

(a) (b)

Figure 4.9: The same synthetic data with the same initialization for the least squares code was used for the fit shown in 4.4a & 4.4b with the difference being that the LBO injection timing offset is either ± 5 ms. The black profiles are the original transport profiles while the blue and purple are the least squares code's inference for the +5 ms and -5 ms LBO timing offset respectively. Also this had $\mathcal{X}_R^2 \approx 4.5$ and 3.37 respectively indicating quite poor fits even if the inferences are coincidentally relatively accurate.

recoverable as a free parameter within the least squares fit, two inferences were performed while keeping the UV and x-ray timing offset fixed to ± 5 ms the actual value used to generate the synthetic data. In contrast to the LBO timing parameter, the UV to x-ray timing offset yields relatively decent matches between the iron spectral lines with $\mathcal{X}_R^2 \approx 1.89$ and 1.78 respectively for the +5 ms and -5 ms fixed delay as seen in figure 4.10. However despite the relatively close matching of the iron spectral lines within the least squares fit, the inferred anomalous transport profiles are clearly inaccurate. This inaccuracy for the anomalous diffusion profile is completely reasonable since a positive (negative) time delay of the x-ray signal is consistent with an underestimate (overestimate) of the diffusion. In fact the least squares routine is utilizing the anomalous diffusion, the more dominant transport channel, to slow down (speed up) the rise of the inverted Fe^{+24} w-line in the case of a negative (positive) time delay. The relative accuracy in matching the iron spectral emission through the inference is only possible due to the broad density profiles of the higher iron chargestates, namely $Fe^{+24,+22}$, that introduce flexibility in the least squares routine to change the transport parameters to inaccurate values to still somewhat match the iron line emission. This is underscored by the fact that for both

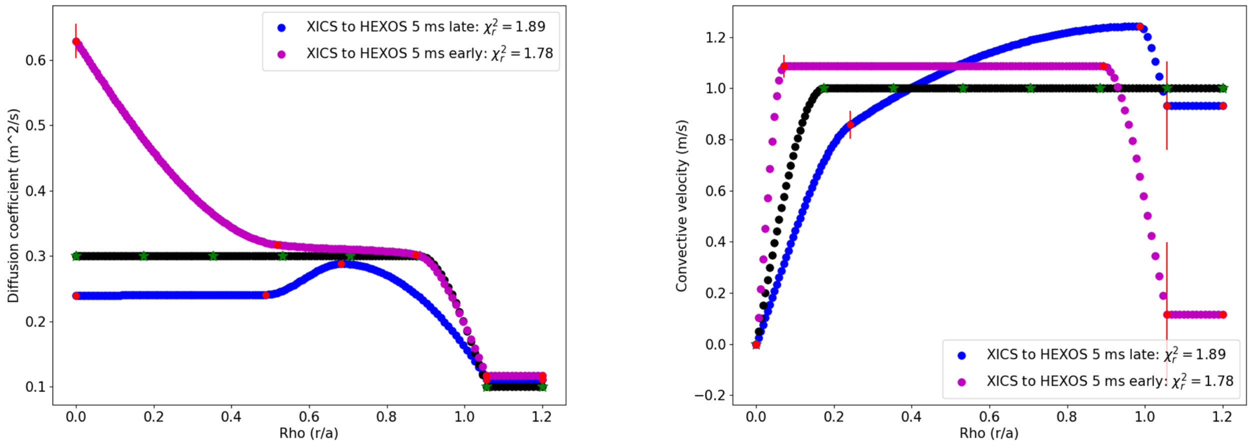

(a)

(b)

Figure 4.10: The same synthetic data with the same initialization for the least squares code was used for the fit shown in 4.4a & 4.4b and in a & b with the difference being that the HEXOS and HR-XIS timing offset is either $\pm$ 5 ms. The black profiles are the synthetic data generating transport profiles while the blue and purple are the least squares code's inference for the +5 ms and -5 ms LBO timing offset respectively. Also this had $\mathcal{X}_R^2 \approx 1.89$ and 1.78 respectively indicating decent match of the spectral lines even though the inferred transport profiles are inaccurate.

of the inferences shown in figure 4.10 the greatest contributors to the total least squares value are the line emission from $Fe^{+24,+22}$. Even more when examining the weighted residuals of these signals, the greatest differences occur on the signal rise due to the smaller number of data points effected and hence contributing less to the total least squares value. Based on the these imposed $\pm$ 5 ms UV to x-ray timing offset tests, it is unclear whether this time shift can be determined through the least squares routine if included as a free parameter. If the least squares routine is used to first find approximately correct parameters and then executed again using these parameters as an initialization, the x-ray timing offset might be useful in accurately inferring the transport profiles. This scenario is however unlikely and including this timing offset as a free parameter can lead to inaccurate inferences as demonstrated in figure 4.10. It should be noted that although $\pm$ 5 ms is a relatively extreme timing offset, these synthetic data tests still demonstrate the sensitivity of the inferred transport profiles to such timing shifts between signals.[g] Therefore including the UV to x-ray spectrometer timing offset as a free parameter within the fit is not recommended or routinely performed due to the increased likelihood of introduced inaccuracies in the inferred transport profiles.

4.1.5 Flat-transport-profiles synthetic data conclusions

The synthetic data was generated from input parameterization based on a real iron LBO experiment with the exception that no classical & neoclassical transport parameters were used and that the anomalous transport profiles were specified at appropriate magnitudes but kept artificially flat. This synthetic data testing demonstrated four key conclusions:

- The spatial information provided by the inverted Fe^{+24} w-line was a necessity for the accurate and unique inference of the anomalous transport profiles.
- The artificially flat anomalous transport profiles demonstrated the achievable spline-knot spatial resolution as evidenced by the overfitting oscillations in the inferred diffusion and convective velocity profiles.
- The synthetic data was generated at expected transport parameter magnitudes, which demonstrated that anomalous diffusive flux is the dominant transport channel for most times and radial positions within the simulation.
- The LBO injection timing can be included as a free parameter and accurately inferred within the fit, while any VUV and x-ray timing offset cannot reliably be inferred.

The first conclusion's importance cannot be overstated that line emission spatial information is critical for the convergence to the genuine transport profiles. From the traditional metrics of least squares, $\mathcal{X}_R^2 \approx 1$ and no structure in the weighted residuals, the quality of the fits were virtually identical with or without the inclusion of the inverted data even though the latter scenario had inaccurate inferences. In fact when the inverted Fe^{+24} w-line data was removed leaving only single sightline data (still including the Fe^{+24} w-line), the anomalous

[g] During the readout of the signal on one of the HEXOS detectors the left most pixel and right most pixel could be as much as 1 ms off from each other. The HR-XIS detector has a 2.5 ms repetition rate and uses its own internal clock meaning drifts or phase differences could arise

diffusion profile was only accurate from $\rho \approx 0.8$ and outward while the anomalous convection velocity was completely inaccurate.[h] The accurate inference of the anomalous diffusion in the region from $\rho \approx 0.8$ to 1.2 is due to the radial localization of the lower iron chargestates, namely $Fe^{+8,12,14,15}$, and due to the large impurity density gradients causing the diffusive flux to be the dominant transport channel in this region.Interestingly this indicates that for the expected and measured temperature profiles in W7-X, the higher iron chargestates have broad density and line emission profiles that need radial localization to more accurately constrain the inference of the anomalous transport profiles. Using the synthetic inverted Fe^{+24} w-line data, the radial resolution effectiveness was tested by generating inverted data with a factor of four fewer radial points, a reduction from forty to ten radial nodes. Performing an inference using this reduced radial resolution inverted Fe^{+24} w-line data was completely sufficient to accurately infer the anomalous diffusion and convective velocity profiles. This decreased resolution test gave confidence in using eight distinct sightlines from the HR-XIS detector instead of calculating an inverted profile since such radial resolutions are completely adequate to accurately infer the anomalous transport profiles.[i]

The second conclusion's importance lies in revealing the anomalous transport's sensitivity in different radial regions and the radial resolution achievable from the given signals. Employing the same number and location of spline-knots to infer the anomalous transport profiles that were used to generate the synthetic data, large oscillations corresponding to overfitting were observed in the core region for inferred the anomalous diffusion and in the edge region for the inferred anomalous convection velocity. In fact the overfitting oscillations increased from core (edge) to edge (core) for the convective velocity (diffusion) due to the convective (diffusive) flux becoming a smaller fraction of the total iron impurity flux in this region. Even with the already enforced flat anomalous transport profiles in the edge region, $\rho = 1.1$ to 1.2, that should limit the deviations from the genuine profiles, the convective velocity still displayed a large oscillation and uncertainty in the edge. To provide similar mitigating effects on the diffusion in the core region, $\rho = 0.0$ to 0.1, the anomalous transport profiles should also be

[h] The proper line integrals were not used in the flat-transport synthetic testing

[i] Note that inversions of the Fe^{+24} w-line data are not possible from OP1.2b experiments presented in this thesis due to vignetting.

inferred in the average-sense in the core. These forced flat anomalous transport regions should help mitigate unphysical inferences by making large displacements more unfavorable due to each flat region encompassing larger radial extent. The overfitting oscillations motivated not only the enforcement of the anomalous transport profiles to be flat in the edge and core regions, but also the reduction in the number of radial spline-knots. Although reducing the number of spline-knots for the anomalous transport profiles decreases the likelihood that the overfitting oscillations will occur, the genuine transport profiles might not be inferred accurately due to the radial profile restrictions. Therefore along with the reduction in the number of spline-knots from eight to five, the two most interior spline-knots were given the freedom to move radially.[j] The subsequent inferences with a reduced number of spline-knots and the inclusion of radially-moving interior knots did indeed yield mostly accurate anomalous transport profiles with one large caveat. The spline-knots for the core diffusion and edge convective velocity were slightly inaccurate, but importantly the inaccuracy was outside the given uncertainty from the least squares fitting routine. This underscores that the uncertainty in the transport profiles are not guaranteed to encompass the true profiles despite using the **exact noise levels** as weights within $lstsq\_STRAHL\_wrap$ and using a reduced number of spline-knots to limit the potential for overfitting. Therefore the spline-knot uncertainties especially for the core diffusion and the edge convective velocity are most likely underestimated for any analysis on real experimental data particularly considering each signal's noise levels are not exactly known.

The third conclusion from the synthetic data is significant for contextualizing the expected behavior of the experimental data. Although the synthetic data was generated with artificial, mostly flat anomalous transport profiles, the magnitudes are consistent with the real experimental values.[7] Therefore a close comparison of the diffusive and convective fluxes can be done at each radial position at select time steps to understand the transport process as modeled within STRAHL. The first and most obvious insight gained about the iron impurity transport is that the anomalous diffusive flux is the dominant transport channel for almost all radial positions and for all times before the iron density profile has reached its equilibrium shape. This means

[j]The synthetic data testing used five spline-knots for the anomalous transport data without a core region of forced flat profiles. In the analysis of the experimental data six spline-knots were used, where the sixth was just added to the core region to enforce this average-sense inference there.

the convective flux is only a significant part of the total iron impurity flux at the inward moving iron density peak that after $\sim$ 100 ms has broadened into a flattened, stiff shape. Corroborating this is the result found from the second conclusion where the uncertainties (and oscillations) were smaller for the core convective velocity spline-knots. Moreover the edge anomalous diffusion uncertainties (oscillations) were also extremely small due to the complete dominance the diffusion transport channel has here. These facts give further insight into the efficacy of each iron chargestates line emission to infer the anomalous transport profiles. For example, the line emission corresponding to $Fe^{+8,12}$ is strictly radially localized to $\rho > 0.9$ and typically returns to background levels well before the iron density profile has reached its equilibrium shape, i.e $<$ 100 ms. That means the temporal shape of the $Fe^{+8,12}$ line emission has almost no influence from the convective velocity hence matching these signals should depend on the anomalous diffusion in this region, the LBO injection timing, the electron temperature in this region, the connection length to the limiter, and the LBO source function.[k] On the otherhand a high iron chargestate with corresponding high signal-to-noise ratio like Fe^{+22}, can easily be emitting longer than 300 ms with some presence in the core region (depending on the electron temperature), providing valuable information on both the anomalous diffusion and convective velocity. The second insight is that although a least squares minimization method doesn't guarantee a global minimum solution, the utter dominance of the anomalous diffusive transport channel gives an opportunity to first infer the anomalous diffusion profile as a most-likely initialization before a second inference is executed for other various parameters (e.g. LBO injection timing, etc) In this way a procedural method has been established with improved confidence of inferring the accurate transport profiles by moving closer to the likely solution in parameter space in the first inference.

The fourth and final conclusion from the flat-transport synthetic data testing is that the LBO injection timing offset can be determined within the inference, while the VUV to x-ray timing offset cannot reliably be included as a free parameter to be accurately inferred. The incorrect LBO injection timing was held fixed at $\pm$ 5 ms and could not be used to accurately

[k]Unfortunately multiple clusters can be seen on the line emission for the lower chargestates (as high as Fe^{+18}) during some iron LBO injections

infer the edge anomalous transport parameters. Importantly the $\mathcal{X}_R^2 > 3$ for the incorrect LBO timing meant that the line emission data match was very poor and in particular for the two lowest chargestates, $Fe^{+8,12}$. Thus the inclusion of an LBO injection timing offset within the least squares routine to be accurately inferred is feasible, especially when it is in a second inference once the anomalous diffusion has been fit to a most-likely initialization profile. Unfortunately when the VUV and x-ray timing offset was held fixed at $\pm$ 5 ms from the true value used to generate the data, the $\mathcal{X}_R^2 < 2$ and there weren't too many structures in the weighted residuals. Only the SOL inferred anomalous diffusion was accurate since the anomalous diffusion in the core could easily be underestimated (overestimated) to slow down (speed up) the x-ray signals being delayed (sped up) by 5 ms. The broad density profiles of Fe^{+24} and Fe^{+22} were enough to alter the anomalous transport profiles to match the signals even though the inverted Fe^{+24} w-line did give spatial localization. The significance of this conclusion is that diagnostic determination of the exact LBO injection timing is less critical than the determination of the relative timing between the diagnostics measuring any of the various iron impurity lines.

4.2 Synthetic data testing utilizing realistic transport profiles

The second part of synthetic data study was performed as a verification of the model used to analyze the real experimental data. In this verification process impurity transport modeling can be characterized, whereby better estimations and understanding of systematic errors in the modeling can be captured. In particular key aspects of the improved modeling such as the proper sightline integration or inclusion of neoclassical & classical transport are used within the synthetic data generation. The details of the model changes will be described in section 4.2.1 while the new model's impacts on the previous synthetic testing's conclusions will be described in section 4.2.2. In terms of better estimating inherent model uncertainties a more comprehensive sensitivity study was performed with this new model where the specific variational tests are discussed in the rest of the sections within 4.2. Additionally an example of the line emission signal matching along with the corresponding inferred anomalous diffusion profile is shown in appendix E.

4.2.1 New model description

- Neoclassical and classical transport profiles were added to an experimentally motivated anomalous transport profile, which consisted of solely an anomalous diffusion profile (i.e. the anomalous convection velocity profile was fixed at 0 $\frac{m}{s}$ for the entire radial extent).
- Only line-integrated sightline signals, each with an independent scale factor, were used for each spectral line bringing the synthetic analysis analogous to the real analysis due to the vignetting on the HR-XIS detector preventing inverted emissivity profiles (see figure 2.3 for sightline definitions).
- The same six spline-knot radial parameterization of the anomalous diffusion profile was used in this synthetic testing as was used with the experimental data analysis.

In order to keep the second round of synthetic testing consistent with the first synthetic study, the same LBO injection was used as a basis. The main impact of using the same LBO injection as a basis was the implementation of the identical kinetic profiles and respective uncertainties. The first notable change over the first synthetic study, was the use of these kinetic profiles to generate the neoclassical & classical transport profiles by means of the NeoTransp code.[74] The neoclassical & classical diffusion and convection velocity, as seen in figure 4.11, are important to include for the chargestate-dependent transport effects. In addition to the added neoclassical & classical transport profiles, realistic anomalous transport profiles were taken from a best match inference of a separate experimental LBO injection, 20180919.037 1st LBO injection. The inference on this particular LBO injection not only was one of the best matches to any of the collected experimental data, but also utilized similar kinetic profiles as the basis LBO injection as seen in figure 4.1. With this as a justification an anomalous diffusion profile was constructed to match the inferred profile, while the convection velocity profile was held at zero just as in the inference. Therefore the first major change with the second round of synthetic modeling has been the transport profiles used in the synthetic data generation: the

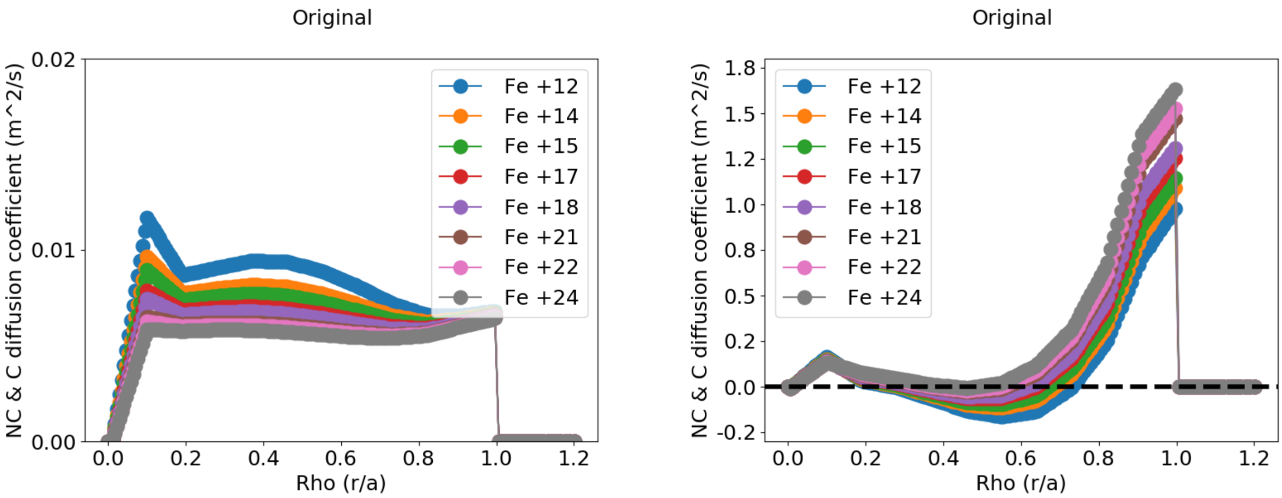

(a) (b)

Figure 4.11: The neoclassical & classical diffusion and convection velocity as calculated from Neotransp for the kinetic profiles from 20180919.049 3rd LBO are shown in (a) and (b) respectively.

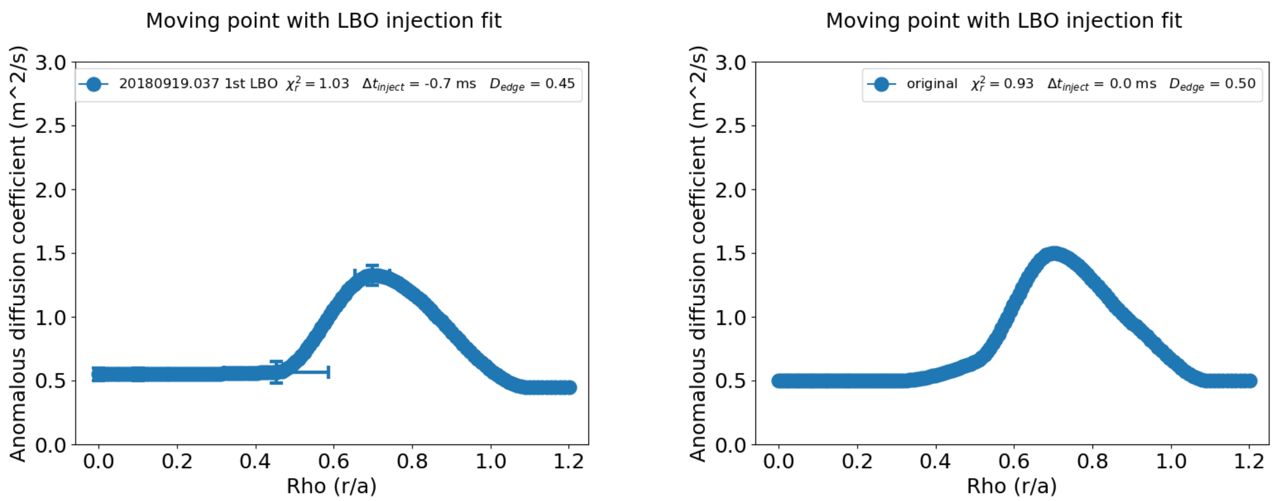

(a) (b)

Figure 4.12: The anomalous diffusion profile inferred for 20180919.037 1st LBO injection is shown in (a), while the new model's synthetic anomalous diffusion profile is shown in (b)

inclusion of neoclassical & classical transport and the use of experimentally motivated anomalous transport profiles.

The next major change to the model was the iron line emission handling in order to make the synthetic study more consistent with the experimental data analysis. The first aspect to bring the iron line emission handling closer to the experimental data analysis was using the real spatial sightline data for every line-of-sight from HEXOS and HR-XIS diagnostics. In this way a proper line integral was calculated using the STRAHL data, more accurately taking into account the spatial information from the various sightlines. Similarly eight lines-of-sight corresponding to the HR-XIS sightlines were generated and used in this synthetic study rather than a single inverted emissivity for the He-like w-line signal. Again these eight sightlines were used to bring the synthetic data study more in line with experimental analysis since the aforementioned experimentally observed vignetting made the He-like inverted emissivities less trustworthy. Also since a very good match to the FeIX signal could never be achieved with the experimental data, it was decided to not use this lowest chargestate signal in this synthetic study. There were a total of fifteen sightline signals generated for the synthetic iron line emisssion completely analogous to measured experimental data: Eight sightlines for the w-line from Fe^{+24} corresponding to a HR-XIS measurement Seven sightlines for the UV line emission from $Fe^{+12,14,15,17,18,21,22}$ corresponding to a HEXOS measurement The final aspects to bring the iron line emission to be consistent with experimental data analysis were the altering of both the line-of-sight and noise scale factors. In particular the line-of-sight scale factors were chosen to bring each sightline's signal level to the same values as measured for the LBO injection used as a basis, i.e. 20180919.049 3rd LBO. With each sightline signal level matched, the same estimate for linear background and noise levels that were determined for the basis LBO injection can be applied. Although the standard method for calculating the noise was employed for the VUV iron lines as seen in equation 4.2, the shot noise was clearly being underestimated when compared to the experimental signal variations.

$$\sigma_{\text{total}} = \sqrt{\sigma^2_{\text{background}} + \alpha^2 \sigma^2_{\text{shot}}} \tag{4.2}$$

Therefore rather than the fit values for α from the basis LBO injection, an increased α value of 6 was used to increase the shot noise contributions and ultimately the total uncertainty levels for the synthetic data generation. With all of these changes to the handling of the iron line emission, this second synthetic study is more analogous to the analysis done on the real experimental data.

The final change for the second synthetic study was the implementation of the recommended radial description discovered from the first synthetic study. Specifically this meant using six spline-knots for the inference of anomalous transport profiles rather than the five used in the first synthetic study. The extra spline-knot was added to accommodate a forced flat anomalous region in the core from ρ 0 to 0.1, while still keeping four spline-knots free for the inferences. In this way the overfitting issues discovered in the edge and core can be minimized by tying the spline-knots at $\rho = 0$ and 1.22 to those at $\rho = 0.1$ and 1.1 respectively. The added core forced-flat region in combination with the two interior spline-knots permitted to move radially should provide enough freedom for the anomalous profiles to fit most shapes.[1]

4.2.2 Confirmation of the flat-transport-profiles synthetic study's results

Procedural method for least squares minimization verified

- The spatial information from the eight x-ray sightlines are sufficient for accurate inference within the new model including proper sightline integrals
- The procedural method yields accurate inferences of the anomalous diffusion profile with the largest inaccuracies occurring in the radial range $\rho \approx 0.6$ to 0.9
- The anomalous convection velocity profile cannot be accurately inferred, i.e. errors $>$ 1.0 $\frac{m}{s}$, and its inclusion as free fit parameters increased the averaged inaccuracies on the anomalous diffusion profile

Utilizing the improvements and changes to the model as detailed in section 4.2.1, the first step in the synthetic study was a verification of the basic results discovered during the flat-transport-profiles synthetic study. One of the most important aspects to verify was the procedural method employed to evaluate real experimental data. As a reminder this procedural

[1]The two moving interior spline-knots are initialized at $\rho \approx 0.43$ and 0.76

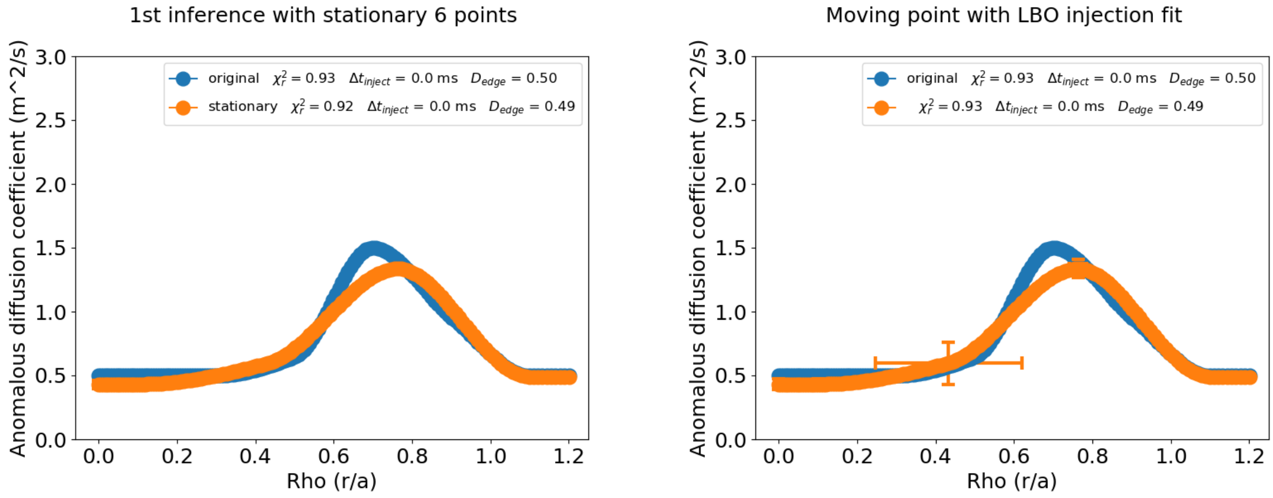

(a) (b)

Figure 4.13: The comparison of the generating anomalous diffusion profile to the inference performed according to the first and second step in the procedural method are shown in (a) and (b) respectively. The inferred diffusion profiles are accurate along with a near perfect matching of the iron line emission with $\mathcal{X}_R^2 = 0.99$

method consisted of two steps: First, perform a least squares minimization with the anomalous convection velocity held at zero, only allowing each iron sightline's scalefactor and the four spline-knots of the anomalous diffusion profile as a free parameters. Second, using the results from the first inference as an initialization perform another least squares minimization with the two interior spline-knots's radial position and the LBO injection time as additional free parameters. The procedure was developed to constrain the inference to the most likely anomalous transport profile. The anomalous diffusive flux is believed to not only be the most dominant transport channel, but also be so dominant that the iron line emission's temporal shapes can mostly be matched without including any other transport channels. This explains the rationale to hold the anomalous convection velocity at zero and not include it within the standard procedure for performing the inferences. The procedural method's goal is to find the most-likely anomalous diffusion profile by means of this aforementioned two-step process.

Employing the first step in the procedural method, the inferred anomalous diffusion profile was accurate with $\mathcal{X}_R^2 = 0.99$ indicating very good matching between the noisy synthetically-generated line emission and the STRAHL modeled signals as seen partially in figure 4.13a and with all of the signal fits in figure E.1. This result is not only encouraging as a confirmation

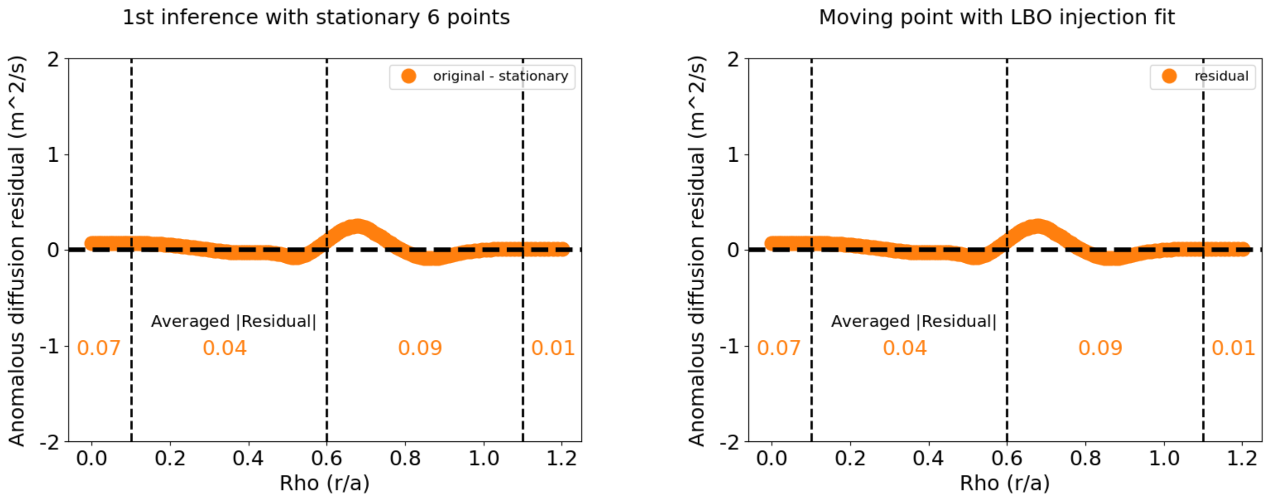

(a) (b)

Figure 4.14: The residual between the original and the inferred anomalous diffusion profiles performed according to the first and second step in the procedural method are shown in (a) and (b) respectively. The average absolute value of the residual for the four radial regions separated by the dashed lines are printed.

of the procedural method, but also more importantly demonstrates that the spatial information provided by the eight sightlines for the Fe^{+24} w-line is equally good as having an inverted w-line emissivity. The flat-transport-profile synthetic study found that reduced spatial resolution on the inverted w-line emissivity was sufficient to infer the accurate transport profiles, but this inference takes it a step further. In this inference an even further reduction in spatial channels (i.e. 8 versus 10) along with individual scale factors for each sightline still provided the necessary spatial information for accurate inferences of the anomalous diffusion profile.

To finalize the confirmation of the procedural method, the second step inference was performed with the moving interior spline-knots and LBO injection timing as free parameters. As seen in figure 4.13b the 2nd inference of the standard method showed very little change from the 1st inference confirming the effectiveness of the procedural method. In fact figure 4.14 shows the residual between the original synthetic-data-generating anomalous diffusion profile and the inferred ones following the procedural method. It is clear that the anomalous diffusion peak at $\rho \approx 0.7$ is not exactly matched even with the radially moving spline-knots and more importantly not captured within the uncertainty estimates returned by the least squares routine as shown in figure 4.13b. Moreover in figure 4.14 the average of the residual's absolute value

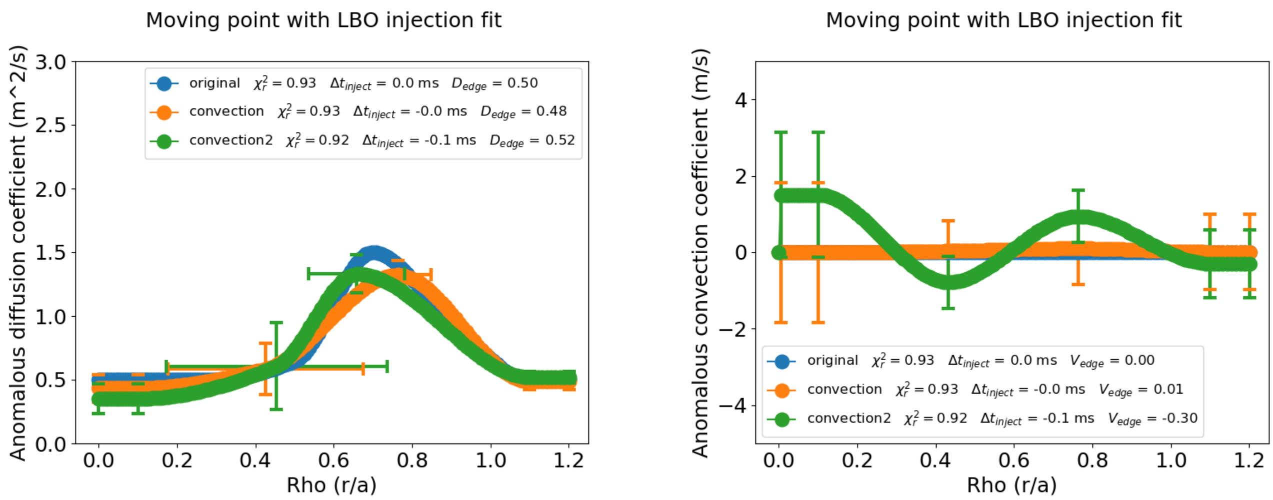

(a) (b)

Figure 4.15: The comparison of the generating anomalous diffusion profile to the 2nd inferences performed according to the procedural method are shown in (a). In (b) the anomalous convection velocity profiles of the 2nd inferences are shown where the labeled "convection2" inference was initialized at a value away from zero.

for the four radial regions (ρ: 0 to 0.1, 0.1 to 0.6, 0.6 to 1.1, and 1.1 to 1.2) are displayed. This clearly shows the averaged inaccuracy in the off-axis radial region, i.e. ρ: 0.6 to 1.1, is the largest. In this case the peak diffusion difference of $\sim 0.1\ \frac{m^2}{s}$ can be mostly attributed to the two interior spline-knots constrained between $\rho = 0.1$ and 1.1 being not sufficient to exactly match the original anomalous diffusion's radial shape. Despite the inferred diffusion profile differences around the peak, the iron line emission can still be exactly matched,$\mathcal{X}_R^2 = 0.99$, with no observable trends in the weighted residuals. This indicates that in the radial range $\rho \approx$ 0.6 to 1.1 the single, central sightlines for the seven UV spectral lines do not provide enough spatial localization to resolve the exact diffusion profile even if more spline-knots were used.

After verifying the standard procedural method, a modified procedure including the anomalous convection velocity in a 2nd inference was tested. This was performed to give perspective on how the accuracy and uniqueness of the inferences are affected when the anomalous convection transport channel is included in the least squares minimization. In figure 4.15 the 2nd inferences including the anomalous convection velocity initialized at two different values are shown. Reassuringly and unsurprisingly the inferred anomalous diffusion profile showed

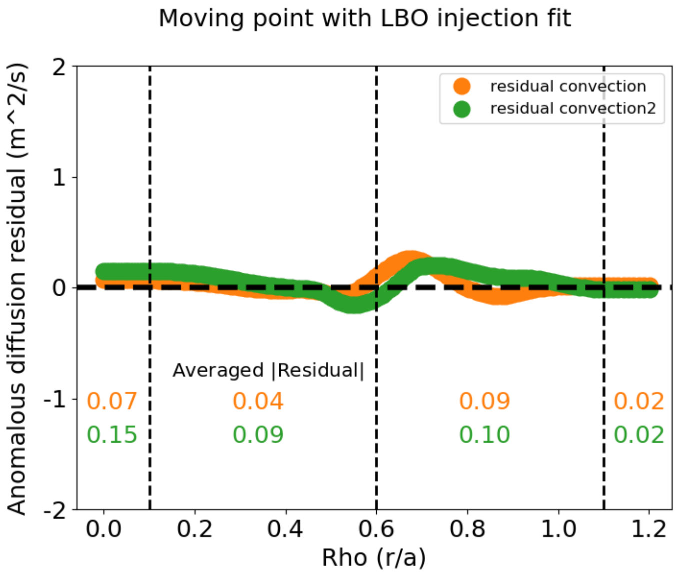

Figure 4.16: The residual between the original and the inferred anomalous diffusion profiles when including and initiating the anomalous convection velocity profile. The average absolute value of the residual for the four radial regions separated by the dashed lines are printed in their corresponding colors.

minimal change when including the convection velocity in the 2nd inference of the procedural method. Interestingly when the convection velocity was initialized at non-zero values (i.e. constant 0.5 $\frac{m}{s}$) for this 2nd inference, the anomalous diffusion profile had increased averaged inaccuracies as shown in figure 4.16. The increase of $\sim 0.15\ \frac{m^2}{s}$ in the core diffusion values is attributed to the least squares routine attempting to increase the diffusive flux to counteract the pinch induced by the negative core convection velocity. Although it is comforting that the anomalous diffusion profile is still accurate in both cases when anomalous convection is included in the 2nd inference, the variations on the order of $\sim 1\ \frac{m}{s}$ in the inferred convection velocity when not initialized at its exact generating values show the insensitivity of the iron line emission signals to the convection channel. Therefore as long as the anomalous diffusion values are expected to be on the order of 0.5 $\frac{m^2}{s}$, the anomalous convection velocity doesn't contribute in any meaningful way to improving the match of noisy synthetically-generated line emission and the STRAHL modeled signals. In fact the inclusion of the anomalous convection velocity could potentially lead to degenerate solutions with the least squares routine finding a local minimum. Also from a physics basis large, i.e. $> 1\ \frac{m}{s}$, convection velocities are not expected in the confined plasma region, especially a negative anomalous convection velocity

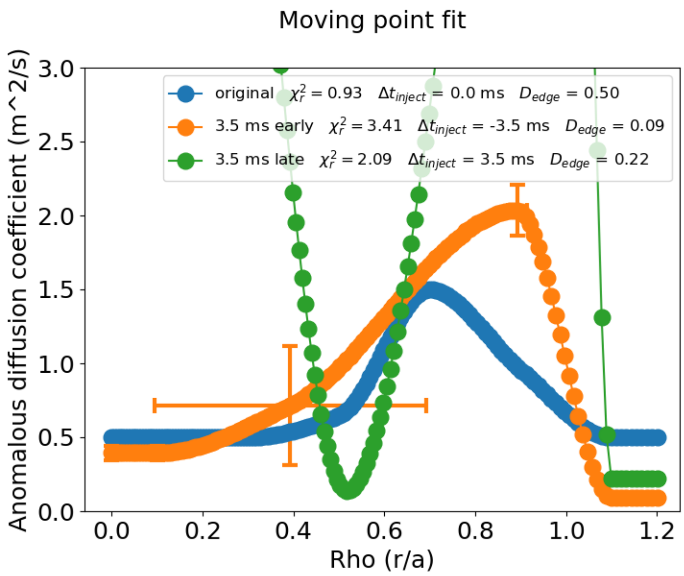

Figure 4.17: The inferences of anomalous diffusion, while holding the LBO injection timing to incorrect values of $\pm$ 3.5 ms.

contributing to a pinch. Therefore in conclusion the standard procedural method was verified, with special consideration that the actual profiles may be outside the returned uncertainties.

LBO injection timing

- Incorrect LBO injection times were verified to have a profound effect, $> 1\ \frac{m^2}{s}$, on the inferred anomalous diffusion profile. Fortunately the iron line emission signals were poorly matched indicating this timing can be determined within the least squares minimization.

As previously discussed in section 4.1.4 the jitter in the laser and the lack of consistent measurements from the fast spectrometer allowed for relatively large uncertainties in the LBO injection timing. Reaffirming the conclusion that the LBO injection time could be accurately inferred within the least squares minimization, a test was performed holding the injection time to $\pm$ 3.5 ms the actual value. Except for the injection timing, the procedural method was employed for the two scenarios where the injection time was held at a value corresponding to 3.5 ms early or late. As seen in figure 4.17 the inferred anomalous diffusion profiles are inaccurate with the 3.5 ms delayed scenario even returning extremely nonphysical values of 15 $\frac{m^2}{s}$ in the core. However fortunately the match to the iron spectral signals were poor, $\mathcal{X}_R^2 > 2.0$, for both scenarios. The large reduced chi-squared values are especially reassuring since the

Fe^{+8} spectral line, the most sensitive signal to the LBO injection time, is not included in this synthetic data study. Therefore without a good match with the iron spectral signals even with the exclusion of the Fe^{+8} line emission means that the LBO injection timing can be determined within the least squares fitting routine in a window of $\pm$ 3.5 ms.

X-ray to VUV timing offset

- Incorrect x-ray to UV timing offsets were verified to have large effect, $> 0.1\ \frac{m^2}{s}$, on the inferred anomalous diffusion profile inside the last-closed-flux-surface. Unfortunately the iron line emission signals were well matched indicating this offset timing cannot reliably be determined within the least squares minimization.

The potential timing offset between HEXOS and HR-XIS was revisited for the second round of synthetic testing to reaffirm the previous conclusions. As discussed in section 4.1.4 when an incorrect relative timing of $\pm$ 5 was given to the x-ray signals, the iron line emission was relatively well matched $\mathcal{X}_R^2 < 1.9$ but with inaccurate inferences of the anomalous transport profiles. This meant that including the timing offset as a free fit parameter could potentially lead to degenerate solutions within the relatively large uncertainty levels of $\pm$ 5 ms Therefore this timing offset was revisited with a much more likely uncertainty level of $\pm$ 2.5 ms[m] Corroborating the previous findings, introducing a timing offset of 2.5 ms did not impede the least squares minimization routine from matching the iron spectral signals ($\mathcal{X}_R^2 \approx 1.1$), but did yield inaccuracies in the anomalous diffusion profile on the order of 0.2 $\frac{m^2}{s}$ from $\rho \approx 0.6$ inward as shown in figure 4.18b. The combination of good iron spectral line matching and inaccurate core anomalous diffusion inferences make it unclear whether including this timing offset as a fit parameter would be beneficial. The encouraging conclusion is that the offsets of $\pm$ 2.5 ms seem to only lead to inaccuracies in the core of 0.3 $\frac{m^2}{s}$. Therefore with unclear benefits of including the offset as a fit parameter and currently no way to determine any offset experimentally, no changes will be made to the procedural method and the input time bases will be considered accurate with respect to each other.

[m]The $\pm$ 2.5 ms is possible if the HEXOS 1 ms resolution and the HR-XIS 2.5 ms resolution lead to a timing offset during data storage of 2.5 ms at greatest

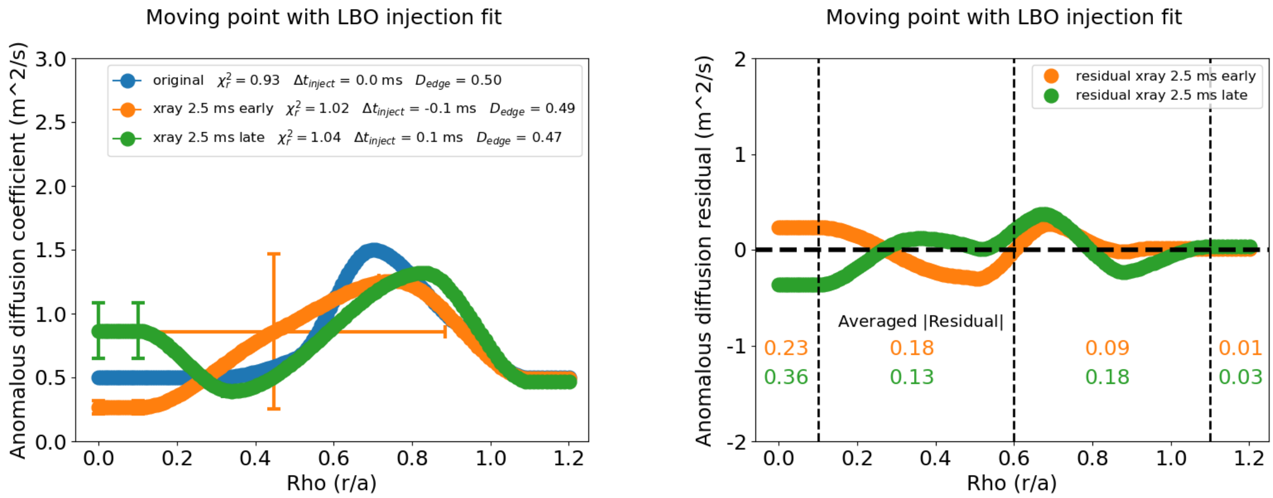

(a) (b)

Figure 4.18: The inferences of anomalous diffusion, while holding the x-ray to VUV timing offset to incorrect values of $\pm$ 2.5 ms is shown in (a), while the residual with the original synthetic-data-generating profile is shown in (b). Unfortunately the inferred diffusion profile is inaccurate from $\rho \sim 0.7$ inward and the $\mathcal{X}^2_R \approx 1.0$ for both cases means this timing offset cannot be included as a free fit parameter within the least squares minimization.

4.2.3 Variation of neoclassical & classical transport profiles

- Scaling the neoclassical & classical transport profiles by factors of two did not substantially add inaccuracies to the inferred anomalous diffusion profile due to the anomalous diffusive flux being the dominant transport channel at diffusion values $\sim 0.5\ \frac{m^2}{s}$

Although W7-X has been optimized in such a way as to minimize the neoclassical transport, understanding its contribution to the uncertainties of the inferred anomalous transport profiles is still critically valuable. In fact the neoclassical & classical transport profiles are important for impurity transport analysis since these profiles are chargestate-dependent and critically are functions of the kinetic profiles present in the plasma. Moreover the kinetic profiles are particularly important for this thesis work since the topic is investigating how iron impurity transport changes at different levels of off-axis ECRH. As mentioned in section 4.2.1 the kinetic profiles,figure 4.1, were used to calculate the nominal neoclassical & classical transport profiles. To understand the impact of variations in the neoclassical & classical transport profiles, inferences were performed while holding all of the neoclassical & classical transport at 50% and 200% these nominal values as seen in figure 4.19.

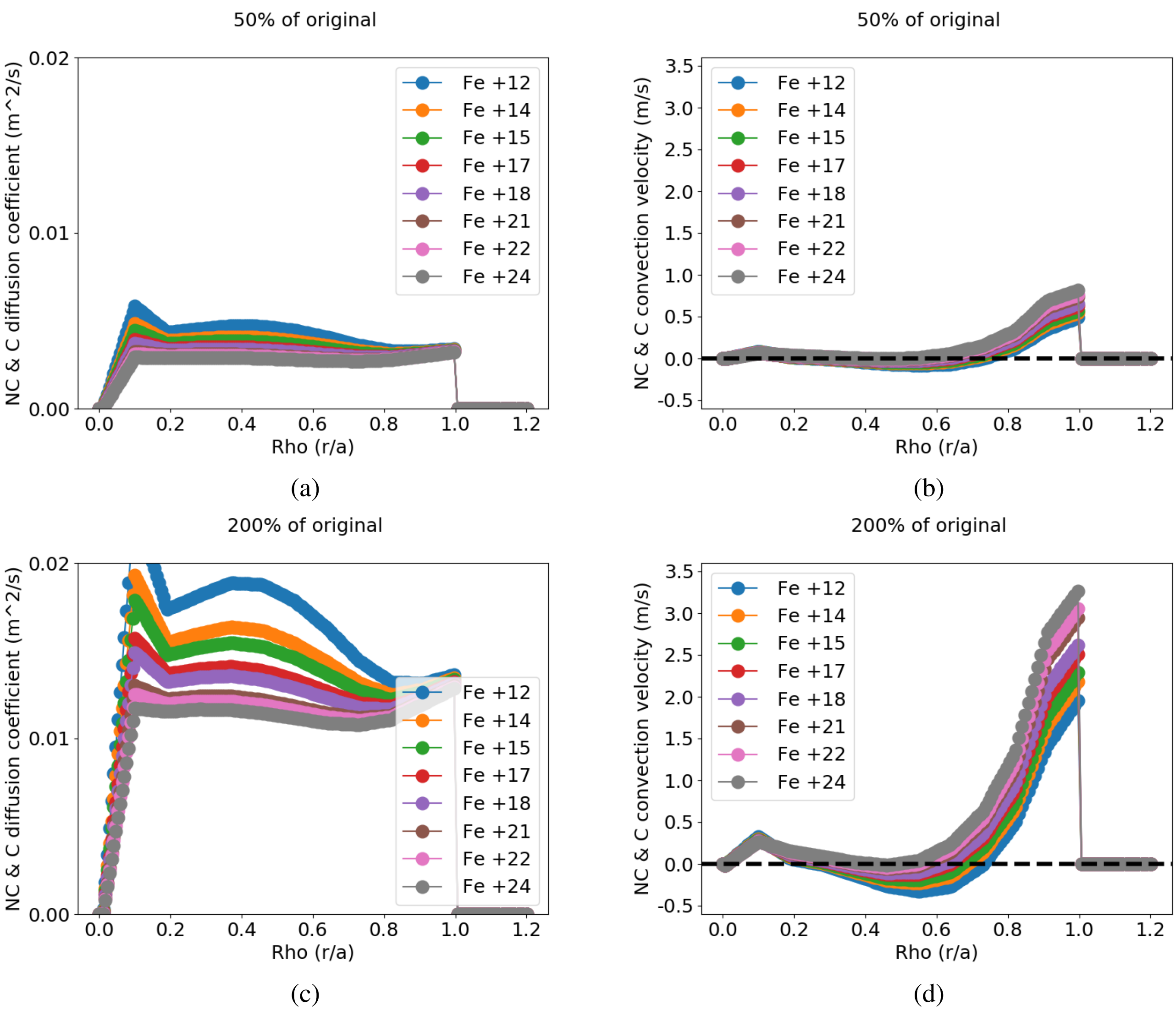

Figure 4.19: The neoclassical & classical diffusion and convection velocities are plotted for the 50% and 200% the nominal case in (a) & (b) and (c) & (d) respectively

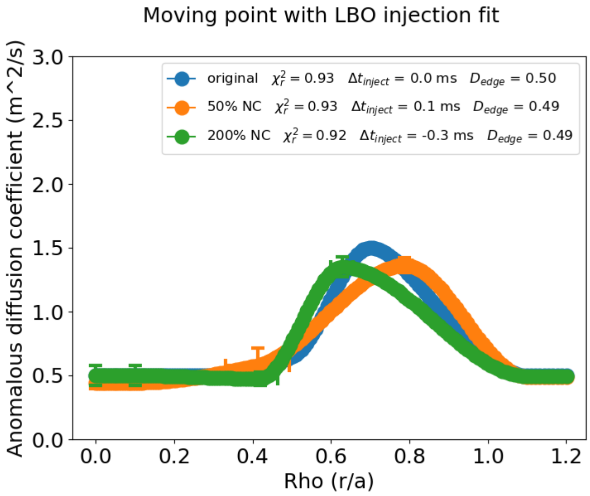

(a)

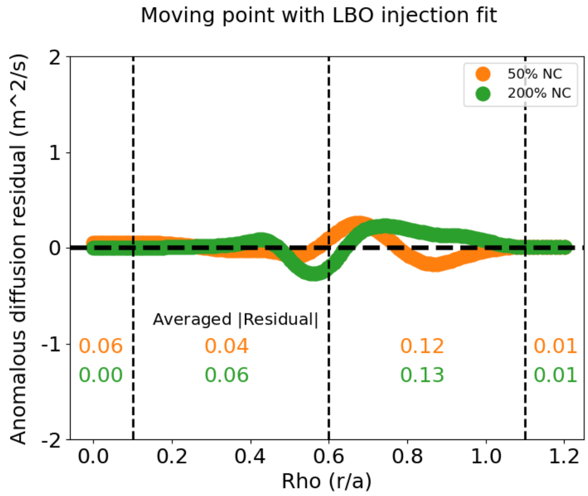

(b)

Figure 4.20: The inferences of anomalous diffusion, while holding the neoclassical & classical transport profiles at incorrect levels of 50% and 200% is shown in (a). In (b) are the residuals between the inferred diffusion and the original synthetic-data-generating profiles. The diffusion profiles are accurate with $\mathcal{X}_R^2 \approx 1.0$ for both cases indicating that potential large inaccuracies in the neoclassical & classical transport profiles have little effect on the inferred anomalous diffusion profile.

After following the procedural method for each incorrect neoclassical & classical transport scenario, the inferred anomalous diffusion profiles show minimal differences with the generating profile and the fit qualities are good. Examining figure 4.20 the factor of four variations in the neoclassical & classical transport seem to only lead to slightly larger inaccuracies for the diffusion profile in the radial range of $\rho = 0.6$ to 1.1 The lack of sensitivity to the neoclassical & classical transport channels is primarily driven by the utter dominance of the anomalous diffusion when present at levels of $\sim 0.5\ \frac{m^2}{s}$ and greater. Even when the convection velocity is present at high levels, i.e in radial range of $\rho = 0.7$ to 1.0, the effects on the inferred anomalous diffusion are small. This phenomenon can be explained by the fact that the chargestates present here are not well-localized and the corresponding line emission from the LBO pulse are relatively short. In fact the convection velocity is more critical for the higher chargestate line emission due to their temporally long signals allowing for impurity density gradients to flatten and hence minimize the effects of diffusive flux as discussed in section 4.1.2. With this understanding only strong convective velocities, $\geq 1.0\ \frac{m}{s}$, in the core plasma or small anomalous diffusion values, $< 0.5\ \frac{m^2}{s}$, near the last closed flux surface should be able to impact the accuracy of the inferred anomalous diffusion profile. Therefore for the realistic anomalous transport profiles used, even large variations in the neoclassical & classical transport should only introduce minimal inaccuracies to the inferences.

4.2.4 Variation of neutral hydrogen profile

- The large uncertainties in the neutral hydrogen density profile don't effect the ability of the least squares minimization routine to match the spectral signals, but in the over-estimation scenario do introduce significant errors, at least $\sim 0.25\ \frac{m^2}{s}$, to the inferred anomalous diffusion for $\rho > 0.6$

Previous work done by [Geiger et al. 7] showed that inferred anomalous transport profiles were most sensitive to changes in the electron temperature, neutral density, and the connection length. In [Geiger et al. 7] the neutral density profile was determined from the filterscope[85] measurements of the hydrogen flux used as input into the KN1D[86] code. Unfortunately the large uncertainty in the filterscope measurements led to $\sim 10^3$ scale between low and high estimations of the neutral density profile, which brought the large variance in the inferred anomalous transport profiles. In the work presented in this thesis, the nominal neutral density profile was taken from [Geiger et al. 7], but scaled down by a factor of three to match the increase in line-integrated electron density. Figure 4.21 shows the factor of 100 difference between the low and high neutral hydrogen scenarios used in this variational study. Similarly to the sensitivity study on neoclassical & classical transport profiles, the neutral hydrogen profile was held at the incorrect high and low scenarios while the procedural method was followed. The second, spatially-moving spline-knot & LBO injection timing inferences are shown in figure 4.22 with their corresponding residuals.

The first conclusion is that utilizing the incorrect neutral hydrogen density profile has little impact on the least squares routine's ability to match the line emission with $\mathcal{X}_R^2 < 1.0$, but unfortunately if given a significant overestimate can return diffusion inaccuracies $\sim 0.5\ \frac{m^2}{s}$. This strong variation observed for the high neutral hydrogen scenario where the edge diffusion values are inferred high and the off-axis diffusion peak is inferred low, are consistent with the increased charge-exchange losses that are calculated for the spectral lines within STRAHL. The

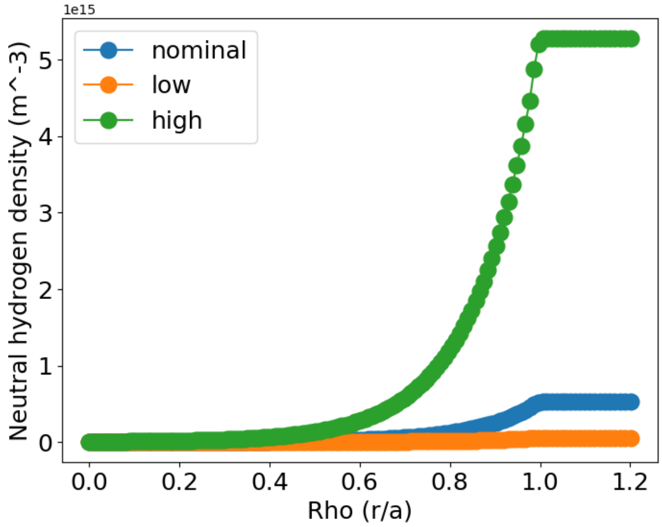

Figure 4.21: The nominal neutral hydrogen profile is shown in blue with the low and high estimate being an order of magnitude scaled down and up respectively.

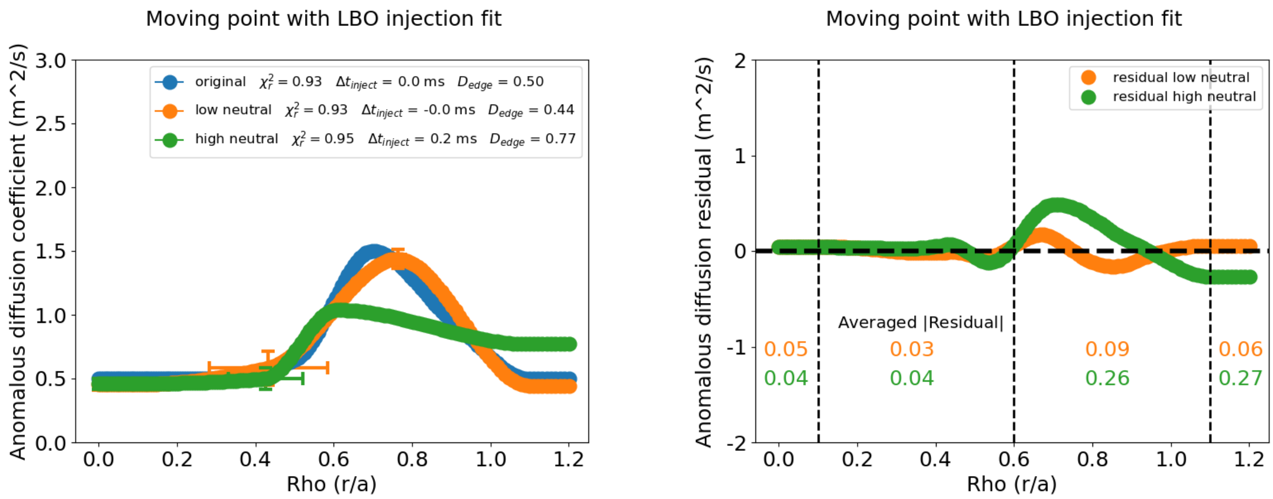

(a) (b)

Figure 4.22: The inferences of anomalous diffusion, while holding the neutral hydrogen density profiles at incorrect levels an order magnitude low and high are shown in (a). In (b) are the residuals between the inferred diffusion profiles and the original synthetic-data-generating profiles. The inferred diffusion profile for the high neutral density scenario is inaccurate with $\mathcal{X}_R^2 \approx 1.0$ indicating that only overestimating the neutral density profile will introduce extra inaccuracies

decreased peaking of the anomalous diffusion observed and the increase in the edge diffusion values is consistent with the least squares inference increasing the diffusive flux to counteract the extra charge-exchange losses. Fortunately there is no noticeable effect between the order of magnitude lower neutral density scenario and the nominal case meaning that uncertainties introduced from having the incorrect neutral hydrogen profile should be able to be mostly mitigated. This can be mitigated because the low neutral hydrogen scenario both matched the line emission and accurately inferred the anomalous diffusion profile. Therefore if the neutral hydrogen profile is suspected to be incorrect for an experimental discharge, a test inference can be performed with the neutral hydrogen profile decreased by an order of magnitude in order to verify previously inferred anomalous diffusion profile. In this way, although having a neutral hydrogen profile too high can lead to rather large diffusion uncertainties in the edge, i.e. $\sim$ 0.25 $\frac{m^2}{s}$, the absolute effect can mostly be mitigated through subsequent least squares runs with decreased neutral hydrogen profiles.

4.2.5 Variation of connection length

One of the key parameters characterizing the scrape-off layer (SOL) plasma is the connection length, the shortest path length along a magnetic field line to a material surface. The connection length present in the edge plasma plays a vital role in determining the flux of particles to the wall. For this work in particular, it is the impact on edge iron impurity flux that compels the connection length sensitivity study. Luckily the connection length only impacts the loss rates for the impurity iron due its inherent non-recycling nature. Therefore the sensitivity studies of connection length attempt to capture the uncertainty levels introduced on the inferred anomalous diffusion from variations in the connection length.

Although a more thorough description of the edge parameterization is described in section 3.2.2, equation (4.3) combines equations (3.2) & (3.3) showing how the impurity radial flux for a chargestate Z varies for a given impurity chargestate density $n_{Z,edge}$, mach number M, connection length L_C, edge diffusion D_{edge}, electron temperature T_e, ion temperature T_i, and main ion mass m.

$$\Gamma_Z = n_{Z,edge}\sqrt{D_{edge}\left(\frac{M}{L_C}\right)\sqrt{\frac{k_b\left(3T_i+T_e\right)}{m}}} \tag{4.3}$$

In fact equation (4.3) fundamentally shows the direct scaling between the edge anomalous diffusion and the connection length.This direct scaling implies that a longer (shorter) connection length will lead to an increase (decrease) in the edge anomalous diffusion for keeping the same radial flux. Unfortunately the least squares inference is performed on line-integrated spectral emission signals and not on measured iron flux rates. This means the model has freedom to match the temporal signals without exactly reproducing the radial flux rates of each iron chargestate. Moreover in the edge region only a single, central sightline is available for each chargestate, meaning there is a lack of radial localization giving more freedom to the least squares routine. As mentioned in section 4.2.1, the anomalous diffusion profile is forced flat in the far SOL region, i.e. ρ = 1.1 to 1.2, in order to minimize the possibility of nonphysical anomalous diffusion inferences.

Besides the radial description of the edge anomalous diffusion, the STRAHL model specifies two different connection lengths to capture two distinct regions in the SOL. The SOL is separated into a divertor-connected and a limiter-connected regions where the former is the larger region with typically longer connection lengths while the latter is the smaller, outermost region with very short connection lengths. More details on each of these regions will be given in the following sections where discussions about the connection length sensitivity tests are presented.

Limiter connection length

- The matching of the iron line emission is insensitive to the limiter connection length variation from 0.5 to 25 m as demonstrated by the $\mathcal{X}_R^2 \approx 1.0$ without visible residual structures.

- The limiter connection length is strongly coupled to the edge anomalous diffusion by establishing the edge flux rate meaning that the anomalous diffusion can be inaccurately inferred at the edge.

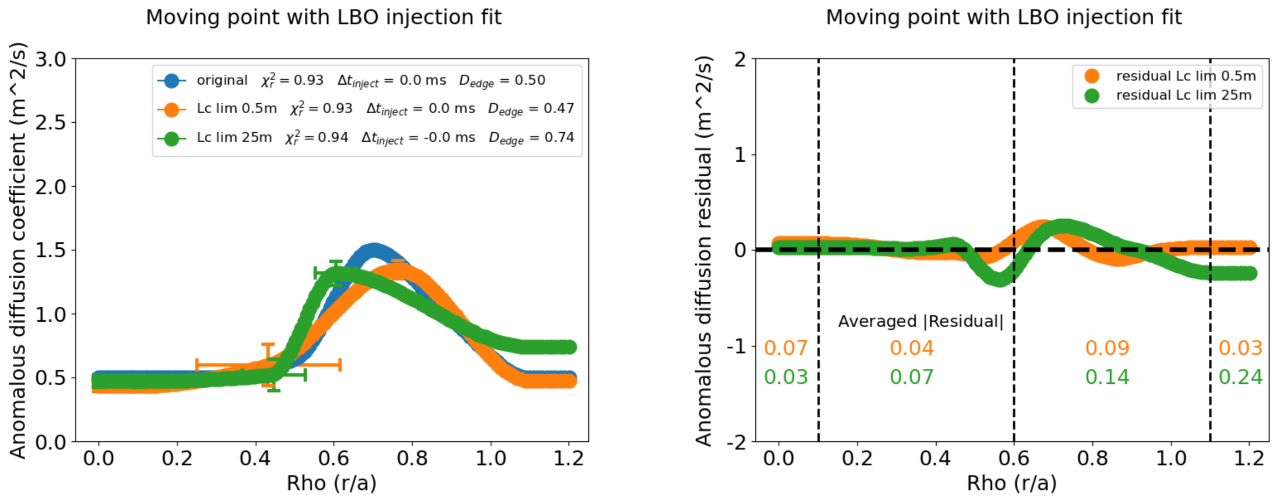

(a) (b)

Figure 4.23: The inferences of anomalous diffusion, while holding the limiter connection length at incorrect values of 0.5 and 25 m are shown in (a) while the corresponding residuals with the original synthetic-data-generating profile is shown in (b). Unfortunately the inferred diffusion profile is inaccurate for the 25 m scenario especially considering there is good signal matching with $\mathcal{X}_R^2 \approx 1.0$

In order to understand the impacts of using an incorrect limiter connection length on the inferred anomalous diffusion profile, a sensitivity study was performed by holding the limiter connection length at the lower and upper bounds. As seen in [Killer et al. 80] the calculated connection length for the W7-X standard magnetic configuration showed a significant increase from ones to tens of meters in the span of a couple centimeters from the plasma edge inward. Therefore the limiter connection length's lower and upper bounds were taken to be 0.5 and 25 m respectively. The synthetic data was generated using the nominal value of 1 m, which is consistent with the previous iron impurity transport work done on W7-X by [Geiger et al. 7]. Also for the inferences performed in this thesis work the limiter-connected region modeled in STRAHL was only composed of the outermost two radial points corresponding to $\sim$ 1 cm radial extent consistent with the small region of low connection lengths in [Killer et al. 80].

After following the standard procedural method, the inferred anomalous diffusion profiles generated from holding the $L_{C,limiter}$ at the incorrect values of 0.5 and 25 m are seen in figure 4.23 The first conclusion from these inferences is that the least squares routine is unfortunately insensitive to the $L_{C,limiter}$ value since a factor of 50 variation didn't detract from the model being able to match the spectral signals. This conclusion is verified by the $L_{C,limiter}$ lower and upper bound scenarios yielding $\mathcal{X}_R^2 \approx 1$ and no obvious structure in the weighted residuals (not shown) for both cases. The insensitivity is partially due to the fact that the lowest iron chargestate line emission, Fe^{+12}, is mostly concentrated inside the LCFS and that the each spectral sightline has an independent free fit scaling factor. The sightline scaling factors are determined within the least squares routine meaning that the model is relatively insensitive to the total iron impurity density. This creates a situation where the line emission can be well-matched but the edge diffusion is inaccurate in an attempt to control the iron flux rate. The demonstrated insensitivity indicates that the limiter connection length should not be included as a free parameter within the least squares routine as it could lead to non-unique inferences.

The second conclusion is that within the $L_{C,limiter}$ lower and upper bounds the anomalous diffusion profile is accurately inferred with the exception of the plasma edge. Although the modeled limiter-connected region is very small (i.e. 2 radial point $\sim$ 1.0 cm) when compared to the entire modeled SOL having a $\sim$ 10 cm radial extent (i.e. 19 radial points), it still plays an outsized role in the impurity iron loss rates. The reason for the limiter-connected region's large impact is due to the low values of connection length and the previously mentioned strong coupling between connection length and edge anomalous diffusion. Therefore the primary inaccuracies being restricted to the SOL plasma can be well understood from the upper bound scenario. In this scenario the factor of 25 increase in $L_{C,limiter}$ over the nominal case yields an increased edge anomalous diffusion in order to keep the iron flux rate constant consistent with equation (3.2). Moreover as seen in figure 4.24 even the lowest iron chargestate used, Fe^{+12}, has low normalized levels of emission in the SOL meaning the diffusion values here have less impact on the model matching the FeXIII signal. Starting at the radial position of $\rho \approx$ 0.9, where the FeXIII line emission has peak intensity, the inferred diffusion profile becomes closer to accurate levels due to the increased iron emission. Even taking into consideration that figure 4.24 is shown at 10 ms after the LBO injection, the approximate time when the FeXIII emission is peaking, the levels of FeXIII line emission in the SOL are still $< 10\%$ underscoring this SOL insensitivity for correct inference of anomalous diffusion. In conclusion the combination of the FeXIII being the lowest chargestate signal and the use of free fit sightline scale factors

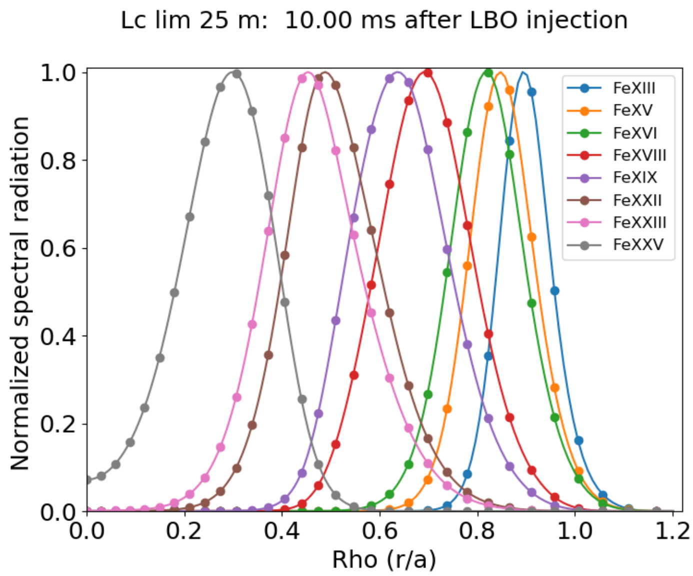

Figure 4.24: The normalized spectral emission from the upper bound scenario, i.e. $L_{C,limiter} =$ 25 m, at 10 ms after the LBO injection time, the approximate time when the line-integrated FeXIII emission is peaked.

has caused the model to be insensitive to the total iron impurity density potentially leading to inaccurate inferences of the edge diffusion, i.e. $\sim 0.2\ \frac{m^2}{s}$

Divertor connection length

- Within the uncertainty range for the divertor connection length, 250 m $\pm$ 50 m, there was no significant impact on the inaccuracies in the inferred anomalous diffusion profile and no impact on the least squares routine's ability to match the signals.

Similarly to the limiter connection length, a sensitivity test was carried out on the divertor connection length whereby least squares inferences are performed while fixing the divertor connection length to it's lower and upper bounds. The noisy synthetic data used for signal matching was generated with the nominal value of 250 m, which is consistent with the previous iron impurity transport work done on W7-X by [Geiger et al. 7]. In particular the divertor connection length was varied up and down by 50 m due to this being the approximate difference between the mean and median reported in [Sinha et al. 79] for the standard magnetic configuration. In contrast to the limiter-connected region, the divertor-connected region is much larger spanning from the last closed flux surface to the outermost $\sim$ 1 cm of the scrape off layer. Therefore the

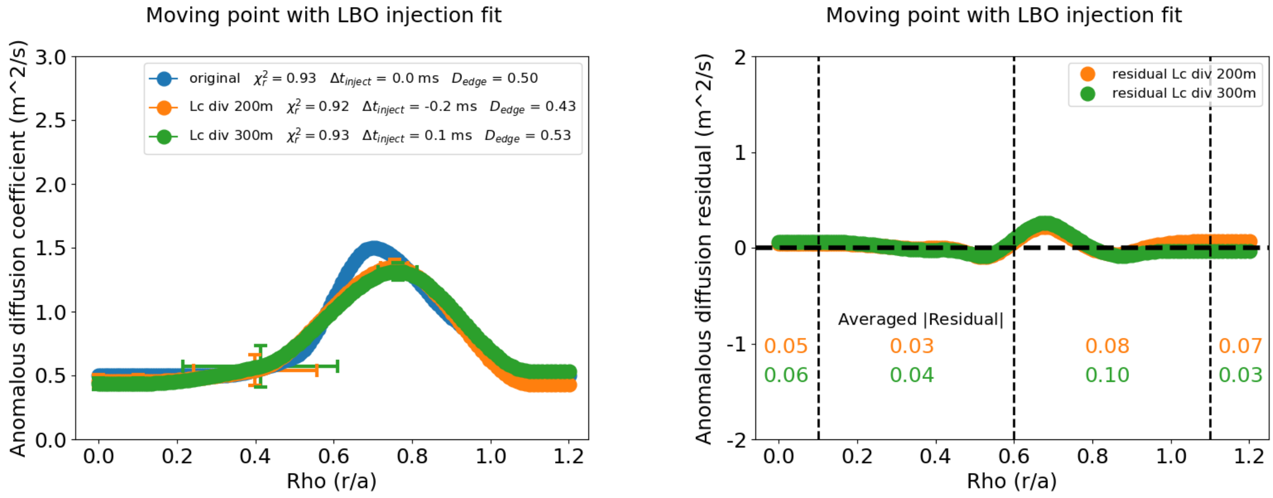

(a) (b)

Figure 4.25: The inferences of anomalous diffusion, while holding the divertor connection length at incorrect values of 200 and 300 m are shown in (a) while the corresponding residuals with the original synthetic-data-generating profile is shown in (b). The diffusion profiles are accurate with $\mathcal{X}_R^2 \approx 1.0$ for both cases indicating that the $\pm$ 50 uncertainty in the divertor connection length has minimal effect on the inferred anomalous diffusion profiles.

majority of the modeled 10 cm SOL is composed of this divertor-connected region typified by longer distances to a first wall and hence smaller iron radial flux loss rate as seen by equation (4.3).

The inferred anomalous diffusion profiles generated from holding the $L_{C,divertor}$ at the incorrect values of 200 and 300 m are seen in figure 4.25. Similarly to the limiter connection length sensitivity study, the first conclusion from these inferences is that the least squares routine is mostly insensitive to the $L_{C,divertor}$ value within the $\pm$ 50 m bounds. The spectral signals are again well-matched with the $L_{C,divertor}$ lower and upper bound scenarios yielding $\mathcal{X}_R^2 \approx 1$ with no obvious structure in the weighted residuals (not shown). Not only does this conclusion indicate that the $L_{C,divertor}$ value shouldn't be included as a free parameter within the least squares inference, but also that the uncertainty bounds on $L_{C,divertor}$ are small enough to not materially influence the inferred solution.

Unsurprisingly the second conclusion is that within the $L_{C,divertor}$ lower and upper bounds the anomalous diffusion profile is accurately inferred. In fact the largest difference between the inferred anomalous diffusion profile and the original, data-generating diffusion profile occurs at $\rho \approx 0.7$, which is far away from the SOL plamsa where the $L_{C,divertor}$ variation is occurring.

The $\sim 0.1\frac{m^2}{s}$ averaged residual is the same inaccuracy observed during the standard procedure using all of the correct model parameters as seen in figure 4.13. This means that the $L_{C,divertor}$ variation had little to no effect on the inferred anomalous diffusion profile inside the last closed flux surface. Now in the $L_{C,divertor} = 200$ m scenario there is a 0.07 $\frac{m^2}{s}$ error in the inferred edge diffusion which is slightly greater than the 0.01 $\frac{m^2}{s}$ error from the nominal standard procedural case. This indicates that there is a slight enough sensitivity of the iron line emission temporal shape to the $L_{C,divertor}$ value to infer accurate edge diffusion values, but not enough sensitivity within the known bounds on $L_{C,divertor}$ to substantially add to inferred diffusion inaccuracies.

4.2.6 Variation of electron temperature profile

Utilizing the synthetic data to perform an electron temperature variational study is quite critical to this thesis work. Not only is this thesis investigating the iron impurity transport over variations in off-axis ECRH deposition which primarily shape the electron temperature profile, but also previous work done by [Geiger et al. 7] demonstrated the electron temperature profile variation had the single largest effect on the inferred anomalous profiles. The potential sensitivity to the electron temperature can be understood as stemming from the fact that the iron chargestate distribution is strongly dependent on T_e and that all of the iron emission lines modeled in this work are primarily driven by electron impact excitation. Therefore to better understand any uncertainties introduced from inaccurate electron temperature profiles, three different T_e profile variational studies will be presented below: edge, core, and whole T_e profile variations. Utilizing the same method as previously described, noisy synthetic data was attempted to be fit through a least squares routine utilizing the fixed lower and upper T_e profiles in order to test their respective effects on the inferred diffusion profile.

Edge electron temperature variation

- The far SOL electron temperature within its uncertainty range, 10 eV $\pm$ 6 eV, has a minimal effect on the inference of the anomalous diffusion profile and the matching of the signals

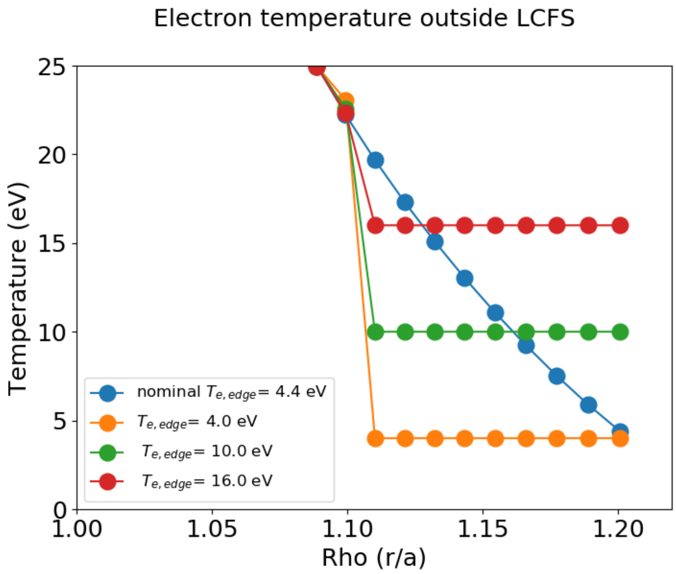

Figure 4.26: The electron temperature at the edge is held at various flat incorrect values

- An indirect coupling between edge T_e and core diffusion was observed, whereby a low edge temperature lead to greater neutral penetration and delay in the LBO injection time which then caused an erroneous core diffusion peaking similar to what was observed in section 4.2.2

The edge electron temperature variational study was performed by altering the T_e values in the far SOL, i.e. $\rho > 1.1$, to be flat. Figure 4.26 shows the forced flat edge electron temperatures which were used in this edge T_e variational study. The justification for only altering the far SOL electron temperatures was to study how the T_e values here impacted the injected neutral iron cloud while minimizing the direct effect on the iron line emission since very little line emission is produced in this region even for the lowest iron chargestate Fe^{+12}. In this way the iron loss rate, see equation (4.3), as a function of T_e and D_{edge} could be tested while employing the standard procedural method. The final results of using the standard procedural method for the T_e profiles shown in figure 4.26 are plotted with the corresponding colors in figure 4.27b As expected the modification of the far SOL electron temperature did not impact the least squares routine from being able to match the synthetic data with the $\mathcal{X}_R^2$ reaching the same level as the original scenario, i.e. holding the data-generating parameters fixed. In addition to the iron line emission signals being well-matched the inferred anomalous diffusion profiles were equally as accurate, with the lone exception being the 4 eV flat edge T_e scenario.

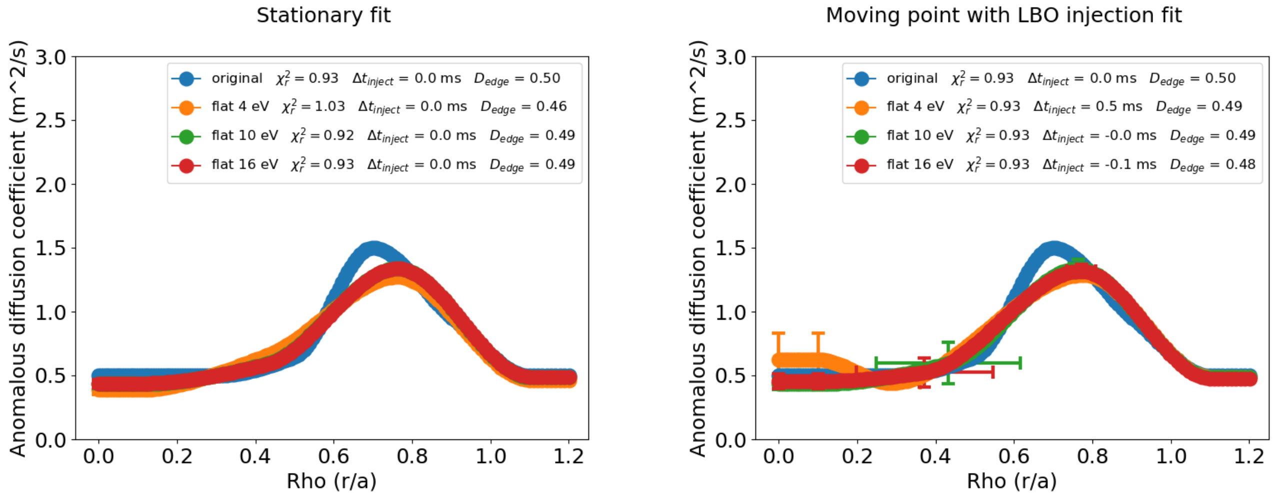

(a) (b)

Figure 4.27: The first stationary inference is shown in (a) with the subsequent moving point & LBO injection timing inference is shown in (b). The inferred anomalous diffusion profiles demonstrate that small edge electron temperature changes can propagate uncertainties in the diffusion profile well into the last closed flux surface all with seemingly good matches to the data, $\mathcal{X}_R^2 \approx 1.0$, when the LBO injection timing is a free fit parameter as shown in (b)

Although the small inaccuracies of the inferred edge diffusion values, i.e. $< 0.02\ \frac{m^2}{s}$, were expected, the peaking of core diffusion values for the 4 eV flat edge T_e scenario was initially unexpected. Upon closer examination the lower electron temperatures of the 4 eV flat edge T_e scenario meant the injected neutral iron cloud could penetrate much further into the SOL as seen in figure 4.28. The deeper penetration of the neutral iron cloud led to higher iron densities present in the plasma and caused the least squares routine to delay the LBO injection timing by 0.5 ms in order to match line emission rise times. In context the resultant core diffusion peaking can be understood from the least squares routine attempting to tailor the diffusion profile to match the eight different sightlines for the He-like FeXXV. This phenomenon was much more pronounced in section 4.2.2, where a 3.5 ms fixed LBO injection delay caused the least squares minimization to drive $> 5.0\ \frac{m^2}{s}$ core diffusion peaking. Although this result seems to indicate that the far SOL electron temperatures have minimal impact on the least squares minimization routine from accurately inferring the diffusion profile, it does demonstrate an unexpected indirect coupling where low edge temperatures can lead to delay in the LBO injection which then can cause erroneous core diffusion peaking. This effect is most obviously observed between the

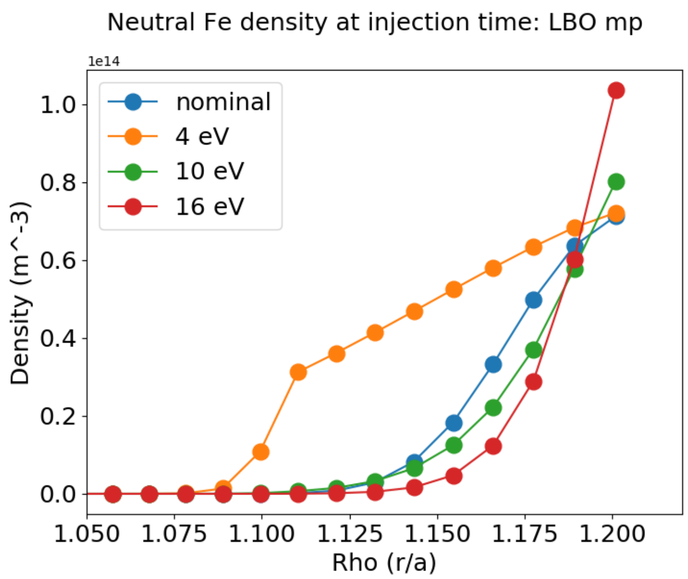

Figure 4.28: The neutral iron spatial distribution taken at the LBO injection time for the final fits using the various electron temperature profiles.

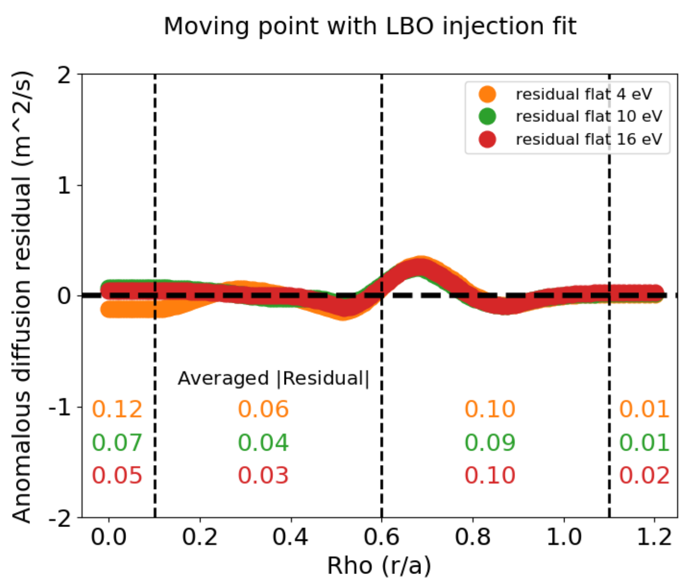

Figure 4.29: The residuals between the inferred anomalous diffusion profiles, as seen in figure 4.27b, with the original synthetic-data-generating profile for the edge T_e variations.

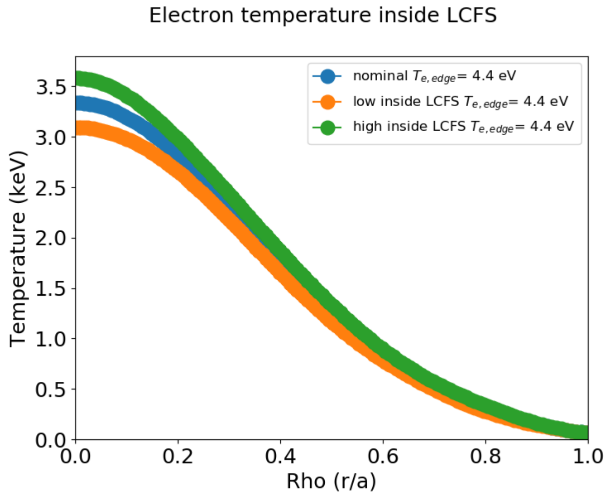

(a)

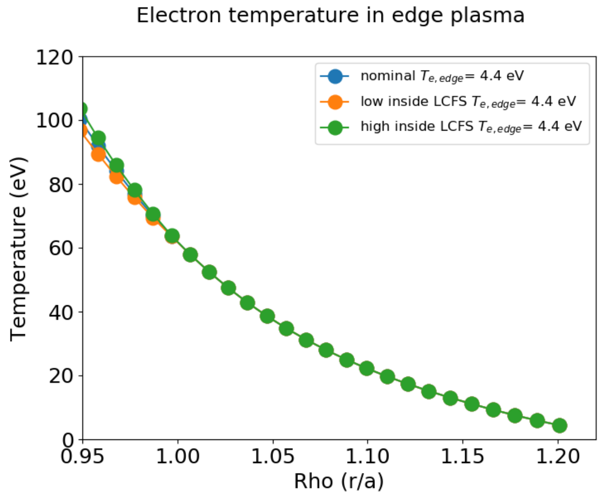

(b)

Figure 4.30: The low and high 1-sigma electron temperature profiles from on axis till the last closed flux surface in (a), while (b) shows how the low and high scenarios have been forced to have the nominal, data-generating edge electron temperatures

1st stationary inference and the 2nd moving point inference for the 4 eV flat edge T_e scenario as seen in figure 4.27

Core electron temperature variation

- The core electron temperature variation of $\Delta T_{e,core} \sim 500$ eV has minimal impact on the accuracy of the inferred anomalous diffusion profile and the matching of the spectral signals

To further isolate the electron temperature effects on $lstsq\_STRAHL\_wrap$'s ability to accurately infer the anomalous diffusion profile, the electron temperature profile's 1-sigma uncertainties were used to create a low and high estimate from the plasma core to the last closed flux surface, LCFS. Outside the LCFS the T_e profiles for the high and low estimates were set equal to the nominal, synthetic data-generating profile as seen in figure 4.30.[n]. This electron temperature variation inside the confined plasma region should provide context to the previous edge T_e variational study to understand how core temperature measurement errors could introduce inaccuracies in the inferred anomalous diffusion profile. Therefore as seen

[n]The entire low and high T_e profiles were shifted up and down respectively to match the electron temperature at the LCFS, ensuring that the electron temperature profiles are continuous across the LCFS while only minimally effecting the core T_e shifts

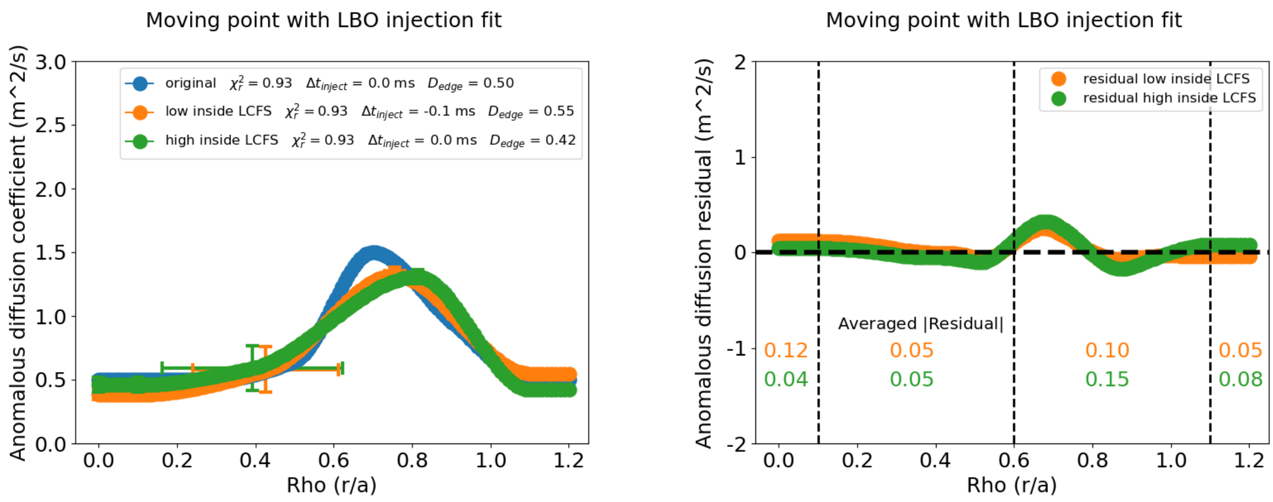

(a) (b)

Figure 4.31: The inferences of anomalous diffusion, while shifting the $T_{e,core}$ values by $\pm$ 250 eV are shown in (a) while the corresponding residuals with the original synthetic-data-generating profile is shown in (b). The inferred anomalous diffusion profiles demonstrate that $T_{e,core}$ changes of $\sim$ 500 eV don't preclude the least square routine from finding the accurate profile all with seemingly good matches to the data, $\mathcal{X}_R^2 \approx 1.0$

in figure 4.31 the results from the procedural method inferences are shown with good line emission signal matching, $\mathcal{X}_R^2 \approx 1.0$, along with inferred diffusion profiles as accurate as the inferences performed with the fixed parameters held at their synthetic data-generating values as seen in figure 4.13.

The major conclusion from this core electron temperature variation is that a $\Delta T_{e,core} \sim$ 500 eV seems to have minimal impact on the accuracy of the inferred anomalous diffusion profile. Comparing to the aforementioned procedural method inference profiles, figure 4.13, the largest deviation occurs in very core and the far edge diffusion.The edge diffusion values are inferred to inaccurate values $\sim 0.05\ \frac{m^2}{s}$ too high (low) for the low (high) core electron temperature scenario. In particular without any substantial difference in the inferred LBO injection time, the edge diffusion value seems to be acting as a boundary condition whereby the lower (higher) T_e has a higher (lower) edge diffusion value to reduce (increase) the inferred anomalous diffusion gradient across the LCFS. Note that the lowest iron chargestate utilized, Fe^{+12}, has line emission that is radially localized between $0.7 < \rho < 1.1$ meaning the edge diffusion values aren't as sensitive for specifying this spectral line's temporal shape (e.g. see figure 4.24). Therefore the additional UV spectral lines in the region from $\rho = 0.7$ to 1.0 are localized by

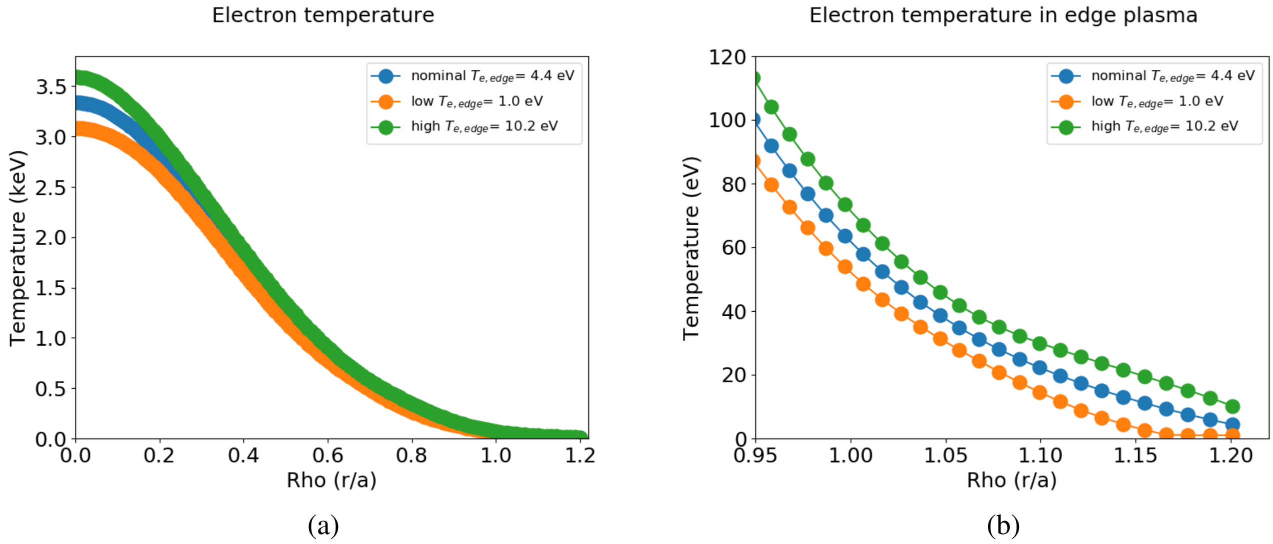

Figure 4.32: The electron temperature uncertainty range from the gaussian process regression fit with a zoom in profile view of the edge electron variation shown in (b)

the specified electron temperature profile in this range. In this way the large ∇T_e in this range helps ensure the line radiation is more spatially localized (hence the accurate inference of the anomalous diffusion profile), but the single, central sightlines for each emission line still yields the least squares routine freedom to alter the diffusion profile gradient to most closely match the emission.

Entire electron temperature variation

- The 1-sigma variation of the whole electron temperature profile introduces inaccuracies to the inferred anomalous diffusion profile, primarily for $\rho > 0.5$, without any degradations to the spectral signal matching.

- The indirect coupling between T_e and the inferred D_{edge} was verified. Specifically the lower (higher) T_e would lead to a higher (lower) inferred D_{edge} by means of delaying (expediting) the LBO injection time.

The last T_e variational study was performed with the 1-sigma uncertainties from the gaussian fit used to shift the entire nominal electron temperature profile up and down as shown in figure 4.32 In performing the entire profile shift direct comparisons can be made with the

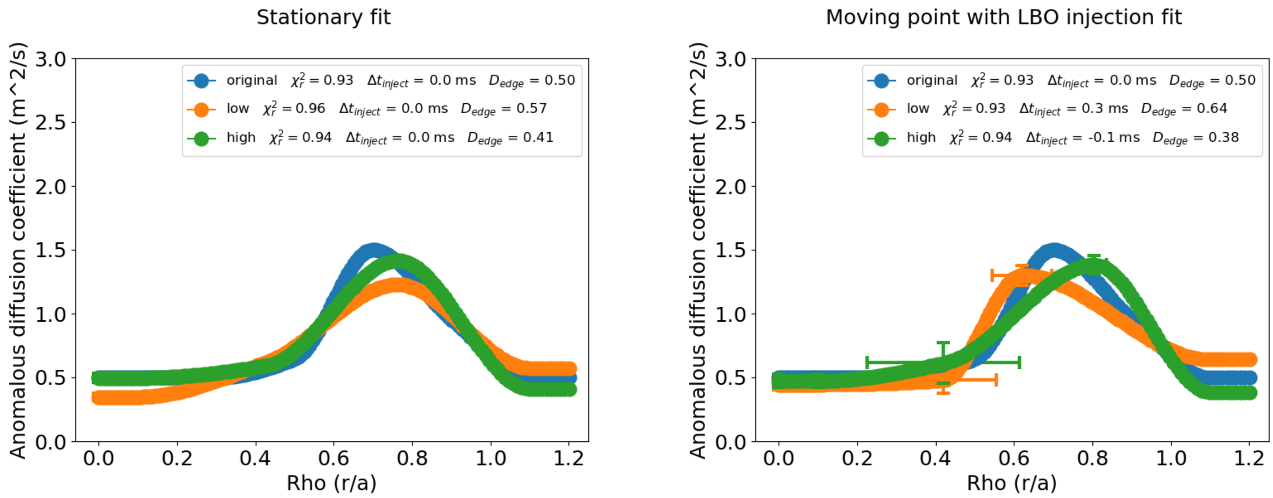

(a) (b)

Figure 4.33: The inferences of anomalous diffusion while holding the electron temperature at the incorrect profile extrema from the fit uncertainties following the standard procedure with the stationary fit shown in (a) and the moving spline-knot & LBO timing fit shown in (b).

previously observed effects from the core and edge variations. However the entire electron temperature profile shift places larger variations percentagewise in the outer regions of the plasma, $\rho \approx 0.7$ to 1.2, as can easily be seen by comparing figure 4.32b to 4.30b Moreover the previously mentioned edge T_e variational study only changed the far SOL T_e where it wouldn't have a direct impact to the spectral emission due to the low percent abundance of even the lowest modeled iron chargestate, Fe^{+12}. Therefore the increased percentage change in the T_e profile in the radial region of $\rho \approx 0.7$ to 1.2 would not only have a direct impact to the calculated spectral emission, but also change the radial position of each chargestate's fractional abundance.

The returned anomalous diffusion profiles from holding the entire T_e profile at the high and low end of their 1-sigma variations are plotted in figure 4.33. The first and expected conclusion is that least squares fitting routine can easily recreate the spectral emission temporal shapes, as evidenced by the $\mathcal{X}_R^2 \approx 1.0$, while using incorrect T_e profiles held at the 1-sigma low or high positions. The emission signal matching in conjunction with the accurate inferences of the anomalous diffusion profile indicate that the electron temperature measurement uncertainties introduce averaged inferred anomalous diffusion inaccuracies $< 0.15\ \frac{m^2}{s}$. Thus with the current levels of uncertainty in the electron temperature measurements, the anomalous diffusion profile

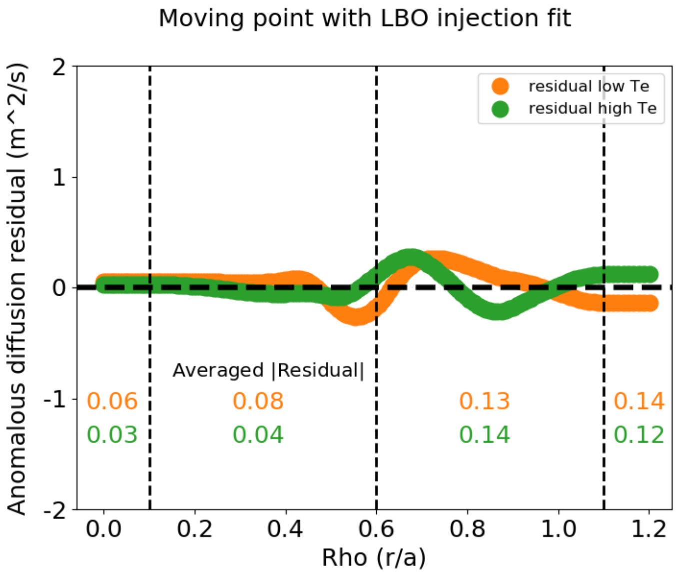

Figure 4.34: The residuals between the inferred anomalous diffusion profiles, as seen in figure 4.33b, with the original synthetic-data-generating profile for the entire T_e profile variations.

should be accurately inferable with the largest uncertainies occurring in the outer half of the radial profile where only a single, central sightline for each iron chargestate is available.

The second conclusion is that the indirect coupling between LBO injection timing and the edge diffusion value observed in the edge variational study was also observed in the entire T_e profile variation. Specifically the low temperature scenario returned a higher edge diffusion, a delayed LBO injection time, and an increased penetration of the neutral iron cloud as seen in figure 4.35. The increased neutral iron penetration from the low T_e values causes the least squares routine to prioritize inferring an elevated edge diffusion since this will increase the transport with minimal impact on matching the spectral line emission due to the negligible emission in the region outside $\rho = 1.1$ This increased edge iron flux is accompanied by a LBO injection delay to ensure the spectral signals' rise time can be accurately matched. The exact opposite effects of a slightly earlier LBO injection, lower edge diffusion, and decreased neutral iron penetration are observed for the high T_e scenario demonstrating the correlation of these effects with the T_e profile.

Finally a shallower (steeper) anomalous diffusion gradient across the LCFS is inferred for the low (high) T_e scenario along with an inward (outward) shifted anomalous diffusion peaking. The inward (outward) shift of the anomalous diffusion peaking for the low (high) temperature

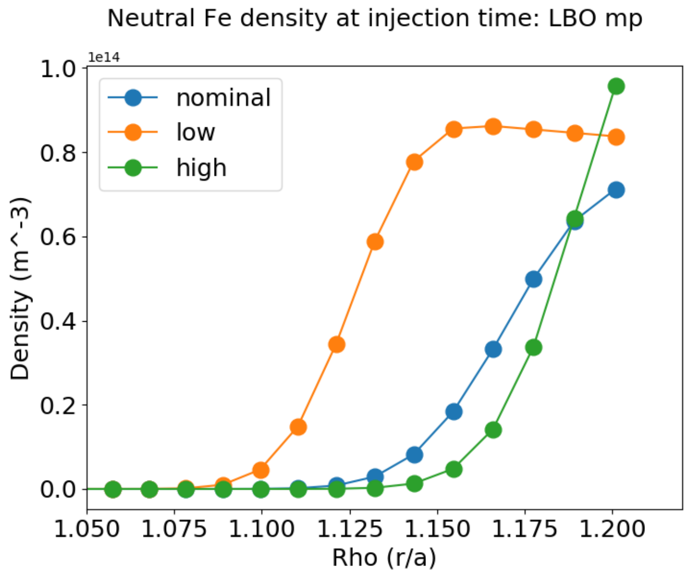

Figure 4.35: The neutral iron spatial distribution taken at the LBO injection time for the final fits using the low and high 1-sigma electron temperature profiles.

scenario is largely a combination of the line emission's dependence on impact excitation and the radial position of the chargestate's fractional abundance. Both the line emission radial distribution and fractional abundance position depend strongly on the specified T_e profile. Moreover for the line emission signals used in this thesis work, there are only single, central sightlines for all iron chargestates below Fe^{+24} meaning the radial localization of emission will most strongly be driven by the T_e profile as seen in figure 4.36. Therefore the high T_e scenario yielding an outward shifted diffusion peak is consistent with greater line emission contributions to the line-integrated signals from radial positions further out, i.e. $\rho > 1.0$ Likewise the inward shifted diffusion peak for the low T_e scenario is consistent with line emission distributions, as seen in figure 4.36a, being inward shifted causing the least squares routine to favor lower diffusion gradients to match the respective chargestate's timetrace.

4.2.7 Variation of LBO injection temporal shape

The last sensitivity study performed was a variation in temporal distribution of the neutral iron LBO injection. As described in section 5.1.3, the experimentally measured line emission shows signs of multiple iron clouds/particles entering the plasma from a single LBO injection event. These multiple iron clouds are not only visibly seen as secondary spikes on a signal's timetrace,

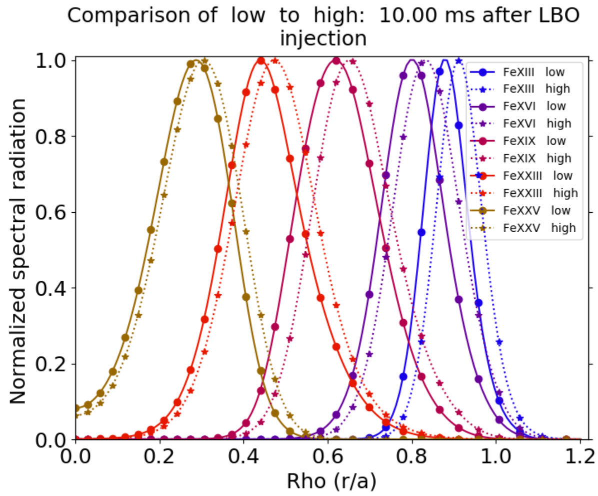

(a)

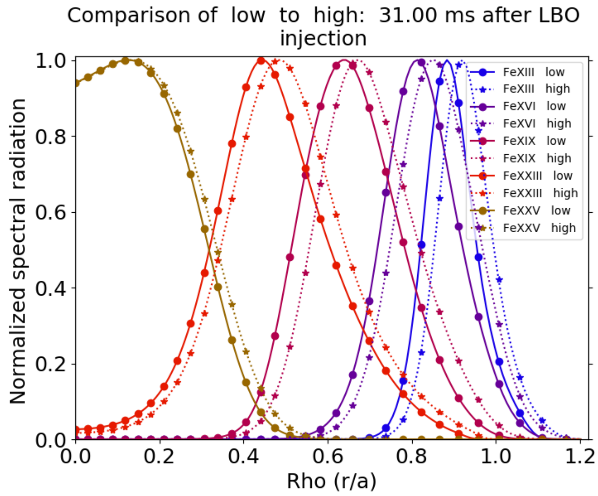

(b)

Figure 4.36: The normalized line emission at 10 and 31 ms after the LBO injection are plotted in (a) and (b) respectively with both the low and high T_e profile scenarios shown in solid and dashed lines respectively. These distributions correspond to the same inferences shown in figure 4.33b.

but also are easily identifiable for chargestates as high as Fe^{+18}. Unfortunately these secondary spikes/peaks in the measured signals distort the decay and even the rise shape of the emission's timetrace, adding uncertainty to the anomalous diffusion profile's inference.

Therefore to better estimate these uncertainties new synthetic data was generated using the nominal parameters except that the LBO injection consisted of two injections separated by 15 ms with the 2nd injection 25% the total number of particles as the 1st in addition to the total injected particles kept equivalent to the previously modeled single injections. Figure 4.37 shows four line emission timetraces from utilizing the double injection model, clearly showing the strong effect on the temporal shape. In this sensitivity study, the double injection noisy synthetic data was attempted to be fit utilizing the standard single injection or with extended duration single injections in order to test their respective effects on the inferred diffusion profile.

Standard single injection

- Modeling a double LBO injection with a single injection causes very large inferred diffusion inaccuracies for $\rho > 0.6$, $\sim 0.4\ \frac{m^2}{s}$, with minimal degradation of the spectral signal matching, $\mathcal{X}_R^2 < 1.7$

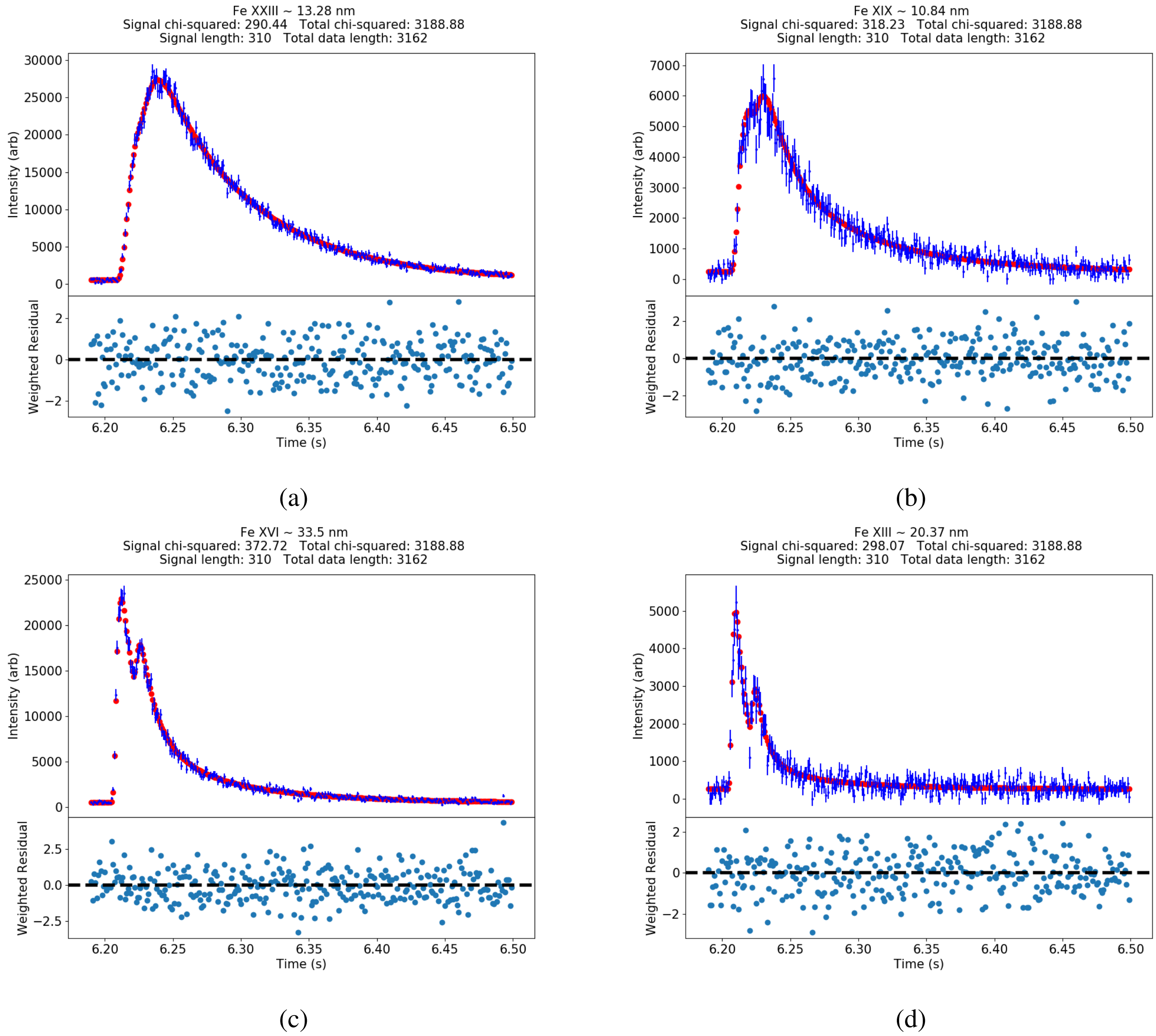

Figure 4.37: The double injection as seen in figure 4.38 was used to generate the above signals in blue, with the modeled fit shown in red.

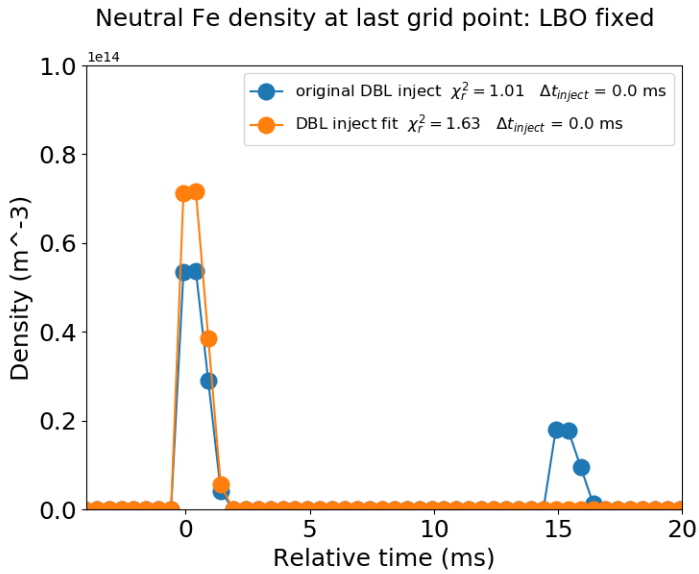

Figure 4.38: The neutral iron density at the outermost spatial position for the synthetic-data-generating double injection shown in blue and the standard injection shape shown in orange. The injection is a double LBO injection where the total number of particles injected is the same as the original, but has a 15 ms delayed injection with 25% of the particles.

- The radial moving spline-knots exacerbates the inaccurate temporal LBO injection modeling, increasing the averged residual error from $\sim 0.15\ \frac{m^2}{s}$ to $\sim 0.4\ \frac{m^2}{s}$
- The temporal shape distortion from a secondary neutral iron cloud 15 ms after the first injection is clearly identifiable on the iron line emission even on chargestates as high as the Fe^{+22} as seen in figure 4.42

As seen in figure 4.38 the standard single injection temporal shape was used to attempt to match the signals produced with aforementioned double injection model. Immediately following the standard procedural method the 1st and subsequent 2nd fit are shown in figures 4.39a and 4.39b respectively.

The first conclusion is that using the standard single LBO injection shape the line emission timetraces can mostly be recreated, i.e $\mathcal{X}_R^2 < 1.5$ after the 2nd fit in the procedural method. Unsurprisingly the inaccuracies in the inferred diffusion profiles are limited to the outer half of the plasma, $\rho > 0.5$, for both the stationary and subsequent moving fit. This result is to be expected due to the single, central sightlines for the UV line emission that are localized in this region giving the least squares routine more leeway in shaping the diffusion profile to match the

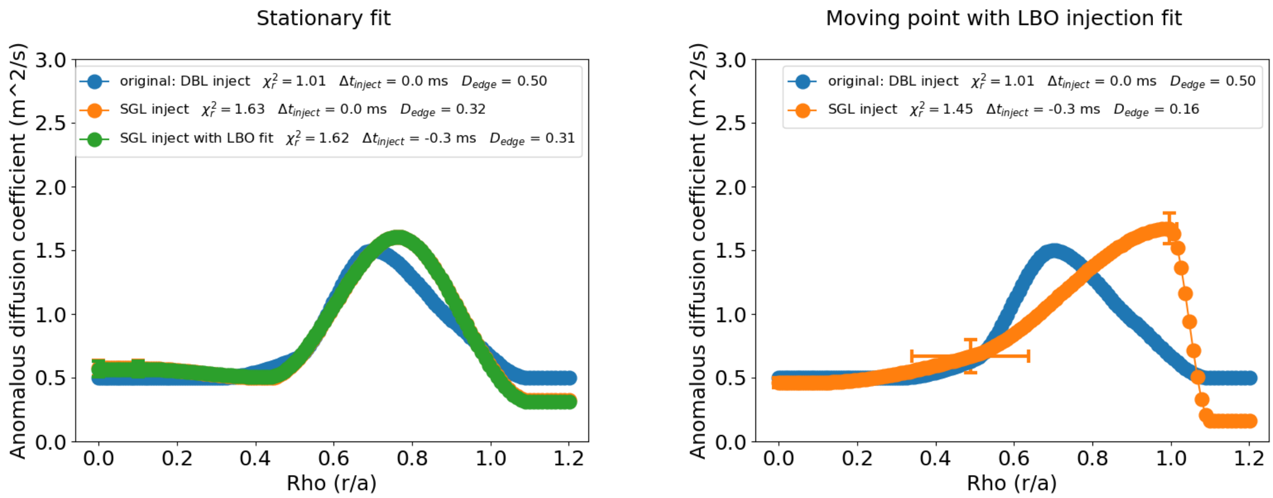

(a) (b)

Figure 4.39: The inference of the anomalous diffusion profile, while using the incorrect single LBO injection shape as seen in figure 4.38 for the initial stationary fit in (a) and the 2nd fit including the moving spline-knots & LBO injection timing in (b). Unfortunately the inferred diffusion profile is inaccurate with $\mathcal{X}_R^2 < 1.7$ indicating that the true LBO injection temporal shape may be needed for accurate inferences.

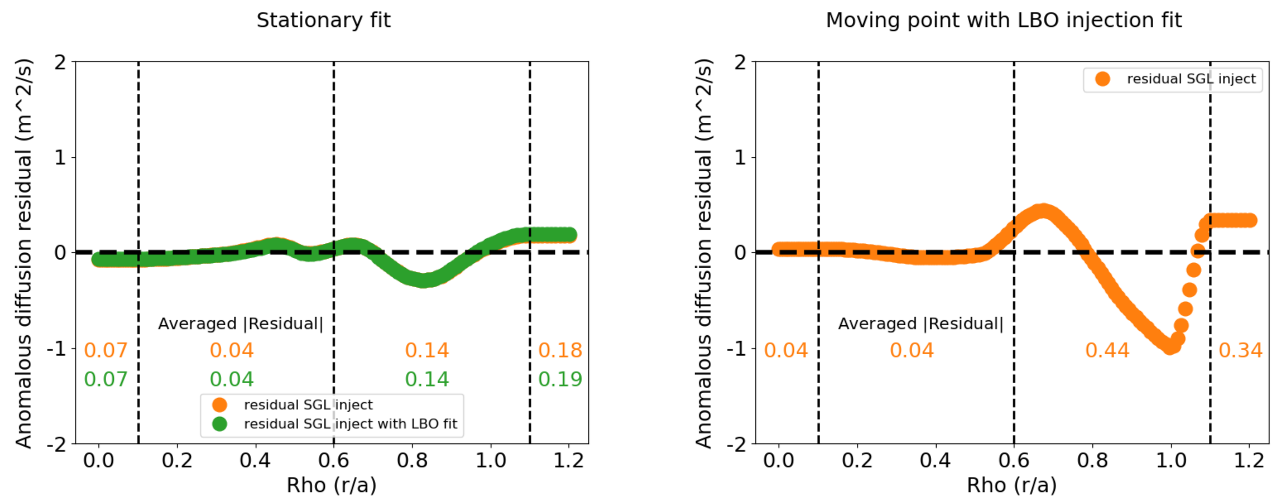

(a) (b)

Figure 4.40: The residuals between the anomalous diffusion profiles shown in figure 4.39 and the original synthetic-data-generating diffusion profile are shown in (a) and (b) respectively.

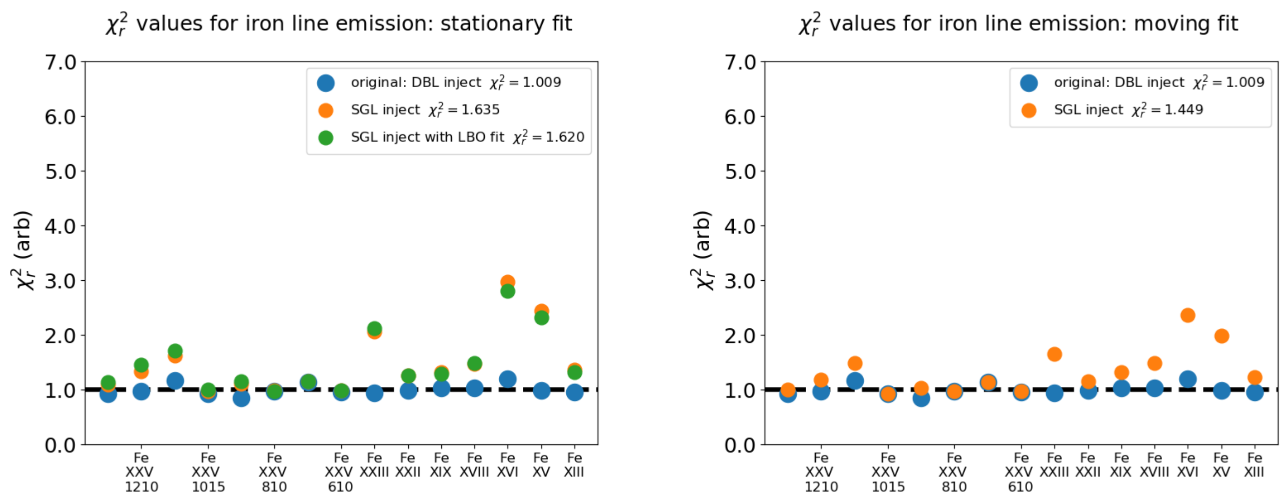

(a) (b)

Figure 4.41: The signal $\mathcal{X}_R^2$'s corresponding to the inferences performed in figure 4.39. The signal $\mathcal{X}_R^2$'s from the initial stationary fit are shown in (a), while the signal $\mathcal{X}_R^2$'s from the 2nd fit including the moving spline-knots & LBO injection timing are shown in (b).

line emission. However the stationary spline-knot inferences yielding more accurate anomalous diffusion profiles than the moving spline-knot inference was unexpected. It is clear from figure 4.39a that it is the inclusion of radially-moving spline-knots not the LBO injection timing that allows the least squares routine to better match the line emission as evidenced by the reduction in $\mathcal{X}_R^2$ in the moving spline-knot inference. Therefore the moving spline-knots have given the least squares routine the freedom to match the distorted temporal line emission shapes from the double injection by driving a large diffusion gradient in the edge plasma. In fact in figure 4.41 the UV lines with the highest average signal-to-noise ratios, i.e. FeXXIII, FeXVI, and FeXV, were the better-matched emission lines when moving spline-knots were included in the 2nd fit as seen in figure 4.39b.

The second conclusion is that the inaccurate description of the LBO injection provides enough uncertainty in the lower chargestates' line emission shape that with only single, central sightlines the introduced inferred anomalous diffusion inaccuracies can be $\sim 1.0\ \frac{m^2}{s}$. For example, the moving spline-knot inference's line emission matching can be seen in figure 4.42 where the four signals are the three highest signal-to-noise ratio UV lines along with the lowest chargestate emission used in the modeling, FeXIII. Examining the single injection model's match to the double injection generated data clearly shows structure in the weighted residuals

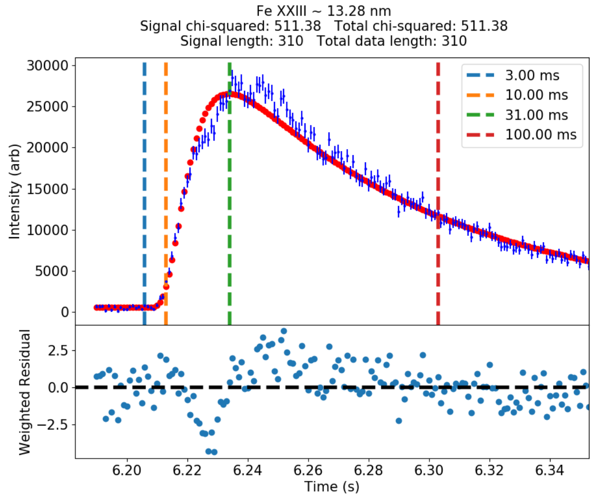

(a)

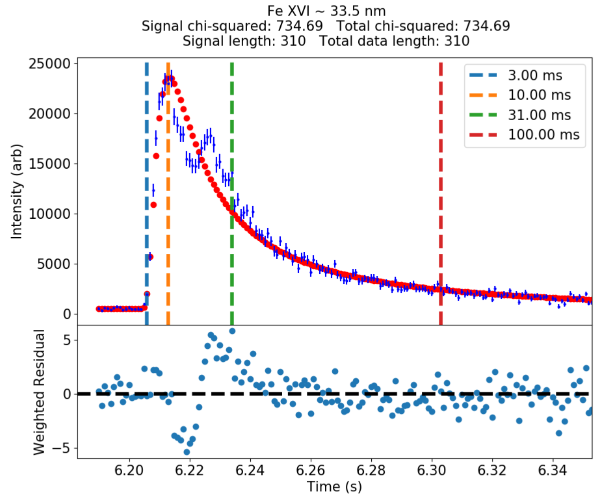

(b)

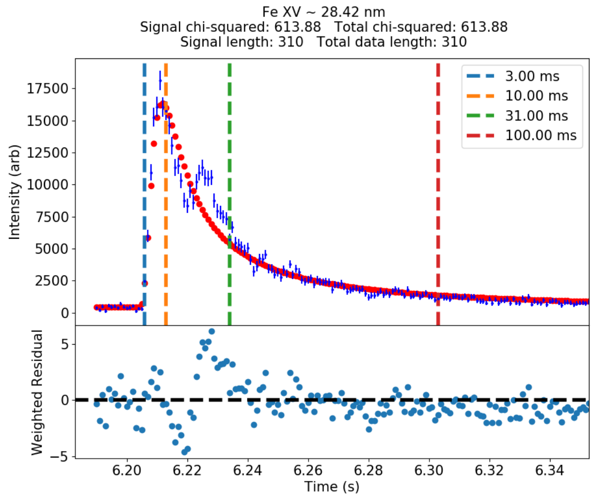

(c)

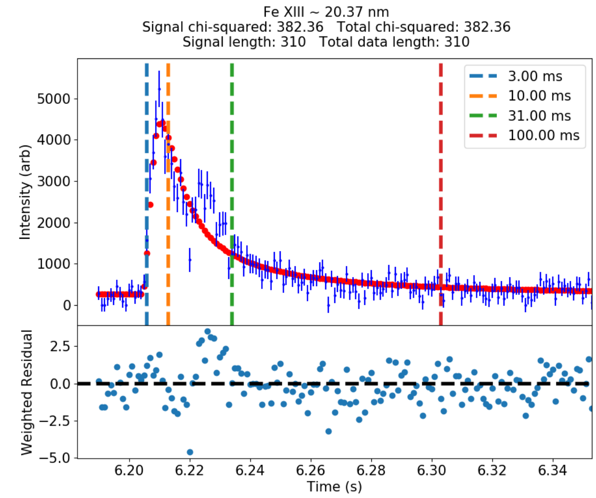

(d)

Figure 4.42: The double injection as seen in figure 4.38 was used to generate the above signals in blue, with the modeled fit using the standard single injection shape along with moving spline-knots & LBO injection timing shown in red (i.e. the inferred diffusion profile from figure 4.39b). Overplotted on each subfigure are vertical dashed lines indicating the 3, 10, 31, and 100 ms after the fit LBO injection time.

indicating an imperfect fit, but not to the extent that would cause the inference to be deemed invalid, i.e. $\mathcal{X}_R^2 \approx 1.45$. The highest chargestate line emission, FeXXIII, clearly shows the largest deviations on the signal rise, while the three lowest chargestates' spectral lines show the largest deviations on the signal decay. This observation is important since the usage of a single LBO injection cannot artificially prolong the lower chargestate emissions like the true double LBO injection does. Therefore under the single LBO injection scenario, the least square routine will simultaneously attempt to decrease the diffusion values to prolong the lowest chargestates' signal decays while delaying the LBO injection time to match the exact rise time. This description now helps explain the decreased inferred diffusion values in the far SOL, the increased diffusion gradient across the LCFS, and the slight delay in the LBO injection that is returned using the single, incorrect LBO model. To better understand this observation, the spectral lines spatial emission distribution can be examined at the same times as those indicated in figure 4.42. Figure 4.43 shows the same spectral lines' normalized emission radial distribution where on a first pass there is minimal differences between the original double injection and the incorrect single injection scenarios. However upon closer examination it is clear that the FeXVI, FeXV, and FeXIII spectral emission distributions are slightly broader for the single injection case and 10 ms after the LBO injection have significant fractional emission in the radial range of $\rho \approx 1.0$ to 1.1, see figure 4.43c. In this way the least squares routine can drive nonphysical gradients in the diffusion profile over the radial range of $\rho \approx 1.0$ to 1.1 without drastically changing the radial distribution of the normalized emission. Also these nonphysical gradients can extend the signal decays by having a small portion of the sightline integrals have contributions from regions with lower diffusion values. The radially-moving spline-knots exacerbate the artificially steep diffusion gradients since all of the modeled spectral lines in this region only have a single, central sightline which cannot fully localize the emission. Thus without an exact measurement of the LBO injection temporal shape, the use of a single LBO injection model can introduce uncertainties in the inferred anomalous diffusion in the outer half of the plasma up to $\sim 1.0\ \frac{m^2}{s}$.

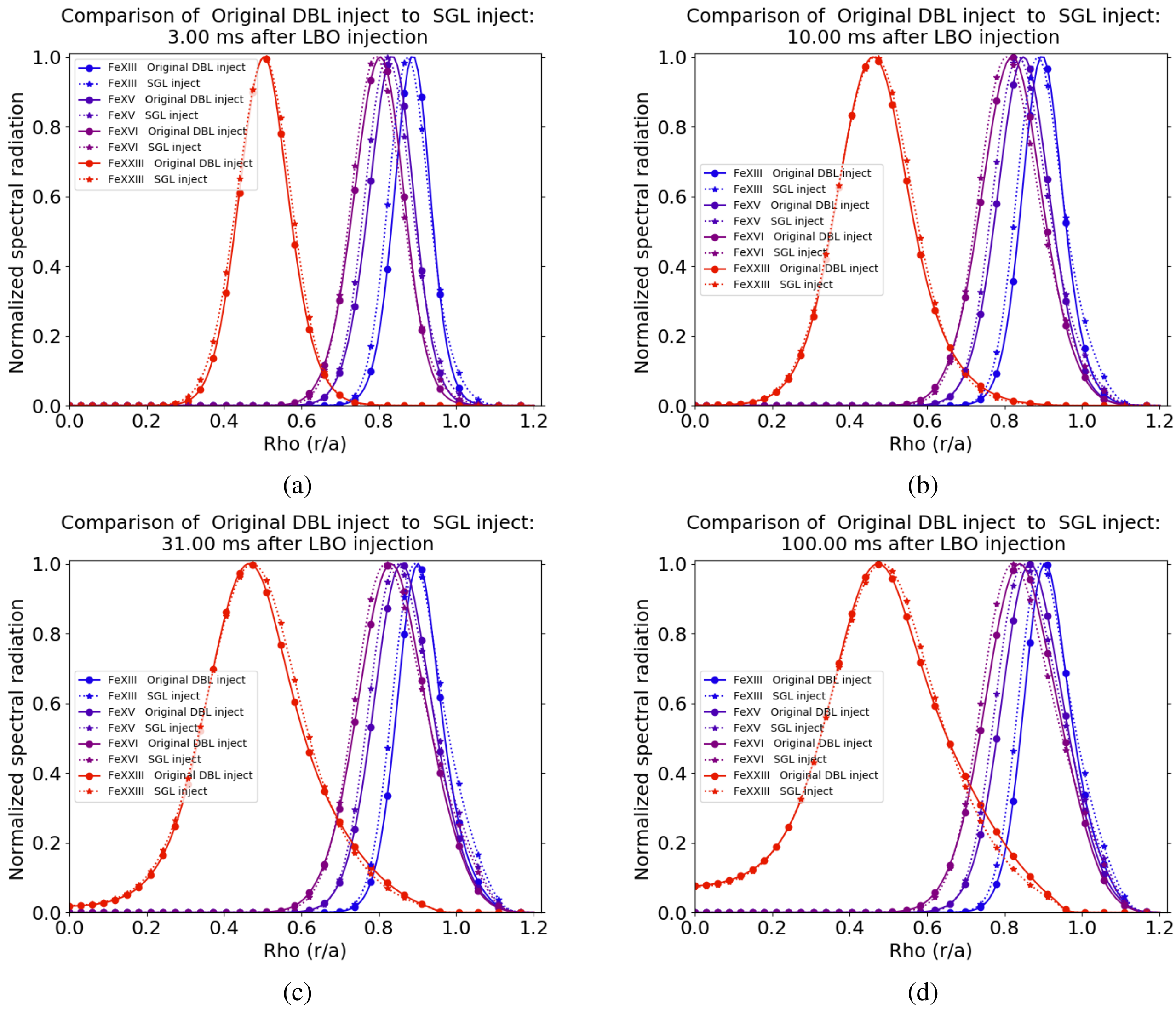

Figure 4.43: The normalized line emission at 3, 10, 31, and 100 ms after the LBO injection for the 2nd fit including the moving spline-knots & LBO injection timing using the standard, incorrect single LBO injection. These distributions correspond to the same inference shown in figure 4.39b).

Extended single injection

- Modeling a double LBO injection with an extended single injection causes very large inferred diffusion inaccuracies for $\rho > 0.6$, $\sim 0.4\ \frac{m^2}{s}$, with minimal degradation of the spectral signal matching, $\mathcal{X}_R^2 < 1.8$

- The single, central sightlines for the UV spectral emission do not provide adequate spatial localization and as such provide the least squares routine freedom to return diffusion profiles with inaccuracies up to $\sim 0.2\ \frac{m^2}{s}$ all the while adequately matching the spectral signals distorted from a double LBO injection. Importantly these inaccuracies are exacerbated by the radially-moving spline-knots with errors increasing to $1.0\ \frac{m^2}{s}$

A single injection model with an extended iron injection was tested to better understand whether the observed spectral emission from a double injected scenario could be more accurately modeled. With no recorded data for the temporal history of the neutral iron cloud as it enters the plasma, perhaps single iron injections of say 4 and 10 ms could better mitigate inference uncertainties. In order to keep these scenarios as accurate as possible the total number of injected particles was kept constant, see figure 4.44, since experimentally this number is more readily verifiable from spot size measurements on the glass iron LBO target.

The 2nd inferences from the procedural method using the extended single injections from figure 4.44 produce nearly identical anomalous diffusion profiles as the standard single injection scenario. In fact the only major differences are the shift in the injection time to be earlier as seen in figure 4.44b and the slight increase in the $\mathcal{X}_R^2$. Therefore exactly analogously to the shorter single injection scenario, the lack of spatial localization of the UV spectral emission in conjunction with radially-moving spline-knots created freedom for the least squares routine to return diffusion profiles with inaccuracies up to $\sim 1.0\ \frac{m^2}{s}$ all the while adequately matching the spectral signals distorted from a double LBO injection.

4.2.8 Realistic transport profile synthetic data conclusions

The synthetic data was generated from input parameterization based on the same real iron LBO experiment as used in section 4.1 with the primary difference being the realistic specification

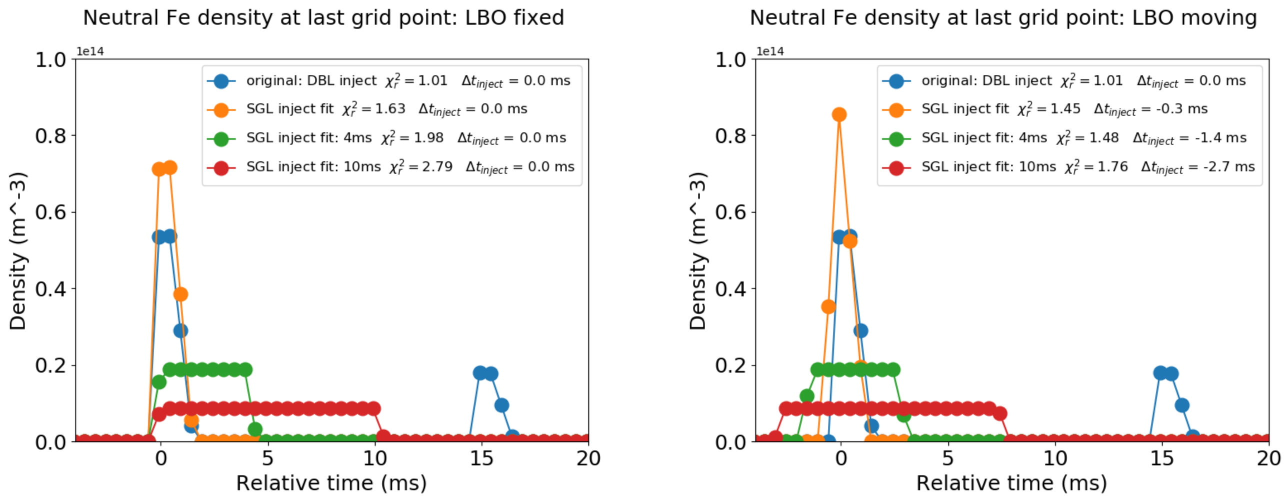

(a) (b)

Figure 4.44: The neutral iron density at the outermost spatial position for the synthetic-data-generating double injection shown in blue with the attempted single injections overplotted for stationary and free LBO injection time in (a) and (b) respectively

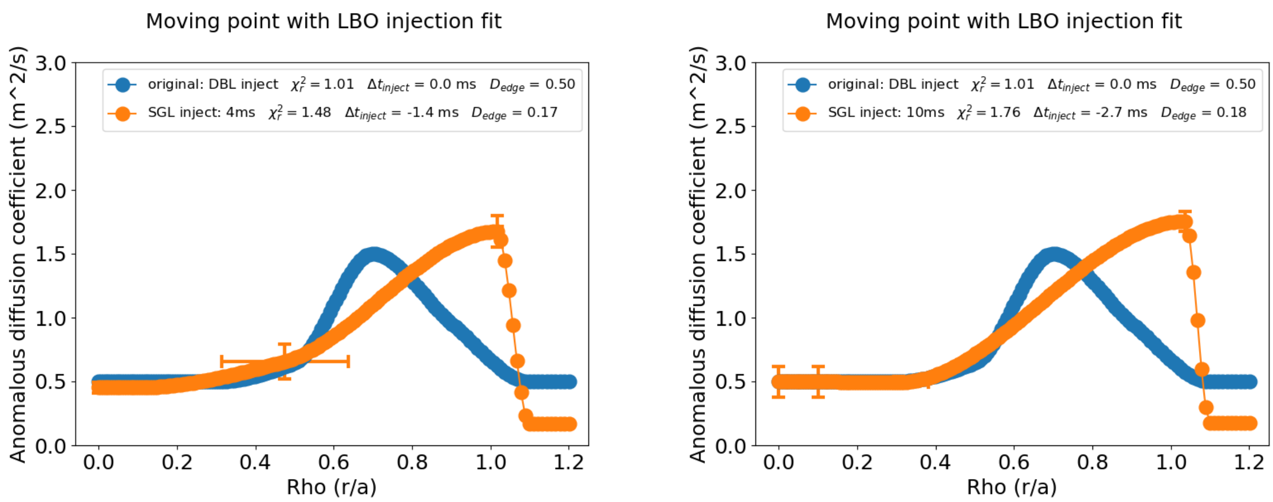

(a) (b)

Figure 4.45: The 2nd inferences of anomalous diffusion following the standard procedural method while also utilizing the incorrect single extended duration LBO injection shapes as seen in figure 4.44 with the 4 ms injection in (a) while the 10 ms injection in (b).

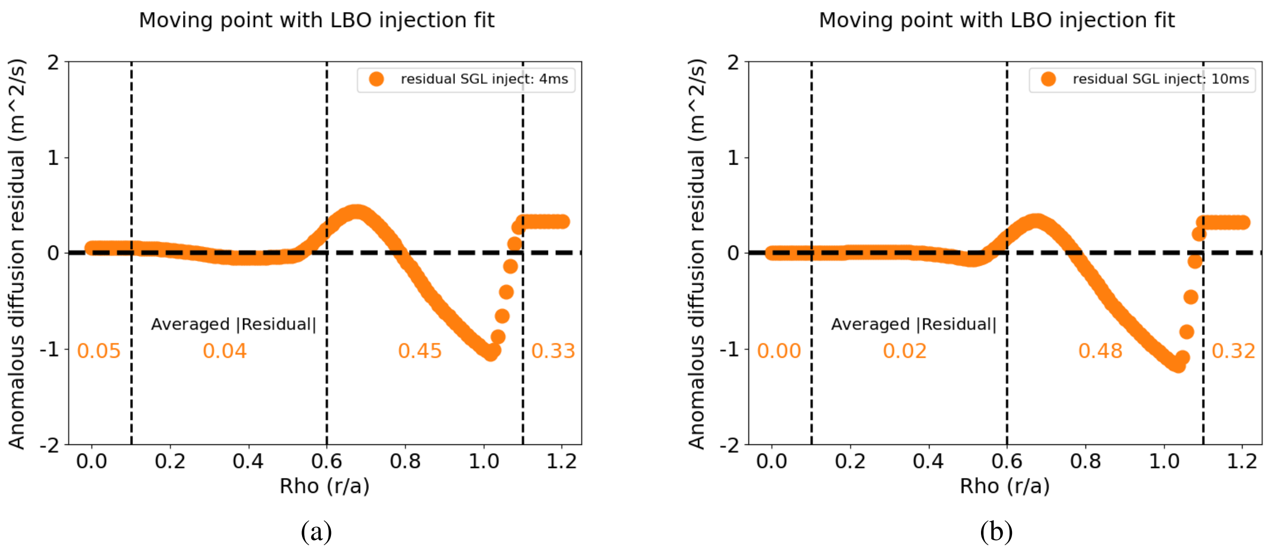

Figure 4.46: The residuals between the anomalous diffusion profiles shown in figure 4.45 and the original synthetic-data-generating diffusion profile are shown in (a) and (b) respectively for the 4ms and 10 ms extended LBO injection scenarios.

of the anomalous diffusion and convection profiles as inspired by an experimental best fit. This synthetic data testing demonstrated four key conclusions:

- Although a procedural method for performing the least squares minimization was affirmed to accurately recover the anomalous diffusion profile, the inferred diffusion profile still didn't exactly match the off-axis peaking present even with the inclusion of radially moving spline-knots.

- Incorrect diagnostic timing offsets have large effects, i.e. $> 0.5\ \frac{m^2}{s}$, on the accuracy of the inferred diffusion profile. However the LBO timing offset can be determined though the least squares minimization, while unfortunately the x-ray to VUV timing offset cannot.

- The accurate inference of the anomalous diffusion profile is minimally effected, i.e. $\sim 0.3\ \frac{m^2}{s}$, by the electron temperature profile variations within its 1-sigma uncertainties.

- The LBO injection temporal shape is critically important for accurate inference of the anomalous diffusion profile.

The confirmation of the procedural method as a viable means to accurately infer the anomalous diffusion profile is critical not only for establishing a process to evaluate the experimental LBO injections, but also for improving the characterization of the model. In fact the procedural method verification demonstrated that the use of eight individual sightlines for the He-like w-line is enough spatial information to accurately constrain the anomalous diffusion profile from plasma mid-radius and inward. This indicates that a single inverted w-line emission profile is not necessary and that having eight different sightline scalefactors doesn't prevent the least squares routine from finding the accurate solution even with an expanded parameter-space. Although the spatial information provided by the eight sightlines was effective in constraining the diffusion profile where $\rho < 0.6$, the exact off-axis peaking of the diffusion profile could not be recovered even with the inclusion of radially-moving spline-knots in the second inference of the procedural method. More importantly the original, data-generating diffusion profile was not within the inferred diffusion spline-knots' uncertainties in both the stationary and moving spline-knot inferences. This is particularly important because the exact parameters[o] and 1-sigma signal uncertainties were used within the least squares routine meaning that using a reduced model with fewer spline-knots introduces a systematic error which dominates the contribution from the uncertainty in the signal measurements. Practically the consequence of model error is that the transport profile's uncertainty given by the least squares routine is not guaranteed to encompass the true profiles. Therefore even in this synthetic data sensitivity study with ideal input parameters and uncertainties, the model still doesn't capture the full uncertainties in the inferred parameters and specifically means the anomalous diffusion profile's errors can be underestimated. In addition to the underestimation of the parameter uncertainties, the procedural method verification reaffirmed the insensitivity of iron line emission to the anomalous convection velocity profile. Although it was shown in section 4.1.2 that the anomalous diffusive flux is the dominant transport channel even at values of $\sim 0.3\ \frac{m^2}{s}$, the procedural method verification demonstrated that at even higher anomalous diffusion values the anomalous convection velocity could return errors $> 1.0\ \frac{m}{s}$. Fortunately the inclusion of the anomalous convection velocity didn't substantially effect the line emission signal matching and didn't increase the errors in the inferred anomalous diffusion profile. However with the

[o]Except the parameters being fit within $lstsq_STRAHL_wrap$

potential errors in the inferred convection velocity on the same order as the magnitudes expected in the experiment, it is better to exclude the anomalous convection velocity profile from inferences in order to minimize the possibility of nonunique inferences.

The second conclusion that incorrect diagnostic timing offsets lead to errors $> 0.5\ \frac{m^2}{s}$ in the inferred diffusion profile is critical for its implications on diagnostic requirements and the procedural method. As already emphasized in the flat-transport-profile conclusions and mentioned in the procedural method verification, the LBO timing offset can be reliably included as a free fit parameter within the least squares routine. The reason it should be included as a free fit parameter is due to the fact that both the iron line emission signal matching and the diffusion profile are sensitive to the absolute LBO timing of the injection. Therefore rather than require a precise measurement of the absolute timing as the neutral iron cloud enters the plasma edge, this LBO injection time can reliably be determined within the least squares routine. In contrast to the LBO injection time, the VUV to x-ray detector timing offset is not sensitive to the line emission signal matching, meaning an incorrect VUV to x-ray timing offset doesn't prevent the least squares routine from matching the iron signals. Unfortunately with an incorrect VUV to x-ray timing offset the iron signals are matched by the manipulation of the anomalous diffusion profile, yielding increased inaccuracies. Therefore the identification of inaccuracies with either diffusion profile and/or detector timing offset is not possible within the least squares fitting routine. This result underscores the importance of the experimental synchronization of detector timebases in order to minimize the inaccuracies in the anomalous diffusion profile introduced from an incorrect detector time offset. Finally during the verification of the procedural method, both diagnostic timing offsets tested within the synthetic studies demonstrated inaccuracies in the anomalous diffusion profile that propagated well into the core plasma. This increased core anomalous diffusion error is of particular importance since it occurred in the region where the increased spatial information provided by the multiple sightlines of the He-like iron line emission reduced diffusion uncertainties for most other parameter variations except for those associated with diagnostic timing offsets.

Motivated from previous results in [Geiger et al. 7] and the potential impacts from an on- to off-axis scan of the ECRH power, the electron temperature variation was closely tested in this realistic transport profile synthetic sensitivity study. Critically the electron temperature profile variations within its 1-sigma uncertainties had minimal impact on the inferred anomalous diffusion profile. Specifically the core T_e variation of $\sim$ 500 eV didn't detract from iron line emission signal matching nor the accurate inference of the anomalous diffusion with inaccuracies $\sim$ 0.1 $\frac{m^2}{s}$ in both the core (ρ ¡ 0.1) and the off-axis regions (0.6 ¡ ρ ¡ 1.1). Moreover the entire T_e profile variation, which included the same $\sim$ 500 eV core T_e change, produced similar results with the largest anomalous diffusion inaccuracies of $\sim$ 0.1 $\frac{m^2}{s}$ located in the off-axis region. The T_e sensitivity test performed in [Geiger et al. 7] varied the entire T_e radial profile but had much larger variations as evidenced by a $\sim$ 2000 eV variation in the core T_e and a $\sim$ 50 eV variation at the last closed flux surface. These larger T_e changes both in magnitude and in percentage of the nominal T_e values led to shifts in the anomalous diffusion values in the core $\sim$ 0.2 $\frac{m^2}{s}$ and in the off-axis region $>$ 1.0 $\frac{m^2}{s}$.[p] Therefore [Geiger et al. 7] work taken in context with this thesis's synthetic sensitivity study of T_e, demonstrate that the T_e profile uncertainties must be resolved enough both in magnitude and percentage (i.e. $T_{core,e} \sim$ 2000 eV is equivalent to $\sim$ 18%) to have minimal impact on the inferred transport profile. For the on- to off-axis transport experiments presented in this thesis the core plasma $T_{core,e}$ uncertainties from the Thomson measurement, i.e. $\pm$ 250 eV, cannot be reduced, but critically are at levels that seem to add no more than $\sim$ 0.15 $\frac{m^2}{s}$ across the profile. This is an important conclusion since the on- to off-axis experiments had $T_{core,e}$ variations of $\sim$ 1000 eV, meaning these T_e profile variations were resolvable enough to have only minor impact on the inferred anomalous diffusion profile.

The fourth and final conclusion from the realistic transport profile synthetic sensitivity study is that the LBO injection temporal shape has the single largest impact on the inference of the anomalous diffusion profile. The double iron injected synthetic data demonstrated a strong shaping effect on the line emission for not only the lower chargestates like Fe^{+12}, but also for some of the highest chargestates $Fe^{+21,22}$. Although the shaping effect on the lower chargestates is more significant, both in signal magnitude and fraction of the LBO time points,

[p]It should be noted that signal data fits were impacted by these large changes in T_e with $\mathcal{X}_R^2$ at 1.15 and 1.25 for the low and high values respectively where the nominal inference had $\mathcal{X}_R^2$ = 1.05

the distortion of the higher chargestates rise time is still non-negligible. This fact highlights the importance of measuring the neutral iron line emission to extract the temporal shape of the injection and if possible optimizing the laser parameters to minimize extraneous flakes. Another unfortunate consequence of using an incorrect temporal LBO injection is its indirect coupling to the outermost radially-moving spline-knot. In this study the spline-knot radial position is inferred further outboard in a region with a large electron temperature gradient because the least squares routine can tailor the diffusion values to better match the line emission.The sensitivity to the large electron temperature gradient region is mainly due to the single, central sightlines for the VUV emission lines in this region yielding radial ambiguity in the line-integrated signal. Therefore in the outer half of the plasma the inferred diffusion spline-knot values and positions are susceptible to increased errors when the true LBO injection's temporal shape isn't used all the while yielding $\mathcal{X}_R^2 < 2.0$. Without multiple sightlines for each VUV spectral line the VUV emission cannot be radially localized enough to reduce the errors in the inferred anomalous diffusion profile or at worst return $\mathcal{X}_R^2 > 3.0$ indicating an inaccurate inference. However in the context of the experiments performed for this thesis work, the VUV spectra are limited to single, central sightlines that make the inferences susceptible to inaccurate diffusion profiles in the outer half of the plasma due to the incorrect LBO injection temporal specification.

4.3 Summary of synthetic data conclusions

The synthetic sensitivity studies detailed throughout this chapter extracted key information about which parameters should add the largest contributions to the inferred anomalous diffusion uncertainties returned from the least squares fitting routine. This is vitally important for estimating the true uncertainties on the experimental LBO injection modeling shown in chapter 6 without the need of performing full Monte-Carlo sampling of all the input parameters. Below is a compiled table of the estimated uncertainties on the anomalous diffusion profile introduced from the uncertainties in various parameters listed. The values are taken from the averaged absolute residuals for the four radial regions defined as $\Delta\rho$: 0 - 0.1, 0.1 - 0.6, 0.6 - 1.1, and 1.1 - 1.2. To estimate the total inaccuracies across the inferred anomalous diffusion profile the individual inaccuracies were assumed to be independent and therefore added in quadrature for

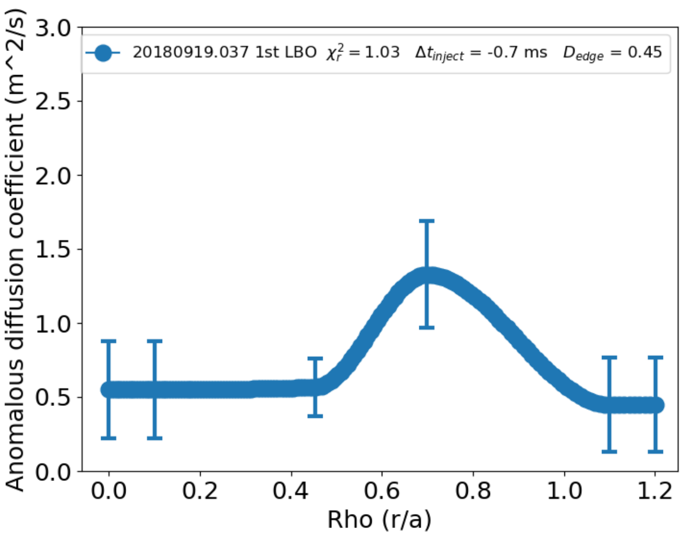

Figure 4.47: The anomalous diffusion profile inferred for 20180919.037 1st LBO injection is shown with the total calculated uncertainties from the realistic transport profile synthetic sensitivity studies.

each radial region.[q] Figure 4.47 gives visual context of the total uncertainties as applied to the real anomalous diffusion profile that inspired the realistic transport profile synthetic sensitivity studies as detailed in section 4.2. This quadrature sum of the diffusion profile inaccuracies will be used in the real experimental analysis as covered in chapter 6. These values will be used in conjunction with the returned parameter uncertainties from $lstsq\_STRAHL\_wrap$'s fit to the experimental data as an estimation for the uncertainties on the inferred anomalous diffusion profile.[r] It should be noted that these uncertainty values are just an estimation and might not encompass the true transport profile. Moreover these values more narrowly apply to an anomalously diffusive dominated plasma, i.e. $D_{anom} \geq 0.3\ \frac{m^2}{s}$ with $v_{anom} \leq 2.0\ \frac{m}{s}$, where potential input parameter couplings have not fully been evaluated. The reader is cautioned about over interpreting the table's absolute uncertainty values below since the total errors given in the last row of the table below are generated by adding the individual errors in quadrature based on the assumption that the uncertainties are independent. Therefore without further uncertainty analysis that can successfully decouple the input uncertainties from one another and

[q]The LBO injection timing errors were not included and only the entire T_e profile inaccuracies were added (i.e. the core and edge T_e errors were excluded)

[r]The returned parameter uncertainties refers here to specifically the anomalous diffusion spline-knot uncertainties that will be treated like an independent error and thus added in quadrature to the synthetically estimated uncertainty.

provide confidence intervals, the total values as detailed in the last row of 4.2 will be used as the estimated uncertainties in the experimental analysis presented in chapter 6.[s]

[s]Note that the grayed out uncertainty sources are not included in the total quadrature sum listed in the last row of 4.2

[t]See footnote s.

[u]See footnote s.

[v]See footnote s.

Table 4.1: Inferred anomalous diffusion profile uncertainties from the synthetic data sensitivity studies

			Average of $\lvert\text{Residual}\rvert$ $\left(\frac{m^2}{s}\right)$ in region ρ				
Uncertainty source	Thesis location	Parameter variations	0 to .1	.1 to .6	.6 to 1.1	1.1 to 1.2	Comment
Procedural method	4.2.2	N.A.	0.07	0.04	0.09	0.01	
Neoclassical & classical transport	4.2.3	50% to 200%	0.03	0.05	0.13	0.01	Uncertainty greatest in $\rho > 0.5$
X-ray to VUV timing offset	4.2.2	±2.5 ms	0.30	0.15	0.13	0.02	Uncertainty localized in core plasma
LBO injection timing[t]	4.2.2	±3.5 ms	5.02	2.29	2.1	0.35	The fits were clearly bad with $\mathcal{X}_R^2 > 2$ and nonphysical diffusion profiles. These error estimates can be ignored since the LBO injection time can be determined within the fit
LBO temporal shape	4.2.7	Outside a 2.5 ms window	0.07	0.04	0.14	0.19	Uncertainty largest in $\rho >$ 0.5 due to only single, central sightlines available for each chargestate

Table 4.2: Inferred anomalous diffusion profile uncertainties from the synthetic data sensitivity studies

			Average of $\lvert\text{Residual}\rvert$ $\left(\frac{m^2}{s}\right)$ in region ρ				
Uncertainty source	Thesis location	Parameter variations	0 to .1	.1 to .6	.6 to 1.1	1.1 to 1.2	Comment
Limiter connection length	4.2.5	0.5 to 25 m	0.05	0.05	0.12	0.13	Uncertainty greatest in $\rho > 0.5$
Divertor connection length	4.2.5	200 to 300 m	0.06	0.03	0.09	0.05	
T_e far SOL[u]	4.2.6	1 to 16 eV	0.08	0.04	0.10	0.02	Edge T_e can cause an incorrect LBO timing leading to more error
T_e core[v]	4.2.6	±250 eV	0.08	0.05	0.12	0.06	Small change observed in core
T_e entire profile	4.2.6	(see above)	0.04	0.06	0.14	0.13	Uncertainty greatest in $\rho > 0.5$
Neutral hydrogen profile	4.2.4	edge from 10^{14} to 10^{16} m^{-3}	0.04	0.04	0.17	0.16	Only the high neutral hydrogen case introduces significant uncertainties
Total errors summed	N.A.	N.A.	**0.33**	**0.20**	**0.36**	**0.32**	The errors are assumed to be independent. Only entire T_e profile variation added and no LBO injection timing errors added.

Chapter 5

Potential uncertainties and systematics examined via experimental data sensitivity studies

This chapter elaborates on the potential uncertainties and systematics that are inherent in the STRAHL code and can arise from $lstsq\_STRAHL\_wrap$. The least squares minimization of the difference between the measured spectral lines and STRAHL modeled lines cannot capture the systematic errors in the inferred transport profiles. The best way to quantitatively capture the true uncertainty for an inverse problem would be to employ a Monte-Carlo method that would generate many sets of input parameters over which a least squares minimization would be performed for every set. However performing a Monte-Carlo sampling in the parameter space of this impurity transport analysis would be prohibitively time consuming as each least squares fitting run typically takes approximately an hour and would need to be performed for every Monte-Carlo point. Therefore a two-step approach was taken to approximate the uncertainties without undertaking a full Monte-Carlo analysis. Performing the synthetic data sensitivity studies, as detailed in chapter 4, was the first step in approximating the inferred transport uncertainties. This first step was initiated in order to give confidence in the least squares method and understand the sensitivity from varying key input parameters over their uncertainties. The second step, and topic of this chapter, was to more thoroughly examine the potential uncertainties inherent to STRAHL and the least squares method. In the discussion of the inherent uncertainties, additional sensitivity studies were performed using **real experimental line emission signals** providing context for the synthetic sensitivity studies. An example of resultant inferences can be found in appendix E where an inference from each of the nominal scenarios for the noisy synthetic data presented in chapter 4 and for the experimental data presented in this chapter are shown. This discussion is important to give context for the confidence interval on the inferred transport profiles in lieu of performing a full Monte-Carlo approach.

The following chapter is divided into two parts, discussing the uncertainties introduced from the STRAHL model itself and from the least squares fitting routine. Therefore the first section will examine the uncertainties inherent from using the STRAHL code to solve for the transport and line radiation from the various iron chargestates. The second section will detail the uncertainties and potential systematics that arise from the least squares python wrapper's design and approach.

5.1 Uncertainties introduced from STRAHL

5.1.1 One dimensional code

- The inherent 1-D assumption within STRAHL does not prevent the least squares routine from matching the observed line emission.
- Wendelstein 7-X is a large aspect ratio stellarator meaning the difference between a volumetrically or toroidal flux defined radial grid is negligible.

The first and most obvious uncertainty associated with STRAHL is that STRAHL is inherently a one-dimensional code used to calculate the transport and emissivity of an impurity species. Although STRAHL was initially developed for an axisymmetric system like a tokamak, the one-dimensional approximation can still be valid for inherently three-dimensional systems like Wendelstein 7-X. The one-dimensional assumption of solving the radial transport indicates that the calculation would be at best accurate in a flux surface averaged sense. This flux surface averaged assumption might seem even bolder with a fully three-dimensional stellarator like Wendelstein 7-X as compared to a tokamak where axisymmetry ensures plasmas can be treated in 2D. For a large aspect ratio stellarator like Wendelstein 7-X, i.e $A \equiv \frac{R_{major}}{a} \approx 10$, the ratio of toroidal flux to the flux surface volume varies minimally with radius meaning the cylindrical form, as seen in equation (3.1), is accurate. Specifically the radial description of the diagnostic profiles whether defined by toriodal flux or volume enclosed are essentially equivalent as shown in figure 5.1. This equivalence is important since the measured radial profiles

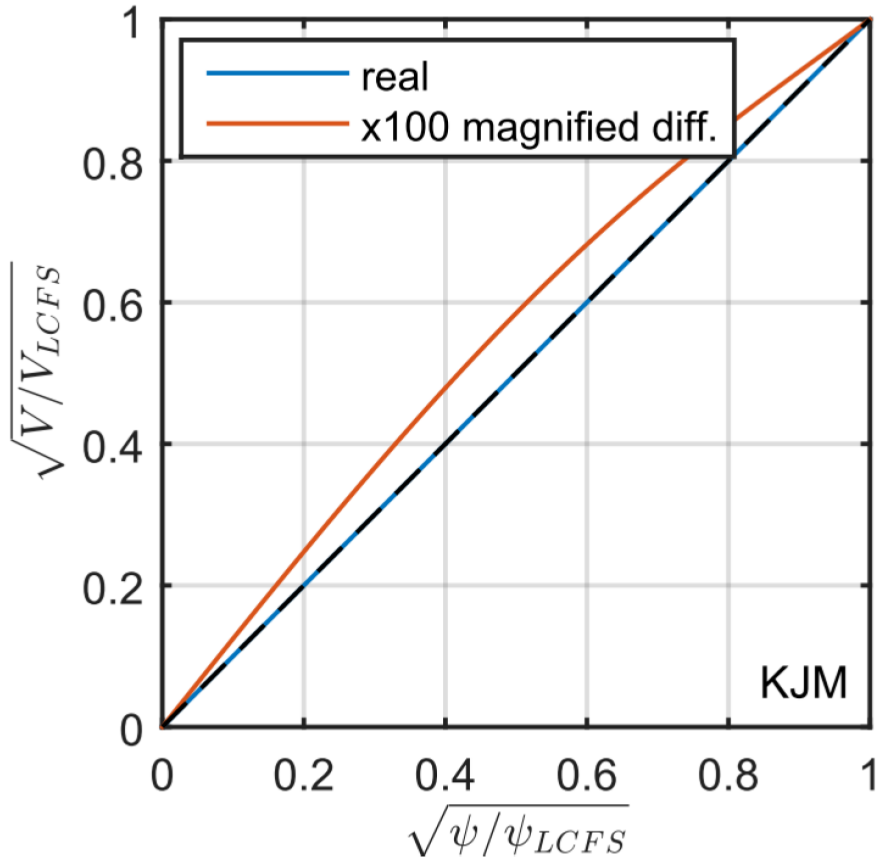

Figure 5.1: Graphic courtesy of Andreas Langenberg demonstrating the equivalence of the radial definition either through toroidal flux or volume of said flux surface[5]

are usually defined in toroidal flux units, while STRAHL solves the impurity flux on a volumetrically defined radial grid. Ultimately the cylindrical approximation for the flux surface averaging does not prevent the STRAHL modeled signals from being able to accurately match the experimentally observed impurity emission lines which will be demonstrated later in the chapter and in chapter 6.

Although the one-dimensional radial approximation is appropriate for the STRAHL calculation and the currently observed line emission signals can be well-matched, any poloidal variations of the impurity species observed in an experiment cannot be characterized. This could be important since recent theory predicts that highly charged impurities are susceptible to density variations on a flux surface and subsequently play a significant role in their radial transport.[87,88,89,28] In particular, [Buller et al. 28] found that highly charged collisional impurities with even moderate electrostatic potential variations on a flux surface can lead to larger neoclassical radial impurity flux. In [García-Regaña et al. 90] it was shown in CERC discharge plasmas that these flux surface variations are larger in the electron root than the ion root.[a]

5.1.2 Atomic data

Another potential uncertainty inherent to STRAHL is the atomic data utilized for solving the radial transport and emission for a given impurity chargestate. Largely the atomic data can be categorized into two sets: the data associated with each impurity chargestates' fractional abundance and the data describing the line emission for each observed atomic transition. The former data is the ionization, recombination, and charge exchange rates of the impurity species, which for the scope of this thesis will only be iron. The latter data necessary is the photon emissivity coefficient for each line transition that describes the spontaneous emission from an upper state population to a lower state.

Ionization, recombination, and charge exchange

- The uncertainties in the ionization and recombination rates are unknown meaning their impact on the inferred anomalous transport profiles is also unknown.
- The thermal charge exchange rates in combination with the neutral hydrogen profile would need to overestimated by an order of magnitude to have a significant impact on the inferred anomalous diffusion profile

The iron ionization, recombination, and charge exchange rates were taken from preexisting density and temperature dependent ADAS, i.e. Atomic Data and Analysis Structure,[77] database files that have been used previously in [7]. The specific ionization, recombination, and charge exchange rate files used were scd00_fe.dat, acd85_fe.dat, and ccd89_fe.dat respectively (see the appendix for the inclusion of these data files). Although these have been used in previous work,[7] the uncertainty on the rates for all three types of processes aren't known at this time.

To test the thermal charge exchange effects from collisions between neutral hydrogen and impurity iron atoms, [Geiger et al. 7] modeled the neutral hydrogen density using the KN1D

[a]See [García-Regaña et al. 87] for further discussion on the magnitude of the impact to impurity transport from electrostatic potential variations on flux surfaces.

code and order of magnitude edge-neutral density measurements from the filterscopes.[85] It was found in the sensitivity study that a large scaling of the neutral density profile, a factor of ~ 50 up and down, led to relatively minor change in the inferred anomalous diffusion profile. In fact there was no change inferred when the neutral density was lowered by a factor of ~ 50 from the expected profile. Only when the neutral density was increased by a factor of ~ 50 from the expected profile was there an impact on the inferred anomalous diffusion profile due to the exceedingly strong charge exchange losses. Therefore the neutral Hydrogen density radial profile shape was taken from [7] and scaled down by a factor of three to roughly match the electron density profile increase in the ECRH off-axis data sets. This profile shape was used for all the experimental least square fits performed in chapter 6 and was the same nominal profile tested in the synthetic sensitivity studies in chapter 4. In fact the conclusions from the sensitivity study performed in [Geiger et al. 7] were corroborated by the synthetic variations of neutral Hydrogen in the section 4.2.4. Specifically those conclusions were that inaccurate neutral hydrogen density profiles with iron would have to be at least an order of magnitude too large to have any effect on the inferred results. Therefore errors in the thermal charge exchange rates in combination with uncertainty in the neutral density profiles have a combined upper bound of a factor $\sim$ 10 where errors of $\sim$ 0.2 $\frac{m^2}{s}$ are possible, see section 5.2.3 for the neutral density profile variations with experimental data.

Photon emissivity coefficients

- Although the uncertainties in PEC values are unknown at this time, the PEC values are mostly constant above $T_e = 100$ eV meaning the largest impacts to the inferred anomalous diffusion profile should be constrained to the plasma edge, $\rho > 0.95$

The iron Photon Emissivity Coefficients or PECs were calculated using a modern set of ADAS codes[91] and were the exact same spectral lines used in [7] except for the exclusion of the Fe IX line. In particular the PEC files only include the electron impact excitation channel to the line emission as the expected largest contribution for the chosen lines, meaning any recombination or charge exchange contribution to these lines were not calculated. Also due to the expected weak density scaling of these PECs in the W7-X parameter regime, the PECs were calculated with a very sparse density grid of two points (10^{18} to 10^{20} m^{-3}) along with a higher resolution temperature grid of 31 points (11 eV to 8.8 keV). The PECs corresponding to the line emission used in this thesis work can be seen in figure 5.2, where except for the He-like iron emission show relatively flat values for all emission lines at electron temperatures greater than 100 eV.[b] The uncertainty in the inferred transport values stemming from the uncertainty in the PEC values is unknown at this time. However from figure 5.2 it is clear that the largest variation in values occurs for electron temperatures below 100 eV or equivalently $\rho > 0.95$ for the experiments presented in this thesis. Therefore the largest potential impact would occur for the lowest chargestates from incorrect contributions to the sightline integrals from the $\rho > 0.95$ radial region. Although incorrect PEC values[c] could shift the radial position of the spectral line emissivity distributions much in the same way as the electron temperature variation did as shown in figure 4.36, the uncertainties introduced to the anomalous diffusion is not expected to be as large as those returned in T_e profile sensitivity studies. The first reason the PEC introduced uncertainties is less than the T_e profile introduced uncertainties is simply that the electron temperature has direct impact on both the ionization (i.e. iron chargestate distributions) and the calculated line emissivity through the PEC values. The second reason is that the incorrect PEC values can be compensated for by the individual scale factors used to match the integrated sightline signal.[d] In conclusion although the exact impact from errors in PEC values on the inferred anomalous diffusion uncertainties is unknown, the largest uncertainty values are expected to be localized from mid-radius outward at values less than the synthetic T_e profile sensitivity discussed in sections 4.2.6 and 5.2.3 due to the larger change to the shape of the PECs values as a function of T_e.

[b] STRAHL does an interpolation on the density and temperature grids to yield the appropriate PECs for given kinetic profiles.

[c] Specifically this refers to both shape and magnitude changes of the PECs as functions of electron temperature.

[d] As mentioned in footnote c, any shape changes of the PEC values versus T_e will slightly shift the radial locations where the emission is stemming, meaning that even though each signal has its own individual scale factor it might not be able to fully compensate for any errors in the PECs.

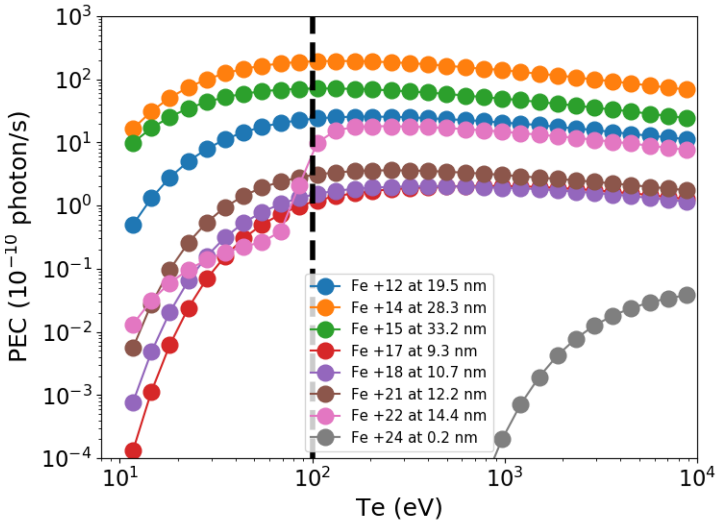

Figure 5.2: The Photon emissivity coefficients at $n_e = 10^{20}\ m^{-3}$ for the iron spectral lines used in this thesis work

5.1.3 LBO source function

The next potential uncertainty within STRAHL is the impurity source function which includes the temporal shape of the iron cloud, the exact time of the injection, the energy of iron atoms, the total number of iron atoms injected, and finally the location and spatial distribution of the iron cloud. Although all of the aforementioned variables can be specified within STRAHL to model an iron injection, including all the variables as free parameters within $lstsq\_STRAHL\_wrap$ would further cast doubt on the uniqueness of the transport parameter inference. Therefore to simplify the fitting and modeling, many of the variables were set to fixed values within $lstsq\_STRAHL\_wrap$ based on experimental measurements and assumptions. In fact for the work presented in this thesis, only the injection timing was given as a free parameter which will be discussed in the least squares fitting section. The justification and uncertainties for leaving all other variables as fixed values will be presented in the following sections.

Temporal shape and neutral energy of LBO injection

- There is clear experimental evidence that many of the iron LBO injections have multiple neutral iron clouds/clusters entering the plasma past the typical 2.0 ms trapezoidal temporal shape.

- Utilizing a 2.0 ms single injection to model multiple neutral iron clouds/clusters entering the plasma can lead to inaccuracies of $\sim 0.3\ \frac{m^2}{s}$ in the inferred anomalous diffusion profile localized predominantly in the outer half of the plasma. The lower iron chargestates have both a shorter line radiation signal, < 100 ms, and only a single, central sightline yielding the least squares routine more freedom to alter the anomalous diffusion profile shape to match the signals. This extra freedom leads to an increase in the inferred diffusion's uncertainties.

- Varying the neutral iron energy from 0.07 to 28 eV had a negligible effect on the inferred anomalous diffusion profile, i.e. $< 0.01\ \frac{m^2}{s}$. Therefore a 20 eV neutral iron energy was specified within all further data analysis.

A visible fast camera was used during a few experiments to measure the typical iron cloud injection into the plasma yielding information on the average cloud velocity and temporal shape. These measurements also helped characterize the number and distribution of iron clusters versus iron atoms within the iron ablation cloud. Although this diagnostic was not available for every LBO injection, the data collected on the iron ablations demonstrated that the majority of the iron was injected as atoms within 2.5 ms and any potential iron clusters would follow within 15 ms. From the visible camera streak images the velocity of atoms and clusters was measured and the energy range was determined to be 0.07 to 28 eV. Based on these streak images the most probable neutral iron energy was 20 eV and it was this value that was used within STRAHL to model the neutral iron injection. During the second half of the divertor campaign, O.P. 1.2b, there was a dedicated spectrometer looking at the LBO injections that captured the Fe I line at 647.6 nm.[e] Nominally this meant the exact temporal shape

[e]All of experimental data presented in this thesis was collected during O.P. 1.2b

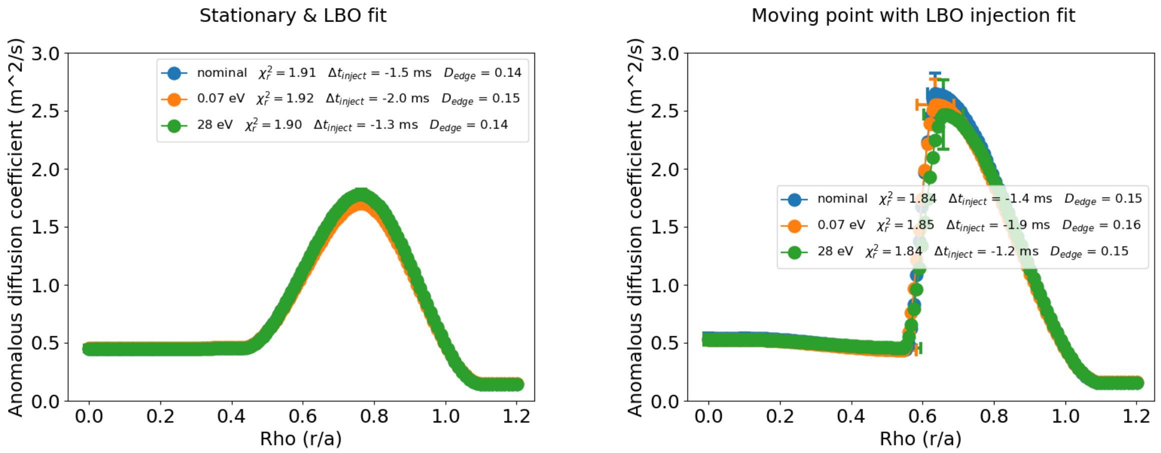

(a) (b)

Figure 5.3: The STRAHL modeled neutral energy was varied between 0.07 and 28 eV for the third iron LBO injection in discharge 20180919.049 In (a) the anomalous diffusion, line emission scale factors, and LBO injection time are the only free parameters within the fit, while (b) included two radial position factors for the interior spline-knots.

function was measured for each LBO injection, but unfortunately due to a triggering and data overwriting issue only the 1st LBO injection within a given W7-X shot was guaranteed to be saved. Therefore without a consistent temporal measurement of a Fe I line, a fixed 2.0 ms trap trapezoidal injection shape as seen in figure 5.4 was used throughout the STRAHL modeling unless otherwise noted.

To test the inferred anomalous diffusion profile's sensitivity to the neutral iron energy, a variational study was performed using the experimental data from the 3rd LBO injection in 20180919.049, the exact same LBO injection that was used as a basis for the synthetic data. The neutral iron energy was held at the values of 0.07 and 28 eV in this variational study with the resultant inferred anomalous diffusion profiles shown in figure 5.3. Although in the first step of the procedural method the resultant inferred anomalous diffusion profile shows a max difference of 0.2 $\frac{m^2}{s}$ (not shown), when a second inference is performed there is a near negligible difference in the inferred diffusion profile among the neutral iron energies as seen in figure 5.3.[f] Therefore the introduced uncertainty for specifying an average neutral iron atom energy of 28 eV versus 0.07 eV is essentially negligible. The small variance in the inferred

[f]The recovery of the same inferred anomalous diffusion profile under the 0.07 and 28 eV scenarios are accompanied by a 0.7 ms relative delay in the LBO injection timing. This is why the first step in the procedural method, without LBO injection timing as a free parameter, returned a difference in the anomalous diffusion profile.

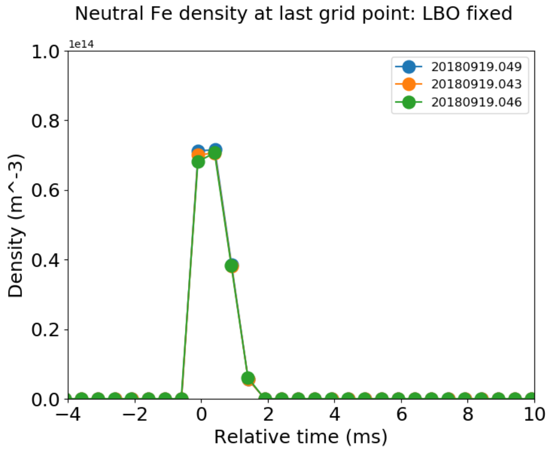

(a)

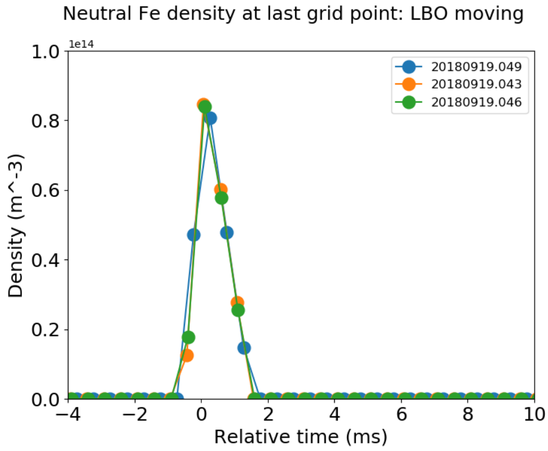

(b)

Figure 5.4: Difference on temporal shape between LBO injection timing as free parameter (b) or held fixed (a) within $lstsq_{S}TRAHL_{w}rap$

diffusion profiles is expected due to the electron temperature and temperature gradients in the edge plasma. Specifically the location of ionization and relative abundance of a particular iron chargestate is essentially unchanged since these factors most strongly depend on the electron temperature gradient and diffusion at the edge.

Next, fixing the iron injection's temporal shape to a 2.0 ms trapezoidal shape within STRAHL introduces two different channels for uncertainty in the inference of transport parameters. The first uncertainty channel arises from the slight distortion of the temporal shape when the exact injection time is left as a free fitting parameter within the least squares python wrapper. As seen in figure 5.4 the shape distortion from allowing the exacting injection timing as a free parameter is very minimal and importantly among the three different LBO injections in the 3.5 MW ECRH off-axis scan is nearly negligible. The exact reason for this shape distortion as seen in figure 5.4b was due to the STRAHL time resolution and the free fit injection time having the exact same step size of 0.5 ms. Fortunately this shape distortion causes $< 1\%$ change in total number of neutral iron atoms injected and doesn't impact the uncertainties in the inferred anomalous diffusion.

The second and much more important uncertainty channel arises from not using the exact temporal shape measured from the dedicated LBO spectrometer (when data is available) to model the LBO injection in STRAHL. As demonstrated in section 4.2.7 the incorrect temporal

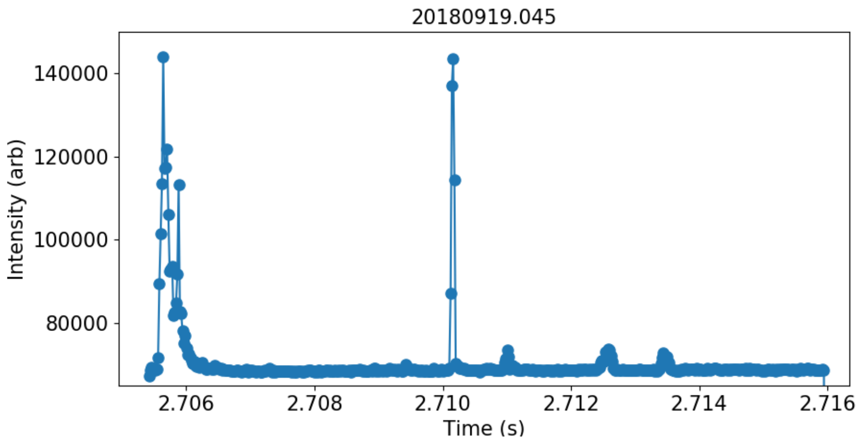

Figure 5.5: The 647.6 nm neutral iron line measured from the fast spectrometer for the first iron LBO injection in discharge 20190919.045

shape can introduce inaccuracies to the inferred anomalous diffusion profile at values > 1.0 $\frac{m^2}{s}$ due to the large impact on the line-integrated signals. For example, the 647.6 nm neutral iron line from the dedicated LBO spectrometer in figure 5.5 indicates that there is a significant iron cluster entering the plasma roughly 5 ms after the initial cloud. The multiple injection hypothesis is corroborated by the measured line-radiation of Fe^{+18} and Fe^{+12} as shown in figure 5.6a and 5.6b respectively. It is evident from figures 5.6a and 5.6b that the STRAHL modeled line-radiation cannot reproduce the exact shape of the measured signals, which will introduce a higher uncertainty in the least squares inference of the transport parameters. As mentioned in section 4.2.7 the measured distortion in the line radiation is more significant for the lower chargestates and subsequently has greater impact on the outer half of the inferred diffusion profile. Moreover the chargestates from Fe^{+22} downward are only measured by the HEXOS system meaning they only have a single, central sightline measurement. This is significant since a single, central sightline measurement yields greater leeway for the least squares routine to shape the diffusion profile to match the measured signals potentially leading to greater inferred inaccuracies. Although the exact impact on the inferred transport parameters is hard to quantify, section 4.2.7 showed the line-radiation shape is most strongly affected by the diffusive transport due to the large radial gradients in the iron density especially for the lower chargestates near the plasma edge. Additionally figure 5.7 shows the impurity radial density profile evolution, where the transport process takes at least ~ 70 ms before the iron profiles have reached an equilibrium

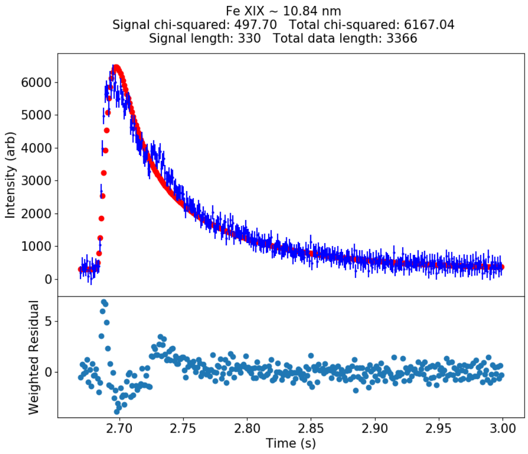

(a)

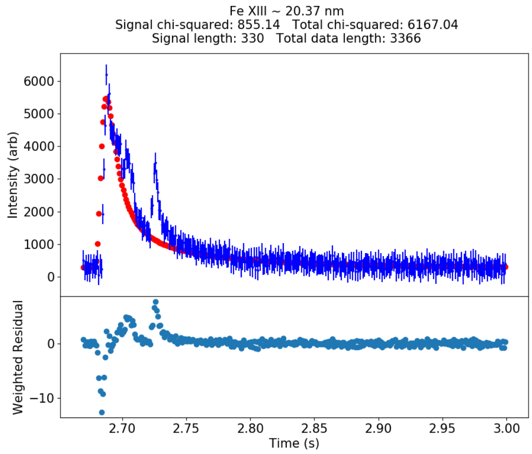

(b)

Figure 5.6: The Fe^{+18} and Fe^{+12} experimental spectral signals in blue are matched with the STRAHL output signals in red from the first iron LBO injection in discharge 20190919.045 as seen in (a) and (b) respectively.

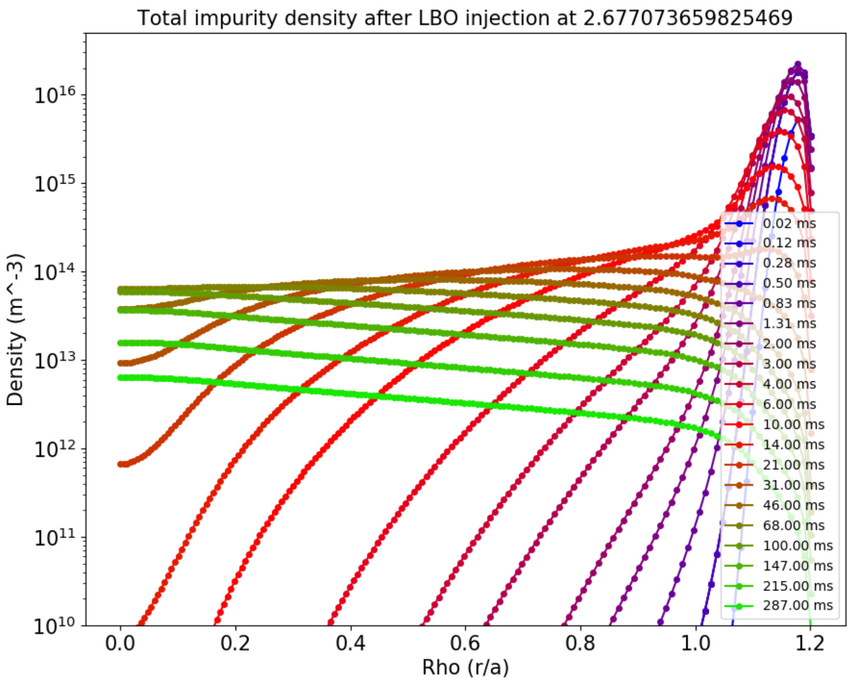

Figure 5.7: The STRAHL calculated iron impurity density from a $lstsq_STRAHL_wrap$ fit using the experimental signals from the 1st LBO injection in 20180919.045

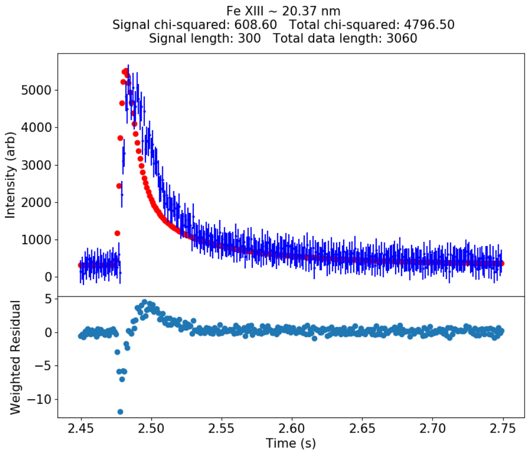

(a)

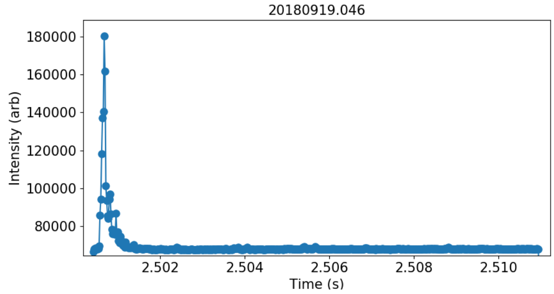

(b)

Figure 5.8: The iron line emission for Fe^{+12} from 20190919.046 1st LBO injection is shown in (a) with the experimental signal in blue and the STRAHL modeled fit in red. During the same LBO discharge the 647.6 nm neutral iron line was measured from the fast spectrometer and is shown in (b)

radial shape. This indicates that the diffusive transport plays a more significant role in these first 70 ms[g], which for the line radiation corresponding to the chargestates of Fe^{+18} and lower encompasses most of the rise & fall in the signal. Therefore even with a single, central sightline measurement for Fe^{+22} and lower, the line radiation's gross shape in the first 70 ms can mostly be matched using a fixed single injection temporal shape. Using this fixed single injection for a clear multiple injection event will increase the uncertainties in the inferred anomalous diffusion profile with the errors mostly concentrated in the $\rho > 0.5$ region. It should be noted that even if the injection does not have any secondary clusters as seen in figure 5.8b, the exact fit for the lowest chargestate in figure 5.8a still doesn't fully capture the signal decay indicating there are other possible outstanding issues.

As a means to corroborate the synthetic sensitivity studies of the LBO temporal shape detailed in section 4.2.7, an inference with a triple LBO injection was performed on the 3rd LBO in 20180919.049. As seen in figure 5.9 the measured spectral emission from Fe^{+18} and Fe^{+12} are attempted to be matched with the nominal 2 ms trapezoidal injection and the ad hoc triple injection for 5.9a & 5.9b and 5.9c & 5.9d respectively. The resultant inferred anomalous

[g] Remember from equation (4.1) the anomalous diffusion will contribute more to the total iron impurity flux when the iron impurity density gradient is large.

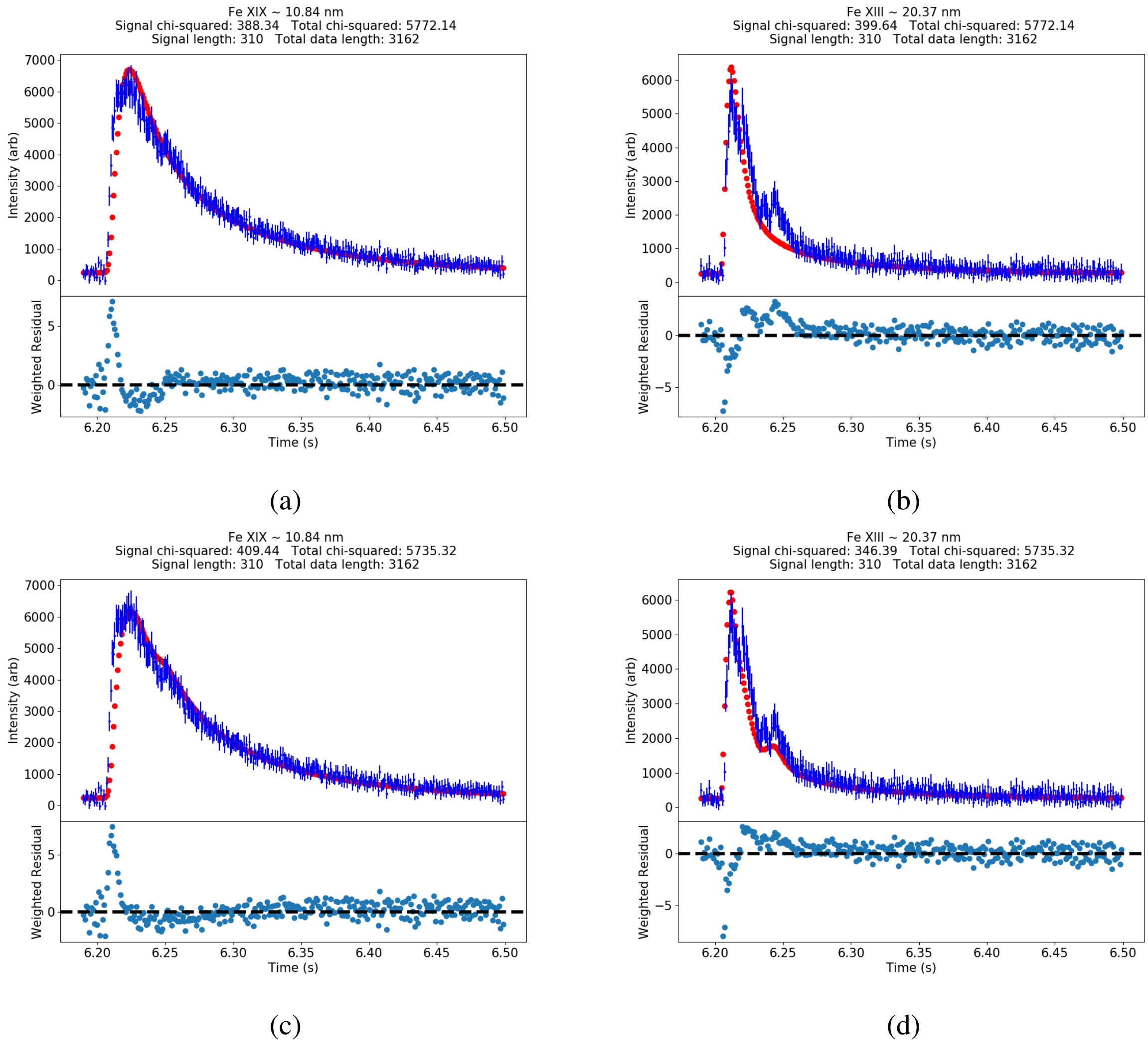

Figure 5.9: The Fe^{+18} and Fe^{+12} line emission signals in blue are matched by the STRAHL modeled signals in red with the nominal 2 ms trapezoidal shape injection in (a) & (b) while an ad hoc triple injection signal match are plotted in (c) & (d).

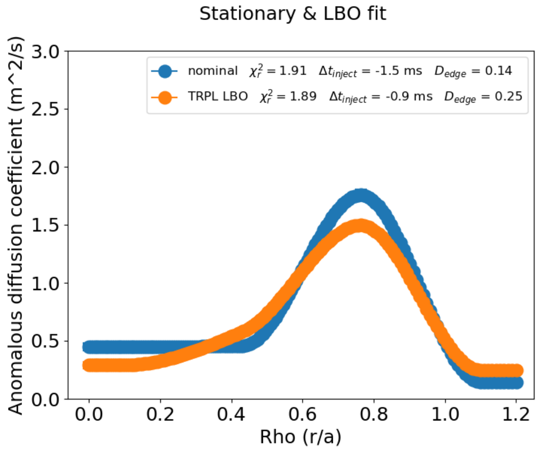

(a)

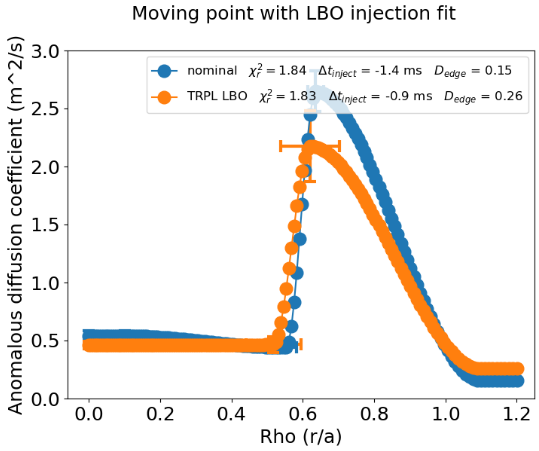

(b)

Figure 5.10: The STRAHL modeled LBO injection temporal shape was varied for the third iron LBO injection in discharge 20180919.049 In (a) the anomalous diffusion, line emission scale factors, and LBO injection time are the only free parameters within the fit, while (b) included two radial position factors for the interior spline-knots.

diffusion profiles shown in figure 5.10 demonstrate that an ad hoc multi-injection LBO model can slightly improve the matching of the line emission signals without large variations in the inferred anomalous diffusion values, $< 0.3\ \frac{m^2}{s}$. Although the second inference with two moving interior spline-knots and LBO injection timing as free parameters show remarkable consistency for both LBO model cases, the steep diffusion gradient at $\rho \approx 0.6$ is most likely nonphysical. Similarly to the conclusions detailed in section 4.2.7, the lower chargestates with only the single, central sightlines do not provide enough radial localization for the emission in $\rho > 0.5$ radial region. Therefore the least squares routine can place artificially large gradients in the diffusion profile in this region to better match the line emission without any physics basis. In particular the radially moving interior spline-knots seem to be the culprit for providing this freedom to the least squares routine. Thus inferred anomalous diffusion profiles with sharp gradients should be considered with skepticism. More details on the possible variations to the initialization and fitting procedure will be described in section 5.2 to verify the inferred solutions. In conclusion the inferred diffusion profile accuracy seems to not only be sensitive to the temporal shape of the LBO injection, but also have inaccuracies of $\sim 0.3\ \frac{m^2}{s}$ predominantly in the outer half of the plasma.

Total number of injected iron atoms

- The total number of particles entering the plasma for the LBO injection presented in this work was determined to be $\sim 1 \times 10^{17}$, a clear non-perturbative iron injection.
- The uncertainty on the inferred diffusion profile introduced from mischaracterizing the total number of iron particles injected should be negligible since each signal's sightline has a free fit parameter for scaling the absolute intensity within the least squares minimization.

The next potential uncertainty within the LBO source function for STRAHL is the total number of iron atoms specified in the LBO injection modeling. As detailed in [68] the glass target for the LBO ablation was coated through Physical Vapor Deposition (PVD) ensuring an even and precise layering of the desired material. All of the iron LBO targets used in this work were 5 μm thick iron layer on top of with a 100 nm thick titanium layer for better energy absorption. Additionally the laser energy, 1 J, and spot size, roughly 3.5 mm diameter, on the glass targets were all the same for every LBO injection presented in this work. Based on the measurements of the iron layer thickness and spot size, the amount of iron ablated and reaching the plasma was determined to be roughly 1×10^{17}. Therefore the STRAHL flux rate of iron atoms for a 2.0 ms trapezoidal shape was chosen ensuring the total atoms injected were 1×10^{17}, yielding a non-perturbative iron injection. Accordingly the uncertainty introduced from mischaracterizing the total number of iron atoms in the STRAHL modeling should be negligible especially considering the iron line-radiation's absolute intensity is left as a free parameter in the least-squares routine.

Location and spatial distribution of LBO injection

- The combination of the SOL temperature equalization for each ECRH total power level, the lowest chargestate's line radiation used in this work corresponding to Fe^{+12}, and the inference of a constant edge diffusion all indicate that the neutral iron spatial distribution should have a near negligible effect on least squares inference.

The final STRAHL LBO source function induced uncertainty is the location and spatial distribution used to model the injection of the iron cloud. Within STRAHL the radial location can be specified as seen in figure C.6 with $r\_source - r\_lcfs$ as the distance outside the last closed flux surface where the neutral source is injected. In the case of figure C.6 with the radial location given as 63 cm[h], STRAHL will use the outermost grid point as the neutral source location since 63 cm is much bigger than the specified width of the scrape-off-layer.[76] The spatial distribution can be specified with the $source\_width\_in$ and $source\_width\_out$ parameters that yield three options: First if the parameters are negative the neutral injection is at a single grid point closest to $r\_source - r\_lcfs$, Second if the parameters are zero the neutral injection follows a exponential decay governed by the ionization determined from the neutral energy and electron profiles, Third if the parameters are positive then their values represent the full-width half-maximum of a gaussian distribution centered at $r\_source - r\_lcfs$. For the work presented here the 2nd option was chosen. Figure 5.11c shows the slight variation in the neutral distributions among the different LBO injections mainly due to the edge diffusion values since the edge temperatures have been equalized, this will be discussed further in section 5.2.3.The uncertainty introduced by using this model for the neutral iron distribution should be minimal since the inferred transport parameters are held constant from ρ = 1.1 to 1.2 and the lowest iron chargestate's line radiation used in the inference is from Fe^{+12}. Therefore the fine profile variations in the far scrape-off-layer should not effect the gross inferences of the transport parameters shown in this work.

5.1.4 Neoclassical and classical transport profiles

- Although there is clear difference between the XICS-derived radial electric fields in the on-to-off axis ECRH scan, the calculated classical & neoclassical convection velocity profiles showed minimal differences.
- The DKES calculated radial electric fields from on-to-off axis kinetic profiles show a near negligible differences, which naturally led to nearly identical classical & neoclassical convection velocity profiles.

[h]63 cm is the actual distance the glass target is from the last closed flux surface

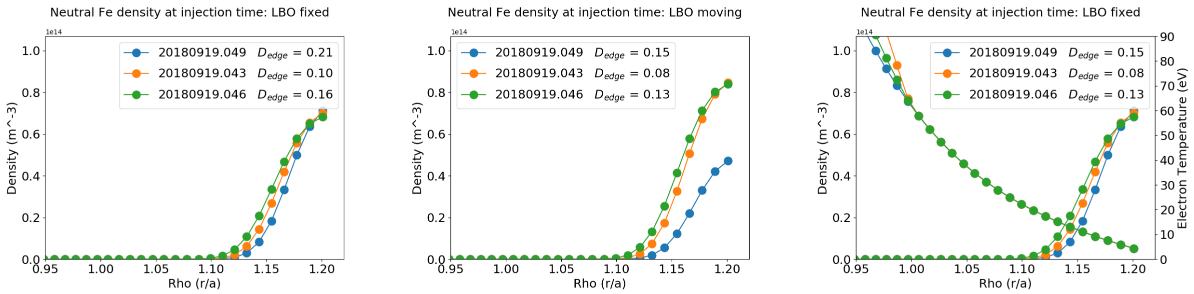

(a) (b) (c)

Figure 5.11: Difference in neutral iron spatial distributions between LBO injection timing as free parameter or held fixed in (a) and (b) respectively. Electron temperature is included in (c) showing the ionization length is the same for the three cases with the difference primarily stemming from the edge diffusion value in the scrape-off-layer

- The scaling of the classical & neoclassical transport profiles by factors of two for the on-axis case in the 3.5 MW experimental dataset reaffirmed the synthetic sensitivity results of a maximum average $\sim 0.15\ \frac{m^2}{s}$ uncertainty occurring in the $0.6 < \rho < 1.1$ radial region.

Another potential uncertainty that is inherent in the STRAHL code is the calculation and implementation of the classical and neoclassical transport profiles. Due to the importance of the classical channel on W7-X[28,30], Neotransp[74] was written to calculate the classical channel and seamlessly call DKES[53] to add in the neoclassical results. Utilizing the Neotransp code to calculate the iron transport parameters for a tracer level of iron can be done self-consistently with the kinetic profiles used first to calculate the radial electric field before calculating the iron diffusion and convection. The iron diffusion and convection can also be calculated using the same kinetic profiles, but with a manual input of an experimental radial electric field, which in this case was derived from the XICS measurements. As seen in figure 5.12 there is a clear difference for the XICS derived radial electric field as more ECRH power is directed off-axis from 5.12a to 5.12c. This difference between on- and off-axis scenarios is not observed for the DKES calculated radial electric fields as shown in 5.12d to 5.12f. Although the XICS derived radial electric fields show a decreasing core value as ECRH is moved off-axis, the Neotransp

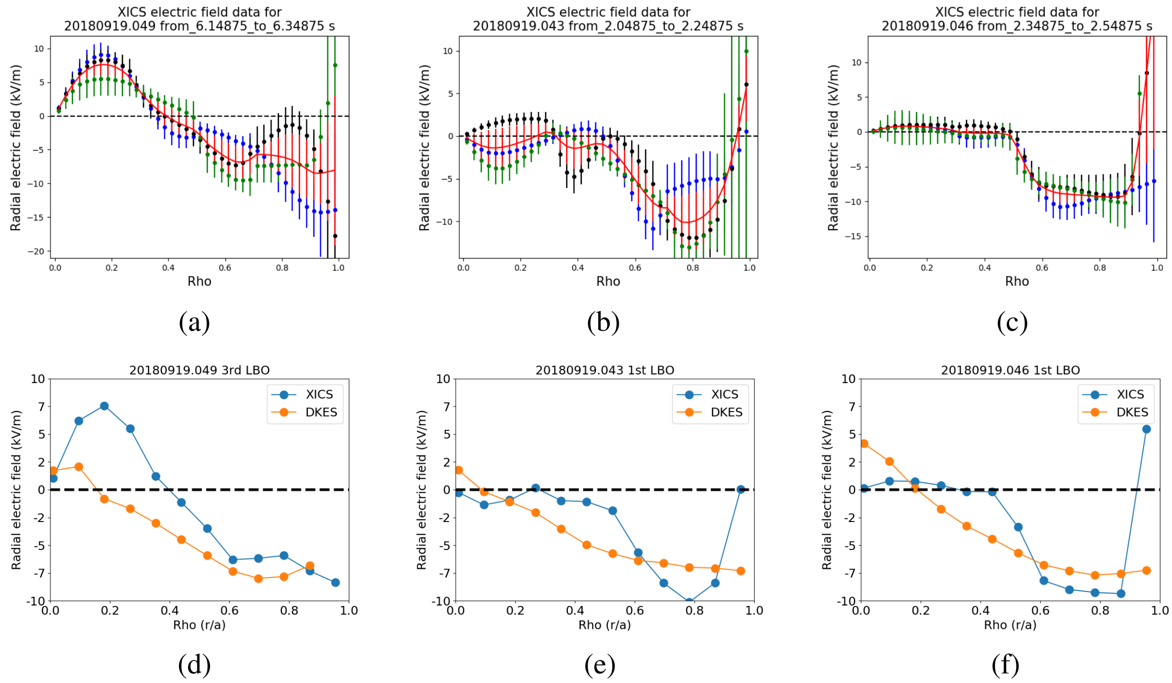

Figure 5.12: The comparison of the radial electric fields for three iron LBO injections at constant total input ECRH power of 3.5 MW, but with varying power directed off-axis. More ECRH power is directed off-axis from (a) to (c) and (d) to (f). Subfigures d to f who both the DKES calculated and the XICS determined radial electric field

calculated diffusion[i] doesn't change and more importantly the convection velocity[j] show minimal variation as seen in 5.13d to 5.13f. Then comparing the convection velocities calculated with either the XICS measured or the DKES derived radial electric fields show no major differences as demonstrated in 5.13. Therefore the uncertainty introduced to the inference of transport parameters by using a measured versus calculated radial electric field within DKES to calculate the iron chargestates' transport parameters isn't very large. This is highlighted by the fact that the inferred anomalous diffusion is at least 50 times larger than the calculated diffusion and that without using any convection channel the observed iron spectral lines could be well matched.

In order to corroborate the resultant uncertainty from the synthetic sensitivity tests of the neoclassical & classical transport profiles from section 4.2.3, the same 50% and 200% variation were utilized on experimental data. With the same input kinetic profiles as the synthetically generated data, the exact same neoclassical & classical transport profiles were utilized on the

[i]This includes both classical and neoclassical channels

[j]See footnote i

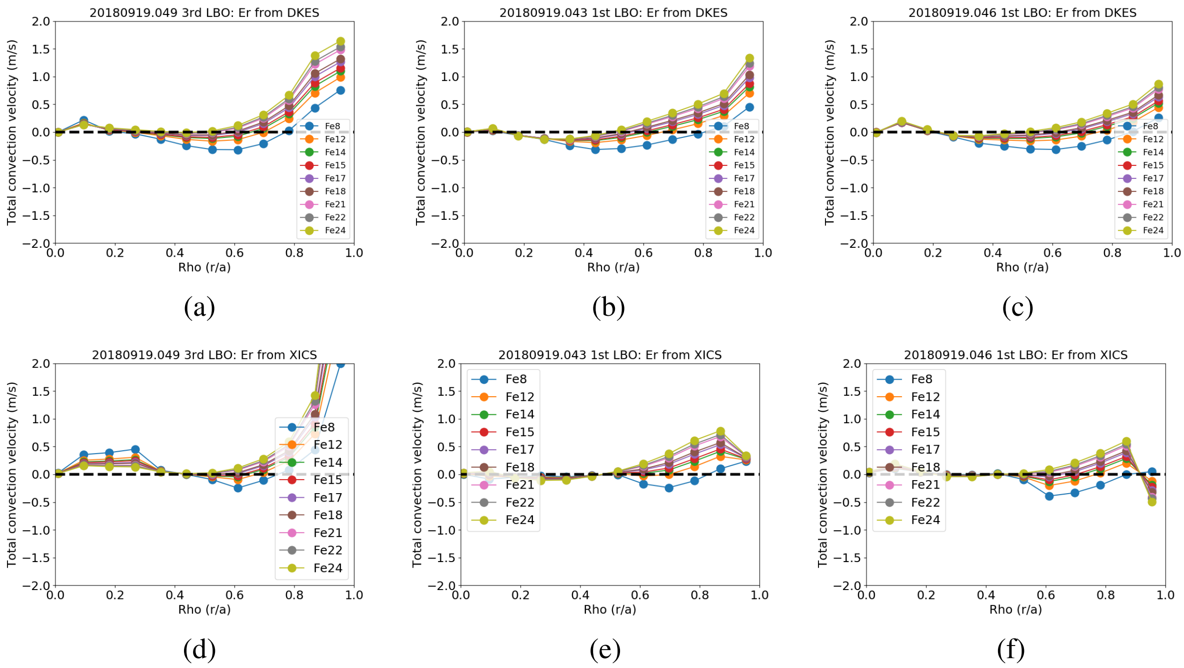

Figure 5.13: The comparison of the total convection velocity for three iron LBO injections at constant total input ECRH power of 3.5 MW, but with varying power directed off-axis. More ECRH power is directed off-axis from (a) to (c) and (d) to (f). Subfigures (a) to (c) utilize a DKES calculated radial electric field, while (d) to (f) utilize a measured radial electric field from XICS

experimental variational study, see figure 4.19 for the exact profiles. Consistent with the synthetic sensitivity study, the impact of scaling the nominal neoclassical & classical transport parameters up factors of two had very little impact on the variance in the inferred anomalous diffusion profile values. The largest difference occurs in the off-axis peaking of the anomalous diffusion values by 0.5 $\frac{m^2}{s}$ for second inference with the moving interior spline-knots as seen in figure 5.14b. However as mentioned in section 5.1.3 this large gradient in the anomalous diffusion profile is most likely nonphysical and a product of the freedom in the least squares parameter-space to match the single sightlines of the lower chargestate signals.[k] Therefore although the $\mathcal{X}_R^2$ are higher for the first inferences of the procedural method, i.e. figure 5.14a, the variation observed in the anomalous diffusion values should be more accurate. This means that the resultant uncertainty of $\sim 0.15\ \frac{m^2}{s}$ from the neoclassical synthetic sensitivity study was reaffirmed through this variational study on real experimental data

[k]This observed phenomenon will be further discussed in section 5.2

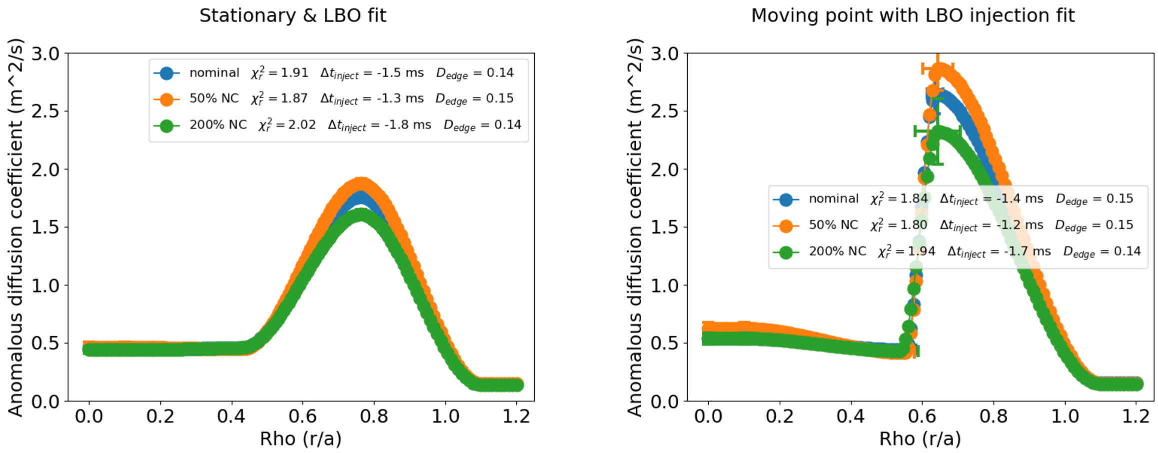

(a) (b)

Figure 5.14: The STRAHL modeled LBO injection temporal shape was varied for the third iron LBO injection in discharge 20180919.049 In (a) the anomalous diffusion, line emission scale factors, and LBO injection time are the only free parameters within the fit, while (b) included two radial position factors for the interior spline-knots.

Now as a final note, the validity of using DKES to calculate the neoclassical transport parameters has to be evaluated carefully since the collisonal operator might not be valid for high Z impurities like iron that are in a higher collisonality regime. For example, figure 5.15 shows that the normalized iron collisonality can be well above unity even for the lower chargestates. To help determine the validity of using DKES, the results can be compared to SFINCS,[92] another drift kinetic equation solver, that has a more accurate form of the linearized Fokker-Planck collision operator. When using the SFINCS code on these LBO injections, the radial electric field recovered is consistent with both the DKES calculated and the XICS measured electric field as seen in figure 5.16 [1]. Although the iron transport parameters from SFINCS haven't presently been calculated, it is believed that the plasma regimes here are still within the validity for DKES calculated transport parameters. Therefore it is believed that the SFINCS calculated transport parameters will not show any large differences with the already presented DKES transport parameters. Thus any uncertainty in the calculated neoclassical & classical transport parameters, even the convection velocity, play a minor role in influencing the inferred transport profiles. The complete dominance of the anomalous diffusion transport channel guarantees it is the only transport channel necessary to recover good matches to the iron line emission.

[1]SFINCS calculations shown here done by Dr. Novimir Pablant and are in shown [Pablant et al. 6] where importantly the plasma profiles used are not identical to the ones used in this work.

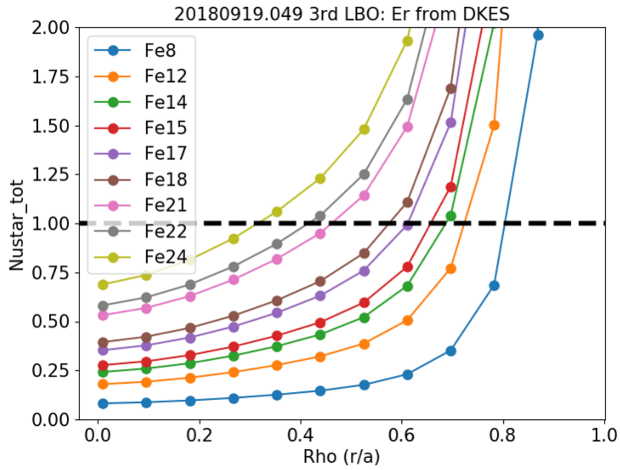

Figure 5.15: DKES calculated normalized collisionality for the iron impurity chargestates used in the least squares inference

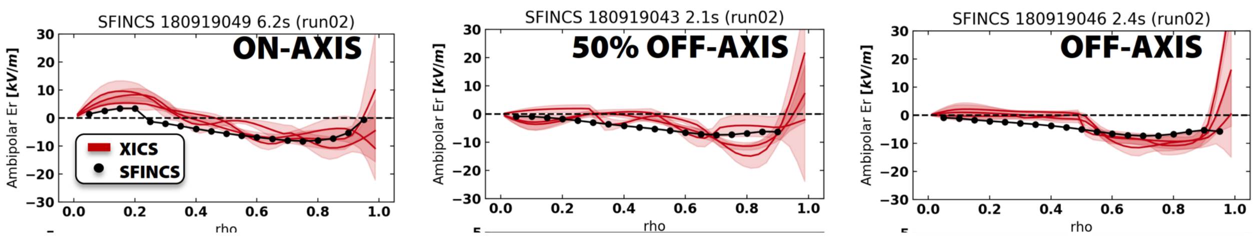

Figure 5.16: SFINCS to XICS derived radial electric field comparison provided by Dr. Novimir Pablant as detailed in [Pablant et al. 6]

5.1.5 Edge parameterization

Finally the last uncertainty associated with the STRAHL code is the edge parameterization of the scrape-off layer, SOL. As discussed in section 3.2.2, the inferred anomalous diffusion can be directly impacted by the edge parameterization because this region determines the iron impurity fluxes both as a source and sink. Critically within the STRAHL model the edge anomalous diffusion value is coupled into the edge loss rate (see section 3.2.2), meaning establishing an accurate as possible approximation of $\tau_{\|,edge}$ from equation (3.2) is vital. As detailed in section 3.2.2, the sensitivity of the $\tau_{\|,edge}$ to edge parameterization can be restricted to the connection lengths due to the connection length and Mach number performing the same role in equation (3.2). Therefore from [Sinha et al. 79] and [Killer et al. 80] respectively a 250 m divertor connection length and a 1 m limiter connection length were established as the edge values to be used in STRAHL. Specifically for the sensitivity testing, the two papers also allowed for the parameter uncertainties for both the limiter and divertor connection length to be estimated. Using these parameter uncertainties consistency variational studies can be performed to corroborate the impact on the returned uncertainties in the anomalous diffusion profile.

Limiter connection length

- Unlike the synthetic study the same limiter connection variation performed on the on-axis case in the 3.5 MW experimental dataset showed a near negligible variation on the inferred anomalous diffusion profile. The difference stems from the nonzero T_i values in the limiter connected region (more details in section 5.2.3)

Utilizing the same parameter variation as detailed above and in section 4.2.5, least square fits were performed with experimental data while fixing the limiter connection length to 0.5 and 25 m. As seen in figure 5.17, holding the limiter connection length at the values of 0.5 and 25 m did not impact the inference of the anomalous diffusion profile at all. Interestingly the synthetic sensitivity study in section 4.23a demonstrated the long limiter connection length of 25 m had a large impact, $\sim 0.3\ \frac{m^2}{s}$, on the inferred edge diffusion values. Previously the coupling between the edge anomalous diffusion and the limiter connection length was strong

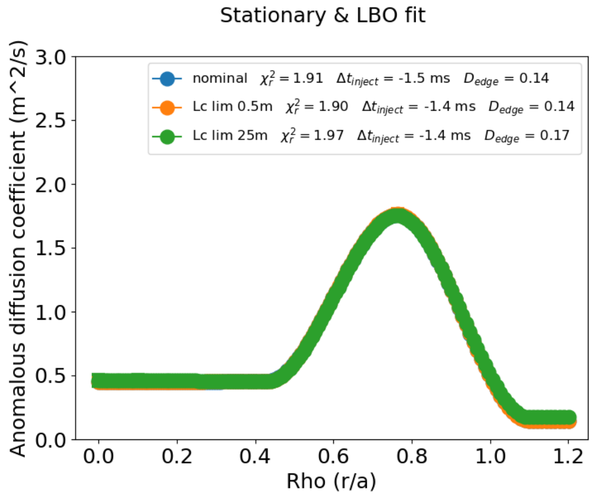

(a)

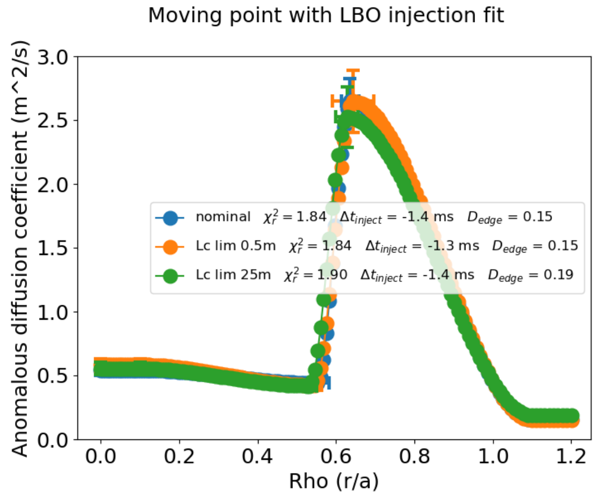

(b)

Figure 5.17: A sensitivity scan over the connections lengths were performed for the 3rd LBO in plasma discharge 20180919.049. In (a) the anomalous diffusion, line emission scale factors, and LBO injection time are the only free parameters within the fit, while (b) included two radial position factors for the interior spline-knots.

and quite important in determining the iron impurity flux even though the limiter-connected region has a small radial extent. The difference with the previous result discussed in 4.2.5 can be understood by the limiter connection length sensitivity study in this section using a shifted ion temperature profile. Specifically the ion temperature was shifted to be equal to the electron temperature in the outer half of the plasma due to the seemingly overestimation of the T_i by $\sim 150eV$ (see section 5.2.3 for more details). Therefore as seen in equation (3.2) the v_{flow} at the edge increased by a factor of two minimizing the percentage impact from the change in limiter connection length and hence minimizing any potential change in the inference of the edge diffusion value. Thus due to the change in the ion temperature profile the uncertainty in the limiter connection length should have a near negligible effect on increasing the uncertainty in the inferred diffusion profile. Hence the previously observed impact of $\sim 0.24\ \frac{m^2}{s}$ in the SOL (see figure 4.23b) when the long limiter connection length was used within the least squares minimization was most likely due to the T_i at the outermost point being held at zero.

Divertor connection length

- Unlike the synthetic study the same divertor connection variation performed on the on-axis case in the 3.5 MW experimental dataset showed much larger variations in inferred anomalous diffusion profile with changes of $\sim 0.5\ \frac{m^2}{s}$ in the off-axis position and $\sim 0.15\ \frac{m^2}{s}$ in the core.
- The inferred diffusion profile change is consistent with keeping the iron flux rate constant since an increased (decreased) $L_{C,divertor}$ leads to a later (earlier) injection time and an increased (decreased) diffusion gradient across the LCFS.

To further understand how variations in the connection length and hence iron impurity loss rates could effect the inference of the anomalous diffusion profile, the divertor connection lengths was altered within its uncertainties. In particular the divertor connection length was varied up and down by 50 m due to this being the approximate difference between the mean and median reported in [Sinha et al. 79] for the standard magnetic configuration. Figure 5.18 shows inferences of the above-stated scenarios on a typical LBO injection for the second-run fits including the LBO injection timing in 5.18a and the moving spline-knot with LBO injection timing in 5.18b. Unfortunately the second inference has the same nonphysical characteristic of artificially steep diffusion gradient, so the interpretation of the divertor variation is not particularly clear from the moving spline-knot results. The synthetic sensitivity study in section 4.2.5 found that the $\pm$ 50 m variation in the divertor connection length led to very minimal inaccuracies in the inferences, i.e $\sim 0.05\ \frac{m^2}{s}$.[m] Interestingly as the divertor connection length is increased the anomalous diffusion gradient & peaking are increased concomitant with a later injection of the LBO. Accompanying this time delay is the slight peaking and radially outward movement of the diffusion profile as $L_{C,divertor}$ is increased. Such a trend is completely consistent with equation (3.2) trying to ensure a constant iron flux by increasing the inferred edge diffusion to counteract the increased connection length. Also it should be noted that the increasing edge diffusion gradient occurs across the last closed flux surface where there is significant

[m]Remember that this sensitivity study used experimental signals, but more importantly had shifted T_i profiles impacting the SOL most significantly.

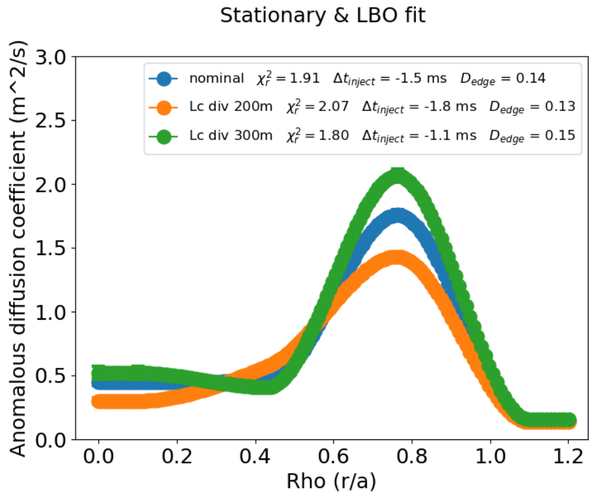

(a)

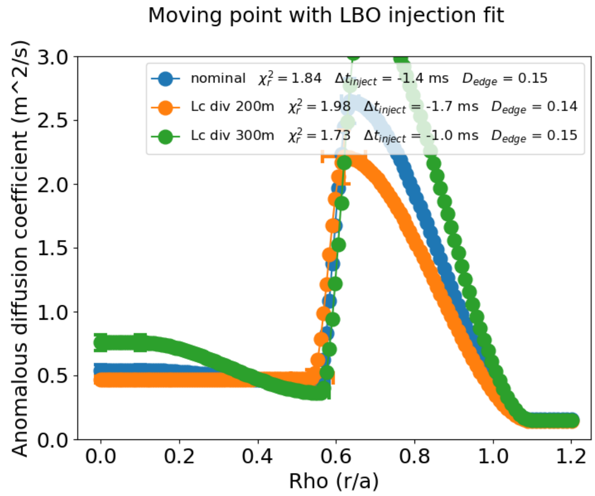

(b)

Figure 5.18: A sensitivity scan over the connections lengths were performed for the 3rd LBO in plasma discharge 20180919.049. In (a) the anomalous diffusion, line emission scale factors, and LBO injection time are the only free parameters within the fit, while (b) included two radial position factors for the interior spline-knots.

contributions of line emission to the three lowest iron chargestates, i.e. $\text{Fe}^{+12,14,15}$. Sadly, the reasonable $L_{C,divertor}$ uncertainties do seem to expand the confidence interval around the location and magnitude of the off-axis anomalous diffusion peaking without any indications of inaccuracy from the fits. Even the second-run fits including the LBO injection time without moving spline-knots in figure 5.18a show the similar trends with diffusion value variations of $\sim 0.5\ \frac{m^2}{s}$ in the off-axis position and core variations of $\sim 0.15\ \frac{m^2}{s}$. In conclusion this variance of the divertor connection length demonstrates the indirect coupling between the edge temperatures, the inferred edge anomalous diffusion, and the LBO injection time via equation (3.2).

5.2 Uncertainties and systematics introduced by parameterization of $lstsq_STRAHL_wrap$

Characterizing impurity transport modeling was the motivation for the variational parameter studies on the least squares inference of the transport profiles. Specifically the goal was to determine whether the inferred solution was unique and to what confidence intervals could the inference be considered accurate. In chapter 4 the details of realistic synthetic data testing provided estimations of whether the modeled signals could be used to accurately infer the transport profiles and which parameters were key for uncertainty estimations. In section 5.1 the details of the STRAHL inherent uncertainties were listed with discussion and estimations of the effects on the inference of transport profiles. In this section the inherent uncertainties introduced from implementing $lstsq_STRAHL_wrap$ and potential systematic errors are discussed. Specifically the radial description of the transport profiles, the sightline signal processing, the procedural method for performing the least squares inference, and the input kinetic profile assumptions will all be discussed in the following sections.

5.2.1 Radial profile function of anomalous transport

- The inclusion of the radial positions as fit parameters for the two interior spline-knots can lead to nonphysical inferred diffusion profiles due to the lack of radial information from the single sightlines for the lower iron chargestate line emission.

As already well-detailed in section 4.1.2 the importance of selecting the number of spline-knots as free parameters within the radial description of the anomalous transport is well established. The synthetic sensitivity testing demonstrated that six spline-knots with four of them being independently inferred had adequate flexibility in parameterizing a flat transport radial profile and an off-axis peaked radial transport profile. The synthetic data testing also demonstrated that the inner core and far edge radial parameterization of the transport profiles were more susceptible to large inferred inaccuracies. This discovery was the main impetus behind forcing the core and edge transport parameters to be forced flat in the radial regions of 0 to 0.1 and 1.1 to 1.2 ρ. Therefore the anomalous diffusion in these regions would be inferred in an averaged-sense helping minimize large gradients in order to improve the accuracy of the inference in the main plasma region, ρ = 0.1 to 1.1. Finally the radial parameterization was chosen to be a one-dimensional monotonic cubic spline between the aforementioned four free spline-knots. The monotonicity is an important characteristic for two main reasons: The first is to ensure that there are no extrema between the specified spline-knots, allowing the least squares routine's transport parameter bounds to be practical. The second reason is that a monotonic function is guaranteed to yield a smooth function helping prevent errors during the least squares routine.

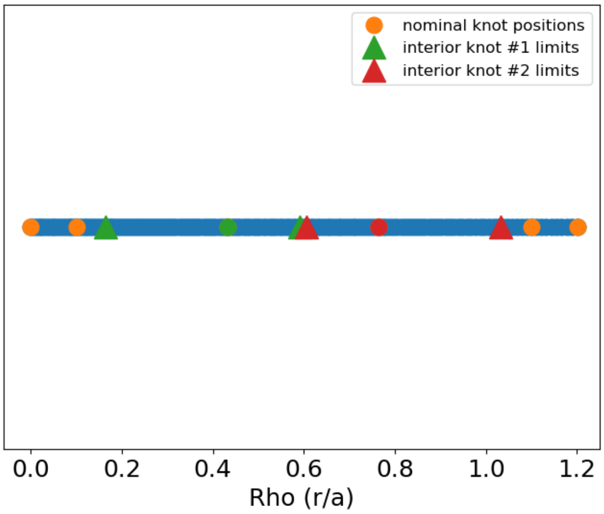

Figure 5.19: The radial grid of the STRAHL calculation is shown in blue circles with the six spline knots parameterizing the anomalous diffusion profile shown in different color circles. The red and green triangles correspond to the extreme positions of the respectively colored interior spline-knot.

In order to improve upon the radial characterization of the transport profiles, the two interior spline-knots (i.e. the two spline-knots closest to $\rho = 0.5$) were also given additional parameters that permitted their position to move radially. As seen in figure 5.19 the limits used for the two interior spline-knots are indicated by the corresponding color triangle. The limits shown are particularly important for the possible diffusion gradients that can be inferred by the least squares routine. The combination of the monotonic radial parameterization causing the diffusion extrema to occur at spline-knot locations and the minimum distance between spline-knots give the least squares routine extra freedom to infer a solution. In fact as demonstrated throughout this chapter (e.g. figure 5.18b 5.17b, 5.14b, etc) there seems to be a minimum in $\mathcal{X}_R^2$ that includes an extremely sharp diffusion gradient centered around the $\rho = 0.6$ position where the two moving spline-knots are closest. In comparison with the inferences that don't include the two interior spline-knots' radial position, the total reduction in $\mathcal{X}_R^2$ is less than 0.1 indicating a small improvement in signal matching. Unfortunately the limits have introduced a systematic error by allowing a nonphysical gradient in this location. The indications that this diffusion gradient is nonphysical are that there is no physics basis for such a steep gradient (e.g. steep gradients in kinetic profiles) and that it occurs in a position where the Fe^{+24} w-line, the

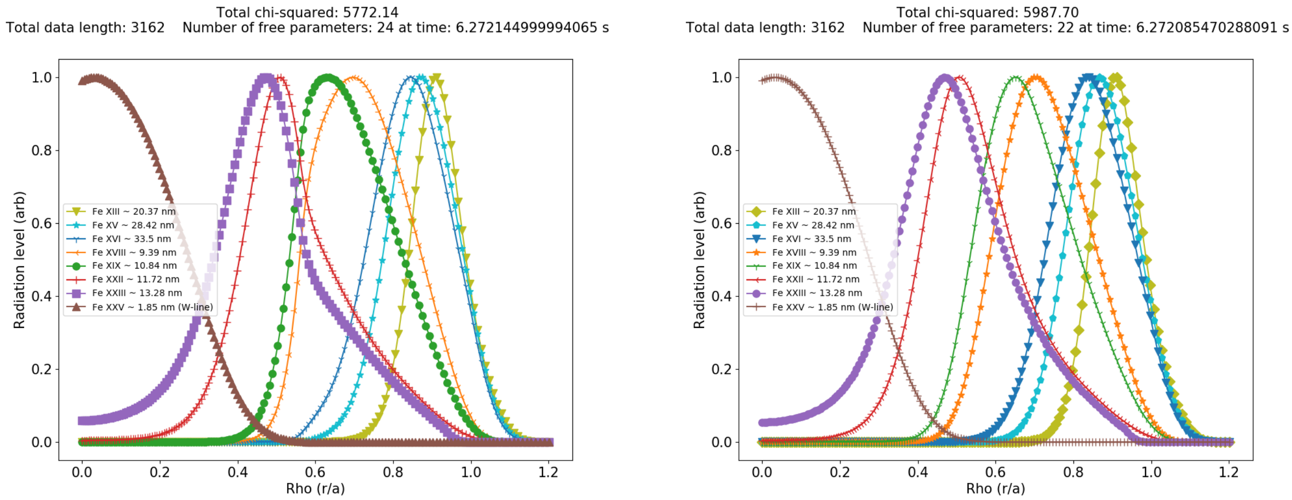

(a) (b)

Figure 5.20: The normalized spectral emission's modeled radial distributions for the measured spectral lines from the 3rd LBO in plasma discharge 20180919.049. In (a) the inference includes two radial position fit parameters for the interior spline-knots in addition to the LBO injection timing parameter, while (b) only includes the LBO injection as an additional free fit parameter.

only spatially resolved signal, has near negligible emission. The radial region surrounding $\rho =$ 0.6 has large fractional emission corresponding to $Fe^{+22,21,18,17}$, the highest chargestates measured with single sightlines. Therefore a sharp diffusion gradient here could tailor the radial contributions to the sightline integrated signals to most closely match the measured temporal line emission. This effect is most obvious when comparing the radial distributions of the normalized line emission with and without the spline-knots' radial positions as a free fit parameters as seen in figure 5.20a and 5.20b respectively. Although including the two radial position fit parameters can lead to an inferred diffusion profile that is nonphysical, the systematic error introduced can still be recognized and avoided by varying the procedural method used. More details on the variation of the procedural method will be described in section 5.2.3, but simply put whenever the two radial position fit parameters are included careful interpretation is needed to avoid systematic errors.

5.2.2 Iron line emission processing

The synthetic data sensitivity studies in chapter 4 demonstrated two key conclusions directly applicable to the iron line emission. One, for the measured iron line emission temporal shapes the anomalous diffusion is the most dominant transport channel. Two, the inclusion of spatial information for the iron line emission is critical for inferring unique and accurate anomalous diffusion profiles. Unfortunately for the work presented in this thesis only the x-ray detectors had multiple sightlines yielding spatial information and even more regrettable is that the data collected for the x-ray system could not be inverted. The primary impurity iron x-ray diagnostic, the HR-XIS system, suffered substantial vignetting during the first divertor campaign on Wendelstein 7-X making any type of data inversion extremely difficult. Therefore to use the data collected by the HR-XIS system, eight evenly spaced and distinct sightlines corresponding to different parts on the detector were used for the spatial information as shown in figure 2.3. Each of these sightlines had their own scaling parameter within the least square routine in order to handle the vignetting rather than a single common factor.[n] The vignetting ensured all the iron line emission used in this work were line-integrated signals since the spectral lines measured with the UV detectors, the HEXOS diagnostic, only had single, central sightline data. Figure 5.21 details the normalized radial position for a typical UV sightline along with the center-most and edge-most x-ray sightlines as a function of major radius. It is clear from this figure how the sightline impact factor, i.e. smallest normalized radial position, varies for the Fe^{+24} W-line sightlines to produce signals that are decoupled from the core providing invaluable spatial information.

Sightline integrals

- The sightline integrals are not expected to contribute any significant uncertainty to the inferred anomalous diffusion profile since the real detector geometry is used and field of view effects has minimal impact on the modeled signals.

[n]The relative transmission for each pixel has been calculated from the vignetting and in theory the eight different scale factors could be tied together in the inference. However some of the line-of-sights' transmission is extremely low meaning the ratio of scale factors has large uncertainties that would introduce more inaccuracy into the inference of the transport parameters

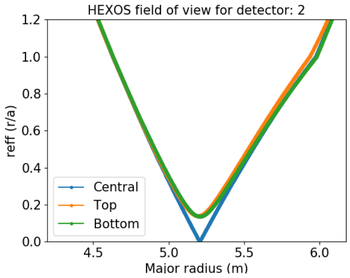

(a)

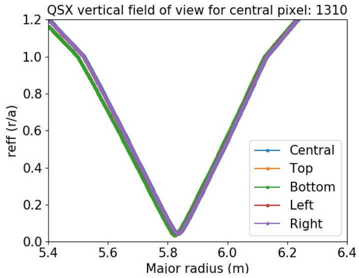

(b)

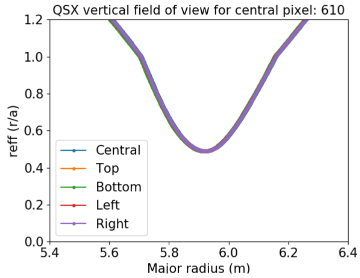

(c)

Figure 5.21: The HEXOS sightline along with the center and edge sightline for the HR-XIS detector is shown for (a), (b), and (c) respectively. The different colors represent the extents of the field of view.

As detailed in section 3.3.3, each STRAHL modeled line emission signal has a corresponding real geometry sightline that is used to correctly sum the STRAHL emission over the radial grid. Moreover every sightline signal has a free scaling factor which is used within the least squares fitting routine meaning the absolute signal intensities (and by extension the iron impurity density) are not fixed. Reexamining figure 5.21, the only field of view effect with any perceptible difference occurs for the UV spectrometer's sightlines in the core plasma. This field of view effect will only be notable for the UV line emission from Fe^{+22} since this chargestate is the only UV-contributing chargestate that has any significant density in the core region due to the temperature profiles present. However since the central line-of-sight is the one implemented in the least squares fitting routine the entire radial extent is still captured in the model. Therefore this field of view correction and more importantly the process of calculating sightline integrals are not expected to contribute any substantial uncertainty to the inference of the transport profiles.

Iron chargestates and corresponding line emission

- Even including a spectral line for every iron chargestate won't guarantee a unique inference of the anomalous diffusion profile due to the iron chargestates' fractional abundance profiles. In fact this is why the higher iron chargestates' spatial data is more effective at constraining the inference of the anomalous transport profiles.

The choice of which iron chargestates and corresponding spectral lines to include in the least squares fit is an important factor in the uncertainty on the inferred anomalous transport profiles. For the work presented in this thesis, the high-efficiency extreme ultraviolet overview spectrometer, HEXOS,[66,67] and the high resolution x-ray imaging crystal spectrometer, HR-XIS,[64,59] were used to collect the spectral emission from the various iron chargestates in the plasma. In particular HEXOS provides a single, central sightline for spectral emission between 2.5 to 161 nm corresponding to seven chargestates, $Fe^{+22,21,18,17,15,14,12}$,[o] and HR-XIS provides the helium-like spectra from Fe^{+24}. Therefore HEXOS generates information on a wide range of chargestates without detailed spatial information, while HR-XIS gives an image with multiple unique sightlines for a single chargestate. This distinction is important since the electron temperature profile present will determine the degree of spatial localization of each chargestate's line emission. A broad electron temperature profile will lead to a broad radial extent of a few chargestates which in turn causes ambiguity in the emission locations for a single line-of-sight measurement. In fact even if it was diagnostically possible to measure line emission for every chargestate which would provide extra constraints on the inference, it still wouldn't be sufficient to guarantee a unique solution with single, central line-of-sight measurements. For the measured and expected temperature profiles in W7-X, the higher the iron chargestate the more effective spatial data is at constraining the inference of the anomalous transport profiles. This is illustrated in figure 5.22, where the fractional abundances of the iron chargestates for the synthetically generated data is plotted as functions of normalized minor radius and electron temperature. The Fe^{+24} abundance is dominant from magnetic axis until ~ 0.55 normalized radius making the HR-XIS diagnostic's ability to provide unique sightlines critical in accurately inferring the anomalous transport profiles. Figure 4.7 perfectly encapsulates this concept when the same number of spectral lines are used, but with only a single sightline for the Fe^{+24} w-line rather than an inverted emissivity profile. Returning to figure 5.22a, the HEXOS data in combination with the eight evenly-spaced sightlines from the HR-XIS provide enough radial coverage and resolution to accurately infer the anomalous transport profiles.

[o] Fe^{+20} atomic and HEXOS data is available, but not implemented in this work. Fe^{+8} is not included since the emission comes from mostly outside LCFS

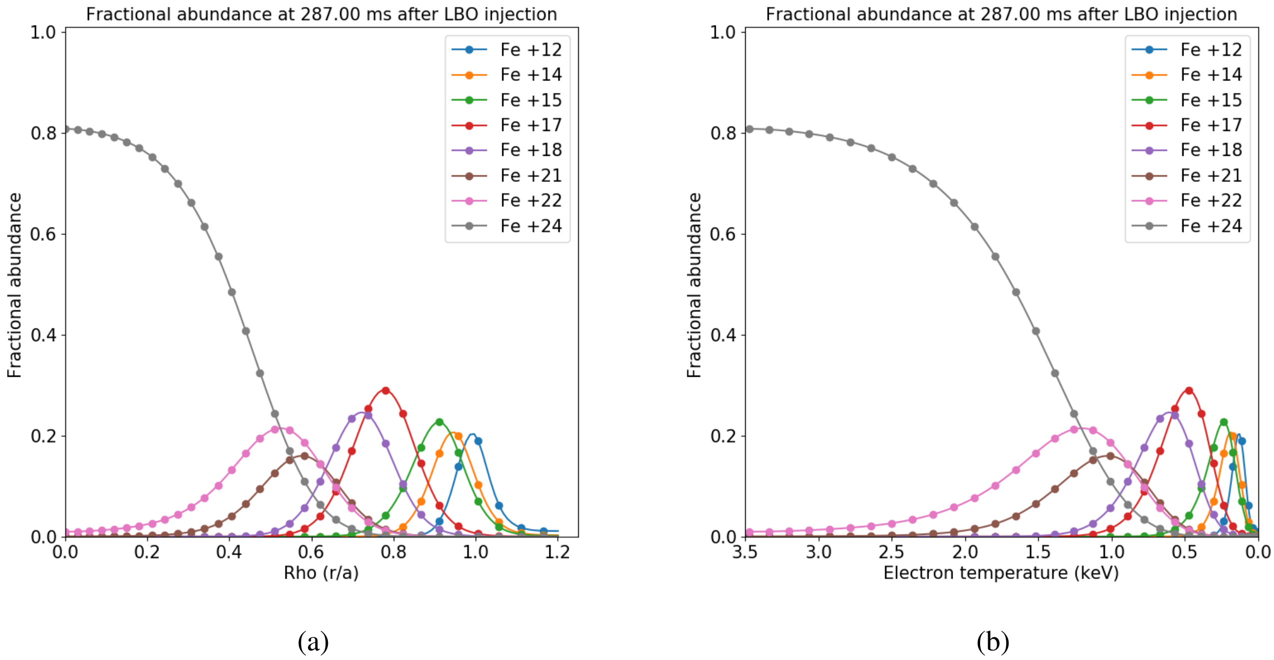

Figure 5.22: The same synthetic data with the same initialization for the least squares code was used for the fit shown in 4.4a & 4.4b. The fractional abundance of the iron chargestates that correspond to the spectral lines used in the inference are plotted at 287 ms after the LBO injection which corresponds to a time when the profile shapes are unchanging. Note in (b) the decreasing temperature used for the x-axis

In terms of reducing the uncertainty, utilizing the Q-line or the beta line in the helium-like spectra measured with HR-XIS and corresponding to the Fe^{+23} and Fe^{+22} chargestate respectively would help localize the correct transport terms based on each line's temporal shape. Unfortunately for the collected data presented in this thesis work, the HR-XIS experienced significant vignetting as seen in figure 5.23b. The vignetting not only increased the signal to noise of the w-line data, but also made calculating inverted emissivities extremely difficult. This is the reason why eight individual sightlines were defined for the HR-XIS detector. Moreover the vignetting shape caused the Q-line and beta line to have very low signal levels calling into question the usefulness of including this data in the inference.

Iron line emission signal uncertainty estimation

Original processing method for signal uncertainties

- The iron line emission was modified with a linear background signal, derived from time points outside the LBO injection, in order to minimize any systematic errors within the fit from non-LBO radiation.
- The UV line emission's noise calculation underestimated the total uncertainty levels even though careful analysis was performed. To rectify this two separate methods were employed: First ansatz scaling factors were used to multiply the various total signal uncertainties and Second an improved estimation for the gain across the UV detectors was performed as detailed in section 5.2.2

The final uncertainties within the iron line emission processing are how the relative weights are determined within the least squares fitting routine and how any background signal is handled within the model. These two topics are particularly crucial since the weights literally determine which data points should contribute more or less to the total least squares sum and any background signal if not properly modeled can add systematic error to the inference. Equation (5.1) shows the general least squares formula with σ_i representing the uncertainty in the ith data point scaling the difference between the ith measured point and ith STRAHL derived

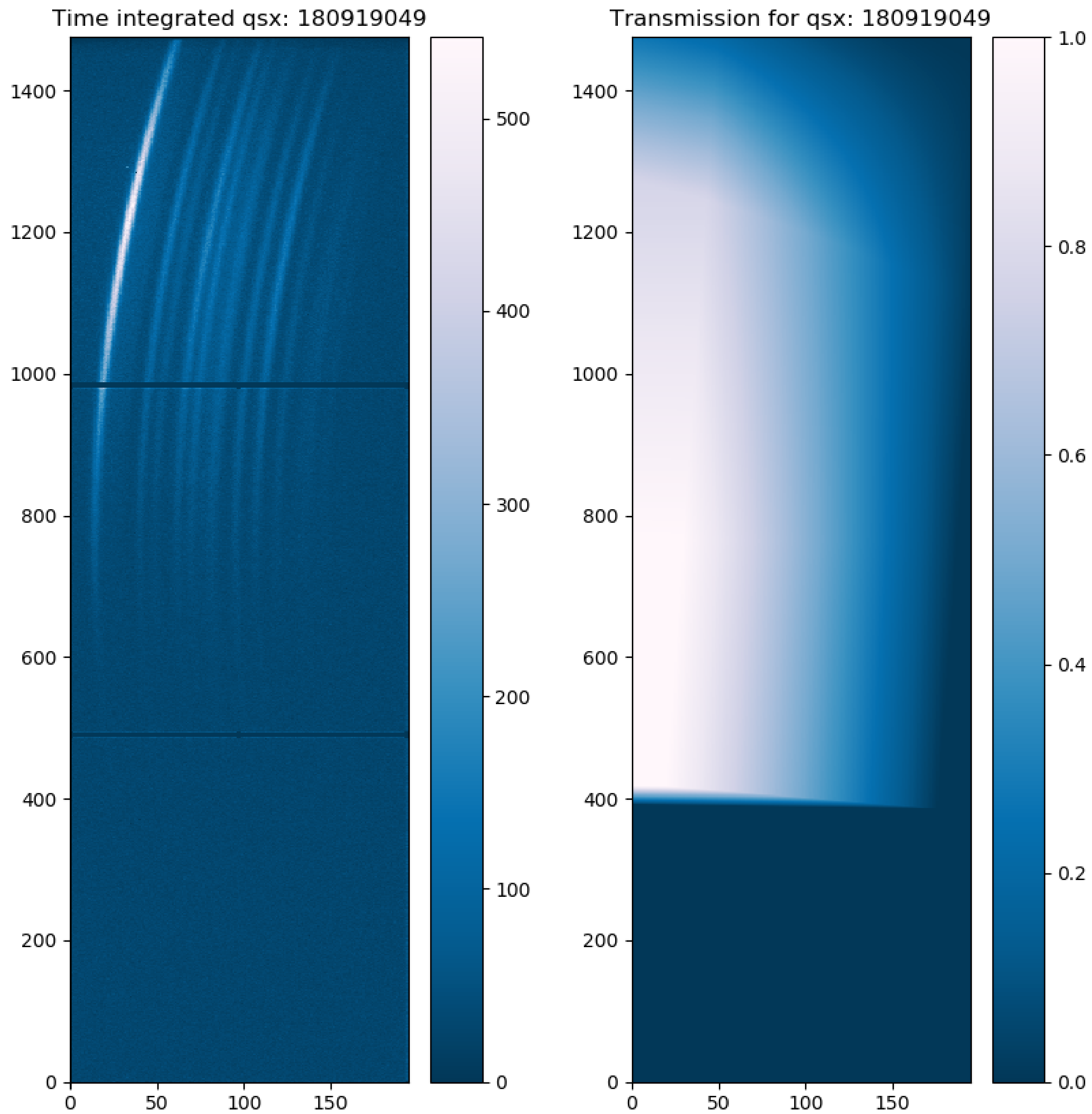

(a) (b)

Figure 5.23: The helium-like iron spectrum is shown in a time integrated image of the HR-XIS detector in (a). The total transmission for the HR-XIS detector is shown in (b) where the incorrect crystal positioning has caused the bad vignetting pattern observed

data point.

$$\min \mathcal{X}^2 = \sum_{i=1}^{N} \frac{\left(\mathrm{Y}_i^{\text{measured}} - \mathrm{Y}_i^{\text{calculated}}\right)^2}{\sigma_i^2} \tag{5.1}$$

In principle the σ_i should be the 1-sigma uncertainties not only to represent each signal appropriately, but also to allow the least squares fitting routine, mpfit,[81] to calculate the correct parameter uncertainties by way of the covariance matrix. Therefore the 1-sigma uncertainties of each spectral line's sightline needs to be estimated as accurately as possible. Before the estimation of the signals' uncertainties using equation (5.2), the method used to process each measured signal should be detailed.

$$\sigma_{\text{total}} = \sqrt{\sigma_{\text{background}}^2 + \alpha^2 \sigma_{\text{shot}}^2} \tag{5.2}$$

For the UV spectral lines measured with HEXOS, each emission line is calculated first by summing up five pixels centered around the NIST defined wavelength for that specific atomic transition. Typically there is an negative offset in the summed signal, so in order to properly scale the entire signal the last thousand data points, corresponding to one second in measurement time well after the plasma discharge had ended, were fit with a simple line using a least squares routine as seen in figure 5.24a. Next the y-intercept value from the least squares fit was subtracted from the signal to boost it above zero since the STRAHL model signal cannot produce any negative values. In addition to the linear fit, the weighted residuals from said fit were binned into thirty different regions to form a histogram and then subsequently fit with a gaussian to determine the approximate standard deviation as depicted in figure 5.24b. The gaussian's standard deviation was then used as an estimate of the background noise in equation (5.2) since it represented any dark current or readout noise in the signal. Finally for each HEXOS derived signal, another simple linear least squares fit was performed on a time window before the LBO injection and after the signal level had returned to background levels as seen in figure 5.25a. Even though in this case the FeXXIII line emission seems extremely constant before and after the LBO injection, determining the linear background is important since it is needed to raise the STRAHL modeled FeXXIII line emission to the measured one shown in the figure 5.24. Also to capture the 1-sigma level uncertainty of the HEXOS derived signals, an ad hoc

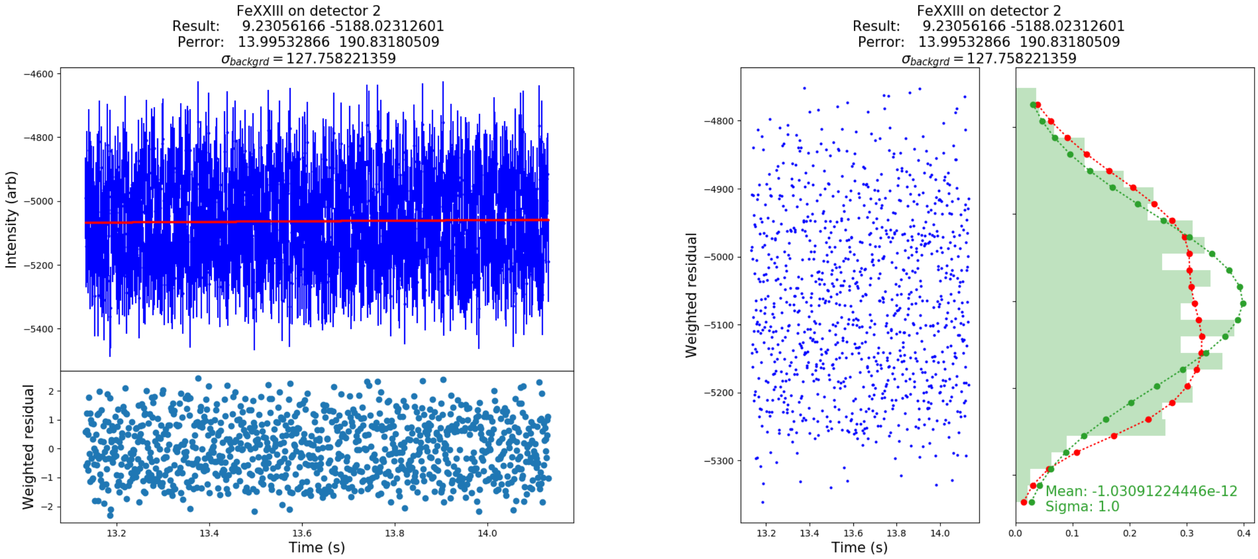

(a) (b)

Figure 5.24: Well after the plasma has ended, a second's worth of data (i.e. one thousand data points) was used to determine the negative offset as seen in (a) and to determine the background noise corresponding to any dark current or readout noise present in the FeXXIII signal in (b). In particular the weighted residuals were binned into a histogram and fit with a gaussian using the standard deviation to make this estimation of background noise levels

α scale factor was added in equation (5.2) to account for any additional noise proportional to the measured signal level. In order to estimate α, the residuals of the line fit to the background levels before and after the LBO injection were used to determine σ_{total}. Using a histogram of the residuals (shown in bottom of figure 5.24a and the bottom left of figure 5.24b) a gaussian fit was performed to determine the standard deviation, which represented σ_{total} when $\alpha = 0$ and $\sigma_{background} = 1$. Next an estimate shot noise was determined from taking a signal level from the line describing the background levels before and after the LBO injection as shown by the red line in figure 5.24a. Therefore using this estimated shot noise in combination with the predetermined readout noise and the estimated total noise, α could be approximated from equation (5.2). Specifically α was determined by forcing the standard deviation of the gaussian fit to a histogram of the linear background fit's weighted residuals to be 1-sigma.

As mentioned previously the HR-XIS diagnostic experienced severe vignetting during the iron impurity transport experiments forcing the helium-like w-line to be treated as eight distinct sightlines rather than performing a singular inversion for an emissivity profile. Each

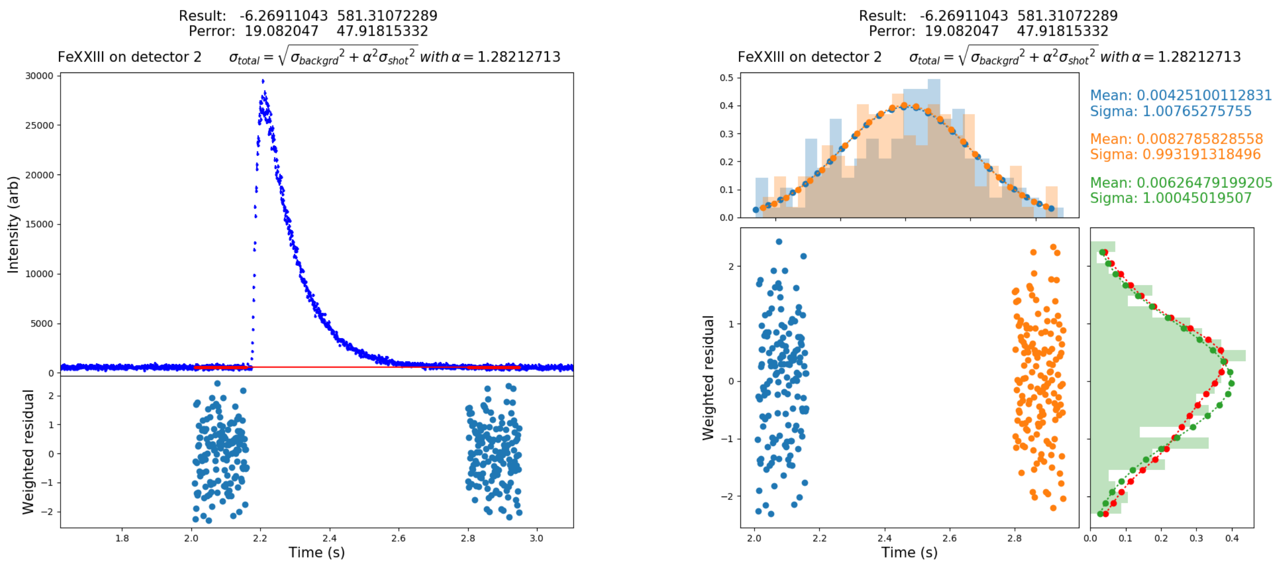

(a) (b)

Figure 5.25: The scaled FeXXIII signal has the background light levels estimated through a simple linear least squares reduction before and after the iron LBO injection in (a). The red points and line represent the linear fit to the background light, while the blue data points is the scaled FeXXIII signal. In (b) the time window before and after the LBO the residuals are binned and fit with a gaussian to determine the appropriate α scale factor in equation (5.2)

w-line line-of-sight was forty pixels vertically, corresponding to $\sim$ 4 cm spatial resolution within the plasma, and anywhere between nine to fourteen pixels wide.[p] The eight sightlines were evenly spaced by one hundred pixels between two neighboring sightlines ensuring the signals weren't directly coupled and had enough counts for decent signal-to-noise ratio. In terms of the uncertainty levels, fortunately the HR-XIS diagnostic is much simpler because the x-ray photons are so energetic that the uncertainty in any recorded counts on any one pixel is predominantly due to shot noise. The shot noise is governed by Poisson statistics and scales with the square root of the signal level, i.e. $\sigma_{\text{total}} \approx \sqrt{\sigma^2_{\text{shot}}} = \sqrt{N_{\text{photons}}}$. Therefore for all of the sightlines corresponding to the helium-like w-line the ad hoc α scale factor could simply set to one without considering any readout/dark noise. However to properly model the HR-XIS sightlines within STRAHL a linear background was still needed to capture any photons measured that weren't from the iron LBO injection as seen in figure 5.26a.

[p]To keep the highest signal to noise ratio possible the width of the integrating box was varied to account for more peaked w-line at cooler temperatures. The width was determined by eye after plotting the spectrum integrated over the vertical pixel range

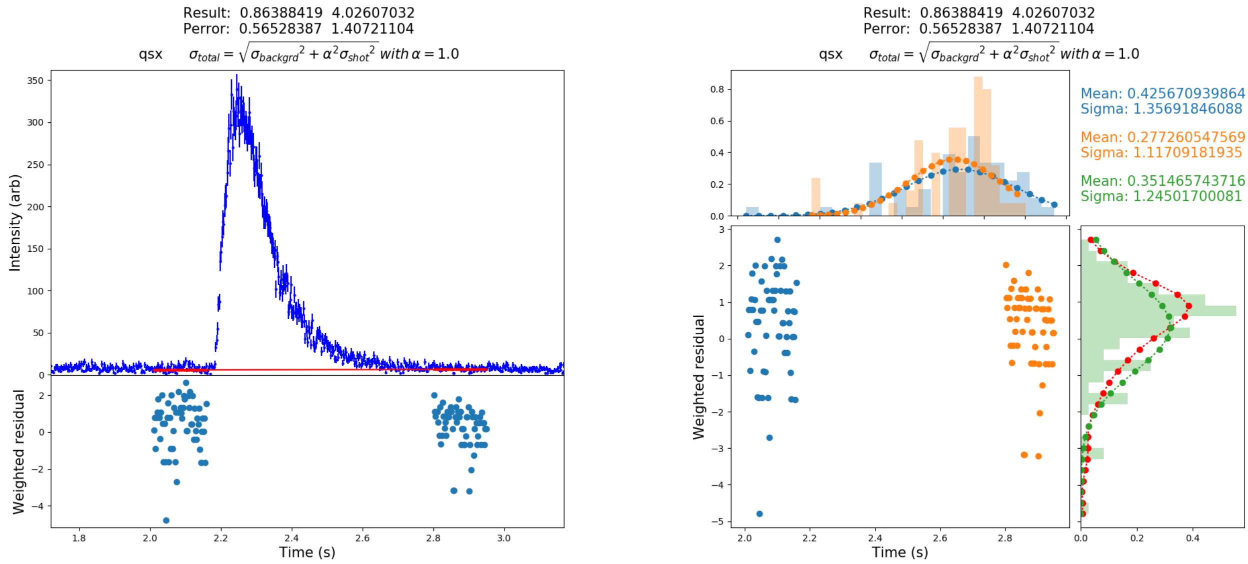

(a)

(b)

Figure 5.26: The HR-XIS diagnostic's central most line-of-sight for the w-line has the background light levels estimated through a simple linear least squares reduction before and after the iron LBO injection in (a). The red points and line represent the linear fit to the background light, while the blue data points is the scaled w-line signal. In (b) the time window before and after the LBO are binned and fit with a gaussian to determine the appropriate α scale factor in equation (5.2)

Unfortunately even though great care was taken to use the fitting techniques described above for both the dark current & readout noise uncertainty and the ad hoc scale factor for shot noise uncertainty, the total signal uncertainties for the HEXOS signals were too low.[q] In particular the same time window of $\sim$ 350 ms was used for every sightline and this meant that the lower chargestates measured by HEXOS had relatively longer regions where the signal level was at the background level. Consequently these HEXOS signals could be unduly influenced by both the systematic error from the linear background levels added and from overly weighting the regions with lower signal levels as observed in figure 5.27. To address this issue all of the HEXOS sightline's $\sigma_{\text{background}}$ were increased to 200.[r] Again unfortunately this still didn't seem to capture the full uncertainty in the HEXOS signals especially the signals with very high number of counts. As an ansatz each HEXOS signal had its σ_{total} scaled by factors varying from

[q]Too low here specifically means that the variation from subsequent time points are outside their individual errorbars even during the smooth variation of the signal (i.e. not during the rapid signal rise due to the LBO injection).

[r]FeXXIII $\sigma_{\text{background}}$ was set to 300

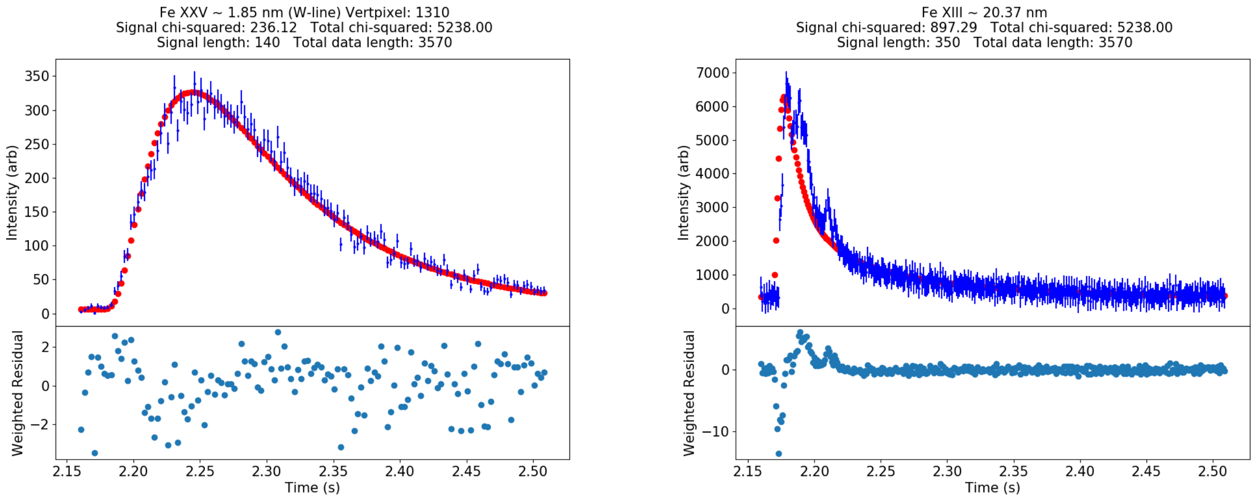

(a) (b)

Figure 5.27: The HR-XIS diagnostic's central most w-line sightline signal for the 1st iron LBO in 180919043 is shown in (a). In (b) is the Fe^{+12} signal for the same iron injection

Table 5.1

Spectral line	Ansatz scaling factor for σ_{total}
FeXXIII	1.8
FeXXII	2.0
FeXIX	1.0
FeXVIII	1.0
FeXVI	3.0
FeXV	3.0
FeXIII	1.5

1 to 3 as seen in table 5.1. Using the 3rd iron LBO injection from shot 180919049, the factors were determined by increasing the levels until the gross spectral line temporal shape could be followed where specifically adjacent data points didn't traverse outside each other's errorbars as seen in figure 5.27b. It should be noted that once these ansatz factors were determined and the $\sigma_{\text{background}}$ set, they were left constant for all of the other direct LBO comparisons.[s] This relative weighting of data points is even more important when considering that the HR-XIS signals are sampled at 2.5 ms versus 1 ms for the HEXOS signals indicating that each HEXOS signal should contribute 2.5 times more to $\mathcal{X}^2_{\text{total}}$.

[s]For the analysis in chapter 6, the signal uncertainty calculations using the ansatz factors detailed in table 5.1 weren't used. In fact all of the on- to off-axis inferred analysis used the point- to-point variation method described in section 5.2.2.

Point-to-point processing method for signal uncertainties

- Rather than use ansatz scaling factors, a point-to-point variation in UV spectral lines' decay phase was employed for estimating the highest average signal gain and subsequently the total uncertainty levels. This method was performed for each LBO injection in the 3.5 MW experimental dataset to verify that each signal's highest average gain yielded similar values.

- Testing the various signal uncertainty estimation methods, three least squares minimizations were performed using the original method detailed in section 5.2.2, the point-to-point method as detailed below, and finally a constant scale factor method. All three returned the same inferred diffusion profile (see figure 5.29) giving confidence that proceeding with the point-to-point method shouldn't increase the uncertainty levels in the anomalous diffusion profile more than 0.1 $\frac{m^2}{s}$.

Finally a point-to-point variation method was employed in order to better calculate the uncertainties in the line-integrated signals from the UV spectral lines. The point-to-point variation method was utilized to capture the true scatter in the decay phase of the spectral signals by first calculating an average gain to understand the contributions from photon statistics. The first step in estimating the point-to-point variation in the signals was to perform a linear interpolation for each datapoint in an emission signal using only two points: the immediately preceding and following point. This interpolation gave a guess value for every datapoint based solely on its adjacent neighbors. Next a residual was calculated between this interpolated signal and the measured line integrated signal as seen in figure 5.28a. In order to ensure appropriate statistical significance, the 25 points preceding and following each datapoint were used to determine the standard deviation of the scatter. This standard deviation, as an estimate of σ_{total}, could then be used in conjunction with equation (5.2) to solve for α^2 or more appropriately an estimated gain in the signal level as seen in figure 5.28b.[t] This process for calculating the gain signal

[t]The structure seen in the residual estimation can have a large impact on the estimation of σ_{total} and ultimately the gain value necessary to satisfy equation (5.2). This is why the average of the gains are taken from the decay phase (i.e. well after the peak signal shown in figure 5.28b with an x) in order to not be impacted by the fast ramp of the signal where residuals will be much larger. In fact when this point-to-point method is applied to synthetic data similar variations are observed (not shown), however accurate average gain values can still be extracted when using the high signal intensity but slowly varying decay phase of the signal.

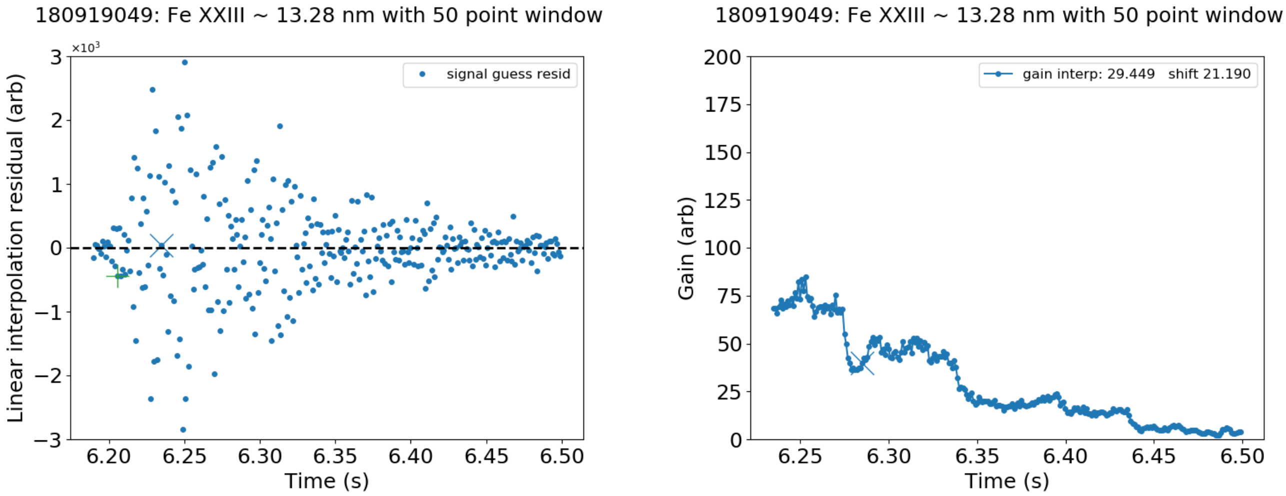

(a) (b)

Figure 5.28: The residual for Fe^{+22} line emission is shown in (a), while (b) depicts the corresponding estimated gain. Note that the variation in the residuals shown in (a) leads to a change in an estimation for σ_{total} from the 50 point windowing, ultimately resulting in non-stationary gains (see footnote t)

Table 5.2

Spectral line	Highest average gain i.e. α^2
FeXXIII	40
FeXXII	25
FeXIX	30
FeXVIII	30
FeXVI	80
FeXV	55
FeXIII	55

value from point-to-point variation was performed on all of the UV line emission for the three experimental LBO discharges that all correspond to the same 3.5 MW input ECRH power level. For each spectral line the highest average gain value during the spectral emission's decay phase was recorded, see table 5.2, and used within equation (5.2) to calculate a smooth σ_{total}. Therefore this point-to-point variation method provided a more accurate estimation for the iron LBO line emission and moving forward is the nominal method used[u]. Moreover in comparison with

[u]The point-to-point method was used as the standard signal uncertainties for the HEXOS sightlines throughout the variational tests in this chapter

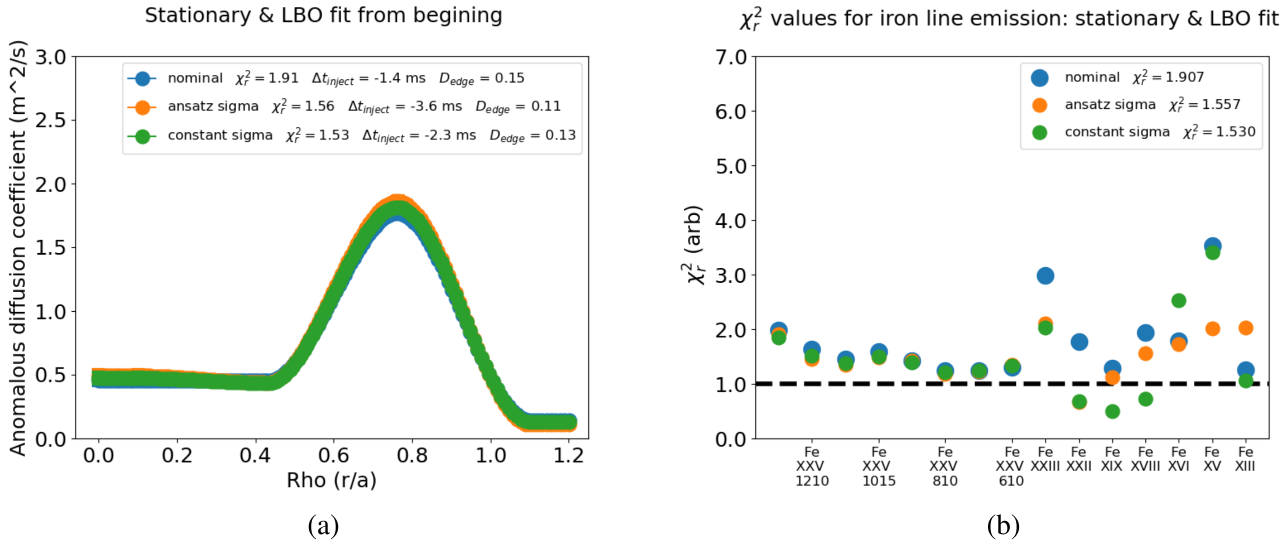

Figure 5.29: The inferred anomalous diffusion profiles for the 3rd iron LBO injection in 180919049 are shown in (a) using the point-to-point, the ansatz scaling factors, and the constant values for every HEXOS signal σ_{total}. In (b) each individual sightline's spectral line emission's $\mathcal{X}_R^2$ are plotted where ideally every signal has $\mathcal{X}_R^2 \sim 1$ for a perfect fit.

the ansatz scale factor method originally used, the spectral lines uncertainties didn't drastically change giving confidence in the calculation.

As a final signal uncertainty estimation on the HEXOS signals for comparison, an additional constant method of setting all $\sigma_{\text{background}}$ to 300 and all α to 6.0 was tested with the least squares routine. In fact figure 5.29 shows that the variation with signal uncertainties has a near negligible effect on the inferred anomalous diffusion profiles as seen in figure 5.29a. Interestingly the constant and ansatz scale factor methods have a significantly lower total $\mathcal{X}_R^2$ indicating an overestimate in the signal uncertainties as evidenced by the individual sightline's $\mathcal{X}_R^2$ in figure 5.29b. These individual $\mathcal{X}_R^2$ are another tool to visualize how well each STRAHL modeled signal matches the experimental data and for figure 5.29b demonstrate how altering the estimation method impacts the overall fit. Surprisingly the LBO injection timing parameter for the ansatz scale factor method was inferred 2.2 ms before the nominal, point-to-point method even though the inferred sightline scale factors and D_{edge} values are only 0.04 $\frac{m^2}{s}$ different. Ultimately the exact 1-sigma uncertainties on the spectral emissions are not achievable, but by the estimations and methods presented above consistent and accurate inferences can be achieved with diffusion value variations less than 0.1 $\frac{m^2}{s}$.

5.2.3 Initialization of least squares minimization

Some key results from the synthetic sensitivity testing performed in chapter 4 were the estimations of the uncertainties introduced from timing offsets, procedural method, and kinetic profiles. From these uncertainties a better understanding of the initialization of the least squares fitting routine was developed. Specifically a procedural method excluding anomalous convection velocity while including the LBO injection timing as a free fit parameter returned accurately inferred anomalous diffusion profiles. However as already illustrated in section 5.2.1 with inferences using experimental data, the inclusion of radially moving spline-knots can lead to nonphysical inferences showing the synthetic sensitivity testing wasn't able to reveal some of the systematic errors. To further explore and understand potential systematic errors, variational testing with the same experimental data is continued in this section. This section discussed the initialization of the least squares fitting routine with regards to the LBO injection timing, the execution of the least squares procedural method, and the kinetic profiles.

LBO injection timing as free fit parameter

- The initialization of the LBO injection timing at 2.5 ms before the first iron spectral signal rise is an appropriate parameterization for the least square minimization.
- The $\pm$ 3.5 ms LBO injection time variation performed with the on-axis case of the 3.5 MW dataset demonstrated the matching of measured signals is sensitive to the LBO injection time even if the difference in $\mathcal{X}_R^2$ between the scenarios is not as large as those for the synthetic testing.
- The experimental variation confirmed the synthetic data testing's conclusions (see section 4.2.2). Specifically the LBO injection time has a large impact on the inferred anomalous diffusion profile, but fortunately this timing parameter can be determined within the least squares fit.

As already discussed in section 4.1.4 the jitter in the LBO laser created a large uncertainty, up to $\pm$ 5 ms, in the exact injection of the neutral iron cloud at the plasma edge. Due to the

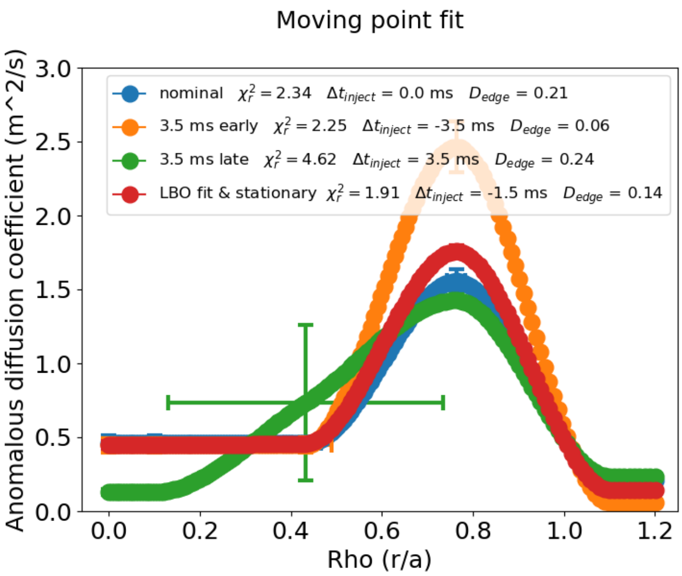

Figure 5.30: The inferred anomalous diffusion profiles for the 3rd iron LBO injection in 180919049 are shown with the LBO injection timing held at 3.5 ms early and late compared to the nominal value. In addition to the moving spline-knot inferences, a stationary LBO injection initialized at the nominal value is shown

inherent timing uncertainty, the LBO injection time was established as 2.5 ms before the first observed iron spectral emission which was always the line radiation from $Fe^{+14,+15}$. Similar to the synthetic sensitivity testing in section 4.2.2, a 3.5 ms shift in the nominal injection time was tested with experimental signals. The resultant inferences from this $\pm$ 3.5 ms variation study can be seen in figure 5.30. The 3.5 ms late scenario showed that the inferred diffusion profile only had large discrepancies with the nominal case in the core, but more importantly could not accurately match the measured spectral signals with $\mathcal{X}_R^2 > 4.0$ The large $\mathcal{X}_R^2$ values safely reaffirm the sensitivity of the spectral signals to the LBO injection time even utilizing experimental measurements. Next the 3.5 ms early case showed consistent inferred diffusion profile characteristics to the synthetic testing in section 4.2.2: Namely an increased off-axis peaking $> 0.5 \ \frac{m^2}{s}$ with $D_{edge} < 0.1 \ \frac{m^2}{s}$ yielding a steep diffusion gradient across the LCFS. A significant difference with the previous synthetic results was the $\mathcal{X}_R^2$ for the 3.5 ms early scenario being approximately equal to the nominal case seemingly casting doubt on the efficacy of including the LBO injection as a free parameter. However the inclusion of the LBO injection as a fit parameter is evident in figure 5.30, which shows a reduction in the $\mathcal{X}_R^2$ by over 0.3 $\frac{m^2}{s}$ in the stationary scenario. Therefore the matching of measured signals is sensitive to the LBO injection time even if the difference in $\mathcal{X}_R^2$ between the scenarios is not as large as those for the synthetic testing in section 4.2.2. This lack of difference between the $\mathcal{X}_R^2$ values for the experimental data is most likely due to the inaccurate description of the LBO temporal shape used to model this injection, see section 5.1.3 and 4.2.7. Taking a closer examination between the stationary case including the LBO injection time and the nominal moving spline-knot case, the anomalous diffusion profile variation is $< 0.2 \ \frac{m^2}{s}$ across the entire profile for a 1.5 ms difference in the timing. This indicates that not only can the LBO injection time be determined internally in the least squares routine, but also the added error in the anomalous diffusion profile should be minimal, i.e $< 0.2 \ \frac{m^2}{s}$. In conclusion the initialization of the LBO injection timing at 2.5 ms before the first iron spectral signal rise and then subsequent use of this time as a fit parameter is appropriate mainly due to the improved experimental signal matching.

Procedural method for least squares minimization

- As first demonstrated in section 5.2.1, including the radial position of the two interior spline-knots can lead to nonphysical gradients in the diffusion profile as seen figure 5.33
- The systematic uncertainty introduced from employing different procedural methods demonstrated not only the importance of the radial information provided by multiple unique sightlines for each spectral line, but also the importance of performing an additional inference without radially moving spline-knots.

The procedural strategy for accurately inferring the anomalous transport profiles was to constrain the parameter space of the least squares minimization routine while still maintaining enough flexibility to match the iron line emission. Not only does including fewer free parameters in the least squares routine speed up the convergence to a solution, but it also limits the routine from inferring nonphysical solutions. Therefore in order to enact this strategy of minimizing the number of free parameters it was important to establish as many fixed parameters as possible using prior knowledge or reasonable assumptions. Based on previous analysis in [Geiger et al. 7] and reaffirmed in section 4.1.2 & 5.1.4, there is every indication that the anomalous diffusion is the dominant transport channel in these W7-X discharges. This led to

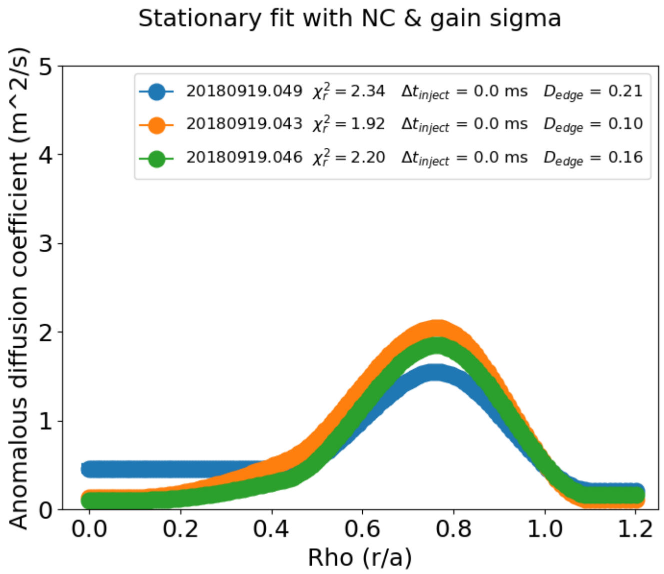

Figure 5.31: First inferences from the least squares routine with only four unique diffusive spline-knots and fifteen signal scale factors used as free parameters. These three LBO injections all have roughly the same density profiles and total input ECRH power, but with various degrees of that power deposited off-axis.

the conclusion that it would be counterproductive to include the anomalous convection velocity profile as a free fit function within the least squares routine. Therefore the standard procedural method as detailed in section 4.2.2, started with the first inference using each sightline scale factor and the four unique anomalous diffusion radial spline-knots as the only free parameters. For every LBO injection presented in this work, these free parameters were initialized as flat values (e.g. 0.1 $\frac{m^2}{s}$) and the first step least squares minimization was performed to generate new and much more likely parameter values. Even though a least squares minimization technique doesn't guarantee finding a unique global solution, these initial inferences with limited number of free parameters routinely produced $\mathcal{X}_R^2 < 2.5$ with most structure in the weighted residuals on the signal rises. These quite good initial fit results, see figure 5.31, reaffirmed the previous assumptions taken, especially the assumption about the anomalous diffusion being the dominant transport channel for these iron LBO injection experiments on W7-X. The corresponding resultant parameters from 5.31 were then used as an initialization, in order to introduce either new free parameters or extra information into the model. For example, the LBO injection time was included as a free parameter for the second inferences as seen in figure 5.32a, while figure 5.32b shows the second inference with both the LBO injection time and the radial position of

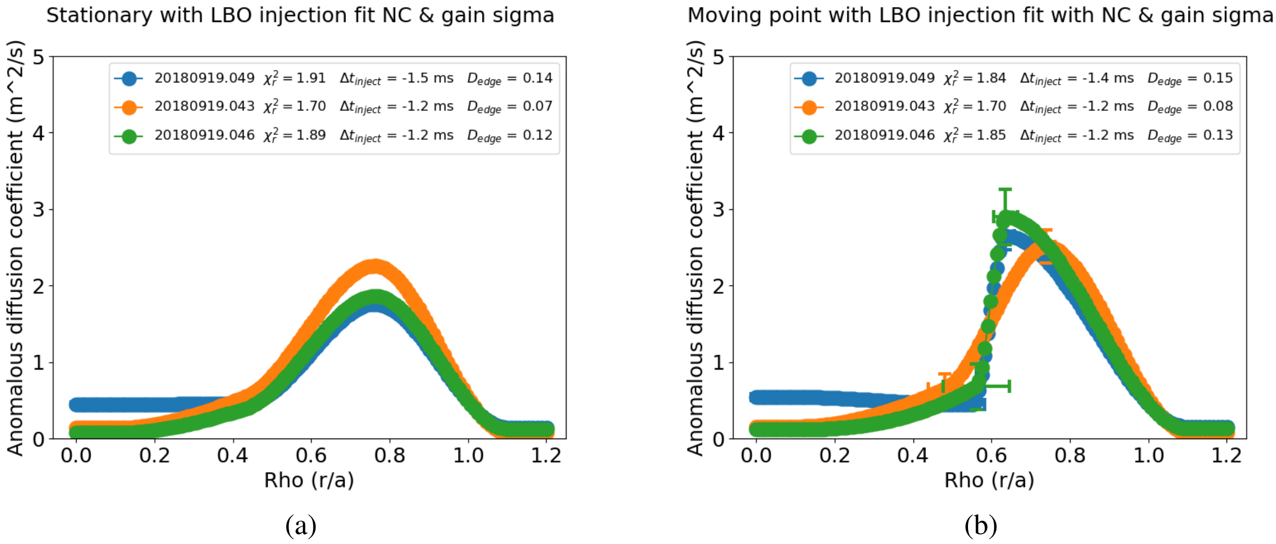

Figure 5.32: The same data is initialized from the ones shown in 5.31 and inferences are performed with the LBO injection timing as a free parameter in (a), while both the LBO timing and the horizontal position of the two interior spline-knots as free parameters in (b)

the two interior spline-knots as extra free parameters. As detailed in section 4.2.2, the nominal procedural method was to first perform a stationary inference of the anomalous diffusion profile (shown in figure 5.31) and then to perform a second inference utilizing the first's result as input with the LBO timing and the radial position of the two interior spline-knots as additional free parameters (shown in figure 5.32b) This nominal procedural method utilized throughout the synthetic uncertainty chapter 4 performed well as a procedural strategy in finding the correct transport profile, however as seen figure 5.32b led to nonphysical diffusion profiles when utilizing real experimental signals. As detailed in section 5.2.1 the limits on the spline-knots' radial positions allow the least squares routine to generate artificially steep diffusion gradients in order to more closely match the line emission. This systematic error introduced from the nominal procedural method, see section 4.2.2, is an important finding for recognizing the procedural method's impact on the inferred profile's uncertainties and subsequent ways to mitigate the systematic errors. For example, this finding led to a new procedure whereby the second inference in the standard procedural method included the LBO injection time as a free parameter, but more importantly didn't include the radial position of the two interior spline-knots. This slightly modified method yielded both very reasonable diffusion profiles and improved $\mathcal{X}_R^2$ values as seen in figure 5.32a. In fact the inclusion of the LBO injection timing parameter reduced

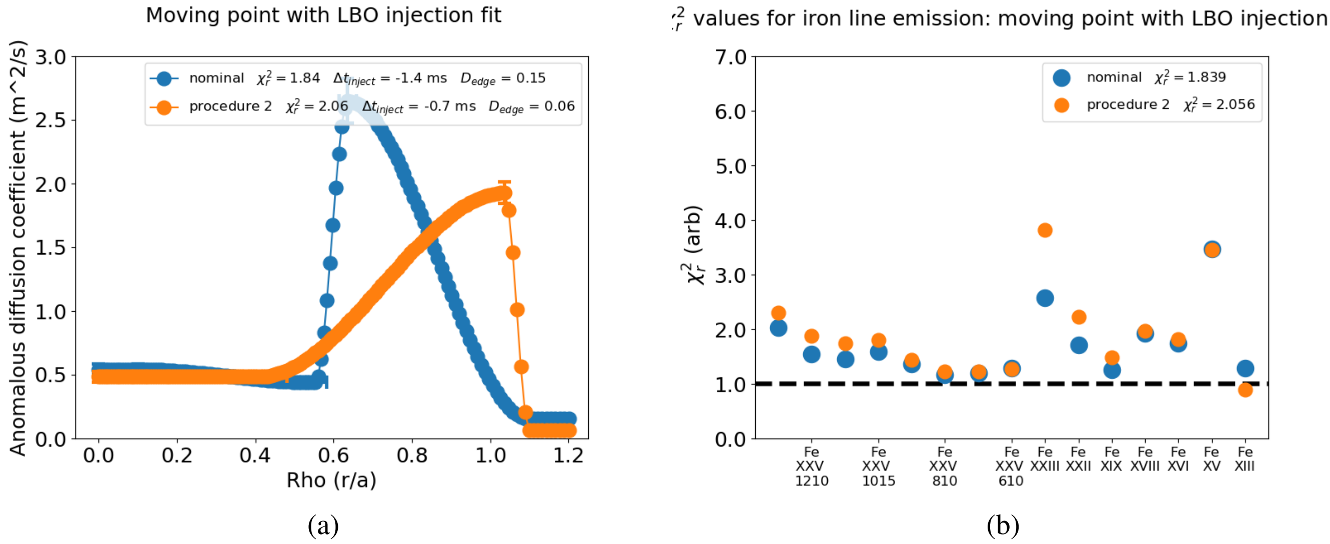

Figure 5.33: The anomalous diffusion profiles for the nominal procedural method and an additional procedural method where all fit parameters are free from the start are plotted in (a). The corresponding $\mathcal{X}_R^2$ values for each iron emission sightline are plotted in (b)

the $\mathcal{X}_R^2$ values ($\sim 0.25\ \frac{m^2}{s}$) significantly more than the inclusion of the radial position of the two interior spline-knots ($\sim 0.05\ \frac{m^2}{s}$). Therefore this additional second inference without utilizing radially moving spline-knots is not only important for the marked decrease in $\mathcal{X}_R^2$ values, but also important for providing a solution guaranteed to not contain any artificially high gradients.

To further demonstrate the systematic errors possibly introduced from a procedural method, an additional test was performed where all of the fit parameters were allowed to be free in both the first and second inference[v]. This additional procedure was performed for the 20180919.049 LBO experimental scenario with the results illustrated in figure 5.33. The systematic errors clearly stem from the radial position parameter's freedom to drive steep diffusion gradient in order to better match the iron line emission signals. If the individual sightline $\mathcal{X}_R^2$ values are examined in figure 5.33b, it is obvious that the largest difference occurs for the Fe^{+22} line emission. As shown in figure 5.20 the higher chargestates have a much larger radial extent of their line emission, meaning the contributions to a single central sightline model signal could occur nearly anywhere inside the LCFS. Taking the Fe^{+22} line emission from figure 5.20 as an example there is a $> 20\%$ normalized emission present in the modeled plasma from $\rho \approx 0.25$ to 0.8! This large radial spread without additional unique sightlines for the Fe^{+22} line emission

[v] i.e. the 15 sightline scale factors, the four unique anomalous diffusion radial spline-knots, the horizontal positions of the two interior spline-knots, and the LBO injection time

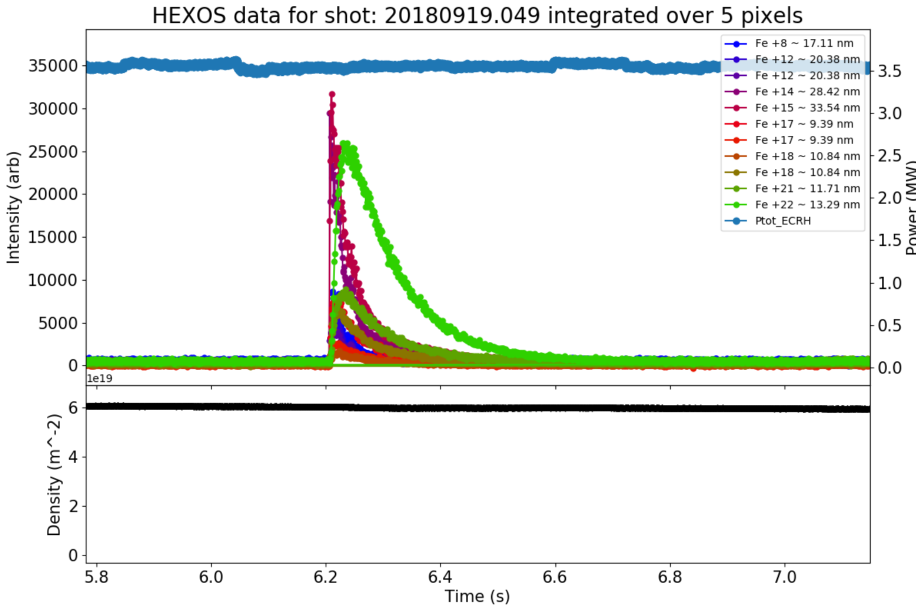

Figure 5.34: The HEXOS iron line emission shown for an iron LBO injection with the ECRH input power and line-integrated density overplotted

allows the least squares routine to tailor the anomalous diffusion profile yielding potentially nonphysical profiles, e.g. figure 5.33a. This reemphasizes not only the importance of the radial information provided by multiple unique sightlines for each spectral line, but also the importance of performing an additional inference without radially moving spline-knots in order to minimize the possibility of moving into nonphysical inference in parameter-space. Finally it should be noted that the diffusion profile's uncertainty stemming from the procedural method should be radially localized, i.e. $\rho > 0.5$, due to the lack radial localization in the line emission in this region.

Initialization of kinetic profiles

The last uncertainty associated with the initialization of the least squares minimization routine arises from the input kinetic profiles. In all of the work presented in this thesis the kinetic profiles are assumed to be constant in time without any variations over the $\sim$ 400 ms of an impurity LBO injection experiment. This time-constant assumption is quite good as shown in figure 5.34 where constant input electron cyclotron heating power along with feedback control of the gas valves yield unchanging line-integrated density measurements well beyond the duration of observed iron emission. With the experimental setup providing time constancy, the only other possible uncertainty from the kinetic profiles is the radial accuracy of said kinetic profiles. Previous work done by [Geiger et al. 7] showed that inferred anomalous transport profiles were most sensitive to changes in the electron temperature, neutral density, and the connection length. The connection length's effects have already been discussed in section 5.1.5 and 4.2.5, therefore the following sections will detail the uncertainties introduced from the neutral density, electron temperature & density, and ion temperature profiles.

Neutral hydrogen profile variation

- The impact on the inferred anomalous diffusion over a factor of 100 change in the neutral density profile is less pronounced ($\sim 0.2\ \frac{m^2}{s}$) than what was found in the synthetic sensitivity testing in section 4.2.4. However the trend in the introduced uncertainty is expected and consistent with increased edge thermal charge exchange discussed in section 5.1.2

In [Geiger et al. 7] the neutral density profile was determined from the filterscope[85] measurements of the hydrogen flux used as input into the KN1D[86] code. Unfortunately the large uncertainty in the filterscope measurements led to $\sim 10^3$ scale between low and high estimations of the neutral density profile, which brought the large variance in the inferred anomalous transport profiles. As detailed in section 4.2.4 the nominal neutral density profile used was a factor of three scaled down profile taken from [Geiger et al. 7] in order to match the corresponding scale increase in line-integrated electron density. Following the exact same procedure from the synthetic data sensitivity testing in section 4.2.4, the nominal density profile was scaled by an order of magnitude smaller and larger before being used within the least squares fit. Figure 5.35 shows the neutral profile variations and the change in the inferred anomalous diffusion profiles for the same iron LBO injection as seen in figure 5.34. The only noticeable difference in the anomalous diffusion profiles occurs in the outer half of the plasma only for the high neutral density scenario. This result is consistent with section 5.1.2 detailing the increased thermal charge-exchange losses from the increased neutral density at the plasma edge. The anomalous diffusion's decreased peaking, $< 0.3\ \frac{m^2}{s}$, at $\rho \approx 0.8$ and the increased D_{edge} inference of $\sim 0.1\ \frac{m^2}{s}$ over the nominal case are both consistent with the least squares inference increasing the diffusive flux to counteract the extra charge-exchange losses. This result is exactly consistent

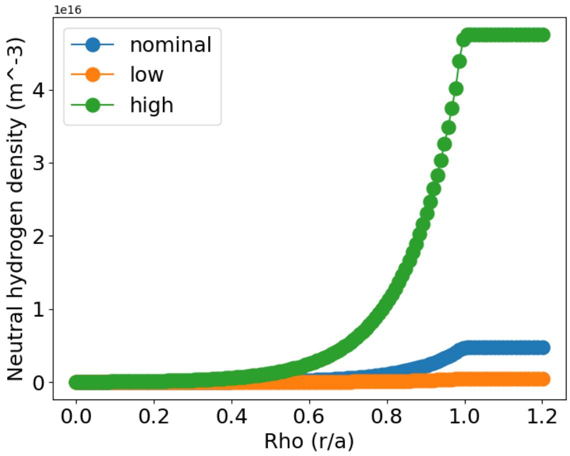

(a)

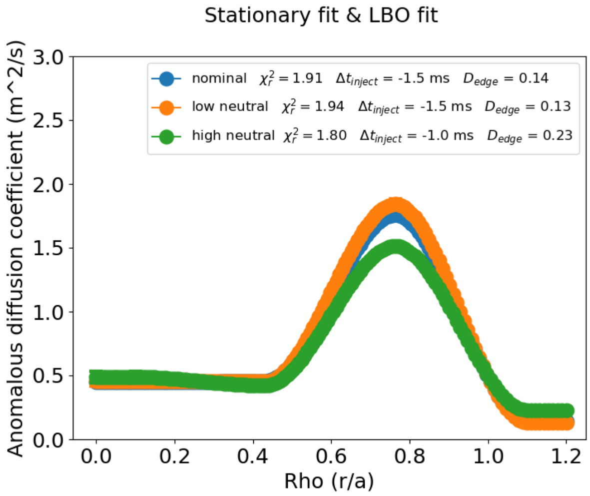

(b)

Figure 5.35: The nominal neutral profile for the 3rd iron LBO injection in discharge 20180919.049 is scaled up and down by an order of magnitude from the nominal profile. The neutral profiles are shown in (a) with the corresponding inferred anomalous diffusion profiles shown in (b) where the inferences do not include radially moving interior spline-knots

with the synthetic sensitivity analysis performed in section 4.2.4, just that the effect from the higher neutral density is less pronounced when using the experimental data from the on-axis case in the 3.5 MW dataset.

Entire electron temperature and density variation

- As expected, the electron density whole profile variation does not substantially impact the inferred anomalous diffusion profile, i.e. $< 0.1\ \frac{m^2}{s}$. Therefore the inferred anomalous diffusion's insensitivity to any n$_e$ profile inaccuracies mean that reducing the uncertainties in the thomson scattering density measurement are not critical for improving the inferences.

- Consistent with the synthetic electron temperature sensitivity testing the low T_e scenario led to a delay in the LBO injection time that caused an increased core diffusion peaking exactly as described in section 4.2.6. In addition, the low T_e scenario demonstrated an increased uncertainty in the diffusion profile for $\rho > 0.5$ due to the lack of spatial resolution from the iron line emission in this region.

- In order to minimize the edge effects on the inferences and improve the cross comparisons for each off-axis ECRH scan, the electron temperature was equalized to the on-axis scenario for the SOL region, i.e. $\rho = 1.0$ to 1.22

A major uncertainty introduced from the kinetic profiles comes from the thomson scattering measurement of the electron pressure. The electron density and temperature profiles provided by thomson scattering diagnostic[71] were taken from three time points around the LBO injection corresponding to $\sim$ 60 ms time difference. The raw data with uncertainties are plotted in figures 5.36a & 5.36b with a gaussian process regression fit of the data overplotted.[72] The output uncertainty of the gaussian process regression's profile was used to subtract/add to the nominally inferred profile as reproduced in figures 5.36c and 5.36d. Naturally these highest and lowest estimations of the electron density and temperature were then taken as inputs into the least squares routine to uncover the relative sensitivity of the anomalous diffusion profile to said variations. Unsurprisingly the electron density profile variations had virtually no effect, i.e. $< 0.1\ \frac{m^2}{s}$, on the inferred profiles as seen in figure 5.37a. Also this insensitivity is consistent with how the least squares minimization is set up: namely the absolute intensity of the line emission is not attempted to be matched and in fact every signal's sightline has a unique scale factor that is a free fit parameter within the minimization. Although the electron density profiles do change from the 1-sigma shifts up & down, the lack of radial localization from the UV spectral emission ($\rho > 0.5$) means that any effects from a different electron density gradient should have minimal influence on the inference. Finally the insensitivity to the n_e profile variations is important primarily for relaxing the restrictions on the measurement and parameterization of the electron density profile without adversely impacting the inference of the anomalous diffusion profile.

Unlike the anomalous diffusion's insensitivity to electron density variations, the low electron temperature scenario demonstrated a larger change to the diffusion profile shape as seen in figure 5.37b. This larger modification of the inferred anomalous diffusion profile was expected and consistent with the previous results found in the synthetic sensitivity testing as detailed in section 4.2.6. The anomalous diffusion's increased sensitivity to T_e as compared to the electron density can be understood by the electron temperature profile's critical role in determining

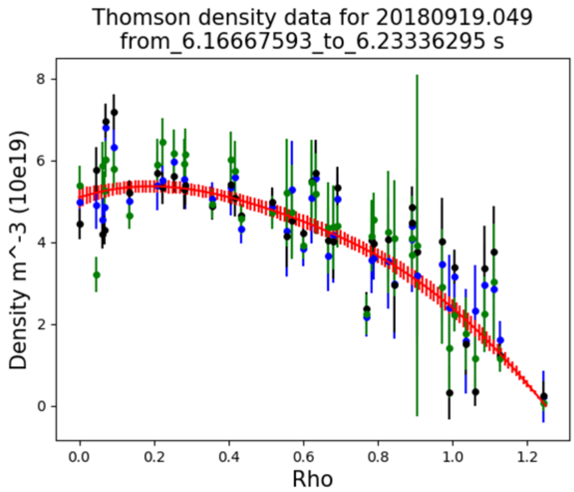

(a)

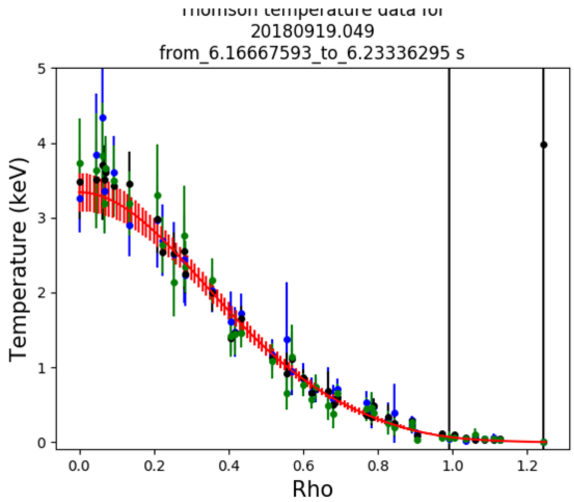

(b)

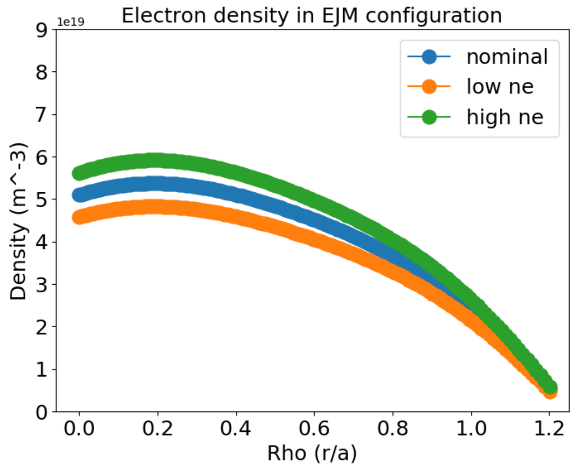

(c)

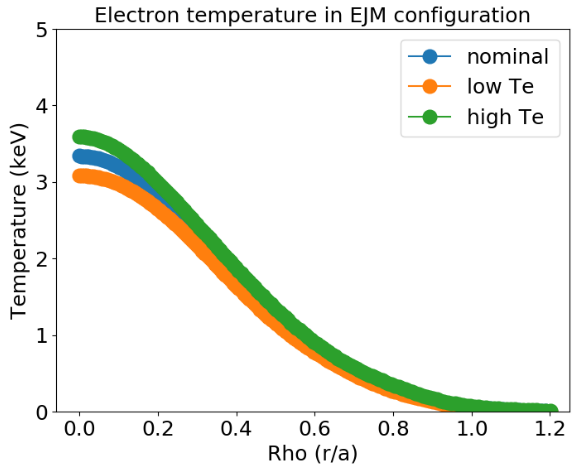

(d)

Figure 5.36: The electron density and temperature for three consecutive time points around the LBO injection time as measured by the thomson scattering system with corresponding gaussian process regression fits overlaid for the on-axis case in the 3.5 MW dataset.

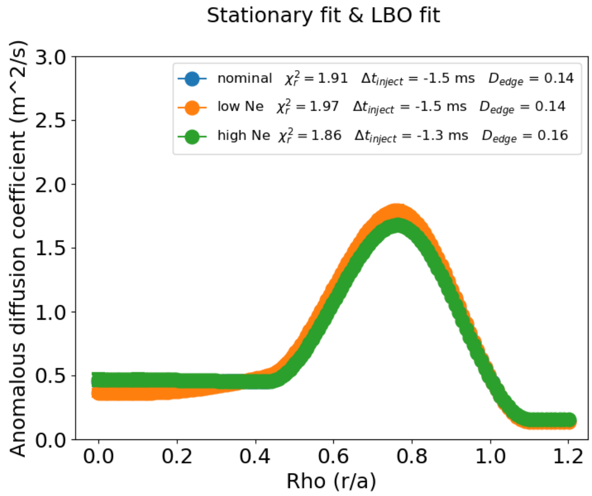

(a)

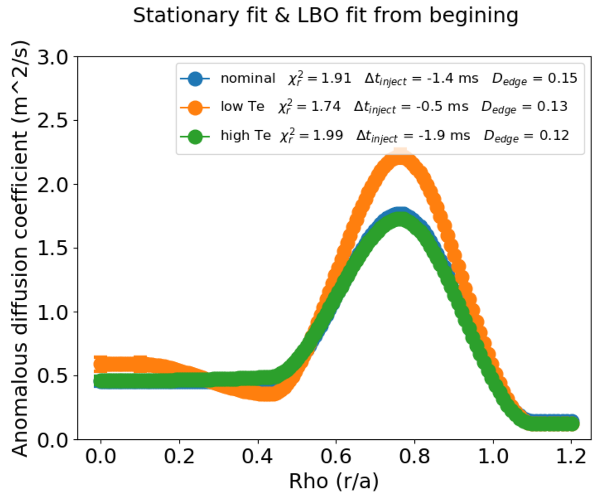

(b)

Figure 5.37: The inferred anomalous diffusion profiles are shown in (a) and (b) for variations in electron density and electron temperature respectively. The fits are for the 3rd iron LBO injection in discharge 20180919.049 including the LBO injection timing as fit a free parameter, but not the radial position of the two interior spline-knots

the ionization locations, the impurity chargestates' fractional abundance, and the strength of the line emission from the electron impact excitation. In particular the low T_e scenario had two characteristics that caused the increased anomalous diffusion profile shaping: First, a 0.9 ms delayed LBO injection time as compared to the nominal T_e case. Second, a radially inward shift of the iron chargestates' line emission distributions. The first characteristic of a large LBO injection time delay, ≥ 0.5 ms, is typically accompanied by an inferred core diffusion peaking as demonstrated in sections 4.2.2 and 4.2.6. The peaked core diffusion keeps the iron from accumulating in the core while matching the spatially resolved signals from the Fe^{+24} spectral emission. The second characteristic, the iron line emission's radial inward shift, indicates the SOL diffusion has even less direct impact on the lower chargestates' spectral emissions. This decreased direct impact of the SOL diffusion in combination with the lack of spatial information for the lower chargestates' line emission provides freedom to the least squares routine to artificially change the inferred anomalous diffusion profile. In fact the increased off-axis diffusion peaking for the low T_e scenario shown in figure 5.37b results in a reduced total $\mathcal{X}_R^2$ primarily due to the improved matching of the lower chargestates' spectral emissions as demonstrated in figure 5.38. Unfortunately the reduction to the total $\mathcal{X}_R^2$ is not an obvious improvement

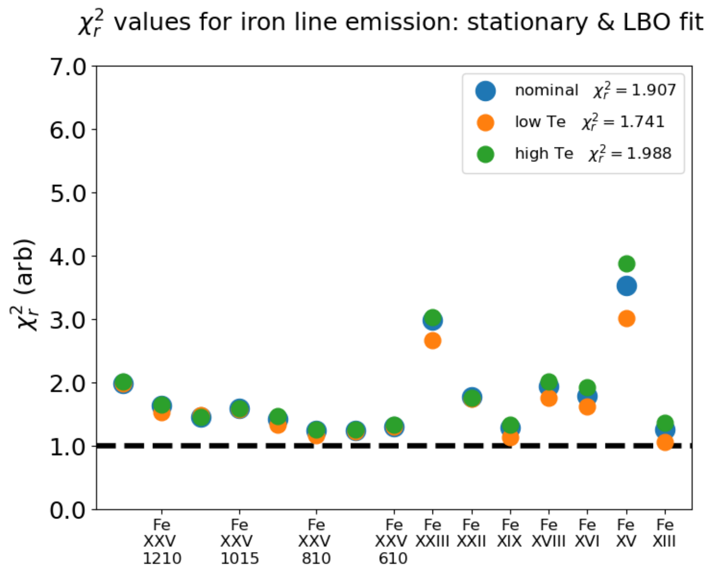

Figure 5.38: The reduced least squares values for each signal in the T_e variation inferences shown in figure 5.37b.

to the characterization of the anomalous diffusion profile. Figure 5.39 shows that the signal with the greatest relative reduction in $\mathcal{X}_R^2$ has large effects from multiple LBO injections that are only modeled with a single injection. Therefore the improved signal matching cannot be attributable to a more accurate inference of the anomalous diffusion profile especially considering the inaccurate description of the LBO injection. Without multiple sightlines for the lower iron chargestates, the radial localization of the line emission will not be sufficient in order to avoid errors from T_e profile inaccuracies. In conclusion the low T_e scenario led to both a delay in the LBO injection time and an inward shift of the iron line emission's radial distributions, which unfortunately contributed to the overall uncertainty in the inferred anomalous diffusion profile.

The T_e variational study performed with experimental data reaffirmed the results found in the synthetic sensitivity testing described in section 4.2.6. Namely it demonstrated that the inaccuracies in T_e profile especially those localized in the edge region could adversely affect the anomalous diffusion profile's inference by the indirect coupling with the LBO injection time. In order to minimize the potential inconsistencies and edge effects for the off-axis ECRH scans presented in chapter 6, the electron temperature from the plasma edge to the LCFS was

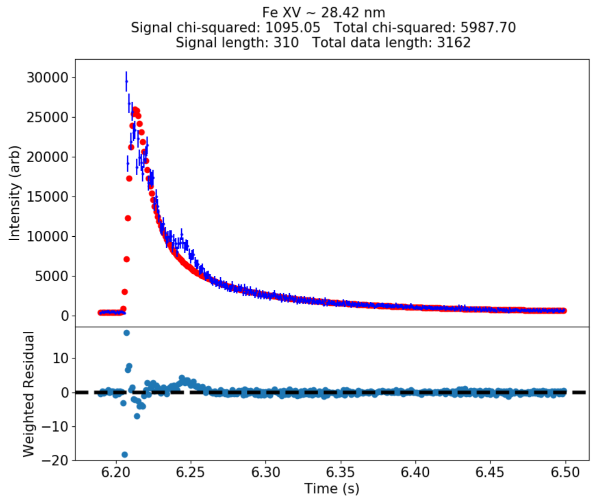

(a)

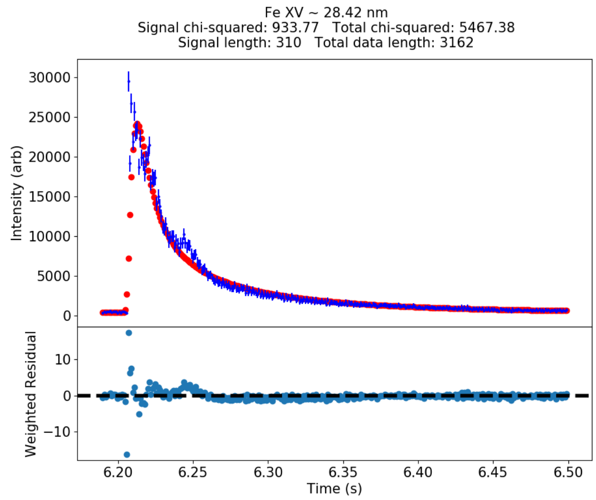

(b)

Figure 5.39: The modeled & measured signals for Fe^{+14} are shown for the nominal and low T_e scenarios in (a) and (b) respectively. These modeled signals are the results from the inferences shown in figure 5.37b.

equalized within an off-axis dataset. Specifically the electron temperature profile for the on-axis scenario was used as a basis to shift the other scenarios to the same T_e at the LCFS before equalizing the T_e outside of $\rho > 1.0$. The electron temperature profiles for the three LBO injections that constitute the 3.5 MW ECRH on- to off-axis dataset are shown in figure 5.40. In this way each total input ECRH power's on- to off-axis scan will have consistent SOL electron temperatures.[w] As discussed in the edge parameterization sections, 3.2.2 & 5.1.5, the electron and ion temperature profiles in the SOL define the characteristic loss time, $\tau_{\parallel,edge}$, as seen in equation (3.2). It is this characteristic loss time that couples together with the edge anomalous diffusion value to determine the iron radial flux in the SOL as demonstrated in equation (3.3). Therefore by establishing a consistent edge electron temperature for each ECRH power level, the core profile effects from the on- to off-axis scan can be better isolated from any SOL mismatching.

Ion temperature profile shift

[w]As detailed in section 5.2.3 each total input ECRH power's on- to off-axis scan will also have consistent SOL ion temperatures. The ECRH is still, even in the off-axis scenarios, still expected to be well within $\rho < 0.5$ meaning that the experiments performed at similar consistent electron densities are not expected to have variations in their SOL temperature profiles.

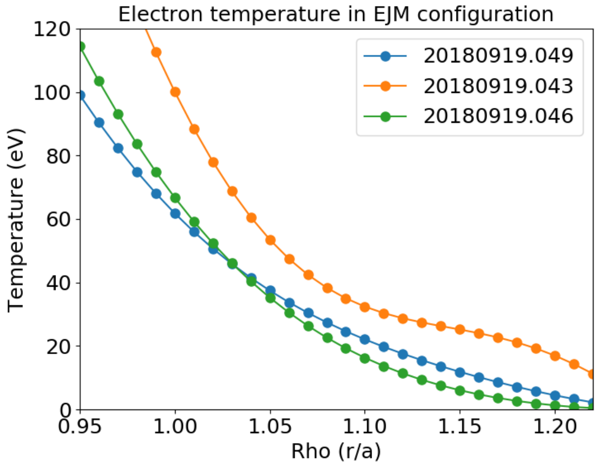

(a)

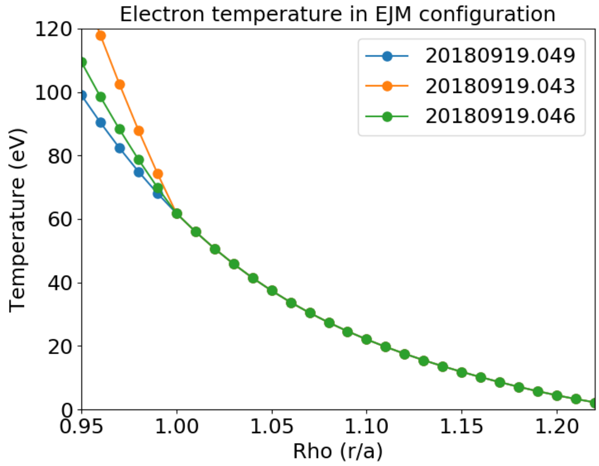

(b)

Figure 5.40: The electron temperature profiles for the 3.5 MW on- to off-axis ECRH scan are shown with the original gaussian process fit to the thomson data shown in (a), while the shifted and equalized T_e profiles shown in (b). The T_e profiles are all equalized from $\rho = 1.0$ to 1.22 with the on-axis case, 20180919.049, used as the standard.

- The ion temperature derived from the XICS measurement is seemingly overestimated in every discharge due to the returned T_i values being ~ 150 eV higher than T_e from $\rho \approx 0.6$ to 1.0. To correct this systematic error the anomalously high T_i was shifted downward by the largest difference between T_i & T_e and then equalized to the T_e values from the largest discrepancy radial location to the plasma edge.

- The ion temperature's variation across an ECRH on- to off-axis scan is minimal meaning the inaccurate characterization in the SOL plasma should have the largest impact on the inferred diffusion's uncertainties. Fortunately the SOL temperatures have all been equalized improving the cross comparisons for each off-axis ECRH scan.

As discussed in section 2.1 the ion temperature profiles were derived solely from the XICS diagnostic since these impurity transport experiments were performed without neutral beam injection needed for a charge-exchange measurement. However as detailed in [Pablant et al. 62] the ion temperature profiles derived from the XICS diagnostic are inexplicably higher than those from the charge-exchange diagnostic by ~ 200 eV. Moreover the XICS diagnostic does not have sightlines outside of $\rho \approx 0.82$ meaning that the estimated ion temperature profiles in the edge are based on forcing a smooth T_i profile to the last closed flux surface where it

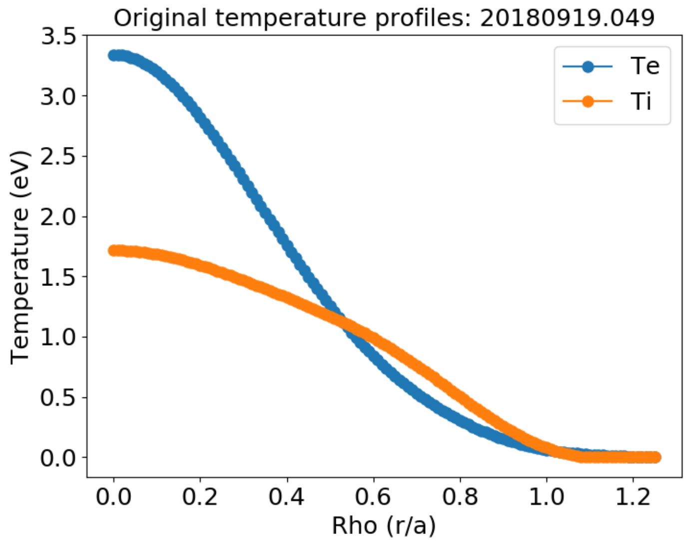

Figure 5.41: The electron and ion temperature profiles for the 3rd LBO injection in plasma discharge 20180919.049 corresponding to the 3.5 MW on-axis ECRH scenario. These are the electron and ion temperature profiles used in chapter 4 for the synthetic data testing.

is required to be 0 eV. Even with the careful corrections done in [Pablant et al. 62], the ion temperature profiles still returned values much higher than even the corresponding electron temperature profile in the outermost portion of the plasma. In fact figure 5.41, shows the comparison between the unshifted ion temperature and electron temperature profiles for the 3.5 MW on-axis ECRH scenario. As a reminder it was this scenario that was used as the basis for both the synthetic sensitivity testing performed in chapter 4 and for the variational confirmation testing performed in this chapter. However the ion temperature profile used in the synthetic chapter, 4, is the original one shown in figure 5.41, while figure 5.42 shows the shifted ion temperature profile used for all of the variational studies in this chapter.

As clearly evident in figure 5.41 the ion temperature shows anomalously higher values than T_e from $\rho \approx 0.6$ to 1.0, an unexpected result for a purely ECRH plasma. This phenomenon of an anomalously higher ion temperature in the range from $\rho \approx 0.6$ to 1.0 was robust for all of the impurity transport discharges used in this work. Therefore to rectify this anomalously high T_i, the entire ion temperature profile was shifted down by the amount that corresponded to the largest discrepancy between T_i and T_e. Then from the radial location where this discrepancy occurred all the way to the plasma edge the ion temperature was set equal to the electron temperature. For example the on-axis scenario shown in figure 5.41 has its largest T_i and T_e

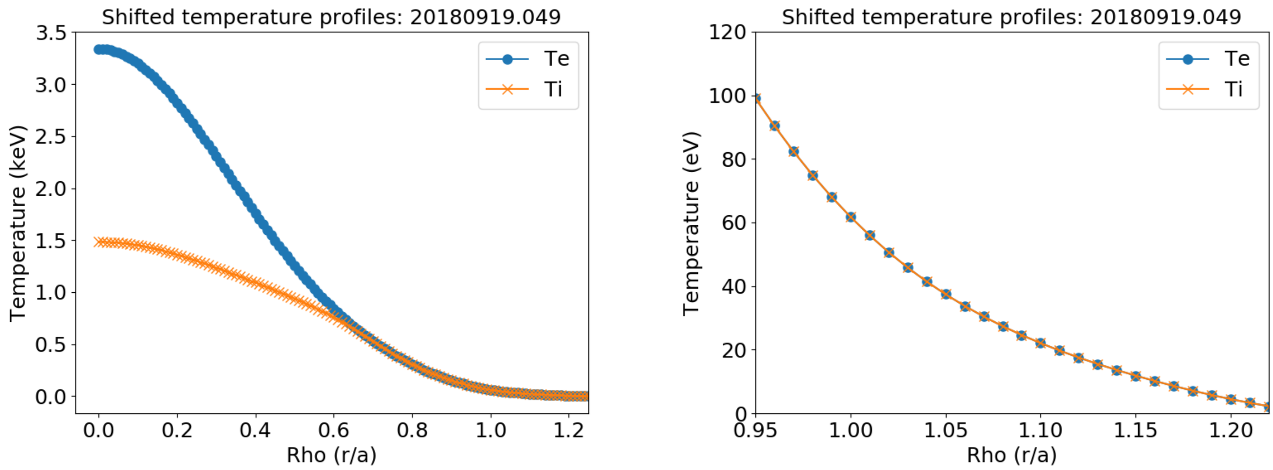

(a) (b)

Figure 5.42: The shifted ion temperature profile used in this chapter's variational testing with experimental data is shown in both (a) and (b). The electron temperature profile is included to demonstrate the equalization of T_i to T_e from $\rho \sim 0.7$ to 1.22.

discrepancy occurring at $\rho = 0.71$ with difference of 230 eV. Figure 5.42 shows the results of the 230 eV downward shift of the entire ion temperature profile and the T_i to T_e equalization from $\rho = 0.71$ to 1.22.

Although figure 5.43 demonstrates the ion temperature profile's stiffness over an on- to off-axis ECRH scan, an accurate characterization within the STRAHL model is still vital for reducing the uncertainty in the inferred diffusion profile. The ion temperature profile's downward shift and equalization to T_e outside of $\rho \approx 0.6$ were both performed to improve this model characterization. In particular the equalization of T_i to T_e in the SOL should have a greater influence on the introduced uncertainty to the inferred anomalous diffusion profile. As mentioned in section 5.2.3 the ion temperature plays a critical role in determining the iron radial flux in the SOL via the characteristic loss time as shown in equations (3.2) and (3.3). In fact if equation (3.2) is closely examined the ion temperature is more heavily weighted than the electron temperature in the SOL region, which underlines the importance of setting the SOL T_i values to be consistent across each power level in an off-axis ECRH scan.

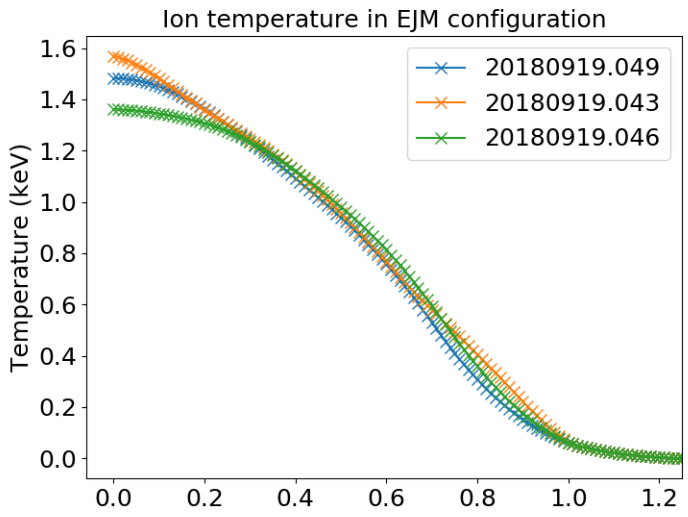

Figure 5.43: The shifted and equalized ion temperature profiles for the 3.5 MW on- to off-axis ECRH scan.

5.3 Conclusion

Performing additional sensitivity studies with experimental line emission signals not only helped reaffirm many of the conclusions from the synthetic studies presented in chapter 4, but also uncovered aspects of the fitting not previously known. Both of these results are important for yielding context on the uncertainty levels of inferred anomalous diffusion profile and whether the solution is unique. To that end the variational studies on the experimental signals resulted in three main conclusions:

- The synthetic sensitivity tests used to determine the accuracy of the least squares fits and to estimate the uncertainty in the anomalous diffusion profile were corroborated with the variational tests performed on experimental data. The most significant corroborated results were the sensitivity of the diffusion profile to the LBO injection timing & temporal shape and the importance of the edge parameterization to the inferred diffusion profile.
- Following the procedural method developed in the synthetic sensitivity chapter can still lead to artificially steep, i.e. nonphysical, anomalous diffusion gradients in the outer half of the plasma from lack of radial localization of line emission.

- Regardless of the method used to estimate the UV signal uncertainties, the inferred anomalous diffusion profiles still converged to the same approximate solution.

Corroborating the synthetic data sensitivity conclusions with the experimental variational testing was important for giving confidence that inferred solutions were consistent and for confirming the significance of specific model parameters. The first corroborated result is that the LBO injection timing and temporal shape have major impacts on the inferred shape of the anomalous diffusion profile. Luckily it was verified that the LBO injection timing could be included as a free parameter in the least squares fit and return consistent results within the ± 3.5 injection window. Unfortunately multiple injections are clearly visible on the decay phase of all Fe^{+18} and lower's line emission. The utilization of a simple 2 ms trapezoidal shape for a clear multiple LBO injection can lead to inaccuracies of $\sim 0.3\ \frac{m^2}{s}$ in the inferred anomalous diffusion profile localized predominantly in the outer half of the plasma. The reason for such sensitivity stems from the compounding of two facts: the line emission signals for these lower chargestates are typically $\leq$ 100 ms and each of these lower chargestates only have a single sightline yielding no spatial localization.

The second, main corroborated result from the real data sensitivity testing was the critical importance of the edge parameterization within the STRAHL model. Specifically, reasonable variance in the SOL temperature can lead to large changes in the inferred diffusion profile. The reduction of the SOL T_e caused greater neutral iron penetration and a delay in the LBO injection timing leading to core peaking in the inferred diffusion. Also the equalization of T_i to T_e in the SOL plasma changes the iron flux rate in this region causing a timing change to the LBO injection or a difference in the inferred D_{edge} or both. This might not seem very surprising or significant, however when taken in context that a $\pm$ 100 m variation in $L_{C,divertor}$ can lead to core plasma variances for the inferred anomalous diffusion profile of $\sim 0.15\ \frac{m^2}{s}$ then is easy to understand the edge parameterization's importance. Overall the edge parameterization importance stems from the lack of direct impact on the signal matching in this region, i.e. reduction to the $\mathcal{X}_R^2$ value, and the possible indirect coupling between the LBO injection timing & the other edge parameters (e.g. D_{edge}, $L_{C,divertor}$, etc.)

The next main result from the sensitivity studies performed using real experimental signals was the systematic uncertainty introduced by varying the procedural method. This systematic uncertainty associated with the procedural method primarily originated from using the radial position of the two interior spline-knots as free parameters within the fit. Specifically the least squares routine could place nonphysical gradients in the diffusion profile to improve the signal matching of the line emission from $\rho = 0.5$ to 1.0. These nonphysical gradients were evident throughout all of the chapter's sensitivity testing whenever the two interior spline-knots were allowed to radially move within the fit. This result critically showed the importance of performing fits without including the radial position of the spline-knots and the importance of multiple sightlines to spatially resolve the line emission.

The final conclusion from the sensitivity studies using experimental data was that regardless of the estimation method for the UV signals' uncertainty levels the inferred anomalous diffusion profile was consistent. This indicates that the estimation method is not critical for finding the same minimum in parameter space and that the added uncertainty to the anomalous diffusion profile should be small (i.e. $< 0.1 \ \frac{m^2}{s}$ see section 5.2.2). The relative insensitivity to the estimation method stems from the fact that the UV lines are all single, central sightlines for one chargestate meaning there is a lack of spatial localization to the emission. The least squares routine has the freedom to alter the diffusion profile to match the line-integrated signals since the radial profiles of the line emission distributions tend to be large (e.g. see figure 5.20). Moreover within the least square routine there is a free parameter for each sightline that scales the line-integrated model signal yielding even more freedom to the routine to slightly change the absolute emission patterns through these scalefactors. Although this result demonstrates the inferred diffusion profile's invariance to the estimation method, it does not mean that the signal uncertainties for the UV lines are unimportant. Having sightlines with much higher signal-to-noise-ratios can cause overfitting, e.g. figure 5.39, that hurts the accuracy of the inference. Therefore in conclusion the estimation of the single sightline line emission is not super critical for the consistent inference of the anomalous diffusion profile, however signal uncertainties should not be underestimated to cause inaccurate overfitting.

Chapter 6

Iron impurity transport with on- and off-axis heating in W7-X

This chapter discusses the off-axis variation of ECRH heating on impurity iron transport in W7-X. The impurity iron transport studies for the datasets discussed were performed in parts of the discharge where the plasma was only heated by ECRH. All of the time windows for the iron LBO injections were chosen with comparable line-integrated density ($\sim 6 \times 10^{19}\ m^{-3}$) and total input ECRH power. Three total input ECRH power levels (2.8, 3.5, and 4.9 MW), with on- to off-axis variation were measured in the standard magnetic configuration (EJM) in W7-X. In the following sections each total input power dataset's main observational results are presented along with the corresponding least squares inferences of the anomalous diffusion profile for each on- and off-axis ECRH variation.

6.1 Iron impurity transport with constant ECRH power in W7-X standard configuration

For adequate comparison the iron LBO injections examined in this thesis were limited to plasmas of similar density, $\overline{n_e} \approx 6 \times 10^{19}\ m^{-2}$, and at similar total ECRH input power levels, $\sim$ 2.8, 3.5, and 4.9 MW. For each total input ECRH power level, three different off-axis heating scenarios were attempted with the 3.5 MW and 4.9 MW being completely successful.[a] After confirming the LBO injections occurred in stationary and roughly equivalent electron density discharges, the first step in the analysis was to examine the global transport times across the datasets.[b] Therefore the global transport times were estimated for each of these iron LBO injections by fitting the decay of the $\sim$ 13.28 nm spectral line from Fe^{+22}. Figure 6.1 displays the

[a]The 2.8 MW dataset doesn't have a middle off-axis LBO injection for comparison.

[b]Where specifically the global transport time is the characteristic time fit from the exponential decay of the line emission.

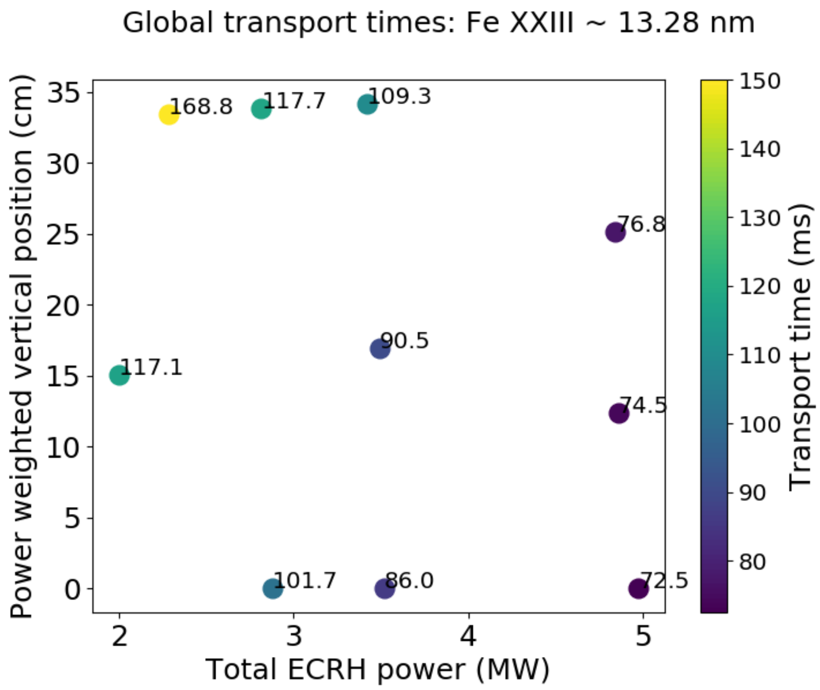

Figure 6.1: The global transport times over the entire ECRH radial deposition position scans at a constant $\overline{n}_e \approx 6 \times 10^{19}\ m^{-2}$ in the W7-X standard magnetic configuration.

global transport time fits on a plot of the total input ECRH power versus the power-weighted average vertical position of the ECRH deposition. Therefore with zero ECRH deposited off-axis the bottom y-axis points in figure 6.1 correspond to fully on-axis ECRH depositions, while the corresponding top points correspond to the most off-axis ECRH deposition. Moreover the vertical groupings of total ECRH power are clearly identifiable into four main constant powers namely $\sim$2.3, 2.8, 3.5, and 4.9 MW.For the 2.8, 3.5, and 4.9 MW scenarios a successful on- to off-axis ECRH deposition scan was completed and in fact the 3.5 and 4.9 MW scenarios included three different positions. As shown in figure 6.1, there was another on- to off-axis ECRH scan at $\sim$ 2.3 MW however this dataset had experimental issues.The first issue was the reproducibility of the ECRH power level where each deposition position was performed at slightly different total ECRH power levels: 2.4, 1.98 ,and 2.28 MW for on- to most off-axis respectively. The second issue was that the on-axis scenario had an LBO injection that was delayed enough to have the preprogrammed input ECRH power ramp up during the iron line emission's decay, which is the reason the global transport estimate was not included in figure

6.1.[c] Although the 2.3 MW dataset can't be included within the STRAHL analysis, the middle and most off-axis scenarios can be included in the global transport time estimates since these scenarios still met the $\overline{n_e} \approx 6 \times 10^{19}\ m^{-2}$ and constant profile requirements. Returning to figure 6.1 there are two main distinguishable effects: the more input ECRH power the shorter the global transport time and the more ECRH power is placed off-axis the longer the iron transport time. The observed global transport time differences suggest that the least squares minimization could potentially reveal radial changes in the inferred anomalous diffusion profiles that led to the observed transport variations.

In order to present the iron LBO injection dataset most effectively this section has been divided into three subsections discussing the 2.8, 3.5, and 4.9 MW ECRH input power levels. However the sections are presented not in ascending total power level, but will first focus on the two power levels at 3.5 and 4.9 MW before diving into the 2.8 MW power level. Specifically the first subsection will have the most detailed analysis focusing on the 3.5 MW dataset because it has three ECRH deposition positions, it has a measurable off-axis trend in global transport time (i.e. $\sim 27\%$ increase), and the on-axis scenario was used as a basis for all the variational uncertainty analysis performed in chapters 4 & 5.Following the presentation of the 3.5 MW analysis, the 4.9 MW dataset will be discussed due to its three ECRH deposition positions and more importantly the weak off-axis trend observed in the global transport time. The 4.9 MW dataset is particularly interesting from a global transport perspective since it is the only power level that always includes ECRH power deposited on-axis for all three deposition scenarios. Finally the 2.8 dataset analysis will be presented, providing important consistency and corroboration checks for the entire on- to off-axis dataset.

[c] There was a third issue with this 2.3 MW dataset, namely that the thomson scattering diagnostic had one of its lasers fail during the most off-axis scenario leaving this LBO injection without electron temperature and density profiles.

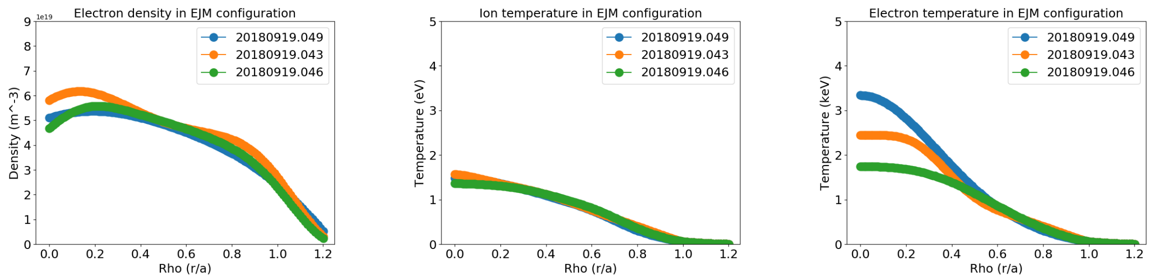

(a) (b) (c)

Figure 6.2: The electron density, ion temperature, and the electron temperature radial profiles are plotted in (a), (b), and (c) respectively for the 3.5 MW input ECRH on- to off-axis scan. Plasma discharge 20180919.049 in blue is completely on-axis exemplified by the peaked electron temperature, while discharge 20180919.046 in green is the most off-axis case with the broader electron temperature profile.

6.1.1 3.5 MW on- to off-axis ECRH scan

Global transport time estimation

- The experimentally derived global iron impurity transport time, τ_I, was determined to increase from $\sim$ 86 to 109 ms as the ECRH was moved from purely on-axis to a completely off-axis deposition position, $\rho \approx 0.4$.

The first step in understanding these off-axis ECRH scans is to examine the measured kinetic profiles during the LBO injection. In figure 6.2 the fit electron density, ion temperature, and electron temperature profiles are shown for the three different ECRH deposition cases all with total ECRH power equal to 3.5 MW: completely on-axis (20180919.049), some off-axis (20180919.043), and most off-axis (20180919.046). Although there are slight differences in the electron density, the major and clear difference is the electron temperature peaking in the plasma core, i.e. $\rho \leq 0.4$, observed for the on-axis scenario. This peaking in the electron temperature can be explained by the change in the deposition position of the gyrotrons as seen in figure 6.3 where the most off-axis case has all of the 3.5 MW deposited at $\rho \approx 0.4$.[d] Next the global impurity transport time, τ_I, can be determined by fitting the exponential decay of the line emission for each heating scenario as a first check on how the global iron transport time changes under a peaked versus broad temperature profiles. To accurately estimate the

[d]The ECRH deposition position is in the W7-X bean plane meaning that $\rho \approx 0.4$ corresponds to a real space deposition position of $\sim$ 35 cm above magnetic axis.

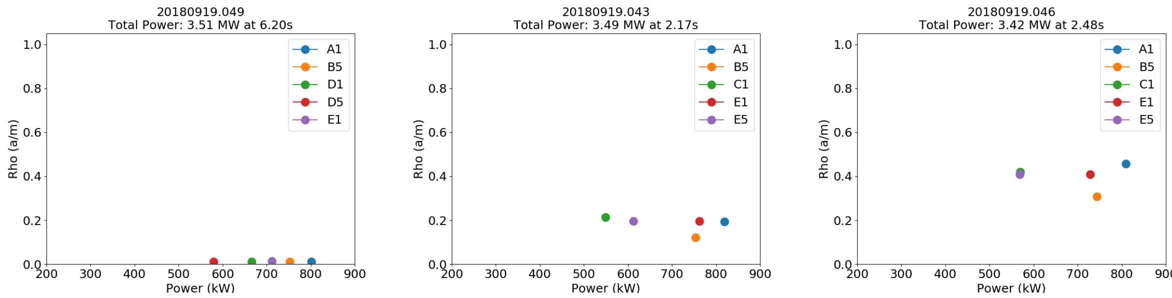

(a) (b) (c)

Figure 6.3: For 3.5 MW iron impurity transport dataset, each gyrotron's normalized radial position of ECRH deposition versus input power is plotted at the time of iron LBO injection with on-axis shown in (a), some off-axis in (b), and most off-axis in (c)

global iron transport time, the total iron impurity density radial profile shape needs to be rigid, which is to say that the entire profile should decay at the same rate. Practically this means a time delay is necessary for the iron density profile to evolve into its rigid shape before the exponential decay can be estimated. To accomplish this estimation, the Fe^{+22}'s 13.28 nm spectral line measured on HEXOS was chosen. This spectral line corresponds to the second highest chargestate measured for the iron spectra and had a very high signal-to-noise ratio. Not only does this mean Fe^{+22} is quite abundant in the core plasma, but also that the observed signal decay should be long compared to the background levels, making accurate transport time estimations feasible. In fact to accomplish an accurate estimation of the transport time, the $\sim$ 250 ms window used to fit the 13.28 nm line's exponential decay was selected to start $\sim$ 65 ms after the signal's maximum. Moreover to increase the accuracy of the exponential decay, a linear background was determined using the data $\sim$ 150 ms before and after the LBO signal to estimate the non-LBO background levels as shown in figure 6.4 . The linear background was then included as fixed values within the fit for the global transport time during the signal's exponential decay phase. This means that any differences observed from the exponential decay as the ECRH power is varied off-axis should be evident in the measured signal and indicate whether the average iron impurity transport has changed. The global iron impurity transport time for each of the three ECRH deposition positions is shown in figure 6.5 going from all on-axis to most off-axis from figure 6.5a to 6.5c. Examining each deposition position's global impurity transport time, there is an increase from $\tau_I \approx 86$ ms to 109 ms as the power is moved

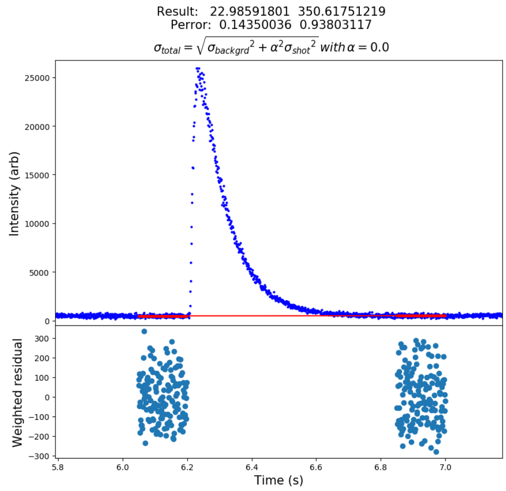

Figure 6.4: The linear background fit on Fe^{+22}'s 13.28 nm spectral line for the 3.5 MW scenario's most on-axis case. This linear background, determined from $\sim$ 150 ms before and after the LBO signal, is included in the global transport time estimate as fixed values within the fit.

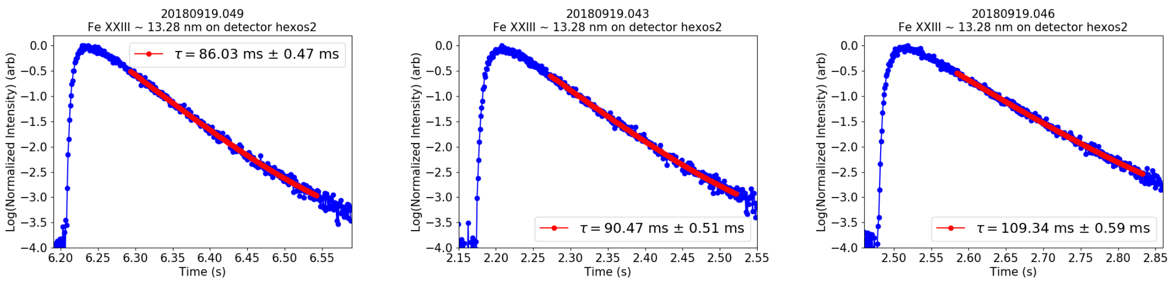

(a) (b) (c)

Figure 6.5: The HEXOS measured line emission for Fe^{+22} is shown versus time for each ECRH deposition position. The global transport time is determined by an exponential fit to the line intensity starting $\sim$ 65 ms after the maximum to ensure that the shape of the iron density profile is rigid

from on- to off-axis respectively. This $\sim 27\%$ increase is consistent with previous iron impurity transport experiments performed with helium as the main working gas in OP1.2a.[58]

Restricting the inference to only the neoclassical & classical channels

- The calculated neoclassical convection velocity showed minimal variation across the on- to off-axis ECRH scan. This was true for both when the radial electric field was self-consistently calculated using DKES (showing near identical E_r) and when the XICS measured radial electric field (demonstrating a clear change from a core electron-root to a weak ion-root confinement as the ECRH was moved from on- to off-axis) was used within DKES.

- As expected, using only the neoclassical & classical transport channels within the least squares minimization cannot reproduce the observed line emission signals, i.e. $\mathcal{X}_R^2 \approx 80$ was the best fit.

As discussed in section 1.3, the radial electric field plays an important role for impurity transport by primarily influencing the neoclassical convection channel. To better understand the role of the radial electric field in this 3.5 MW off-axis ECRH scan, the reader is encouraged to return to section 5.1.4 for an in depth discussion. In particular figure 5.12 and combined in figure 6.6 show the measured radial electric fields from the XICS diagnostic and the corresponding DKES calculated radial electric fields based on the kinetic profiles shown in figure 6.2. The important element from figure 6.6 is that while the XICS measured radial electric fields show a clear difference between the on-axis & off-axis cases, the DKES calculated radial electric fields do not. The XICS measured radial electric fields demonstrate a small radial electric field from $\rho \leq$0.5 inward for the off-axis cases, while a strong positive electric field for the on-axis case. This along with the strong electron temperature peaking in the on-axis case indicates that this dataset is a scan from a core electron-root to a weakly ion-root confinement as ECRH is moved off-axis. SFINCs runs were performed for this 3.5 MW dataset (as detailed in [Pablant et al. 6]) confirming the general trend of a core electron-root to a weakly ion-root confinement regime as the ECRH deposition was placed further off-axis. Therefore although

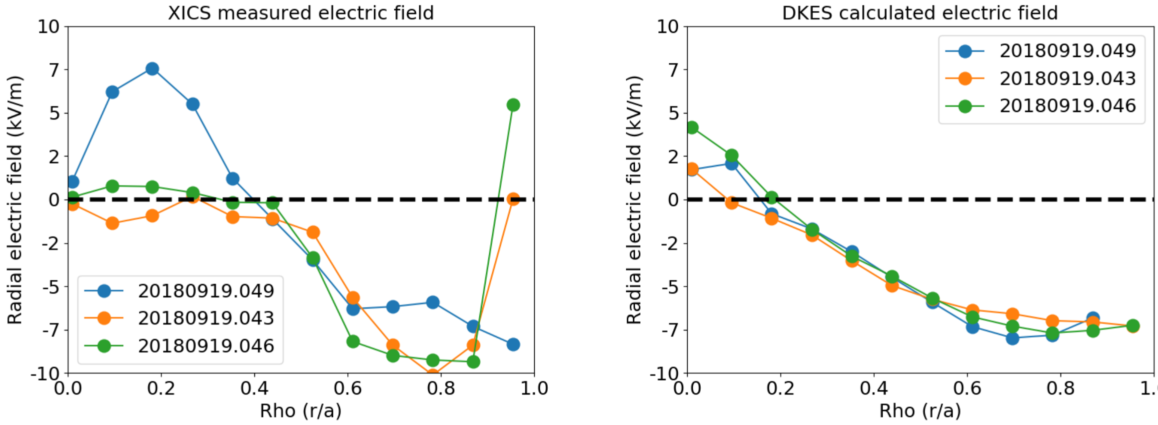

(a) (b)

Figure 6.6: A comparison of the 3.5 MW off-axis ECRH scan dataset's XICS measured radial electric fields in (a) and the DKES calculated radial electric fields in (b)

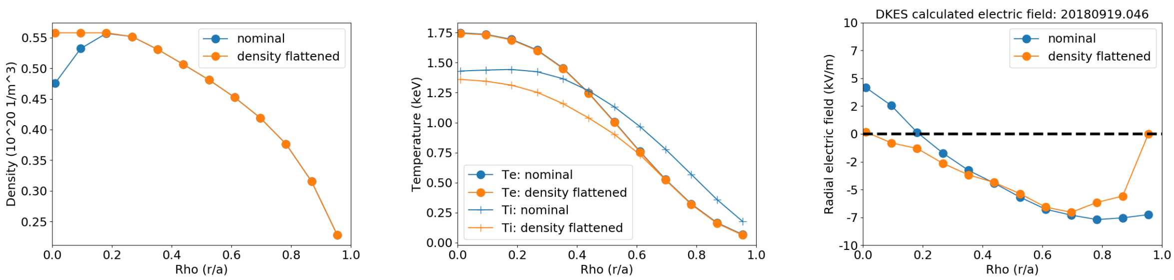

(a) (b) (c)

Figure 6.7: A comparison of the 3.5 MW off-axis ECRH scenario with a hollow versus flat density profile shown in (a) with the electron & ion temperature shown in (b) revealing the core impact to the radial electric field calculated from DKES in (c). The ion temperature downshift is discussed in 5.2.3 and the reason why the E_r is different in the edge for the modified case.

there is qualitative agreement between the XICS and DKES radial electric field values as discussed in detail in 5.1.4, the lack of an on- to off-axis variation in the DKES calculated E_r is troublesome. The main reason for this discrepancy is the slightly hollow density profiles shown in figure 6.2a causing the scenarios to have a more positive core radial electric field. Both the off-axis scenarios have more pronounced hollow profiles than the on-axis case causing a larger impact to the radial electric field calculated from DKES, as shown for the most off-axis scenario in figure 6.7 when the hollow profile is altered to be flat.[e] Thus a relatively small change in the core density for the off-axis scenarios recovers the qualitative agreement with the XICS

[e]Some of the observed change in the outer portion, i.e. $\rho \geq 0.5$ stem from ion temperature profile shifts performed, see section 5.2.3 for more details.

measured radial electric field's trend from electron-root to weakly ion-root as ECRH is moved off-axis. Although this flattening of the core density profile changes the DKES calculated radial electric field, the corresponding DKES convection velocities are not substantially different (not shown).

Returning again to section 5.1.4 and specifically figure 5.13, the neoclassical & classical convection velocity profiles are plotted using the DKES and the XICS derived radial electric fields for each ECRH position. Unsurprisingly the iron chargestates' convection velocities calculated from the DKES derived radial electric fields are virtually identical for the three ECRH deposition positions. Somewhat surprisingly the XICS derived radial electric fields yield very similar convection velocity profiles across the ECRH variation and show minimal difference with the DKES derived convection velocities.Therefore the lack of change in the calculated convection velocities from the core density flattening is consistent with the already demonstrated small difference between using the XICS measured versus DKES derived radial electric field to calculate the convection velocity as seen in figure 5.13. This means that no matter which radial electric field is used within DKES the total convection velocities for the iron chargestates show minor variations across a change from electron-root to weakly ion-root confinement. Combined with the calculated total diffusion coefficients, see figure 6.8, not only do the neoclassical & classical transport coefficients have low absolute values stemming from the W7-X optimization, but also show very little variation across the ECRH deposition position despite the strong T_e peaking and positive radial electric field shown for the on-axis scenario. This lack of variation combined with a significant global transport time shift is the first indication that solely using the neoclassical & classical transport channels probably won't explain the differences in the observed iron impurity transport.

Finally with the comparison of the neoclassical & classical transport profiles across the on- to off-axis scan finished, these transport profiles can be used within STRAHL to check how well the measured iron line emission can be matched without any added anomalous transport. In fact if these neoclassical & classical transport profiles are solely used within a STRAHL least squares minimization, the iron spectral lines' time traces can in no way be matched using

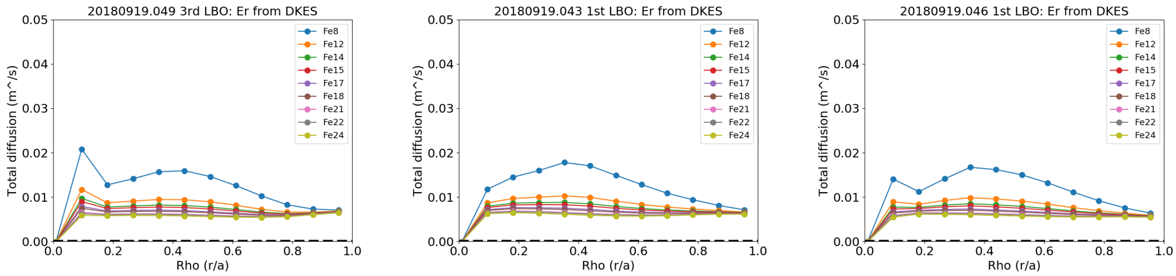

(a) (b) (c)

Figure 6.8: The sum of the neoclassical and classical diffusion coefficients for the various iron chargestates used in the inference are shown for the on-axis (a), some off-axis (b), and most off-axis (c) cases. These diffusion coefficients were calculated using the radial electric field from DKES (see figure 6.6b)

the least squares routine. Figure F.1 shows the inadequacy of solely using classical & neoclassical transport parameters for reproducing the iron spectral lines for the 3.5 MW on-axis case. With a $\mathcal{X}_R^2 \approx 80$ and very obvious structures in the weighted residuals, a need for additional transport channels to match the data is transparent. Not only does the poor matching to the experimental data indicate that the observed iron transport cannot be explained solely from classical & neoclassical transport, but also that the total transport is underestimated as demonstrated by the long/slow evolution of the STRAHL modeled signals when only using the classical & neoclassical transport.

Including the anomalous transport channels within the inference

- The inclusion of the anomalous diffusion transport channel was necessary to reproduce the experimental signals with high fidelity, e.g. $\mathcal{X}_R^2 \leq 2.0$. In fact when using only the anomalous convective velocity in conjunction with the neoclassical & classical transport channels the best signal matching was still quite poor, i.e. $\mathcal{X}_R^2 \approx 37$. This clearly demonstrates that the iron impurity transport is dominated by anomalous diffusive flux.

- As discussed in section 5.1.5 variations in edge parameterization can propagate uncertainties in the inferred anomalous diffusion profile well inside the plasma LCFS. This propagation can occur because the least squares routine has the freedom to adequately match the single sightlines per iron chargestate localized predominantly in the outer half of the plasma.

Testing the relative importance between the anomalous diffusive and convective channels in matching the observed signals can be easily done by including only one transport channel as fit parameters within the inference. To first perform this sensitivity comparison, the anomalous diffusion profile is zeroed out meaning only the anomalous convection velocity profile will be used in conjunction with the neoclassical & classical transport channels. If an anomalous convective velocity profile is specified with free parameters as described in section 5.2.1 for the STRAHL inference, the signals once again cannot be adequately matched. In fact performing a second fit with the inclusion of the LBO injection timing and radially moving interior spline-knots for the anomalous convective velocity profile as free parameters still can't reproduce the observed signals as seen in figure F.2. Although the reduced least squares value, $\mathcal{X}_R^2 \approx 45$, has improved by a factor of two compared to only using the classical & neoclassical transport channels, the fit is still categorically poor. In fact neither the fast rise times in the lower chargestates' line emission (e.g. see figures F.2e & F.2d) nor the fast signal decay in the highest iron chargestate (e.g. see figure F.2a) could be simultaneously matched. The inherent directionality of the convection channel limits its ability to match the iron line emission signals. For example, the fast rise times could in theory be explained by very strong inward directed convection velocity, but would then lead to much longer than observed transport times (e.g. see figure F.2a with near infinite transport time). This indicates that the lone addition of anomalous convection to the classical & neoclassical transport channels is insufficient to accurately match the iron impurity transport observed during these experiments.

However when anomalous diffusion is included with the classical & neoclassical transport channels in the least squares minimization the observed iron line emissions can be well-matched without any need for an anomalous convection. Figure 6.9 shows the results of an inference performed using the anomalous diffusion profile as the only new additional free parameters within the fit. With a $\mathcal{X}_R^2 \approx 1.9$ and minimal structures in the weighted residuals, the need for including the anomalous diffusion is evident from figure 6.9.

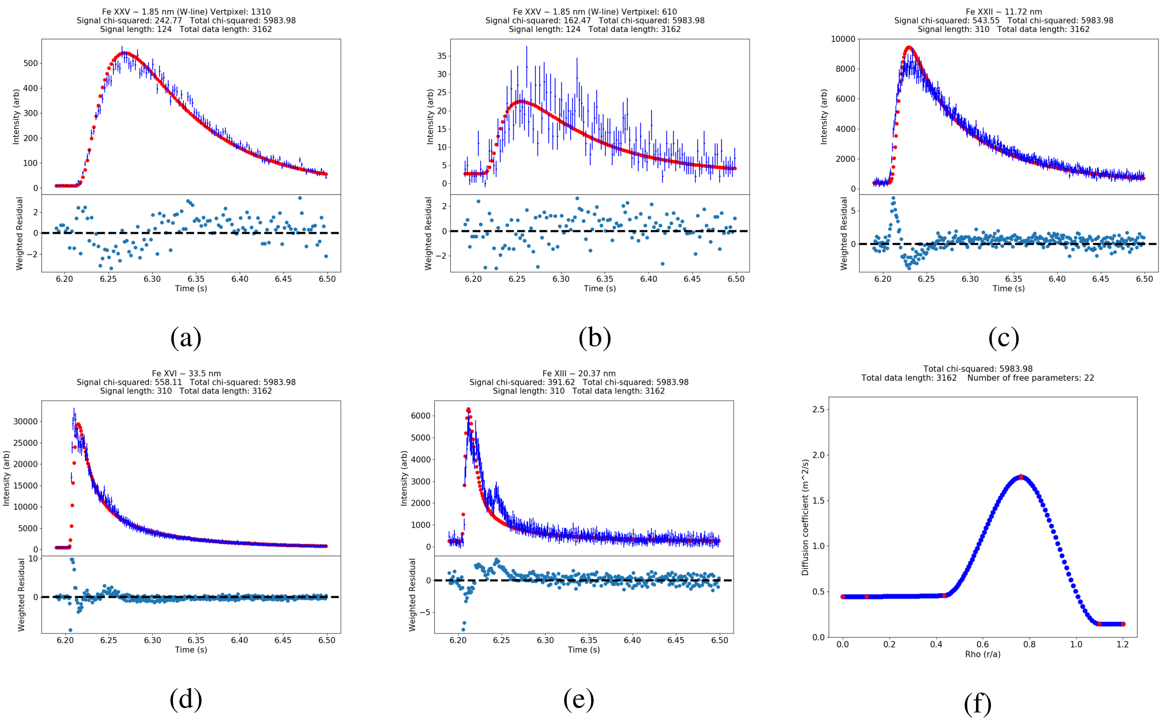

Figure 6.9: The signals from the 3rd LBO in discharge 180919049 are shown in blue with the attempted matching from the STRAHL inference are shown in red with the weighted residuals plotted below. The inference is performed on the scale parameters for the signals and the anomalous diffusion profile, as seen in (f), with the classical & neoclassical transport profiles included. The classical & neoclassical transport profiles are the same as the ones used in figure F.1

The drastic improvement in the quality of the fit by including the anomalous diffusive transport channel cannot be overstated. The incredible improvement to the fit when only adding the anomalous diffusion channel to the neoclassical & classical transport indicates two important conclusions. First, the level of anomalous diffusion necessary to match the iron line emission is at least ~ 50 times higher than the calculated classical and neoclassical diffusive values. Examining the inferred anomalous diffusion profile in figure 6.9f, the smallest values are at least a factor of ~ 50 larger than what is predicted from the classical & neoclassical diffusion from DKES (see figure 6.8a) meaning the observed iron transport is not neoclassical. This expected result is consistent with the previous work performed by [Geiger et al. 7] where inferred levels of anomalous diffusion were ~ 100 times larger than neoclassical values. Second, a density gradient proportional diffusion seems to be by far the most dominant transport channel. In the previous scenario using only the anomalous convection velocity, the unidirectional nature of the convection velocity meant that the fast rise times and faster-than-neoclassical decay could not simultaneously fit. The combination of the fast rise times and the short global transport time confirm that the anomalous transport is dominated by the diffusive channel. Not only is this finding identical to the previous work done by [Geiger et al. 7], but also when the anomalous convection is fit alongside the anomalous diffusion channel the inferred diffusion profile & the $\mathcal{X}_R^2$ are minimally changed (not shown).

Equipped with the understanding that the anomalous diffusive transport is the most critical transport channel in these iron impurity experiments, the inferred anomalous diffusion profiles can be evaluated for the on- to off-axis ECRH dataset. In figure 6.10 the inferred anomalous transport profiles are plotted for the three cases at the 3.5 MW total input power: completely on-axis (20180919.049), some off-axis (20180919.043), and most off-axis (20180919.046). Interestingly the inferred diffusion profiles are of similar magnitude and shape for all three ECRH scenarios even when the two interior spline-knots radial positions are left as free parameters.[f] All three inferences are good matches to the line emission signals, i.e. $\mathcal{X}_R^2 \leq 1.9$ with some

[f] In figure 6.10b, the inferred diffusion profiles' sharp gradients at $\rho \approx 0.6$ for the on- and most off-axis scenarios are most likely nonphysical (see section 5.2.1)

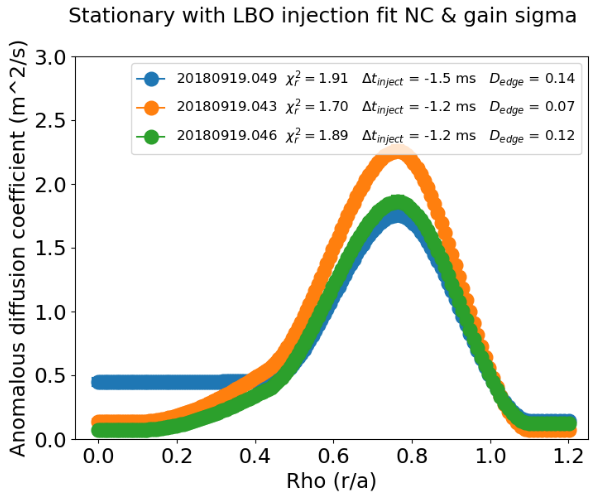

(a)

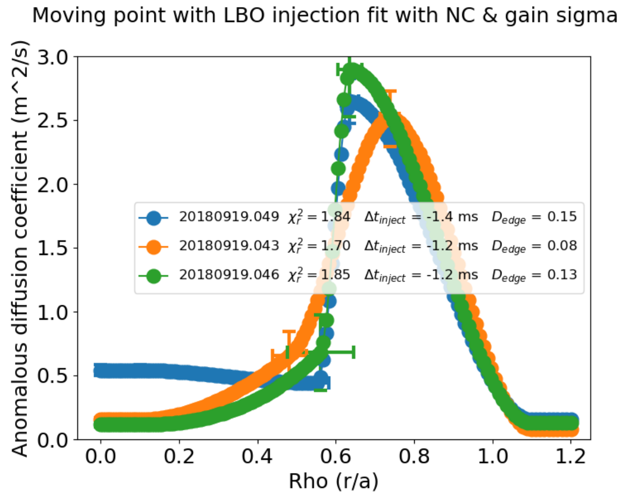

(b)

Figure 6.10: The inferred anomalous diffusion profiles included the LBO injection timing as a free parameter and with the classical & neoclassical transport profiles taken from the DKES calculated profiles in figure 5.13 and 6.8 for the convection velocity and diffusion respectively. The inferences are performed with (a) and without (b) the two interior spline-knots allowed to move radially.

structure in the weighted residuals primarily from injection shape mischaracterization as illustrated in figure 6.9.[g] Although the returned uncertainties for the diffusion spline-knots are very small as seen in figure 6.10, the conclusion that these diffusion profiles are distinguishable from one another is incorrect when the systematic uncertainties, derived from the sensitivity studies performed in chapter 4 and 5, are considered. Even taking into consideration that these diffusion profiles are indistinguishable, the close examination of an individual profile can reveal potential systematic error. For example, the mid off-axis case's inference shown in figure 6.10a could have overfitting errors due to the lack of spatial localization for the line emission in the outer half of the plasma. The delayed LBO injection time, the depressed D_{edge} value, and the increased diffusion gradient across the LCFS are potential signs of overfitting the lower chargestates' line emission. As discussed in the section on edge parameterization, 5.1.5, the single sightline per iron chargestate yields freedom to the least squares routine to drive larger diffusion gradients in the outer half of the plasma as a means to improve the signal matching. This underscores the importance of establishing a consistent edge parameterization within an on- to off-axis dataset in order to better isolate any SOL mismatching from core effects.

[g]See section 5.1.3 for more discussion on the LBO temporal shape's impact

Fixed edge anomalous diffusion for consistent edge parameterization

- Establishing a fixed anomalous diffusion for the edge plasma, i.e. D$_{edge}$ $= 0.15\ \frac{m^2}{s}$ for $\rho \geq 1.1$, allows for consistent comparison among the inferences within an on- to off-axis ECRH dataset. With a constant total ECRH power there should be minimal edge profile variations among an on- to off-axis dataset and importantly reduces the possibility of uncertainties propagating inside the LCFS.

- In order to keep the edge parameterization consistent, the SOL T$_e$ profiles for each on- to off-axis dataset (i.e. all with the same constant total power) were set to the on-axis case as described in section 5.2.3 and the T$_i$ was equalized to T$_e$ in the outer plasma region as described in section 5.2.3.

- The 3.5 MW on- to off-axis dataset has indistinguishable inferred anomalous diffusion profiles when the more realistic uncertainty levels taken from the sensitivity studies from chapter 4 are applied.

As alluded to in the last section, additional least squares inferences were performed with the edge parameterization consistent within each on- to off-axis dataset. These inferences were performed due to two main justifications: One, the SOL plasmas during this on- to off-axis dataset should be nearly identical due to the near constant total ECRH power and the same kinetic profiles (except for T$_e$) Two, the modeled edge parameters can propagate uncertainty into the core as demonstrated by the sensitivity studies in chapter 4 and 5. Specifically keeping the edge parameterization consistent meant the SOL T$_e$ profiles were all set to the on-axis case as described in section 5.2.3, T$_i$ was equalized to T$_e$ as described in section 5.2.3, and finally the anomalous edge diffusion value was fixed at D$_{edge}$ = 0.15 $\frac{m^2}{s}$. The result of performing these inferences are shown in figure 6.11, where the anomalous diffusion profile matching is even better especially outside of mid-radius, $\rho > 0.5$. The close similarities of the inferred anomalous diffusion profiles shown in figure 6.11 should be taken with reservations. Unfortunately from the synthetic and experimental sensitivity testing in chapters 4 and 5 respectively, it is well-established that the spline-knot parameter uncertainties are underestimated as seen in

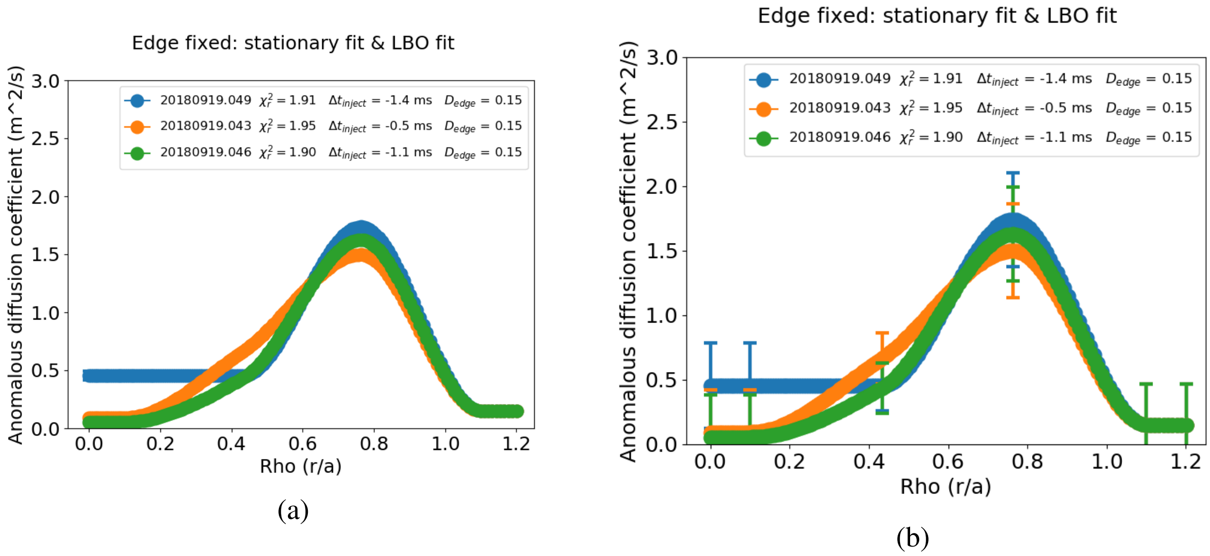

Figure 6.11: The inferred anomalous diffusion profiles included the LBO injection timing as a free parameter and the classical & neoclassical transport profiles taken from the DKES calculated profiles in figure 5.13 and 6.8 for the convection velocity and diffusion respectively. The profiles are exactly the same except plotted with the least squares returned uncertainty in (a) and the total uncertainty from the synthetic sensitivity studies in (b).

figure 6.11. In fact the extra uncertainties on the anomalous diffusion profile either introduced from the potential inaccuracies in input parameters or from systematic errors in modeling are shown in figure 6.11b. Once these systematic uncertainties are considered, the inferred anomalous diffusion profiles in this on- to off-axis ECRH scan cannot be distinguished based on the work presented in this thesis. Therefore even though the results in figure 6.11a seemingly indicate the difference between on- and off-axis ECRH scenarios is predominantly from changes to core diffusive transport, the inclusion of the total synthetically-derived uncertainties in figure 6.11b make that conclusion speculative.

6.1.2 4.9 MW on- to off-axis ECRH scan

Global transport time estimation

- Due to the 4.9 MW ECRH on- to off-axis scan always having two gyrotrons depositing power on-axis, the experimentally derived global iron impurity transport time, τ_I, showed near negligible increase from $\sim$ 73 to 77 ms as the ECRH deposition position was moved from purely on-axis to a mostly off-axis.

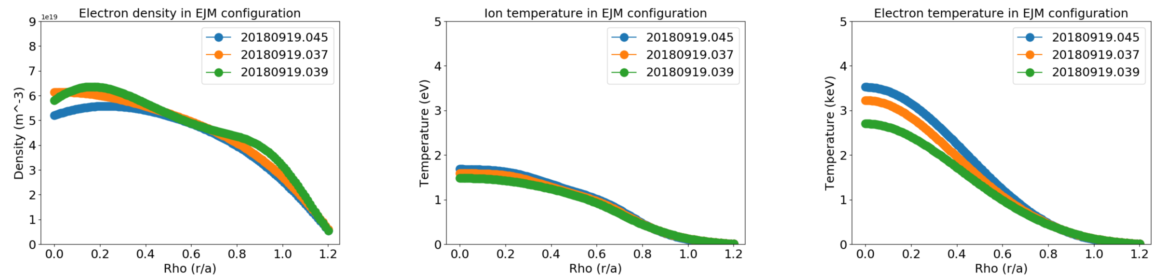

(a) (b) (c)

Figure 6.12: The electron density, ion temperature, and the electron temperature radial profiles are plotted in (a), (b), and (c) respectively for the 4.9 MW input ECRH on- to off-axis scan. Plasma discharge 20180919.045 in blue is completely on-axis, while discharge 20180919.039 in green is the most off-axis scenario.

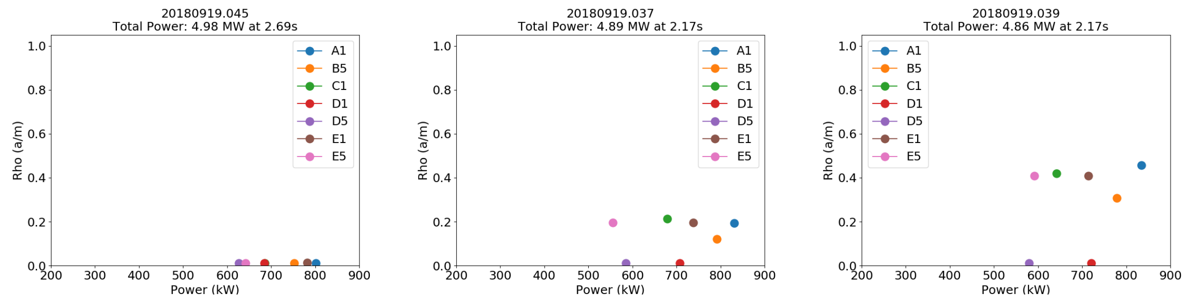

(a) (b) (c)

Figure 6.13: For 4.9 MW iron impurity transport dataset, each gyrotron's normalized radial position of ECRH deposition versus input power is plotted at the time of iron LBO injection with on-axis shown in (a), some off-axis in (b), and most off-axis in (c)

The 4.9 MW on- to off-axis ECRH dataset is valuable for its unique experimental setup as the only power level that always had ECRH power deposited on-axis. In this way the 4.9 MW dataset can almost be considered a control since the electron temperature profile variations are much smaller percentagewise between the on- and off-axis scenarios. Figure 6.12 shows the fit electron density, ion temperature, and electron temperature profiles for the three different ECRH deposition cases all with total ECRH power equal to 4.9 MW: completely on-axis (20180919.045), some off-axis (20180919.037), and most off-axis (20180919.039). The slight electron temperature peaking between the on- and off-axis scenarios can be explained by constant ECRH on-axis from two gyrotrons as seen in figure 6.13.

After reviewing the ECRH deposition positions and the kinetic profile plots, the impurity iron transport time can be estimated using the same method as discussed in section 6.1.1. Unlike the 3.5 MW dataset, the iron transport times are expected to only have a slight extension as

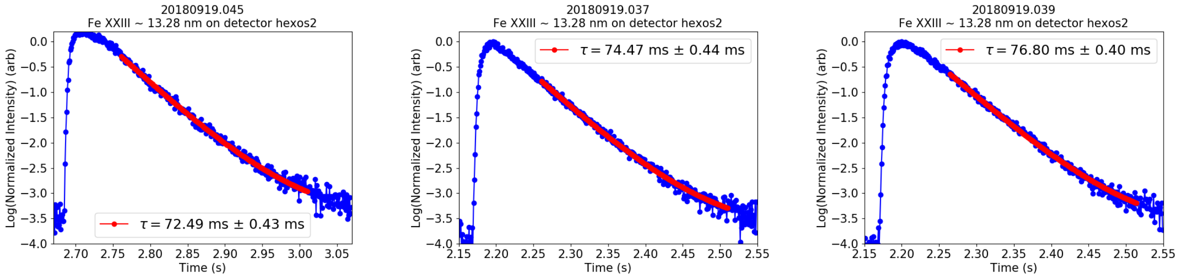

(a) (b) (c)

Figure 6.14: The HEXOS measured line emission for Fe^{+22} is shown versus time for each ECRH deposition position. The global transport time is determined by an exponential fit to the line intensity starting $\sim$ 65 ms after the maximum to ensure that the shape of the iron density profile is rigid

the ECRH power is moved further off-axis. This is under the assumption that with only a slight peaking in the electron temperature profile as shown in figure 6.12c the average iron impurity transport should have a corresponding slight increase leading to a modest decrease in the transport times. In fact figure 6.14 confirms our exact expectation with the fully on-axis to mostly off-axis ECRH scenarios yielding $\tau_I \approx$ 73 ms to 77 ms respectively. Not only do these global transport times indicate that the average iron transport is the same across the 4.9 MW dataset, but also match the scaling expected for the ECRH input power.[58] In comparison with the 3.5 MW dataset, the two extra gyrotrons always kept on-axis for the 4.9 MW scenarios lead to a reduction in the iron transport time of $\sim$ 13 ms for the fully on-axis cases.

Fixed edge anomalous diffusion for consistent edge parameterization

- Mischaracterizing the LBO injection's temporal shape had profound impacts to both the inferred anomalous diffusion profile, i.e. changes $> 0.6\ \frac{m^2}{s}$, and to the subsequently estimated modeled τ_I, i.e. changes $\leq$ 10 ms.

- Although the inferred diffusion profiles across the 4.9 MW ECRH on- to off-axis scan were indistinguishable, the similarity of the diffusion profiles were consistent with the observed similarity in both the $\frac{T_i}{T_e}$ ratios and the experimentally derived transport times, τ_I.

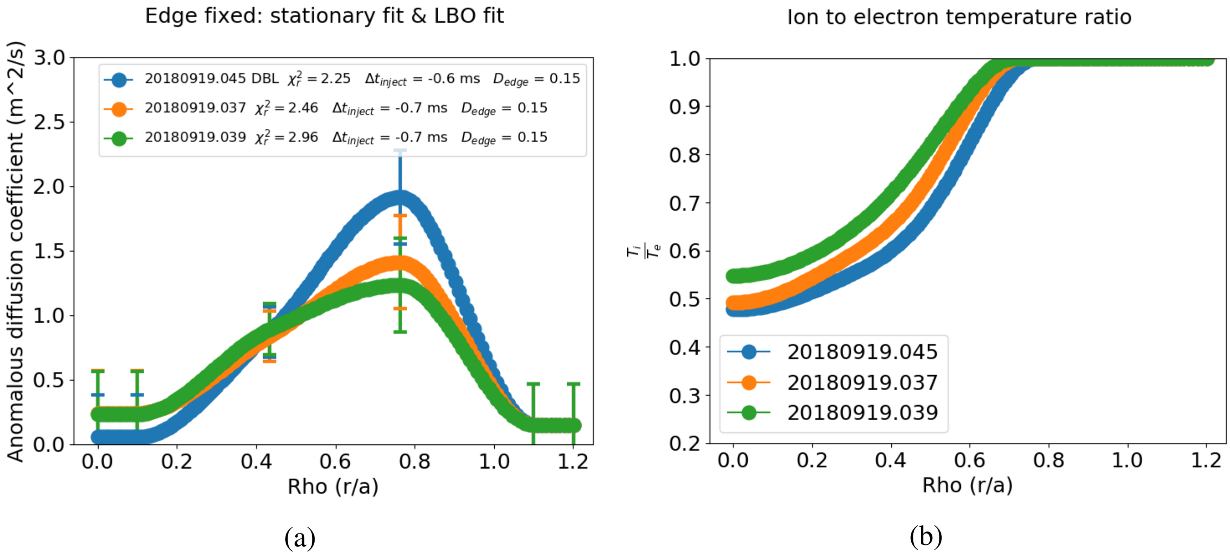

Figure 6.15: The inferred anomalous diffusion profiles are shown in (a) which included the LBO injection timing as a free parameter and the classical & neoclassical transport profiles taken from the DKES calculated profiles. There are two on-axis inferences shown in (a) where the SGL used the standard LBO injection shape, while the DBL used a 2nd LBO injection delayed by 40 ms from the first. In (b) is the $\frac{T_i}{T_e}$ ratio for the three ECRH scenarios.

Following the same procedure as described in section 6.1.1, the least squares minimization was performed for each ECRH deposition position while forcing the inferred flat region in the SOL to a fixed value, i.e. $D_{edge} = 0.15 \ \frac{m^2}{s}$. The inferred anomalous diffusion profiles are shown in figure 6.15, where unfortunately the signal matching is worse for all three scenarios with $\mathcal{X}_R^2 \geq 2.25$. These larger $\mathcal{X}_R^2$ values are not unexpected for plasma discharges with higher electron temperatures. In higher electron temperature scenarios not only are the signal levels higher magnifying the signal distortion from the inaccurate LBO injection specification, but also the signals have an increased radial broadening and outward shift of their distributions causing wider radial regions that contribute to the single line-integrated signals.[h] In addition to the increased $\mathcal{X}_R^2$ values, the 4.9 MW on- to off-axis scan has two main conclusions that both reemphasize the indistinguishability of the inferred anomalous diffusion profiles.

The first major conclusion is derived from figure 6.16a, where it illustrates the correct specification of the iron LBO's temporal shape is vitally important for accurate inferences of the anomalous diffusion profile. The simultaneous drop of the $\mathcal{X}_R^2$ by ~ 0.7 and the off-axis

[h]See sections 4.2.6 and 5.2.3 for more discussion on how the electron temperature impacts the inference of the anomalous diffusion profile.

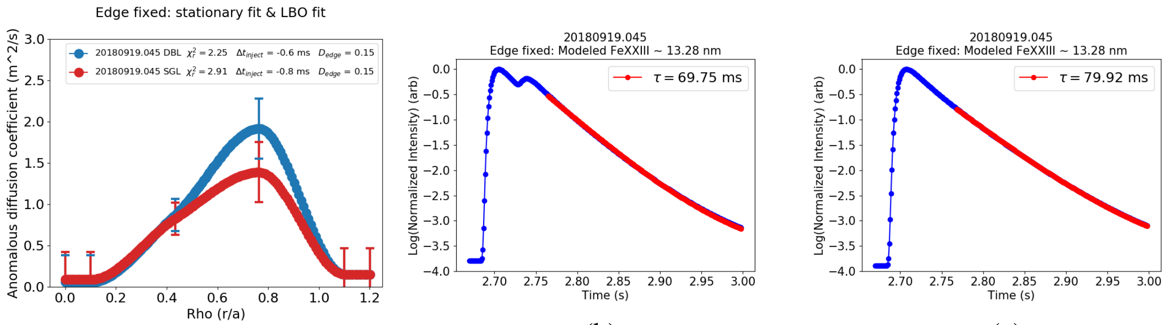

(a) (b) (c)

Figure 6.16: The inferred anomalous diffusion profiles shown in (a) include the LBO injection timing as a free parameter and have LBO parameterizations that correspond to the standard LBO injection shape (labeled with SGL) and the standard injection shape with an additional LBO injection delayed by 40 ms from the first (labeled with DBL). Next the STRAHL modeled line emission corresponding to Fe^{+22}'s 13.28 nm line is shown for the on-axis scenario with the double injection in (b) and the single injection in (c). The global transport time is determined by an exponential fit to the line intensity starting $\sim$ 65 ms after the maximum to ensure that the shape of the iron density profile is rigid

increase of $\sim 0.6\ \frac{m^2}{s}$ in the inferred anomalous diffusion when a smaller secondary neutral iron injection is included in the model illustrates the importance of accurate LBO temporal shape parameterization. The significance of LBO temporal shape parameterization for accurately inferring diffusion profiles was discussed extensively in sections 4.2.7 and 5.1.3. In particular section 4.2.7 demonstrated that a small secondary LBO injection delayed 15 ms from the initial injection could noticeably alter each signal's line-integrated shape for chargestates Fe^{+22} and lower. Emphasizing this point the STRAHL modeled signals for the Fe^{+22} line emission can be used to estimate the resultant global transport time based of the best fit diffusion profiles shown in figure 6.16a. As figure 6.16 illustrates, the same time window for the standard single LBO model injection versus a double LBO model injection yield τ_I estimations shifted by ~ 10 from one another. Although the more accurate double injection model brings the τ_I estimation within 3 ms of the experimentally derived value, the inferred diffusion profile from this double injection model is still well within the systematic uncertainties demonstrated in chapters 4 and 5. Therefore the double injection model has better constrained the uncertainty introduced from the inaccurate parameterization of the neutral iron injection, but not to an extent where discussions about the radial features in the diffusion profile would be meaningful.

The second major conclusion is illustrated by figure 6.15, where the consistency in the experimentally determined τ_I across the on- to off-axis scan is corroborated by the similar $\frac{T_i}{T_e}$ ratios and similarly inferred diffusion profiles. Although the consistency of inferring the same broad diffusion profile for each ECRH deposition position is reassuring, the comparison of this dataset to the 3.5 MW scenarios immediately demonstrates the futility of over interpreting these profile shapes. Rather than over analyze the inferred diffusion profile shapes, this 4.9 MW on- to off-axis ECRH scan is notable for the minimal change to the measured global transport time, i.e. a τ_I increase from $\sim$ 73 to 77 ms respectively. Interestingly this minimal change in τ_I is seemingly correlated with the ion-to-electron temperature ratio as shown in figure 6.15b. This correlation is consistent with the 3.5 MW dataset where when the revisiting figure 6.2 the simultaneous drop in the core T_e by $\sim$ 1.5 keV with negligible changes to the ion temperature create a significant change to the $\frac{T_i}{T_e}$ ratios and to the τ_I. Therefore even though the specifics of each inferred diffusion's radial shape happens to be indistinguishable according to the uncertainty levels calculated in chapter 4, the measured iron transport times correlation with the $\frac{T_i}{T_e}$ ratio is consistent with the similarity in the inferred anomalous diffusion profiles.

6.1.3 2.8 MW on- to off-axis ECRH scan

Global transport time estimation

- The experimentally derived global iron impurity transport time, τ_I, was determined to increase from $\sim$ 102 to 118 ms as the ECRH was moved from purely on-axis to a completely off-axis deposition position, $\rho \approx 0.4$.

As mentioned in section 6.1, the 2.8 MW dataset only had two successful iron LBO injections at $\overline{n}_e \approx 6 \times 10^{19}\, m^{-2}$ for the on- to off-axis scan. Fortunately the two successful injections were the on-axis and most off-axis scenarios yielding the largest contrast in the electron temperature profiles. Figure 6.17 shows the electron density, ion temperature, and electron temperature profiles for the two cases with the completely on-axis (20180919.044) and most off-axis (20180919.046) scenarios labeled. Indeed the on-axis scenario's T_e profile shows a large core peaking over the off-axis scenario very similar to the 3.5 MW dataset. In this way

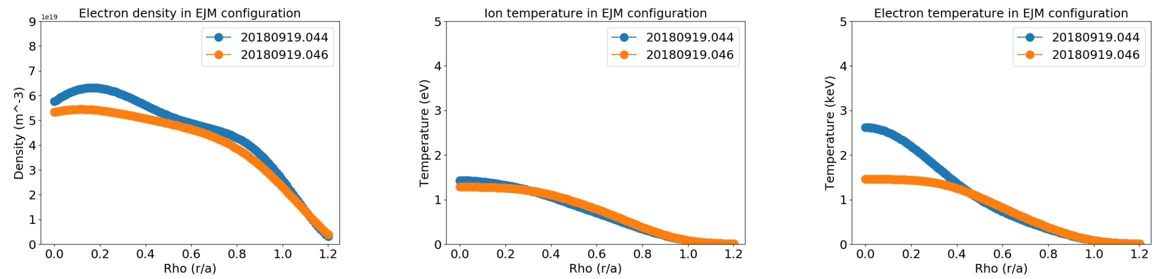

(a) (b) (c)

Figure 6.17: The electron density, ion temperature, and the electron temperature radial profiles are plotted in (a), (b), and (c) respectively for the 2.8 MW input ECRH on- to off-axis scan. Plasma discharge 20180919.044 in blue is completely on-axis exemplified by the peaked electron temperature, while discharge 20180919.046 in orange is the most off-axis case with the broader electron temperature profile.

(a) (b)

Figure 6.18: For 2.8 MW iron impurity transport dataset, each gyrotron's normalized radial position of ECRH deposition versus input power is plotted at the time of iron LBO injection with on-axis shown in (a) and most off-axis in (b). (See footnote i on spacing)

the 2.8 MW dataset should be valuable for its resemblance to the 3.5 MW dataset, yielding more data points to put both the 3.5 MW and 4.9 MW datasets in context. In order to achieve the variance in the electron temperature profiles shown, the two ECRH scenarios with the specific radial deposition positions of the gyrotrons are shown in figure 6.18.[i]

Following the same procedure for estimating the global transport as first described in section 6.1.1, the observed exponential decay of the Fe^{+22}'s 13.28 nm spectral line was fit to determine τ_I. Unlike the 4.9 MW dataset, the iron LBO injections for both ECRH deposition positions did not have any obvious secondary iron clusters causing τ_I estimation errors. As such the fit of FeXXIII's exponential decay had no obvious complications with the on-axis and off-axis scenarios yielding $\tau_I \approx 102$ and 118 ms respectively as depicted in figure 6.19. The

[i]The middle space is left intentionally blank for consistency with the other power levels and to specifically emphasize this 2.8 MW dataset is composed of the on-axis and most off-axis scenarios.

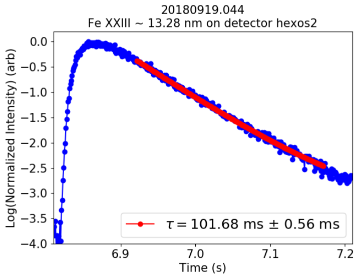

(a)

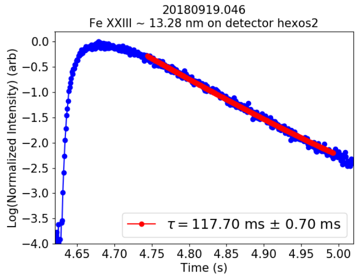

(b)

Figure 6.19: The HEXOS measured line emission for Fe^{+22} is shown versus time for each ECRH deposition position. The global transport time is determined by an exponential fit to the line intensity starting $\sim$ 65 ms after the maximum to ensure that the shape of the iron density profile is rigid. (See footnote i on spacing)

first observation from these two global transport time estimations is the confirmation of the expected increase in the transport time as a larger fraction of the ECRH power is placed off-axis. Although this trend is consistent with the 3.5 MW dataset, the enhanced transport time for off-axis ECRH deposition is still a smaller increase percentagewise than those observed for the 3.5 MW dataset. The second observation is that the 102 ms transport time for the on-axis scenario is consistent with the observed ECRH power scaling where as less ECRH power is injected the global transport time increases.[58] More details and discussion on the global transport times for the entire dataset is presented in section 6.2.

Fixed edge anomalous diffusion for consistent edge parameterization

- Even though the inferred diffusion profiles for the 2.8 MW on- to off-axis dataset were indistinguishable from each other & those from the other power levels, the inferred diffusion levels were less than the 4.9 and 3.5 MW datasets'. This trend is consistent with the observed trends in both the $\frac{T_i}{T_e}$ ratios and the τ_I.

After the global impurity transport times were estimated, the next step in the dataset's analysis was naturally the least squares inference of the anomalous diffusion profile. As mentioned previously the inferences attempted to minimize the uncertainty from inconsistent SOL modeling by establishing consistent edge temperature models as discussed in sections 5.2.3 & 5.2.3 in addition to holding $D_{edge} = 0.15 \frac{m^2}{s}$. The resulting inferred anomalous diffusion profiles, depicted in figure 6.20, had the same characteristics as the 3.5 and 4.9 MW datasets'

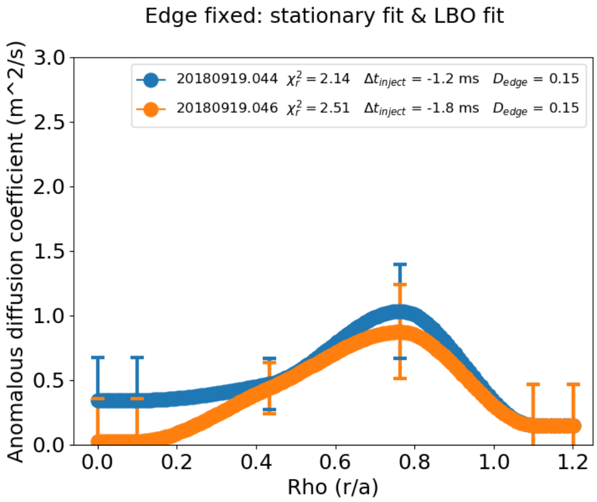

(a)

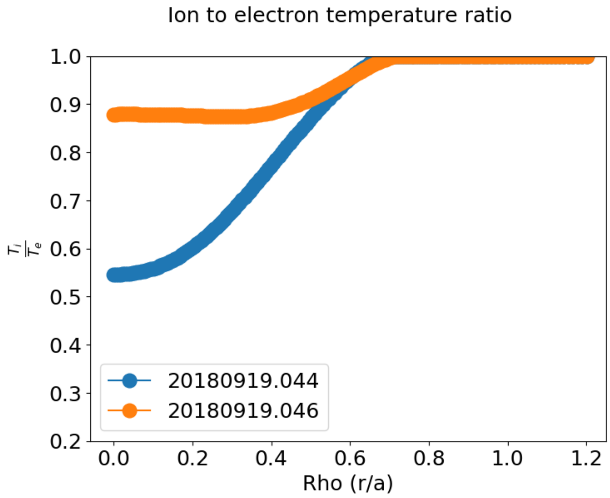

(b)

Figure 6.20: The inferred anomalous diffusion profile is shown in (a) which included the LBO injection timing as a free parameter and the classical & neoclassical transport profiles taken from the DKES calculated profiles. In (b) is the $\frac{T_i}{T_e}$ ratio for the two ECRH scenarios.

inferences. The first and most obvious shared characteristic across the 2.8, 3.5, and 4.9 MW datasets is the indistinguishability of the inferred anomalous diffusion profiles. In fact the indistinguishability covers all scenarios across the datasets with even the 4.9 on-axis scenario and the 2.8 MW off-axis scenario falling within the uncertainty levels despite the difference in the global transport time (118 ms versus 73 ms respectively). The second shared characteristic with the 3.5 MW dataset is the identical trend of a large variation in the $\frac{T_i}{T_e}$ ratio from the on- to off-axis scan seemingly not reflected in the inferred anomalous diffusion profiles. The 2.8 and 3.5 MW datasets returned near identical anomalous diffusion profiles despite the clear estimated difference in the global transport times. Although it is encouraging that the returned diffusion profiles for the 2.8 MW scenarios have lower diffusive peaking than the 3.5 or 4.9 MW scenarios, this trend is currently unverifiable due to the large uncertainties on the anomalous diffusion profiles. Therefore the large central electron temperature peaking as a larger fraction of ECRH power is deposited on-axis returns distinguishable global transport times, but indistinguishable anomalous diffusion profiles when systematic uncertainties are taken into account.

6.2 Overview of the on- to off-axis ECRH scan in the standard magnetic configuration

6.2.1 Observational results

- The on- to off-axis scans performed at constant total power demonstrated that as a larger fraction of ECRH was deposited off-axis there was an increase in the $\frac{T_i}{T_e}$ ratio for $\rho \leq 0.6$ along with an enhancement of the global transport time, τ_I.

- The iron impurity transport was marginally sensitive to the core electron temperature peaking. Within the on- to off-axis scans the electron temperatures in the core, $\rho \leq 0.4$, were observed to change by as much as $\sim$ 1.5 keV with a relatively small impact on the global transport time, i.e. τ_I was enhanced by at most 27% as core T_e decreased.

- The on-axis ECRH power scan from 4.9 to 2.8 MW reduced the core T_e from $\sim$ 3.5 to 2.7 keV. Although the core T_e reduction was nearly identical to the 4.9 MW on- to off-axis dataset (the same $\sim$ 3.5 keV reduced to 2.6 keV), the global transport time enhancement was substantially larger for the on-axis power scan (i.e. $\sim$ 73 to 102 ms) than the on- to off-axis scan (i.e. $\sim$ 73 to 77 ms)

- Unlike the on- to off-axis datasets, the on-axis ECRH power scan had significant variations in the $\frac{T_i}{T_e}$ profiles in the outer region of the plasma, i.e. $0.6 \leq \rho \leq 0.8$. This variation combined with fact that a similar $\sim$ 900 eV drop in core T_e during the 4.9 MW on- to off-axis dataset did not significantly change the global transport time indicates that the kinetic profile's magnitude/shape outside mid-radius has a greater impact on the observed iron impurity transport than core T_e variations.

After analyzing each ECRH power level's on- to off-axis scans, the next step in the analysis is synthesizing these individual results for a more comprehensive picture of iron impurity transport across the entire dataset. The first step in this synthesis is a discussion of the observable characteristics across all the on- to off-axis scans. Specifically the observable characteristics of most interest in the on- to off-axis ECRH scans are the temperature profile variations and the global transport time estimates. As seen in figure 6.21 the 4.9, 3.5, and 2.8 MW on- to

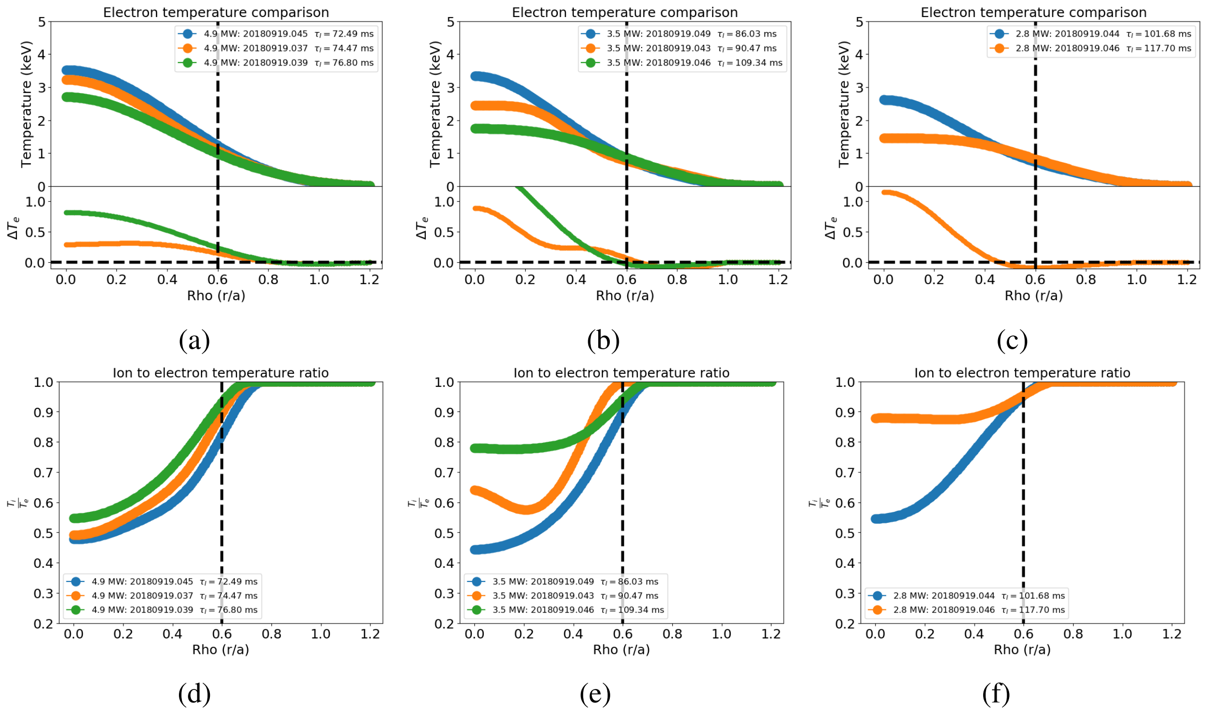

Figure 6.21: The 4.9, 3.5, and 2.8 MW ECRH on- to off-axis T$_e$ profiles are shown in (a-c) with their corresponding $\frac{T_i}{T_e}$ ratios shown in (d-f). For the electron temperature profiles the respective difference from the on-axis case is plotted below to illustrate the variations caused from the off-axis ECRH scan. Also note that the global impurity iron transport time, i.e. τ_I, are included in the legend for each heating scenario.

off-axis ECRH scans have their electron temperatures plotted in (a-c) with the corresponding ion-to-electron temperature ratios in (d-f) with every heating scenario's estimated global transport time listed in the legend. Examining the electron temperature profiles in figure 6.21 there are two obvious common characteristics for the on- to off-axis scans. The first shared characteristic of the on- to off-axis datasets is the electron temperature profile's equivalency outside $\rho = 0.6$ with the only major T$_e$ profile shaping occurring in the plasma core. This indicates that the ECRH deposition position varying from an on-axis to the most off-axis position, $\rho \approx 0.4$, primarily causes a flattening of T$_e$ profile in the core. The second shared characteristic is the relative weak scaling of the global transport time with core electron temperatures. This is evidenced in every on- to of-axis scan with each dataset demonstrating a core T$_e$ reduction and relatively small increase in the global transport time. In fact the largest enhancement of the global transport time, i.e. 27% increase, occurred in the 3.5 MW dataset where the on- to off-axis core electron temperature reduction was 1.5 keV, the largest core T$_e$ reduction among the three power levels. Reinforcing the observed insensitivity of the impurity iron's global transport time to the core electron temperature magnitude was the 4.9 MW dataset's minimal increase of τ_I by 4 ms even though a $\sim$ 800 eV reduction in T$_e$ had occurred. Interestingly the on- to off-axis datasets had unchanging ion temperature profiles meaning that within an on- to off-axis scan the only major kinetic profile discrepancy was the core electron temperature.[j] Therefore the core electron temperature variation within an on- to off-axis scan is the major contribution to the observed correlation between the core ion-to-electron temperature ratio and the global iron transport time. As shown in figure 6.21, the increasing core $\frac{T_i}{T_e}$ ratio for the 3.5 and 2.8 MW datasets coincides with the observed increasing iron transport time, τ_I, while the 4.9 MW dataset demonstrated the simultaneous small change to the core $\frac{T_i}{T_e}$ and τ_I. This ion-to-electron ratio is important not only for the neoclassical transport due to the influence on the radial electric field (see sectionD.1), but also for its impact on anomalous transport by changing the conditions necessary for instability onset (see section D.1). A further discussion on the impact of the $\frac{T_i}{T_e}$ is included in the section 6.2.3.

After examining the on- to off-axis observational results, it is useful to examine the on-axis ECRH power scan inherent within the entire on- to off-axis dataset. First, the iron transport time scaled as expected with the deposited ECRH power, $\tau_I \propto P_{ECRH}^{-0.59}$, confirming previous work.[58, 93] Second, the reduction in the deposited power for the on-axis ECRH power scan returned many of the same observational characteristics as the movement of ECRH deposition further off-axis did in the on- to off-axis scans. Specifically the similar observational characteristics were the increase in global transport time in conjunction with the reduction of the electron temperature profile. However as shown in figure 6.22 there are significant differences with the on-axis power scan's observational results. The most obvious difference is the large, i.e $\sim$ 300 eV, reduction in the ion temperature profiles as on-axis power was lowered from 4.9 to 2.8 MW. Even with the ion temperature profile's systematic errors, see section 5.2.3 for a discussion on ion temperature profile shifts, this observed reduction is measurable. Furthermore unlike the

[j]See figures 6.12b, 6.2b, and 6.17b for the ion temperature profile rigidness as ECRH deposition position was altered.

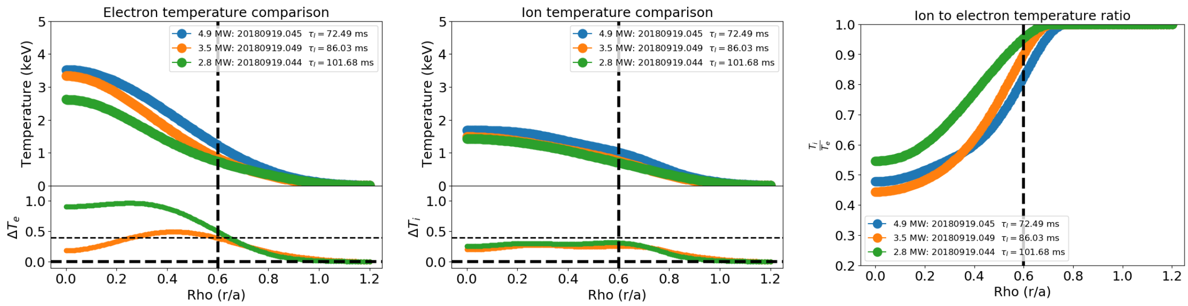

(a) (b) (c)

Figure 6.22: The 4.9, 3.5, and 2.8 MW ECRH on-axis T$_e$ and T$_i$ profiles are shown in (a) and (b) respectively with their corresponding $\frac{T_i}{T_e}$ ratios shown in (c). For the electron and ion temperature profiles the respective difference from the 4.9 MW case is plotted below with horizontal dashed lines at 0 and 400 eV to illustrate the variations caused from the ECRH power scan. Also note that the global impurity iron transport time, i.e. τ_I, are included in the legend for each heating scenario.

unchanging electron & ion temperature profiles in an on- to off-axis scan, the temperature reduction extended outside the plasma core with significant temperature differences as far as $\rho = 0.8$ as shown in figure 6.22a. In fact although the on-axis power scan's T$_e$ profile had similar ~ 1.0 keV core electron temperature changes as the on- to off-axis scans, the power scan had the additional electron temperature variation of ~ 300 eV across the region $0.6 \leq \rho \geq 0.8$. Therefore the on-axis power scan clearly impacted the electron and ion temperature profiles' broadness with significant modification outside $\rho = 0.6$, unlike the on- to off-axis scans' impact solely on the core electron temperature peaking.

The change in the temperature profiles' broadness had a more profound influence on the iron impurity transport than the core electron temperature peaking alone. The iron impurity transport times, included in the legends in figure 6.22, had a 40% increase as the temperature profiles' broadness was reduced as a consequence of decreasing the input ECRH power. Interestingly even though the power scan displayed a similar core electron temperature reduction as the 4.9 MW on- to off-axis scan (~ 900 versus 800 eV respectively), the core ion-to-electron temperature ratio showed minimal change, i.e. $\Delta\frac{T_i}{T_e} \leq 0.15$, due to increased ECRH power raising the ion temperature profile. However due to the ion and electron temperature profiles' change in broadness, the power scan's $\frac{T_i}{T_e}$ ratio outside mid-radius had a much larger disparity

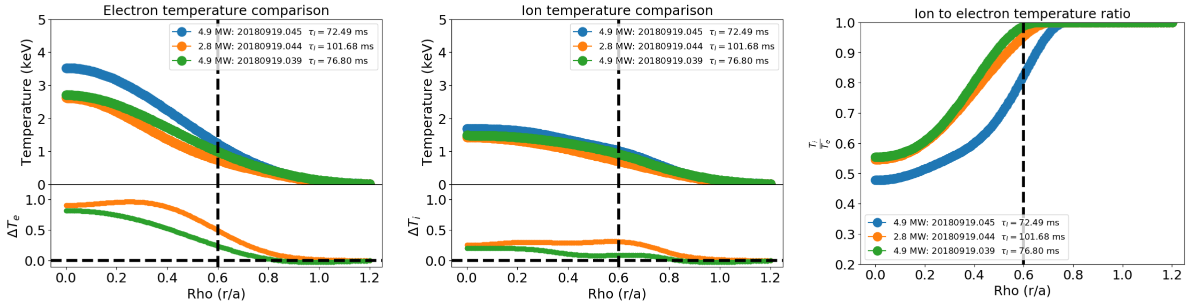

(a) (b) (c)

Figure 6.23: The 4.9 MW on-axis, 2.8 MW on-axis, and the 4.9 MW most of-axis scenarios have their T_e and T_i profiles are shown in (a) and (b) respectively with their corresponding $\frac{T_i}{T_e}$ ratios shown in (c). For the electron and ion temperature profiles the respective difference from the 4.9 MW on-axis case is plotted below to illustrate the variations caused from either the ECRH power scan or the off-axis deposition scan. Also note that the global impurity iron transport time, i.e. τ_I, are included in the legend for each heating scenario.

between low and high power as shown with the $\rho = 0.6$ dashed line in figure 6.22c. This reemphasizes that it is the electron and ion temperature profiles' magnitude/shape outside the plasma core, i.e. $\rho \geq 0.4$, that has a greater impact on the iron impurity transport for these plasmas. In fact figure 6.23 shows this observational result through the temperature profile comparisons among the 4.9 MW on-axis, 4.9 MW most off-axis, and the 2.8 MW on-axis scenarios. The 4.9 MW most off-axis and the 2.8 MW on-axis scenarios have the same core electron temperature, but outside $\rho = 0.2$ both T_e and T_i profiles start to diverge in magnitude with the 2.8 MW on-axis scenario having much narrower temperature profiles. Although there isn't a significant difference in the $\frac{T_i}{T_e}$ ratios between the 2.8 MW on-axis and 4.9 MW most off-axis scenarios, the decreased magnitude and narrower profiles of T_e and T_i for $\rho \geq 0.4$ led to a significant increase in the iron transport time, i.e. ~ 77 to 102 ms. Therefore examining the ECRH power scan's observational results has not only reaffirmed that a purely core T_e variation has a smaller effect on the iron impurity transport, but also that the temperature profiles' magnitude/shape outside the core, i.e. $\rho \geq 0.4$, has a much larger impact on the observed iron impurity transport.

6.2.2 Inferred results

- The experimentally observed iron line emission could only be well-matched when the anomalous diffusion channel was included within the least squares inference. The dominance of the anomalous diffusive channel strongly suggests that turbulent transport is the main transport mechanism during these W7-X plasma discharges.

- The uncertainty estimation performed in this thesis assumed linear independent errors and subsequently couldn't fully decouple induced uncertainties from the systematic errors & input inaccuracies. Thus without an uncertainty analysis that can provide confidence intervals (e.g. Markov Chain Monte Carlo approach), the differences in the inferred diffusion profile within an ECRH on- to off-axis dataset cannot be resolved.

- The inferred anomalous diffusion profiles for the on-axis ECRH power scan demonstrate a distinguishable difference outside mid-radius even when taking into account the uncertainties derived from the sensitivity studies in chapter 4. As on-axis ECRH power is decreased there is a decrease in diffusion profile peaking outside mid-radius that is consistent with the concomitant increase of global transport time (τ_I) and the ion-to-electron temperature ratio ($\frac{T_i}{T_e}$).

After analyzing each ECRH power level's on- to off-axis scan and the on-axis ECRH power scan, it is useful to consolidate the observational results with the inferred anomalous diffusion profiles in order to generate comprehensive conclusions. Naturally the very first and most obvious unified conclusion is the sheer dominance of the anomalous diffusion transport channel over all other transport channels. This dominance was demonstrated in two ways: The first way occurred through the isolation of the neoclassical & classical transport channels from the anomalous diffusive and convective transport channels. As shown in sections 6.1.1 & 6.1.1, the measured iron line emission could not be matched when the anomalous diffusion transport channel was excluded from the least squares inference. The second way the anomalous diffusion demonstrated its dominance as a transport channel was the necessary levels to reproduce the iron line emission were at the very least an order of magnitude to two orders of magnitude greater than the neoclassical & classical diffusion combined, i.e. $0.1 \leq$ D$_{anomalous}$ ≤ 3.5 $\frac{m^2}{s}$ versus D$_{neoclass\ \&\ class}$ $\leq 0.2\ \frac{m^2}{s}$. These two aspects combined give very strong indications that these W7-X plasma discharges are dominated by turbulent transport. In fact [Wegner et al. 40] recently not only demonstrated that in similar plasma conditions the plasma's transport is turbulently-dominated, but also identified the specific turbulent mode (i.e. ion temperature gradient) that lead to the observed transport changes. Without the neoclassical transport reduction from the W7-X magnetic field geometry optimization, this identification of turbulently dominated transport would have been extremely difficult.

The next conclusion is that each on- to off-axis scan performed at constant total ECRH power had indistinguishable inferred anomalous diffusion profiles when the uncertainties derived from the sensitivity studies were considered. The sensitivity studies performed in chapters 4 & 5 demonstrated that the LBO temporal parameterization, i.e. both the injection timing & temporal shape, and the STRAHL edge parameterization had the largest impact on the inferred diffusion profiles. Although these variational style synthetic studies are unable to decouple induced uncertainties from the systematic errors and input inaccuracies, they importantly highlight key parameters that if their uncertainties were reduced would significantly improve the confidence interval for the inferred anomalous diffusion profiles. Following this method both a more comprehensive error analysis approach (e.g.Markov Chain Monte Carlo) should be undertaken to decouple parameter uncertainties and additional experimental data should be collected in an attempt to better minimize induced errors (e.g. temporal parameterization of the neutral LBO injection & adding multi-chord x-ray diagnostic for improved spatial localization of the emission). Although further minimization of these uncertainties is beyond the scope of this thesis, it is important to note that the inference of the anomalous diffusion profile is minimally effected by the electron temperature profile variations within its current 1-sigma uncertainties as detailed in chapter 4. Thus with the electron temperature variations across the ECRH power and deposition position datasets falling outside the T$_e$'s uncertainty levels, resolving the radial variations of the inferred anomalous diffusion profiles potentially becomes possible once the more significant contributions to the systematic uncertainties are minimized.

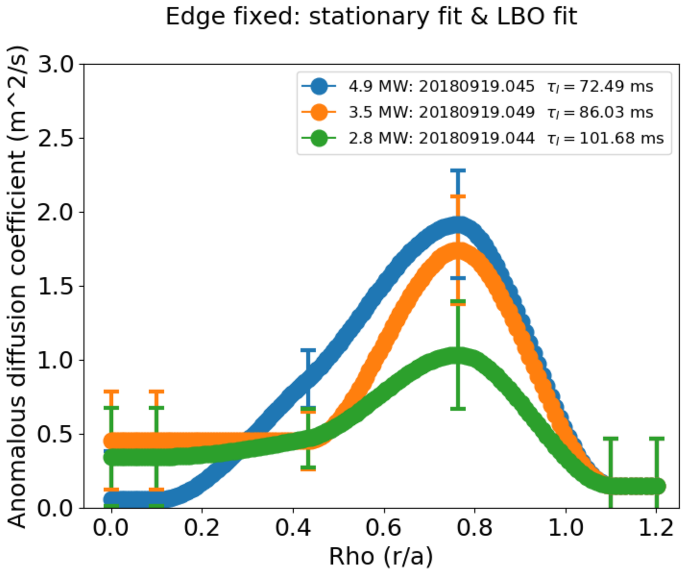

Figure 6.24: The inferred anomalous diffusion profiles are shown for the on-axis scenarios at 4.9, 3.5, and 2.8 MW with their corresponding global transport time labeled

The final conclusion is that the on-axis ECRH power scan demonstrated a clear difference in the inferred anomalous diffusion profiles outside mid-radius that is consistent with the observed concomitant increase in the global transport time and ion-to-electron temperature ratios. This fact is exhibited most clearly through figure 6.24 where the inferred diffusion profiles for the on-axis ECRH power scan are shown. From this figure it is clear that the diffusion profiles for the 4.9 and 2.8 MW scenarios are distinguishable at the spline-knot position of $rho \approx 0.76$ and importantly show an increase in the anomalous diffusion values with ECRH input power. This is the well known ECRH power scaling of transport times already noted through the experimentally derived global transport times as shown in figure 6.24's legend and discussed in section 6.2.1. Therefore it is reassuring that the inferred diffusion profiles reflect the characteristics observed for the on-axis ECRH power scan, namely an increase in diffusion profile peaking outside mid-radius corresponding to broader electron temperature profiles and shorter global transport times.

In addition to the on-axis ECRH power scan, the similarity of each on- to off-axis dataset's inferred diffusion profiles is consistent with the observed scaling of global transport time (τ_I) and the ion-to-electron temperature ratio ($\frac{T_i}{T_e}$). The on- to off-axis datasets demonstrated large core electron temperature variations corresponding to modest changes in the global transport time. Although the exact shaping and differences among the radial diffusion profiles is unknown within the uncertainty levels, the inferred diffusion profiles similarity in shape and magnitude qualitatively reflect this observed trend in the global transport time and the $\frac{T_i}{T_e}$ ratio. The consistency of the inferred diffusion profiles matching the observed trends in the τ_I and $\frac{T_i}{T_e}$ contribute confidence that the least squares routine is matching the signals well enough to reflect the global transport effects but unfortunately not precise enough for radial profile interpretations of the inferred anomalous diffusion for all scenarios.

6.2.3 Discussion of anomalous transport mechanisms

- The dominance and necessity of the anomalous diffusive flux channel is corroborated by the gyrokinetic simulations performed in [García-Regaña et al. 1], where irrespective of whether the turbulence was driven by ITG or TEM instabilities, it was found that the dominant impurity transport channel was ordinary, charge-independent diffusion.

- Across the entire ECRH on- to off-axis dataset as either more ECRH power is moved off-axis or less total ECRH power is deposited both the $\frac{T_i}{T_e}$ and the τ_I increases.

  - In the ECRH power scan the increases at the off-axis position in the $\frac{T_i}{T_e}$ and τ_I were accompanied by decreases in D_{anom}. This observational evidence is consistent with a suppression of ITG induced turbulent transport and previous work done by [Wegner et al. 40].

  - The on- to off-axis ECRH scans had the $\frac{T_i}{T_e}$ ratio increasing with the τ_I, however the $\frac{T_i}{T_e}$ ratio only varied in the core where the T_e profile's peaking was altered and where the ion temperature gradient would be very small. Indicating ITG induced turbulent transport is much less likely as an explanation for the observed τ_I variation and that the mechanism is likely dependent on the core electron temperature.

The final step in evaluating the entire dataset is a discussion on the possible mechanism(s) for the observed dominance of the anomalous diffusive transport. The usual mechanisms driving an instability attributable to turbulent transport are the ion temperature gradient (ITG), the electron temperature gradient (ETG), and the trapped electron mode (TEM). It is expected that the largest drivers of impurity transport for W7-X are the ion-temperature gradient (ITG) and the trapped electron mode (TEM) since these instabilities have a scale length on the order of the ion's larmor radius.[k] Numerical simulations in [94, 33] have indicated that typical TEM driven impurity transport should be at low levels. However recent quasilinear and nonlinear gyrokinetic simulations of impurity transport in W7-X were used to calculate the transport coefficients for ITG, ETG, TEM driven turbulence.[1] Importantly the results from the work by [García-Regaña et al. 1] demonstrated that the turbulent transport was dominated by ordinary diffusion (i.e. proportional to the impurity density gradient) for both ITG and TEM driven turbulence at nearly the same levels for similar normalized gradient scale lengths. This result is consistent with the observational conclusions from this thesis, namely that an ordinary, charge-independent anomalous diffusion was necessary to match the iron line emission and the anomalous diffusion was by far the most dominant transport channel. Although [García-Regaña et al. 1]'s result might indicate that it is mainly the steady-state iron impurity density gradient that is dictating the anomalous transport, these calculations were all performed at $T_e = T_i$ without any potential electron temperature peaking changing the threshold for the ITG instability onset. Moreover the work done by [Proll et al. 33] demonstrated that there were multiple types of TEM instabilities including ones driven by an electron temperature gradient rather than the classical picture of an electron density gradient. Therefore the potential mechanism(s) in this on- to off-axis ECRH dataset causing the change in the iron impurity transport is not verifiable with the present analysis, but can be discussed for consistency and likelihood for either ITG or TEM (or some combination thereof) induced turbulence.

Recent work by [Wegner et al. 40] confirmed ion temperature gradient (ITG) driven turbulent transport for a trace iron impurity in the W7-X standard magnetic configuration. Specifically [Wegner et al. 40] demonstrated that iron impurity transport was sensitive to the ion-to-electron temperature ratio whereby lower $\frac{T_i}{T_e}$ plasmas were observed to have increased electron

[k] In [39] stellarators should not be as susceptible to turbulent transport driven on the scale lengths of the electron larmor radius like the the electron temperature gradient instability

density fluctuations and increased anomalous diffusive flux. This result was observed experimentally through a decrease in the global transport time concomitant with a decrease in $\frac{T_i}{T_e}$ and an increase in n_e fluctuations. Moreover it has been predicted for the W7-X standard magnetic configuration that as $\frac{T_i}{T_e}$ increases the critical value for the normalized ion temperature gradient length, needed to excite the ITG mode, also increases.[95] In order to confirm that the observed impurity transport changes were related to a change in the ITG driven turbulent diffusion, [Wegner et al. 40] performed linear gyro-kinetic calculations for the critical values of the normalized ion temperature gradient length, a/L_{T_i}. Armed with these critical values, i.e. $a/L_{T_{\mathrm{i,\,crit}}}$, the onset of ITG turbulence could be evaluated as a function of the local $\frac{T_i}{T_e}$ and a/L_{T_i}. Therefore this comparison corroborated that the increased iron transport times, the decreased electron density fluctuations, and the decreased inferred diffusion values could be attributable to a suppression of the ITG induced turbulence.

Before extending the comparison to this thesis's dataset, it is important to note that the iron LBO injections performed in [Wegner et al. 40] altered the $\frac{T_i}{T_e}$ ratio by dropping the centrally applied ECRH from $\sim$ 5 to 2 MW. Therefore the inherent ECRH power scan presented in this thesis is a great analog for comparison of the observational and inferred results. In the least squares minimization performed by [Wegner et al. 40], the same least squares minimization code as was used in [Geiger et al. 7], the inferred anomalous diffusion profiles yielded a substantial decrease in the off-axis position, $\sim$ 1.5 $\frac{m^2}{s}$ at $\rho \approx 0.6$, as the central ECRH power was decreased from 5 to 2 MW. Comparing [Wegner et al. 40]'s and the inherent ECRH power scan's inferred anomalous diffusion profiles led to two important conclusions. The first and encouraging conclusion is the returned similarity in both shape and magnitude for the inferred anomalous diffusion profiles for the 3 MW scenario in [Wegner et al. 40] and the on-axis 3.5 MW scenario shown in figure 6.11. These results were achieved using completely separate least squares minimization codes giving confidence in the accuracy and consistency of the approach taken in the analysis presented in this thesis.[1] The second conclusion was that both datasets follow the trend of an increased anomalous diffusion peaking outside mid-radius as the local $\frac{T_i}{T_e}$

[1] In fact taking into account the on- to off-axis dataset was performed at higher densities ($\overline{n_e} \approx 6 \times 10^{19}$ versus 4×10^{19} m^{-2}) yielding increased $\frac{T_i}{T_e}$ makes the slightly lower inferred diffusion values expected.

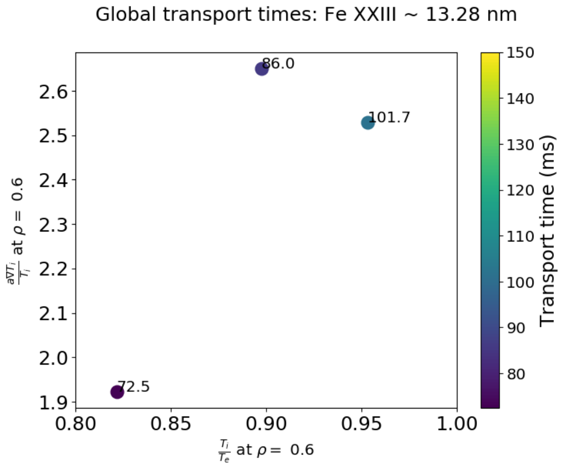

Figure 6.25: The on-axis ECRH power scan demonstrating the scaling of the normalized ion temperature gradient length with $\frac{T_i}{T_e}$ at the radial position of $\rho = 0.6$

ratio was lowered. The concomitant increase in the iron transport time with the local $\frac{T_i}{T_e}$ ratio is consistent with the observational result that the temperature profiles' magnitude/shape outside the core, i.e. $\rho \geq 0.4$, has a much larger impact on the observed iron impurity transport. As further verification of consistency between the two power scans, the electron density fluctuations could be examined for a variation indicative a turbulence modification. Unlike the analysis in [Wegner et al. 40], the data from the phase contrast imaging diagnostic[96] used to measured electron density fluctuations have not been analyzed for these LBO injections. Therefore no direct information is currently available on possible turbulence changes stemming from the ion temperature gradient (ITG) or from trapped electron mode (TEM) instabilities.

To exactly apply the same analysis in [Wegner et al. 40] to the ECRH power scan dataset presented in this thesis, both the $\widetilde{n_e}$ levels would need to be evaluated and more importantly gyro-kinetic simulations for the $a/L_{T_{\mathrm{i,\,crit}}}$ would need to be performed. However the dataset can be checked for consistency with this ITG suppressed picture by evaluating the scaling of the iron transport time versus a local normalized ion temperature gradient length and a local ion-to-electron temperature ratio. In fact this exact plot is produced for the on- to off-axis ECRH dataset in figure 6.25, where the both the temperature ratio and the normalized gradient length are evaluated at the same radial position as in [Wegner et al. 40], $\rho = 0.6$. The clear trend of the iron transport time increasing from 72.5 to 141.6 ms as the $\frac{T_i}{T_e}$ ratio increases from ~ 0.82 to 0.98 is evident from figure 6.25. This type of scaling is the expected trend if the suppression in turbulent transport driven by the ITG instability was the correct mechanism explaining the observed iron transport modification. Along with the concomitant increase of $\frac{T_i}{T_e}$ with τ_I, the normalized ion temperature gradient length also increases as the ECRH power is reduced. This is where a gyro-kinetic simulation for each ECRH scenario would be able to determine whether the critical length, i.e. $a/L_{T_{\mathrm{i,\,crit}}}$, increases faster than this rising gradient length.[m] Ultimately without this numerical verification on whether the ITG instability is properly suppressed, the transport changes cannot be fully attributable to ITG turbulent diffusion, however importantly all of the observable characteristics for a modification in the iron impurity transport through ITG suppression are consistent for the ECRH power scan, e.g. an increase at an off-axis position in $\frac{T_i}{T_e}$ accompanied with a decrease in D_{anom} and increase in τ_I.

Moving onto the on- to off-axis datasets, the similar scaling of $\frac{T_i}{T_e}$ with τ_I is generally observed. However critically the only major variation in the $\frac{T_i}{T_e}$ ratio occurred in the plasma core rather than an off-axis position as was detailed in section 6.2.1. The flat and unchanging ion temperature profiles for these datasets indicate that modifications to the ITG instability were unlikely the cause for the observed τ_I change. The lack of temperature profile variations outside mid-radius, exactly where the ion temperature gradient has non-negligible values, would seem to indicate that the driver for the ITG instability had negligible variations during the on- to off-axis scans. Although the cause for the observed τ_I change in these on- to off-axis scans is unconfirmed especially without any gyrokinetic calculations performed, the observed smaller variation in the τ_I looks to be a consequence of a different transport mechanism. In fact the strong variation of the core electron temperature profile in combination with unchanging ion temperature profiles and consistent electron density profiles across an on- to off-axis dataset seemingly indicate that the observed impurity iron transport modification is attributable to these core T_e profile variations. Unfortunately, the mechanism affecting the iron impurity transport during an off-axis ECRH scan is even more unclear than the ECRH power scan. In

[m] In fact the 2.8 and 3.5 MW scenarios are intriguing in that they show a nearly identical $a/L_{T_{\mathrm{i}}}$ (see figure 6.25) but with a increase in the τ_I by 18%, meaning the increase in the $\frac{T_i}{T_e}$ ratio from 0.9 to 0.95 should also increase the $a/L_{T_{\mathrm{i,\,crit}}}$ value necessary to excite the ITG mode. Therefore the difference of $\sim$ 15 ms in their estimated transport times could indicate that this critical $a/L_{T_{\mathrm{i,\,crit}}}$ value has increased faster than the observed normalized ion temperature gradient scale length.

fact from the work done by [Proll et al. 33], the numerical simulations uncovered not only hybrid instabilities (i.e. coupling between ITG, ETG, TEMs), but also new drivers for instabilities characteristically similar to already specified modes, e.g. the trapped electron modes driven by an electron temperature gradient rather than the traditional electron density gradient. Therefore although the on- to off-axis datasets had the similar scaling of $\frac{T_i}{T_e}$ with τ_I, the observed characteristics don't indicate an ITG suppression mechanism and point to a weak dependence on the core electron temperature profile.

In conclusion, the total on- to off-axis ECRH dataset demonstrates impurity transport variations across both total input power and radial deposition position. These iron impurity injections can only be well-matched when anomalous diffusion is used as a transport channel within the least squares minimization. In fact the anomalous diffusion transport channel is the most dominant transport channel in these plasma discharges with neoclassical & classical levels at a minimum an order of magnitude lower. Even though the inferred anomalous diffusion profiles could not be sufficiently differentiated from one another due to the inherent uncertainties introduced from inaccurate input parameters and systematic errors, their consistency in matching the observed trends in the τ_I and $\frac{T_i}{T_e}$ contribute confidence that the least squares routine is matching the signals well enough to reflect the global transport effects. Finally the exact mechanism explaining the observed transport changes cannot be conclusively confirmed without added signals and importantly gyrokinetic calculations performed for these discharges. However the observed characteristics for the ECRH power scan are consistent with ITG driven turbulent diffusion being suppressed as the $\frac{T_i}{T_e}$ ratio outside mid-radius is increased. On the other hand the on- to off-axis ECRH scans with unchanging ion temperature profiles are much less likely to have ITG suppression as the explanation for the observed τ_I variation and consequently indicate that the mechanism is likely dependent on the core electron temperature profile.

References

[1] J. M. García-Regaña, M. Barnes, I. Calvo, F. I. Parra, J. A. Alcusón, R. Davies, A. González-Jerez, A. Mollén, E. Sánchez, J. L. Velasco, and et al. Turbulent impurity transport simulations in wendelstein 7-x plasmas. *Journal of Plasma Physics*, 87(1):855870103, 2021.

[2] P Helander, C D Beidler, T M Bird, M Drevlak, Y Feng, R Hatzky, F Jenko, R Kleiber, J H E Proll, Yu Turkin, and P Xanthopoulos. Stellarator and tokamak plasmas: a comparison. *Plasma Physics and Controlled Fusion*, 54(12):124009, nov 2012.

[3] R. Dux. Impurity transport in tokamak plasmas. *IPP Report 10/27, Max-Planck-Institut fur Plasmaphysik, Garching*, 2004.

[4] Alexander Charles Ince-Cushman. *Rotation Studies in Fusion Plasmas via Imaging X-ray Crystal Spectroscopy*. PhD thesis, Aug 2008.

[5] A. Langenberg. Radial unit comparison. 2017.

[6] N. Pablant, A. Langenberg, A. Alonso, J. Baldzuhn, C.D. Beidler, S. Bozhenkov, R. Burhenn, K.J. Brunner, A. Dinklage, G. Fuchert, O. Ford, D.A. Gates, J. Geiger, M. Hirsch, U. Höfel, Ye.O. Kazakov, J. Knauer, M. Krychowiak, H. Laqua, M. Landreman, S. Lazerson, H. Maaßberg, O. Marchuck, A. Mollen, E. Pasch, A. Pavone, S. Satake, T. Schröder, H.M. Smith, J. Svensson, P. Traverso, Y. Turkin, J.L. Velasco, A. von Stechow, F. Warmer, G. Weir, R.C. Wolf, and D. Zhang and. Investigation of the neoclassical ambipolar electric field in ion-root plasmas on w7-x. *Nuclear Fusion*, 60(3):036021, feb 2020.

[7] B. Geiger, Th. Wegner, C.D. Beidler, R. Burhenn, B. Buttenschön, R. Dux, A. Langenberg, N.A. Pablant, T. Pütterich, Y. Turkin, T. Windisch, V. Winters, M. Beurskens, C. Biedermann, K.J. Brunner, G. Cseh, H. Damm, F. Effenberg, G. Fuchert, O. Grulke, J.H. Harris, C. Killer, J. Knauer, G. Kocsis, A. Krämer-Flecken, T. Kremeyer, M. Krychowiak, O. Marchuk, D. Nicolai, K. Rahbarnia, G. Satheeswaran, J. Schilling, O. Schmitz, T. Schröder, T. Szepesi, H. Thomsen, H. Trimino Mora, P. Traverso, and D. Zhang. Observation of anomalous impurity transport during low-density experiments in w7-x with laser blow-off injections of iron. *Nuclear Fusion*, 59(4):046009, feb 2019.

[8] Thomas Sunn Pedersen, Ralf König, Maciej Krychowiak, Marcin Jakubowski, Jürgen Baldzuhn, Sergey Bozhenkov, Golo Fuchert, Andreas Langenberg, Holger Niemann, Daihong Zhang, Kian Rahbarnia, Hans-Stephan Bosch, Yevgen Kazakov, Sebastijan Brezinsek, Yu Gao, and Novimir Pablant and. First results from divertor operation in wendelstein 7-x. *Plasma Physics and Controlled Fusion*, 61(1):014035, nov 2018.

[9] T. Klinger, T. Andreeva, S. Bozhenkov, C. Brandt, R. Burhenn, B. Buttenschön, G. Fuchert, B. Geiger, O. Grulke, H.P. Laqua, N. Pablant, K. Rahbarnia, T. Stange, A. von Stechow, N. Tamura, H. Thomsen, Y. Turkin, T. Wegner, I. Abramovic, S. Äkäslompolo, J. Alcuson, P. Aleynikov, K. Aleynikova, A. Ali, A. Alonso, G. Anda, E. Ascasibar, J.P. Bähner, S.G. Baek, M. Balden, J. Baldzuhn, M. Banduch, T. Barbui, W. Behr, C. Beidler, A. Benndorf, C. Biedermann, W. Biel, B. Blackwell, E. Blanco, M. Blatzheim, S. Ballinger, T. Bluhm, D. Böckenhoff, B. Böswirth, L.-G. Böttger, M. Borchardt, V. Borsuk, J. Boscary, H.-S. Bosch, M. Beurskens, R. Brakel, H. Brand, T. Bräuer, H. Braune, S. Brezinsek, K.-J. Brunner, R. Bussiahn, V. Bykov, J. Cai, I. Calvo, B. Cannas, A. Cappa, A. Carls, D. Carralero, L. Carraro, B. Carvalho, F. Castejon, A. Charl, N. Chaudhary, D. Chauvin, F. Chernyshev, M. Cianciosa, R. Citarella, G. Claps, J. Coenen, M. Cole, M.J. Cole, F. Cordella, G. Cseh, A. Czarnecka, K. Czerski, M. Czerwinski, G. Czymek, A. da Molin, A. da Silva, H. Damm, A. de la Pena, S. Degenkolbe, C.P. Dhard, M. Dibon, A. Dinklage, T. Dittmar, M. Drevlak, P. Drewelow, P. Drews, F. Durodie, E. Edlund, P. van Eeten, F. Effenberg, G. Ehrke,

S. Elgeti, M. Endler, D. Ennis, H. Esteban, T. Estrada, J. Fellinger, Y. Feng, E. Flom, H. Fernandes, W.H. Fietz, W. Figacz, J. Fontdecaba, O. Ford, T. Fornal, H. Frerichs, A. Freund, T. Funaba, A. Galkowski, G. Gantenbein, Y. Gao, J. García Regaña, D. Gates, J. Geiger, V. Giannella, A. Gogoleva, B. Goncalves, A. Goriaev, D. Gradic, M. Grahl, J. Green, H. Greuner, A. Grosman, H. Grote, M. Gruca, C. Guerard, P. Hacker, X. Han, J.H. Harris, D. Hartmann, D. Hathiramani, B. Hein, B. Heinemann, P. Helander, S. Henneberg, M. Henkel, J. Hernandez Sanchez, C. Hidalgo, M. Hirsch, K.P. Hollfeld, U. Höfel, A. Hölting, D. Höschen, M. Houry, J. Howard, X. Huang, Z. Huang, M. Hubeny, M. Huber, H. Hunger, K. Ida, T. Ilkei, S. Illy, B. Israeli, S. Jablonski, M. Jakubowski, J. Jelonnek, H. Jenzsch, T. Jesche, M. Jia, P. Junghanns, J. Kacmarczyk, J.-P. Kallmeyer, U. Kamionka, H. Kasahara, W. Kasparek, Y.O. Kazakov, N. Kenmochi, C. Killer, A. Kirschner, R. Kleiber, J. Knauer, M. Knaup, A. Knieps, T. Kobarg, G. Koc-sis, F. Köchl, Y. Kolesnichenko, A. Könies, R. König, P. Kornejew, J.-P. Koschinsky, F. Köster, M. Krämer, R. Krampitz, A. Krämer-Flecken, N. Krawczyk, T. Kremeyer, J. Krom, M. Krychowiak, I. Ksiazek, M. Kubkowska, G. Kühner, T. Kurki-Suonio, P.A. Kurz, S. Kwak, M. Landreman, P. Lang, R. Lang, A. Langenberg, S. Langish, H. Laqua, R. Laube, S. Lazerson, C. Lechte, M. Lennartz, W. Leonhardt, C. Li, C. Li, Y. Li, Y. Liang, C. Linsmeier, S. Liu, J.-F. Lobsien, D. Loesser, J. Loizu Cisquella, J. Lore, A. Lorenz, M. Losert, A. Lücke, A. Lumsdaine, V. Lutsenko, H. Maaßberg, O. Marchuk, J.H. Matthew, S. Marsen, M. Marushchenko, S. Masuzaki, D. Maurer, M. Mayer, K. Mc-Carthy, P. McNeely, A. Meier, D. Mellein, B. Mendelevitch, P. Mertens, D. Mikkelsen, A. Mishchenko, B. Missal, J. Mittelstaedt, T. Mizuuchi, A. Mollen, V. Moncada, T. Mönnich, T. Morisaki, D. Moseev, S. Murakami, G. Náfrádi, M. Nagel, D. Nau-joks, H. Neilson, R. Neu, O. Neubauer, U. Neuner, T. Ngo, D. Nicolai, S.K. Nielsen, H. Niemann, T. Nishizawa, R. Nocentini, C. Nührenberg, J. Nührenberg, S. Ober-mayer, G. Offermanns, K. Ogawa, J. Ölmanns, J. Ongena, J.W. Oosterbeek, G. Orozco, M. Otte, L. Pacios Rodriguez, N. Panadero, N. Panadero Alvarez, D. Papenfuß, S. Paqay, E. Pasch, A. Pavone, E. Pawelec, T.S. Pedersen, G. Pelka, V. Perseo, B. Peterson, D. Pi-lopp, S. Pingel, F. Pisano, B. Plaum, G. Plunk, P. Pölöskei, M. Porkolab, J. Proll, M.-E.

Puiatti, A. Puig Sitjes, F. Purps, M. Rack, S. Récsei, A. Reiman, F. Reimold, D. Reiter, F. Remppel, S. Renard, R. Riedl, J. Riemann, K. Risse, V. Rohde, H. Röhlinger, M. Romé, D. Rondeshagen, P. Rong, B. Roth, L. Rudischhauser, K. Rummel, T. Rummel, A. Runov, N. Rust, L. Ryc, S. Ryosuke, R. Sakamoto, M. Salewski, A. Samartsev, E. Sanchez, F. Sano, S. Satake, J. Schacht, G. Satheeswaran, F. Schauer, T. Scherer, J. Schilling, A. Schlaich, G. Schlisio, F. Schluck, K.-H. Schlüter, J. Schmitt, H. Schmitz, O. Schmitz, S. Schmuck, M. Schneider, W. Schneider, P. Scholz, R. Schrittwieser, M. Schröder, T. Schröder, R. Schroeder, H. Schumacher, B. Schweer, E. Scott, S. Sereda, B. Shanahan, M. Sibilia, P. Sinha, S. Sipliä, C. Slaby, M. Sleczka, H. Smith, W. Spiess, D.A. Spong, A. Spring, R. Stadler, M. Stejner, L. Stephey, U. Stridde, C. Suzuki, J. Svensson, V. Szabó, T. Szabolics, T. Szepesi, Z. Szökefalvi-Nagy, A. Tancetti, J. Terry, J. Thomas, M. Thumm, J.M. Travere, P. Traverso, J. Tretter, H. Trimino Mora, H. Tsuchiya, T. Tsujimura, S. Tulipán, B. Unterberg, I. Vakulchyk, S. Valet, L. Vano, B. van Milligen, A.J. van Vuuren, L. Vela, J.-L. Velasco, M. Vergote, M. Vervier, N. Vianello, H. Viebke, R. Vilbrandt, A. Vorköper, S. Wadle, F. Wagne. Overview of first wendelstein 7-x high-performance operation. *Nuclear Fusion*, 59(11):112004, jun 2019.

[10] G. J. Hartwell, S. F. Knowlton, J. D. Hanson, D. A. Ennis, and D. A. Maurer. Design, construction, and operation of the compact toroidal hybrid. *Fusion Science and Technology*, 72(1):76–90, 2017.

[11] J D Lawson. Some criteria for a power producing thermonuclear reactor. 70(1):6–10, jan 1957.

[12] A. Gibson and J. B. Taylor. Single particle motion in toroidal stellarator fields. *The Physics of Fluids*, 10(12):2653–2659, 1967.

[13] John R. Cary, C. L. Hedrick, and J. S. Tolliver. Orbits in asymmetric toroidal magnetic fields. *The Physics of Fluids*, 31(6):1586–1600, 1988.

[14] R.L. Dewar and S.R. Hudson. Stellarator symmetry. *Physica D: Nonlinear Phenomena*, 112(1):275–280, 1998. Proceedings of the Workshop on Time-Reversal Symmetry in Dynamical Systems.

[15] Donald A. Spong. 3d toroidal physics: Testing the boundaries of symmetry breaking. *Physics of Plasmas*, 22(5):055602, 2015.

[16] Per Helander. Theory of plasma confinement in non-axisymmetric magnetic fields. *Reports on Progress in Physics*, 77(8):087001, jul 2014.

[17] H. E. Mynick. Transport optimization in stellarators. *Physics of Plasmas*, 13(5):058102, 2006.

[18] W. D. D'haeseleer, W. N. G. Hitchon, J. D. Callen, and J. L. Shohet. *Flux Coordinates and Magnetic Field Structure: A guide to a Fundamental Tool of Plasma Theory*. Springer-Verlag, 1991.

[19] G. Grieger, W. Lotz, P. Merkel, J. Nührenberg, J. Sapper, E. Strumberger, H. Wobig, R. Burhenn, V. Erckmann, U. Gasparino, L. Giannone, H. J. Hartfuss, R. Jaenicke, G. Kühner, H. Ringler, A. Weller, and F. Wagner. Physics optimization of stellarators. *Physics of Fluids B: Plasma Physics*, 4(7):2081–2091, 1992.

[20] Jürgen Nührenberg. Development of quasi-isodynamic stellarators. *Plasma Physics and Controlled Fusion*, 52(12):124003, nov 2010.

[21] Craig Beidler, Günter Grieger, Franz Herrnegger, Ewald Harmeyer, Johann Kisslinger, Wolf Lotz, Henning Maassberg, Peter Merkel, Jürgen Nührenberg, Fritz Rau, Jörg Sapper, Francesco Sardei, Ruben Scardovelli, Arnulf Schlüter, and Horst Wobig. Physics and engineering design for wendelstein vii-x. *Fusion Technology*, 17(1):148–168, 1990.

[22] T Klinger, A Alonso, S Bozhenkov, R Burhenn, A Dinklage, G Fuchert, J Geiger, O Grulke, A Langenberg, M Hirsch, G Kocsis, J Knauer, A Krämer-Flecken, H Laqua, S Lazerson, M Landreman, H Maaßberg, S Marsen, M Otte, N Pablant, E Pasch, K Rahbarnia, T Stange, T Szepesi, H Thomsen, P Traverso, J L Velasco, T Wauters, G Weir,

and T Windisch and. Performance and properties of the first plasmas of wendelstein 7-x. *Plasma Physics and Controlled Fusion*, 59(1):014018, oct 2016.

[23] T. Klinger. 16 - wendelstein 7-x. In George H. Neilson, editor, *Magnetic Fusion Energy*, pages 493–505. Woodhead Publishing, 2016.

[24] A. Dinklage, C. D. Beidler, P. Helander, G. Fuchert, H. Maaßberg, K. Rahbarnia, T. Sunn Pedersen, Y. Turkin, R. C. Wolf, A. Alonso, T. Andreeva, B. Blackwell, S. Bozhenkov, B. Buttenschön, A. Czarnecka, F. Effenberg, Y. Feng, J. Geiger, M. Hirsch, U. Höfel, M. Jakubowski, T. Klinger, J. Knauer, G. Kocsis, A. Krämer-Flecken, M. Kubkowska, A. Langenberg, H. P. Laqua, N. Marushchenko, A. Mollén, U. Neuner, H. Niemann, E. Pasch, N. Pablant, L. Rudischhauser, H. M. Smith, O. Schmitz, T. Stange, T. Szepesi, G. Weir, T. Windisch, G. A. Wurden, D. Zhang, I. Abramovic, S. Äkäslompolo, A. Ali, J.Alcuson Belloso, P. Aleynikov, K. Aleynikova, R. Alzbutas, G. Anda, E. Ascasibar, J. Assmann, S.-G. Baek, J. Baldzuhn, M. Banduch, T. Barbui, M. Barlak, K. Baumann, W. Behr, C. Beidler, A. Benndorf, O. Bertuch, M. Beurskens, C. Biedermann, W. Biel, D. Birus, E. Blanco, M. Blatzheim, T. Bluhm, D. Böckenhoff, P. Bolgert, M. Borchardt, V. Borsuk, J. Boscary, H.-S. Bosch, L.-G. Böttger, R. Brakel, H. Brand, Ch. Brandt, T. Bräuer, H. Braune, S. Brezinsek, K.-J. Brunner, B. Brünner, R. Burhenn, R. Bussiahn, V. Bykov, Y. Cai, I. Calvo, B. Cannas, A. Cappa, A. Card, A. Carls, L. Carraro, B. Carvalho, F. Castejon, A. Charl, F. Chernyshev, M. Cianciosa, R. Citarella, Ł Ciupiński, G. Claps, M. J. Cole, F. Cordella, G. Cseh, A. Czermak, K. Czerski, M. Czerwinski, G. Czymek, A. da Molin, A. da Silva, G. Dammertz, A. de la Pena, S. Degenkolbe, P. Denner, T. Dittmar, C. P. Dhard, M. Dostal, M. Drevlak, P. Drewelow, Ph. Drews, A. Dudek, G. Dundulis, F. Durodie, P. van Eeten, G. Ehrke, M. Endler, D. Ennis, E. Erckmann, H. Esteban, T. Estrada, N. Fahrenkamp, J.-H. Feist, J. Fellinger, H. Fernandes, W. H. Fietz, W. Figacz, J. Fontdecaba, O. Ford, T. Fornal, H. Frerichs, A. Freund, M. Führer, T. Funaba, A. Galkowski, G. Gantenbein, Y. Gao, J.García Regaña, M. Garcia-Munoz, D. Gates, G. Gawlik, B. Geiger, V. Giannella, N. Gierse, A. Gogoleva, B. Goncalves, A. Goriaev, D. Gradic,

M. Grahl, J. Green, A. Grosman, H. Grote, M. Gruca, O. Grulke, C. Guerard, P. Hacker, L. Haiduk, K. Hammond, X. Han, F. Harberts, J. H. Harris, H.-J. Hartfuß, D. Hartmann, D. Hathiramani, B. Hein, B. Heinemann, P. Heitzenroeder, S. Henneberg, C. Hennig, J.Hernandez Sanchez, C. Hidalgo, H. Hölbe, K. P. Hollfeld, A. Hölting, D. Höschen, M. Houry, J. Howard, X. Huang, M. Huber, V. Huber, H. Hunger, K. Ida, T. Ilkei, S. Illy, B. Israeli, A. Ivanov, S. Jablonski, J. Jagielski, J. Jelonnek, H. Jenzsch, P. Junghans, J. Kacmarczyk, T. Kaliatka, J.-P. Kallmeyer, U. Kamionka, R. Karalevicius, H. Kasahara, W. Kasparek, Y. Kazakov, N. Kenmochi, M. Keunecke, A. Khilchenko, C. Killer, D. Kinna, R. Kleiber, M. Knaup, A. Knieps, Th. Kobarg, F. Köchl, Y. Kolesnichenko, A. Könies, M. Köppen, J. Koshurinov, R. Koslowski, R. König, F. Köster, P. Kornejew, R. Koziol, M. Krämer, R. Krampitz, P. Kraszewsk, N. Krawczyk, T. Kremeyer, Th. Krings, J. Krom, M. Krychowiak, G. Krzesinski, I. Ksiazek, G. Kühner, T. Kurki-Suonio, S. Kwak, M. Landreman, R. Lang, S. Langish, H. Laqua, H. P. Laqua, R. Laube, S. Lazerson, C. Lechte, M. Lennartz, W. Leonhardt, L. Lewerentz, Y. Liang, Ch. Linsmeier, S. Liu, J.-F. Lobsien, D. Loesser, J.Loizu Cisquella, J. Lore, A. Lorenz, M. Losert, L. Lubyako, A. Lücke, A. Lumsdaine, V. Lutsenko, J. Maisano-Brown, O. Marchuk, M. Mardenfeld, P. Marek, S. Marsen, M. Marushchenko, S. Masuzaki, D. Maurer, K. McCarthy, P. McNeely, A. Meier, , and the W7-X Team. Magnetic configuration effects on the wendelstein 7-x stellarator. *Nature Physics*, 14(8):855–860, Aug 2018.

[25] W Lotz, P Merkel, J Nuhrenberg, and E Strumberger. Collisionless alpha -particle confinement in stellarators. *Plasma Physics and Controlled Fusion*, 34(6):1037–1052, jun 1992.

[26] Robert C. WOLF, Craig D. BEIDLER, Rainer BURHENN, Joachim GEIGER, Matthias HIRSCH, Johann KISSLINGER, Henning MAASSBERG, Arthur WELLER, Andreas WERNER, and the Wendelstein 7-X Team. From wendelstein 7-x to a stellarator reactor. *Plasma and Fusion Research*, 5:S1011–S1011, 2010.

[27] C.D. Beidler, K. Allmaier, M.Yu. Isaev, S.V. Kasilov, W. Kernbichler, G.O. Leitold, H. Maaßberg, D.R. Mikkelsen, S. Murakami, M. Schmidt, D.A. Spong, V. Tribaldos,

and A. Wakasa. Benchmarking of the mono-energetic transport coefficients—results from the international collaboration on neoclassical transport in stellarators (ICNTS). *Nuclear Fusion*, 51(7):076001, jun 2011.

[28] S. Buller, H. M. Smith, P. Helander, A. Mollén, S. L. Newton, and I. Pusztai. Collisional transport of impurities with flux-surface varying density in stellarators. *Journal of Plasma Physics*, 84(4):905840409, 2018.

[29] P. Helander and D.J. Sigmar. *Collisional Transport in Magnetized Plasmas*. Cambridge Monographs on Plasma Physics. Cambridge University Press, 2005.

[30] S. Buller, A. Mollén, S. L. Newton, H. M. Smith, and I. Pusztai. The importance of the classical channel in the impurity transport of optimized stellarators. *Journal of Plasma Physics*, 85(4):175850401, 2019.

[31] C.D Beidler, W.N.G Hitchon, and J.L Shohet. "hybrid" monte carlo simulation of ripple transport in stellarators. *Journal of Computational Physics*, 72(1):220–242, 1987.

[32] C D Beidler and W N G Hitchon. Ripple transport in helical-axis advanced stellarators: a comparison with classical stellarator/torsatrons. *Plasma Physics and Controlled Fusion*, 36(2):317–353, feb 1994.

[33] J. H. E. Proll, P. Xanthopoulos, and P. Helander. Collisionless microinstabilities in stellarators. ii. numerical simulations. *Physics of Plasmas*, 20(12):122506, 2013.

[34] *Fusion Physics*. Non-serial Publications. INTERNATIONAL ATOMIC ENERGY AGENCY, Vienna, 2012.

[35] E.J. Doyle (Chair Transport Physics), W.A. Houlberg (Chair Confinement Da Modelling), Y. Kamada (Chair Pedestal, Edge), V. Mukhovatov (co Chair Transport Physics), T.H. Osborne (co Chair Pedestal, Edge), A. Polevoi (co Chair Confinement Da Modelling), G Bateman, J.W Connor, J.G. Cordey (retired), T Fujita, X Garbet, T.S Hahm, L.D Horton, A.E Hubbard, F Imbeaux, F Jenko, J.E Kinsey, Y Kishimoto, J Li, T.C Luce, Y Martin, M Ossipenko, V Parail, A Peeters, T.L Rhodes, J.E Rice, C.M Roach,

V Rozhansky, F Ryter, G Saibene, R Sartori, A.C.C Sips, J.A Snipes, M Sugihara, E.J Synakowski, H Takenaga, T Takizuka, K Thomsen, M.R Wade, H.R Wilson, ITPA Transport Physics Topical Group, ITPA Confinement Database, Model Group, ITPA Pedestal, and Edge Topical Group. Chapter 2: Plasma confinement and transport. *Nuclear Fusion*, 47(6):S18–S127, jun 2007.

[36] ITER Physics Expert Group on Confin Transport, ITER Physics Expert Group on Confin Database, and ITER Physics Basis Editors. Chapter 2: Plasma confinement and transport. *Nuclear Fusion*, 39(12):2175–2249, dec 1999.

[37] R. Burhenn, Y. Feng, K. Ida, H. Maassberg, K.J. McCarthy, D. Kalinina, M. Kobayashi, S. Morita, Y. Nakamura, H. Nozato, S. Okamura, S. Sudo, C. Suzuki, N. Tamura, A. Weller, M. Yoshinuma, and B. Zurro. On impurity handling in high performance stellarator/heliotron plasmas. *Nuclear Fusion*, 49(6):065005, apr 2009.

[38] Josefine Henriette Elise Proll. *Trapped-particle instabilities in quasi-isodynamic stellarators*. PhD thesis, jan 2014.

[39] G. G. Plunk, P. Xanthopoulos, G. M. Weir, S. A. Bozhenkov, A. Dinklage, G. Fuchert, J. Geiger, M. Hirsch, U. Hoefel, M. Jakubowski, A. Langenberg, N. Pablant, E. Pasch, T. Stange, D. Zhang, and the W7-X Team. Stellarators resist turbulent transport on the electron larmor scale. *Phys. Rev. Lett.*, 122:035002, Jan 2019.

[40] Thomas Wegner, Jorge Alberto Alcuson, Benedikt Geiger, Adrian von Stechow, Pavlos Xanthopoulos, Clemente Angioni, Marc N A Beurskens, Lukas Böttger, Sergey A Bozhenkov, Kai Jakob Brunner, Rainer Burhenn, Birger Buttenschön, Hannes Damm, Eric M Edlund, Oliver P Ford, Golo Fuchert, Olaf Grulke, Zhouji Huang, Jens P Knauer, Falk Kunkel, Andreas Langenberg, Novimir Antoniuk Pablant, Ekkehard Pasch, Kian Rahbarnia, Jonathan Schilling, H Thomsen, and Lilla Vano. Impact of the temperature ratio on turbulent impurity transport in wendelstein 7-x. *Nuclear Fusion*, sep 2020.

[41] Albert Mollen. *Impurity transport in magnetically confined fusion plasmas*. PhD thesis, Goteborg, 2015.

[42] P. Helander, J. H. E. Proll, and G. G. Plunk. Collisionless microinstabilities in stellarators. i. analytical theory of trapped-particle modes. *Physics of Plasmas*, 20(12):122505, 2013.

[43] G. G. Plunk, P. Helander, P. Xanthopoulos, and J. W. Connor. Collisionless microinstabilities in stellarators. iii. the ion-temperature-gradient mode. *Physics of Plasmas*, 21(3):032112, 2014.

[44] G. G. Plunk, J. W. Connor, and P. Helander. Collisionless microinstabilities in stellarators. part 4. the ion-driven trapped-electron mode. *Journal of Plasma Physics*, 83(4):715830404, 2017.

[45] P. Helander, S. L. Newton, A. Mollén, and H. M. Smith. Impurity transport in a mixed-collisionality stellarator plasma. *Phys. Rev. Lett.*, 118:155002, Apr 2017.

[46] S. L. Newton, P. Helander, A. Mollén, and H. M. Smith. Impurity transport and bulk ion flow in a mixed collisionality stellarator plasma. *Journal of Plasma Physics*, 83(5):905830505, 2017.

[47] Masanori Nunami, M. Nakata, S. Toda, and H. Sugama. Gyrokinetic simulations for turbulent transport of multi-ion-species plasmas in helical systems. *Physics of Plasmas*, 27:052501, 05 2020.

[48] J M García-Regaña, R Kleiber, C D Beidler, Y Turkin, H Maaßberg, and P Helander. On neoclassical impurity transport in stellarator geometry. *Plasma Physics and Controlled Fusion*, 55(7):074008, jun 2013.

[49] A. Mollén, M. Landreman, H. M. Smith, S. Braun, and P. Helander. Impurities in a non-axisymmetric plasma: Transport and effect on bootstrap current. *Physics of Plasmas*, 22(11):112508, 2015.

[50] M. Yokoyama, H. Maassberg, C. D. Beidler, V. Tribaldos, K. Ida, F. Castejón, T. Estrada, A. Fujisawa, T. Minami, T. Shimozuma, Y. Takeiri, J. Herranz, S. Murakami, and H. Yamada. Common features of core electron-root confinement in helical devices. *Fusion Science and Technology*, 50(3):327–342, 2006.

[51] M. Yokoyama, H. Maaßberg, C.D. Beidler, V. Tribaldos, K. Ida, T. Estrada, F. Castejon, A. Fujisawa, T. Minami, T. Shimozuma, Y. Takeiri, A. Dinklage, S. Murakami, and H. Yamada. Core electron-root confinement (CERC) in helical plasmas. *Nuclear Fusion*, 47(9):1213–1219, aug 2007.

[52] H. Maassberg, R. Burhenn, U. Gasparino, G. Kühner, H. Ringler, and K. S. Dyabilin. Experimental and neoclassical electron heat transport in the lmfp regime for the stellarators w7-a, l-2, and w7-as. *Physics of Fluids B: Plasma Physics*, 5(10):3627–3640, 1993.

[53] W. I. van Rij and S. P. Hirshman. Variational bounds for transport coefficients in three-dimensional toroidal plasmas. *Physics of Fluids B: Plasma Physics*, 1(3):563–569, 1989.

[54] Y Nakamura, Y Takeiri, R Kumazawa, M Osakabe, T Seki, B.J Peterson, K Ida, H Funaba, M Yokoyama, N Tamura, A Komori, S Morita, K Sato, K Narihara, S Inagaki, T Tokuzawa, S Masuzaki, J Miyazawa, N Noda, T Mutoh, T Shimozuma, K Kawahata, Y Oka, H Suzuki, N Ohyabu, T Akiyama, N Ashikawa, M Emoto, P Goncharov, M Goto, H Idei, K Ikeda, S Imagawa, M Isobe, O Kaneko, H Kawazome, K Khlopenkov, T Kobuchi, A Kostrioukov, S Kubo, Y Liang, T Minami, T Morisaki, S Murakami, S Muto, K Nagaoka, Y Nagayama, H Nakanishi, Y Narushima, K Nishimura, T Notake, H Nozato, S Ohdachi, S Okamura, T Ozaki, A Sagara, T Saida, K Saito, S Sakakibara, R Sakamoto, M Sasao, M Sato, M Shoji, N Takeuchi, K Tanaka, M.Y Tanaka, K Toi, Y Torii, K Tsumori, K.Y Watanabe, T Watari, Y Xu, H Yamada, I Yamada, S Yamamoto, T Yamamoto, S Yoshimura, Y Yoshimura, M Yoshinuma, K Itoh, T Mito, K Ohkubo, I Ohtake, T Satow, S Sudo, T Uda, K Yamazaki, K Matsuoka, O Motojima, Y Hamada,

and M Fujiwara. Plasma performance and impurity behaviour in long pulse discharges on LHD. *Nuclear Fusion*, 43(4):219–227, mar 2003.

[55] N. Tamura, C. Suzuki, S. Satake, Y. Nakamura, M. Nunami, H. Funaba, K. Tanaka, M. Yoshinuma, K. Ida, and S. Sudo. Observation of the ech effect on the impurity accumulation in the lhd. *Physics of Plasmas*, 24(5):056118, 2017.

[56] Rainer Burhenn, Jürgen Baldzuhn, Rudolf Brakel, Hartmut Ehmler, Louis Giannone, Peter Eckhard Grigull, Jens Knauer, Maciej Krychowiak, Matthias Hirsch, Katsumi Ida, Henning Maassberg, Gerald Kent McCormick, Ekkehard Pasch, Henning Thomsen, Arthur Wel, W7-As Team, Ecrh Group, and NI Group. Impurity transport studies in the wendelstein 7-as stellarator. *Fusion Science and Technology*, 46(1):115–128, 2004.

[57] Y. Nakamura, N. Tamura, M. Kobayashi, S. Yoshimura, C. Suzuki, M. Yoshinuma, M. Goto, G. Motojima, K. Nagaoka, K. Tanaka, R. Sakamoto, B.J. Peterson, K. Ida, M. Osakabe, and T. Morisaki. A comprehensive study on impurity behavior in lhd long pulse discharges. *Nuclear Materials and Energy*, 12:124 – 132, 2017. Proceedings of the 22nd International Conference on Plasma Surface Interactions 2016, 22nd PSI.

[58] A Langenberg, F Warmer, G Fuchert, O Marchuk, A Dinklage, Th Wegner, J A Alonso, S Bozhenkov, K J Brunner, R Burhenn, B Buttenschön, P Drews, B Geiger, O Grulke, M Hirsch, U Höfel, K P Hollfeld, C Killer, J Knauer, T Krings, F Kunkel, U Neuner, G Offermanns, N A Pablant, E Pasch, K Rahbarnia, G Satheeswaran, J Schilling, B Schweer, H Thomsen, P Traverso, and R C Wolf and. Impurity transport studies at wendelstein 7-x by means of x-ray imaging spectrometer measurements. *Plasma Physics and Controlled Fusion*, 61(1):014030, Nov 2018.

[59] G. Bertschinger, W. Biel, H. Jaegers, and O. Marchuk. Compact imaging bragg spectrometer for fusion devices. *Review of Scientific Instruments*, 75(10):3727–3729, 2004.

[60] M. Bitter, K. W. Hill, A. L. Roquemore, P. Beiersdorfer, S. M. Kahn, S. R. Elliott, and B. Fraenkel. Imaging x-ray crystal spectrometers for the national spherical torus experiment. *Review of Scientific Instruments*, 70(1):292–295, 1999.

[61] N A Pablant, M Bitter, R Burhenn, L Delgado-Aparicio, R Ellis, D Gates, M Goto, K W Hill, A Langenberg, S Lazerson, M Mardenfeld, S Morita, G H Neilson, T Oishi, and T S Pedersen. Measurement of core plasma temperature and rotation on w7-x made available by the x-ray imaging crystal spectrometer (xics). *Invited papers to be published in a special issue of Plasma Physics and Controlled Fusion.*, 38F(P1.076), 7 2014.

[62] N. A. Pablant, A. Langenberg, J. A. Alonso, M. Bitter, S. A. Bozhenkov, O. P. Ford, K. W. Hill, J. Kring, O. Marchuck, J. Svensson, P. Traverso, T. Windisch, and Y. Yakusevitch. Correction and verification of x-ray imaging crystal spectrometer analysis on wendelstein 7-x through x-ray ray tracing. *Review of Scientific Instruments*, 92(4):043530, 2021.

[63] N. A. Pablant, A. Langenberg, A. Alonso, C. D. Beidler, M. Bitter, S. Bozhenkov, R. Burhenn, M. Beurskens, L. Delgado-Aparicio, A. Dinklage, G. Fuchert, D. Gates, J. Geiger, K. W. Hill, U. Höfel, M. Hirsch, J. Knauer, A. Krämer-Flecken, M. Landreman, S. Lazerson, H. Maaßberg, O. Marchuk, S. Massidda, G. H. Neilson, E. Pasch, S. Satake, J. Svennson, P. Traverso, Y. Turkin, P. Valson, J. L. Velasco, G. Weir, T. Windisch, R. C. Wolf, M. Yokoyama, and D. Zhang. Core radial electric field and transport in wendelstein 7-x plasmas. *Physics of Plasmas*, 25(2):022508, 2018.

[64] A Langenberg, N Pablant, Thomas Wegner, P Traverso, O Marchuk, Tiziana Bräuer, B Geiger, Golo Fuchert, S Bozhenkov, E. Pasch, Olaf Grulke, F Kunkel, Carsten Killer, Dirk Nicolai, G Satheeswaran, K Hollfeld, B. Schweer, T Krings, Philipp Drews, and R Wolf. Prospects of x-ray imaging spectrometers for impurity transport: Recent results from the stellarator wendelstein 7-x (invited). *The Review of scientific instruments*, 89:10G101, 10 2018.

[65] A. Langenberg, Th. Wegner, N. A. Pablant, O. Marchuk, B. Geiger, N. Tamura, R. Bussiahn, M. Kubkowska, A. Mollén, P. Traverso, H. M. Smith, G. Fuchert, S. Bozhenkov, H. Damm, E. Pasch, K.-J. Brunner, J. Knauer, M. Beurskens, R. Burhenn, and R. C.

Wolf. Charge-state independent anomalous transport for a wide range of different impurity species observed at wendelstein 7-x. *Physics of Plasmas*, 27(5):052510, 2020.

[66] W. Biel, G. Bertschinger, R. Burhenn, R. König, and E. Jourdain. Design of a high–efficiency extreme ultraviolet overview spectrometer system for plasma impurity studies on the stellarator experiment wendelstein 7-x. *Review of Scientific Instruments*, 75(10):3268–3275, 2004.

[67] H. Thomsen, A. Langenberg, D. Zhang, G. Bertschinger, C. Biedermann, W. Biel, R. Burhenn, B. Buttenschön, K. Grosser, R. König, M. Kubkowska, O. Marchuk, N. Pablant, L. Ryc, and T.S. Pedersen and. Startup impurity diagnostics in wendelstein 7-x stellarator in the first operational phase. *Journal of Instrumentation*, 10(10):P10015–P10015, oct 2015.

[68] Th. Wegner, B. Geiger, F. Kunkel, R. Burhenn, T. Schröder, C. Biedermann, B. Buttenschön, G. Cseh, P. Drews, O. Grulke, K. Hollfeld, C. Killer, G. Kocsis, T. Krings, A. Langenberg, O. Marchuk, U. Neuner, D. Nicolai, G. Offermanns, N. A. Pablant, K. Rahbarnia, G. Satheeswaran, J. Schilling, B. Schweer, T. Szepesi, and H. Thomsen. Design, capabilities, and first results of the new laser blow-off system on wendelstein 7-x. *Review of Scientific Instruments*, 89(7):073505, 2018.

[69] V. Erckmann, P. Brand, H. Braune, G. Dammertz, G. Gantenbein, W. Kasparek, H. P. Laqua, H. Maassberg, N. B. Marushchenko, G. Michel, M. Thumm, Y. Turkin, M. Weissgerber, A. Weller, W7-X ECRH Team at IPP Greifswald, W7-X ECRH Team at FZK Karlsruhe, and W7-X ECRH Team at IPF Stuttgart. Electron cyclotron heating for w7-x: Physics and technology. *Fusion Science and Technology*, 52(2):291–312, 2007.

[70] B. Plaum, C. Lechte, W. Kasparek, S. Gaiser, A. Zeitler, V. Erckmann, M. Weißgerber, A. Bechtold, M. Busch, and B. Szcepaniak. Design of a remote steering antenna for ecrh heating in the stellarator wendelstein 7-x. *Fusion Engineering and Design*, 96-97:568–572, 2015. Proceedings of the 28th Symposium On Fusion Technology (SOFT-28).

[71] E. Pasch, M. N. A. Beurskens, S. A. Bozhenkov, G. Fuchert, J. Knauer, and R. C. Wolf. The thomson scattering system at wendelstein 7-x. *Review of Scientific Instruments*, 87(11):11E729, 2016.

[72] M.A. Chilenski, M. Greenwald, Y. Marzouk, N.T. Howard, A.E. White, J.E. Rice, and J.R. Walk. Improved profile fitting and quantification of uncertainty in experimental measurements of impurity transport coefficients using gaussian process regression. *Nuclear Fusion*, 55(2):023012, jan 2015.

[73] Jens Knauer, P. Kornejew, H. Trimino Mora, Matthias Hirsch, A. Werner, and Robert C. Wolf. A new dispersion interferometer for the stellarator wendelstein 7-x. 2016.

[74] H. M. Smith. Neotransp, 2019.

[75] K. Behringer. Description of the impurity transport code 'strahl'. Technical report, Abingdon, 1987.

[76] R. Dux. *STRAHL User Manual*, 2006.

[77] The ADAS project, version 2.1, 1995-2019.

[78] Carsten Killer. Personal communication, September 30th 2018.

[79] P. Sinha, H. Hölbe, T.S. Pedersen, and S. Bozhenkov and. Numerical studies of scrape-off layer connection length in wendelstein7-x. *Nuclear Fusion*, 58(1):016027, nov 2017.

[80] Carsten Killer, Olaf Grulke, Philipp Drews, Yu Gao, Marcin Jakubowski, Alexander Knieps, Dirk Nicolai, Holger Niemann, Aleix Puig Sitjes, and Guruparan Satheeswaran and. Characterization of the w7-x scrape-off layer using reciprocating probes. *Nuclear Fusion*, 59(8):086013, jun 2019.

[81] Craig B. Markwardt. Non-linear least squares fitting in idl with mpfit, 2009.

[82] N. A. Pablant, R. E. Bell, M. Bitter, L. Delgado-Aparicio, K. W. Hill, S. Lazerson, and S. Morita. Tomographic inversion techniques incorporating physical constraints for line

integrated spectroscopy in stellarators and tokamaks. *Review of Scientific Instruments*, 85(11):11E424, 2014.

[83] Jörg Schacht, Heike Laqua, Marc Lewerentz, Ina Müller, Steffen Pingel, Anett Spring, and Andreas Wölk. Overview and status of the control system of wendelstein 7-x. *Fusion Engineering and Design*, 82(5):988–994, 2007. Proceedings of the 24th Symposium on Fusion Technology.

[84] J. Schacht, D. Naujoks, S. Pingel, A. Wölk, U. Herbst, S. Degenkolbe, A. Winter, R. Vilbrandt, and H.-S. Bosch. Realization of the requirements for a safe operation of wendelstein 7-x. *Fusion Engineering and Design*, 152:111468, 2020.

[85] L. Stephey, G. A. Wurden, O. Schmitz, H. Frerichs, F. Effenberg, C. Biedermann, J. Harris, R. König, P. Kornejew, M. Krychowiak, and E. A. Unterberg. Spectroscopic imaging of limiter heat and particle fluxes and the resulting impurity sources during wendelstein 7-x startup plasmas. *Review of Scientific Instruments*, 87(11):11D606, 2016.

[86] B. LaBombard. Kn1d: A 1d space, 2d velocity, kinetic transport algorithm for atomic and molecular hydrogen in an ionizing plasma. 2001.

[87] J.M. García-Regaña, C.D. Beidler, R. Kleiber, P. Helander, A. Mollén, J.A. Alonso, M. Landreman, H. Maaßberg, H.M. Smith, Y. Turkin, and J.L. Velasco. Electrostatic potential variation on the flux surface and its impact on impurity transport. *Nuclear Fusion*, 57(5):056004, mar 2017.

[88] A Mollén, M Landreman, H M Smith, J M García-Regaña, and M Nunami. Flux-surface variations of the electrostatic potential in stellarators: impact on the radial electric field and neoclassical impurity transport. *Plasma Physics and Controlled Fusion*, 60(8):084001, jun 2018.

[89] Iván Calvo, José Luis Velasco, Félix I. Parra, J. Arturo Alonso, and José Manuel García-Regaña. Electrostatic potential variations on stellarator magnetic surfaces in low collisionality regimes. *Journal of Plasma Physics*, 84(4):905840407, 2018.

[90] J M García-Regaña, T Estrada, I Calvo, J L Velasco, J A Alonso, D Carralero, R Kleiber, M Landreman, A Mollén, E Sánchez, and C Slaby and. On-surface potential and radial electric field variations in electron root stellarator plasmas. *Plasma Physics and Controlled Fusion*, 60(10):104002, aug 2018.

[91] T. Pütterich, E. Fable, R. Dux, M. O'Mullane, R. Neu, and M. Siccinio. Determination of the tolerable impurity concentrations in a fusion reactor using a consistent set of cooling factors. *Nuclear Fusion*, 59(5):056013, mar 2019.

[92] M. Landreman, H. M. Smith, A. Mollén, and P. Helander. Comparison of particle trajectories and collision operators for collisional transport in nonaxisymmetric plasmas. *Physics of Plasmas*, 21(4):042503, 2014.

[93] A. Langenberg. Iron transport time estimation. 2020.

[94] J. H. E. Proll, P. Helander, J. W. Connor, and G. G. Plunk. Resilience of quasi-isodynamic stellarators against trapped-particle instabilities. *Phys. Rev. Lett.*, 108:245002, Jun 2012.

[95] A. Zocco, P. Xanthopoulos, H. Doerk, J. W. Connor, and P. Helander. Threshold for the destabilisation of the ion-temperature-gradient mode in magnetically confined toroidal plasmas. *Journal of Plasma Physics*, 84(1):715840101, 2018.

[96] E. M. Edlund, M. Porkolab, Z. Huang, O. Grulke, L.-G. Böttger, C. von Sehren, and A. von Stechow. Overview of the wendelstein 7-x phase contrast imaging diagnostic. *Review of Scientific Instruments*, 89(10):10E105, 2018.

[97] P. J. Traverso, D. A. Maurer, D. A. Ennis, G. J. Hartwell, M. M. Goforth, S. D. Loch, A. J. Pearce, and M. R. Cianciosa. Thomson scattering diagnostic system design for the compact toroidal hybrid experiment. *Review of Scientific Instruments*, 85(11):11D852, 2014.

[98] Edward T. Gerry and D. J. Rose. Plasma diagnostics by thomson scattering of a laser beam. *Journal of Applied Physics*, 37(7):2715–2724, 1966.

[99] D. J. Schlossberg, G. M. Bodner, M. W. Bongard, R. J. Fonck, J. A. Reusch, and C. Rodriguez Sanchez. A novel, cost-effective, multi-point thomson scattering system on the pegasus toroidal experiment (invited). *Review of Scientific Instruments*, 87(11):11E403, 2016.

[100] D. M. Ponce-Marquez, B. D. Bray, T. M. Deterly, C. Liu, and D. Eldon. Thomson scattering diagnostic upgrade on diii-d. *Review of Scientific Instruments*, 81(10):10D525, 2010.

[101] D. Johnson, N. Bretz, D. Dimock, B. Grek, D. Long, R. Palladino, and E. Tolnas. Multichannel thomson scattering systems with high spatial resolution (invited). *Review of Scientific Instruments*, 57(8):1856–1861, 1986.

[102] Dustin H. Froula, Siegfried H. Glenzer, Neville C. Luhmann, and John Sheffield. Chapter 4 - noncollective scattering. In Dustin H. Froula, Siegfried H. Glenzer, Neville C. Luhmann, and John Sheffield, editors, *Plasma Scattering of Electromagnetic Radiation (Second Edition)*, pages 69–102. Academic Press, Boston, second edition edition, 2011.

[103] I. H. Hutchinson. *Principles of Plasma Diagnostics*. Cambridge University Press, 2 edition, 2002.

[104] 2021.

[105] N. L. Schoenbeck, D. J. Schlossberg, A. S. Dowd, R. J. Fonck, and G. R. Winz. A compact multichannel spectrometer for thomson scattering. *Review of Scientific Instruments*, 83(10):10E330, 2012.

[106] Haiyin Sun. *Laser Diode Beam Propagation Basics*, pages 21–37. Springer Netherlands, Dordrecht, 2012.

[107] Mikhail Polyanskiy. Refractiveindex.info.

[108] Paul Lutus. Opticalraytracer, 2017.

[109] *Photomultiplier Tubes Basics and Applications*. Hamamatsu Photonics, 3a edition, 2007.

[110] H. Haken and H. C. Wolf. *Molecular physics and elements of quantum chemistry: introduction to experiments and theory*. Springer, 2011.

[111] Marcus Johannes van de Sande. *Laser scattering on low temperature plasmas: high resolution and stray light rejection*. PhD thesis, 2002.

[112] C. M. Penney, R. L. St. Peters, and M. Lapp. Absolute rotational raman cross sections for n2, o2, and co2. *J. Opt. Soc. Am.*, 64(5):712–716, May 1974.

Appendices

Appendix A

Thomson scattering diagnostic on the Compact Toroidal Hybrid

This appendix begins with a brief introduction to the Compact Toroidal Hybrid (CTH) experiment where design & installation work on a thomson scattering diagnostic was performed for completion of this thesis. Then the appendix continues on to describe the design and partial implementation of a thomson scattering system on CTH.[97] Therefore the appendix is split into five sections with the first section introducing CTH before covering the basics of thomson scattering as a plasma diagnostic in the second section. Following this introduction the CTH specific beamline and collection optics are each discussed in the next two sections with details covering the design choices and hardware implementation. Finally the last section covers the initial measurements performed to confirm signal levels and system alignment.

A.1 Compact Toroidal Hybrid (CTH)

The Compact Toroidal Hybrid (CTH) is a low aspect ratio ($\frac{R}{a} \approx 3.5$) five-field period torsatron with a continuously wound helical coil (i.e. $l = 2$ & $m = 5$) providing the majority of the toroidal field with key parameters found in table A.1.[10] Although CTH can generate nested flux surfaces in a pure stellarator fashion, the predominant CTH operation occurs in the hybrid mode where a central solenoid provides both poloidal field and ohmic heating to the plasma through transformer action. In fact figure A.1 shows CTH nested flux surfaces during an ohmic discharge with the shaded color corresponding to the magnetic field strength ($|B|$) and the gray lines representing individual field lines. The unique coil geometry of CTH provides experimental flexibility in the shaping of the nested magnetic flux surfaces by controlling the relative poloidal field contributions from the helical field coil versus the ohmically

Parameter	Dimension
Major radius (R_0)	0.75 m
Inner vacuum vessel radius (a_{vessel})	0.29 m
Toroidally averaged B-field along the magnetic axis (B_0)	0.64 T
Input ECRH heating	$\leq$ 15 kW
Input OH heating	$\leq$ 100 kW
Average plasma minor radius (a_0)	0.2 m
Line-averaged density (n_{e})	$\leq 5.0 \times 10^{19}\,\mathrm{m}^{-3}$
Electron temperature (T_{e})	$\leq$ 200 eV
Discharge length	$\leq$ 200 ms

Table A.1: CTH key parameters (see [Hartwell et al. 10] for more details)

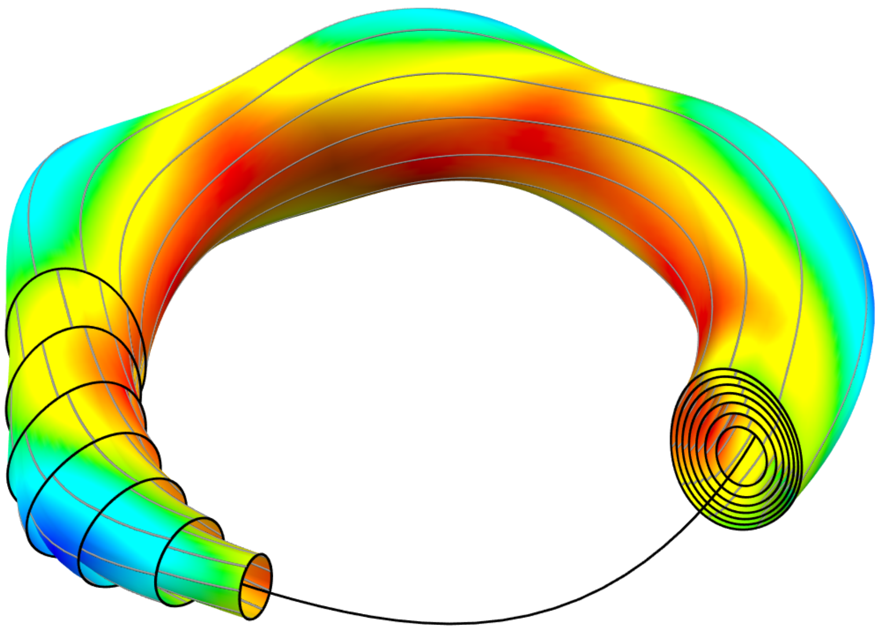

Figure A.1: The magnetic field lines in gray are displayed on the nested flux surfaces of CTH during an ohmic discharge with the color indicating the normalized strength of the magnetic field with red corresponding to higher levels of $\langle|B|\rangle$.

driven plasma current. Accordingly CTH has the ability to study plasma phenomena under both stellarator-like and tokamak-like operation. When operating with a hybrid discharge by ohmically-driving toroidal plasma current, CTH mainly focuses on disruption and Magneto-HydroDynamic (MHD) instability studies. Although CTH has these tokamak-like discharges, it still is far from axisymmetric and in no way has its magnetic field optimized for improved confinement. Therefore as discussed in section 1.1.1 particles can be helically trapped causing rapid losses due to the poloidal localization of the trapped particle leading to drifts off the flux surface. However as a device investigating MHD instabilities and current-driven disruptions as a function of applied external 3D fields, the lack of transport optimization is not important.

Although impurity transport studies were not performed on CTH, its basic magnetic geometry can provide context for the Wendelstein 7-X optimization as will be discussed in the next subsection. Additionally much of the work performed for the completion of this thesis went towards the design and partial implementation of a thomson scattering diagnostic on CTH as detailed in the following sections.

A.2 Thomson scattering as a plasma diagnostic

The use of thomson scattering as a plasma diagnostic not only has a long history,[98] but also an essential role in the routine measurements of electron temperature & density profiles in many fusion-relevant devices.[71,99,100,101] A thomson scattering diagnostic uses a laser, a monochromatic light source, to directly probe the velocity distribution of a chosen plasma species (e.g. typically electrons) via the elastic scattering of photons off the free charged particles of said species. The active probing of the charged species's velocity distribution yields the species's temperature from the doppler broadening of the scattered signal and the species's density from the total number of scattered photons. Figure A.2 shows a basic thomson scattering diagnostic schematic with the two major components of the laser beamline and the collection optics highlighted. Specifically the schematic shows the interaction region of an input laser beam and plasma creating a thomson scattered signal that is then imaged & dispersed onto a detector. The dispersion of the scattered light away from the input laser wavelength can then be used to determine the species temperature in the interaction region (e.g. the electron temperature as

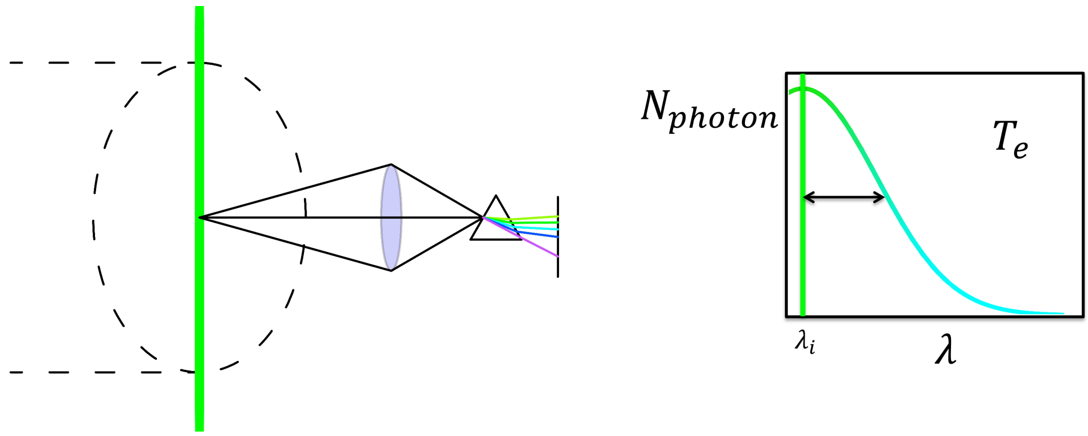

Figure A.2: A basic schematic of a thomson scattering diagnostic is shown with its two major components: the laser beamline and the collection optics. The schematic shows the imaging of a laser beamline interacting with a plasma column, indicated by the dashed lines, with the dispersed thomson scattered signal mapped onto a detector. Additionally the doppler broadening of the thomson signal from an electron fluid is shown with the temperature derived from the width of the wavelength shift.

indicated in figure A.2), while the total number of thomson scattered photons captured by the detector can be used to determine the species's density in the interaction region.

In order to understand how the scattered thomson signal is used to derive plasma parameters like a species's temperature and density, it is useful to examine the fundamental incoherent thomson scattering process.[a] Figure A.3 shows a linearly polarized plane wave labeled with the electric and magnetic field components colored red and blue respectively incident on a charged particle q. This plane wave propagating in $\hat{k_i}$ direction is incident on a charged particle q moving at a velocity $\vec{v_q}$. The oscillating electric field of this incident plane wave causes the charged particle q to accelerate along the polarization axis, giving rise to a dipole radiation pattern perpendicular to the plane wave's polarization (i.e. $\hat{E}$).[103] In order to solve for the emitted radiation's wavelength (i.e. thomson scattered signal) it is important to note that there are two doppler shifts present. First in the charged particle q's rest frame the incident laser's frequency, ω_i, is shifted by $\vec{k_i} \cdot \vec{v_q}$. Second in the detector's rest frame the frequency of collected light, ω_s, is shifted by $\vec{k_s} \cdot \vec{v_q}$. Therefore due to the elastic scattering process conserving energy, the

[a]An incoherent thomson scattering process occurs when the incident wavelength is much smaller than the debye length in the plasma. If the incident light's half wavelength is on the order of the debye sphere's diameter the plasma responds collectively yielding information about the ions rather than the electrons. For CTH relevant conditions an incident wavelength of $\lambda_i \approx 241$ μm would be necessary for collective effects to be present. See [102] for more discussion on the difference between collective and non-collective thomson scattering.

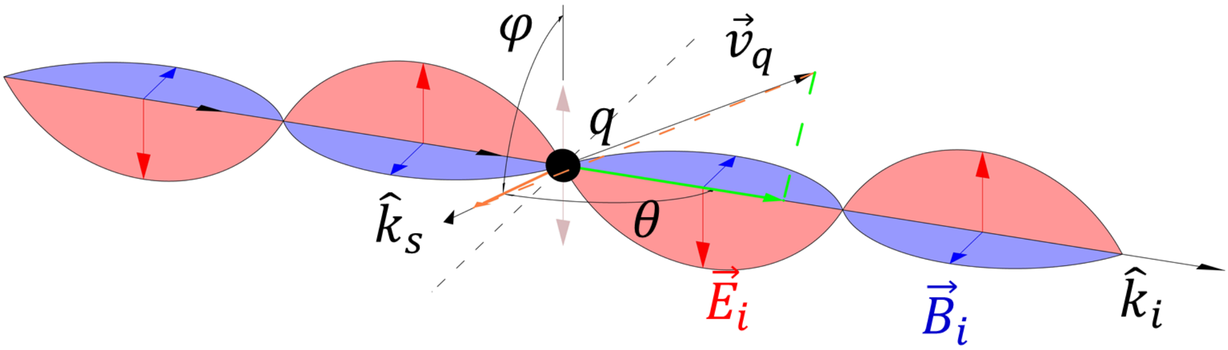

$$\omega_i - \left(\vec{k}_i \cdot \vec{v}_q\right) = \omega_s - \left(\vec{k}_s \cdot \vec{v}_q\right)$$

Figure A.3: A diagram demonstrating the basic thomson scattering process with a linearly polarized plane wave $\hat{k}_i$ at frequency ω_i incident on a charged particle q moving at a velocity $\vec{v_q}$ with a detector in the $\hat{k}_s$ direction. The double doppler shift is shown vectorially and in the equation below the diagram utilizing the conservation of energy in the charged particle's rest frame.

incident laser frequency and the thomson scattered frequency must be the same in the charged particle's rest frame leading to $\omega_s = \omega_i + \left(\vec{k_s} - \vec{k_i}\right) \cdot \vec{v_q}$ as shown in A.3. Next the total average scattered power per unit solid angle for a group of charged particles q can be written as equation A.1 according to [102]

$$\frac{d\langle P_s\rangle}{d\Omega dv_{q\,\hat{k}}} = n_q V^2 \left(\frac{\epsilon_0 c}{2}\|\vec{E_i}\|^2\right) r_q^2 \sin^2\phi \; f\left(v_{q\,\hat{k}}\right) \tag{A.1}$$

where n_q is the species q's particle density, V is the scattering volume, $\|\vec{E_i}\|$ is the magnitude of incident electric field of the plane wave, r_q is the classical charged particle radius for species q, ϕ is the azimuthal angle indicated in figure A.3, $f\left(v_{q\,\hat{k}}\right)$ is the velocity distribution function of the group of charged particles q, and $v_{q\,\hat{k}} \equiv \left(\vec{k_s} - \vec{k_i}\right) \cdot \vec{v_q}$. Assuming the species q is thermally equilibrated, the velocity distribution function can be written as a normal distribution, i.e. $f\left(v_{q\,\hat{k}}\right) = n_q\sqrt{\frac{m_q}{2\pi k_b T_q}} \exp\left(-\frac{m_q v_{q\,\hat{k}}^2}{2k_b T_q}\right)$. Combining this velocity distribution with average scattered power for dipole radiation shown in equation (A.1), the total number of photons expected at the detector (i.e. $N_{photons\,@\,detector}$) for thomson scattering off an electron fluid can be written as equation (A.2).

$$N_{photons\,@\,detector} = \left(\frac{N_{laser\,photons}\,(n_e r_e^2)\,(L\Omega T)\sin^2\phi}{\sqrt{\pi}\left[\lambda_i\sqrt{\frac{8k_bT_e}{m_ec^2}}\sin\left(\frac{\theta}{2}\right)\right]} \right) \exp\left(-\frac{(\lambda_s-\lambda_i)^2}{\left[\lambda_i\sqrt{\frac{8k_bT_e}{m_ec^2}}\sin\left(\frac{\theta}{2}\right)\right]^2} \right) \tag{A.2}$$

In equation (A.2), the variables not previously defined are as follows: $N_{laser\,photons}$ is the number of incident laser photons, L is the length of the scattering volume, Ω is the solid angle subtended by the collection optics, T is the unitless transmission factor taking into account all of the detection system's losses, k_b is the Boltzmann constant, and T_e is the electron temperature. Examining equation (A.2) shows that $N_{photons\,@\,detector} \propto n_e$ and that the half-width half-max (HWHM) of the wavelength distribution yields $HWHM \propto \sqrt{T_e}$. Therefore if the thomson scattered signal's dispersion can be measured on the detector, the temperature of the measured species (e.g. electrons) can easily be determined. Moreover if the input laser power and optical detection system are well characterized then the measured species's density can also be determined through an absolute account of the thomson scattered photons. Also note that equation (A.2) shows the scattering process generates a dipole radiation pattern from the $\sin^2\phi$ term. This means that in order to maximize the thomson signal measured, the collection optics location should be placed perpendicular (i.e. $\phi = 90\circ$) to the laser polarization.

Armed with a basic understanding of an incoherent thomson scattering process in a plasma and how this process can be used to diagnose a plasma species, the next step is understanding the general characteristics and requirements for a thomson scattering diagnostic. A thomson scattering diagnostic provides a non-invasive, non-perturbative, local, and internal measurement via the elastic scattering of photons off of free charged particles. Non-invasive means that no physical probe or mechanism needs to be immersed in the plasma to determine the plasma properties as already discussed above. Non-perturbative means that although the incident photons interact with the free charged particles (e.g. electrons) the total input energy and more importantly the transferred energy is negligible compared to the plasma. Local & internal means that the thomson scattered signal only originates from the photon scattering volume and that this scattering volume, typically designed to be small e.g. $\sim 0.1\ cm^{-3}$, can be imaged even if it is located in the plasma interior. In addition to these beneficial qualities, these local & internal measurements can yield global plasma parameters for magnetic confining devices with flux surfaces since Magnetohydrodynamics (MHD) says constant pressure surfaces and magnetic surfaces coincide to first order (i.e. $\nabla\overleftrightarrow{p} = \vec{j} \times \vec{B} \quad \Rightarrow \quad \vec{B} \cdot \nabla\overleftrightarrow{p} = 0$). Therefore a single thomson scattering system using local measurements of electron temperature and density can be used to characterize the entire magnetic surface's electron pressure.

Although there are many beneficial characteristics of a thomson scattering diagnostic as described above, there are difficult technical obstacles to overcome before these advantages can be realized. The major technical obstacles all stem from the extremely small thomson scattering cross section which for an electron is shown in equation (A.3).

$$\sigma_e = \frac{8}{3}\pi r_e^2 = \frac{e^4}{6\pi\epsilon_0^2 \left(m_e c^2\right)^2} \;=\; 6.65 \times 10^{-29}\ m^2 \tag{A.3}$$

This low cross section places stringent requirements on the input light source and the thomson detection system in order to generate a measurable signal. To better understand the approximate thomson signal level, the ratio of scattered power to input power can be examined for a characteristic CTH scenario using equation (A.4), where r_e is the classical electron radius, n_e is the electron density in the thomson scattering volume, L is the length of the scattering volume, and $d\Omega$ is the solid angle subtended by the thomson collections optics.

$$\begin{gathered}\frac{P_{scattered}}{P_{input}} \approx r_e^2 n_e L d\Omega \\ \frac{P_{scattered}}{P_{input}} \approx \left(7.9 \times 10^{-30}\, m^2\right)\left(10^{19}\, m^{-3}\right)(0.01\, m)\,(0.04\, sr) = 3.14 \times 10^{-14}\end{gathered} \tag{A.4}$$

There are three conclusions from the CTH estimation using equation (A.4): first, the input power (i.e. incident number of photons) needs to be extremely high to even recover a measurable signal, second the low number of scattered photons indicate that a large viewing solid angle is necessary, and third any background signals need to be carefully controlled in order to not washout the signal. In order to overcome these major technical obstacles it is clear that a high power laser, large & fast optics, and a good stray light mitigation system are all necessary for a successful thomson scattering diagnostic on CTH. The design strategies and hardware implementation of the CTH thomson scattering diagnostic to overcome the technical obstacles will be discussed in the next two sections with the first one covering the laser beamline and the second covering the collection optics system.

A.3 CTH laser beamline design and hardware

The objectives of the CTH thomson scattering beamline design were to transmit the full power beam without damaging any optical components, place the beam waist on the CTH mid-plane, ensure the beam polarization is as close to perpendicular to the collection optics as possible, minimize the number of optical components, create a consistent beam width through the plasma region, and to minimize the stray laser light from entering the collection optics. In the next three sections the design and hardware used to accomplish these objectives will be discussed. The first section introduces the laser source chosen for the CTH thomson system and details the major beamline geometry constraints specific to CTH. The next section introduces the brewster window design used for full transmission of the laser pulses through the CTH vaccum vessel terminating in an external beam dump. The last section outlines the specific geometry considerations, design, and hardware for the stray laser light baffles installed to minimized the background signal from the laser line.

A.3.1 CTH geometry considerations and gaussian beam calculation

Initially both a vertical and horiztonal thomson scattering system design were evaluated on CTH to determine the most feasible scattering geometry. After examining the horizontal system, where the laser pulse would be fired along the mid-plane of the machine, it was determined that the potential stray light would be too difficult to mitigate and any baffle system would use too much available port space. Both of these issues can be seen in figure A.4. In terms of stray light mitigation the horizontal design is much more daring as any stray light that would reflect off the inner wall of the vacuum vessel could wash out the signal. Another important disadvantage to the horizontal system is such a beamline would require a baffle system that makes an oblique angle with the 18” side ports, using too much valuable diagnostic space. Therefore

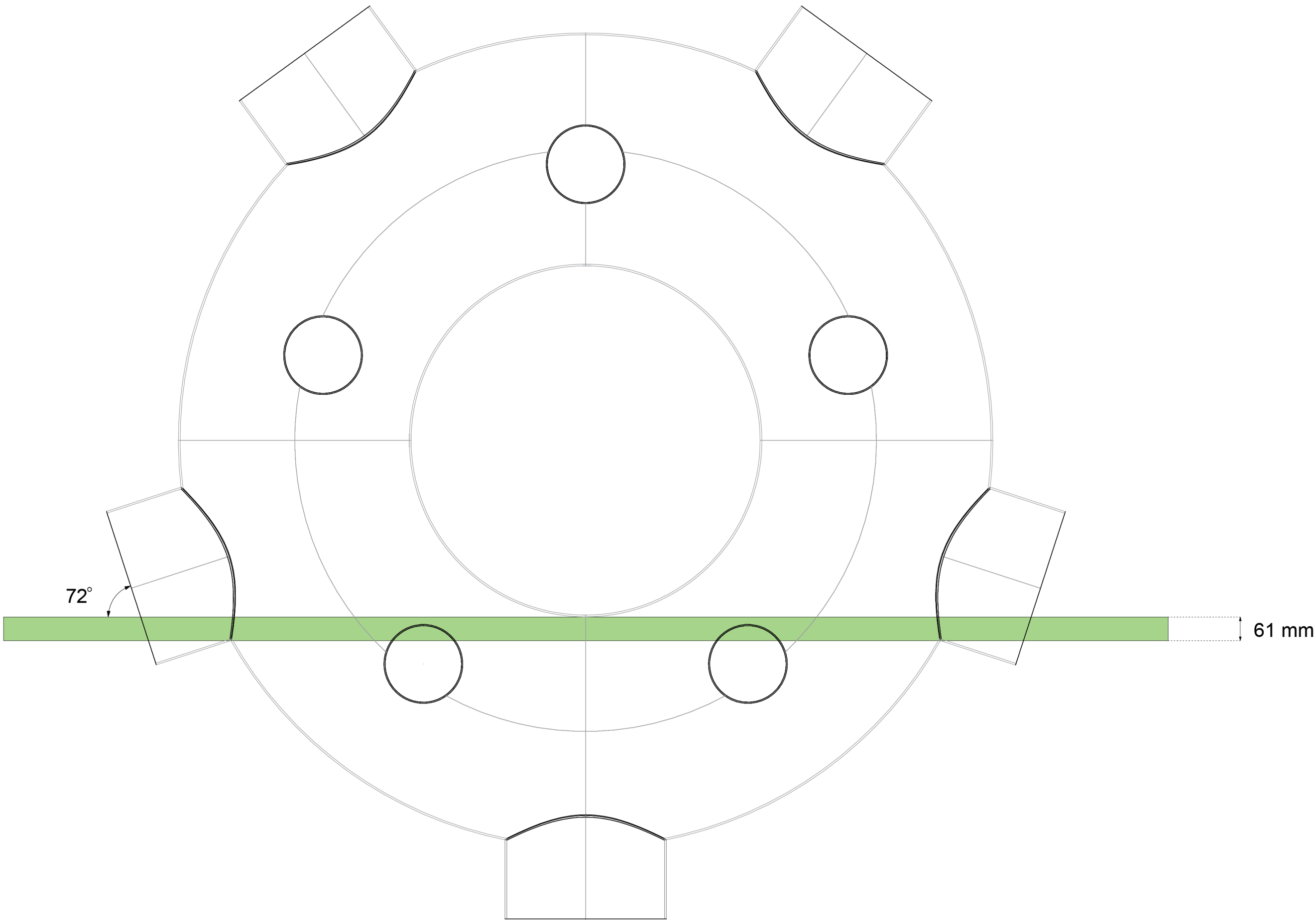

Figure A.4: A top down view of the CTH vacuum vessel showing the mid-plane extent ($\sim$ 61 mm) from the inner wall to the outer port positions for a potential thomson laser beamline.

a vertical laser beamline was determined to be the better option since the solid angle for the collection optics is roughly the same, the scattered light can almost be completely mitigated, and only the two 10” vertical ports are used for the beamline.

In order to achieve this vertical beamline for a thomson scattering dianostic on CTH, an extremely bright light source is necessary as detailed in section A.2. Therefore a frequency doubled, Q-switched Continuum Powerlite DLS 2 J Nd:YAG laser was selected.[104] Specifically the CTH thomson system design[97] utilizes the frequency doubled option at 532 nm capable of delivering 2 Joule pulses with full-width half-max of $\sim$7 ns at a 10 Hz repetition rate.[b] This high power in the visible spectrum combined with availability of commercially off-the-shelf low $f/\#$ spectrometers with high efficiency volume phase holographic (VPH) transmission gratings and high quantum efficiency image intensified charged coupled devices (ICCDs) motivated the CTH thomson system design.[c] Moreover this frequency doubled option not only provided an intense input power, but also made beam & aperture alignment much simpler being in the visible spectrum.

Implementing the vertical thomson scattering system in the simplest geometry meant placing the laser & optical table in a room above the CTH device. This design choice meant that all of the turning mirrors could be kept on the optical table and an added half-wave plate to control the polarization wasn't necessary. Both of these consequences improved the beamline setup by providing a large & stable area to maximally separate the mirrors for more precise beam steering and by keeping the number of optical elements to a minimum for maximum beam energy transmission. Figure A.5 shows the basic beamline schematic detailing the laser table layout in (a) and the vertical beamline distance to the CTH mid-plane in (b). Adding the listed distances in figure A.5 yields a total distance of 7.895 m from the laser head to the CTH mid-plane where for symmetry considerations is the desired location for the beam waist, i.e. minimum beam diameter.[d] With a 12 mm beam diameter at the laser head, the beam needed to be focused not only for increasing the beam intensity in the plasma, but also for shrinking the size of the laser

[b]The 10 Hz repetition rate only allows a single measurement in the ohmically heated discharges ($\leq$ 100 ms) and at most two measurements for pure stellarator discharges ($\leq$ 150 ms)

[c]This design approach was based off the Pegasus thomson scattering system ([99, 105])

[d]The beam diameter is defined as the $\frac{1}{e^2}$ width or the width that corresponds to the points where the beam intensity has dropped by the factor $\frac{1}{e^2} \approx 0.135$

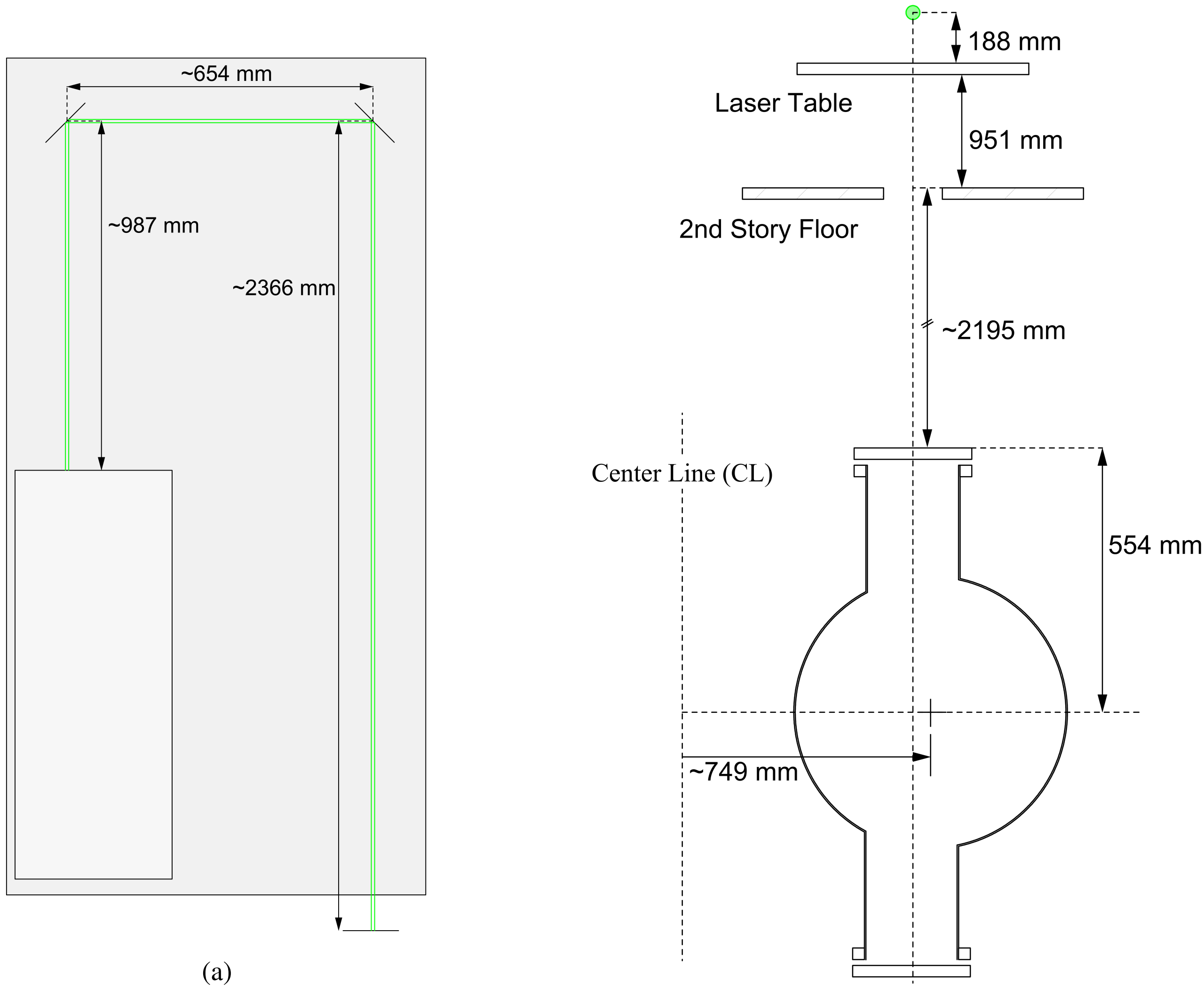

(a)

(b)

Figure A.5: The laser beamline layout on the laser table with the three turning mirrors is shown in (a) and the vertical distance from the laser table to the vacuum vessel mid-plane is shown in (b) (~ 3.88 m)

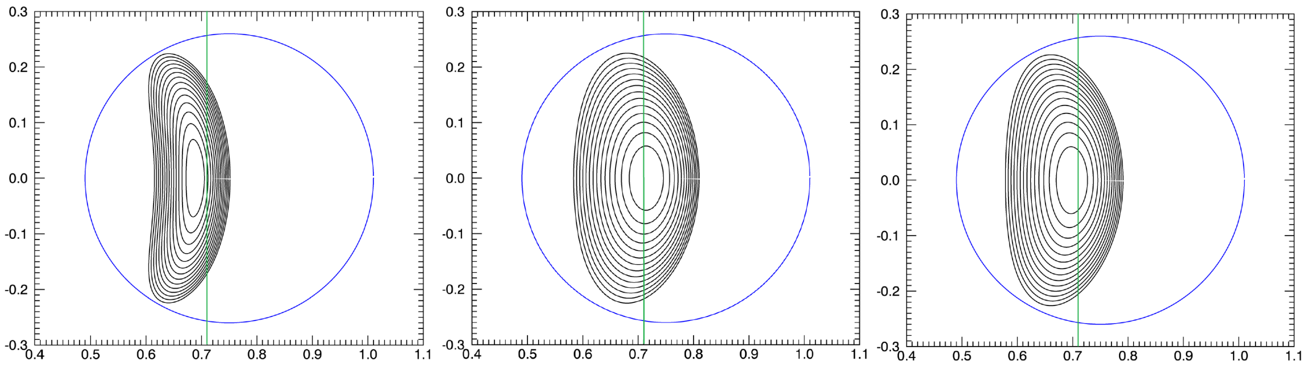

Figure A.6: The vertical laser beamline path is shown in green as it intersects flux surfaces at three different time points during a plasma discharge for CTH. Also the blue circle represents the CTH vacuum vessel.

volume to be imaged onto a detector. In order to keep in line with the objectives of the thomson beamline design the focusing was performed with a single anti-reflection coated lens whose positioning is discussed in section A.3.2.

Finally although the vertical thomson scattering system was the better option, this design still had many challenges to overcome. The first challenge stems from the fact the two 10" top and bottom ports are not centered on the vacuum vessel (see figure A.5b). This is important since the CTH magnetic field settings, especially the amount of inductively driven plasma current, determine where the beamline intersects with the magnetic flux surfaces. Fortunately as demonstrated in figure A.6, even during a large plasma current leading to a radial outward displacement of the flux surfaces, the beamline still passes very close to the magnetic axis.[e] A second and more significant challenge was also associated with the top & bottom 10" ports. Although the CTH vacuum vessel was built within specification, the top & bottom 10" ports for the thomson beamline were displaced from each other in almost the worst way causing their centers to be shifted by 0.348". The top & bottom 10" ports not sharing a common center meant a custom rotatable flange had to be designed (see figure B.1) with this 0.348" offset from the center. Furthermore the installation of the custom non-centered flange on the bottom 10" port was much more difficult since the stray laser light baffling (discussed in section A.3.3) had to

[e]Finally it should be noted that the magnetic axis typically stays between 0.69 and 0.72 m (as measured from the center of the torus) while the proposed beamline will have a radial location of 0.71 m as shown in figure A.6.

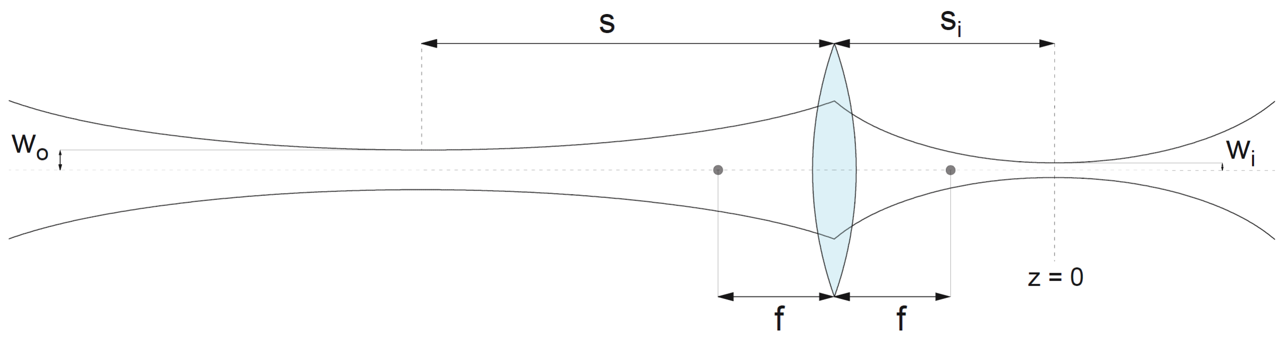

Figure A.7: The basic single lens diagram for a gaussian beam propagating through a lens with a focal length f where the input beam has a beam waist w_o at position s. The output beam waist w_i at the image location a distance s_i from the lens but defined in local coordinates at $z = 0$.

be illuminated to ensure proper alignment of the apertures that wouldn't cause beam clipping. A third challenge with the vertical thomson system was the limitation of the concrete floor allowing only 0.78 m of space below the 10" bottom port for the exit Brewster window. This space limitation combined with the necessity of a symmetric beamline about the CTH mid-plane placed additional restrictions on how close the entrance Brewster window could be to the optical table. This restriction on the Brewster window location, discussed in section A.3.2, was also critical for determining the positions and characteristics of both the single focusing lens and the stray laser light baffling.

Therefore a gaussian beam calculation was performed to determine the possible single lens positions and focal lengths that will result in the desired beam profile for the given CTH geometry considerations. The laser beam profile from the Continuum Powerlite DLS 2 J Nd:YAG laser can be accurately modeled using gaussian beam optics where for a single thin lens figure A.7 demonstrates the key features. Applying the CTH geometry considerations to the thin lens gaussian beam equation as shown in equation (A.5), the focal length can be determined for a given total distance from laser head to CTH mid-plane ($A \approx$ 7.895 m), a given laser head location (s), and the given Raleigh range ($Z_{Raleigh}$) out of the laser head or the distance along the beam required for the beam radius to be enlarged by a factor of $\sqrt{2}$.[106]

$$s + s_i = A \quad \Rightarrow \quad s + \frac{sf\left(s-f\right) + fZ_{Raleigh}^2}{\left(s-f\right)^2 + Z_{Raleigh}^2} = A$$

$$f = \frac{\left(Z_{Raleigh}^2 - s^2 + 2As\right) \pm \sqrt{\left(Z_{Raleigh}^2 - s^2\right)^2 + 4AZ_{Raleigh}^2\left(2s-A\right)}}{2A} \tag{A.5}$$

Therefore equation (A.5) applies the constraints of CTH symmetry about the mid-plane for a total distance $A \approx$ 7.895 m to yield an appropriate focal length lens for a given placement distance s away from the output laser head. The beam's Raleigh range out of the laser head can be calculated based on the half-angle divergence detailed on the specification sheet,[104] i.e. $Z_{Raleigh} = \frac{w_o}{\theta_{half}}$ with known beam radius $w_o = 6 \times 10^{-3}$ m and beam half-angle divergence $\theta_{half} = 0.225 \times 10^{-3}$ rad yielding $Z_{Raleigh} \approx$ 26.67 m.

Although equation (A.5) is useful for determining a range of focal length lenses and their corresponding positions to utilize in the CTH thomson beamline design, it still doesn't detail the beam profiles along the beamline. In order to calculate the beam diameter as a function of distance along the beamline (z), the thin lens gaussian beam equations from [106] and reproduced in (A.6) were combined to generate an equation for the focused beam radius as a function of focal length & distance from the beam waist.

$$w_i = \frac{w_o f}{\sqrt{\left(f-s\right)^2 + Z_{Raleigh}^2}} \quad \text{and} \quad w\left(z\right) = w_o\sqrt{1 + \left(\frac{z}{Z_{Raleigh}}\right)^2}$$

$$w_i\left(f, z\right) = w_o f \sqrt{\frac{1 + \left(\frac{z}{Z_{Raleigh}}\right)^2 \left(\frac{\left(f-s\right)^2 + Z_{Raleigh}^2}{f^2}\right)^2}{\left(f-s\right)^2 + Z_{Raleigh}^2}} \tag{A.6}$$

It is important to note that the origin for the distance along the beamline occurs at the beam waist meaning that $z = 0$ is located at the minimum beam radius as shown in figure A.7. Finally the focal length formula shown in equation (A.5)[f] can be plugged into equation (A.6)

[f]Where the negative root is used to retrieve real focal lengths

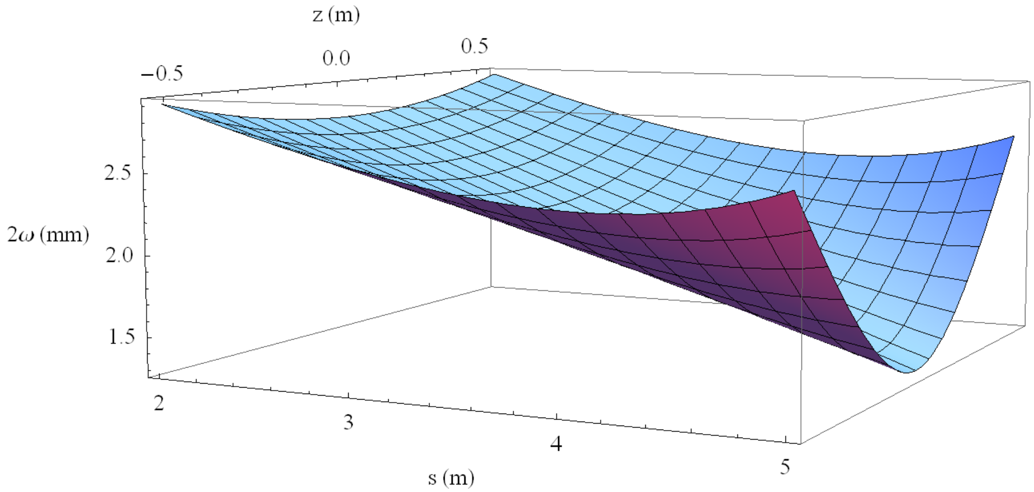

Figure A.8: The focused beam diameter ($2w_i$) contour is plotted as a function of distance from the beam waist, i.e. distance from CTH mid-plane (z), and the single lens distance from the laser head (s). This beam diameter contour was calculated for a real gaussian beam using the parameters: $w_0 = 6$ mm, $A = 7.895$ m, and $Z_{Raleigh} = 26.67$ m

yielding a formula for the beam radius as a function of the distance from the focused beam waist (z) and the lens's distance from the laser head (s). Figure A.8 shows the resulting contour of the focused beam diameter, $2 \times w_i\,(s,\, z)$, demonstrating the variation of the beam profile from the top port entrance to bottom port entrance, $z \to (-.533\,m,\, 0.533\,m)$, at different lens distances from the laser head, $s \to (2\,m,\, 5\,m)$. The beam profiles show greater variation as the focusing lens's distance from the laser head is increased which is consistent with the decreasing focal length necessary to satisfy the CTH geometry constraints. Critically this demonstrates a single focusing lens at locations with $s < 4$ m not only generates beam profiles more consistent through the vacuum vessel, but also provides a simple, robust installation on the optical table without any extra beamline mounts.

A.3.2 Brewster window design and vacuum integration

With a general description of the laser beamline for the CTH thomson system, the next step is ensuring a safe, reliable method of propagating the beam through the vacuum vessel with the stray laser light kept to a minimum. The first step toward this goal of minimizing the stray laser light along the beamline was using a vacuum window at the Brewster angle. The Brewster's angle can be easily calculated using snell's law, $n_1 \sin(\theta_1) = n_2 \sin(\theta_2)$, and remembering

$\theta_1 + \theta_2 = 90°$ is the necessary condition to ensure the parallel polarization is refracted along the plane of the window, i.e. minimizing the reflected laser light off the window. Combining these two conditions yields equation (A.7) for the Brewster's angle θ_B, which after plugging in the index of refraction values from [107] for fused silica at the frequency doubled wavelength of 532 nm yields $\theta_B \approx 55.6°$

$$\theta_B = \tan^{-1}\left(\frac{n_{window}}{n_{air}}\right) \quad \Rightarrow \quad \theta_{B\,quartz} = \tan^{-1}\left(\frac{1.46071}{1.00027}\right) = 55.597° \tag{A.7}$$

Utilizing this Brewster's angle a custom nipple was designed, see figures B.2a through B.2i for the design document, that employed a double o-ring seal for the 4" fused silica window connection and a rotatable flange for the vacuum vessel connection. This double o-ring sealing technique meant the window could be rapidly replaced even when at high vacuum since as seen in figure A.9a the custom nipple had a bleed valve installed along with a gate valve separating it from the vacuum vessel. The rotatable flange's connection to the gate valve ensured that the Brewster window could be placed in the correct orientation for the beam polarization to be aligned with the Brewster window surface maximizing beam transmission. As evident in figure A.12b the beamline components are symmetric about the CTH mid-plane due to the symmetric design constraint of placing the beam waist at the CTH mid-plane as discussed in section A.3.1. Therefore the height constraint imposed by the 0.78 m distance from the 10" bottom port to the concrete floor established the position of each Brewster window $\sim$ 1.211 m from the CTH mid-plane as depicted schematically in figure A.9b.

Another important consequence of the double o-ring seal design was the large 4" diameter Brewster windows necessary for ensuring an adequate clear aperture. Moreover these laser grade windows as commercially off-the-shelf components have a wider thickness than is necessary for safely keeping vacuum. With a thickness of 0.5", these windows contributed to significant beam displacement as the laser is transmitted through the vacuum vessel. This beam displacement was calculated beforehand not only for expediting the beamline alignment process, but also for determining the effective beam spot size that could contribute to stray laser

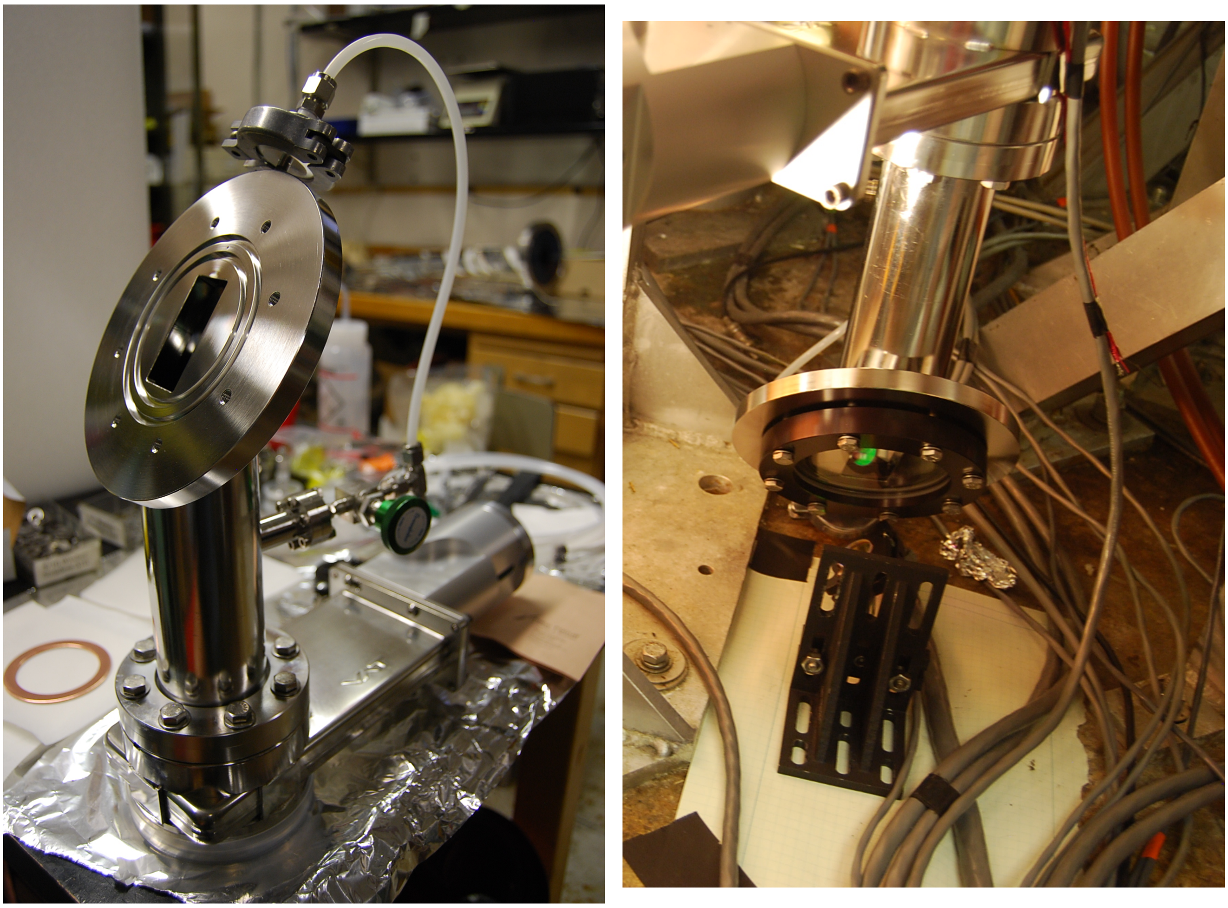

(a)

(b)

Figure A.9: In (a) the custom Brewster window nipple showing the differentially pumped double o-ring grooves without the 4” fused silica window installed. Also note the bleed valve installed on the nipple body and the rotatable flange attaching the nipple to a gate valve. In (b) the bottom/exit Brewster window nipple is installed on CTH showing the clearance from the concrete floor is enough for the ISO flange for differential pumping and an inclusion of a turning mirror for future beam dump.

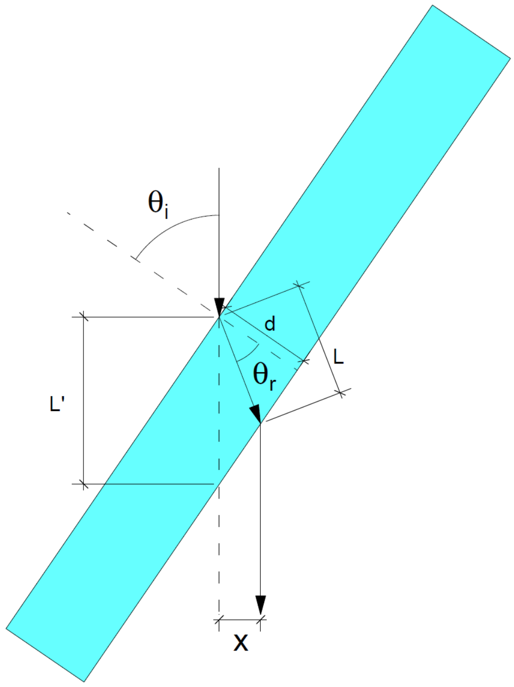

Figure A.10: Brewster window diagram where θ_i is the angle of incidence, θ_r is the angle of refraction, d is the thickness of the window, L' is the distance that would have been traveled by the light ray if the window was not there, L is the distance the light ray traveled inside the window, and X is the beam displacement once it has passed completely through the window.

light. Using a schematic of the Brewster window, shown in figure A.10, the beam displacement labeled as x can be calculated using simple geometry where L is the beam length in the window, θ_r is the angle of refraction, d is the window thickness, and θ_i is the angle of incidence. The two geometrical relations that determine the beam displacement are $L\cos(\theta_r) = d$ and $L\sin(\theta_i - \theta_r) = x$, where from figure A.10 it can be seen that $\theta_i = \theta_{B\,quartz} = 55.597°$, $\theta_r = 90° - \theta_i = 34.403°$, and $d = 0.5$". Solving the geometrical relations for the beam displacement as shown in equation (A.8), the resultant beam displacement is over half a centimeter.

$$x = \frac{d\sin(\theta_i - \theta_r)}{\cos(\theta_r)} \quad \Rightarrow \quad x = 5.564\,mm \tag{A.8}$$

This significant beam displacement was particularly important for estimating how the beam spot size on the Brewster window could contribute to stray laser light. Since stray laser light is generated from scattering off defects in the quartz window, the beam spot size was overestimated to be the nominal spot size on the air-side of the quartz window plus this displacement distance. As will be detailed in section A.3.3, this overestimated "effective beam spot size" was used to constrain the baffling system design in order to keep the stray laser light at a minimum.

Before the installation of the Brewster windows, the assumed best choice for the single focusing lens was a commercially off-the-shelf $f = 5.0$ m option.[97] This decision was based off the gaussian beam calculation in section A.3.1 demonstrating the lens could be mounted on the optical table while still producing a consistent beam diameter, i.e. ≤ 3 mm, inside the plasma and a beam waist on the CTH mid-plane. However during the in situ beamline alignment, it was discovered that the focused beam was damaging the 4" laser-grade Brewster window. Fortunately due to the double o-ring seal design, the damaged window could easily be replaced and critically the damaged window could be rotated to an undamaged section for further testing purposes. After extensive testing with a variety of focal length lenses (i.e. $f =$ 5.0, 4.0, 3.0, 2.0 m), it was found that only the $f = 2.0$ m option didn't incur any visible damage on the window and that the critical laser spot size at the Brewster window leading to damage on the window's exit surface was ~ 6 mm in diameter.[g] Figure A.11 shows the comparisons between the gaussian beam calculated diameters and the measured diameters from the laser burns using the $f = 2.0$ m lens in its nominal position. In particular the brown points in figure A.11 correspond to laser burns performed on the thomson optical table with the $f = 2.0$ m lens at its gaussian beam calculated position using extra turning mirrors, while the green diamond represents the beam diameter from an in situ laser burn at the Brewster window surface. Although the measured beam diameter at the Brewster window was > 6 mm with no signs of damage even after tens of laser pulses incident, the positioning of the $f = 2.0$ m lens was not optimal since it had to mounted ~ 0.728 m below the laser room floor.[h] Even after the unforeseen window damage excluding all but the shortest focal length option and even using a suboptimal mounting structure for this $f = 2.0$ m lens, the three most important thomson beamline objectives of transmitting as much power as possible, placing the beam waist on the CTH mid-plane, and minimizing the number of optical components could still be achieved. In the next section the ramifications of switching to the $f = 2.0$ m lens are discussed.

[g] At roughly ~ 1.7 J per pulse the fluence for a 6 mm diameter beam is $\sim 6\ \frac{J}{cm^2}$.

[h] In fact the lens had to be mounted off of a translation stage attached to a temporary 80-20 aluminum rail structure formed into a T-shape such that the top of the T-shape rested on the laser room floor.

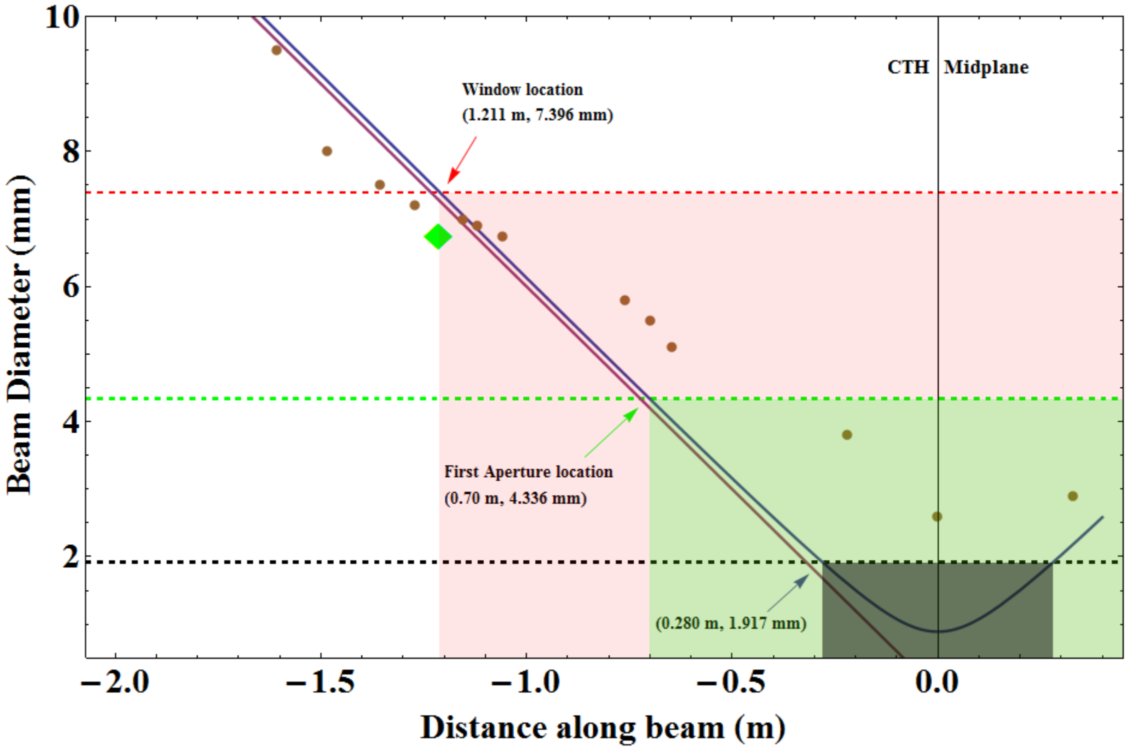

Figure A.11: The beam diameter as a function of distance along the beamline is shown for the gaussian beam calculation (blue line), the simple geometrical estimation (purple line), and the measured diameters from laser burns (brown circles) for a single $f = 2.0$ m lens. The key locations and the predicted gaussian beam diameters are noted for the Brewster window (red box & dashed line), the primary baffle aperture (green box & dashed line), and the extent of the poloidal cross section (black box & dashed line). Note that the green diamond represents a measured diameter from an in situ laser burn at the Brewster window surface. Also note the diameter measurements as estimated from the burns are not exact and can easily have $\pm$ 0.5 mm errorbars.

A.3.3 Baffling design for stray laser light mitigation

Finally with the general beamline chosen the next step was to minimize the stray light inside the vacuum vessel since the thomson signal could easily be washed out due to the small ratio of the thomson signal to input laser power as demonstrated by equation (A.4). The first step in this process, figuring out the laser spot size on the input Brewster window, has already been accomplished in the last section (see A.3.2). This beam spot size can be thought of as the stray laser light's source size since it is the light scattering off of defects in the Brewster window that will lead to laser light reflecting within the vacuum vessel potentially scattering into the thomson collection optics. In order to prevent this possibility, a two-aperture baffle system was designed that would contain the stray laser light within the opposing symmetric baffle and the 10" port. As shown in figure A.12a there are two stray light cones (SLC): the primary stray light, defined as the diffuse laser light scattered off the Brewster window, and the secondary stray light, defined as the diffuse laser light scattered off the primary aperture. The primary SLC (shown by the solid red lines in figure A.12a) demonstrates how the marginal rays from the beam spot size on the Brewster window and the primary aperture would still be constrained within the opposing baffle system. Note that the primary SLC is not symmetric about the entrance port's centerline due to the beam refraction in the Brewster window causing a non-symmetric laser spot size. To ensure both the primary SLC and the secondary SLC (shown by the dashed blue lines in figure A.12a) travel down the opposing baffles and 10" port respectively without providing a direct reflection to the collection optics, simple geometrical constraints were imposed on the design to determine the baffle dimensions.

Using a simple schematic as shown in figure A.13 the key distances along the laser beamline can be defined and used within the geometrical constraints for the symmetric two aperture baffle system design. The geometrical constraints will be used not only to solve for the distances along the laser beamline (as shown in figure A.13), but also to solve for the primary aperture diameter (d_1) and the secondary aperture diameter (d_2) of the baffle system. Therefore using figure A.13 as a guide the simplest and first constraint is the laser beam must fit through the primary aperture meaning that the focused beam diameter at the primary aperture

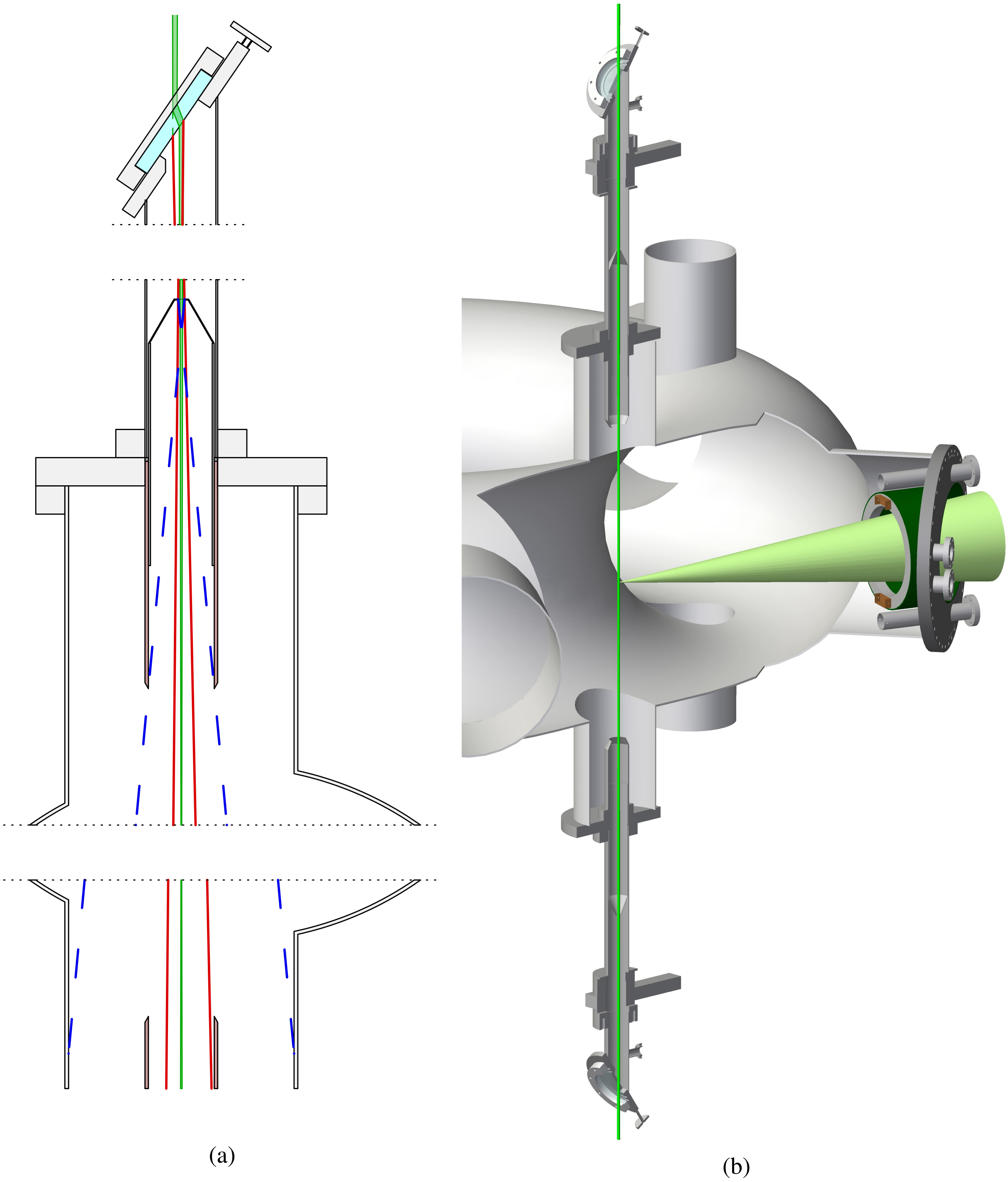

Figure A.12: In (a) the CTH thomson beamline is shown (green) traversing the vacuum vessel with the primary stray light cone (solid red line) and the secondary stray light cone (dashed blue line) explicitly shown to emphasize their capture by the exit baffling and port respectively. In (b) a cut-away of the CTH vacuum vessel with the thomson scattering geometry is shown with all of the thomson vacuum components. Additionally (b) shows the expected solid angle acceptance of the thomson collection optics via the light green cone.

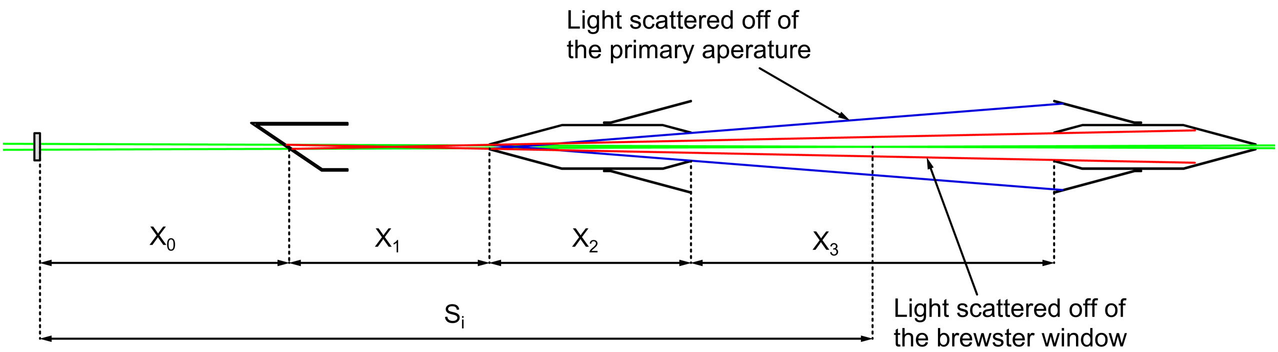

Figure A.13: A basic schematic demonstrating the important distances in the laser beamline (green) that are used within the geometrical constraints for the symmetric two-aperture baffling system on CTH. The schematic shows the critical components along with the primary and secondary SLC shown in red and blue respectively. x_0 is the distance between the single focusing lens and the Brewster window, x_1 is the distance between the Brewster window and the primary aperture of the entrance baffle, x_2 is the distance between the primary and secondary aperture, x_3 is the distance between the secondary apertures of the entrance and exit baffles, and S_i is the distance from the focusing lens to the CTH midplane where the beam waist is placed.

($d_{beam\,at\,d_1}$) needs to be smaller than the primary aperture diameter as shown in equation (A.9).

$$d_1 > d_{beam\,at\,d_1} \tag{A.9}$$

The next constraint is that the primary SLC needs to fit within the secondary aperture of the exit baffles as demonstrated in equation (A.10).

$$d_2 > \left(\frac{x_1 + x_2 + x_3}{x_1}\right)(d_1 + d_w) - d_w \tag{A.10}$$

Next to ensure the stray light is minimized as much as possible the secondary SLC is required to fit within the opposing 10” port leading to equation A.11 where the inner diameter of the 10” port is only 8” or ~ 203 mm.

$$203\,mm > \left(\frac{x_2 + x_3}{x_2}\right)(d_2 + d_1) - d_1 \tag{A.11}$$

As mentioned the baffling design is symmetric with the exact same entrance and exit baffles in addition to the same entrance and exit Brewster window distances. Therefore as depicted by figure A.12b the top and bottom beamline components can be identical simplifying the entire design. Finally it is important to note that the baffles can't be placed too far into the top and bottom 10" ports as a direct line-of-sight to the thomson collection optics could lead to saturating the detector with stray laser light.

The next step in the baffling design was to apply the CTH relevant distances to the geometrical constraints established in equations (A.9), (A.10), and (A.11). In fact two important distances specific to the CTH vertical beamline are the distance from the bottom 10" port down to the concrete floor is only $780\,mm$ and the baffle system can only stick into the 10" port $170\,mm$ without giving a direct line-of-sight to the collection optics. Combining these two distances means that $170\,mm + 780\,mm = 950\,mm$ is the total allowed distance from the furthest the baffles can extend into the 10" port to the concrete floor. In order to maximize the distance between the Brewster window and the baffle's second aperture it was chosen: $x_1 + x_2 = 800\,mm$ as the extra $150\,mm$ is necessary space for a turning mirror and a beam dump. Additionally based on the CTH vacuum vessel model the $170\,mm$ extension of the entrance and exit baffles into the 10" top and bottom ports respectively sets the distance between the secondary apertures at $x_3 = 720\,mm$ as shown schematically in figure A.13. Finally to minimize both the primary and secondary SLCs the distances between the Brewster window and the first aperture, x_1, and between the first aperture and the second aperture, x_2, were set equal to each other as shown in equation (A.12).

$$x_1 + x_2 = 800\,mm \qquad x_1 = x_2 = 400\,mm \tag{A.12}$$

Now applying the beamline parameters to the geometry constraints leads to the first critical inequality where the beam diameter at the location of the first aperture has to satisfy $d_1 > 3.083\,mm$.As discussed in section A.3.2, the original beamline was designed with a commercially off-the-shelf $f = 5.0$ m focusing lens leading to the $3.083\,mm$ result at the primary aperture. Even though the baffle system was designed using a $f = 5.0$ m focusing lens in the gaussian beam calculation, the primary aperture diameter was set to $\frac{1}{4}$" ($6.35\,mm$) to ensure more laser power is transmitted and to ease beam alignment. Fortunately once the $f = 2.0$ m focusing lens was employed in order to prevent Brewster window damage, in situ laser power tests were performed with the baffling installed confirming minimal beam clipping with $\sim 90\%$ transmitted energy. Returning to section A.3.2's discussion of beam displacement through the Brewster window, the original gaussian beam calculation also used the $f = 5.0$ m focusing lens leading to an effective laser spot size on the Brewster window of $d_w = 3.555\,mm{+}5.564\,mm = 9.119\,mm$. Plugging in x_1, x_2, x_3, d_1, and d_w into the geometrical constraint for the secondary aperture shown in equation (A.10) resulted in $d_2 > 49.663\,mm$. This inequality meant that the inner diameter of the stainless steel tube used to mount the primary aperture onto could be employed as the second aperture (see the specification drawing B.3b for more details). Therefore the 2.26" inner tube diameter was used as the secondary aperture for the baffle system, namely $d_2 = 57.404\,mm$ The final geometrical constraint for the secondary SLC fitting within the 10" port (see equation (A.11)) was verified with the SLC diameter of $\sim$ 177 mm being smaller than the 8" or $\sim$ 203 mm inner port diameter.

Once the dimensions of the baffle system were determined, the simplest design that would simultaneous satisfy the beamline requirements, afford an easy installation, and use as many commercially available parts as possible was conceptualized. The chosen design had three main components: the primary aperture stainless steel tube (see figure B.3a), the secondary aperture stainless steel tube (see figure B.3b), and a clamping shaft collar to hold the baffle system together. The baffle component containing the primary aperture was the most custom part needing welds between the commercially available stainless steel cone & tube and an additional weld of a ring around the tube. Besides this primary aperture baffle component, the other two main components needed minor machining and were off-the-shelf components. Moreover the design allowed for simple and robust installation as shown in figures A.14a, A.14b, and A.14c. Specifically the primary aperture baffle was designed to fit inside the secondary aperture baffle with the distance between apertures precisely determined by the ring weld stopper on the primary aperture baffle. This ring also had the correct dimensions to snugly fit on the inner diameter lip of the $2\frac{3}{4}$" nipple, ensuring the distance between the Brewster window and the primary aperture was maintained. The last component, the clamping shaft collar, held the entire baffle system to the 10" flange regardless if the baffle system was installed on the bottom or top 10" ports (see A.12b for orientation reference). Finally as evident in figure A.14, all the

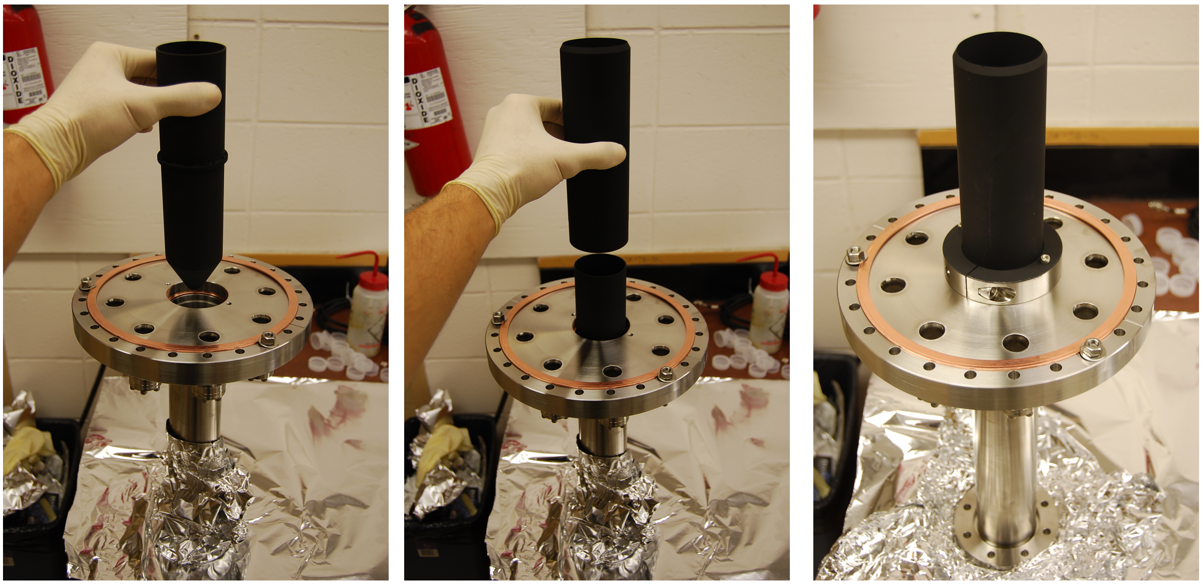

(a) (b) (c)

Figure A.14: In (a) the primary aperture baffle component, blackened to reduce stray laser light reflections, is being installed into the 10" flange and the $2\frac{3}{4}$" nipple, with the welded ring holding the baffle in position. In (b) the secondary aperture baffle component is fit over the primary baffle. Finally in (c) the clamping collar, whose face is also blackened with vacuum compatible paint, is attached first to the 10" flange and then tightened to hold the entire baffle system in place.

baffling components were coated with vacuum compatible black paint in order to reduce the reflectivity of the system.

A.4 CTH collection optics design and hardware

As seen from equation (A.4) the Thomson scattered signal is extremely small even using a high powered laser as a light source. Therefore the collection optics must be optimized to gather as much light as possible and to guide the thomson scattered light onto the detector. A simple schematic depicting the general optical components of a thomson scattering diagnostic system can be seen in figure A.15. It is important to highlight that the detector requirements (e.g. $\sim 1\,ns$ response time and low-light sensing) make it the most expensive and inflexible component of the collection system. Therefore the first step in the optimization process is to choose a detector and match the etendue for each of the components following the light backwards from the detector to the scattering volume. However in the following subsections

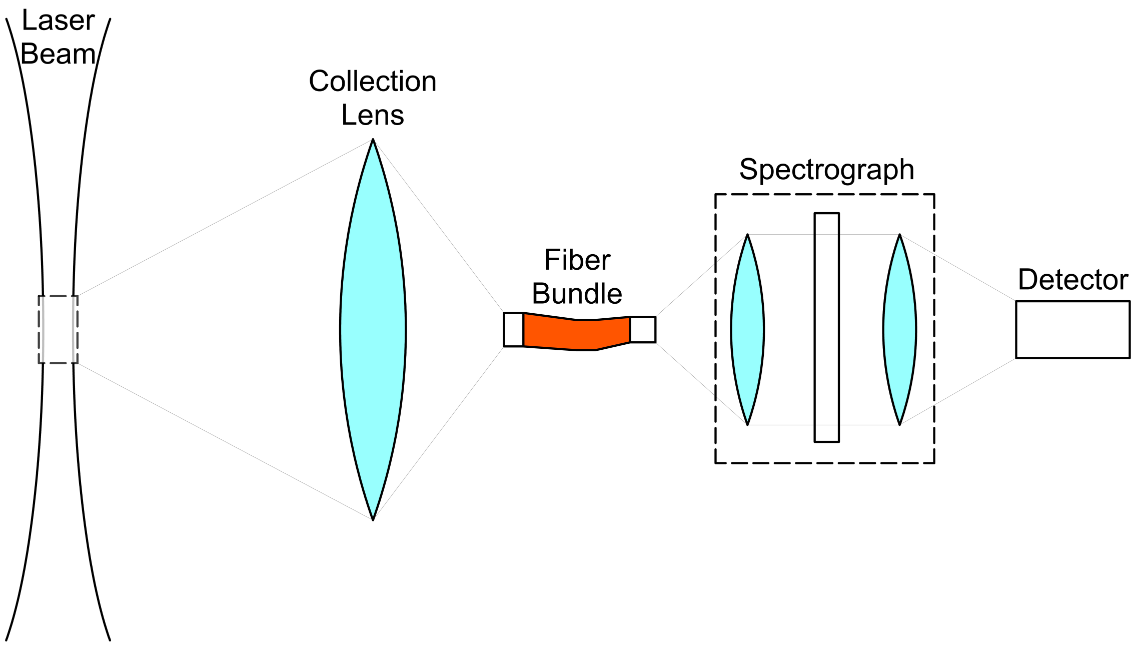

Figure A.15: A basic cartoon of the major optical components of CTH's thomson scattering collection system.

the thomson scattering collection system will be presented in the reverse process starting from vacuum window and finishing at the detector.

A.4.1 Reentrant collection optics flange

As discussed in section A.3.1, the only feasible thomson scattering geometry in CTH was a vertical beamline through the top and bottom 10" ports meaning that a custom reentrant flange needed to be designed and purpose built to view this beamline. The goals of the reentrant flange were to provide the largest clear aperture possible, to minimize the distance between the focusing optics and the beamline, and to view the beamline from a sightline as close to perpendicular as possible. The design document for the specification of the thomson scattering collection optics flange can be found in figures B.4a through B.4g.

The first step to achieve the above goals was to establish the beamline location since not only are the top and bottom 10" ports not centered on the vacuum vessel (see figure A.5b), but also these two 10" ports don't share a common center. In fact figure A.16 shows a top schematic view of the custom collection optics flange installed on CTH in the correct orientation, where

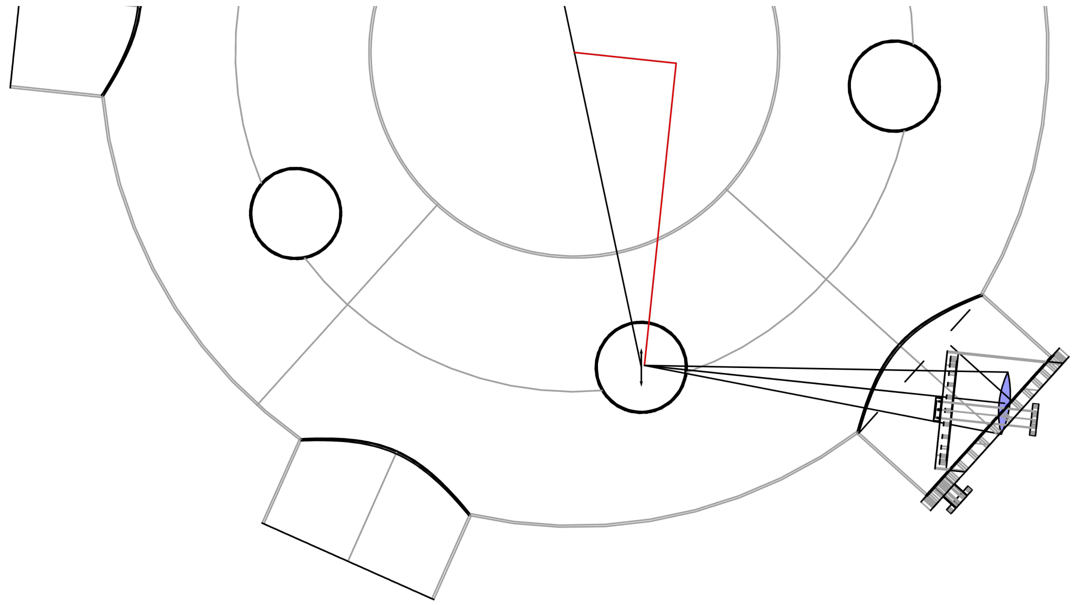

Figure A.16: Top view of CTH vacuum vessel with 18" reentrant thomson scattering flange shown. The red lines depict the measured position of the center of the top 10" port where the beamline is located. Note that this measured position of the beamline location is not the nominal center of the 10" port. The black arrows show the laser polarization, which has $\sim$ 86° angle with the vector perpendicular to the cartoon collection lens shown. Also the distance from the laser axis to the center of the cartoon collection lens is $80\,cm$.

critically the red lines show the measured location of the beamline from CTH's machine coordinate origin. Moreover figure A.16 shows the correct orientation of the laser polarization (see small black arrows) as it propagates through CTH allowing for an estimation of the angle between the beam polarization and the vector perpendicular to a potential collection lens leading to a value of $\theta_{polarization} = 86.371°$.

The next step in the design of this custom viewport was the pursuit of the largest possible clear aperture viewing the thomson scattering volume. To achieve this goal, the reentrant tube was chosen to fit a standard, commercially available 10" conflat zero-length fused silica viewport. However such a choice meant that a standard 18" conflat flange could only accommodate a $54°$ rotation before infringing on the 18" flange's conflat knife-edge spacing, meaning that the polarization angle of $\theta_{polarization} = 86.371°$ and depicted in figure A.16 demonstrated the best situation possible for the design of the 18" reentrant flange (see figure A.17 for good visualization on the spacing for the reentrant tube). It should also be noted that reentrant tube accommodating a 10" zero-length fused silica viewport not only provided a clear aperture of

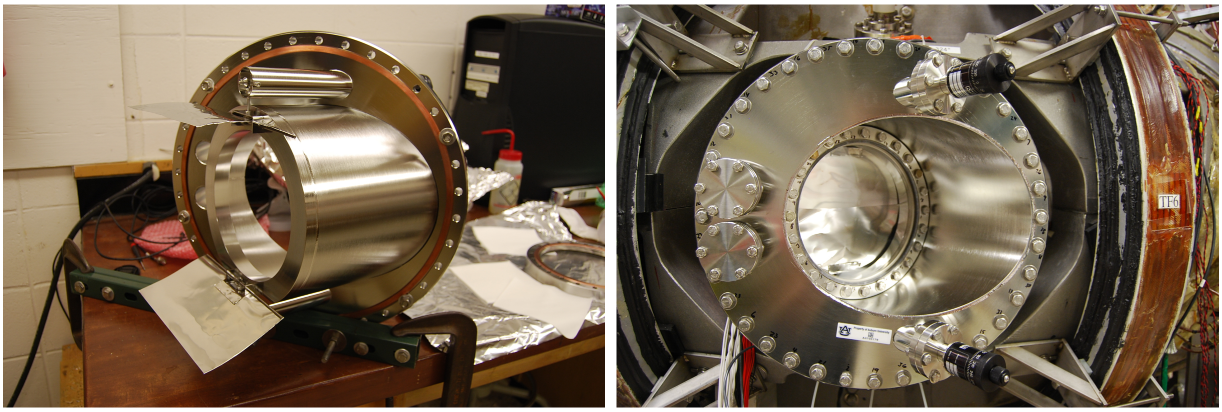

(a) (b)

Figure A.17: In (a) the collection optics flange is on the bench in order to fix the shutters before the entire flange is installed on CTH. In (b) collection optics flange is installed on CTH with the two rotation feedthroughs used to control the shutters for the 10" window. Also note the two extra standard $2\frac{3}{4}$" ports for supplemental diagnostic access.

7.78", but also gave extra flexibility in the alignment positioning of the collection optics inside this reentrant tube.

The last step in achieving the three main goals of the 18" custom collection optics flange was determining the extent the reentrant tube could safely extend within the 18" port. The top view depicted in figure A.16 shows the inward most part of the reentrant tube stays well within the 18" port by the dashed line indicating the midplane position where the 18" port opens up to vacuum vessel. This reentrant tube design allowed for the collection optics to be placed closer than $80\,cm$ shown by the cartoon collection lens, with a minimum distance of $\sim 71.5\,cm$. Although minimizing the distance between the collection optics & the beamline and achieving the largest possible clear aperture were necessary for a successful reentrant flange design, they also meant a complicated shuttering system was necessary to protect the window from plasma coating during glow discharge cleaning. Figure A.17a shows the original shutter design with two stainless steel shims connected to their own rotary feedthrough (see figure A.17b) via two sets of miter gears. The large clear aperture and deep extension into the 18" port required not only two shutters to fully cover the 8" window, but also that the shutters be flexible enough to bend across the inner 18" port wall in order to prevent the shutters protruding too deep into the vacuum vessel and acting as a limiter. Unfortunately this design was problematic and didn't consistently work due to the flex in the 18" flange after the conflat gasket was crushed causing the small miter gears to slip. Ultimately this design was altered to move each shutter's axis mounting off their $2\frac{3}{4}$" reentrant half nipple in addition to using larger miter gears to minimize the possibility of teeth slippage.[i]

A.4.2 Collection optics off-the-shelf design

The CTH thomson scattering system was designed to be a single spatial point measurement on the magnetic axis that is viewed via the 18" reentrant flange as described in section A.4.1. The goals of the thomson collection optics were to maximize the signal via the fastest optics (i.e. lowest $f/\#$) possible, ensure the correct demagnification for input into a fiber bundle, provide a robust optical setup for ease of alignment, and finally have a simple design using off-the-shelf components.

In the initial design of the CTH thomson scattering system performed in [97], the collection optics design was based off a single custom manufactured, anti-reflection coated aspheric lens with aperture area of 150 cm^2 and $f/\# \approx 1$. Unfortunately such a lens was not readily available as an off-the-shelf component and importantly would be prohibitively expensive for a single spatial point measurement. Therefore to accomplish the goals of the thomson collection optics, it was decided to use off-the-shelf PCX condenser lenses since these type of lenses are commercially available at large diameters, short focal lengths (i.e. very low $f/\#$), and can be ordered with an anti-reflection coating.[j] As detailed in section A.4.1, the thomson viewing window was a standard 10" conflat UV-grade fused silica window with 7.78" clear aperture, which effectively capped the largest possible diameter for the collection optics. Therefore two different lens from Edmund optics were identified as a possibility: a 150 mm and 200 mm diameter lens each with a $f/2$.[k]

In order to evaluate each lens and the combination of these lenses, the free software OpticalRayTracer[108] was used to predict the optical properties of the various setups. From this optical modeling it was determined the combination of a 200 mm and 150 m lens in sequence

[i]The task of redesigning and fixing the shutters was completed by fellow graduate student Nicholas Allen

[j]A PCX condenser lens stands for plano-convex which will suffer from much larger spherical aberrations than a corresponding aspheric lens.

[k]See footnote j

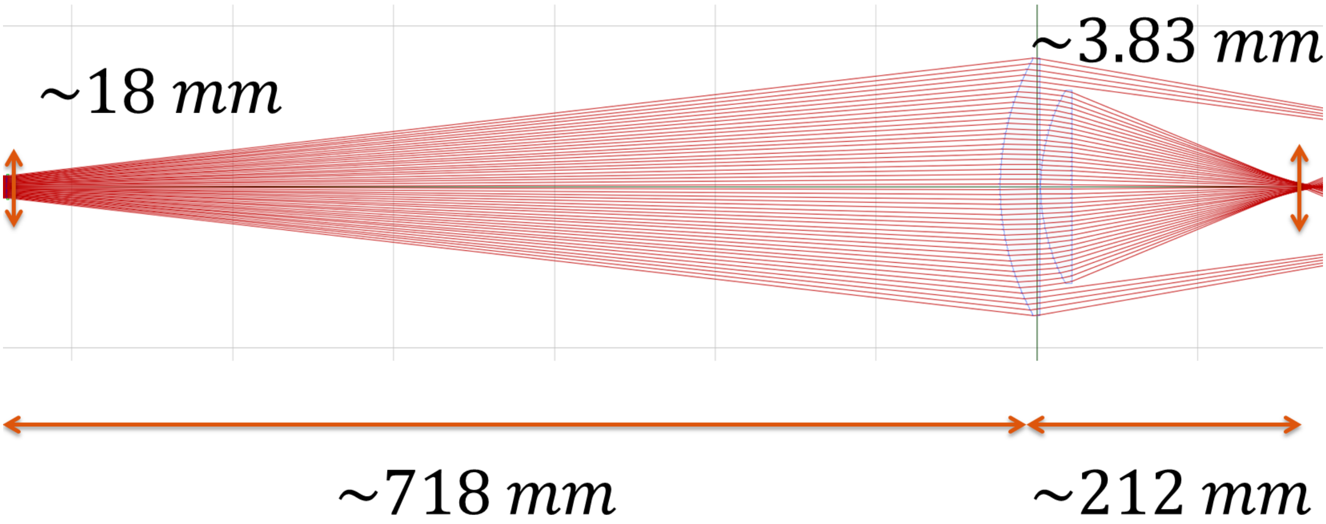

Figure A.18: Using the OpticalRayTracer free software the focusing properties of a combination of 200 mm and 150 mm plano convex lens made from N-BK7 were calculated for 532 nm light. The 18 mm represents the possible distance along the laser beamline that could be imaged, the 718 mm distance represents the closest the front 200 mm lens could be to the beamline, the 212 mm represents the location of smallest image size, and the 3.83 mm is the height of the image at the 212 mm location.

was the best option since it provided a large clear aperture ($\sim$ 155 mm) with small $f/\#$ ($\sim$ 1.39) as shown in figure A.18. The ray tracing performed using the OpticalRayTracer software was instrumental for not only validating a proof of design, but also for providing an estimation on the spherical aberration impact to image location and magnification. In figure A.18 the outermost rays clearly demonstrate the spherical aberration with a much shorter focal length meaning that using the entire clear aperture will not necessarily yield a sharp image at the nominal image plane. Luckily for the thomson scattering system, achieving a sharp image of the laser beamline at the input fiber bundle is not necessary since it is just the total number of photons doppler shifted that is necessary for an estimation of the electron density and temperature. It is for this reason simple plano-convex lenses can be utilized within this optical system.

Once the ray tracing results helped verify the optical design for achieving the collection optics goals for a large aperture, low $f/\#$, and viable demagnification, an appropriate custom optics mount was designed to hold the 200 and 150 mm optical system. The design document for the collection optics mount machined out of Delrin can be found in figures B.5a through B.5e. After the collection optics mount was fabricated, the optics were tested in order to verify

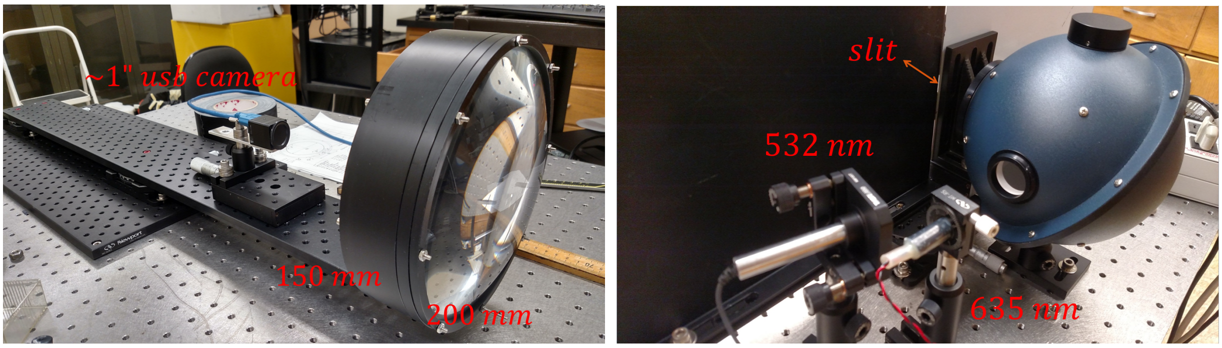

(a) (b)

Figure A.19: In (a) the collection optics mount is attached to the end of the 4” by 36” optical breadboard and the 12” by 24” optical breadboard used as a removable table top for the thomson collection optics system. Note that the 1” usb camera is mounted off a translation stage to perform the image plane testing. In (b) the two laser sources (i.e. 532 and 635 nm) are positioned to enter an integrating sphere that then illuminates a 15 mm by 2.5 mm slit which mimics the thomson beamline.

the optical properties predicted from the ray tracing model. As shown in figure A.19 the collection optics were tested on the bench using a 15 mm by 2.5 mm slit mimicking the thomson laser beamline and a 1” usb camera mounted at the input fiber bundle position for image verification. The slit was illuminated by a red (635 nm) and green (532 nm) laser via an integrating sphere to simulate the thomson signal and to verify chromatic effects would be minimal. Using a translation stage for the 1” usb camera mount, the image distance could be varied to confirm the optimum position for collecting the most amount of light. Figure A.20 shows the results from the image plane bench testing for three different image plane distances: 214.95 mm, 217.49, and 220.03 mm shown in figure A.20a, A.20b, and A.20c respectively. As predicted in the optical ray tracing (see figure A.18), the optimum distance for collecting the most light was not at the nominal image plane ($\sim$ 220 mm) but at a closer distance ($\sim$ 214). This position at $\sim$ 214.95 turns out to encompass the highest percentage of the light emitted over a fixed area as demonstrated in figure A.21. This fact is true even though the image at $\sim$ 214.95 looks defocused as shown in figure A.20a. Ultimately this bench testing not only validated the optical ray tracing modeling performed, but also helped determine the appropriate size for the input fiber bundle size as will be discussed in section A.4.3.

The final key design feature of the collection optics was the flexible mounting system that allowed the collection optics to be placed as close to the vacuum window as possible,

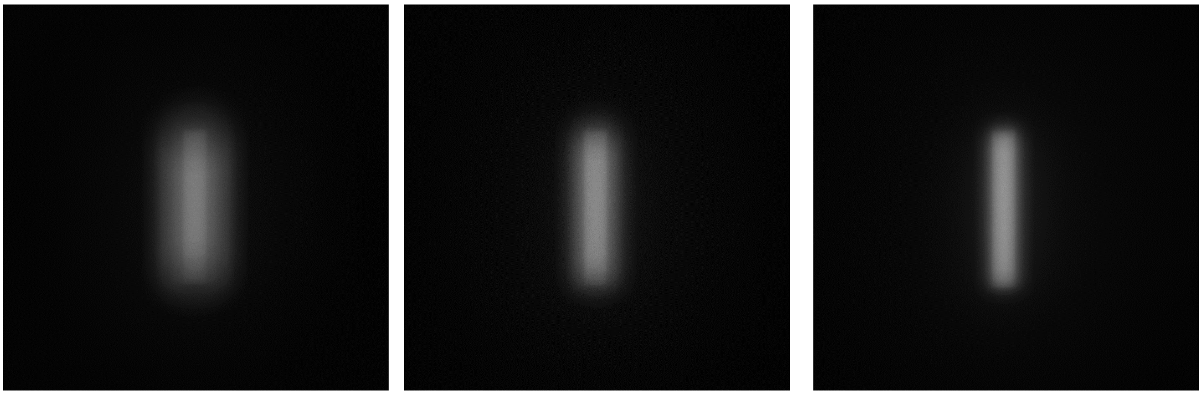

(a) (b) (c)

Figure A.20: The output of the 1" usb camera is shown for three different image plane distances from the collection optics bench testing shown in figure A.19. The image distances are 214.95 mm, 217.49, and 220.03 mm respectively for (a), (b), and (c).

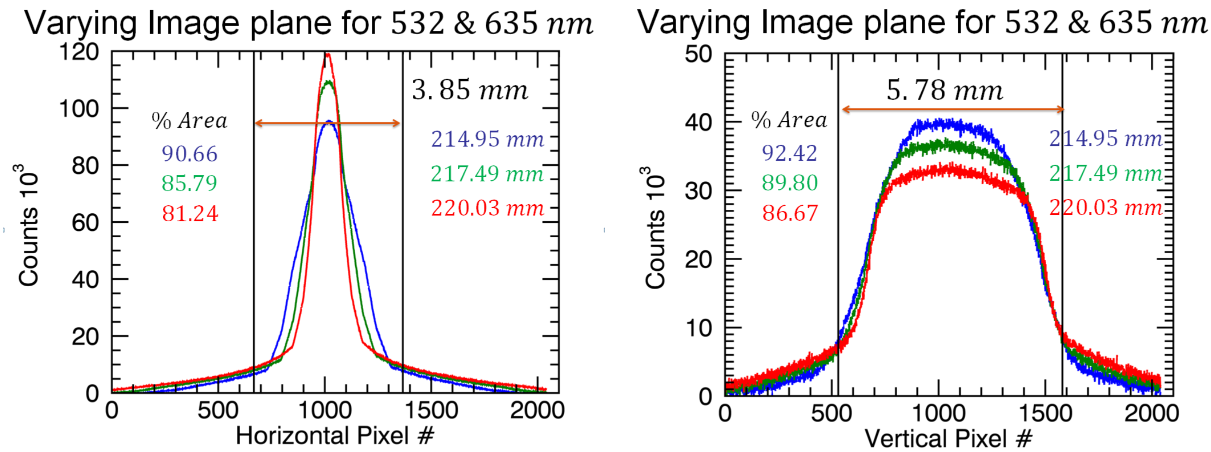

(a) (b)

Figure A.21: The vertical and horizontal binning of the images shown in figure A.20 are shown in (a) and (b) respectively. Importantly the total percentage of the signal that falls within the 3.85 mm for the vertical binning in (a) and the 5.78 mm horizontal binning in (b) are calculated and demonstrate the defocused image location at $\sim$ 214.95 is the best position to collect the highest percentage of the signal.

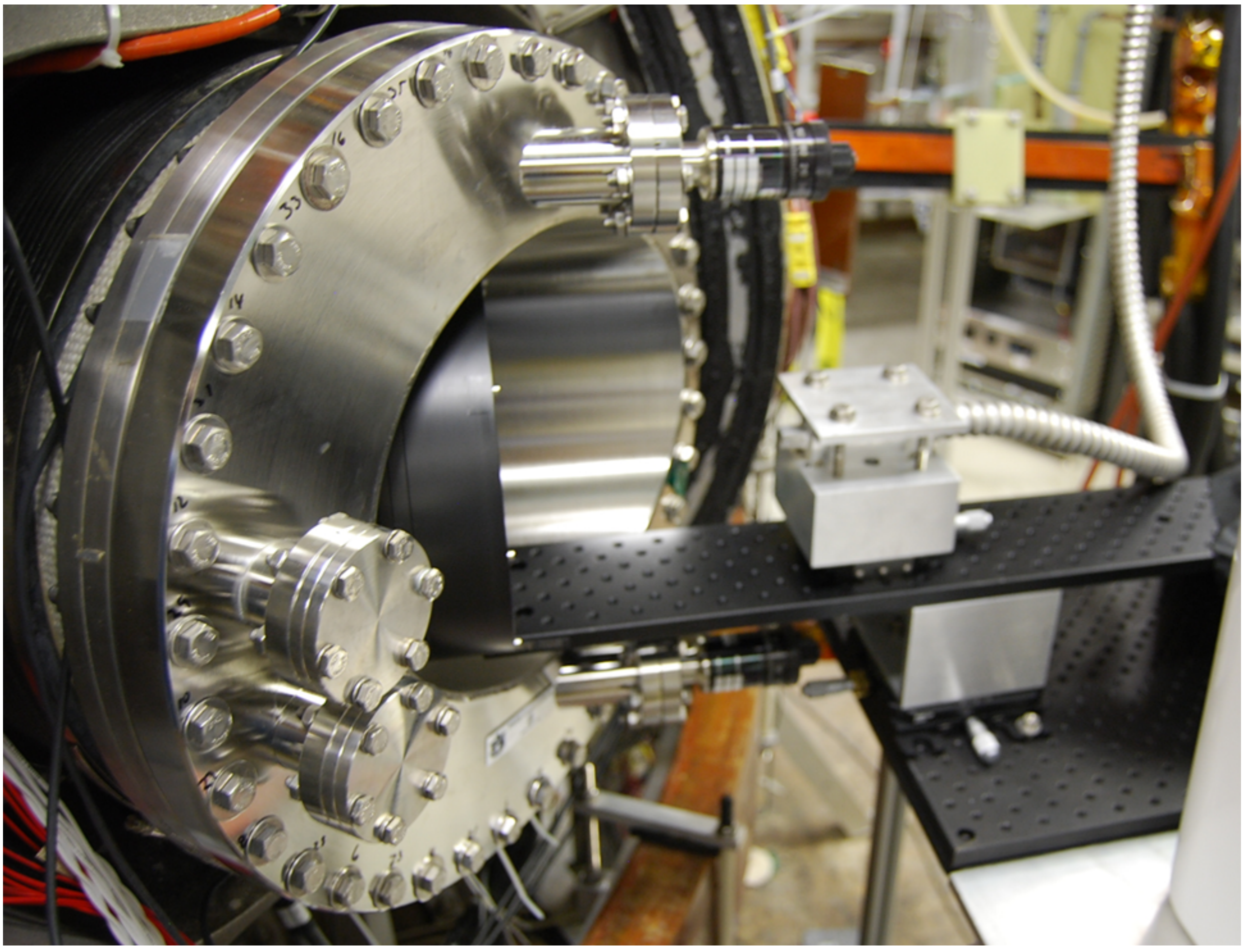

Figure A.22: The thomson scattering collection optics mounted on CTH with the 4” by 36” optical breadboard placing the optics right outside the 18” reentrant port while keeping the fiber bundle in the correct imaging location (i.e. $\sim$ 214 mm as measured from the front of the Delrin mount).

ensured that the fiber bundle was always on the optical axis, provided an easy way to adjust the alignment, and was easily removable for any other diagnostic that wanted to use the reentrant flange’s 10” UV-grade window. The first two benefits listed above for the CTH collection optics were accomplished by designing the collection optics mount to attach at the end of an off-the-shelf 4” by 36” optical breadboard. In fact figure A.22 shows this 4” by 36” optical breadboard providing both the length necessary to place the collection optics right at the reentrant window and the rigid structure to ensure the collection optics fiber bundle was always on the optical axis. Also shown in figure A.22 is one of the two two-axis rotation translation stages that connect the 4” by 36” optical breadboard to another 12” by 24” breadboard acting as a tabletop. Critically the two-axis rotation translation stages are mounted on the 12” by 24” optical tabletop with the maximum distance (i.e. 24”) in order to provide fine angle adjustments of the entire optical axis on the 4” by 36” optical breadboard. In this way small linear translations that are perpendicular to the optical axis and not identical in magnitude for both the stages would allow the mounted 4” by 36” optical breadboard to slightly rotate on the stages. Such a design meant the collection optics position could easily be optimized in situ ensuring the thomson beamline was being adequately imaged. Finally the last benefit designed into the collection optics was a 12” by 24” optical breadboard that acted as the optical table for the entire CTH collection optics system. This 12” by 24” optical breadboard was modified to sit on four stainless steel precision balls allowing for the breadboard to be quickly removed and placed exactly back into position. Practically this meant the entire CTH collection optics system could be quickly demounted and moved out of the way for other diagnostics to use the 10” fused silica window (e.g. coherence imaging diagnostic), while not worrying about the thomson collection optics alignment being ruined.

A.4.3 Input fiber bundle, spectrometer, and detector setup

The last major components for the CTH collection optics design completed for this thesis work are the input fiber bundle, the spectrometer, and the single Photomultiplier tube (PMT) used as a test detector. The two primary goals of these components are to conserve and to disperse the thomson scattered signal collected via the optics detailed in section A.4.2. As referenced in the introduction of section A.4 the first step in the thomson collection system design process is ensuring that the thomson scattered signal is conserved as it propagates through all the optical elements. In other words this signal conservation goal is just the maximization (or very least matching) of the geometrical extent through all the optical elements. The definition of the geometrical extent can be seen in equation A.13 where n is the index fo refraction, S is the area of some emitting/collecting surface element, and θ is the polar angle from a spherical coordinate system.

$$dG = n^2\left(dS\cos\theta\right)d\Omega = n^2\left(dS\cos\theta\right)\left(\sin\theta d\theta d\phi\right) \quad \Rightarrow \quad G = \pi n^2 S\sin^2\theta \qquad \text{(A.13)}$$

Usually this geometrical extent optimization process starts with the detector due to the high performance requirements and subsequent high cost making it the most likely optical component that will restrict the geometrical extent. However for consistency with the previous sections, this section will continue following the thomson scattered signal as it is transmitted through the various optical components before ultimately arriving at the detector as shown in the cartoon A.15.

Following this outline, section A.4.2 already demonstrated the necessary location and approximate area for a needed fiber bundle to collect the thomson scattered light from a $\sim$ 15 mm long by 2.5 mm wide source. In fact figure A.21 demonstrates that a 5.78 mm long by 3.85 mm wide collection area would capture $\sim$ 90% of the scattered light. Therefore using this area as a basis for an approximate size of the fiber bundle, a specification document was created for a fiber bundle design, see B.6. The best commercial option for this design came from Fiberguide industries, which manufactures a hard clad silica core fiber (SPCH200) with high OH for lower attenuation in the visible spectrum and a high numerical aperture of $NA = 0.37$. Using the dimensions for the individual fibers it was determined that 450 fibers arranged in a 25 rows ($\sim$ 5.87 mm) by 18 columns ($\sim$ 3.62 mm) layout most closely matched the desired dimensions as shown in figure A.23 Armed with the dimensions and location for the fiber bundle, the geometrical extent can be calculated for both the collection optics and the corresponding fiber bundle shown in figure A.23. In order that the thomson signal is conserved the geometrical extent for the fiber bundle's ability to accept light should be greater than or equal to the geometrical extent for the fiber bundle viewing the collection optics. Employing equation (A.13) the geometrical extent for the fiber bundle's ability to accept light can be calculated as seen in equation (A.14)

$$G_{fiber} = \pi n^2 S_{fiber} \sin^2\theta = \pi S_{fiber} \Big(NA\Big)^2 = \pi \left(18.696\, mm^2\right) \Big(0.37\Big)^2 = 8.041\, mm^2 sr \tag{A.14}$$

Then the next step is conserving the geometrical extent from the collection lens onto the fiber bundle meaning that the geometrical extent for fiber bundle viewing the collection optics better be less than the previous geometrical extent calculated in (A.14). Performing this calculation as shown in equation (A.15), it is clear that the fiber bundle due to its high numerical aperture

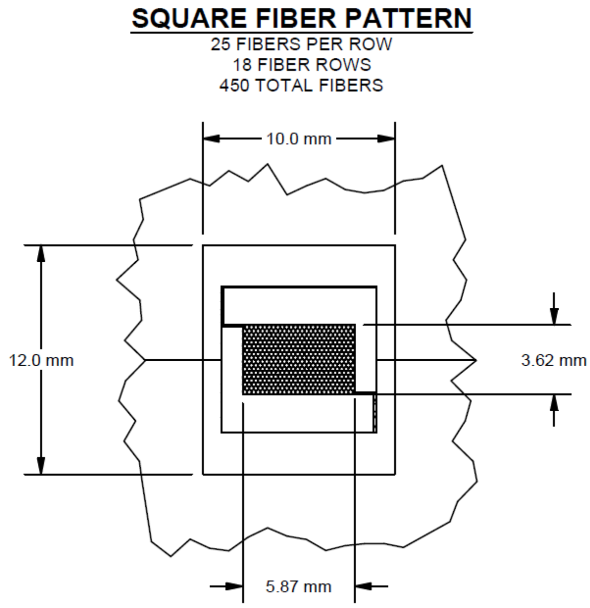

(a)

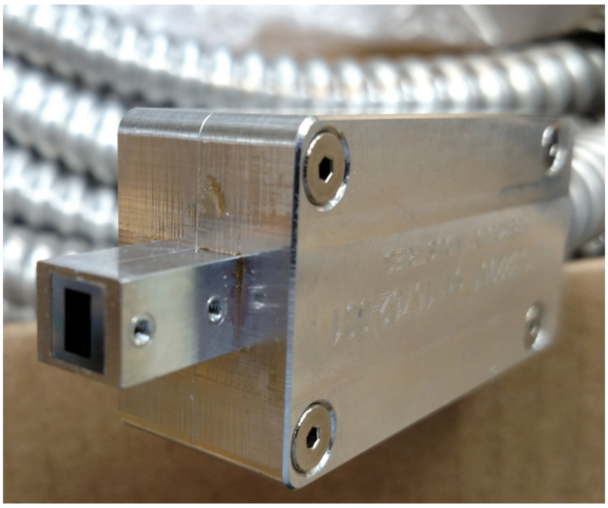

(b)

Figure A.23: The designed fiber bundle for collecting the thomson beamline image is shown in (a) and the same designed Fiberguide industries built fiber bundle is shown in (b)

fibers can readily accept all the light that the collection optics passed onto it.[l]

$$G_{collection} = \pi n^2 S_{fiber} \sin^2 \left[\tan^{-1} \left(\frac{155\,mm}{2\,(214\,mm)} \right) \right] \quad \Rightarrow \quad G_{collection} = 6.8102\,mm^2 sr \tag{A.15}$$

Next the fiber bundle is repacked into an elongated rectangular shape (i.e. the 450 fibers are arranged in 75 rows by 6 columns) as shown in figure A.24. This repacking is important for two reasons: first this repacking helps take advantage of the extended vertical clear aperture afforded by the spectrometer and second the thin fiber bundle width ($\sim$ 1.23 mm as shown in A.24a) will minimize the spectral wavelength mixing at the spectrometer output.[m] Finally as the last aspect of the collection optics fiber bundle, the reshaped end was designed to easily mount into the modified snap-in connector for the spectrometer as shown in figure A.25.

As just mentioned the fiber optic bundle was designed to couple the scattered and background light into a Holospec f/1.8 imaging spectrometer made by Kaiser Optical Systems with

[l]The caveat here is that there is a packing loss in the fiber bundle that is roughly 12% or that 88% of the light falling on the 5.87 mm by 3.62 mm area is transmitted

[m]The extended vertical clear aperture wasn't accurate. See the next paragraph for more details.

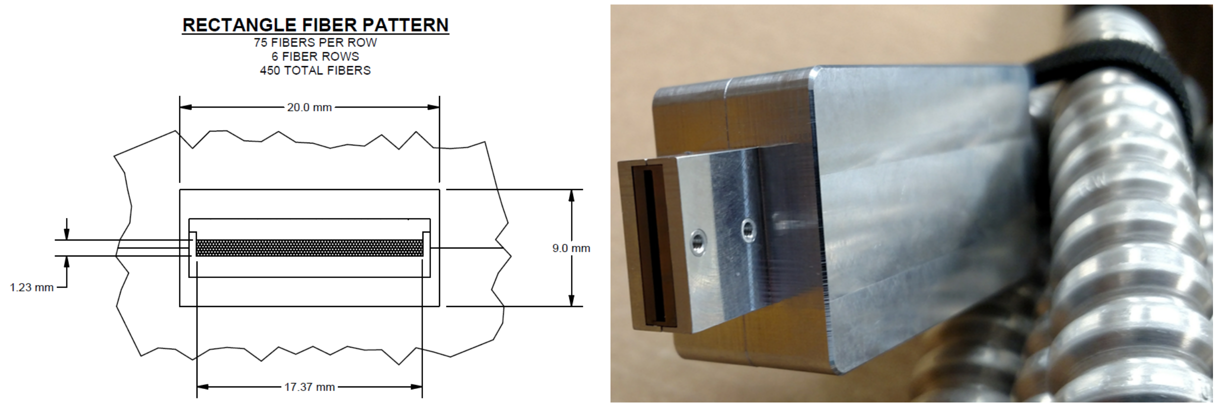

(a) (b)

Figure A.24: The design for the reshaped end of the collection optics fiber bundle that is meant for input into the spectrometer is shown in (a) and the same reshaped Fiberguide industries built fiber bundle is shown in (b). To be clear these images correspond to the opposite end of the fiber bundle in A.23

Figure A.25: The fiber bundle attaches to the input side of the Holospec spectrometer using set screws (see figure A.24b for reference) on the snap-in optical mount. Unfortunately using this setup places the fiber bundle input not in the focal plane of the internal optics of the spectrometer.

(a)

(b)

Figure A.26: The layout of the Holospec f/1.8 imaging spectrometer made by Kaiser Optical Systems with anti-reflection coated optics and 532 nm laser notch filter is shown in (a). In (b) the custom volume phase holographic grating with linear dispersion at the output/detector plane of 1.135 nm/mm (i.e. 533.1 to 563.3 nm over 26.6 mm) is shown.

anti-reflection coated optics and volume-phase holographic transmission grating shown in figure A.26a and A.26b respectively. Although the fiber optic bundle was designed to simply connect via set screw to the spectrometer's removable input adapter, this turned out to be a mistake since no matter the image plane location at the output plane the input fiber bundle could never be placed fully in focus. The results of this first mistake is that the resolution of the spectrometer is slightly worse when the fibers are not in focus at the output plane which is something to consider for potentially adding cross-correlation to the spectrometer's separate wavelength channels at the output plane. Unfortunately there was a second and more important mistake: the spectrometer's slit focusing optics can't capture the full vertical extent of the input fiber bundle even when the fiber bundle is translated along the spectrometer's optical axis. This was unexpected because the spectrometer's manual indicated the spectrometer's input optics could accept $\sim 18\,mm$ vertical input (measured to be $18.4\,mm$)[n] Bench testing with the Holospec spectrometer confirmed that the total usable height was $\sim$ 13 mm and that the issue was related to the aperturing occuring at the slit focusing optics. Figure A.27 was produced from bench testing with the spectrometer demonstrating the aperturing happening that effectively reduced the transmitted signal by $\sim \frac{13}{17.37}$. Moving on from these two mistakes, the custom volume-phase holographic transmission grating shown in figure A.26b was selected to isolate the laser line 532 nm from reaching the output plane and more importantly select only

[n]From the HoloSpec user manual: "...the optics are well corrected over a height of $16\,mm$, so the spectrograph can be used over $16\,mm$ without a slit."

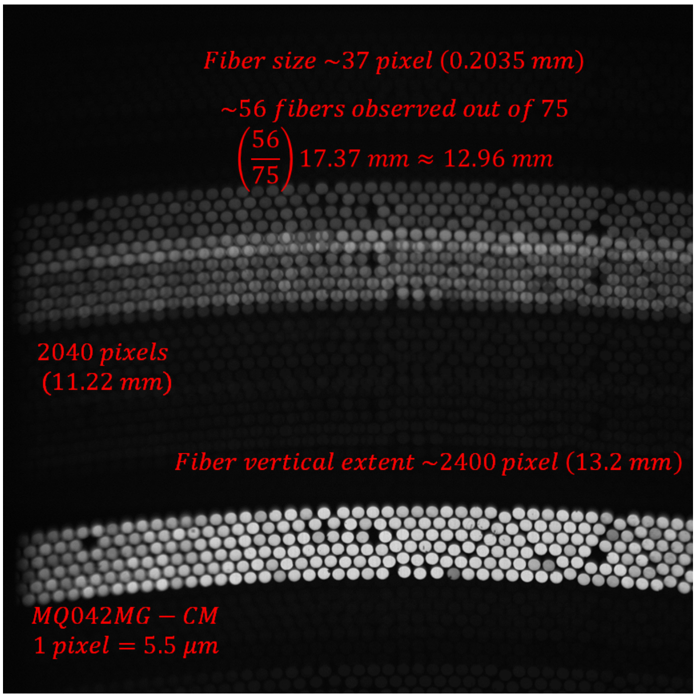

Figure A.27: The fiber bundle was clipped in the vertical direction due to the slit focusing optics only having a clear aperture of $\sim$ 13 mm or $\frac{56}{75}$ fibers visible at one time. The image was produced using the 1"usb camera at the spectrometer output plane and a neon arc lamp as the light source.

the red-shifted side of the doppler shifted thomson signal (i.e. 533.1 nm to 563.3 over the 26.6 mm output plane). It should be noted that red-shifted side of the 532 nm laser line was chosen due to the relatively fewer impurity spectral lines present in the wavelength range 533.1 to 563.3 nm. Also if the amount of stray laser light entering the spectrometer is still unacceptable using this grating, a notch or cut-on interference filter can be mounted at the Holospec input slit and used for spectral discrimination.

As final bench testing for the spectrometer, the induced curvature on the output plane was measured. This curvature shown in figure A.28 is important for establishing the correct wavelength channels for the thomson scattering measurement and for designing an output fiber bundle that prevents coupling between these wavelength bins by matching the curvature.[o] Also note that the necessary fiber type is different due to a higher numerical aperture needed by these fibers to not throw away light at the spectrometer's output plane. Unfortunately the necessary fiber bundle(s) from the spectrometer output plane to indivdual PMT detectors needed for a

[o]The basic design for an input detector fiber bundle is shown in figure B.8.

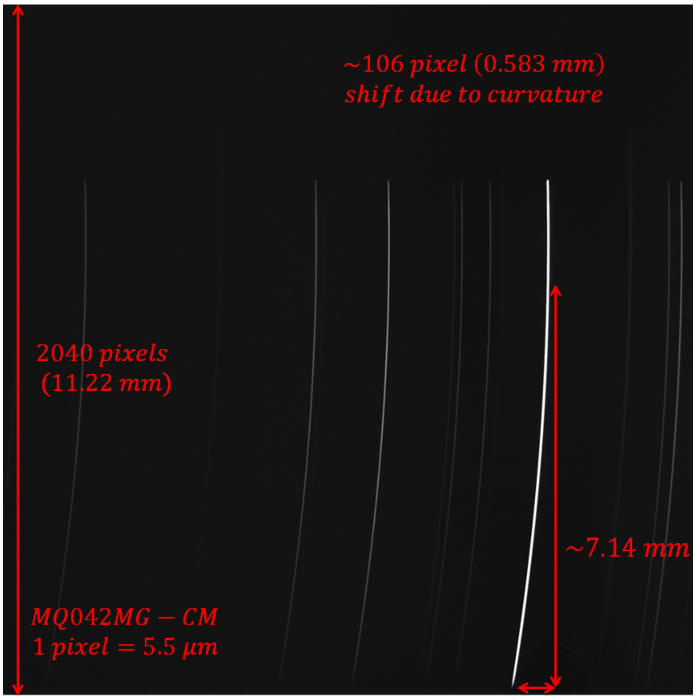

Figure A.28: Using the 1" usb camera, a neon arc lamp, and the custom volume-phase holographic transmission grating the curvature induced on the Holospec's output plane from the low $f/\#$ is measured.

working thomson scattering diagnostic was never fully finished because it was desired to first measure and confirm thomson scattered signal levels were close to those predicted for the CTH geometry. Figure A.29 demonstrates schematically how the detector input fiber bundles would be laid out and operate. Although initial designs have been prepared for a fully operational thomson system on CTH, without a means to discriminate the wavelength channels an electron temperature and density measurement cannot be accomplished.

Finally the last optical component in the CTH collection optics system is the detector. The initial CTH thomson scattering design described in [97] planned to use an intensified charged-coupled device (ICCD) camera as the detection element for the single spatial point thomson scattered light measurement. The unique advantage of choosing an ICCD as a detector is that multiple spatial points can be incident on a single detector where typically the wavelength dispersion of the thomson scattered signal is incident on the detector's horizontal axis while the vertical axis has multiple spatial points. This is very different than the traditionally-used polychromators which have multiple detectors (i.e. PMTs) for a single spatial point since each detector is used for a specific wavelength range (see [101, 71] for good examples of this type

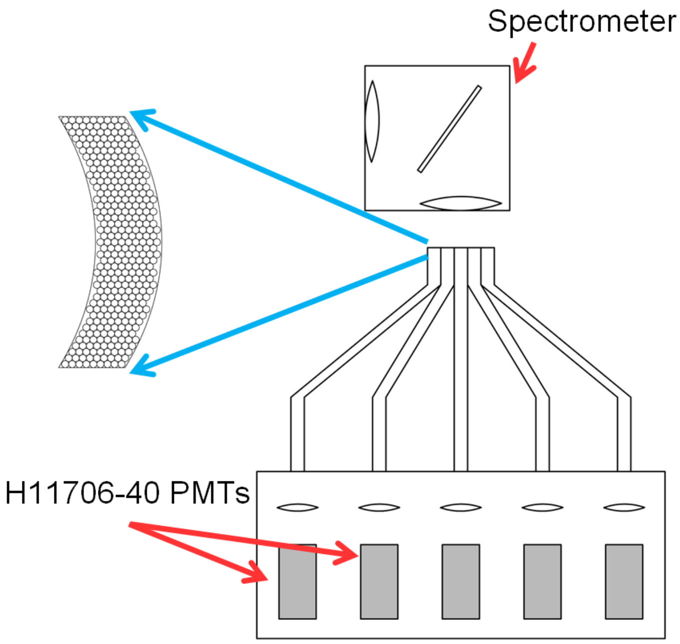

Figure A.29: A schematic demonstrating how a curved fiber bundle(s) at the spectrometer output would be used to directly feed into five different PMT detectors (Hammatsu H11706-40) to use as the wavelength bins in the calculation of the doppler broaden thomson signal.

of detection system). The main drawback of the using an ICCD detector is that the measured signal is an integrated signal (converting from photo-electrons to photons through a phosphor screen is a slow process $> 200\,ns$) meaning a background channel is necessary to validate the measured signal. The power in using an ICCD detector is the versatility in having multiple spatial points and wavelength channels on a single detector, but with the caveat that each spatial channel requires a corresponding background channel (see [99] for an example of such a system).

Rather than attempt to measure a time-integrated signal using an ICCD, it was decided to use commercially available and a relatively cheap (i.e. $\sim$ \$3000) photomultiplier tube from Hammatsu to perform signal level tests and verifications. The Hamamatsu H11706-40 PMT module was chosen for its large effective area (i.e. 5 mm diameter), fast gating (i.e. FWHM of 1 ns), high quantum efficiency in the visible (i.e. $\sim 40\%$ at 550 nm), and high signal gain (i.e. $\sim 10^3$ to 5×10^5). Therefore a single Hamamatsu H11706-40 PMT module was purchased to perform Raman scattering experiments off of neutral nitrogen gas in CTH, to measure plasma background light levels for typical CTH plasmas, and finally to measure thomson scattered

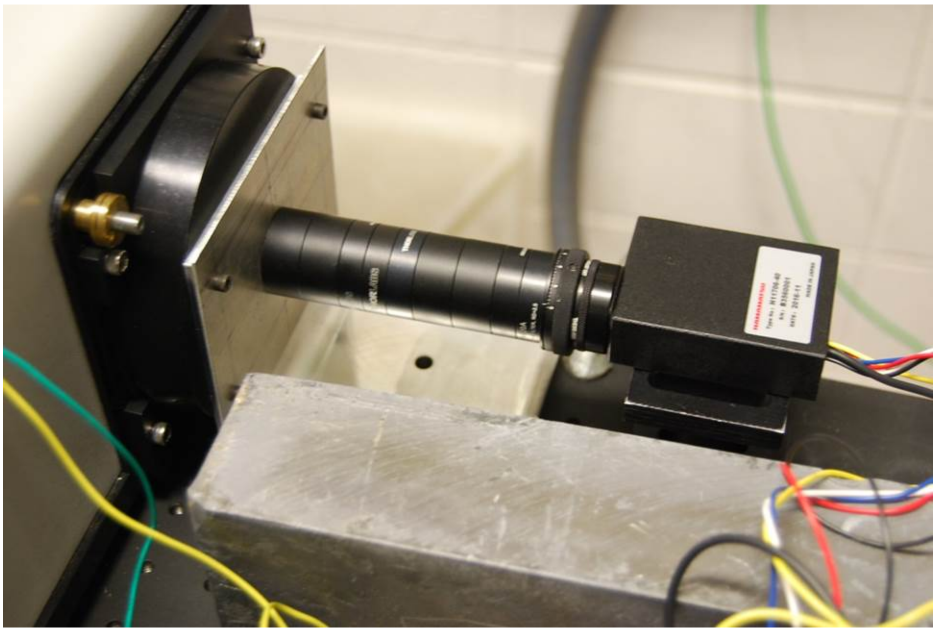

Figure A.30: A picture demonstrating a simple plate mount with a few optical elements for attaching the Hamamatsu PMT to the center of the output plane of the spectrometer.

light. In order to accomplish these experiments the PMT module was connected to the output plane of the Holospec spectrometer using a simple plate and some optical components as shown in figure A.30. To measure the output signal the PMT output was fed into a 1 GHz oscilloscope and integrated into CTH's trigger system, with the Powerlite laser system supplying the laserhead flash trigger to successfully acquire signal via the oscilloscope.[p] The advantage of the PMT coupled with a fast oscilloscope is that the time history of the laser pulse and any measured scattered signal can be visualized and corroborated with each other. Due to the PMT's output impedance of 50 Ohms, a simple resistor circuit designed by John Dawson was implemented and schematically shown in figure A.31.

Also from [109], the Hamamatsu photomultiplier handbook, the expected current collected at the anode can be expressed by equation (A.16) where μ is the gain from the dynode stages and $\tau_{laser\,pulse}$ is the pulse length of the laser.

$$I_{signal\,at\,anode} = \mu \frac{e}{\tau_{laser\,pulse}} \left(n_{photo-electrons}\right) \tag{A.16}$$

[p]It is important to note that unexpectedly this PMT required a modulating trigger voltage to ensure the photocathode would stay off.

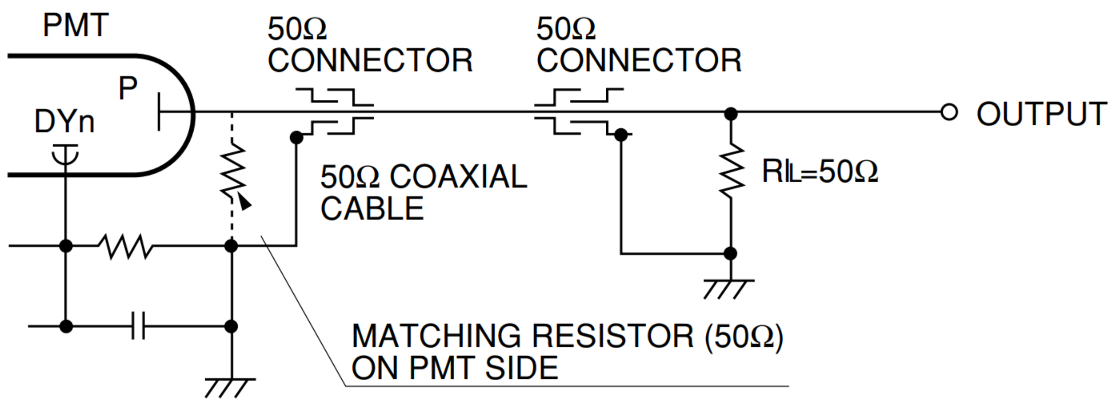

Figure A.31: A circuit showing the connection between the PMT output signal and the fast oscilloscope as designed by John Dawson.

As mentioned earlier the PMT current has a fast response time ($\sim$ 1 ns) meaning the typical laser pulse shown in figure A.32 can be resolved. However the short pulse width does contribute to the signal-to-noise ratio calculation as evidenced by equation (A.16) where B is the bandwidth of the measured signal, F is the excess noise factor for the PMT based on the dynode structure, I_{dark} is the dark current at the last anode, and I_{amp} is the noise from any amplifier circuit.

$$SNR = \frac{I_{signal\,at\,anode}}{\sqrt{2eBF\mu\left(I_{signal\,at\,anode} + 2I_{dark}\right) + I_{amp}^2}} \tag{A.17}$$

Using equation (A.17) the signal-to-noise ratio can be calculated for the expected thomson scattered signals entering the Hamamatsu H11706-40 PMT module.[q]

A.5 Signal estimations and preliminary measurements of the thomson system

A.5.1 Thomson scattering modeling and measurements

Before delving into the details of the signal estimations it is important to summarize key values for the CTH single spatial point thomson scattering system as listed in table A.2. Utilizing the values from table A.2, the thomson scattered signal per unit wavelength can be estimated from equation (A.1) at various possible electron temperatures (i.e. $T_e \approx$ 50, 100, 150, and 250

[q]The Hamamatsu H11706-40 PMT module has a 2 μA max average current output meaning that it might rail from background noise before a thomson signal is measured. The impact of this 2 μA max average current output is not clear.

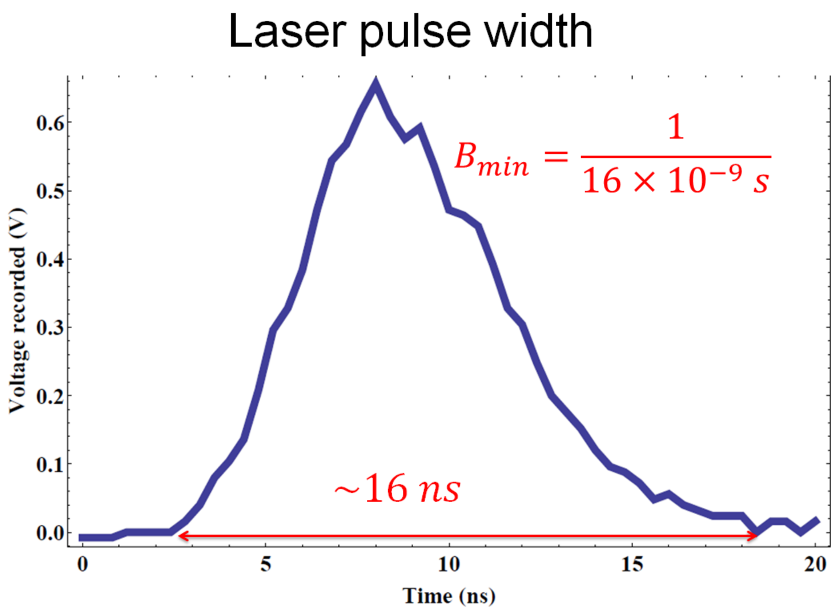

Figure A.32: A typical laser pulse width measured using a fast diode placed behind a laser turning mirror on the optical table. The B_min represents the minimum bandwidth that the PMT detector takes and is used within the signal-to-noise ratio as seen from equation (A.17)

Parameter	Dimension
System etendue	1.36 mm^2 sr
Collection optics effective $f/\#$ on axis	$\sim$ 1.39
Collection optics effective focal length	$\sim$ 215 mm
Scattering length	$\leq$ 1.4 cm
Laser energy	1.7 J
Scattering wavelength	532 nm
PMT active area	19.63 mm^2
Estimated excess noise factor	$\sim$ 1.6
Average PMT quantum efficiency	$\sim$ 0.39
Estimated system transmission	$\sim$ 0.37
$\frac{Total\, photo-electrons}{10^{19}\, plasma\, electron}$	$\sim 10^4$
$\frac{Total\, electrons\, collected\, per\, channel}{10^{19}\, plasma\, electron}$	$\sim 10^3$
S/N ratio per channel	$\sim$ 8 to 40

Table A.2: CTH single spatial point thomson scattering design parameters

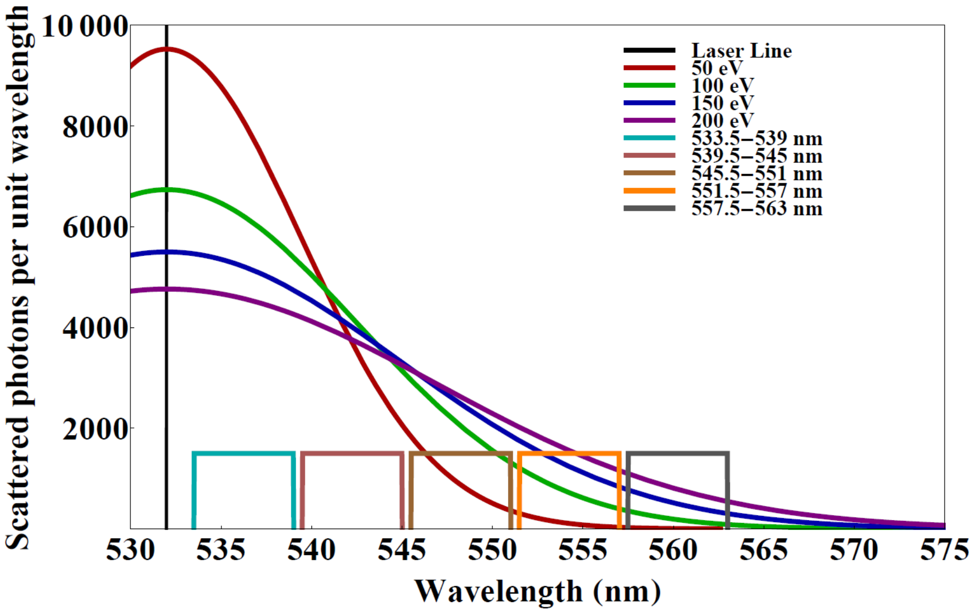

Figure A.33: The scattered photons per unit wavelength using CTH relevant parameters and for four different electron temperature scenarios (i.e. $T_e \approx$ 50, 100, 150, and 250 eV). Also the proposed five different wavelength bins are shown that would be used experimentally to determine the T_e from the doppler broadening in the thomson scattered signal.

eV). The result from this estimation using these CTH relevant parameters is shown in figure A.33.[r] Note that figure A.33 also includes five different wavelength regions corresponding to 5.5 nm bins or roughly $\sim$ 4.85 mm on the output plane of the Holospec spectrometer using the custom VPH grating. These 5.5 nm wavelength regions with 0.5 nm (or $\sim$ 0.44 mm) spacing between them would be utilized as individual signals collected via their own fiber bundle and PMT detector.

Next the same calculation for the thomson scattered signal can be performed, however this time the expected signals for each of the five proposed wavelength regions, shown in figure A.33, can be examined as a function of electron temperature. The result of this calculation is depicted in figure A.34 where the expected signal levels for the two wavelength regions above 551 nm are only a few thousand photons. In order to better understand how the scattered photons at each wavelength region's detector translates into measurable signal, a signal-to-noise ratio can be calculated for the Hamamatsu PMT detectors as detailed in section A.4.3 via equation (A.17). Plugging in the typical values for this PMT module (excess noise factor $F \approx 1.6$ and $I_{dark} \approx 1nA$, and I_{amp} assumed to be 0) each channel's SNR is plotted in

[r]All of the estimations shown in this section are for plasma electron densities of $1\times 10^19\ m^3$

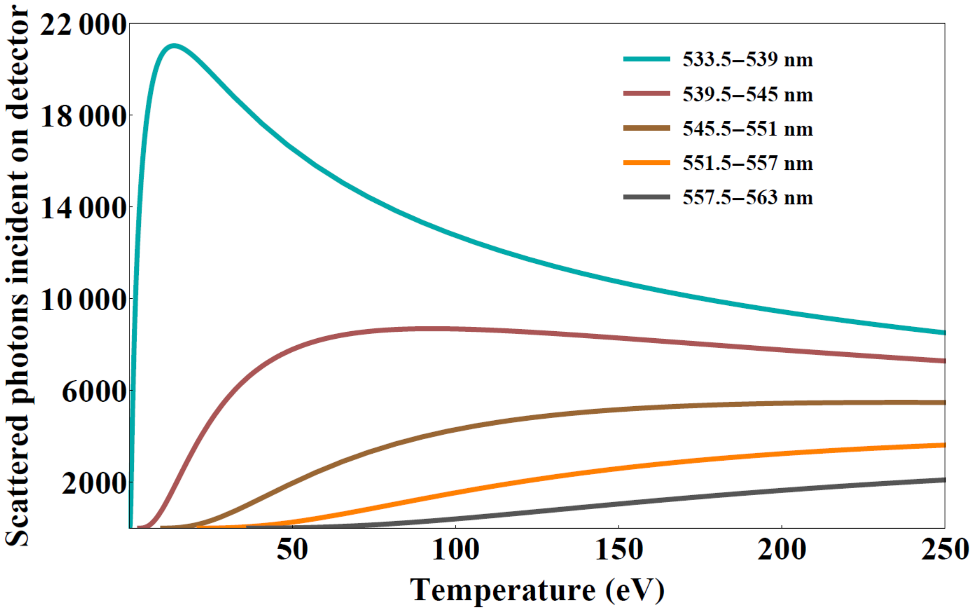

Figure A.34: The scattered photons for each wavelength region are plotted as a function of T$_e$. Note that at CTH relevant temperatures (i.e. T$_e$ < 250 eV) the outer most channels would have low number of incident photons on the PMT photocathode.

figure A.35. The signal-to-noise calculation demonstrates that using this PMT module for CTH relevant parameters should return reasonable signals, i.e. SNR $\geq$ 8, for any plasma with $n_e \geq 1 \times 10^19$ and with T$_e \geq$ 100 eV on the magnetic axis. This thomson scattering system design only becomes problematic for the colder less dense pure stellarator plasmas where it wouldn't be surprising to find $n_e \approx 1 \times 10^18$ and T$_e \approx$ 50 eV on the magnetic axis. The bigger problem posed by these pure stellarator plasma is the low electron density aspect since the signal- to-noise ratio scales like $\sqrt{n_e}$ for all the wavelength channels making any estimations of n_e or T_e with reasonable errorbars more difficult.

After demonstrating a single spatial point thomson system based on this Hamamatsu PMT tube was feasible, actual plasma background data was measured. The results of nearly identical plasma shots are shown in figure A.36 where the only major difference is the gain setting on the PMT module. Encouragingly the change in gain setting from 0.5 to 0.7 V led to a roughly order of magnitude change in the PMT gain which was also reflected in the measured signal levels from the plasma. In contrast to the estimated signal levels for the small 5.5 nm wavelength windows, the background data was collected with the optical setup shown in figure A.30 meaning that the PMT was collecting light from $\sim$ 535 to 562 nm. In this way the

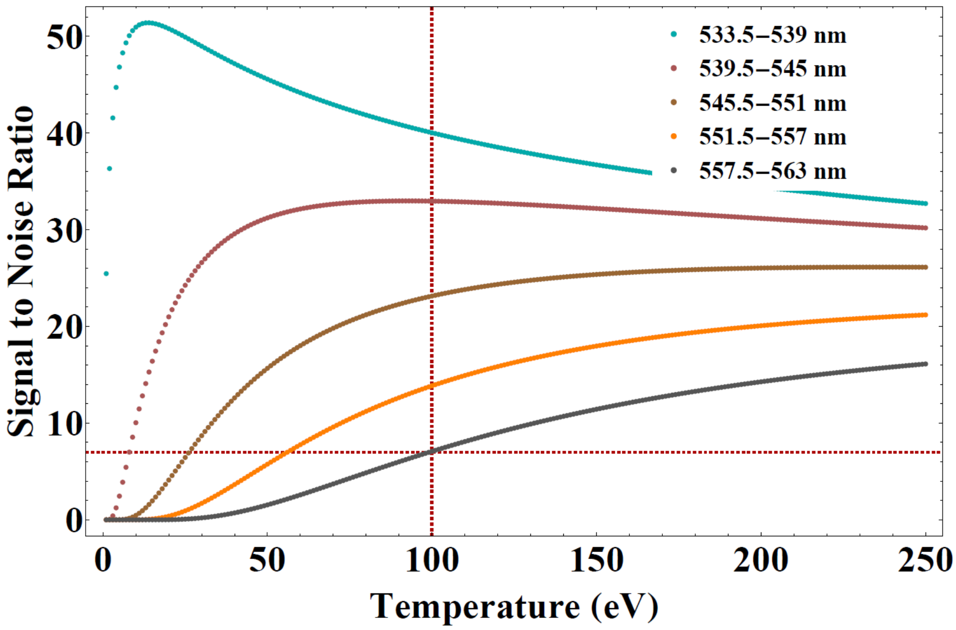

Figure A.35: The signal-to-noise ratios for each wavelength region are plotted as a function of T$_e$. Note that at T$_e$ = 100 eV the signal noise to ratio for the furthest doppler shifted channel is only $\sim$ 8.

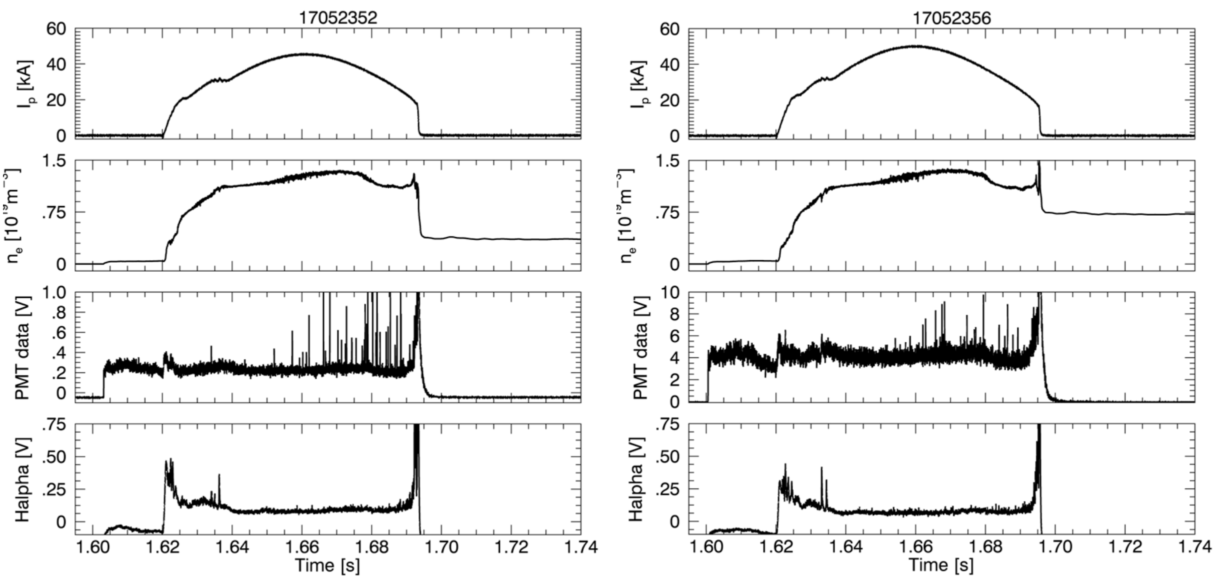

(a)

(b)

Figure A.36: In near identical plasma shots as demonstrated by the similar shapes to the plasma densities, plasma current, and H-α levels, the plasma background was measured using the PMT across 22.86 mm of the spectrometer output plane ($\sim$ 535 nm to 562 nm) as shown in figure A.30. The PMT signals in (a) have a gain on the PMT of 0.5 V (corresponding to $\mu \approx 2 \times 10^4$), while in (b) the gain is set to 0.7 V (corresponding to $\mu \approx 2 \times 10^5$)

background plasma signal was quite high even for low levels of gain (i.e. $\mu \approx 2 \times 10^4$), while as a reminder the thomson signal estimations presented via figures A.33 to A.35 all had the maximum gain setting of $\mu \approx 4.7 \times 10^5$ equivalent to a 0.8 V setting on the PMT.

Therefore when the time came to measure thomson scattered signals from CTH plasmas, the high plasma background signal even at a low gain setting for the PMT was one of the many reasons no thomson light was observed. Although the high levels of plasma background light did force the oscilloscope to be on too high of a voltage per division setting where any expected time-resolved thomson signal would be in the noise, there were plenty of other issues common with bringing a new diagnostic online. In particular due to the mismatch in impedance between the oscilloscope and the PMT neither of the original circuits worked as expected (one using a transimpedance amplifier and the other simple ratio of resistors) leading to a an observed ringing signal from the PMT.[s] Fortunately the ringing was resolved via the circuit setup shown in figure A.31 by John Dawson. This ringing was solved in time to allow additional Raman scattering calibration measurements from neutral nitrogen gas, but sadly CTH plasma operation was suspended and the thomson laser beamline had to be disassembled in preparation for building HVAC upgrades.

A.5.2 Raman scattering modeling and measurements

Although the thomson scattering signal was not successfully measured, the modeling and measurments of rotational Raman scattering in neutral nitrogen gas were performed. In general for a diatomic molecule like nitrogen when incident monochromatic light impacts the gas it can excite the molecule into vibrational and rotational excited states that after some time relax to some lower level emitting either redshifted (called stokes) or blueshifted (anti-stokes) light depending on the energy difference from the excited and relaxed state.[110] For the specific application here the energy shifts associated with nitrogen's vibrational states are much larger than can be measured at the output plane of the spectrometer with anti anti-stokes vibrational lines being well outside the single PMT spectral coverage of 535 to 562 nm. Therefore the

[s] Also it should be noted there was time crunch during this time since the leach science center was about to have its HVAC system upgraded meaning CTH had to stop operation and the thomson scattering beamline had to be disassembled.

only Raman scattering signals detectable with the thomson scattering setup as shown in figure A.30 are the stokes rotational transitions that have the selection rules $\Delta J = +2$ where J is the rotational quantum number.[110,111t]

Therefore to model the Stokes rotational transitions for nitrogen gas the first step is to write down the general scattering signal calculation as shown by equation (A.18).

$$\frac{d\langle P_s\rangle}{d\Omega d\lambda_s} = P_i n L \frac{d\sigma}{d\Omega} f\left(\lambda_s\right)$$

$$\frac{d\langle P_s\rangle}{d\lambda_s} d\lambda_s = P_i n L \frac{d\sigma}{d\Omega} \Delta\Omega f\left(\lambda_s\right) d\lambda_s \tag{A.18}$$

Equation (A.18) says that the average scattered power per unit wavelength (i.e. $\frac{d\langle P_s\rangle}{d\lambda_s}$) is equal to the product of the incident power (P_i), the number of states (n), the length of the scattering volume(L), the differential cross section ($\frac{d\sigma}{d\Omega}$), the subtended solid angle ($\Delta\Omega$), and the distribution of states as function of scattered wavelength ($f\left(\lambda_s\right)$). Next using this equation as a guide and consulting the work by [Sande M. 111] the Stokes rotational Raman scattered power can be written as equation (A.19)

$$\frac{d\langle P_{j\to j+2}\rangle}{d\lambda_j} = P_i L \Delta\Omega \left[n_j \left(\frac{d\sigma}{d\Omega}\right)_{j\to j+2}\right] \tag{A.19}$$

where n_j, the density distribution of state j, is given by equation (A.20)

$$n_j = \frac{n g_j \left(2j+1\right) \exp\left[\frac{-Bhcj(j+1)}{k_b T}\right]}{\Sigma_j g_j \left(2j+1\right) \exp\left[\frac{-Bhcj(j+1)}{k_b T}\right]} \tag{A.20}$$

where g_j is a degeneracy term depending on whether j has an even or odd value, B is the rotational constant for N_2 molecule with the used value taken from [112], h is the planck constant, c is the speed of light, k_b is the Boltzmann constant, T is the N_2 gas temperature, and where $\left(\frac{d\sigma}{d\Omega}\right)_{j\to j+2}$, the differential cross section, is given by equation (A.21)

$$\left(\frac{d\sigma}{d\Omega}\right)_{j\to j+2} = \frac{64\pi^4}{45} \frac{3\left(j+1\right)\left(j+2\right)}{2\left(2j+1\right)\left(2j+3\right)} \frac{\frac{3}{4}\gamma^2}{\lambda^4_{j\to j+2}} \tag{A.21}$$

[t]It should be noted that rayleigh scattering or the elastic scattering of the light occurs incident wavelength.

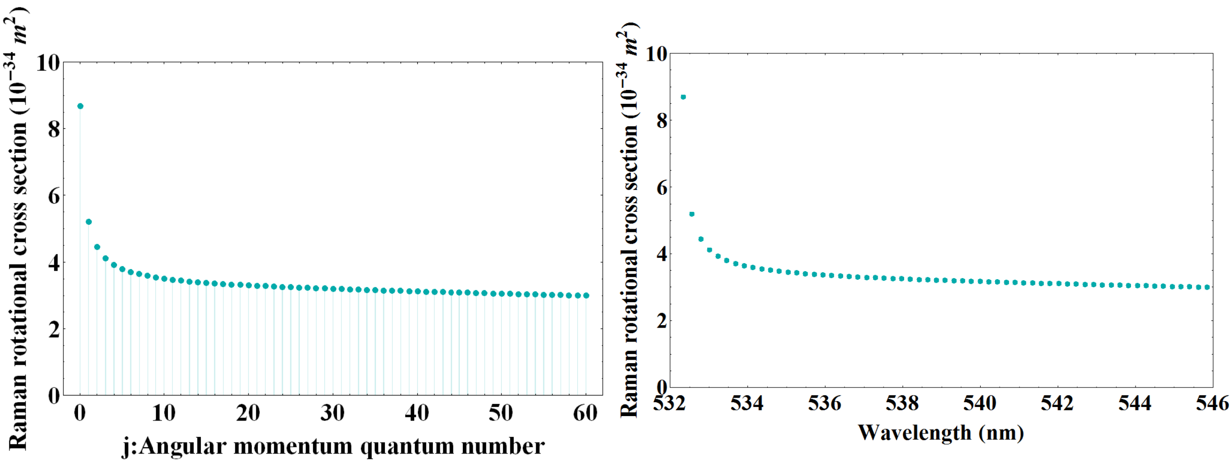

(a) (b)

Figure A.37: The same differential cross section for the Stokes rotation Raman scattered light from N_2 gas is plotted in both (a) and (b) with the sole difference is the indepent variable being the rotational quantum number j in (a) and the expected wavelength of scattered light in (b).

Finally note that γ is the molecular-polarizability anisotropy for N_2 and its value was taken from [Sande M. 111].

Solving equation (A.21) for the differential cross section for Stokes rotational Raman scattering under the assumptions that this is a perpendicular Raman cross section for 532 nm incident laser light the results are plotted in figure A.37 Critically this is the exact same result as obtained by [Sande M. 111] (see right side of figure 2.7 in [Sande M. 111]) giving confidence in the implementation of Stokes rotational Raman scattered model.

Next the total Raman scattered photons as a function of wavelength can be calculated by plugging the result for the differential cross section from equation (A.21) and equation (A.20) into equation (A.19) and solving. Plotting the results from this procedure leads to figure A.38 where the estimated signal collected by the PMT would be the convolution of the plotted heavyside function and the Raman scattered photons. After performing this convolution the number of photo-electrons and even the PMT's estimated output voltage can be estimated as functions of pressure of N_2 gas as shown in figure A.39

Finally with these estimations for the Stokes rotational Raman scattering from N_2, the experimentally measured data can be analyzed and compared to the predictions. Figure A.40 shows both the laser pulse as measured by a fast diode on the optical table and the corresponding Raman scattered signal. In fact the evidence is quite convincing that the pulse measured by the

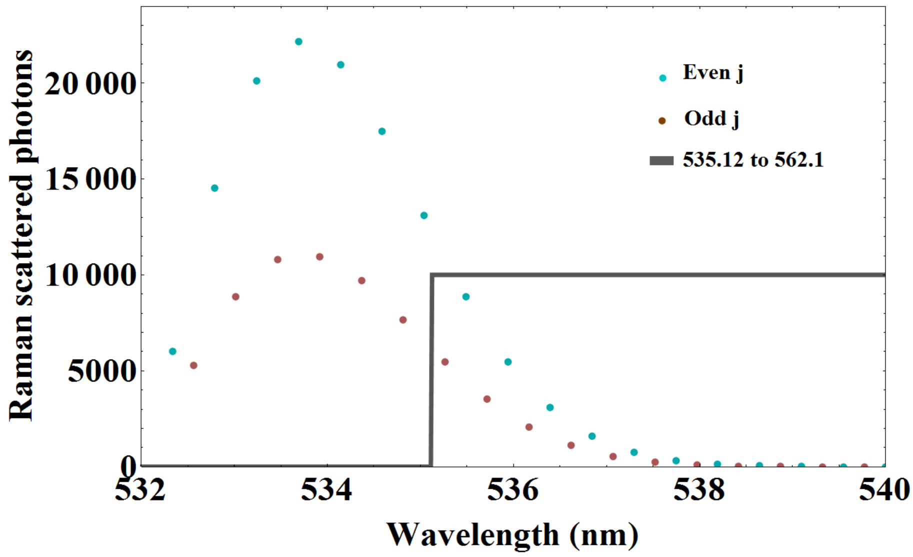

Figure A.38: The Stokes rotational Raman signal is plotted for both odd and even rotational quantum number j as functions of wavelength. Also note that a heavy-side function is included to demonstrate the wavelength range (i.e. ≥ 535.12 nm) where the Hamastsu PMT can measure on the spectrometer output plane.

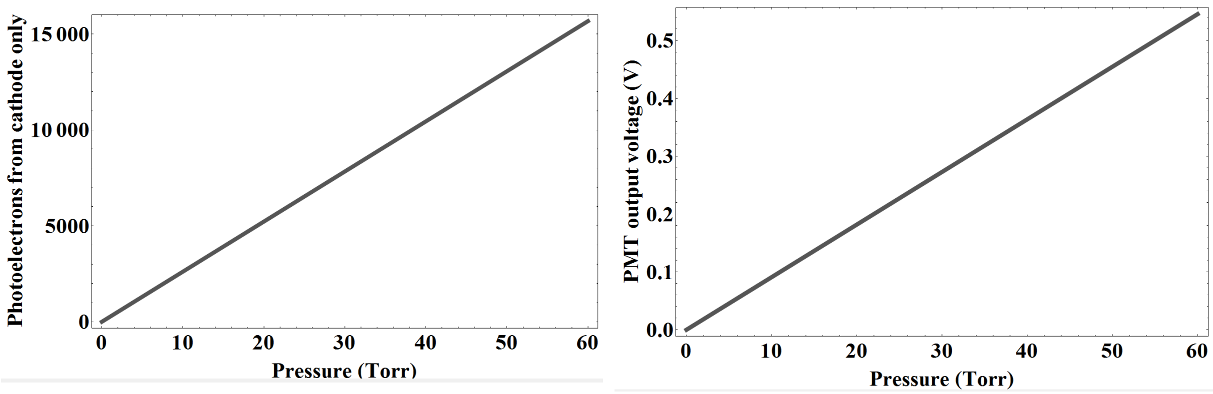

(a)

(b)

Figure A.39: In (a) the estimated photo-electrons generated at the cathode (i.e. before gain is added via dynode stage cascade) is calculated as a function of N_2 gas pressure. In (b) the analysis is taken one step further by examining the peak voltage output from the PMT at given N_2 gas pressures.

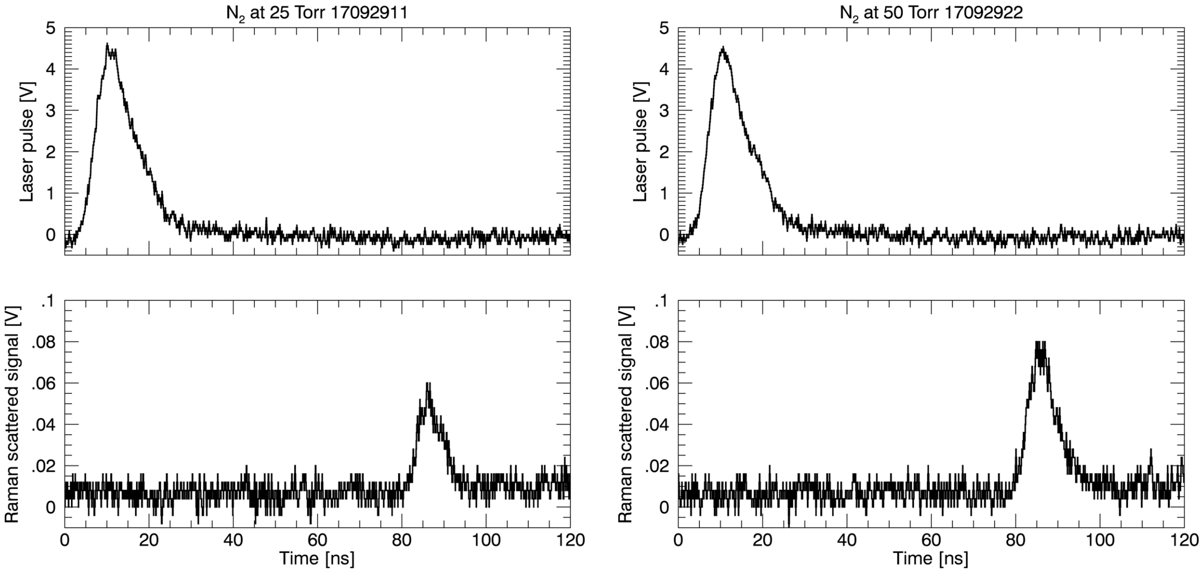

(a) (b)

Figure A.40: In both (a) and (b) the laser pulse is shown as measured by a fast diode mounted behind the first turning mirror along with the Raman scattered signal for N_2 at 25 and 50 Torr respectively. Note that in both cases the Raman signal is delayed by $\sim$ 80 ns, which is consistent with a $\sim$ 24 m of distance the light has to traverse from the laser to the PMT detector giving strong confidence in the veracity of the measurement.

PMT is from Raman scattered light in CTH. The first piece of evidence that this is true is that the pulse shapes are very similar wih nearly identical pulse lengths.[u] The other compelling piece of information from the plots in figure A.40 is that the Raman scattered signls have an appropriate time delay between the fast diode measured pulse and the PMT meaured pulse. Understanding that light move $\sim$ 3 m every 10 ns then the $\sim$ 80 ns delay between the two types of signals is an extra $\sim$ 24 m that the PMY pulse has to travel. Adding up the beamline distances, the distance along the optical path from the laserhead to the detecor is $\sim$ 24 m ($\sim$ 7.8 m to propagate to CTH midplane plus the extra 1 m to enter the fiber bundle and finally the 15 m long fiber bundle add up to a number very close to the $\sim$ 24 m). Another encouraging conclusion from figure A.40 is that the higher the density of N_2 the more intense the PMT measured signals became.

Finally after collecting all the Raman scattered measurements, the results can be coalesced to compare with the model estimations. Figure A.41 shows a range of photo-electrons from 500

[u]The PMT data is definitely noisier so these pulse could be the exact same pulse length, but those parts of the signals could be in the noise.

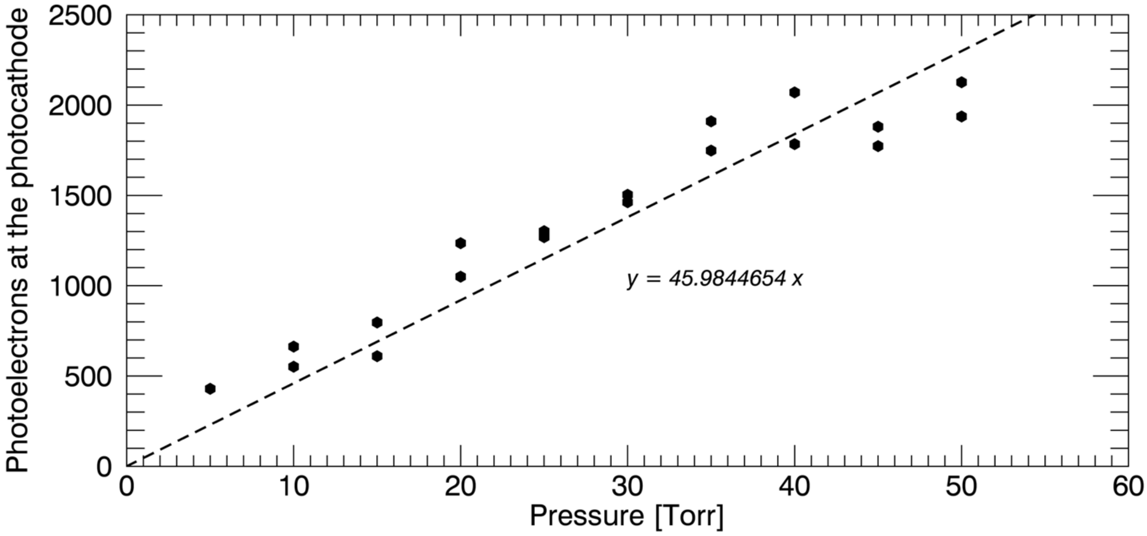

Figure A.41: The Raman scattered signals as measured by the PMT were transformed into photo-electrons at the cathode (i.e. before any gain would be applied) versus the measured N_2 pressure.

to 2000 as the nitrogen pressure was increased from 5 to 50 Torr. Comparing this result to those obtained in figure A.39a, it seems the measured values are about a factor of five lower than those estimated via the model. This factor of five is not too worrisome because the errorbar in the laser energy measurement could be as much as a factor of two. Moreover in the setup of the PMT as seen in figure A.30 a simple lens system was used in between the spectrometer & the PMT and it definitely did not focus the $\sim$ 22 mm output plane down on the 5 mm diameter photocathode correctly.

Appendix B

CTH thomson scattering techincal drawings

This appendix contains the technical drawings on CTH created for the thomson scattering diagnostic.

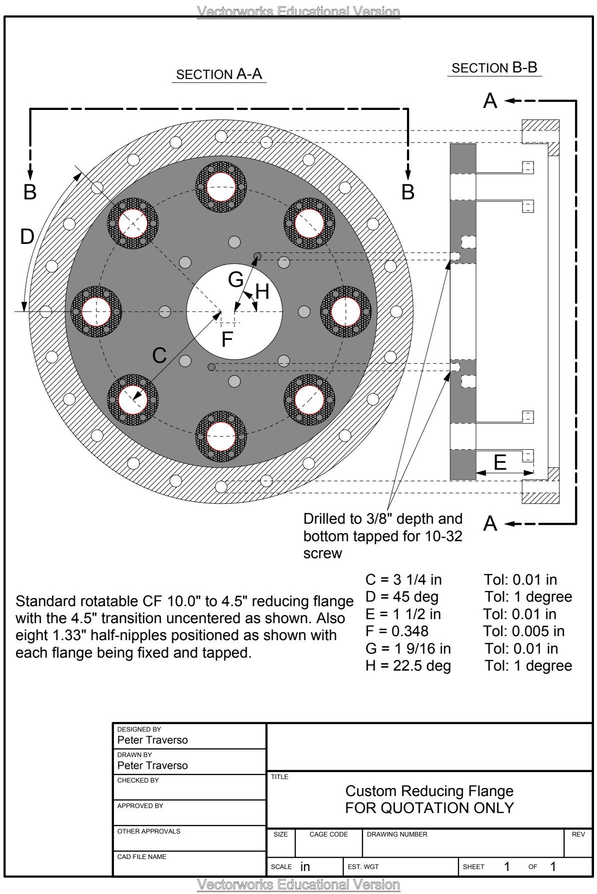

Figure B.1: The non-centered zero-length reducing flange for the bottom 10" port on CTH that is used to connect the vacuum vessel to the nipple containing the laser light baffling

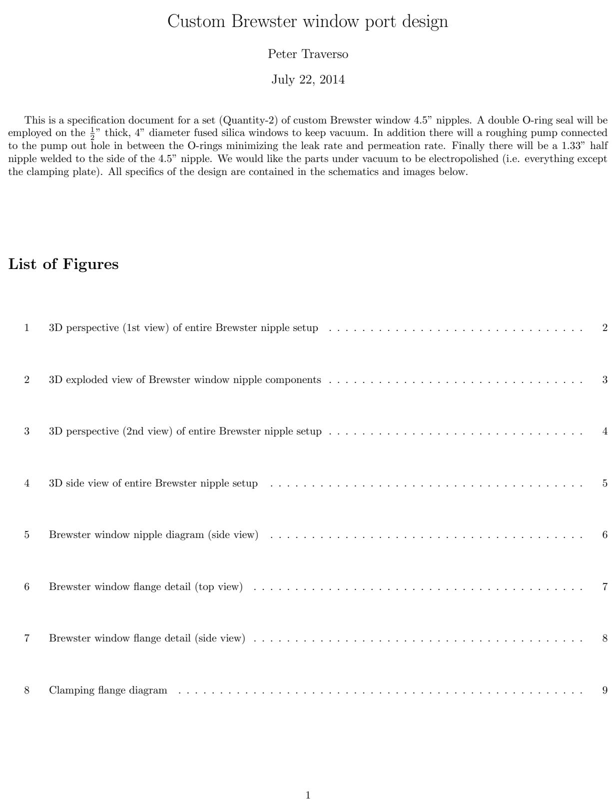

Custom Brewster window port design

Peter Traverso

July 22, 2014

This is a specification document for a set (Quantity-2) of custom Brewster window 4.5" nipples. A double O-ring seal will be employed on the $\frac{1}{2}$" thick, 4" diameter fused silica windows to keep vacuum. In addition there will a roughing pump connected to the pump out hole in between the O-rings minimizing the leak rate and permeation rate. Finally there will be a 1.33" half nipple welded to the side of the 4.5" nipple. We would like the parts under vacuum to be electropolished (i.e. everything except the clamping plate). All specifics of the design are contained in the schematics and images below.

List of Figures

1

(a) Brewster window design document (1 of 9)

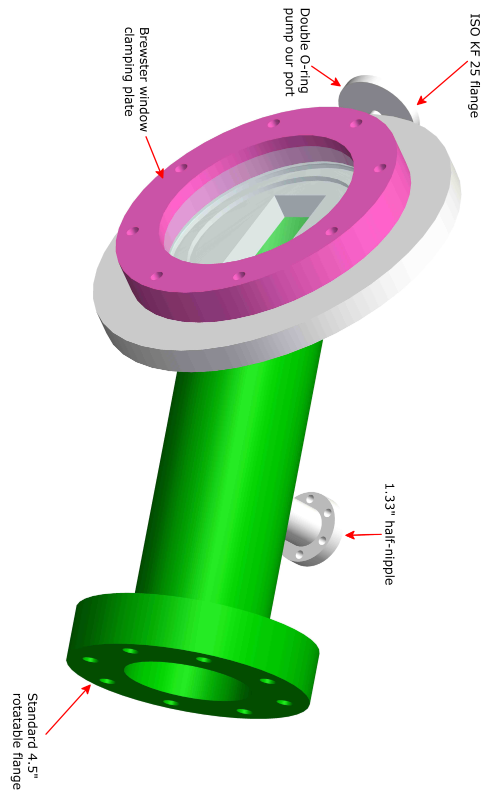

Figure 1: 3D perspective (1st view) of entire Brewster nipple setup
2

(b) Brewster window design document (2 of 9)

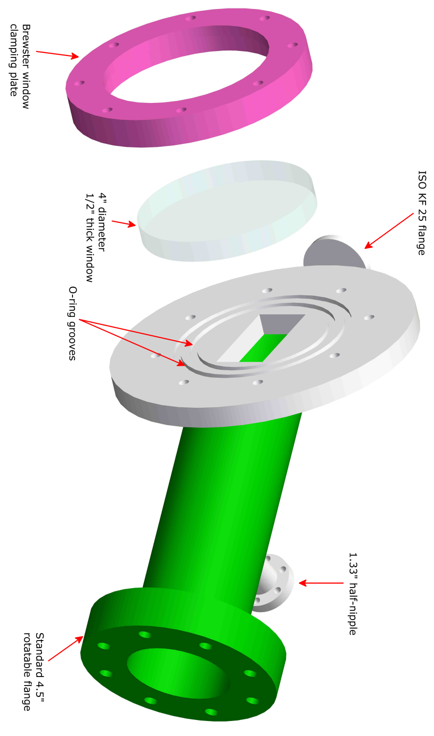

Figure 2: 3D exploded view of Brewster window nipple components

3

(c) Brewster window design document (3 of 9)

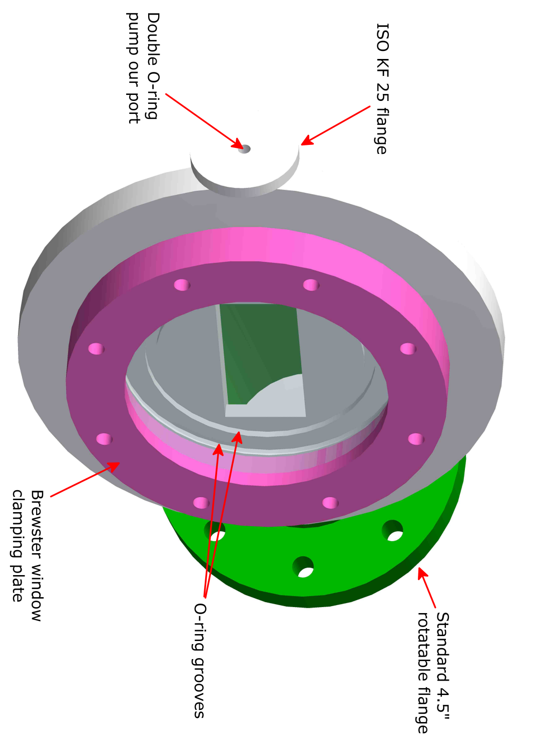

Figure 3: 3D perspective (2nd view) of entire Brewster nipple setup

4

(d) Brewster window design document (4 of 9)

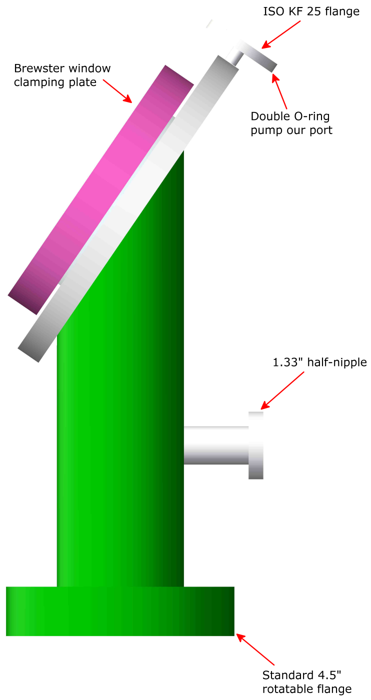

Figure 4: 3D side view of entire Brewster nipple setup

5

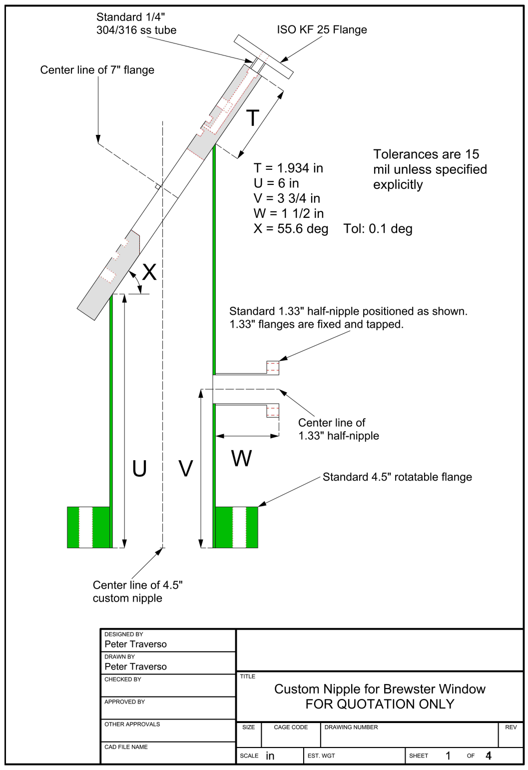

Figure 5: Brewster window nipple diagram (side view)

6

(e) Brewster window design document (5 of 9)

(f) Brewster window design document (6 of 9)

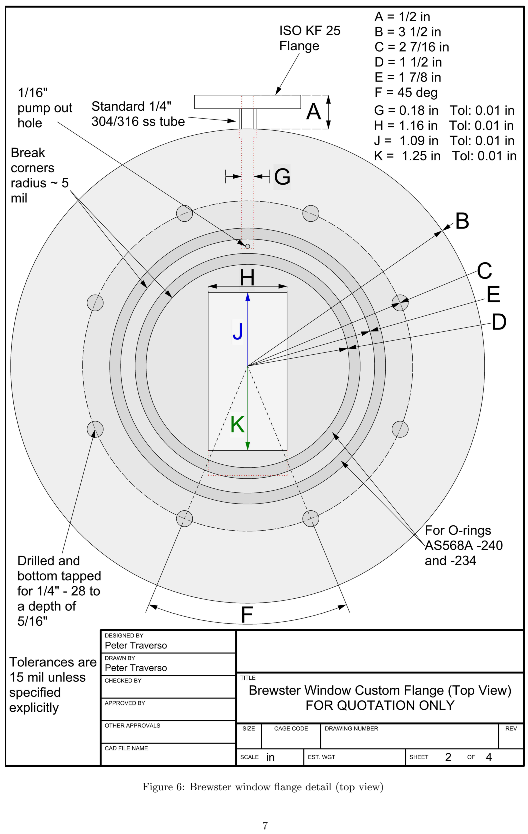

(g) Brewster window design document (7 of 9)

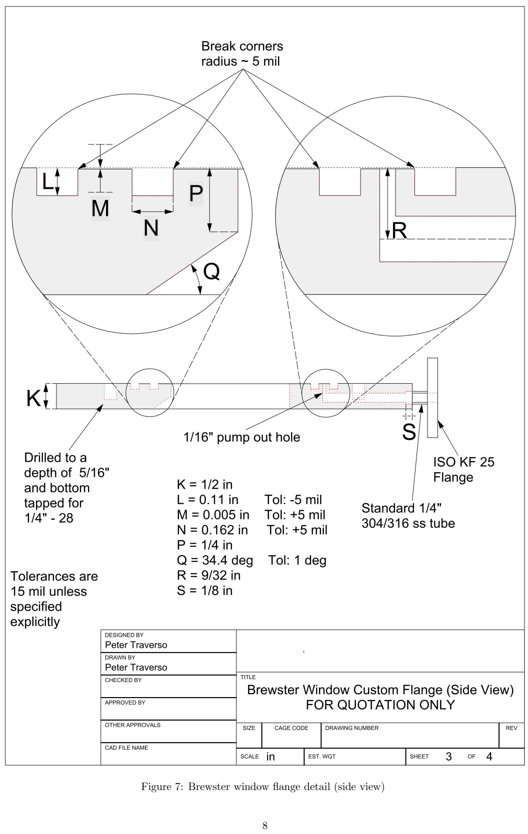

(h) Brewster window design document (8 of 9)

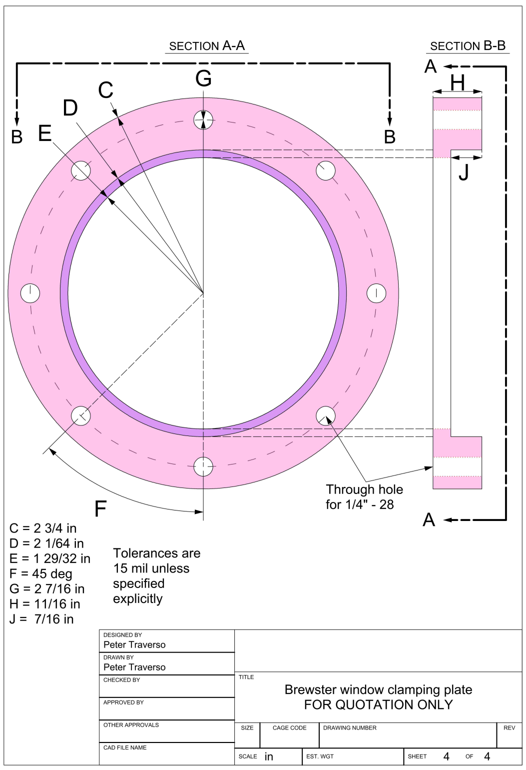

Figure 8: Clamping flange diagram

9

(i) Brewster window design document (9 of 9)

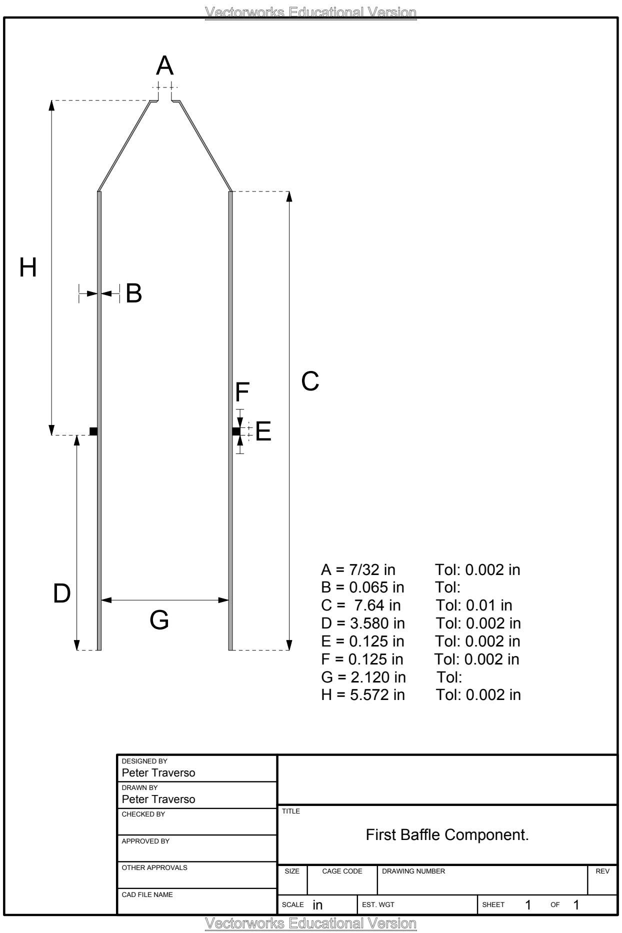

(a) Baffle top cone

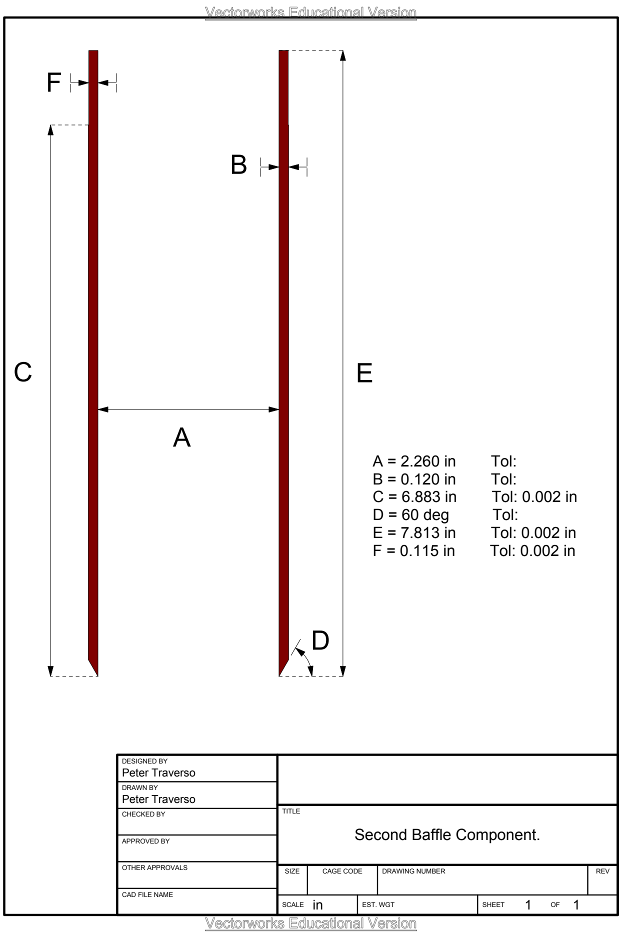

(b) Baffle bottom cone

Custom viewport

Peter Traverso

April 14, 2015

This is a specification document for a single custom 18" Stainless Steel (SS) flange with a reentrant viewport mounted at angle of $54^{o} \pm 1^{o}$ with respect to the 18" SS flange. The reentrant viewport is to be made of 1/8" 304/316 Stainless Steel (SS) tubing with I.D. of 10-1/16" such that a 10-1/16" CF bored flange (with all other measurements standard for 10" CF bored flange) can be welded to the 1/8" tubing as shown in images/diagrams following. The reentrant viewport is designed to accommodate a standard 10" CF zero length fused silica viewport, i.e. NorCal ZVQ-800 or equivalent (not shown in images/diagrams but would like it included in the quotation). Also welded to the face of the 10-1/16" CF bored flange on the vacuum side will be two (2) symmetrically placed 304/316 SS brackets as shown in following images/diagrams. In addition there are four (4) 2.75" half nipples welded to this 18" SS flange. Two (2) of the 2.75" nipples are parallel with the reentrant viewport, while the other two (2) are perpendicular to the 18" SS flange face. Parts under vacuum are to be electropolished. All specifics of the design are contained in the schematics and images below. Manufacturers machine drawings to be approved by Auburn before a bid is awarded, but before final construction.

List of Figures

1

(a) Collection optics flange design document (1 of 7)

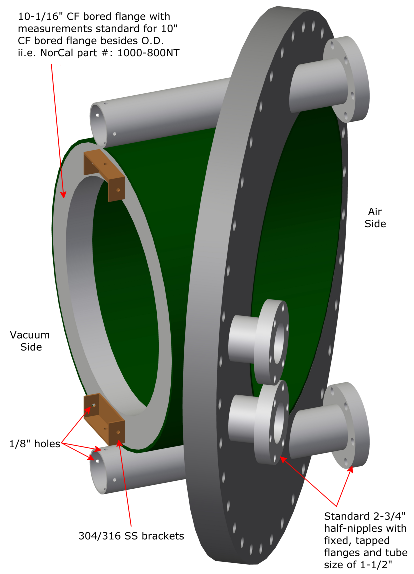

Figure 1: 3D perspective (1st view) of entire Custom 18" flange

2

(b) Collection optics flange design document (2 of 7)

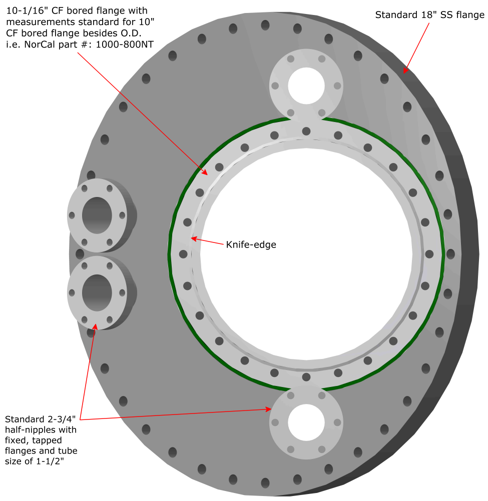

Figure 2: 3D perspective (2nd view) of entire Custom 18" flange

3

(c) Collection optics flange design document (3 of 7)

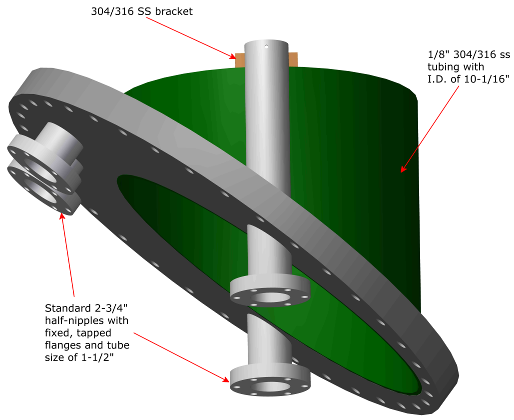

Figure 3: 3D perspective (3rd view) of entire Custom 18" flange

4

(d) Collection optics flange design document (4 of 7)

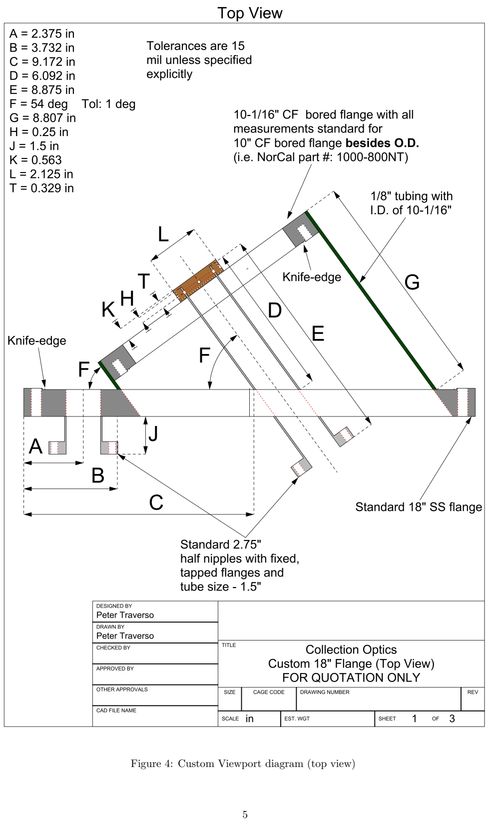

(e) Collection optics flange design document (5 of 7)

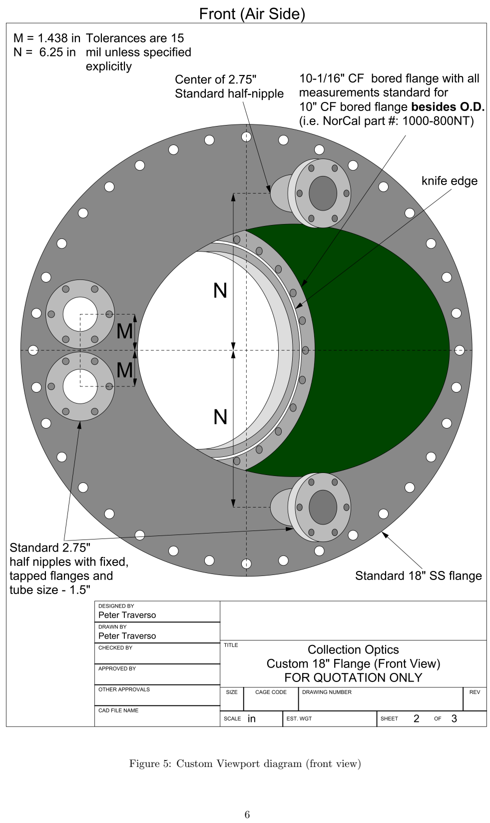

(f) Collection optics flange design document (6 of 7)

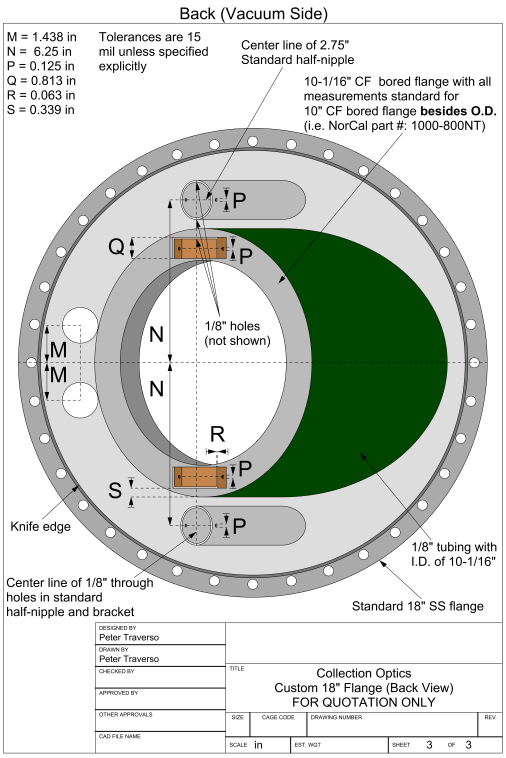

Figure 6: Custom Viewport diagram (back view)

7

(g) Collection optics flange design document (7 of 7)

Custom Collection Optics Lens Mount

Peter Traverso

March 14, 2017

This is a specification document for a single custom 212 mm Delrin optics lens mount. The optics lens mount is designed to mount to standard optical breadboards commercially off the shelf, specifically a 4" by 24" anodized aluminum double-density breadboard from Thorlabs. The Delrin optics lens mount is to be clamped together with standard 316 Stainless Steel 4-40 hex bolts and to be attached to the aforementioned breadboard by standard 316 Stainless Steel 1/4-20 hex bolts. All specifics of the design are contained in the schematics and images below.

List of Figures

1

(a) Collection optics holder design document (1 of 5)

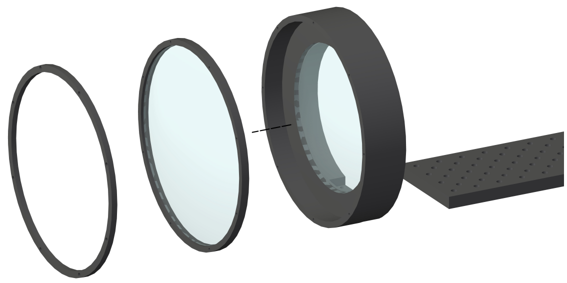

Figure 1: 3D perspective (1st view) of entire assembly including the two lenses (200 mm and 150 mm respectively)

Figure 2: 3D perspective (2nd view) of entire assembly including the two lenses (200 mm and 150 mm respectively)

2

(b) Collection optics holder design document (2 of 5)

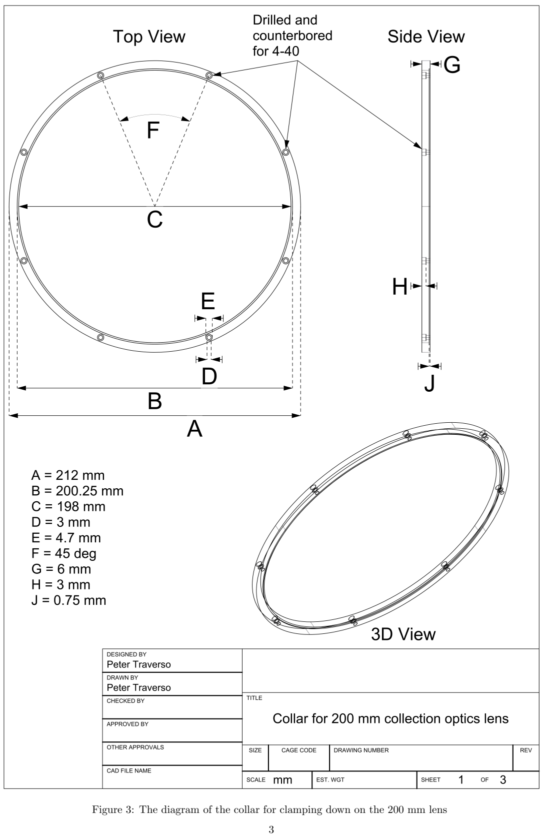

(c) Collection optics flange design document (3 of 5)

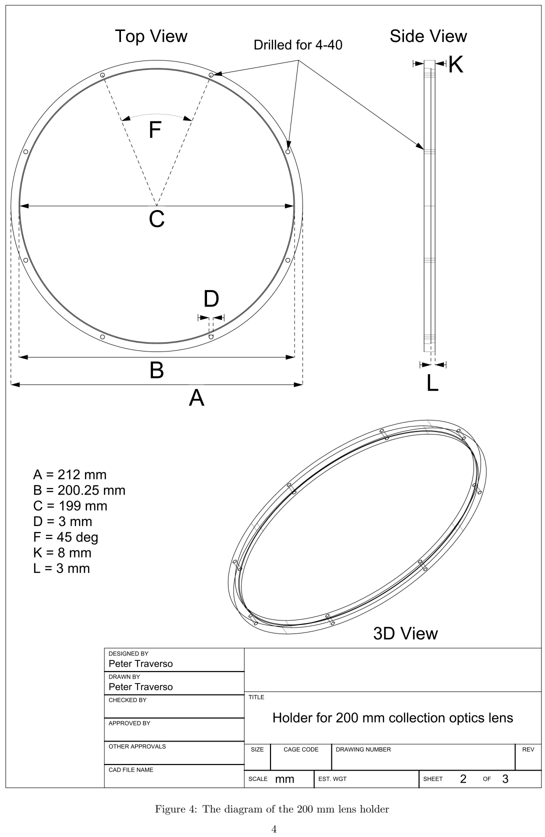

(d) Collection optics holder design document (4 of 5)

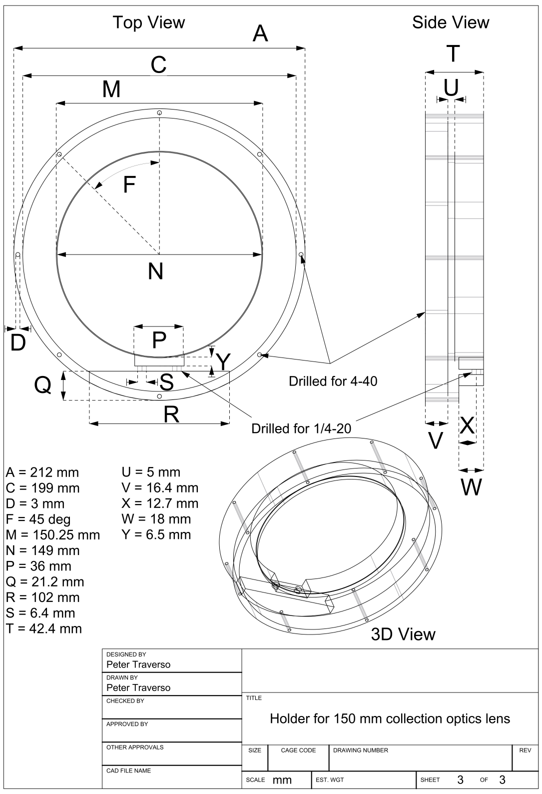

Figure 5: The diagram of the 150 mm lens holder

5

(e) Collection optics holder design document (5 of 5)

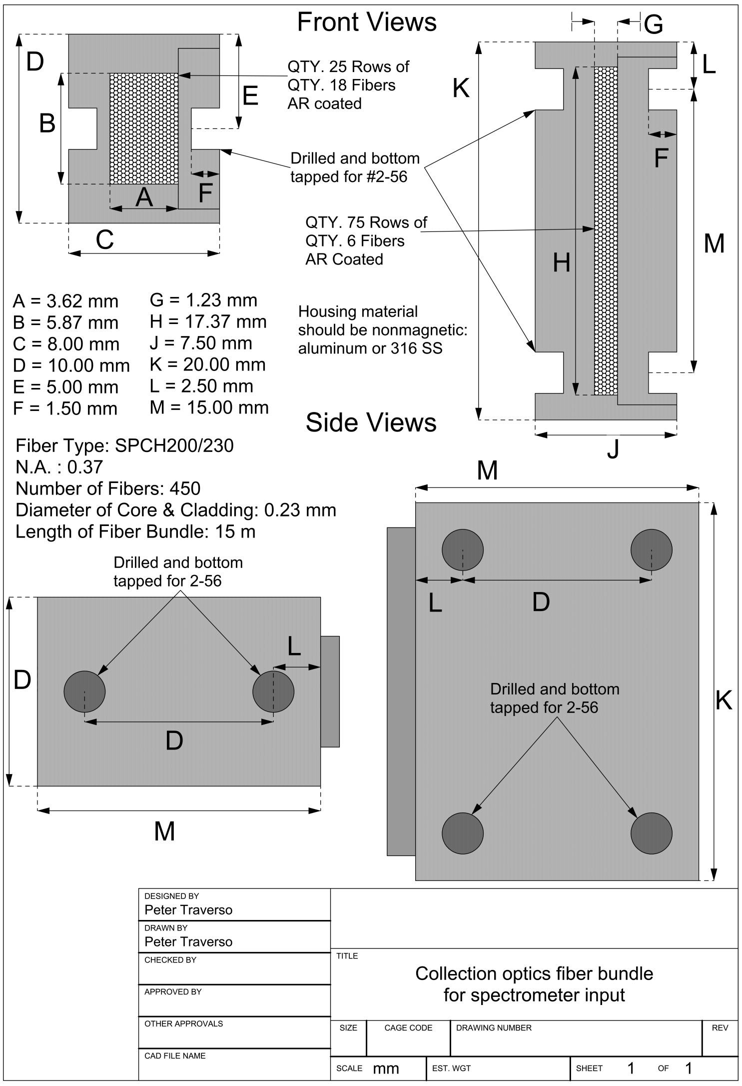

Figure B.6: The specification document detailing the fiber bundle transporting the thomson scattered light from the collection optics into the spectrometer.

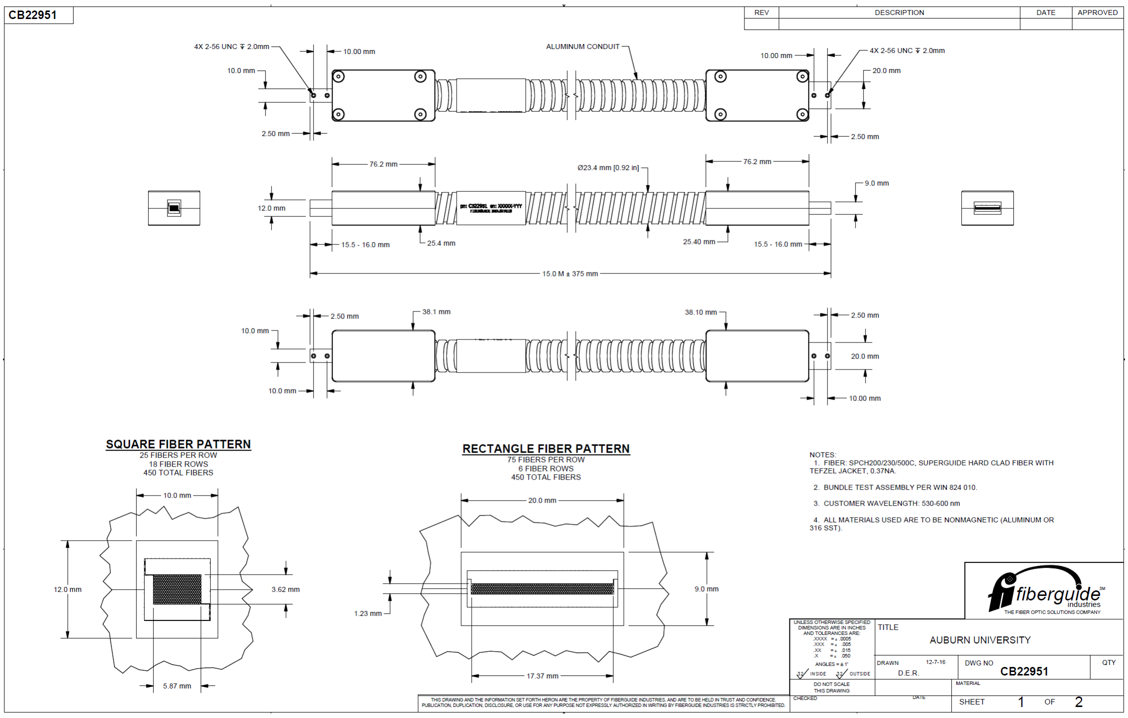

Figure B.7: The specification document produced by Fiberguide Industries for the fiber bundle transporting the thomson scattered light from the collection optics into the spectrometer.

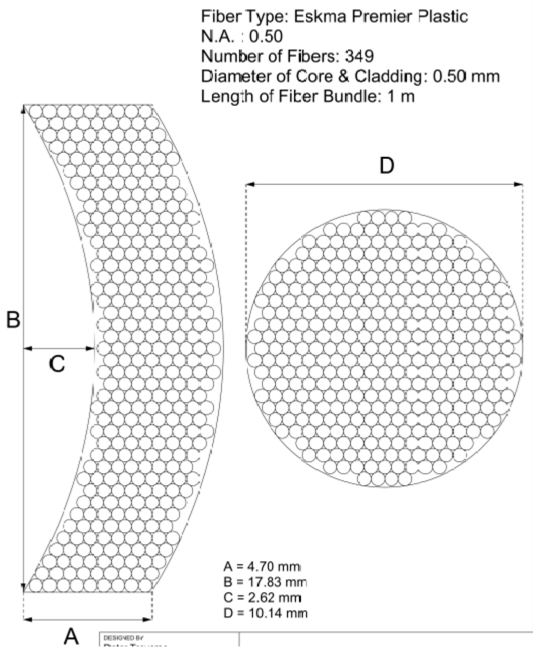

Figure B.8: The preliminary design document for the spectrometer routing to the detector fiber bundle.

Appendix C

STRAHL input files

This appendix contains example input files necessary to execute STRAHL[75] as detailed in section 3.2. For understanding these files in detail see the STRAHL user manual, [Dux R. 76], and [3] for more context/discussion.

```
cv  rho volume(LCFS)[cm]   R_axis[cm]   U_loop[V]    time[s]
      51.2692195          551.1939539        0.0       0.0000


cv  number of grid points  points up to separtrix  fourier coefficients
             28                     21                       0


cv  sqrt( (Psi-Psi_ax) / (Psi_sep - Psi_ax) )
   0.00000   0.03993   0.07987   0.11984   0.15985   0.19994   0.24010
   0.28039   0.32089   0.36169   0.40300   0.44509   0.48833   0.53322
   0.58041   0.63079   0.68565   0.74693   0.81765   0.90073   1.00000
   1.01566   1.03186   1.04840   1.06527   1.08250   1.10013   1.11812


cv     rho volume / rho_volume(LCFS)
   0.00000   0.03993   0.07987   0.11984   0.15985   0.19994   0.24010
   0.28039   0.32089   0.36169   0.40300   0.44509   0.48833   0.53322
   0.58041   0.63079   0.68565   0.74693   0.81765   0.90073   1.00000
   1.01566   1.03186   1.04840   1.06527   1.08250   1.10013   1.11812

cv   large radius low field side / R_axis
   0.00000   0.00000   0.00000   0.00000   0.00000   0.00000   0.00000
   0.00000   0.00000   0.00000   0.00000   0.00000   0.00000   0.00000
   0.00000   0.00000   0.00000   0.00000   0.00000   0.00000   0.00000
   0.00000   0.00000   0.00000   0.00000   0.00000   0.00000   0.00000

cv   large radius high field side / R_axis
   0.00000   0.00000   0.00000   0.00000   0.00000   0.00000   0.00000
   0.00000   0.00000   0.00000   0.00000   0.00000   0.00000   0.00000
   0.00000   0.00000   0.00000   0.00000   0.00000   0.00000   0.00000
   0.00000   0.00000   0.00000   0.00000   0.00000   0.00000   0.00000

cv  safety factor
   0.00000   0.00000   0.00000   0.00000   0.00000   0.00000   0.00000
   0.00000   0.00000   0.00000   0.00000   0.00000   0.00000   0.00000
   0.00000   0.00000   0.00000   0.00000   0.00000   0.00000   0.00000
   0.00000   0.00000   0.00000   0.00000   0.00000   0.00000   0.00000

cv  fraction of circulating particles
   0.00000   0.05000   0.10000   0.15000   0.20000   0.25000   0.30000
   0.35000   0.40000   0.45000   0.50000   0.55000   0.60000   0.65000
   0.70000   0.75000   0.80000   0.85000   0.90000   0.95000   1.00000
   1.01037   1.02074   1.03111   1.04148   1.05185   1.06222   1.07259

cv  Integral( dl_p / B_p) [m/T]
   0.00000   0.03993   0.07987   0.11984   0.15985   0.19994   0.24010
   0.28039   0.32089   0.36169   0.40300   0.44509   0.48833   0.53322
   0.58041   0.63079   0.68565   0.74693   0.81765   0.90073   1.00000
   1.01566   1.03186   1.04840   1.06527   1.08250   1.10013   1.11812

cv  < B_total > [T]
   0.00000   0.00000   0.00000   0.00000   0.00000   0.00000   0.00000
   0.00000   0.00000   0.00000   0.00000   0.00000   0.00000   0.00000
   0.00000   0.00000   0.00000   0.00000   0.00000   0.00000   0.00000
   0.00000   0.00000   0.00000   0.00000   0.00000   0.00000   0.00000

cv  < B_total**2 > [T**2]
   0.00000   0.00000   0.00000   0.00000   0.00000   0.00000   0.00000
   0.00000   0.00000   0.00000   0.00000   0.00000   0.00000   0.00000
   0.00000   0.00000   0.00000   0.00000   0.00000   0.00000   0.00000
   0.00000   0.00000   0.00000   0.00000   0.00000   0.00000   0.00000

cv  < 1./B_total**2 > [1/T**2]
   0.00000   0.00000   0.00000   0.00000   0.00000   0.00000   0.00000
   0.00000   0.00000   0.00000   0.00000   0.00000   0.00000   0.00000
   0.00000   0.00000   0.00000   0.00000   0.00000   0.00000   0.00000
   0.00000   0.00000   0.00000   0.00000   0.00000   0.00000   0.00000
```

Figure C.1: Example of STRAHL's input grid file

```
INFO:   op1.2b  divertor    Pecrh=5MW   input=

cv    time-vector
    1
   6.00000


cv    Ne-Funktion
      'interpa'


cv     x-coordinate
      'volume rho'


cv   # of interpolation points
      126


cv   x-grid for ne-interpolation
0.0000000000000 0.0100000000000 0.0200000000000 0.0300000000000 0.0400000000000
0.0500000000000 0.0600000000000 0.0700000000000
0.0800000000000 0.0900000000000 0.1000000000000 0.1100000000000 0.1200000000000
0.1300000000000 0.1400000000000 0.1500000000000
0.1600000000000 0.1700000000000 0.1800000000000 0.1900000000000 0.2000000000000
0.2100000000000 0.2200000000000 0.2300000000000
0.2400000000000 0.2500000000000 0.2600000000000 0.2700000000000 0.2800000000000
0.2900000000000 0.3000000000000 0.3100000000000
0.3200000000000 0.3300000000000 0.3400000000000 0.3500000000000 0.3600000000000
0.3700000000000 0.3800000000000 0.3900000000000
0.4000000000000 0.4100000000000 0.4200000000000 0.4300000000000 0.4400000000000
0.4500000000000 0.4600000000000 0.4700000000000
0.4800000000000 0.4900000000000 0.5000000000000 0.5100000000000 0.5200000000000
0.5300000000000 0.5400000000000 0.5500000000000
0.5600000000000 0.5700000000000 0.5800000000000 0.5900000000000 0.6000000000000
0.6100000000000 0.6200000000000 0.6300000000000
0.6400000000000 0.6500000000000 0.6600000000000 0.6700000000000 0.6800000000000
0.6900000000000 0.7000000000000 0.7100000000000
0.7200000000000 0.7300000000000 0.7400000000000 0.7500000000000 0.7600000000000
0.7700000000000 0.7800000000000 0.7900000000000
0.8000000000000 0.8100000000000 0.8200000000000 0.8300000000000 0.8400000000000
0.8500000000000 0.8600000000000 0.8700000000000
0.8800000000000 0.8900000000000 0.9000000000000 0.9100000000000 0.9200000000000
0.9300000000000 0.9400000000000 0.9500000000000
0.9600000000000 0.9700000000000 0.9800000000000 0.9900000000000 1.0000000000000
1.0100000000000 1.0200000000000 1.0300000000000
1.0400000000000 1.0500000000000 1.0600000000000 1.0700000000000 1.0800000000000
1.0900000000000 1.1000000000000 1.1100000000000
1.1200000000000 1.1300000000000 1.1400000000000 1.1500000000000 1.1600000000000
1.1700000000000 1.1800000000000 1.1900000000000
1.2000000000000 1.2100000000000 1.2200000000000 1.2300000000000 1.2400000000000
1.2500000000000


cv  DATA   nominal
5.094749791764936e+13 1.0000000000000 1.0055580041998 1.0108228469233
1.0157910489590 1.0204596158401 1.0248260644377 1.0288884471423 1.0326453714867
1.0360960130986 1.0392401201854 1.0420780083398 1.0446105452507 1.0468391258283
1.0487656391717 1.0503924296099 1.0517222546074
1.0527582425631 1.0535038534041 1.0539628443952 1.0541392428132 1.0540373261787
1.0536616097227 1.0530168398317 1.0521079914797
1.0509402672140 1.0495190951447 1.0478501236062 1.0459392106533 1.0437924072392
1.0414159337008 1.0388161499377 1.0359995203214
1.0329725748439 1.0297418682835 1.0263139392081 1.0226952705081 1.0188922528658
1.0149111522070 1.0107580817764 1.0064389790795
1.0019595875694 0.9973254426264 0.9925418611040 0.9876139334649 0.9825465173324
0.9773442311217 0.9720114463248 0.9665522770207
0.9609705653142 0.9552698616867 0.9494533997031 0.9435240651424 0.9374843603698
0.9313363655846 0.9250816993616 0.9187214815460
```

Figure C.2: Example of STRAHL's plasma profile input file

```
cv main ion brems       SXR     spectral brems      thermal CX     NBI CX
             0           0        0                   1            0

cv  diagnostic lines
      1

cc begin atomicData
acd:acd85_fe.dat           recombination
scd:scd00_fe.dat           ionisation
prb:prb00_fe.dat           continuum radiation
plt:pltic_fe.dat           line radiationplt  (old file, 97_fe.dat, pltls_fe.dat is replaced)
ccd:ccd89_fe.dat           thermal charge exchange
prc:prc89_fe.dat           thermal charge exchange continuum radiation
pls:plsx2_fe.dat           line radiation in SXR range
prs:prsx2_fe.dat           continuum radiation in SXR range
fis:sxrfl10.dat            sensitivity of SXR for 10microm-Be-foil
brs:brs05320.dat           spectral bremsstrahlung
cc end atomic Data

********************Diagnostic Lines********************
cd     excitation     recombination   charge exchange
          1                 0               0

cd    num. of lines
        11

cd   charge of ion      wavelength(A)     half width of window(A)       file extension
         8                170.9                      20                      'ben'
        12                203.700                    20.                     'ben'
        14                284.200                    20.                     'ben'
        15                335.000                    20.                     'ben'
        17                93.900                     20.                     'ben'
        18                108.400                    20.                     'ben'
        19                121.800                    20.                     'ben'
        21                117.200                    20.                     'ben'
        22                132.700                    20.                     'ben'
        23                1.86                      0.07                     'ben'
        24                1.85                      0.07                     'ben'
```

Figure C.3: Example of STRAHL's iron atomic data input file

```
4
6.2030   0.0
6.2035   9.091e+19
6.2037   9.091e+19
6.2050   0.0
```

Figure C.4: Example of a STRAHL iron impurity injection input file

```
1           12
2           26
3    5.127E-01   1.031E+01   4.378E+00   2.196E+00   1.135E+00   5.227E-01
     1.364E-01  -1.311E-01  -3.275E-01  -4.756E-01  -5.883E-01  -6.747E-01
     -7.421E-01  -7.961E-01  -8.405E-01  -8.778E-01  -9.097E-01  -9.373E-01
     -9.611E-01  -9.819E-01  -1.000E+00  -1.016E+00  -1.030E+00  -1.043E+00
     -1.054E+00  -1.065E+00  -1.074E+00   1.065E-01   9.579E-02   7.793E-02
     6.093E-02   4.493E-02   3.015E-02   1.582E-02   1.770E-03  -1.190E-02
     -2.502E-02  -3.751E-02  -4.949E-02  -6.106E-02  -7.236E-02  -8.352E-02
     -9.458E-02  -1.055E-01  -1.164E-01  -1.272E-01  -1.379E-01  -1.485E-01
     -1.591E-01  -1.696E-01  -1.800E-01  -1.904E-01  -2.007E-01
4    5.127E+00   4.666E+03   1.844E+03   1.003E+03   6.330E+02   4.377E+02
     3.250E+02   2.549E+02   2.078E+02   1.744E+02   1.497E+02   1.312E+02
     1.169E+02   1.057E+02   9.677E+01   8.959E+01   8.370E+01   7.876E+01
     7.459E+01   7.100E+01   6.786E+01   6.510E+01   6.266E+01   6.050E+01
     5.859E+01   5.689E+01   5.537E+01   1.258E+02   7.214E+01   5.132E+01
     3.983E+01   3.247E+01   2.763E+01   2.433E+01   2.192E+01   2.007E+01
     1.861E+01   1.746E+01   1.655E+01   1.583E+01   1.527E+01   1.484E+01
     1.450E+01   1.423E+01   1.403E+01   1.387E+01   1.373E+01   1.363E+01
     1.355E+01   1.349E+01   1.345E+01   1.344E+01   1.345E+01
5    9.741E+00   3.565E+03   1.097E+03   5.383E+02   3.319E+02   2.347E+02
     1.813E+02   1.488E+02   1.274E+02   1.125E+02   1.015E+02   9.324E+01
     8.676E+01   8.159E+01   7.735E+01   7.384E+01   7.089E+01   6.838E+01
     6.622E+01   6.434E+01   6.269E+01   6.123E+01   5.993E+01   5.876E+01
     5.771E+01   5.676E+01   5.589E+01   8.793E+00   1.534E+00   3.610E-01
     3.170E-01   5.448E-01   8.873E-01   1.268E+00   1.669E+00   2.072E+00
     2.474E+00   2.872E+00   3.264E+00   3.650E+00   4.031E+00   4.407E+00
     4.778E+00   5.144E+00   5.506E+00   5.865E+00   6.221E+00   6.574E+00
     6.924E+00   7.273E+00   7.619E+00   7.963E+00   8.305E+00
6    1.436E+01   3.692E+03   1.473E+03   7.327E+02   4.345E+02   2.908E+02
     2.142E+02   1.695E+02   1.412E+02   1.221E+02   1.085E+02   9.846E+01
     9.076E+01   8.474E+01   7.989E+01   7.593E+01   7.263E+01   6.984E+01
     6.746E+01   6.542E+01   6.363E+01   6.206E+01   6.067E+01   5.945E+01
     5.835E+01   5.736E+01   5.646E+01   3.559E+00  -9.321E+00  -1.029E+01
     -8.634E+00  -6.770E+00  -5.268E+00  -4.099E+00  -3.152E+00  -2.349E+00
     -1.647E+00  -1.021E+00  -4.493E-01   7.226E-02   5.610E-01   1.021E+00
     1.459E+00   1.879E+00   2.280E+00   2.668E+00   3.046E+00   3.414E+00
     3.773E+00   4.122E+00   4.463E+00   4.799E+00   5.130E+00
7    1.897E+01   2.858E+03   1.332E+03   7.596E+02   4.889E+02   3.396E+02
     2.497E+02   1.934E+02   1.569E+02   1.325E+02   1.156E+02   1.034E+02
     9.436E+01   8.732E+01   8.178E+01   7.729E+01   7.358E+01   7.051E+01
     6.791E+01   6.569E+01   6.377E+01   6.209E+01   6.062E+01   5.933E+01
     5.818E+01   5.716E+01   5.623E+01  -1.975E+01  -2.890E+01  -2.893E+01
     -2.621E+01  -2.253E+01  -1.878E+01  -1.555E+01  -1.289E+01  -1.080E+01
     -9.122E+00  -7.755E+00  -6.622E+00  -5.620E+00  -4.741E+00  -3.948E+00
     -3.221E+00  -2.557E+00  -1.941E+00  -1.364E+00  -8.198E-01  -3.029E-01
     1.882E-01   6.548E-01   1.103E+00   1.536E+00   1.955E+00
8    2.358E+01   2.253E+03   1.084E+03   6.476E+02   4.342E+02   3.170E+02
     2.437E+02   1.939E+02   1.591E+02   1.344E+02   1.165E+02   1.035E+02
     9.382E+01   8.646E+01   8.077E+01   7.620E+01   7.246E+01   6.937E+01
     6.677E+01   6.456E+01   6.266E+01   6.102E+01   5.959E+01   5.833E+01
     5.721E+01   5.622E+01   5.533E+01  -4.164E+01  -4.896E+01  -4.672E+01
     -4.201E+01  -3.752E+01  -3.303E+01  -2.855E+01  -2.446E+01  -2.087E+01
     -1.781E+01  -1.526E+01  -1.315E+01  -1.139E+01  -9.891E+00  -8.568E+00
     -7.382E+00  -6.314E+00  -5.337E+00  -4.434E+00  -3.595E+00  -2.816E+00
     -2.081E+00  -1.386E+00  -7.272E-01  -1.011E-01   4.966E-01
9    2.820E+01   1.798E+03   8.798E+02   5.374E+02   3.649E+02   2.705E+02
     2.134E+02   1.743E+02   1.460E+02   1.252E+02   1.096E+02   9.793E+01
     8.911E+01   8.241E+01   7.715E+01   7.297E+01   6.961E+01   6.679E+01
     6.442E+01   6.241E+01   6.070E+01   5.922E+01   5.793E+01   5.680E+01
     5.580E+01   5.492E+01   5.413E+01  -4.988E+01  -6.069E+01  -5.829E+01
     -5.187E+01  -4.607E+01  -4.114E+01  -3.623E+01  -3.142E+01  -2.694E+01
     -2.289E+01  -1.938E+01  -1.635E+01  -1.380E+01  -1.157E+01  -9.628E+00
     -7.917E+00  -6.325E+00  -4.865E+00  -3.524E+00  -2.277E+00  -1.110E+00
     -1.334E-02   1.023E+00   2.010E+00   2.944E+00   3.839E+00
10   3.281E+01   1.350E+03   6.808E+02   4.234E+02   2.922E+02   2.196E+02
     1.762E+02   1.470E+02   1.257E+02   1.097E+02   9.763E+01   8.845E+01
     8.144E+01   7.605E+01   7.185E+01   6.845E+01   6.569E+01   6.341E+01
     6.149E+01   5.985E+01   5.846E+01   5.725E+01   5.620E+01   5.528E+01
```

Figure C.5: Example of a neoclassical & classical iron transport coefficient input file for STRAHL. The iron transport coefficients were calculated with the Neotransp code.

```
               M A I N  I O N

cv    background ion:  atomic weight    charge
                           1.0           1.0

        G R I D - F I L E
cv    shot      index      from VMEC file
      19049       0

                   G R I D   P O I N T S   A N D   I T E R A T I O N

cv     rho = r**K (->K)      number of grid points      dr_0       dr_1
             1.2                    100                 0.3         0.6

cv      max. iterations at fixed time  stop iteration if change below(%)
               2000                         1.e-4

                  S T A R T   C O N D I T I O N S

cv    start new=0/from old impurity distribution=1     shot   at    time  index
                        0                              11111         2.0    0

                        O U T P U T

cv    save all cycles = 1, save final and start distribution = 0
                     1

                      T I M E S T E P S

cv    number of changes (start-time+... +stop-time)
                 2

cv    time    dt at start    increase of dt after cycle     steps per cycle
      6.15        1.e-4               1.0                        5
      6.50        1.e-2               1.0                        10


           S T A R T   I M P U R I T Y   E L E M E N T S
      (for each impurity one input line needed in this block)

cv     number of impurities
                1

cv     element   atomic weight  energy of neutrals(eV)
       'Fe'          55.8               20.0
                   S O  U R C E

cv#      r_source-r_lcfs(cm)  constant rate(1/s)   time dependent rate from
file(1/0)
               15.0                0.0e0                      1

cv    divertor puff   source_width_in(cm)    source_width_out(cm)  prompt redep
            0                0.0                       0.0               0
                    E D G E ,  R E C Y C L I N G

cv    decay length of impurity outside last grid point(cm)
                          -1.0

cv    Rec.:ON=1/OFF=0   wall-rec.  Tau-div->SOL(ms)   Tau-pump(ms)
           0              0.0            1.e9             1.e9


          E N D   I M P U R I T Y   E L E M E N T S

                                              Connection lengths [m]      Mach #
cv#    r_bound-r_lcfs (cm)  r_lim-r_lcfs(cm)   to divertor   to limiter    SOL
Flow
          15.0                 8.0                250.          10.        0.2
```

Figure C.6: Example of a main input file for STRAHL execution

```
cv   additional sheath voltage [V]
            0.


  D E N S I T Y, T E M P E R A T U R E  AND N E U T R A L  H Y D R O G E N  F O R  CX

cv    take from file with:    shot        index
                              19349         9


                   N E O C L A S S I C A L     T R A N S P O R T
                                   7=W7-X neoDKES
                 NEOART with
     0 = off,  >0 = % of Drift,    2= one stage     no BP      max        min
cv  <0 =figure out, but dont use   3= all stages   contrib   rho_pol   rho_pol
               100.0                   4              1          1.0       0.0

                   A N O M A L O U S     T R A N S P O R T

cv    # of changes for transport
                   1

cv    time-vector
         0.0000

cv      Diffusion  [m^2/s]
        'interp'

cv#     # of interpolation points
                   2

cv#     rho polodial grid for interpolation
           0.0    1.0

cv#     D[m^2/s]
           0.5     0.5

cv    Drift function       Drift Parameter/Velocity
        'interp'                'velocity'

cv#     # of interpolation points
           2

cv#     rho polodial grid for interpolation
          0.0    1.0

cv#    v[m/s]
          0.5     0.5

cv    # of sawteeth     inversion radius
           0                 25.

cv    times of sawteeth
           1.5
```

Figure C.6: Continuation of an example of a main input file for STRAHL execution

Appendix D

$lstsq\_STRAHL\_wrap$'s input files

This appendix contains example input files used by $lstsq\_STRAHL\_wrap$, the STRAHL wrapper that performs the least squares minimization for the anomalous transport profiles.

```
{
    "12": {
        "lineintegrated": {
            "1": {
                "name": "20180919.049_signalFeXIII_data_from_detect_2_intensity_corrected_over_1000_pixel_width_5",
                "typeofsignal": "lineintegrated",
                "detector": "hexos2",
                "elementsymbol": "Fe",
                "title": "Fe XIII ~ 20.37 nm",
                "chargestate": 12,
                "backgroundnoisesig": 200,
                "scalingshotnoisesig": 1.5664403,
                "timeflag": 1,
                "starttime": 6.19,
                "endtime": 6.50,
                "startrho": -1,
                "endrho": -1,
                "typeofbackground": "linear",
                "slope": -10.2231972,
                "yintercept": 321.82832577,
                "scaleguess": 0.25,
                "exponentialscaleterm": 0.0,
                "exponentgrowthterm": 0.0,
                "rhofilename_lineofsight": "/draco/u/petr/Peter_Python/w7x_20180919.049_HEXOS_sightline_rhopos_fordetector_2.csv"
            }
        }
    },
    "14": {
        "lineintegrated": {
            "1": {
                "name": "20180919.049_signalFeXV_data_from_detect_3_intensity_corrected_over_1000_pixel_width_5",
                "typeofsignal": "lineintegrated",
                "detector": "hexos3",
                "elementsymbol": "Fe",
                "title": "Fe XV ~ 28.42 nm",
                "chargestate": 14,
                "backgroundnoisesig": 200,
                "scalingshotnoisesig": 2.31341282,
                "timeflag": 1,
                "starttime": 6.19,
                "endtime": 6.50,
                "startrho": -1,
                "endrho": -1,
                "typeofbackground": "linear",
                "slope": -3.73236522,
                "yintercept": 447.6482798,
                "scaleguess": 0.2,
                "exponentialscaleterm": 0.0,
                "exponentgrowthterm": 0.0,
                "rhofilename_lineofsight": "/draco/u/petr/Peter_Python/w7x_20180919.049_HEXOS_sightline_rhopos_fordetector_3.csv"
            }
        }
    },
    "15": {
        "lineintegrated": {
            "1": {
```


Figure D.1: An example of iron line emission data input file for the python least squares inference routine (1 of 7)

```
                    "name":
                    "20180919.049_signalFeXVI_data_from_detect_3_intensity_corrected_over_100
                    0_pixel_width_5",
                    "typeofsignal": "lineintegrated",
                    "detector": "hexos3",
                    "elementsymbol": "Fe",
                    "title": "Fe XVI ~ 33.5 nm",
                    "chargestate": 15,
                    "backgroundnoisesig": 200,
                    "scalingshotnoisesig": 1.88853529,
                    "timeflag": 1,
                    "starttime": 6.19,
                    "endtime": 6.50,
                    "startrho": -1,
                    "endrho": -1,
                    "typeofbackground": "linear",
                    "slope": -23.85263271,
                    "yintercept": 621.93078027,
                    "scaleguess": 0.8,
                    "exponentialscaleterm": 0.0,
                    "exponentgrowthterm": 0.0,
                    "rhofilename_lineofsight":
                    "/draco/u/petr/Peter_Python/w7x_20180919.049_HEXOS_sightline_rhopos_forde
                    tector_3.csv"
                }
            }
        },
        "17": {
            "lineintegrated": {
                "1": {
                    "name":
                    "20180919.049_signalFeXVIII_data_from_detect_1_intensity_corrected_over_1
                    000_pixel_width_5",
                    "typeofsignal": "lineintegrated",
                    "detector": "hexos1",
                    "elementsymbol": "Fe",
                    "title": "Fe XVIII ~ 9.39 nm",
                    "chargestate": 17,
                    "backgroundnoisesig": 200,
                    "scalingshotnoisesig": 3.43845978,
                    "timeflag": 1,
                    "starttime": 6.19,
                    "endtime": 6.50,
                    "startrho": -1,
                    "endrho": -1,
                    "typeofbackground": "linear",
                    "slope": -10.61974885,
                    "yintercept": 257.54057931,
                    "scaleguess": 1.9,
                    "exponentialscalterm": 0.0,
                    "exponentgrowthterm": 0.0,
                    "rhofilename_lineofsight":
                    "/draco/u/petr/Peter_Python/w7x_20180919.049_HEXOS_sightline_rhopos_forde
                    tector_1.csv"
                }
            }
        },
        "18": {
            "lineintegrated": {
                "1": {
                    "name":
                    "20180919.049_signalFeXIX_data_from_detect_2_intensity_corrected_over_100
                    0_pixel_width_5",
                    "typeofsignal": "lineintegrated",
```

Figure D.1: Continuation of an example of iron line emission data input file for the python least squares inference routine (2 of 7)

```
                "detector": "hexos2",
                "elementsymbol": "Fe",
                "title": "Fe XIX ~ 10.84 nm",
                "chargestate": 18,
                "backgroundnoisesig": 200,
                "scalingshotnoisesig": 2.8890522,
                "timeflag": 1,
                "starttime": 6.19,
                "endtime": 6.50,
                "startrho": -1,
                "endrho": -1,
                "typeofbackground": "linear",
                "slope": -21.0549887,
                "yintercept": 381.62854564,
                "scaleguess": 2.2,
                "exponentialscalterm": 0.0,
                "exponentgrowthterm": 0.0,
                "rhofilename_lineofsight": "/draco/u/petr/Peter_Python/w7x_20180919.049_HEXOS_sightline_rhopos_fordetector_2.csv"
            }
        }
    },
    "21": {
        "lineintegrated": {
            "1": {
                "name": "20180919.049_signalFeXXII_data_from_detect_2_intensity_corrected_over_1000_pixel_width_5",
                "typeofsignal": "lineintegrated",
                "detector": "hexos2",
                "elementsymbol": "Fe",
                "title": "Fe XXII ~ 11.72 nm",
                "chargestate": 21,
                "backgroundnoisesig": 200,
                "scalingshotnoisesig": 1.0,
                "timeflag": 1,
                "starttime": 6.19,
                "endtime": 6.50,
                "startrho": -1,
                "endrho": -1,
                "typeofbackground": "linear",
                "slope": 0.15893455,
                "yintercept": 396.860549,
                "scaleguess": 4.0,
                "exponentialscalterm": 0.0,
                "exponentgrowthterm": 0.0,
                "rhofilename_lineofsight": "/draco/u/petr/Peter_Python/w7x_20180919.049_HEXOS_sightline_rhopos_fordetector_2.csv"
            }
        }
    },
    "22": {
        "lineintegrated": {
            "1": {
                "name": "20180919.049_signalFeXXIII_data_from_detect_2_intensity_corrected_over_1000_pixel_width_5",
                "typeofsignal": "lineintegrated",
                "detector": "hexos2",
                "elementsymbol": "Fe",
                "title": "Fe XXIII ~ 13.28 nm",
                "chargestate": 22,
```


Figure D.1: Continuation of an example of iron line emission data input file for the python least squares inference routine (3 of 7)

```
                    "backgroundnoisesig": 300,
                    "scalingshotnoisesig": 1.24381819,
                    "starttime": 6.19,
                    "endtime": 6.50,
                    "typeofbackground": "linear",
                    "slope": 22.59847441,
                    "yintercept": 351.73259213,
                    "scaleguess": 4.0,
                    "rhofilename_lineofsight": "/draco/u/petr/Peter_Python/w7x_20180919.049_HEXOS_sightline_rhopos_fordetector_2.csv"
                }
            }
        },
        "24": {
            "lineintegrated": {
                "1": {
                    "name": "20180919.049_qsx_Wline_horpixel_36to50_vertpixel_1290to1331",
                    "typeofsignal": "lineintegrated",
                    "detector": "qsx",
                    "elementsymbol": "Fe",
                    "title": "Fe XXV ~ 1.85 nm (W-line)",
                    "chargestate": 24,
                    "backgroundnoisesig": 0.0,
                    "scalingshotnoisesig": 1.0,
                    "starttime": 6.19,
                    "endtime": 6.50,
                    "typeofbackground": "linear",
                    "slope": 1.34461305,
                    "yintercept": 0.03704084,
                    "scaleguess": 1.6,
                    "pixelindex": 1310,
                    "rhofilename_lineofsight": "/draco/u/petr/Peter_Python/w7x_20180919.046_HRXIS_sightline_rhopos_forpixel_1310.csv"
                },
                "2": {
                    "name": "20180919.049_qsx_Wline_horpixel_27to39_vertpixel_1190to1231",
                    "typeofsignal": "lineintegrated",
                    "detector": "qsx",
                    "elementsymbol": "Fe",
                    "title": "Fe XXV ~ 1.85 nm (W-line)",
                    "chargestate": 24,
                    "backgroundnoisesig": 0.0,
                    "scalingshotnoisesig": 1.0,
                    "timeflag": 1,
                    "starttime": 6.19,
                    "endtime": 6.50,
                    "startrho": -1,
                    "endrho": -1,
                    "typeofbackground": "linear",
                    "slope": 1.47319299,
                    "yintercept": -1.0802392,
                    "scaleguess": 1.6,
                    "exponentialscaleterm": 0.0,
                    "exponentgrowthterm": 0.0,
                    "pixelindex": 1210,
                    "rhofilename_lineofsight": "/draco/u/petr/Peter_Python/w7x_20180919.046_HRXIS_sightline_rhopos_forpixel_1210.csv"
                },
                "3": {
                    "name": "20180919.049_qsx_Wline_horpixel_20to32_vertpixel_1090to1131",
                    "typeofsignal": "lineintegrated",
```


Figure D.1: Continuation of an example of iron line emission data input file for the python least squares inference routine (4 of 7)

```
                "detector": "qsx",
                "elementsymbol": "Fe",
                "title": "Fe XXV ~ 1.85 nm (W-line)",
                "chargestate": 24,
                "backgroundnoisesig": 0.0,
                "scalingshotnoisesig": 1.0,
                "timeflag": 1,
                "starttime": 6.19,
                "endtime": 6.50,
                "startrho": -1,
                "endrho": -1,
                "typeofbackground": "linear",
                "slope": 1.41567787,
                "yintercept": -1.69221254,
                "scaleguess": 1.6,
                "exponentialscaleterm": 0.0,
                "exponentgrowthterm": 0.0,
                "pixelindex": 1110,
                "rhofilename_lineofsight":
                "/draco/u/petr/Peter_Python/w7x_20180919.046_HRXIS_sightline_rhopos_forpixel_1110.csv"
            },
            "4": {
                "name": "20180919.049_qsx_Wline_horpixel_15to27_vertpixel_995to1036",
                "typeofsignal": "lineintegrated",
                "detector": "qsx",
                "elementsymbol": "Fe",
                "title": "Fe XXV ~ 1.85 nm (W-line)",
                "chargestate": 24,
                "backgroundnoisesig": 0.0,
                "scalingshotnoisesig": 1.0,
                "timeflag": 1,
                "starttime": 6.19,
                "endtime": 6.50,
                "startrho": -1,
                "endrho": -1,
                "typeofbackground": "linear",
                "slope": -0.4085418,
                "yintercept": 9.48518386,
                "scaleguess": 1.6,
                "exponentialscaleterm": 0.0,
                "exponentgrowthterm": 0.0,
                "pixelindex": 1015,
                "rhofilename_lineofsight":
                "/draco/u/petr/Peter_Python/w7x_20180919.046_HRXIS_sightline_rhopos_forpixel_1015.csv"
            },
            "5": {
                "name": "20180919.049_qsx_Wline_horpixel_10to22_vertpixel_890to931",
                "typeofsignal": "lineintegrated",
                "detector": "qsx",
                "elementsymbol": "Fe",
                "title": "Fe XXV ~ 1.85 nm (W-line)",
                "chargestate": 24,
                "backgroundnoisesig": 0.0,
                "scalingshotnoisesig": 1.0,
                "timeflag": 1,
                "starttime": 6.19,
                "endtime": 6.50,
                "startrho": -1,
                "endrho": -1,
                "typeofbackground": "linear",
                "slope": 1.11867401,
                "yintercept": -1.48964055,
```


Figure D.1: Continuation of an example of iron line emission data input file for the python least squares inference routine (5 of 7)

```
                "scaleguess": 1.6,
                "exponentialscaleterm": 0.0,
                "exponentgrowthterm": 0.0,
                "pixelindex": 910,
                "rhofilename_lineofsight": "/draco/u/petr/Peter_Python/w7x_20180919.046_HRXIS_sightline_rhopos_forpixel_910.csv"
            },
            "6": {
                "name": "20180919.049_qsx_Wline_horpixel_9to21_vertpixel_790to831",
                "typeofsignal": "lineintegrated",
                "detector": "qsx",
                "elementsymbol": "Fe",
                "title": "Fe XXV ~ 1.85 nm (W-line)",
                "chargestate": 24,
                "backgroundnoisesig": 0.0,
                "scalingshotnoisesig": 1.0,
                "timeflag": 1,
                "starttime": 6.19,
                "endtime": 6.50,
                "startrho": -1,
                "endrho": -1,
                "typeofbackground": "linear",
                "slope": -0.42507007,
                "yintercept": 7.28096247,
                "scaleguess": 1.6,
                "exponentialscaleterm": 0.0,
                "exponentgrowthterm": 0.0,
                "pixelindex": 810,
                "rhofilename_lineofsight": "/draco/u/petr/Peter_Python/w7x_20180919.046_HRXIS_sightline_rhopos_forpixel_810.csv"
            },
            "7": {
                "name": "20180919.049_qsx_Wline_horpixel_10to20_vertpixel_690to731",
                "typeofsignal": "lineintegrated",
                "detector": "qsx",
                "elementsymbol": "Fe",
                "title": "Fe XXV ~ 1.85 nm (W-line)",
                "chargestate": 24,
                "backgroundnoisesig": 0.0,
                "scalingshotnoisesig": 1.0,
                "timeflag": 1,
                "starttime": 6.19,
                "endtime": 6.50,
                "startrho": -1,
                "endrho": -1,
                "typeofbackground": "linear",
                "slope": -0.37277325,
                "yintercept": 5.62200721,
                "scaleguess": 1.6,
                "exponentialscaleterm": 0.0,
                "exponentgrowthterm": 0.0,
                "pixelindex": 710,
                "rhofilename_lineofsight": "/draco/u/petr/Peter_Python/w7x_20180919.046_HRXIS_sightline_rhopos_forpixel_710.csv"
            },
            "8": {
                "name": "20180919.049_qsx_Wline_horpixel_12to21_vertpixel_590to631",
                "typeofsignal": "lineintegrated",
                "detector": "qsx",
                "elementsymbol": "Fe",
                "title": "Fe XXV ~ 1.85 nm (W-line)",
```


Figure D.1: Continuation of an example of iron line emission data input file for the python least squares inference routine (6 of 7)

```
                    "chargestate": 24,
                    "backgroundnoisesig": 0.0,
                    "scalingshotnoisesig": 1.0,
                    "timeflag": 1,
                    "starttime": 6.19,
                    "endtime": 6.50,
                    "startrho": -1,
                    "endrho": -1,
                    "typeofbackground": "linear",
                    "slope": -0.21809285,
                    "yintercept": 4.12869521,
                    "scaleguess": 1.6,
                    "exponentialscaleterm": 0.0,
                    "exponentgrowthterm": 0.0,
                    "pixelindex": 610,
                    "rhofilename_lineofsight": "/draco/u/petr/Peter_Python/w7x_20180919.046_HRXIS_sightline_rhopos_forpixel_610.csv"
                }
            }
        }
    }
```


Figure D.1: Continuation of an example of iron line emission data input file for the python least squares inference routine (7 of 7)

Appendix E

Synthetic data and experimental data resultant inferences

This appendix contains the resultant iron spectral signal matching and anomalous diffusion profile for the realistic transport profile synthetic data found in section 4.2 and shown in figure E.1. Also this appendix contains the resultant iron spectral signal matching and anomalous diffusion profile for the 3rd LBO in discharge 180919049 that was used in chapter 5 for the sensitivity studies and shown in figure E.2.

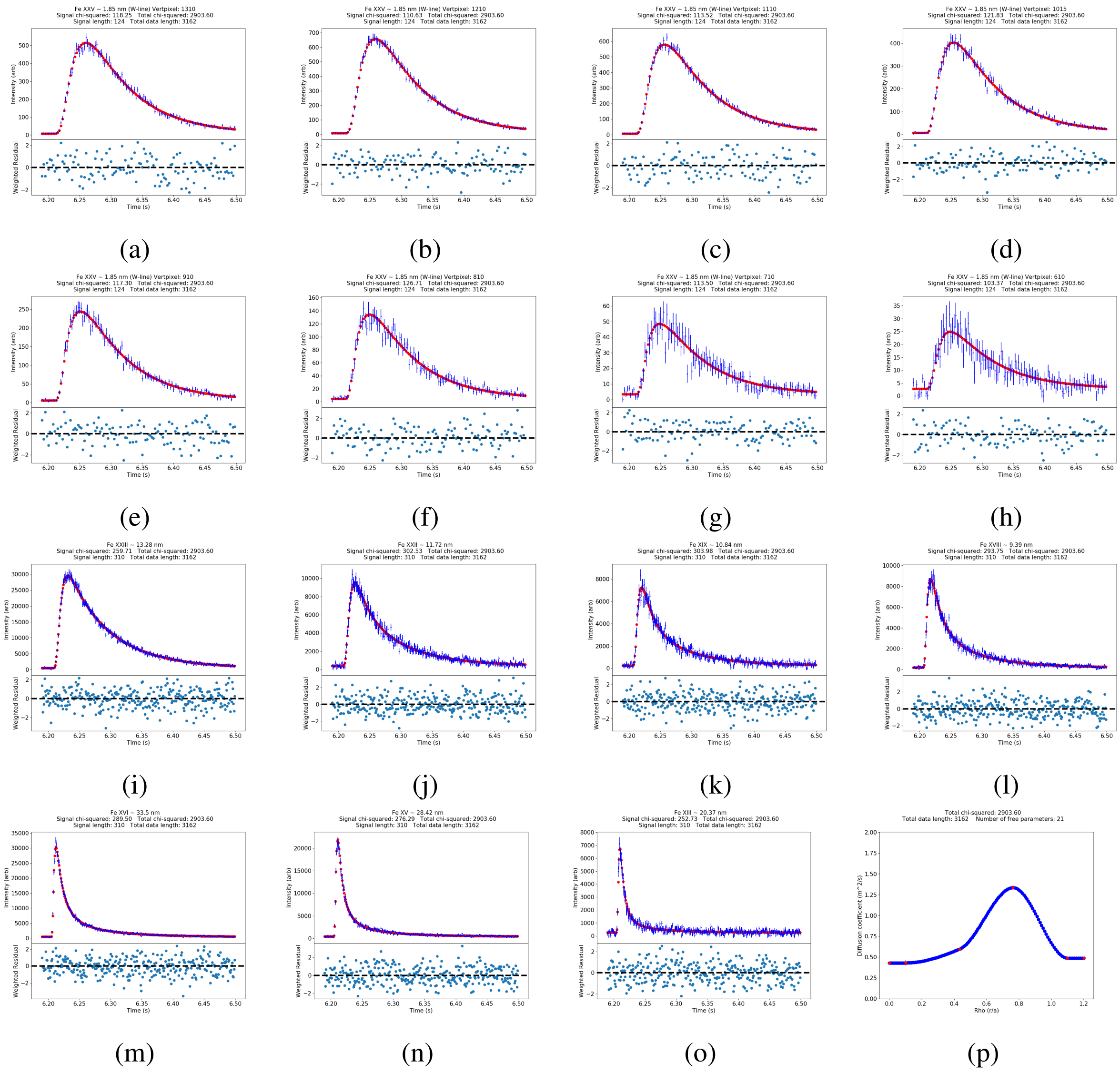

Figure E.1: All of the realistic transport profile noisy synthetic data found in section 4.2 are shown in blue with the attempted matching from the STRAHL inference are shown in red with the weighted residuals plotted below. The inference is performed on the scale parameters for the signals' sightlines, the LBO injection time, and the anomalous diffusion profile, as seen in (), with the classical & neoclassical transport profiles included.

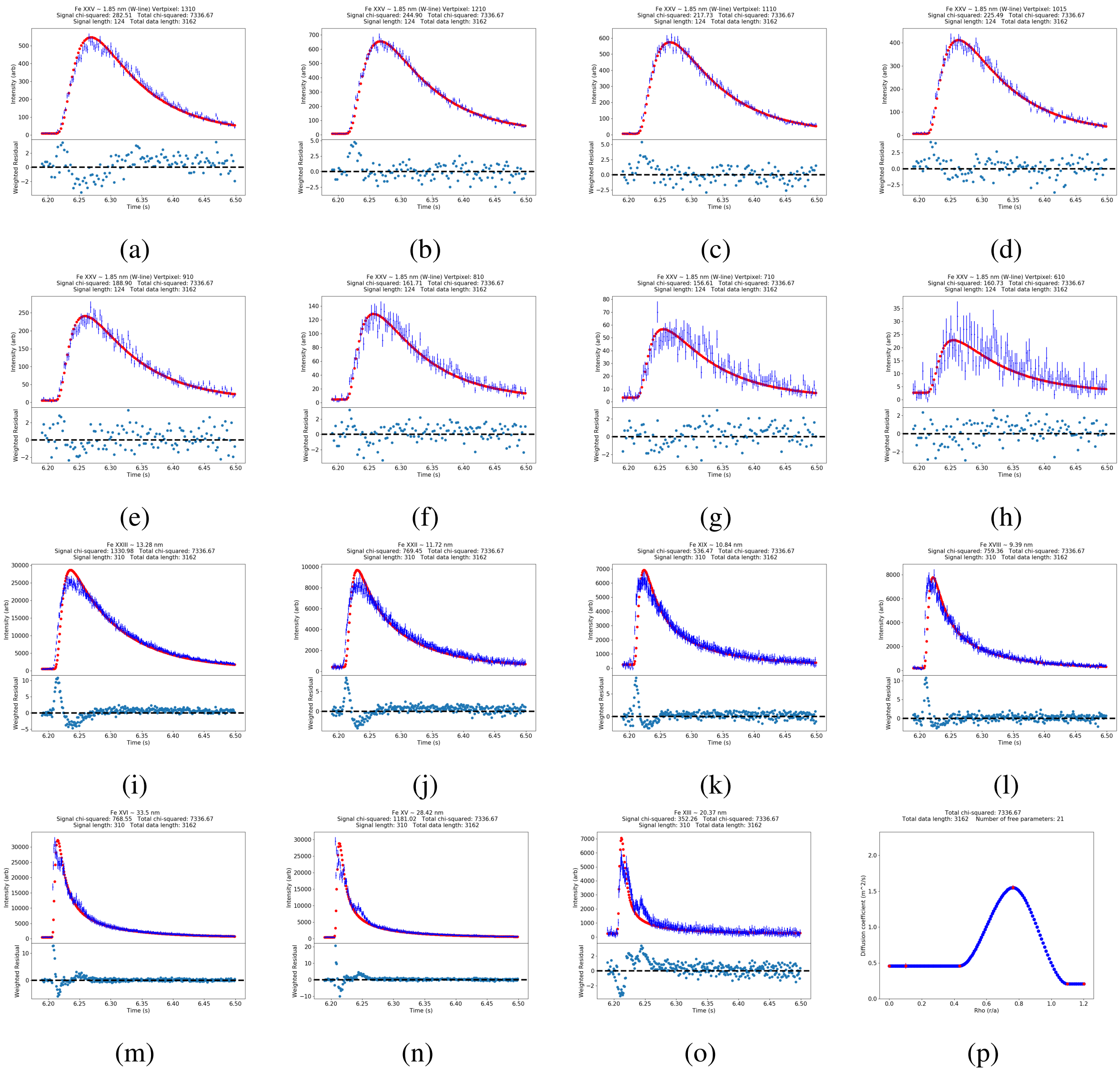

Figure E.2: Select signals from the 3rd LBO in discharge 180919049 are shown in blue with the attempted matching from the STRAHL inference are shown in red with the weighted residuals plotted below. The inference is performed on the scale parameters for the signals' sightlines, the LBO injection time, and the anomalous diffusion profile, as seen in (), with the classical & neoclassical transport profiles included.

Appendix F

Neoclassical & classical resultant inferences

This appendix contains all of the resultant fits using only neoclassical & classical transport channels (see figure F.1) and using only the anomalous convective velocity channel in addition to the neoclassical & classical transport channels (See figure F.2).

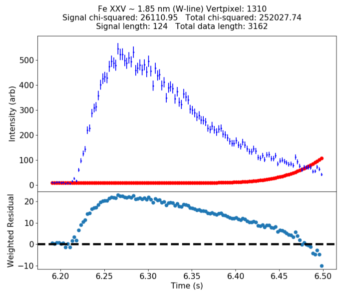

(a)

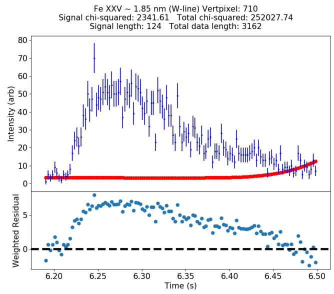

(b)

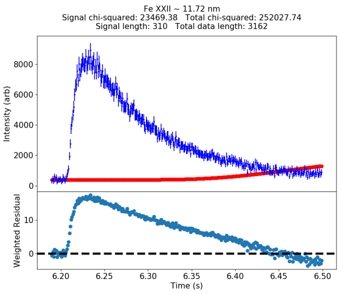

(c)

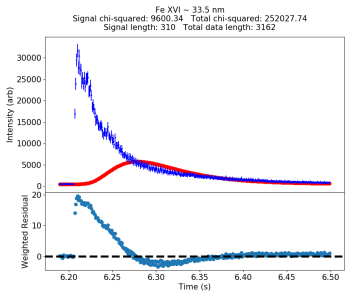

(d)

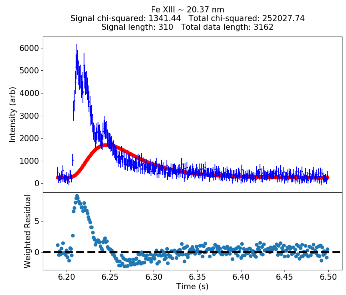

(e)

Figure F.1: Select signals from the 3rd LBO in discharge 180919049 are shown in blue with the attempted matching from the STRAHL inference are shown in red with the weighted residuals plotted below. The inference is performed on the scale parameters for the signals using only the classical & neoclassical transport parameters (an ad hoc 0.1 $\frac{m^2}{s}$ anomalous diffusion was added in the SOL to allow the iron to migrate in and following the work done by [Geiger et al. 7]). The classical & neoclassical transport diffusion used can be seen in figure 6.8a while the convection velocity used can be seen in figure 5.13a

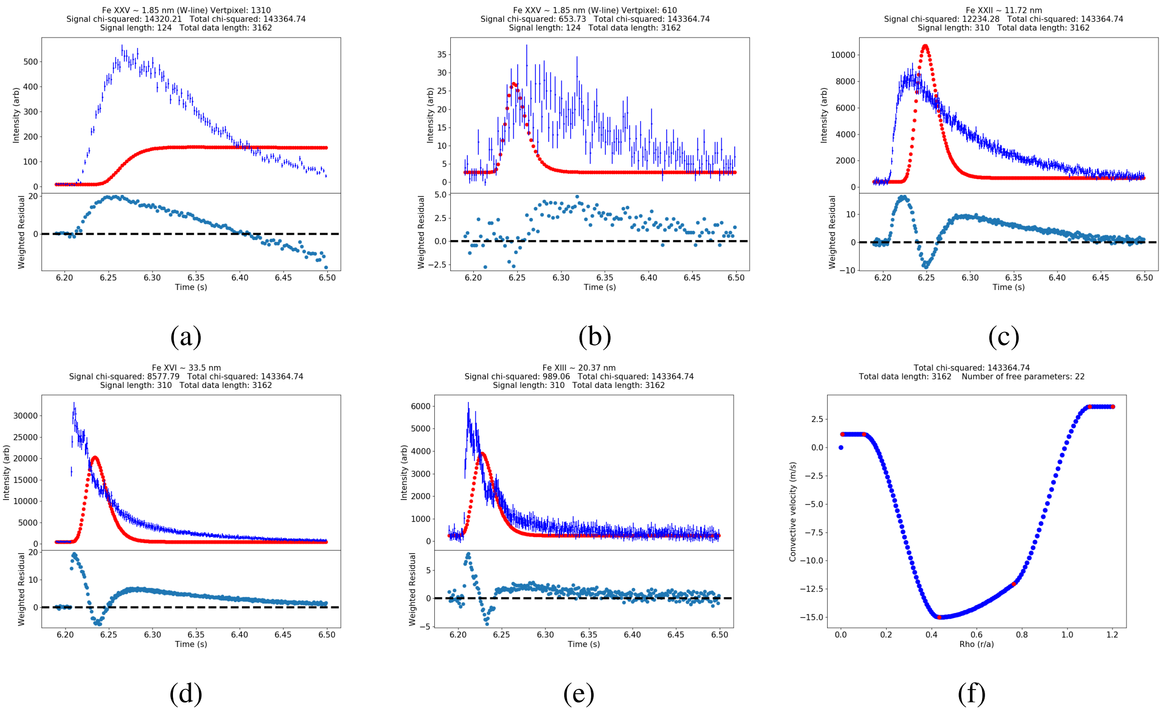

Figure F.2: Select signals from the 3rd LBO in discharge 180919049 are shown in blue with the attempted matching from the STRAHL inference are shown in red with the weighted residuals plotted below. The inference is performed on the scale parameters for the signals' sightlines, the LBO injection time, and the anomalous convection profile, as seen in (f), with the classical & neoclassical transport profiles included. The classical & neoclassical transport profiles are the same as the ones used in figure F.1